UNCLASSIFIED

AD NUMBER

ADB004729

LIMITATION CHANGES

TO:

Approved for public release; distribution is unlimited.

FROM:

Distribution authorized to U.S. Gov't. agencies only; Critical Technology; MAR 1975. Other requests shall be referred to Federal Aviation Administration, Supersonic Transport Office, 800 Independence Avenue, SW, Washington, DC 20590. This document contains export-controlled technical data.

AUTHORITY

faa ltr, 26 apr 1977

THIS PAGE IS UNCLASSIFIED

THIS REPORT HAS BEEN DELIMITED
AND CLEARED FOR PUBLIC RELEASE
UNDER DOD DIRECTIVE 5200.20 AND
NO RESTRICTIONS ARE IMPOSED UPON
ITS USE AND DISCLOSURE.

DISTRIBUTION STATEMENT A

APPROVED FOR PUBLIC RELEASE;
DISTRIBUTION UNLIMITED.

AD B004729

Report No. FAA-SS-73-11-2

SST Technology Follow-On Program—Phase II NOISE SUPPRESSOR/NOZZLE DEVELOPMENT VOLUME II

NOISE TECHNOLOGY

J. Atvars, C. P. Wright, C. D. Simcox

Boeing Commercial Airplane Company
P.O. Box 3707
Seattle, Washington 98124

AD No. ____
DDC FILE COPY

D6-42443
March 1975

FINAL REPORT

Task III

Approved for U.S. Government only. This document is exempted from public availability because of restrictions imposed by the Export Control Act. Transmittal of this document outside the U.S. Government must have prior approval of the Supersonic Transport Office.

DDC
RECEIVED
JUN 27 1975
A

Prepared for
FEDERAL AVIATION ADMINISTRATION
Supersonic Transport Office
800 Independence Avenue, S.W.
Washington, D.C. 20590

The contents of this report reflect the views of the Boeing Commercial Airplane Company, which is responsible for the facts and the accuracy of the data presented herein. The contents do not necessarily reflect the official views or policy of the Department of Transportation. This report does not constitute a standard, specification, or regulation.

TECHNICAL REPORT STANDARD TITLE PAGE

1. Report No. FAA-SS-73-11-2	2. Government Accession No.	3. Recipient's Catalog No.
4. Title and Subtitle: SST Technology Follow-On Program—Phase II, Noise Suppressor/Nozzle Development, Volume II, Noise Technology		5. Report Date: March 1975
		6. Performing Organization Code
7. Author(s): J. Atvars, C. P. Wright, C. D. Simcox		8. Performing Organization Report No. D6-42443
9. Performing Organization Name and Address: Boeing Commercial Airplane Company, P.O. Box 3707, Seattle, Washington 98124		10. Work Unit No.
		11. Contract or Grant No. DOT-FA-72WA-2893
12. Sponsoring Agency Name and Address: Federal Aviation Administration, Supersonic Transport Office, 800 Independence Avenue S.W., Washington, D.C. 20590		13. Type of Report and Period Covered: Final Report, Task III
		14. Sponsoring Agency Code

15. Supplementary Notes

S. Blatt, DOT/SST Technical Monitor

16. Abstract

Jet noise suppression, a major problem in the development of quiet airplane systems, has experienced a substantial technology advance as described in this report. Fundamental technology development has led to a better understanding of nozzle aerodynamics, noise generation and noise transmission processes. This report describes the results of a systematic, model-scale, multitube nozzle test program which generated far-field jet noise data, jet noise-source location data, flow-profile data and jet noise data recorded in a wind tunnel to evaluate flight effects. The effects of various suppressor components are discussed in turn. They include: unsuppressed nozzle, multitube nozzles, hardwall ejectors and acoustically-lined ejectors. The analysis covers the full range of acoustic parameters: sound pressure levels, sound power levels, perceived noise levels, 1/3-octave-band spectra, and directivity effects. Analytical studies on jet noise reduction with simple gas shields are discussed, as are studies on the effects of jet noise-source locations and flow profiles on the acoustic lining effectiveness in ejectors. Selected jet noise and flow-profile backup data to this analysis can be found in volume III of this document.

17. Key Words	18. Distribution Statement
jet noise jet noise suppression multitube jets ejectors ejector/suppressors acoustical linings	Approved for U.S. Government only. This document is exempted from public availability because of restrictions imposed by the Export Control Act. Transmittal of this document outside the U.S. Government must have prior approval of the Supersonic Transport Office.

19. Security Classif. (of this report)	20. Security Classif. (of this page)	21. No. of Pages	22. Price
Unclassified	Unclassified	373	

Form DOT F 1700.7 (8-69)

DN

390145

PREFACE

This is one of a series of final reports on noise and propulsion technology submitted by the Boeing Commercial Airplane Company, Seattle, Washington, 98124, in fulfillment of Task III of Department of Transportation Contract DOT-FA-72WA-2893, dated 1 February 1972.

To benefit utilization of technical data developed by the noise suppressor and nozzle development program, the final report is divided into 10 volumes covering key technology areas and a summary of total program results. The 10 volumes are issued under the master title, "Noise Suppressor/Nozzle Development." Detailed volume breakdown is as follows:

			Report No.
Volume I	–	Program Summary	FAA-SS-73-11-1
Volume II	–	Noise Technology	FAA-SS-73-11-2
Volume III	–	Noise Technology–Backup Data Report	FAA-SS-73-11-3
Volume IV	–	Performance Technology Summary	FAA-SS-73-11-4
Volume V	–	Performance Technology–The Effect of Initial Jet Conditions on a 2-D Constant Area Ejector	FAA-SS-73-11-5
Volume VI	–	Performance Technology–Thrust and Flow Characteristics of a Reference Multitube Nozzle With Ejector	FAA-SS-73-11-6
Volume VII	–	Performance Technology–A Guide to Multitube Suppressor Nozzle Static Performance: Trends and Trades	FAA-SS-73-11-7
Volume VIII	–	Performance Technology–Multitube Suppressor/Ejector Interaction Effects on Static Performance (Ambient and 1150° F Jet Temperature)	FAA-SS-73-11-8
Volume IX	–	Performance Technology–Analysis of the Low-Speed Performance of Multitube Suppressor/Ejector Nozzles (0-167 kn)	FAA-SS-73-11-9
Volume X	–	Advanced Suppressor Concepts and Full-Scale Tests	FAA-SS-73-11-10

PRECEDING PAGE BLANK-NOT FILMED

ACKNOWLEDGEMENT

The achievements of this program are the result of efforts of many individuals besides the authors. The following contributions are gratefully acknowledged:

S. J. Cowan	-	Analytical Two-Dimensional Jet Noise Shielding Model
J. D. Nuhse	-	Jet Noise Source Distributions on Related Flow Profiles
F. G. Strout	-	Flight Effects on Jet Noise Suppression
C. F. Wintermeyer	-	Acoustically-Lined Ejector Test Program
S. Mariano	-	Acoustic Impedance for Linings with Grazing Flow and Analytical Studies of Noise-Source Location Effects and Flow Profile Effects on Acoustic Lining Attenuation
F. W. Hollatz	-	Overall Help with Computations and Graphical Arrangements in this Report

PRECEDING PAGE BLANK-NOT FILMED

SUMMARY

Jet noise suppression technology has always been based upon empirical techniques derived from ad hoc testing of various suppressor nozzles. Far too often this approach has led to suppressor designs which lacked the practicability of a flightworthy installation, had inadequate thrust performance and had excessive weight and drag penalties. A coordinated effort among acoustic, propulsion, and other technologies was used in this program to avoid such pitfalls.

The high velocity jet noise-suppression studies described in this report have led to a better understanding of nozzle aerodynamics, jet noise generation and transmission processes. These studies were conducted on a model scale and in a systematic manner. They generated static far-field jet noise data, and jet noise-source location data in conjunction with flow profile data. Noise generating mechanisms were successfully identified with certain jet-flow regions and properties. Jet noise-suppression characteristics were investigated for each suppressor component independently, as well as for integrated suppressor systems. The basic knowledge that was acquired from these studies was applied in the design of a full-scale suppressor-system demonstrator which is described in volume X. The full-scale test results confirmed the veracity of this jet noise-suppression technology.

The following is the current status of the high-velocity jet noise-suppression technology. The far-field noise spectrum generated by a multitube jet noise-suppressor nozzle is composed of a number of noise sources:

Low frequencies:
1. Postmerged jet mixing turbulence noise.
2. Facility or engine core noise.

High frequencies:
3. Elemental jet mixing turbulence noise.
4. Shock (or screech) noise.
5. Spiral-mode flow-instability noise.

The multitube nozzle, postmerged jet noise is generated in a downstream region which has flow characteristics similar to a simple jet. The gas conditions (P_T, T_T and V_J) in the post-merged jet region are equal to the average conditions in a round jet which has expanded to a diameter equal to the multitube array diameter. The postmerged jet noise level for a given nozzle velocity is primarily a function of nozzle-array area ratio. Test-facility core noise was detected in the low-frequency part of the spectrum only at low jet velocities.

The multitube nozzle, premerged jet noise is generated in a region close to the nozzle-exit plane where the elemental structure of the multitube jets can still be detected in the flow. The outer row of jets in the multitube-nozzle efflux appear to shield the noise generated by the inner jets. The premerged jet noise level for a given nozzle velocity is primarily a function of the number of tubes in the array. Multitube-nozzle-jet shock noise is usually prominent only for cold supersonic jets. The spiral-mode flow-instability noise becomes discernable in

PRECEDING PAGE BLANK-NOT FILMED

the high-frequency part of the jet noise spectrum for nozzle pressure ratios above 2.5, and is most prominent at angles close to 90^{o} from the jet axis.

Hardwall ejectors surrounding multijet flows increased noise suppression across the whole jet noise spectrum. High-frequency suppression is achieved by the relative velocity effect on the noise sources inside the ejector and by changes in noise-source efficiencies due to interaction with wall reflections. Low-frequency noise suppression is mainly the result of more efficient jet mixing reducing the kinetic energy in the postmerged jet region. Acoustical linings in the ejector wall provide an additional means of suppressing the jet noise generated inside the ejector.

A series of noise tests conducted in a low-speed wind tunnel have provided insight into the forward velocity (flight) effects on jet noise suppression. The peak noise from an unsuppressed round convergent nozzle, and from multitube nozzles without ejectors varies simply as a function of relative velocity. The peak noise from suppressors with ejectors has to be analyzed in two parts. The premerged noise from within the ejector is influenced by the forward velocity effects, while the postmerged noise downstream of the ejector behaves as a simple jet, i.e., it varies as a function of relative velocity.

This program has clearly demonstrated that the success of an experimental approach to jet noise-suppression technology is dependent on a systematic noise-generation mechanisms study. Only then can the knowledge be extended in a rational manner to the design of suppressor systems.

CONTENTS

CONTENTS–Continued

CONTENTS–Continued

FIGURES

FIGURES—Continued

FIGURES–Continued

FIGURES–Continued

FIGURES—Continued

FIGURES—Continued

FIGURES—Continued

FIGURES—Continued

FIGURES–Continued

FIGURES–Continued

SYMBOLS AND ABBREVIATIONS

A	Fully expanded jet cross-sectional area
A*	Nozzle throat area
A_8	Nozzle exit area
alt	Altitude
AR	Area ratio = $\frac{\text{total cross-sectional area}}{\text{primary flow area}}$
AR_8	Nozzle exit flow area ratio
AR_{EJC}	Ejector area ratio = $\frac{\text{ejector cross-sectional area}}{\text{primary nozzle flow area}}$
a_o	Speed of sound in air
C_{Fg}	Gross thrust coefficient
CPA	Close-packed array
c	Local speed of sound
D	Round convergent nozzle diameter
D_E	Equivalent round convergent nozzle diameter
d	Diameter; perforated plate hole diameter
dB	Decibel
dia	Diameter
ET	Elliptical tubes
^oF	Degree Fahrenheit
ft/sec	Feet per second
freq	Frequency
f	Frequency in Hz
f_1, f_2	Unknown functions
H	Distribution function
Hz	Hertz
HNTF	Hot Nozzle Test Facility
h	Duct height
Im	Imaginary part
i	$\sqrt{-1}$
J_n	Bessel function
k	Wave number
kHz	Kilo Hertz
L	Ejector length; acoustic lining length
lb/sec	Pounds per second
L_c	Jet core length
L_s	Jet supersonic core length
L/D	Ejector length to diameter ratio
L/D_E	Ejector length to equivalent primary nozzle diameter ratio
M	Mach number
M_o	Mach number steady flow; grazing flow Mach number

PRECEDING PAGE BLANK-NOT FILMED

SYMBOLS AND ABBREVIATIONS (Cont.)

M_J	Jet Mach number
M_p	Particle Mach number
N_o	Number of tubes in outer row
N_t	Total number of tubes in multitube nozzle
NC	Nonconvergent tube ends
OASPL	Overall sound pressure level
O/B	Octave band
P_s	Static pressure
psi	Pounds per square inch
P_T	Total pressure
PNL	Perceived noise level
PNdB	Units of perceived noise level
PR	Nozzle pressure ratio
PWL	Sound power level
p	Pressure
Q	Acoustic energy flux
R	Reflected wave; resistive impedance; flow resistance
rad	Radius
RA	Radial array (nozzle)
R_e	Real part
R/C	Round convergent (nozzle)
Ref.	Reference
rms	Root mean square
rpm	Revolutions per minute
^oR	Degree Rankine
RT	Round tubes (nozzle)
SN	Strouhal number
SL	Sideline
SPL	Sound pressure level
SPLFA	Space averaged SPL in 1 Hz bandwidth
SST	Supersonic transport
s	Spacing between nozzle centers
s_1, s_2	Particle displacements
sec	Second
T	Transmitted wave
T_o	Ambient sea level temperature
T_J	Jet total temperature
T_T	Total temperature
t	Time, perforated plate thickness
u	Particle velocity
V	Velocity
V_J	Jet velocity

SYMBOLS AND ABBREVIATIONS (Cont.)

V_{JI}	Ideal fully-expanded jet velocity
$V_{J\ mix}$	Fully-mixed jet velocity
V_o	Steady flow velocity
V_R	Relative velocity
$V_{R\ post}$	Relative velocity of postmerged jet
V	Airplane velocity; wind tunnel velocity
WIF	Wall Isolation Test Facility
w	Particle velocity
X	Distance from nozzle exit plane
Y	Nondimensional acoustic admittance
Z	Acoustic impedance
x, y, z	Coordinates
a	Variable function
a_n	Weighting parameter
β	Variable function
δ	Dirac function
ϵ_m	Fourier series parameter
η	Nondimensional coordinate
η_s	Noise source coordinates
θ	Angle; temperature ratio (T/T_o)
λ	Wavelength; pressure ratio (P/P_o)
μbar	Microbar (dynes per square-cm.)
ξ	Nondimensional coordinate
ξ_s	Noise source coordinates
ρ	Gas density
ρ_o	Ambient air density
σ	Perforated plate open area ratio
$\sigma_j^{(1)}, \sigma_j^{(2)}$	Pole locations
τ_m	Energy flux parameter
ϕ	Angle
Ω	Phase
ω	Angular frequency

1.0 INTRODUCTION

The purpose of this volume is to describe in detail the high-velocity jet noise suppression technology work conducted during this program. The basic philosophy was to associate the geometric variations of nozzles and ejectors to flow patterns and these in turn to mechanisms associated with noise and propulsion aspects. In order to achieve this goal a systematic, model scale, experimental program was conducted to study the different jet noise sources by varying one test or geometric parameter at a time and then synthesizing the results to create a physical model of jet noise generation and suppression. The experimental program was supplemented with analytical studies to establish a solid foundation in areas where previous work was lacking.

The basic jet noise suppression concept pursued in these studies consists of a multitube mixer nozzle with or without an ejector shroud. The ejector may or may not be acoustically lined. The multitube concept was chosen because past studies (refs. 1 and 2), have shown it to be the only way to achieve high noise-suppression levels at supersonic jet velocities.

The main emphasis in the experimental program was placed on static acoustic testing of parametrically related multitube nozzles and hardwall ejectors. Thrust performance data was always acquired in conjunction with the acoustic data to assure data repeatability and to establish test conditions accurately. The thrust performance results are reported in volume IV of this report. In addition to the controlled nozzle parametric studies, more involved multitube suppressor designs were tested to establish the relative importance of various techniques for controlling the acoustic energy after it has been generated by the jet. Acoustic effects of temperature and velocity profile control were also studied.

Further insight into the jet noise generating mechanisms was gained through studies of noise-source frequency distributions along the jet axis using the "wall isolation technique" (refs. 3 and 4). Examination of the jet wake was also conducted by measuring mean flow properties in both radial and axial directions and thus observing the mixing properties between the primary jet and the ambient atmosphere.

Ejector acoustic lining development was an extension of the work reported in reference 5, and consisted of studies of double-layer or broadband absorbers and "distributed" linings. Lining impedance tests were conducted in the presence of grazing flow to enhance the analytical or prediction model described in volume VII. Analytical studies were conducted to investigate the effects of variations of noise-source locations and ejector internal flow profiles on jet noise absorption by acoustic linings.

The above experimental studies were conducted over a range of jet temperatures (ambient $\leq T_T \leq 1150^{\circ}F$) and nozzle pressure ratios ($2 \leq PR \leq 4$).

Previous experience, both analytical and experimental, has indicated that significant thrust-performance losses for suppressor nozzles can result from low-speed external flow as, for example, during airplane takeoff and climbout. Similarly, an airplane's forward velocity affects

jet noise generation and radiation. The jet noise suppressor system's acoustic performance, in the final analysis, has to be evaluated with forward flight effects taken into account. Therefore, representative suppressor configurations from the above static program were tested for acoustic performance in a low-speed wind tunnel and the results are reported in this document.

2.0 JET NOISE TEST FACILITIES AND TECHNIQUES

Most of the jet noise suppression program's model scale testing was accomplished at three facilities located in Seattle, Washington. The latest techniques in acoustic free-field data acquisition and data processing were employed in order to handle the large volume of test results. Direct measurement of acoustic free-field data, as described below, was of utmost importance in maintaining the high level of accuracy of the basic noise spectra necessary for fundamental jet noise research. The model scale test hardware used in this program is described in section 3.0.

2.1 TEST FACILITIES

2.1.1 THE HOT NOZZLE TEST FACILITY

The Hot Nozzle Test Facility (HNTF) was the most extensively used facility for both acoustic and propulsion testing in this program. It is a static test facility for the determination of jet exhaust nozzle propulsion performance and related exterior noise fields. The facility has a maximum airflow capacity of 40 lb/sec, and can be used to measure axial thrusts up to 2000 lb with a repeatability of 0.5% of the full-scale reading. Nozzle pressure ratios of 4.0 and total temperatures of 2500^{O}F can be achieved for continuous operation. The average primary total temperatures are determined from an area-weighted rake containing seven shielded chromel/alumel thermocouples approximately 4 in.upstream of the nozzle mounting flange. A similar rake arrangement for total pressure is located 180^{O} relative to the temperature rake. The nozzle centerline is 5 ft 8 in. above ground level.

The arena for acoustic measurements consists of a smooth, flat concrete surface as shown in figure 1. The arena is large enough to allow acoustic far-field measurements to be made on a 50-ft-radius centered on the test nozzle exit. Noise measurements are limited, however, to the quadrant of 90^{O} to 180^{O} from the nozzle inlet axis. Building surfaces in the vicinity of the test stand are covered with 4-in.-thick, acoustically absorptive material to minimize sound reflections into the acoustic arena.

Microphone arrays consisted of far-field and near-field groups. Near-field microphones were placed parallel to the jet axis at a distance of two ft and positioned at angles corresponding to the angular distribution of the far-field array. The far-field array consists of two sets of microphones; one set in the ground plane, and the second at the horizontal plane containing the jet axis (figs. 2 and 3). Microphones were located at 10^{O} increments from 90^{O} to 150^{O} with the addition of a 155^{O} microphone (angle relative to nozzle inlet axis). Both arrays were at a 50-ft polar radius.

Bruel and Kjaer 1/4-in. model-4136 pressure microphones without windscreens were used in the ground installations. Special precautions, such as heaters and silica gel dehumidifier cartridges, were used to prevent condensed moisture from affecting the transducer performance.

The extended concrete surface provided essentially an infinite acoustic baffle, resulting in fairly uniform pressure doubling over the frequency range of interest of 200 Hz to 80 kHz. This technique allowed spectra to be measured which were free-field in shape, but 6 db above free-field in level. Data could then be easily corrected to free-field levels for further analysis. The centerline-height microphones were Bruel and Kjaer 1/4-in. Model-4135 free-field units with the diaphragms pointed at the sound source and protected by wind-screens. The data from the centerline microphones was only used to monitor and verify that the data acquired by the ground microphones was not affected by acoustic shadowing caused by wind or temperature gradients across the ground plane.

2.1.2 THE WALL ISOLATION FACILITY

The Wall Isolation Facility (WIF) was used mainly for jet noise-source location tests. It was, however, also used as a backup for the HNTF, because it could be operated in a conventional way for measuring far-field noise from jet exhaust nozzles. It also had the capability of coupling two burner systems in parallel to provide independently variable coannular jets that were used to study temperature and velocity gradient effects on the suppressor nozzle's acoustic performance. The WIF did not have a thrust measuring capability and therefore had to rely only on air and fuel flow measurements, plenum pressure, and temperature measurements to establish nozzle test conditions.

The WIF consists of a scale-model jet located entirely inside a 20- by 50- by 20-ft test cell. This is shown schematically in figure 4. The facility is fed by a 300 psi air supply with a maximum mass flow of 40 lb/sec. The maximum total jet temperature attainable is 2000^{o}F. The burner and nozzle system is mounted on tracks and exhausts through a circular aperture in the front wall (fig. 5). A telescoping section in the burner's air supply line enabled the nozzle exit plane to be withdrawn from a position flush with the exterior wall to a point 8 ft inside the cell. For the multitube nozzles investigated, this corresponded to a travel of approximately 26 equivalent R/C nozzle diameters.

Three of the test cell walls are constructed of brick while the fourth, which faces the outdoor acoustic arena, is constructed of two sections of 1/4-in. steel plate 14 in. apart with the space between the plates filled with sand. This construction minimized the transmission of sound from within the test cell through the wall to the outside arena. The steel plate was cut to form the aperture through which the jet exhausted from the cell. The aperture is a truncated cone thirty-six in. at the outside wall which widens at a 45^{o} half-angle inwards (fig. 4).

An iris mechanism (fig. 6) was mounted flush against the outside wall concentric with the fixed aperture. The diameter of the remote controlled iris could be varied continuously from 5 to 36 in.

The outside face of the front wall is completely covered with 4-in. of fiberglass, with a 2-in. air space between the glass and the wall to minimize reflections. When acoustic measurements were being taken, a 4-in.-thick layer of fiberglass was placed on the ground covering an area of 4-ft on either side of the jet axis and extending 22-ft in the downstream axial direction.

The WIF was also used for conventional testing of exhaust nozzles where their location relative to the far-field microphone array was fixed. In this program the WIF was used specifically in a test series requiring coannular flows to study temperature and velocity gradient effects.

Two burner systems were mounted parallel as shown in figure 7. The independently controllable hot flows entered a coannular plenum chamber which supplied air to the test nozzles.

In the outside arena, (figs. 8 and 9) eight microphones were mounted vertically over the jet centerline on a boom having a 25-ft radius curvature about the aperture center. They were mounted at 10^{o} intervals beginning at 20^{o} from the exhaust direction of the jet axis and continuing up to 90^{o}. The acoustic far-field pressures were measured by 1/4-in. Bruel and Kjaer condenser microphones having a flat frequency response (after correction) from 50 Hz to 80 kHz.

2.1.3 THE LOW-SPEED WIND TUNNEL

The forward velocity effects on noise generation and radiation from jet exhaust nozzles was studied in the Boeing 9- by 9-ft Induction Tunnel Facility (fig. 10).

The tunnel includes acoustically-lined panels on the ceiling and side walls of the test section, a burner to heat the facility's compressed air supply to the required total temperature, and a traversing microphone system to acquire sideline acoustic data at selected angles. The wind tunnel is powered by a turboprop engine that induces ambient air through the test section at velocities up to 165 knots (278 ft/sec). The propeller turns at a constant rpm and controls tunnel velocity by varying pitch. For this test series, noise data were obtained with the tunnel off and at 165 knots. The tunnel air flows through a large, rectangular bell-mouth inlet, a flow straightening grid, and a diffuser, prior to reaching the 9-by 9-ft constant area test section. The flow is then diffused and expelled from the tunnel by the four-bladed propeller. A kerosene burner is located within the model's nacelle and incorporates a propane gas spark ignition system. During the test, the burner heated the nozzle air to a constant 1150^{o}F. The nacelle installation included a boundary-layer bleed to better simulate the boundary layer of an actual engine installation. Nozzle pressure ratio, total temperature, tunnel velocity and traversing microphone positions are monitored and set within the facility's control room.

The acoustic instrumentation consisted of two 1/4-in. Bruel and Kjaer Model-4135 microphones with bullet-shaped grip caps. One of the microphones was mounted on a traversing mechanism capable of remote positioning from 70^{o} to 165^{o} relative to the inlet axis. The second microphone was in a fixed location at 120^{o} from the inlet and on the opposite side of the jet axis, and served as a reference for the traversing microphone. Both microphones were at the jet centerline height and on a sideline 2 ft from the jet axis.

2.2 ACOUSTIC DATA ACQUISITION AND ANALYSIS

A typical set of acoustic data acquisition instrumentation used in this program is shown in block diagram form in figure 11 and a general overview in figure 12. Noise data from up to twelve microphones was recorded for sixteen seconds during stabilized nozzle pressure ratio conditions on a fourteen-track analog tape recorder for subsequent analysis after test completion. Basic analysis of the recorded acoustic data was performed in a separate facility in the Boeing Acoustical Laboratory in Seattle, Washington. The basic analysis system consists of an analog tape reproducer, General Radio Model-1921, 1/3-octave analyzer, time code reader, PDP8-1 computer, digital magnetic tape recorder, and associated monitor, control, interface and peripheral service equipment (figs. 13 and 14).

The operator controls the analysis through a teletype keyboard used for entering calibration, frequency response compensation, and measurement point identification information into the computer. The General Radio analyzer includes a bank of twenty-seven 1/3-octave-band filters, covering the frequency range of 200 to 80 kHz. The filters meet International Standard IEC 225 and U.S.A. Standard 51.11-1966 Class III requirements and are calibrated with both sine wave and random noise inputs. The true rms detector section of the analyzer has a dynamic range of 60 dB and a resolution of ± 0.25 dB. The square law response of the detector is verified by the two sine wave insert method per IEC 179, Paragraph 8.5.

Frequency response compensation and sensitivity calibration information are added to the 1/3-octave-band data in the computer, and the output on a digital magnetic tape is in a format compatible with existing CDC-6600 computer software. All components of the reduction system are periodically certified to the manufacturer's specifications by the Boeing Flight Test Calibration Laboratory.

2.2.1 INSTRUMENTATION CALIBRATION

To insure proper data quality as well as day-to-day repeatability all acoustic systems were calibrated on a regular basis. Three types of calibration were performed on the data acquisition system prior to recording test data. The first determined the frequency response of the microphone preamplifier and power supply. This was performed before and after each test using the electrostatic actuator method illustrated in the block diagram in figure 15. The sweep oscillator frequency is referenced to an electronic counter, certified and calibrated by the Boeing Flight Test Laboratory. The Boeing Flight Test Calibration Laboratory maintains test standards, references, and equipment with calibration accuracy traceable to the U.S. Bureau of Standards.

The second calibration, using the sweep oscillator in figure 15 was done to determine the relative response of the signal conditioning amplifiers, acquisition recorder and data reduction tape reproducer. An electrical insert signal was applied to the data system in the form of a sine wave frequency sweep from 200 Hz to 80 kHz. The sweep was recorded on the acquisition system, then reproduced on the data reduction system to determine the response of that portion of the instrumentation. When the frequency response of the system relative to 250 Hz had been determined, corrections were computed for each 1/3-octave- band and applied to the data during reduction to obtain a uniform (flat) system response at all frequencies within the data bandwidth.

The third calibration was an end-to-end sensitivity check, performed each day before and after a test. An acoustic pistonphone calibrator with a constant, known sound pressure level (SPL) at 250 Hz was applied to each microphone, and the calibrator signal recorded on magnetic tape. This reference was used during the data reduction process to determine system sensitivity. The device used was a Bruel and Kjaer Model-4220 pistonphone which has a certification traceable to the U.S. Bureau of Standards through a secondary standard maintained by the Boeing Metrology Laboratory.

2.2.2 ACOUSTIC DATA ANALYSIS FORMAT

A standardized acoustic data analysis procedure was followed during the preliminary stages of each test program. The main objective was to arrange the large volume of test data into various convenient formats that would expedite the final engineering analysis. The data output from the acoustics laboratory was in the form of digitized 1/3-octave-band spectra that were stored on digital magnetic tape. First, the digitized data was plotted through a computer controlled procedure to provide easy visibility in order to ascertain data quality and acceptability. The digitized data were then normalized for atmospheric absorption effects to a standard day of 77°F and 70% relative humidity. In the case of data from the HNTF, the ground microphone spectra were also corrected to free-field levels by simply lowering the spectrum levels by 6 dB. Noise data measured in the WIF with the overhead microphone array were already free-field level. Noise data in this final form were stored on a digital magnetic tape data bank for further analysis.

Overall sound pressure levels (OASPL) presented in this report are the computed sum of the measured 1/3-octave-band levels in each spectrum.

Sound power levels (PWL) were calculated using a computer program. Sound pressure levels from each microphone location were assumed to be constant in a 10° arc centered at the microphone position. Assuming an axisymmetric sound field, an integral procedure was used to calculate the total sound power radiated through the surface of revolution about the jet axis described by the arc 85° to 158° at 50-ft distance. Noise in the forward arc was assumed to be zero. (Note: Atmospheric absorption of sound over the propagation distance was included to give the effective sound power of the source.).

Perceived noise levels (PNL) were calculated over an extrapolated distance for the subjective evaluation of the jet noise suppressor systems. In this case the model scale data were transformed in frequency and normalized for both measurement distance and nozzle geometric scale to full size values before extrapolation and calculation of PNL. The extrapolation procedure is based on four Society of Automotive Engineers (SAE) publications (refs. 6, 7, 8 and 9) and takes into account:

- Spherical divergence (AIR 876)
- Number of engines and engine shielding (AIR 876)
- Atmospheric absorption (ARP 866)

- Extra ground attenuation (AIR 923)
- Perceived noise level calculation (ARP 865)

2.3 JET NOISE SOURCE LOCATION DATA ACQUISITION AND ANALYSIS

The test procedures and the data analysis techniques for jet noise-source location tests in the WIF were different from the normal far-field noise tests conducted with jet exhaust nozzles. Therefore, these differences are described separately below.

2.3.1 TEST PROCEDURES

For a given test configuration and test condition the jet flow boundary was first determined by means of a total head probe radially traversing the flow at a number of axial locations. This boundary was arbitrarily defined to be that radial position at which the average total pressure is 0.2 inches of water above ambient. This boundary determined the minimum orifice diameter that could be used at a given axial position without impingement of the flow on the iris plate.

Beginning with the jet fully extended (nozzle exit plane flush with the outer wall and the iris fully open) the baseline measurement was recorded (fig. 16.1). The jet was then retracted a short distance into the cell as in figure 16.2. With the jet fixed in that position a set of measurements was made for each of several orifice diameters. The first was taken at the smallest diameter for which there was no flow impingement and successive measurements were taken at increasing orifice diameters. This procedure was repeated at each location as the jet was withdrawn step-by-step into the room (figs. 16.3 to 16.n). Although a set of measurements was made at each step, only one of the measurements contributed a point to the distribution curve. The measurement used was the one taken for that orifice opening which provided maximum isolation of sound within the cell and which generated the least amount of orifice interaction noise. The result of all these measurements is a curve like that shown in figure 16.n for each frequency band.

2.3.2 DATA ANALYSIS

The acoustic data was recorded and analyzed in the same way as described in section 2.2.2. The normalized data from the data bank was used to calculate space averaged sound pressure level (SPLFA) spectra in bands 1 Hz wide for each of the nozzle's axial locations.

The SPLFA versus axial distance (X/D) data was then processed to obtain source distributions in a manner suggested by Potter and Jones (ref. 3). The procedure consisted of taking the SPLFA data for a given frequency band as a function of X/D and curve-fitting an analytical function to it. An example of the curve fit and of the analytical function used is shown in figure 17. The chosen function is of a form which has zero slope at $X/D = 0$ and then is continuously negative in the downstream direction. The negative derivative of the function gives the noise density distribution curve, figure 18, which represents the apparent jet noise-source locations along the jet axis. The word apparent is used because this experimental

technique "sees" the noise sources as they emerge from the jet surface and hence fails to account for propagation paths inside the jet.

2.4 LOW-SPEED WIND TUNNEL ACOUSTIC DATA ACQUISITION AND ANALYSIS

The test procedures and data handling in the low speed wind tunnel associated with jet noise measurements are described below.

2.4.1 TEST PROCEDURES

For a given nozzle-test installation, noise data was first acquired with the tunnel turned off. Jet noise data were recorded for approximately 20 seconds with the traverse microphone positioned at a series of angles from 70^{o} to 165^{o} relative to the inlet centerline. Noise data for the fixed microphone was recorded each time and served as a reference for condition repeatability and comparison with the traverse microphone when positioned at the same angle. Following the static runs the wind tunnel was turned on and flight jet noise data were recorded with the gas conditions set at the same total temperature and pressure ratio as the static gas conditions (equal ideal jet velocity). Thus, the test variable is tunnel velocity, with changes in jet noise attributed to this parameter.

2.4.2 DATA ANALYSIS

The acoustic data was recorded and analyzed in the same way as described in section 2.2. The normalized acoustic data from the data bank were then scaled and extrapolated to an arbitrary 100 ft sideline for further analysis. This was done in two steps. The first extrapolation employed model scale frequencies and corrected the SPL's from a 2-ft sideline to a 50-ft polar arc. This was done to correct for atmospheric absorption of high frequency noise thus providing a better comparison with far-field model data that was measured on a 50-ft polar arc. The second step scaled the data and extrapolated to a 100-ft sideline where OASPL and PNL values were calculated. Two values of PNL were calculated for each spectrum; one using the scaled measured frequency/SPL values, the other applying a 1/3-octave-band frequency shift in consideration of Doppler effects. Since the wind tunnel technique does not include Doppler effects, this added calculation was necessary for later analysis.

3.0 TEST HARDWARE

The model scale acoustic test hardware that was fabricated and used in this program is described in the table below. The multitube nozzles are identified as to the number of tubes; area ratio (AR); tube distribution, i.e., close-packed array (CPA) or radial array (RA); and tube description, i.e., round tubes (RT) or elliptical tubes (ET); with round convergent ends (RC) or nonconvergent ends (NC). The hardwall ejectors used in the program are identified in the following table by area ratio. All of the ejectors used had flight type inlets. Schematic drawings and photographs of the test hardware are presented in figures 19 through 37.

TEST HARDWARE

NOZZLE	DESCRIPTION
4.16-in. RC	4.16-in. round convergent reference nozzle
6-in. RC	6-in. round convergent reference nozzle
37T-3.3 AR-CPA-RT/RC	37 Tubes, 3.3 Area Ratio, Close-Packed Array, Round Tubes with Round Convergent Ends
7T-3.3 AR-CPA-ET/RC	7 Tubes, 3.3 Area Ratio, Close-Packed Array, Elliptical Tubes with Round Convergent Ends
19T-3.3 AR-CPA-ET/RC	19 Tubes, 3.3 Area Ratio, Close-Packed Array, Elliptical Tubes with Round Convergent Ends
37T-3.3 AR-CPA-ET/RC	37 Tubes, 3.3 Area Ratio, Close-Packed Array, Elliptical Tubes with Round Convergent Ends
61T-3.3 AR-CPA-ET/RC	61 Tubes, 3.3 Area Ratio, Close-Packed Array, Elliptical Tubes with Round Convergent Ends
37T-2.75 AR-CPA-ET/RC	37 Tubes, 2.75 Area Ratio, Close-Packed Array, Elliptical Tubes with Round Convergent Ends
37T-4.5 AR-CPA-ET/RC	37 Tubes, 4.5 Area Ratio, Close-Packed Array, Elliptical Tubes with Round Convergent Ends
37T-6.0 AR-CPA-ET/RC	37 Tubes, 6.0 Area Ratio, Close-Packed Array, Elliptical Tubes with Round Convergent Ends
37T-3.3 AR-RA-RT/NC	37 Tubes, 3.3 Area Ratio, Radial Arrangement, Round Tubes with Nonconvergent Ends
37T-4.5 AR-RA-ET/RC	37 Tubes, 4.5 Area Ratio, Radial Arrangement, Elliptical Tubes with Round Convergent Ends

PRECEDING PAGE BLANK-NOT FILMED

TEST HARDWARE (Cont.)

NOZZLE	DESCRIPTION
31T-2.75 AR-RA-ET/RC	31 Tubes, 2.75 Area Ratio, Radial Arrangement, Elliptical Tubes with Round Convergent Ends
42T/Annulus-3.3 AR-CPA-ET/RC	42 Tubes with Annulus and Plug, 3.3 Area Ratio, Close-Packed Array, Elliptical Tubes with Round Convergent Ends, Variable Annulus Width
61T-3.1 AR-CPA-RT/NC	61 Tubes, 3.1 Area Ratio, Close-Packed Array, Round Tubes with Nonconvergent Ends
61T(Canted)-3.1 AR-CPA-RT/NC	61 Tubes with the Outer Row of 24 Tubes Canted Outwards, 3.1 Area Ratio, Close-Packed Array, Round Tubes with Nonconvergent Ends
85T-3.1 AR-CPA-RT/NC	85 Tubes, 3.1 Area Ratio, Close-Packed Array, Round Tubes with Nonconvergent Ends
EJECTOR	
2.5 AR	Cylinderical Ejector, 6.57-in.-diameter, 4.16-in.-long
3.1 AR	Cylinderical Ejector, 7.31-in.-diameter, 4.16-in.-long
3.7 AR	Cylinderical Ejector, 7.98-in.-diameter, 4.16-in. long
3.7 AR	Cylinderical Ejector, 7.98-in.-diameter, 24-in. long

4.0 JET NOISE RESULTS

4.1 JET NOISE POWER CHARACTERISTICS OF REGULAR MULTITUBE NOZZLES

Understanding the acoustic power characteristics of jet exhaust nozzles helps in the formulation of the noise generating mechanisms involved, as well as providing information useful in normalizing the acoustic results. Since this program's objectives are to study supersonic jet noise suppression, data were acquired only over the supersonic jet velocity range. Many geometric parameters of multitube nozzles were investigated, but the only significant variables for regular or close-packed arrays (CPA) were found to be tube number and nozzle-array area ratio. Variables having second order effects on suppression will be discussed later in the report.

The total jet noise power levels as a function of the number of tubes are shown in figure 38 for a nominal nozzle area ratio of 3.3. The noise power level generally decreases with increasing tube number. The noise power suppression attained relative to a R/C nozzle is shown in figure 39. The noise suppression varies from about 4.5 to 6.5 dB for the 7-tube nozzle up to 7.5 to 11 dB for the 61-tube nozzle.

The total jet noise power levels as a function of nominal nozzle area ratio for 37-tube nozzles are shown in figure 40. Area ratio appears to have an impact on only the higher pressure ratio (velocity) results. The noise power suppression attained relative to a R/C nozzle is shown in figure 41. For the high-temperature jets the noise suppression does not appear to have a simple relationship with nozzle pressure ratio. For the smaller AR nozzles the low pressure ratios show highest suppression, while at the largest area ratio, the high pressure ratios tend to give the best suppression, reaching about 11 dB.

The jet noise power levels normalized by the commonly used function of $-10 \log \rho^2 A$ and plotted against ideal jet velocity are shown in figures 42 and 43 as a function of tube number and nozzle area ratio respectively. The apparent discrepancies in test data for overlapping velocity points going from one jet temperature to the next indicates that more complex noise-generating mechanisms are present in supersonic jets than just jet turbulence. Consequently in the following sections, the acoustic power analysis is conducted by identifying and isolating the various noise-source mechanisms to give a better insight into supersonic jet noise suppression.

4.1.1 MULTITUBE-NOZZLE NOISE SOURCES

Figure 44 is a schematic of a typical multitube jet. This sketch should be referred to in the following discussion. Five sources of noise were considered to dominate the multitube-nozzle composite noise spectrum:

(1) Jet premerging (and merging) turbulence noise.

(2) Jet postmerging turbulence noise.

(3) Spiral-mode flow-instability noise.

(4) Shock noise.

(5) Burner core noise.

The effect of each noise source on the power spectrum is illustrated in figure 45 for the 7-tube, 3.3 AR nozzle. Premerged jet turbulence generates broadband noise which results in the high frequency peak of the typical double-peak multielement noise spectrum. The postmerged jet turbulence generates broadband noise composing the low frequency peak of the spectrum. Shock noise is a tone component that tends to occur only at near ambient total temperatures. Sometimes a second harmonic of shock noise is apparent. Spiral-mode flow-instability noise (ref. 10) affects a relatively narrow band of frequencies, noticeable at low values of total temperature. The facility's burner core noise is composed of tones and broadband noise affecting the lower frequency portion of the spectrum, especially at low jet velocities. Burner core-noise interference was reduced significantly during the latter part of this test program by modifying the HNTF burner.

4.1.1.1 Premerged Jet Turbulence Noise

The premerging jet noise tends to be the most annoying source of multitube-nozzle noise when the nozzle pressure ratio is less than 3.0. For SST noise suppression systems, premerging jet noise is particularly troublesome at cutback over the community after sufficient altitude has been gained during takeoff. The premerged jet generates high frequency noise in a region extending from the nozzle exit plane to where the elemental jets coalesce.

The dimensions of this region are such that an acoustically absorbent, lined shroud of practical size can be installed around the jet premerging region thus reducing this source of noise. The effect of unlined ejectors will be discussed in section 4.1.2 of this document.

The premerged jet noise, adjusted by removing that contributed by spiral-mode flow-instability and shocks, is assumed to be primarily turbulence noise generated in the mixing regions of the elemental jets. Premerged jet turbulence noise contributes to the high frequency peak of the jet noise spectrum.

Supersonic flow adds to the complexity of determining the premerged jet noise characteristics of multitube suppressor nozzles. When the jet Mach number is increased, the fully expanded area of each elemental jet increases, thus decreasing the flow area ratio, since the array's base area is relatively unchanged. This results in a shortened, premerged jet region as the nozzle pressure ratio is increased. Also, the potential (and supersonic) core dimension lengthens as Mach number increases, which may lead to core penetration of the jet merging region for small area ratio arrays. Most of the turbulence noise is generated near the end of the core, and a significant range in turbulence-noise generation may be expected for small AR nozzles.

The jet flow area ratio in this study is related to the fully expanded jet area, e.g., $AR_8(A^*/A)$. This provides correlation of acoustic data with area ratio which is in turn a function of pressure ratio. Figure 46 shows the range of flow area ratios for each nozzle in this parametric study over the range of pressure ratios from 2.0 to 4.0.

The premerged jet turbulence noise power levels with the components of shock and spiral-mode flow-instability noise removed are shown in figures 47 and 48. The power levels are shown as a function of jet velocity and have been normalized by 10 log $(\rho + \rho_0)^2 A$. The density term is proportional to the mean density of the jet mixing region, which has been shown to be a useful relationship in expressing multitube-nozzle noise values (ref. 1). The normalized premerged jet turbulence noise power levels tend to show a roll-off for some configurations at the higher jet velocities. This is believed to be primarily due to the decrease in flow area ratio, with the potential cores of the elemental jets penetrating into the post-merged jet region. Premerged jet turbulence noise power level for 37-tube nozzles, as a function of flow area ratio, show noise level increases because the premerged jet region lengthens. Increasing the tube number (i.e., decreasing the tube size) lowers the premerged jet turbulence-noise power level. The amount of noise reduction increases with jet velocity.

The premerged jet turbulence noise is expected to have a spectrum peak frequency related to the Strouhal number, fd/V. The dimension d is proportional to the diameter of a fully-expanded elemental jet in a multitube-nozzle array. The peak frequency of the pre-merging jet noise was obtained from the measured power spectra for the various multitube nozzles tested. Those spectra which were badly distorted by the effects of postmerging, shock, or spiral-mode flow-instability components were rejected in this analysis.

Figure 49 shows the Strouhal numbers (SN) calculated from the available data using the fully-expanded elemental jet diameter $d(A/A^*)^{0.5}$. The multitube nozzle premerged noise peak frequency correlates with a simple jet (4.1-in. RC), but there is a significant scatter of values. This scatter is partly related to gas total temperature and partly to number of tubes in the nozzle array. Modifying the SN empirically by $(T_T/T_0)^{0.5}$ to account for temperature effects and by $0.0043N_T$ to account for tube number effects, the data can be made to normalize to a value of 0.6 as shown in figure 50. Hence the premerged jet noise peak-frequency can be approximated by:

$$f = \frac{(0.6 - 0.0043N_T)V_J}{d\left(\frac{A}{A^*}\right)^{0.5}\left(\frac{T_T}{T_0}\right)^{0.5}}, \text{ Hz} \qquad (1)$$

The total temperature effect on premerged jet noise peak frequency is not too surprising; Bushell (ref. 11) has shown that a theoretical argument exists for applying $(T_T/T_0)^{0.26}$ to the basic Strouhal number for simple, subsonic jets.

The reason for premerged jet noise peak frequency to be dependent on the number of tubes in the array is not so obvious. Flow profile measurements show that the axis of the outer row of elemental jets in a multitube array bend towards the center of the array, tending to merge with the second row of elemental jets. This bending of the flow axis could be attributed to crossflow created by the demand for secondary flow by the mixing process of elemental jets within the array. As the number of tubes in an array increases, the demand for secondary flow increases, also resulting in further bending of the outer row of jets. When the outer and second row of jets merge, a larger diameter jet is created which will shift the premerged jet noise peak frequency to a lower frequency.

Another reason that has been offered is the probable transfer of momentum from the outer jets to the inner jets, indicated by the shorter core lengths for the outermost rows of jets. The secondary crossflow reduces the degree of turbulence in the outer-row jets with an accompanying lowering of premerged jet noise peak frequency. The transfer of momentum to the inner jets would raise their turbulence levels, but this effect is masked by the shielding properties of the outermost row of jets. Figure 51 shows the individual flow axes and lengths of the respective supersonic core regions measured with the 61-tube, 3.3 AR nozzle (PR = 3.0 and T_T = 1000°F). The bending of the outermost jet is apparent as well as the shorter core lengths.

After comparing all of the multitube nozzle, premerged jet noise spectra acquired in this program, a general spectrum shape for this source of noise is proposed in figure 52. The very high frequency end of the proposed spectrum is affected by uncertainties present in the model scale data due to ultrasonic sound propagation loss and microphone calibration corrections. In general, however, the proposed spectrum shape is very similar to that of a simple jet.

4.1.1.2 Postmerged Jet Turbulence Noise

The postmerged jet turbulence noise has been particularly troublesome when considering suppressor nozzle systems for SST application. The high nozzle pressure ratios, e.g., PR $\geq$ 3.0, necessary for takeoff will usually result in the postmerged jet noise being the prime source of noise. The postmerged jet is a considerable distance downstream of the nozzle exit plane, so that a practical length lined ejector can not absorb this noise.

The postmerged jet exhibits flow properties very similar to the simple jet. The elemental jets mix with secondary flow and merge together some distance downstream. A large diameter core is formed with well defined boundaries as shown in figure 53 for the 61-tube, 3.3 AR nozzle. With nozzle PR of 3.0 and total temperature of 1000°F (V_J = 2191 ft/sec) the postmerged jet core conditions as measured were PR = 1.6 and T_T = 675°F which is equivalent to a jet velocity of 1315 ft/sec. The diameter of the postmerged jet core is very nearly equal to the diameter of the multitube nozzle.

The effective diameter of the postmerged jet core is a necessary parameter needed to predict noise level and the postmerged noise frequency spectrum. Noise level is proportional to the jet diameter squared while the frequency spectrum is related to the Strouhal number, fD/V.

The diameter of the postmerged jet core was determined by measuring the distance at the $0.5(T_J + T_O)$ points from the temperature profiles taken with the various multitube (CPA) nozzles. It was found that for all practical purposes the postmerged jet core diameter can be assumed to be equal to the multitube-nozzle array flow diameter at the exit plane.

The postmerged jet noise power levels, derived from the low frequency peak of the noise spectra, for the various multitube nozzles are shown in figures 54 and 55 for variations in area ratio and tube number respectively. It can be seen that the area ratio is the major parameter affecting postmerged noise levels, with the noise decreasing with increasing area ratio.

The postmerged jet noise power levels can be normalized by ($-10 \log \rho_c^2 A_c$) if ρ_c and A_c are taken to represent the conditions of density and flow area in the postmerged jet region. Good correlation between multitube-nozzle postmerged jet power levels and simple R/C nozzle noise is shown in figure 56. Measured values of postmerged jet density and area for the various nozzles were used in the normalizing procedure. Figure 56 also shows good agreement between the test data and predicted "clean jet" power levels for velocities above about 1500 ft/sec. For lower jet velocities, test facility core noise is thought to affect the sound power levels.

H. Lu (ref. 11) has developed a numerical technique for calculating the static temperature and velocity profiles as a function of axial location in a simple round jet. The calculations are based on the initial nozzle exit conditions in the jet. As a simple jet mixes with the atmosphere the cross-sectional area increases. The ratio of the cross-sectional area, at same axial distance, to the fully-expanded jet area provides an area ratio term. It has been found that there is good agreement between the predicted average gas conditions in a simple jet and the measured gas conditions in a multitube-nozzle, postmerged jet as a function of area ratio as shown in figure 57. Hence it can be concluded that the gas conditions in the postmerged jet core can be predicted from round jet mixing theory by calculating the average conditions in a simple jet at the appropriate axial location (area ratio).

It is commonly accepted that for subsonic jets, the 1/3-octave-band noise spectrum peaks at a Strouhal number of approximately 0.22. It can be seen in figure 58 that the postmerged noise from multitube nozzles also peaks at about the same Strouhal number except for flow area ratios above 4.0. The apparent increase in Strouhal number for large AR nozzles may be due to the interference from premerged jet noise in the test data because the postmerged jet noise levels are lower and are approaching premerged noise levels in that part of the spectrum. It is therefore concluded that for multitube nozzles of $AR < 4.0$, a normalized spectrum shape (fig. 59) can be used to describe the postmerged jet noise spectrum. The proposed spectrum shape also approximates that from a simple R/C nozzle.

4.1.1.3 Spiral-Mode Flow-Instability Noise

A component of supersonic jet noise has been tentatively identified as spiral-mode flow-instability source radiation. This noise source is apparent in R/C nozzle spectra as well as in multitube suppressor nozzle noise spectra.

The mechanism for spiral-mode flow-instability, according to C. K. Tam (ref. 10), is the selective amplification of flow disturbances by shock cells in the jet which results in large scale flow instabilities downstream. These large scale flow instabilities are believed responsible for transferring jet kinetic energy into noise radiation. Tam predicted the existence of two dominant noise-source frequencies as a result of spiral-mode flow-instability, but from the results acquired in this program, only the high frequency mode has been detected.

Multitube-nozzle test data indicates that spiral-mode flow-instability is the dominant noise source for $PR \geq 2.5$ in cold jets. High jet velocity associated with hot jet conditions results in jet premerging turbulence noise levels dominating over the spiral-mode noise.

The peak spiral-mode frequency found in the measured spectra agrees with Tam's theoretical predictions as shown in figures 60 and 61. It has been found that the higher order terms of Tam's equation can be neglected without loss of accuracy using the following equation.

$$f = \frac{1.202\, a_o}{\pi\, d} \left(\frac{M_J + 1}{M_J - 1}\right)^{0.5} \left(1.436 - 0.361 \frac{V_J}{a_o}\right)^{-1} \qquad (2)$$

a_o is the speed of sound in air

d is the fully expanded flow diameter of an elemental jet

The spiral-mode flow-instability noise apparent in the power spectra is especially noticeable in noise spectra recorded at 90^o relative to the nozzle inlet axis (figs. 62 and 63). As tube number increases the spiral-mode flow-instability noise power decreases (fig. 64). Nozzle area ratio has little effect on spiral-mode noise levels. At nozzle pressure ratios less than 2.5 ($M_J < 1.22$) the evidence of spiral-mode noise was difficult to detect. When the spiral-mode frequency agrees with the 2nd harmonic of the shock noise frequency, 3- to 5-dB higher power levels resulted. An estimate of the spiral-mode noise spectrum and beam pattern has been made using the test data and is shown in figure 65.

4.1.1.4 Shock Noise

Shock or screech tones were present in the baseline R/C nozzle test spectra at supersonic jet velocities. For cold and low temperature jets, shock noise was also detected in the multitube nozzle spectra. The multitube nozzles, however, showed no tendency to radiate shock noise under hot flow conditions. When the spiral-mode flow-instability noise frequency coincided with the shock noise or its harmonics there was significant amplification of both noise components. The following empirical equation has been derived from test data to predict the fundamental screech-tone frequency in the jet noise spectra.

$$f_M = \frac{a_o}{K\, d(PR - 1.89)^{0.5}}, \text{ for } PR \geq 1.89 \qquad (3)$$

where a_o = speed of sound
d = fully expanded jet diameter from each tube or nozzle
PR = nozzle pressure ratio
K = constant
= 1.57 for R/C nozzle
= 2.74 for multitube nozzles

4.1.1.5 Test Facility Burner Core Noise

Model scale test facilities, such as the HNTF, that employ burners to raise jet temperature have traditionally shown high background noise levels. The background noise is associated with the burners and other upstream perturbances in the test rig. The burner core noise contains both tones and broadband components that mainly affect the low frequency portion of the noise spectrum. This unwanted noise is not well understood and can interfere

with the normal jet noise analysis. It can, however, lend a degree of realism to the analysis, because similar burner core noise components have been detected radiating from the nozzles of full scale engines.

In a continuing effort to improve test facilities The Boeing Company has modified the burner designs to reduce this internal noise source. Progressively during this program, the test facility's burner noise was reduced to the level where it could no longer be detected in the jet noise spectra. Consequently care had to be taken with the early test data, because it contained burner core noise. A very interesting sidelight to the facility's burner noise problem was the discovery that the multitube nozzles appeared to suppress this noise component when compared to the baseline R/C nozzle. Noise reductions of 5 to 10 dB were observed in the low frequency parts of the spectrum. This phenomena of burner core noise reduction with the multitube nozzles is attributed mainly to the change in cross-sectional area (change in impedance) in the duct upstream of the nozzle, causing some of the acoustic energy to be reflected back into the duct. This results in an acoustic transmission loss which can be expressed as:

$$\triangle \text{dB} = 10 \log \frac{\left(1 + A_1/A_2\right)^2}{4\, A_1/A_2} \qquad (4)$$

for wave lengths (λ) > duct diameter (D)
where A_1 = duct area
A_2 = nozzle area

In the case of the multitube-nozzle tests, $A_1/A_2 = 9.75$ so that a noise reduction of the order of 4.7 dB could be expected.

In the case of full scale engines, the area ratio between the duct and nozzle would be much smaller, say on the order of 3.0, in which case the expected noise reduction would be about 1.2 dB.

4.1.1.6 Composite Jet Noise

Supersonic jet noise characteristics as shown in the previous sections can be difficult to analyze due to the many noise-source mechanisms present. To summarize the above discussions two typical examples of the relative noise power levels of the supersonic jet noise components are shown in figures 66 and 67 for a 37-tube nozzle. For ambient jet temperatures in figure 66 spiral-mode flow-instability noise component dominates the total power level. For high temperature jets, however, in figure 67 the jet turbulence noise dominates and the spiral-mode noise can be neglected.

4.1.2 MULTITUBE NOZZLES WITH HARDWALL EJECTORS

In typical SST applications, engine nacelles have a variable area secondary exhaust nozzle which is required to optimize nozzle performance during the total flight envelope, i.e., takeoff, transonic acceleration and supersonic cruise. During the takeoff phase, this secondary nozzle acts like an ejector relative to the primary flow nozzle. For jet noise suppressor installations this secondary nozzle or ejector is a very convenient adjunct. A properly sized ejector with respect to the multitube nozzle can improve noise suppression. Secondly, the ejector provides a means of supporting acoustically absorbent materials that will further attenuate jet exhaust noise.

A number of multitube nozzle/ejector configurations have been tested in the past (refs. 1, 2 and 5). Acoustically lined ejectors have suppressed premerged jet noise by as much as 12 dB. Loose fitting hardwall ejectors have shown little effect on suppressor nozzle radiated noise.

When the ratio of the ejector diameter to the nozzle array diameter approached unity, noise suppression of 1 to 2 PNdB was possible with a tight-fitting hardwall ejector (ref. 1). Noise generated by multielement jets surrounded by a hardwall ejector apparently propagated downstream beyond the ejector exit and into the far-field unaffected. When the ejector fits tightly around the jet efflux, the velocity of secondary flow between the elemental jets and ejector wall increases, providing some suppression of premerged jet noise seemingly due to the relative velocity effect. Similar results have been obtained in this test program. In addition it was noted that a hardwall ejector can provide substantial reduction of postmerged jet noise as well as higher amounts of suppression of premerged jet noise.

The 31-tube, 2.75 AR nozzle was tested with three hardwall ejectors with area ratios of 2.6, 3.1 and 3.7. The noise power spectra for each configuration are shown in figures 68 through 70 for nozzle pressure ratios of 2.0, 3.0 and 4.0, where T_T = 1150°F. The smallest ejector in all cases results in the lowest premerged noise levels (high frequencies). The best results were attained at the lowest pressure ratio. At PR = 4.0 the effect of the ejector on jet radiated noise was considerably diminished. This may be due to lengthening of the elemental jets potential and supersonic cores at higher Mach numbers resulting in the premerged jets extending beyond the ejector exit.

The jet noise power suppression achieved by the three ejector configurations is shown in figure 71 for PR = 2.0. The smaller ejectors achieved 0 to 3.0 dB suppression of *postmerged* jet noise. This was considered unusual since the postmerged jet region is beyond the ejector exit. As discussed in section 4.6.7, jet velocity profiles taken at the ejector exit indicate that the kinetic energy of the multitube-nozzle postmerged jet is reduced when an ejector is installed. One may conclude that an ejector promotes better mixing of the premerged jet region to result in the lower postmerged jet velocity.

Suppression of premerged jet noise by the 2.6 AR ejector was unexpectedly high, e.g., 6.7 dB at 10 kHz. This amount of suppression is substantially greater than would be expected from the relative velocity effect. A possible explanation of these high values of suppression is shown schematically in figure 72. The region of high turbulence in the outer row of jets is situated in a relatively localized part of the jet mixing region. Since noise generation is

associated with jet turbulence, one may assume that the prime noise sources are being convected downstream in the jet mixing region where maximum shear exists. The frequency of the sound sources is a function of the width of the jet mixing region according to the Strouhal number relationship. This means that specific frequencies radiated by turbulence will emanate predominantly from localized parts of the jet mixing region. If this condition exists it is possible that the radiation efficiency of the noise sources can be affected by reflections from the ejector wall by effectively short circuiting the load impedance. The fact that the 2.6 AR ejector's maximum suppression of the premerged jet noise coincided with the premerged noise peak frequency was as a result of a fortuitous choice of the ejector dimensions.

Varying phase relationships are expected to exist between different source frequencies and their reflected signals so that a series of maxima and minima should be apparent in the ejector's premerged jet noise-suppression spectra. A series of maxima and minima can be observed in the noise suppression spectra in figure 71 and the peaks and valleys can be related as multiples of $\lambda/4$ as shown.

There is not sufficient data available at this time to either confirm this or suggest some other hypothesis of noise suppression by hardwall ejectors. More work should certainly be conducted in this area since the test data shown in figure 71 demonstrates the existence of some hitherto unrecognized suppression mechanism which may be used to enhance jet noise suppression for nozzle/ejector configurations.

Figures 73, 74 and 75 summarize the postmerged and premerged jet noise power levels for 31-, 37- and 61-tube nozzles with ejectors. As suggested above, the premerged noise power is reduced by a combination of relative velocity effects and wall reflection effects inside the ejectors while the postmerged jet noise is reduced by a small amount, presumably due to improved mixing within the ejector, resulting in lower kinetic energy in the postmerged jet. All of the combinations of nozzles and ejectors show substantially the same trends.

4.2 JET NOISE DIRECTIVITY CHARACTERISTICS OF REGULAR MULTITUBE NOZZLES

The directivity of radiated jet noise is an important consideration when evaluating jet noise-suppressor characteristics. Noise power analysis, as discussed in section 4.1, provides information about noise generation and overall noise levels, but fails to account for noise radiation paths or beaming effects. In jet noise suppressor analysis, jet noise directivity effects relative to a given observer (e.g., under the flight path or on a sideline from the flight path) are very important. This happens as a result of varying sound propagation losses with varying distances between the jet noise source and the far-field observer.

The single R/C nozzle has a simple directivity pattern because it is usually dominated by only one noise generating mechanism, jet turbulence. The OASPL directivity characteristics of multitube-nozzle jet noise is the result of several noise generating mechanisms, and consequently, it is best to analyse each noise component separately. The noise power signature of the multitube-nozzle noise components has been shown to possess many of the characteristics of a R/C nozzle. In this section of the report the noise directivity characteristics of multitube-nozzle jet noise suppressors will be compared against the R/C nozzle.

4.2.1 ROUND CONVERGENT NOZZLE

The far-field jet noise beam patterns radiated by the R/C nozzle efflux are shown in figure 76 for a nozzle pressure ratio of 2.0 and total temperatures of 60°F, 500°F and 1150°F respectively. The beam patterns are of 1/3-octave bands at intervals of one octave throughout the noise spectrum. It is generally accepted that maximum noise generation occurs in the jet mixing region near the end of the potential core. The mean frequency of noise radiated near the potential core tip is related to the Strouhal number, $fd/V \approx 0.22$. Lower frequencies are radiated largely from the fully-turbulent region beyond the potential core. Higher frequencies are considered to be radiated from the jet mixing region upstream of the potential core tip. The data shown in figure 76, being recorded at a constant nozzle pressure ratio, has dual variables of jet temperature and velocity. For the supersonic jet velocities, the high frequency data is hard to interpret with both temperature and velocity varying.

The lower frequencies, however, being generated in the subsonic regions of the jet, show the typical trends of peaking progressively further away from the jet axis with increasing velocity and temperature. In figure 77 the jet temperature was kept constant showing a comparison of directivity effects as a function of jet velocity alone. Again the typical trends of a conical jet are shown where lower frequencies peak closer to the jet axis than higher frequencies and where an increase in velocity refracts the noise away from the jet axis. Evidence of spiral-mode flow-instability noise is indicated by a secondary peak in the 4000 Hz band at 90° for the V_J = 2545-ft/sec case in figure 77.

Figures 78 and 79 show the noise directivity at the peak frequency for the R/C nozzle, i.e., $0.22 = fd/V$. The ambient temperature jet peaks at an angle of 150° which is nearer the jet axis than a hot jet. At 1150°F, jet noise peaks at 140° to the nozzle inlet axis. An increase in pressure ratio from 2.0 to 4.0 tends to cause a change in directivity away from the jet axis.

4.2.2 MULTITUBE NOZZLES

The far-field jet noise beam patterns radiated by a multitube nozzle exhaust are shown in figure 80 for nozzle pressure ratios of 2.0 and 4.0 at a jet temperature of 1150°F. The beam patterns are of 1/3-octave bands at intervals of one octave across the spectrum. The multitube nozzle jet noise spectra are composed of a number of noise components as discussed earlier; therefore, the beam patterns will be analyzed broadly in terms of premerged and postmerged jet noise characteristics. In figure 80 the frequency bands up to 2000 Hz could be considered to be representative of the postmerged jet noise component and the frequencies above 2000 Hz representative of the premerged jet noise component. It can be seen that the postmerged noise tends to be more directive, peaking at angles close to the jet axis, especially for the high pressure ratios. The premerged noise peaks at angles away from the jet axis, but the beam patterns are quite flat or omnidirectional. The trends are somewhat similar to those shown for the R/C nozzle in figure 77.

The postmerged jet peak-noise directivity of multitube nozzles of 3.3 AR are shown in figures 81 and 82 for PR = 2.0 and 4.0 at T_T = 1150°F. The test data from nozzles with tube numbers varying from 7 to 61 collapses within a bandwidth shown. At nozzle PR = 2.0 the postmerged noise appears to peak between 150° and 155°. For higher jet velocities (PR = 4.0) the postmerged noise is refracted away from the jet axis and peaks at angles between 130° and 150°. In figures 81 and 82 the R/C nozzle's beam patterns are shown for comparison and it can be seen that at the higher pressure ratios (e.g., 4.0) the multitube-nozzle postmerged noise has a very similar characteristic. At the lower pressure ratios the premerged noise in the total spectrum is relatively high compared to the postmerged jet noise and is harder to separate out in component form, so that the postmerged noise beam pattern between 90° and 130° is probably affected by the premerged noise component.

Area ratio has a more pronounced effect on postmerged jet noise directivity than does the tube number, as shown in figures 83 and 84 versus 81 and 82. At PR = 2.0 and T_T = 1150°F the postmerged jet peak frequency directivity is relatively broad with the maximum at 130° - 140° for the larger AR nozzles (fig. 83). As the area ratio becomes smaller the postmerged jet noise beam pattern narrows considerably with the maximum occurring at 150°. It should be kept in mind that the amount of postmerged jet noise generated by a large AR nozzle is much less than that produced by a small AR nozzle. The premerged jet peak noise directivity for the same nozzles and gas conditions are shown in figures 85 and 86. Again the test data for varying tube number as well as nozzle area ratio collapses within a bandwidth shown. The directivity of premerged jet noise in all cases is braoder than the postmerged or R/C nozzle jet noise. In other words the R/C nozzle's beam pattern can not be ussed to approximate the premerged jet noise directivity. There is only a slight change in the peak angle with a change in nozzle pressure ratio.

The effect of spiral-mode flow-instability noise on premerged jet noise can be seen in figure 87. The spiral-mode noise as explained in section 4.1.1.3 is quite directive and peaks at 90° to the jet axis. The beam pattern between 120° and 155° is not pure spiral-mode flow-instability noise, but is a combination with premerged jet turbulence noise.

The jet turbulence noise directivity characteristics for multitube nozzles with a nominal AR of 3.3 are summarized in figures 88 through 91. For a PR = 2.0 the postmerged jet turbulence noise directivity for T_T = 60°F, 500°F and 1150°F is shown in figure 88. The cool-jet noise peaks nearer to the jet axis than do the hot jets, except the 500°F-jet appears to peak further away from the jet axis than does the 1150°F-jet, i.e., 140° versus 150°. The reason for this is not understood. It is possible that an adverse temperature profile from the burner was affecting directivity; however, no measured data is available to substantiate this hypothesis. An estimate of mean postmerged jet noise beam patterns is shown in figure 88. The dashed portions of the beam patterns are predictions assuming that interference from premerged jet turbulence, spiral-mode flow-instability, and burner core noise were absent.

At PR = 4.0 the postmerged jet noise is considerably more directive at $60°F \leq T_T \leq 1150°F$ than at lower pressure ratios, e.g., PR = 2.0. This is shown by figures 88 and 89. The higher-temperature jet noise peaks further away from the jet axis than does the low-temperature jet at PR = 4.0.

The premerged jet turbulence noise becomes more directive when the pressure ratio is increased from 2.0 to 4.0 (figs. 90 and 91). The high levels between 90^{o} and 120^{o} in figure 91 are due to spiral-mode flow-instability interference.

The postmerged jet turbulence noise has been shown to have beam pattern and noise power characteristics similar to a simple jet. It appears that existing simple jet noise prediction methods can be adapted to predict multitube-nozzle postmerged-jet turbulence noise, however subtle influences such as the temperature profile in the postmerged jet core should be considered. The premerged jet noise characteristics of multitube nozzles is not so directly related to a simple jet and further investigations are warranted to fully understand the effects of tube spacing, total temperature, pressure ratio, relative tube sizing, etc., on this source of jet noise.

4.2.3 MULTITUBE NOZZLES WITH HARDWALL EJECTORS

The effect of a hardwall ejector on multitube-nozzle jet noise has been shown in a previous section of this report to introduce a relative velocity effect and changes in noise-source efficiency due to reflections off the ejector wall. These mechanisms largely affect premerged (high frequency) noise; however, the presence of the ejector seems to promote jet mixing thus reducing postmerged jet noise levels also. By examining jet noise beam patterns one can see the hardwall ejector has a decided affect on noise directivity, especially at lower nozzle pressure ratios.

Figure 92 shows 1/3-octive-band beam patterns measured with the 31-tube, 2.75 AR nozzle with and without hardwall ejectors installed, i.e., 2.6 AR, 3.1 AR, and 3.7 AR sized ejectors, for PR = 2.0 and $T_T = 1150^{o}F$. All three ejectors were of the same length, i.e., 2 D_E long. It is apparent that the directivity of the premerged jet noise is affected significantly with reductions in noise noticeable at angles greater than 110^{o}, re: nozzle inlet axis. Similar effects on jet noise directivity have been observed in previous programs (ref 5). An explanation for this directivity effect of hardwall ejectors has been proposed in reference 5, which suggests that noise reflected from the ejector walls arrives at the exit and is then refracted away from the jet axis as it propagates through the velocity gradients existing beyond the ejector exit plane. The shorter wavelengths common to the higher frequencies are affected more by refraction resulting in less noise radiated near the jet axis. This effect is especially apparent with a tight-fitting ejector, e.g., 2.6 AR ejector. A schematic of the noise-refraction process with a tight-fitting ejector is illustrated in figure 93.

As the ejector AR is increased in figure 92, it can be seen that the refractive effect on the high frequencies is reduced. This is most likely due to the reduced velocity gradients across the ejector exit of the looser ejectors. All three ejectors shown had a negligible effect on the postmerged jet noise directivity.

The hardwall ejectors had a considerably different affect on multitube-nozzle radiated jet noise at higher pressure ratios (fig 94). The 2.6 AR ejector increased the premerged jet noise power level at PR = 4.0. Since the fully expanded jet flow area increases as Mach number increases, it is possible that the jet efflux from the 31-tube nozzle was severely scrubbing the ejector walls adding to the generation of high frequency noise. The larger AR ejectors, where ejector-wall scrubbing should not be a problem still showed very little in the way of noise reduction or

directivity effects. Nagamatsu (ref. 13) had concluded that maximum noise from a supersonic jet radiates from a region near the supersonic core tip. Noise-source location tests discussed in section 4.6 confirm this hypothesis. Consequently it can be established that at PR = 4.0 the peak noise sources for the above ejectors are downstream of the exit plane and in that case the ejectors can not be expected to influence the jet noise characteristics to any extent. The suppression that is evident at the higher pressure ratios may be due entirely to the effect of relative velocity on noise generation.

4.3 PERCEIVED NOISE CHARACTERISTICS OF REGULAR MULTITUBE NOZZLES

In the previous sections, jet noise generation and suppression mechanisms have been discussed in physical terms. Human hearing, however, is more sensitive to some noise frequencies than others. Kryter and his co-workers (ref 14) have set up a calculation procedure for perceived noise level (PNL) in dB, also called PNdB which is supposed to take into account people's annoyance to certain noise qualities. Ratings in terms of PNL's are widely used for aircraft noise evaluation and are now an integral part of aircraft noise certification as per FAR 36 (ref 15). For high speed aircraft, jet noise is mainly a problem during the full power takeoff phase of flight and for noise certification purposes. This translates to a sideline noise case. In this section the jet noise suppression characteristics are reexamined in light of the annoyance weighted PNL scale, and also takes into account the changes in jet noise spectra due to atmospheric absorption over long distances (i.e., sideline noise).

The model scale suppressor nozzle data recorded on a 50-ft polar arc in the HNTF was extrapolated to 2128-ft sideline and then converted to PNL's as described in section 2.2.2. In an attempt to generate realistic PNL values the following standard set of aircraft/flight parameters were used in the PNL computation program:

1.	Number of engines:	4
2.	Airplane altitude for max. noise	1000 ft
3.	Engine attitude (angle of incidence + climb angle)	20^{o}
4.	Ambient temperature:	$77^{o}F$
5.	Relative humidity:	70%
6.	Observer location:	2128-ft sideline
7.	Scale factor:	1 to 8

The computed PNL values were derived from free-field noise levels. Presented PNL values include a +3 PNdB correction to represent nominal ground reflection interference adjustments.

4.3.1 ROUND CONVERGENT NOZZLE

A 4.16-in. diameter, R/C nozzle, equivalent to an unsuppressed jet engine nozzle of 6-sq ft exit area (full scale), served as a reference to derive the values of PNdB suppression. Maximum perceived noise levels *normalized* by 10 log ρ^2A are shown in figure 95 compared to a curve predicted using the SAE procedure of reference 6.

The measured values are generally within ±2 PNdB of the SAE prediction. The SAE predicted PNL curve was used in this report to determine multitube-nozzle PNL suppression characteristics.

The R/C nozzle PNL beam patterns are shown in figure 96 for a jet temperature of 1150°F. The results are very similar to the polar SPL beam patterns shown in figures 78 and 79 except that for the higher pressure ratios on a sideline basis, the maximum PNL occurs 10° further away from the jet axis. Another interesting feature is the relatively rapid increase in noise occurring at the 90° angle as the pressure ratio is increased. This increase appears to be related to the spiral-mode flow-instability discussed in section 4.1.1.3.

4.3.2 MULTITUBE NOZZLES

It was shown in the previous section that peak PNL's from R/C nozzles can be *normalized* by $-10 \log \rho^2 A$. Perceived noise from multitube nozzles has to be treated in two parts. The postmerged jet noise which has physical properties similar to a simple jet will normalize by $-10 \log \rho^2 A$. Multitube-nozzle jet noise which is dominated by the premerged jet turbulence noise, on the other hand normalizes with $-10 \log (\rho + \rho_0)^2 A$, (ref. 1). Examples of *normalized* multitube-nozzle peak PNL results are shown in figure 97. At pressure ratios greater than 3.0 postmerged jet noise dominates and PNL values *normalize* by subtracting $10 \log \rho^2 A$. For pressure ratios less than 3.0, premerged jet noise dominates and PNL values *normalize* by subtracting $10 \log (\rho + \rho_0)^2 A$. The PNL *normalization* relationships are useful in making PNL predictions for a given multitube-suppressor/nozzle configuration when engine size and gas conditions are variables.

In order to evaluate sideline noise suppression of various multitube nozzles it is necessary to analyze beam patterns as shown in figures 98 and 99, because the customary way of expressing PNL suppression is "peak-to-peak". As can be seen in figures 98 and 99, the reference R/C nozzle peaks at 130° to 140°, depending on jet velocity, while at the same time the various multitube nozzles peak from 110° to 140° depending on whether premerged or postmerged noise dominates the extrapolated jet noise spectrum.

PNL suppression, over a range of nozzle area ratios, tube numbers and pressure ratios are summarized in figure 100. At the lowest pressure ratio condition the smallest area ratio shows the best PNL suppression. PNL suppression decreases from 10 to 8 PNdB as nozzle AR varies from 2.75 to 6.0. When pressure ratio is increased to 4.0, the larger area ratios show the best suppression. PNL suppression increases from 11 to 16 PNdB as area ratio is varied from 2.75 to 4.5 at PR = 4.0. The jet postmerging noise tends to be dominant at PR = 4.0, and multitube nozzles with greater spacing between tubes (greater area ratios) generate lower noise levels. As area ratio increases beyond 4.5 the premerged jet *shielding* advantage common to multitube nozzles becomes less evident and noise-suppression values decrease.

In general the PNL suppression increases as the number of tubes increase. The 61-tube nozzle provides approximately 5 PNdB more suppression than the 7-tube nozzle. The relatively small differences in noise suppression between 7 and 61 tubes apparently is due to two factors. The first reason is the larger tube diameter for the 7-tube nozzle. The premerged-jet noise spectrum peaks at a lower frequency for the 7-tube nozzle, because of the Strouhal number relationship, causing that noise to be weighted in a region of lower sensitivity to the human ear. Secondly, the postmerged jet-noise levels for a given AR are not significantly different whether the nozzle has 7 tubes or 61 tubes. This means the low-frequency portion of the noise spectrum does not change appreciably with tube number.

4.3.2.1 Sideline Noise Suppression versus Static Thrust Loss

Static thrust loss characteristics of multitube nozzles are discussed in detail in volume 4 of this report. To get the proper perspective on the relative importance of various suppressor components on noise suppression and associated thrust losses it is necessary to compare the suppressor results as shown in figures 101 through 104. It must be remembered, however, that these values of sideline noise suppression versus percent of static thrust loss are derived from model-scale test configurations and their absolute values are very dependent on the care and ability to fabricate scaled test hardware. In some instances thrust performance gains are made with increased hardware scale as will be shown in volume 10 in the discussion of full-scale test results.

Several observations can be made from PNL suppression versus the percent of thrust loss: (1) variations in tube length affect thrust grossly, but has little effect on suppression; (2) the noise-suppression to thrust-loss ratio improves as velocity (or pressure ratio) increases. An exception to this is when jet postmerging noise dominates at very high pressure ratios; (3) better noise-suppression to thrust-loss ratios occur as the tube number decreases; however, high levels of suppression are attained only by a large number of tubes.

At low pressure ratios, i.e., PR = 2.0 and T_T = 1150°F, representative of engine power-cutback conditions the smaller AR multitube nozzles provide the highest noise-suppression to thrust-loss values. At high pressure ratios, i.e., PR = 4.0 and T_T = 1150°F, representative of engine power takeoff conditions, the nozzles with an AR of 4.5 tended to provide the best suppression to thrust-loss values.

The noise suppression/thrust loss characteristics for the 7-, 19-, 37- and 61-tube, AR 3.3 nozzles are summarized in figure 105. As pressure ratio increases from 2.0 to 4.0, the 61-tube nozzle reaches a noise suppression plateau of 13.5 PNdB while the 7-tube nozzle appears capable of improving its suppression values at higher pressure ratios. This is partly due to the slightly greater tube-spacing ratio common to the 7-tube, AR 3.3 nozzle which provides relatively less jet postmerging noise. Greater tube-spacing ratios delay jet coalescence and reduce the jet postmerging noise. Although the multitube-nozzle noise data shown in figure 105 came from nozzles with the same nozzle area ratios, the tube-spacing ratios between tubes in the outer row in the peripheral direction varied as follows:

Nozzle	Tube Spacing Ratio*
7 Tubes, 3.3 AR - CPA	1.717
19 Tubes, 3.3 AR - CPA	1.687
37 Tubes, 3.3 AR - CPA	1.667
61 Tubes, 3.3 AR - CPA	1.66

*Tube spacing ratio is defined here as the distance between tube centers divided by tube exit diameter.

4.3.3 MULTITUBE NOZZLES WITH HARDWALL EJECTORS

The general characteristics of suppressor nozzles with hardwall ejectors have been discussed in sections 4.1.2 and 4.2.3. The extrapolated sideline PNL's show similar trends, e.g., loose-fitting hardwall ejectors, because of insufficient length, have little effect on suppression values. An ejector with too small an AR relative to the nozzle can result in wall scrubbing accompanied by excessive noise suppression loss. The major effect observed in the suppressor/ejector results on the PNL scale is the more pronounced directivities shown in figure 106. At the lower nozzle pressure ratio (PR = 2.0) all of the ejectors beam towards 110^{o} and then as the pressure ratio is increased, the beam pattern swings to 130^{o} at PR = 4.0.

The actual sideline noise peak PNL reductions for this particular set of nozzle/ejector combinations are shown as a function of jet velocity in figure 107. The 2.6 AR ejector experienced excessive wall scrubbing from the jet efflux for PR $>$3.0 resulting in structural vibrations and rapid loss in noise suppression with velocity. The bare nozzle attained 13 PNdB suppression compared to approximately 16 PNdB with the best hardwall ejector.

4.3.3.1 Sideline Noise Suppression versus Static Thrust Loss

Static thrust loss characteristics of multitube nozzles with ejectors are discussed in detail in volume 4 of this report. An example demonstrating the impact of ejector thrust performance on acoustic evaluation of suppressor systems is shown in figure 108. Under static conditions, most ejectors will augment the overall thrust of an exhaust system. Compared to a bare multitube nozzle, an ejector suppressor will have a *gain* in the thrust coefficient as shown in figure 108. The amount of thrust augmentation depends on many factors as discussed in volume 4, hence the example shown should not be interpreted as being typical of all ejector systems. A case in point is the sharp change in thrust performance between the AR 3.1 and 3.7 ejectors. The 3.7 AR ejector was not long enough to achieve fully-mixed exit conditions and consequently suffered a degradation of both thrust and acoustic performance. For the example shown in figure 108, the best suppressor/ejector system showed a combined performance of 16 PNdB for 1.5% thrust *gain* versus the bare multitube nozzle of 12.5 PNdB for 1% thrust *loss*.

4.4 JET NOISE CHARACTERISTICS OF IRREGULAR MULTITUBE NOZZLES

The jet noise characteristics of regular multitube-nozzle arrays have been discussed in great detail in the previous sections. There is no reason for restricting jet noise suppressor nozzle design to so called regular arrays which have the same tube diameters and equidistant spacing of the elements. It is quite possible that irregular tube spacing and element size may have some distinct advantages. To investigate these possibilities various additional suppressor nozzles were designed and tested and the results and conclusions are reported below.

4.4.1 RADIAL-ARRAY MULTITUBE NOZZLES

The geometric description of radial-array nozzles is given in section 3.0. The philosophy behind the radial-array multitube nozzle was essentially to improve thrust performance by providing unrestricted radial paths for ambient air to ventilate the nozzle base plate and thus

reduce the base drag as described in volume 4. The noise charaeteristies of radial arrays were found to be similar, but not the same as regular arrays of the same tube number and nozzle AR.

Sound power calculations show that the premerged noise levels for radial arrays are slightly higher than for the corresponding regular arrays (fig. 109). The premerged noise beam patterns in figures 110 and 111, on the other hand, are very similar. Therefore, the increase in premerged jet noise is thought to be due to a combination of loss in shielding by the outer row of tubes and to the lengthened premerged jets radiating more high-frequency noise because they are spaced further apart in the radial array. Postmerged jet noise levels in figure 112 are unaffected by the type of tubular array, but the beam patterns in figures 113 and 114 show a shift away from the jet axis. This change in directivity of the postmerged jet noise is strongest at the higher jet velocities and will consequently affect extrapolated sideline PNL's. It has been found that the sideline PNL's for radial-array nozzles are higher than for corresponding regular arrays causing the jet noise-suppression levels relative to a R/C nozzle to be lower by approximately 1 PNdB, as shown in figures 115 and 116.

4.4.2 COMBINATION MULTITUBE/FLOW ANNULUS AND CENTERBODY NOZZLE

The geometric description of this compound nozzle containing tubes in the outer row, surrounding an annular flow passage and a centerbody, is given in section 3.0. This nozzle was tested to see whether the jet efflux from the outer row of tubes could effectively shield annulus-flow mixing noise in the center of the jet. The nozzle was designed to simulate the 61-tube, 3.3 AR, close-packed-array nozzle in the following aspects (fig. 117): (i) the nozzle-array diameter was made equal, (ii) the two outer rows of 42 tubes were identical in size and spacing.

The annulus flow around the centerbody became the variable parameter.

A comparison of sound power spectra is shown in figure 118 between the regular 61-tube nozzle and a range of annulus sizes with the 42-tube nozzle. It ean be seen that the premerged noise levels compare reasonably well; the small changes in level are the result of increased elemental jet length for the zero-annulus configuration and postmerged noise overlap for the 1.067-in. annulus configuration. It is the low-frequency, postmerged jet noise that shows the most dramatic differences. These differences can best be explained by examining the flow profiles in figure 119. The annulus flow is attached to the tapering centerbody and does not mix with the ambient air as rapidly as does the tubular flow round the periphery leaving a high velocity core a long distance downstream which accounts for the high postmerged jet noise levels. In contrast, when the annulus is closed off completely, the peripheral jet flows mix out without attaching to the centerbody, resulting in very low postmerged velocities and correspondingly low noise levels. This latter-type of flow is characteristic of separated flow on the centerbody which invariably is associated with high nozzle-base-pressure losses.

The sideline PNL suppression attained by the annulus-type nozzles are compared with the 61-tube nozzle in figure 120. At the lowest jet velocity (PR = 2.0) the noise suppression values are identical for annulus heights up to 0.533 in., beyond which a fall-off takes place. At higher jet velocities where the postmerged jet noise levels become dominant, all the annulus configurations are inferior to the regular 61-tube design for the reasons explained above.

4.4.3 MULTITUBE NOZZLES WITH VARYING OUTER-TUBE-ROW CHARACTERISTICS

A set of multitube nozzles was tested to evaluate the effectiveness of the jets in the outer row of a multitube nozzle in shielding the noise from the central cluster of jets. This part of the study was performed using only nozzle geometric variations. Variations in gas dynamic conditions in the outer tube row will be discussed in section 4.5.5.

The regular-array, 61-tube nozzle was used as a geometric and acoustic reference. A second 61-tube nozzle was tested which had the 24 tubes in the outer row canted outward (see section 3.0 for description) to delay the jet merging action with the central cluster of jets, as well as with each other, in the outer row. The delay in jet merging was thought to be a means of reducing low frequency postmerged jet noise, provided that the premerged jet noise shielding remained unaffected. This could also be thought of as a means of increasing the multijet AR without changing the nacelle diameter of an engine. A third multitube nozzle was tested which had the 24 tubes in the outer row replaced by 48 smaller ones of the same equivalent flow area as described in section 3.0. This nozzle then had a total of 85 tubes, except that the central cluster of 37 tubes was still the same as in the regular 61-tube nozzle. The purpose of the 85-tube nozzle was to see if the reduced element size in the outer row would lead to lower premerged noise levels (up to 3 dB) provided that the shielding of the noise from the central cluster was not degraded.

4.4.3.1 Sound Power Characteristics

A comparison of the total SPL's of the three nozzles is shown in figure 121 for a range of jet temperatures and nozzle pressure ratios. No conclusive trends can be seen in the data from this point of view. Separating the power spectrum into its components of premerged and postmerged jet noise yields a clearer picture.

The normalized premerged jet noise power levels are shown in figure 122 for the various configurations tested. For jet velocities up to 2000 ft/sec, the premerged jet noise level varies as the 4th to 5th power of V_J. For jet velocities greater than 2000 ft/sec the sound power increases at about the 2.7th power of V_J. Next, figure 122 shows that canting of the outer row of tubes has led to higher premerged jet noise levels (up to 1 dB) probably because the delayed mixing resulted in an increased length of the premerged jet region. On the other hand the 85-tube configuration shows a decrease in the premerged jet noise levels of about 1.5 dB which is less than the expected 3 dB if shielding by the outer jets had been maintained.

The flow through the smaller tubes in the outer rows was blocked off selectively to investigate the effect of spacing between the outer jets and the central cluster. Figure 122 shows that when the shielding jets are closer to the central cluster they are more effective in reducing premerged jet noise than when they are spaced further away. There must be some optimum distance between the outer shielding jets and the central cluster as shown in figure 123.

Multitube-nozzle postmerged jets have flow properties similar to a simple jet as discussed in section 4.1.1.2. It was also suggested that postmerged jet-core velocity and density could be calculated from simple round-jet mixing theory by choosing an appropriate axial location that corresponded in cross-sectional area to that of the multitube-nozzle array. Such calculations were performed to obtain ρ_c and V_{Jc} for the various multitube nozzles enabling normalized

postmerged jet noise power levels to be compared in figure 124 with the typical jet noise power curves reproduced from figure 56. It can be seen that the 61-tube nozzle's postmerged jet noise is close to the predicted "clean" jet curve. The 85-tube nozzle's postmerged jet noise is about 3.5 dB higher because the smaller jets in the outer rows mix-out faster leaving a smaller diameter, higher velocity jet core. Canting the outer row of tubes outward is shown to be beneficial for postmerged jet noise reduction because of the increase in the flow AR in the postmerged jet region.

The relative comparison of premerged and postmerged jet noise power levels is shown in figures 125 and 126. In all cases the postmerged jet noise increases more rapidly with nozzle pressure ratio than does the premerged jet noise. It can also be seen that the 61-tube nozzles are postmerged jet noise dominated only at the very high nozzle pressure ratios, whereas the 85-tube nozzles are postmerged jet noise dominated over almost the whole jet velocity range. Blocking the outer row of tubes on the 85-tube nozzle reduced the premerged jet noise relative to the nozzle with the second row of tubes blocked.

Combining the results of the premerged and postmerged jet noise power levels for the basic nozzles in figure 127, it can be seen that for a given nozzle AR it is possible to manipulate the component noise levels by changing the characteristics of the outer row of elements. These tests were not designed to determine the degree of optimization possible with these methods.

4.4.3.2 Jet Noise Directivity Characteristics

The premerged jet noise peak frequency band directivity characteristics are shown in figures 128 and 129 for the three multitube-nozzle configurations. The premerged jet noise beam patterns are quite broad as is typical for multitube nozzles. There are only small differences in the beam-pattern shape among the three nozzle configurations over a wide range of nozzle pressure ratios ($2.0 \leq PR \leq 3.8$). Typically the premerged jet noise peaks between 110^{o} and 130^{o} on a polar basis. Extrapolated sideline beam patterns, especially on a PNL basis, become more directive as will be shown in the following section.

The postmerged jet noise peak frequency band directivity characteristics are shown in figures 130 and 131. The postmerged jet noise is more directive, peaking closer to the jet axis (140^{o} to 155^{o}) and it exhibits the typical jet velocity trend where with increasing velocity, the postmerged jet noise peaks further away from the jet axis. Figures 130 and 131 also show that the 85-tube nozzle, postmerged jet noise, relative to the 61-tube nozzle, is much higher at angles closer to the jet axis than at other angles.

4.4.3.3 Perceived Noise Level Suppression

The test data from the three multitube nozzles were extrapolated to a 2128-ft sideline and converted to the PNL scale to provide a subjective evaluation of the manipulation of the flow from the outer row of tubes. The normalized results are shown in figures 132 and 133 as a function of jet temperature and velocity together with a standard noise curve for the unsuppressed round jet. The PNL suppression values relative to the R/C jet are shown in figure 134. Because the premerged jet noise levels of the 85-tube nozzle are lower than the 61-tube nozzle it shows higher suppression levels at the lower pressure ratios. At the higher nozzle

pressure ratios the 85-tube nozzle starts to lose its advantage because the postmerged jet noise becomes significant. Blocking the outer row of tubes in the 85-tube nozzle had a small advantage at the lower pressure ratios compared to blocking the second row of tubes. This is the same trend that was observed with the premerged jet noise power results in section 4.4.3.1.

The sideline PNL directivity characteristics for the multitube nozzles are shown in figure 135 for two jet velocities. At the lower jet velocity premerged jet noise dominance causes the PNL to peak between 120^{o} and 130^{o} followed by a very rapid fall-off as the jet axis is approached. At the higher jet velocity, postmerged jet noise influence in the spectrum tends to broaden the beam pattern mainly by boosting the noise levels close to the jet axis, especially for the 85-tube nozzle.

Therefore it can be concluded that the characteristics of the outer tube row of a multitube nozzle will mainly affect the premerged jet noise component. Proper structuring of the flow in the outer row of tubes can lead to improved jet noise suppression as long as the premerged jet noise component is the dominant noise source. Canting the outer row of tubes outward can be a means of increasing the jet flow AR and thus reducing the postmerged jet noise component when this noise source is dominant. This latter result is achieved at the expense of the delay in the merging of the outer row of jets and higher premerged jet noise levels.

4.5 JET NOISE SHIELDING

The reduction of jet noise can be accomplished either by modifying the noise generation processes or by modifying the transmission paths between the source and the receiver. In the latter case a sound barrier or a shield is used to reflect the sound away from the observer. In this section the principles of gas shields will be discussed together with a simple experiment which was used to demonstrate these principles. Later the shielding concept will be used to discuss and interpret the experimental results from the very complex flow and noise fields of a multitube nozzle with different velocity and temperature characteristics in the outer tube row relative to the inner cluster of jets.

A number of papers have treated the problem of sound propagation through fluids with changing thermodynamic properties and velocity. The problem of sound refraction in the atmosphere when the wind is blowing was treated by Lord Rayleigh (ref. 16). Rayleigh gave the conditions which must be satisfied by the acoustic waves as the media varies. He showed that the phase velocity and wave-number component tangent to a plane of constant properties must be the same for the waves on each side of the plane. It is these conditions which are responsible for the cutoff phenomena (to be explained later) which is the most valuable characteristic of the gas layer shield.

Miles (ref. 17) developed the solution for the reflection and transmission coefficients of sound at a single flow discontinuity. He also pointed out that the vortex sheet (the discontinuity in velocity) could become unstable and that a resonance could occur which amplified the incident sound waves. Miles solved the problem of plane waves incident on a plane discontinuity. All other similar papers on the subject have also used plane waves and plane discontinuities and it is these conditions which limit the application of past theoretical work to the jet noise problem.

Ribner (ref. 18) also treated the single discontinuity problem in terms of the equivalent aerodynamic problem of flow over a wavy wall. Ribner pointed out that three fundamentally different phenomena can occur: (1) ordinary reflection and transmission, (2) total reflection with an exponentially-decaying disturbance in the second medium, and (3) amplified reflection and transmission. He also examined the energy balance and concluded that the moving fluid is the source of energy for the amplified waves.

Yeh (ref. 19) solved the problem of two surfaces of discontinuity which gives a layer of fluid between two semi-infinite regions. He unfortunately used the wrong boundary conditions, but he published a corrected solution in reference 20. It is this solution which has been used to generate the curves presented in this report.

There seemed to be only one published experimental study of the shielding phenomena. Jones (ref. 21) performed an experiment using an 0.75-in.-diameter cold jet as the noise source and a sheet of acetylene flame as the shielding layer. His experimental results showed a 7 dB maximum noise reduction. For measurements made perpendicular to the jet there was good agreement between theory and experiment, but for angles closer to the jet axis, the trends of the theory did not agree with the data. A possible explanation is that the disagreement between theory and experiment occurred because the distributed nature of the noise source (the jet) was not accounted for in the theoretical calculations. Although not a good check of the theory, nor an optimum configuration, Jones' experiment did demonstrate that noise reduction is possible with a shielding gas layer and that the concept should be pursued further.

4.5.1 ANALYTICAL APPROACH FOR A TWO-DIMENSIONAL MODEL

Yeh's theoretical model (ref. 20) was used to calculate the results given in this report. The geometry of the model and the resulting equations are shown below. Some theoretical results are then discussed.

The model consists of three semi-infinite layers of moving fluid separated by vortex sheets. The layers may have different velocities, densitites, sound speeds and specific heat ratios, however, the properties of each layer are assumed uniform within the layer. A sketch of the physical model and nomenclature of the problem are shown in figure 136.

The wave configuration in figure 136 shows ordinary reflection and transmission. The incident pressure is a plane wave of wave number, k_0, incidence angle, θ_0 and unit amplitude, |1|. The reflected wave has an amplitude, |R| and leaves vortex sheet A with an angle, θ_R (= 180 - θ_0). Part of the incident wave is refracted at A, penetrates into the shielding layer (region one) and travels at an angle, θ_1. This wave is then incident on vortex sheet B, again undergoes reflection and refraction, with the final transmitted wave of amplitude, |T| propagating into region two. The reflected waves in the shielding layer have not been shown in the figure because they do not appear in the final solutions for |R| and |T|.

The above description is not the only way the waves can be configured in the problem. There are a number of possible wave patterns, depending on the incident wave angle θ_0, the fluid properties and velocities in the three regions. These configurations will be discussed after the equations are introduced.

The equations which describe the wave propagation through the three-layered region are given below. It is assumed that the waves are all periodic and plane and that the problem is steady state. The vortex sheets are assumed to have negligibly small deflection due to the sound waves and to be hydrodynamically stable.

Continuity of wave number and phase velocity at the vortex sheets give the following equations of constraint.

$$k_o \operatorname{Sin} \theta_o = k_1 \operatorname{Sin} \theta_1 = k_2 \operatorname{Sin} \theta_2 \tag{5}$$

$$k_o(V_o \operatorname{Sin} \theta_o + c_o) = k_1(V_1 \operatorname{Sin} \theta_1 + c_1) = k_2(V_2 \operatorname{Sin} \theta_2 + c_2) \tag{6}$$

Applying the boundary conditions of continuity, pressure, and displacement at the vortex sheets and then solving for the complex amplitude of the reflected and transmitted waves gives

$$R = e^{2ik_o d \operatorname{Cos} \theta_o} \frac{[(1 - \Gamma_1 \Gamma_2) \operatorname{Cos}(k_1 d \operatorname{Cos} \theta_1) - i(\Gamma_1 - \Gamma_2) \operatorname{Sin}(k_1 d \operatorname{Cos} \theta_1)]}{[(1 + \Gamma_1 \Gamma_2) \operatorname{Cos}(k_1 d \operatorname{Cos} \theta_1) + i(\Gamma_1 + \Gamma_2) \operatorname{Sin}(k_1 d \operatorname{Cos} \theta_1)]} \tag{7}$$

$$T = \frac{2e^{ik_o d \operatorname{Cos} \theta_o}}{[(1 + \Gamma_1 \Gamma_2) \operatorname{Cos}(k_1 d \operatorname{Cos} \theta_1) + i(\Gamma_1 + \Gamma_2) \operatorname{Sin}(k_1 d \operatorname{Cos} \theta_1)]} \tag{8}$$

where Γ_1 and Γ_2 are defined as

$$\Gamma_1 = \frac{\rho_o c_o^2 \operatorname{Sin} 2\theta_1}{\rho_1 c_1^2 \operatorname{Sin} 2\theta_o} \tag{9}$$

$$\Gamma_2 = \frac{\rho_1 c_1^2 \operatorname{Sin} 2\theta_2}{\rho_2 c_2^2 \operatorname{Sin} 2\theta_1} \tag{10}$$

Equations 5 through 10 are the solution of the wave equation for the problem. They are rearranged below to give some physical insight into the phenomena and to show the effect of flow and the fluid properties.

4.5.1.1 Interpretation of Analytical Results

Because of the constraints on continuity of wave number and phase velocity at the vortex sheets (equations 4 and 5), there are ranges of angles for the incident wave which completely change the character of the solution. Solving equations 4 and 5 for $\operatorname{Sin} \theta_1$ gives

$$\operatorname{Sin} \theta_1 = \frac{\frac{c_1}{c_o} \operatorname{Sin} \theta_o}{1 - \left(\frac{V_1 - V_o}{c_o}\right) \operatorname{Sin} \theta_o} \tag{11}$$

As long as the value of the right side of the equation lies in the range of minus one to plus one, θ_1 is real and a wave propagates into region one. When the value is outside this range, θ_1 becomes complex and the character of the solution changes so that instead of a propagating wave, an exponentially decaying disturbance occurs in region one. An identical relationship exists for θ_2 in terms of the wave and fluid properties in regions one and two. Setting Sin θ_1 and Sin θ_2 equal to ± 1 gives equations for θ_0 and θ_1 in terms of the acoustic speeds and velocities of the regions. The angles thus determined are called the cut-off angles.

The cut-off angle θ_1 is shown as a function of the velocity difference between the layers in figure 137. Curves are shown for three values of the sound speed ratio. The regions of wave transmission and exponential decay are indicated. It is seen that increasing the sound speed ratio increases the region of exponential decay.

There is a region (not shown) at high relative speeds where wave motion again appears and there is considerable amplification of the incident sound waves. This region lies outside the range of variables pertinent to the shielding problem.

There is no energy propagation associated with the exponential disturbance. All of the incident energy is reflected at the interface ($|R| = 1.0$). If region one were infinite in the negative y direction, the exponential disturbance would decay to zero and there would be no further effect. However, region one is of finite thickness and regions one and two are generally moving relative to one another. As a result of the finite thickness, vortex sheet B has small ripples due to the exponential disturbance. If the relative velocity between regions one and two is supersonic (based on the sound speed in region two), then waves are produced in region two. The energy for these waves comes from the flow, not from acoustic transmission through region one. The transmission coefficient $|T|$ will have a finite but generally small value.

From the above discussion it is seen that *cut-off* does not generally mean total isolation of region two from the noise in region zero, but it will be shown in the numerical results to follow that the attenuation is quite large for flows of practical interest. Because of the large attenuation in the cut-off region, it is desirable to adjust the properties and velocities to cause as large a cut-off region as possible. In particular, since the source of the noise generally has an angle of maximum intensity, it is desirable to insure that this angle falls within the cut-off region for the shielding layer.

In order to demonstrate the potential of noise reduction by gas shielding, a numerical example is evaluated below. The theoretical noise reduction was calculated using a three layer shielding model.

The following conditions were assumed in figure 136:

(a) Mach number equals one in regions 0 and 1 and Mach number equals zero in region 2.

(b) Sonic speed ratio between the shielding gas (region 1) and region 0 of two (shielding gas temperature approximately 1500°F). Ambient air (region 2) and region 0 have the same sonic speed.

(c) All flows have the same static pressures and specific heats.

The equations can be arranged so that the shielding layer thickness, d (region 1) always appears in combination with the wave number of the incident wave, k_o. Thus the results can be applied to any configuration by choosing appropriate values of d to correspond with the wave number of the major noise source.

It should be noted that a constant wave number does not imply a constant frequency because of the motion of the fluid. The relation between the frequency received by a stationary observer and the wave number in region zero is

$$f = \frac{k_o}{2\pi}(V_o \operatorname{Sin} \theta_o + c_o). \qquad (12)$$

There are two incident wave cut-off angles for the assumed flow condition. The region zero - region one interface (fig. 138) has a cut-off at $\theta_o = 160.5^o$ and the region one - region two cut-off is at $\theta_o = 210^o$. The first cut-off (160.5^o) is the most important.

Incident waves with angles from 90^o (jet axis) to 160.5^o are completely reflected at the interface. An exponentially decaying disturbance exists in region one and there is greatly reduced transmission to the surroundings (region two). Figures 138 and 139 show the theoretical transmission and reflection coefficients as a function of the incident wave angle for a representative value of $k_o d$, The cut-off range includes the angles of maximum noise intensity for jets (approximately 135^o in these coordinates) thus the shielding layer would be very effective. If the sonic speed ratio between regions one and zero (c_1/c_o) is reduced to 1.5 (which corresponds to a temperature of approximately 625^oF for the shielding flow), the cut-off angle becomes 150^o which still includes the angle of maximum noise intensity.

It must be emphasized that the noise reductions for an actual jet would not be as large as indicated in figure 138. The distributed noise sources will create waves which will reach the observer by different paths through the shielding layer. The observed noise will be a weighted average which includes the source characteristics as well as the shielding layer effects.

There are two ranges of incident wave angle where there is amplification of the sound (figure 138). The first range from 158^o to 165^o has less than 1 dB amplification and is negligible for that reason. The second range from 208^o to 213^o has up to 5 dB amplification. However, no acoustic energy propagates upstream in a supersonic jet, therefore, this region is of no physical significance for this problem.

Figure 140 shows the transmission coefficient spectrum for a few values of the incident wave angle. In the cut-off region ($90^o \leq \theta_o \leq 160.5^o$) the transmission coefficient is a monotonic decreasing function of k_o and becomes very small (large negative value of 20 log |T|) as the incident wave angle approaches the jet axis ($\theta_o = 90^o$). In the transmission region ($160.5^o \leq \theta_o \leq 210^o$) the transmission coefficient is a periodic function which oscillates with increasing frequency and decreasing amplitude as θ_o is increased.

For the angle of maximum jet noise (135^o) the spectrum shows that all but the very lowest frequencies are strongly attenuated. For example, if d = 1 ft, there is 5 dB of attenuation at 30 Hz.

One important result seen in the transmission coefficient spectrum is that as long as the angles for maximum jet noise intensity lie in the cut-off region, the shielding layer thickness d can be small and still provide substantial attenuation.

Figure 141 shows the angle of the transmitted wave as a function of the angle of the incident wave. The refraction effect of the shielding layer gives a shadow region $90^{o} \leq \theta_2 \leq 150^{o}$. In the range from $90^{o} \leq \theta_1 \leq 160.5^{o}$ a very weak wave exists in region two because there is cut-off at the region zero - region one interface. From $162.5^{o} \leq \theta_1 \leq 210^{o}$ there is transmission at both interfaces and for $210^{o} \leq \theta_1 \leq 270^{o}$ the region one - region two interface has cut-off and there is only an exponentially decaying disturbance in region two.

The calculated results for the above example show that a substantial noise reduction can be obtained with the gas-layer shielding concept. Because of the simplified theoretical model the calculated attenuation in the cut-off region is larger than could be expected for the actual flow. A better estimate of the actual attenuation could be obtained from further experimental and theoretical work.

4.5.1.2 Experimental Verification of the Gas Shielding Concept

A simplified experiment was conducted to verify the theoretical gas shielding concepts developed in the previous sections. The experiment was designed to model the theoretical problem as closely as possible. A two-dimensional heated jet was used as a shielding layer. Acoustic waves were generated by a point source located sufficiently far away from the shielding jet, so that plane waves could be considered as impinging on the shield.

The experimental apparatus consisted of a two-dimensional nozzle, an acoustic source and an array of microphones. A schematic of the test setup is shown in figure 142. The nozzle had a nominal exit height of 1 in. and width of 12 in. giving an eccentricity of 1/12. The contraction ratio was 8. The air was taken from the plant's air supply, heated with an in-line burner and diffused into a plenum before entering the nozzle. Temperature and pressure measurements were made in the jet to ensure that an adequately two-dimensional flow was obtained and to provide necessary inputs for the theoretical analysis. The shield exit pressure ratio was 1.3 and the exit's total temperature was 700°F.

An oscillator, amplifier and driver with horn were used for the narrow band acoustic source. The source was placed 10 ft from the shield to obtain approximately plane acoustic waves at the shield. The source was moved along a 10-ft arc to vary the incident sound-wave angle while maintaining a constant distance from the shield.

The transmission loss across the shield was determined by measuring the change in source intensity just behind the shield with and without the shield in operation. Both narrowband filtering and crosscorrelation techniques were used for data reduction. Because of the limited source sound intensity and the proximity of the microphones to the shield, there were some operating conditions for which the shield noise completely masked the source. For these conditions, crosscorrelation between the electrical input to the source and the microphone signal was used to extract the source signal. Reduction of the same data by both techniques showed ±1 dB agreement for the measured transmission loss.

Precautions were taken to ensure that the actual transmission loss was being measured. Initially, the transmission loss across the shield was determined for four transverse microphone positions behind the shield. It was desirable to minimize the shield noise level at the microphone without receiving sound-source energy diffracted around the shielding jet. Baffles were erected to reduce diffraction around the shield.

The positions of the noise source (driver) and of the microphones are given in the following table:

Microphone No.	x in.	z in.	(y = 0)
1	8	2.5	
2	12	3.0	
3	16	3.5	
4	20	4.0	

DRIVER POSITIONS (aimed at x = 12 in., z = 0 in.)

θ_o (Nominal)	x in.	z in.
90	12.0	-120.0
100	-8.8	-118.2
110	-29.0	-112.8
120	-48.0	-103.9
125	-56.8	-98.3
130	-65.1	-91.9
135	-72.8	-84.8
140	-79.9	-77.1

The results of this simple test are shown in figure 143. The test results in general verify the trends predicted by the theory. At angles between 90^o and 120^o from the jet inlet axis there is very little, if any, transmission loss. Beyond 120^o, when the jet axis is approached, there is significant noise reduction which correlates well with the predicted noise cutoff.

4.5.2 JET NOISE SHIELDING EFFECTS INHERENT IN MULTITUBE JETS

Many investigators in the past have conjectured that the observed premerged jet noise suppression characteristics of multitube nozzles were due to some form of shielding of the noise from the central cluster of jets by the outer row of jets.

Middleton and Clark (ref. 22) have suggested that the flow from a multitube nozzle which is visible to the observer (fig. 144) is chiefly responsible for the noise radiated to the far field from the premerged jet region. An efficiency factor for the noise generated by one jet in the outer row of a multitube array is described as being $(1/2 + 1/n_o)$ where n_o is the number of tubes in the outer row of the array.

The efficiencies of equal-sized tubes may be added so their total output is equal to $(n_o/2 + 1)$ which is the total efficiency e_n. The difference in dB levels, according to Middleton and Clark,

between the noise of an equivalent area simple jet and that due to a multitube nozzle with tube diameters of d is

$$10 \log \frac{d^2 e_n}{D^2} \tag{13}$$

Gray, Gutierrez and Walker (ref. 23) proposed a premerged jet shielding hypothesis which assumes that noise generated within the jet cluster of a multitube nozzle cannot radiate through the outer mixing zone of a jet in the outer row. In order to achieve shielding, it is further assumed that the spreading initial-mixing zones of adjacent outer jets merge together and form a scalloped shield (fig. 144), upstream of the axial location of maximum noise generation. The spreading scalloped shield region generates the premerged jet noise observed by a far-field observer. The premerged noise is related to the mixing region defined by the angle θ and the number of jets in the outer row.

$$\theta = 2 \left[90^o - \sin^{-1} \left(\frac{1/2 + s\,(x/d)}{1 + g/d} \right) \right] \text{for } 120^o \geqslant 90^o \tag{14}$$

$$\theta = 2 \sin^{-1} \left(\frac{1 + g/d}{1 + 2s(x/d)} \right) \qquad \text{for } \theta \leqslant 90^o \tag{15}$$

The ratio of θ to 360^o may be interpreted as the radiation efficiency of each tube in the outer row.

s is the jet spreading slope, approximately 1/10

x/d is the distance downstream where maximum noise is generated, a variable depending on M_J

g/d is the tube-to-tube gap-diameter ratio, peripheral spacing ratio between tubes in the outer row

As part of the multitube nozzle premerged jet noise analysis in this program, an alternate shielding hypothesis was developed. The region of a supersonic jet where maximum noise radiation occurs is near the end of the supersonic core (ref. 13). According to H. Lu (ref. 12), the maximum kinetic energy in a supersonic jet occurs in the region near the end of the potential core. If one associates noise level with jet kinetic energy it follows that maximum turbulence-noise generation will occur at the end of a potential core. This noise could very well be channeled down the jet by shock structure and radiated out to the far field where the jet becomes subsonic. If this is the case the geometry of merging flows in a multitube nozzle at the end of the elemental jet's potential core may be a significant relationship in premerged jet noise.

The radius of the 10% V_J contour in a simple jet is approximately equal to the fully-expanded jet diameter. This was determined for pressure ratios ranging from 2.0 to 4.0 using H. Lu's method for jet flow definition. Assuming that significant turbulence noise occurs in the jet

mixing region where adjacent flows have not merged, the acoustie effieieney of eaeh tube in the outer row can be estimated:

$$e_n = \frac{180 + \frac{360}{No} - 2\cos^{-1}\frac{s}{2d}}{360} \qquad (16)$$

No is the number of tubes in the outer row
s is the spacing between nozzle axis
d is the fully-expanded elemental jet diameter

The amount of premerged jet turbulence noise suppression one may expect from this relationship is:

$$\text{PWL suppression} = -10 \log \left(\frac{180 + \frac{360}{No} - 2\cos^{-1}\frac{s}{2d}}{360} \right), \text{dB} \qquad (17)$$

To evaluate the above hypotheses, as well as generate additional test data that could give more insight into this subject of shielding, a speeial test program was eonducted. A 61-tube, 3.1 AR nozzle was used in a dual-flow mode, where one heated air source supplied the eentral eluster of 37 tubes and a second heated air source supplied the outer row of 24 tubes. The air sourees could be controlled for pressure ratio and temperature independently of eaeh other. Initially a test was conducted where the nozzle was run first with one air supply (37 central tubes) then with the seeond air supply (24 outer tubes) and finally with both flows (61 tubes). Figure 145 shows the results of this test in terms of sound power speetra. The low frequeney peak of the spectrum, eaused by the postmerged jet turbulence, experiences a large reduetion in level when the outer row of 24-tubes-only is operating. There is no signifieant differenee in premerged jet noise level apparent between the 24-tube and 61-tube cases. This provides good support for the argument that the outer row of jets from a multitube nozzle ean effectiveiy shield the premerged jet noise generated by the innermost jets.

The noise power level normalized for differences in the nozzle exit area are shown in figure 146 as a function of jet velocity. The 24-tube configuration attained 9.6 dB suppression. The 61-tube configuration, premerged jet noise levels were approximately the same as the 24-tube eonfiguration, however, beyond 2550 ft/sec thc 61-tube nozzle shows less noise. At this point the total noise level of the 61-tube nozzle shows a marked increase in level due to the eontribution of postmerged jet noise. Apparently, there are ehanges oeeurring in the region where the jets merge whieh may be a funetion of nozzle pressure ratio or jet veloeity causing a transfer of energy from the premerged jet to the postmerged jet. The greater demand for secondary flow by the eentral jets as pressure ratio increases eauses the axes of the outer jets to bend inwards resulting in a shorter premerged jet region.

The 24-outer-tube or annulus configuration resulted in a constant 9.6 dB suppression for the velocity range of 2072 ft/see to 2771 ft/sec. This annulus array of jets probably does not experience a significant ehange in the geometry of the jet merging region, since the demand for secondary air inside the array is much less than for the 61-tube configuration. The 24-annulus-tube eonfiguration noise data provides an opportunity to eheck the geometric

shielding hypothesis expressed by Middleton and Clark (ref. 22) and Gray, Gutierrez and Walker (ref. 23) and the procedure developed in this program.

The results of the predicted noise reductions relative to a round nozzle of equal area using the above three methods are summarized in figure 147. All three methods fall short of the 9.6 dB suppression measured. This could mean that another mechanism of suppression is involved besides the geometric shielding concept and is not accounted for in any of the three methods.

In the late fifties, Greatrex (ref. 24) published the results of an experimental program with two parallel jets in close proximity. These tests with subsonic jets indicate the radiated noise can be reduced beyond the value expected from geometric shielding depending on jet separation distance, (fig. 148). About 2 to 2.5 dB additional reduction of jet noise was realized at an $s/d \approx 1.5$. Rollin, (ref. 25) noticed a reduction in jet noise power which approached an optimum at a spacing ratio of 1.5. In this study a greater reduction in noise power resulted when the flow was supersonic.

Consequently possible explanation to the reduction in noise beyond that expected from geometric shielding is the existance of acoustic and/or flow-mutual coupling between adjacent jets which could result in (1) lowered acoustic efficiency in the turbulence noise generation mechanism or (2) cancellation of turbulence noise by the phase relationships set up between the adjacent jets' noise producing regions.

4.5.3 JET NOISE SHIELDING BY TEMPERATURE AND VELOCITY CONTROL IN MULTITUBE JETS

The 61-tube nozzle, used in the dual-flow test setup described in section 4.5.4, was further tested to evaluate the effect of temperature and velocity control in the outer row of jets on the overall shielding characteristics of jet noise. The tests were conducted by keeping the flow conditions constant in the central cluster of 37 tubes and varying either temperature or pressure ratio in the outer row of 24 tubes. The following sets of test data were acquired.

Primary Supply (Central 37 Tubes)			Secondary Supply (Outer Row of 24 Tubes)		
PR_1	T_{T1}	$V_{J1(ideal)}$	PR_2	T_{T2}	$V_{J2(ideal)}$
3.8	1500°F	2771 ft/sec	1.64	1500°F	1772 ft/sec
			2.05	1500°F	2105
			2.7	1500°F	2438
			3.8	1500°F	2771
			1.98	1000°F	1772
			2.73	1000°F	2105
			4.1	1000°F	2438
			3.8	1070°F	2438
3.8	1500°F	2771 ft/sec	3.8	690°F	2105

Primary Supply (Central 37 Tubes)			Secondary Supply (Outer Row of 24 Tubes)		
PR_1	T_{T1}	$V_{J1(ideal)}$	PR_2	T_{T2}	$V_{J2(ideal)}$
2.73	1000°F	2105 ft/sec	2.0	500°F	1439
			3.0	500°F	1772
			1.54	1000°F	1439
			1.94	1000°F	1747
			2.73	1000°F	2105
			1.38	1500°F	1443
			1.64	1500°F	1772
			2.05	1500°F	2105
			2.7	1500°F	2438
2.73	1000°F	2105 ft/sec	2.73	580°F	1772
2.0	1000°F	1784 ft/sec	1.4	1500°F	1474
2.0	1000°F	1784 ft/sec	1.2	1500°F	1095
			2.0	1500°F	2072
			2.5	1500°F	2351
			3.0	1500°F	2548
			3.5	1500°F	2697
			3.8	1500°F	2771
NO FLOW					
2.0	1500°F	2072 ft/sec			
2.5	1500°F	2351			
3.0	1500°F	2548			
3.5	1500°F	2697			
3.8	1500°F	2771			
			NO FLOW		

4.5.3.1 Noise Power Characteristics

The jet noise shielding by temperature and velocity control of the flow from the outer-tube row was first analyzed from the noise power point of view. Figures 149 through 153 show the 1/3-octave-band power spectra arranged so that comparisons can be made on the basis of constant secondary total temperature (T_{T2}), pressure ratio (PR_2) or fully-expanded jet velocity (V_{J2}).

A high temperature, low velocity flow from the outer row of tubes can be used to shield the high frequency jet noise as shown in figure 149. Keeping the secondary flow temperature constant, while decreasing the flow velocity, further decreases the high frequency noise levels. This indicates that the noise level is predominantly due to the noise generated by the outer tube row. An estimated power spectrum for the noise generated by the central cluster of 37 tubes has been included to provide a gross indication of the noise shielding offered by the outer row of jets. Estimated spectrum was derived from 61-tube test data by adjusting the pre- and postmerged parts of the power spectrum by the following method.

It was assumed that the postmerged jet noise is proportional to the total flow area while the premerged jet noise was proportional only to the outer row jet flow area. Figure 145 shows that these assumptions for estimating the 37-tube-array noise level from 61-tube measured data is justifiable, as long as the jet velocities are high enough to provide adequate shielding. The comparison in figure 149 between the estimated and measured power spectra also assumes superposition of noise levels to hold true. It is recognized that the latter is a gross assumption since secondary effects of mutual coupling between jet elements, crossflow mixing effects and relative velocity effects have been ignored. Nevertheless, figure 149 shows that dropping the jet velocity in the outer Tube row decreases the premerged jet noise power level. It is very interesting to note in figure 150 that similar shielding and noise reduction effects can be achieved when the flow temperature in the outer tube row is lower than the central cluster.

The effect of varying the secondary flow velocity by varying the flow temperature (i.e., constant nozzle PR) is shown in figure 151. It shows again that the premerged jet noise part of the spectrum is determined by the flow velocity in the outer row of tubes. Figures 152 and 153 provide further evidence that the velocity in the outer tube row is the significant parameter, because variations of secondary nozzle pressure ratio and jet temperature show very small changes in noise power levels.

In the above spectral comparisons the jet flow density effects have been ignored. In order to take the density effects on the premerged jet noise generation into account, the premerged jet noise total power was calculated and then normalized with respect to the flow area and gas density in the outer row of jets. First, the 61-tube nozzle data is shown in figure 154 where all the jet elements have the same gas conditions (monoflow). This normalized premerged jet noise power curve was used as a reference in the following comparisons. Figures 155 and 156 show again that as the jet velocity in the outer row of tubes is reduced shielding of the noise from the inner cluster of jets becomes less effective. Secondly, for a given velocity, the lower-temperature flow in the outer row of tubes seems to form a more effective shield than does a hot flow.

The multitube nozzle's postmerged jet noise power is a function of the mean postmerged jet flow conditions and is not significantly affected by velocity gradients in the premerged jet region. Figure 157 shows the postmerged jet noise power levels from the dual-flow tests, and even though the flow conditions in the outer tube row were varied over a wide range of jet temperature and velocity, there is little effect on postmerged jet noise power levels. The gas conditions of the 37 tubes in the central cluster dominate the postmerged jet noise power.

4.5.3.2 Jet Noise Directivity

The above discussion showed that the outer row of jets appeared to shield the premerged jet noise generated by the central cluster of jets. It was shown that shielding was mainly a function of the jet velocity and temperature in the outer tube row. The previous discussion, however, provided only a gross overview of the problem, because the refraction effects of velocity and temperature flow profiles can not be seen from sound power results. The refractive effects can only be obtained from directivity curves.

A typical set of directivity curves is shown in figure 158 for the peak 1/3-octave band of the premerged jet noise. These data have been normalized for the flow area and gas density in the outer row of jets. The noise levels stratify as a function of the jet velocity in the outer tube row (V_{J2}) which was also shown previously in figure 151. Using the monoflow 61-tube data as a reference, it is possible to further normalize the directivity curves according to the velocity exponents shown in figure 154 (i.e., -10n log V_{J2}/V_{J1}(, where n = 3.1 for $V_{J2} >$ 2000 ft/sec and n = 4.3 for $V_{J2} <$ 2000 ft/sec). When the directivity curves are normalized for the jet velocity, good agreement is seen in figure 159 for the example where the outer row of tubes effectively shields the noise from the inner cluster. Choosing an example where the shielding effectiveness of the outer jets has been reduced we get the results shown in figures 160 and 161. First, figure 160 clearly shows the refractive effect at angles greater than 120°. This effect was discussed in sections 4.5.2 and 4.5.3 and can be represented schematically as shown in figure 162. The outer row of jets forms a hot turbulent gas sheath around the central array of jets. Noise generated by the higher-velocity inner jets radiates through this cylindrical sheath. At angles close to the jet axis the noise is cut-off (see section 4.5.2) while at higher angles it passes through the sheath and probably gets refracted. Lu (ref. 26) has developed a more complex analysis technique for the calculation of sound propagation paths through fluid layers. Using his prediction technique a simulated case of the 61-tube nozzle was computed and the results obtained are shown in figure 163. These results again show the large noise reductions due to refraction at angles close to the jet axis.

The directivity curves in figure 161 have been normalized for the jet velocity differences in the outer row. The normalized curves show that the noise levels at 130° to 160° approach a noise floor which is caused by the noise generated by the outer row of jets.

The noise levels between 90° and 120° are indicative of the shielding effectiveness of the outer row of jets. Because the data at these angles does not collapse as it did in figure 159, it is assumed that the levels shown are representative of the noise leakage from the central cluster. The directivity curves over the arc of 90° to 120° were found to be approximately parallel to each other for all the cases tested with dual flow. This meant that a generalized trend for the effects of shielding over the arc 90° to 120° could be derived as follows. In this derivation a simple superposition of noise components was assumed. A comparison was made between three typical measured noise curves in the form presented in figure 164. The curves were:

Curve a, noise measured for outer 24 jets
Curve b, noise measured for inner 37 jets
Curve c, noise measured for all 61 jets

The apparent shielding of the noise from the inner cluster of 37 jets is given by subtracting curve a from curve c. This apparent shielding is replotted in figure 165 as a function of velocity of the shielding outer row of jets. This curve applies only to the case where the inner cluster of 37 jets is operated at V_{J1} = 2771 ft/sec. For other primary jet conditions other shielding curves could be derived using the above approach.

The model for explaining multitube-nozzle, dual-flow premerged jet noise characteristics which emerges from the analysis of measured data may be described by the schematic shown in figure 166. When the outer row jet velocity is substantially lower than the inner central-

array jet velocity, a very peaked premerged jet noise beam pattern results. The central-array jets tend to dominate the 90° to 130° arc noise level, while the outer-row jets tend to dominate the 140° to 160° arc noise level. The central-array jet noise is attenuated in the 90° to 120° arc by the outer-row jet flow due to acoustic impedance (ρc) mismatch and turbulance scattering. In the 120° to 160° arc the central-array jet noise is greatly attenuated by severe refraction and reflection of noise by the outer row jet turbulence. There is an indication that this severely refracted noise is being radiated downstream, affecting overall noise levels in the 150° - 160° arc. There is probably a relative velocity effect on central-array jet noise levels which will tend to decrease the source of premerged jet noise also. There may be mutual coupling effects (flow and/or acoustic) between the outer row of jets and the inner array of jets which will affect premerged jet noise levels. The test data from this program, however, is insufficient to resolve quantitatively all the mechanisms involved in dual-flow premerged jet noise characteristics.

The postmerged jet noise beam patterns of a wide range of outer-tube row gas conditions are shown in figure 167 for the peak 1/3-octave postmerged jet noise band. The beam patterns are very similar to that from the 37-tube cluster alone and appear to be little affected by jet velocity variations in the outer tube row. The directivity characteristics of the dual-flow test series is best summarized in figures 168 and 169. Comparing the beam patterns of the monoflow case of the 61-tube nozzle with various dual-flow configurations, it can be seen that the low frequency, postmerged jet noise characteristics are not affected while significant changes are observed in the high frequency premerged jet noise domain. The premerged jet noise effects are characterized by two phenomena: shielding effects by the outer row of jets in the arc between 90° and 120°, and refractive/reflective effects at angles beyond 120°.

4.5.3.3 Perceived Noise Level Suppression

These dual-flow multitube nozzle tests were run primarily to provide jet noise suppression technology information to better understand jet noise suppression mechanisms. Consequently, jet noise suppression in absolute terms is incidental to these studies. However, for completeness of analysis the effects of the major jet noise variables were also evaluated on the PNL scale. The most logical basis for the PNL evaluation would be to make the comparisons on a constant thrust basis. But, since thrust could not be measured in the dual-flow mode of the test facility, a very close approximation is to evaluate the results at constant nozzle pressure ratio. Figure 170 shows the peak sideline PNL suppression attained by the 61-tube nozzle. It can be seen that relative to the monoflow case, noise suppression is improved by reducing the jet temperature in the outer tube row. Conversely, an increase in the outer jet temperature degrades the jet noise suppression. These changes in the peak sideline noise suppression, however, are simply due to changes in the premerged jet noise levels as a result of jet velocity variations in the outer tube row.

4.6 APPARENT JET NOISE-SOURCE DISTRIBUTIONS AND RELATED FLOW PROFILES

Identification of noise source locations in jet flows is of utmost importance in jet noise suppressor studies. Coupled with flow profile data, source location information can give further insight into the jet noise generating mechanisms. The experimental technique used was the "wall isolation technique" of Potter and Jones (ref. 3) and MacGregor and Simcox

(ref. 4). R/C nozzle and multitube suppressors, with and without hardwall ejectors, were evaluated. The following nozzle and jet variables were evaluated:

- Jet temperature
- Jet velocity
- Nozzle tube number
- Nozzle AR
- Type of nozzle tube array
- Nozzles with hardwall ejectors

The results from the source location tests are reported in this section.

4.6.1 NOISE-SOURCE DISTRIBUTION VARIATION WITH JET TEMPERATURE

Tests were conducted with a R/C nozzle and a 37-tube, AR 3.3 nozzle to determine the temperature effect on noise-source locations. Figures 171 and 172 show the apparent distances from the nozzle exit plane of the centers of the noise-producing volumes of the jets in the various 1/3-octave bands. The nozzle pressure ratio was kept constant (PR = 3.0) while the temperature was varied from 500°F to 1150°F. It can be seen that jet temperature has only a small effect on the axial distribution of the acoustic sources both in simple and multitube nozzle jets. The postmerged jet noise sources in the multitube jet appear to show a minor downstream movement with increasing jet temperature. The lack of movement of the high-frequency noise sources with jet temperature can be explained by using Nagamatsu's argument (ref. 13) that in supersonic jets the peak noise-source locations occur at the tip of the supersonic core which is only pressure ratio (Mach number) sensitive (fig. 173). The postmerged jet noise sources of a multitube jet occur in a subsonic flow region and hence do not follow the above argument. Instead, they are simply a function of mean jet velocity which is higher for the hot jet as shown by the flow profiles in figure 174. These higher velocities delay the decay of the postmerged jet and thus the low-frequency noise sources are found further downstream.

Since jet noise sources of any given frequency band occur over a large volume, looking at source location results in terms of peak values, figures 171 and 172, may not be sufficient. Hence, to see if jet temperature changes have any additional effects not perceptible in figures 171 and 172 the data is shown in figures 175 and 176 for a jet flow region whose boundaries represent a reduction in sound power of one half from the maximum or -3 dB. No new trends with jet temperature can be seen. It is interesting to observe, however, how compact the high-frequency noise-source volume is for the multitube jet as compared to the simple conical jet. Secondly, the high-frequency jet-noise sources occur very close to the multitube-nozzle exit plane.

4.6.2 NOISE SOURCE DISTRIBUTION VARIATION WITH NOZZLE PRESSURE RATIO

Tests were conducted with a R/C nozzle and a 37-tube, AR 3.3 nozzle where the jet temperature was kept constant at 1150°F and the nozzle pressure ratio varied between 2.0 and 4.0. The resultant distributions of the peak noise sources are shown in figures 177 and 178. It is quite apparent that significant changes in source locations occur with varying pressure ratio for the R/C nozzle, lesser variations are seen for the multitube nozzle. The

trend shown is for the noise sources to move downstream with increasing nozzle pressure ratio. As pointed out in section 4.5.1 the noise-source location trends in supersonic jets can be related to the supersonic core tip which is a function of jet Mach number and nozzle diameter. Since Mach number is a function of nozzle pressure ratio, the core lengths and the high frequency noise sources are PR dependent. Figures 177 and 178 show the supersonic core lengths relative to the test data and generally confirm the measured noise-source location trends. The multitube nozzle results in figure 178 do not appear to show as large a variation with pressure ratio only because the data has been normalized with respect to the equivalent R/C nozzle diameter. The premerged jet noise sources are characterized by the elemental jet dimensions and hence *appear* to be more compact relative to the single (large) R/C jet in figure 177.

The postmerged jet, low frequency noise sources are dependent on the local subsonic velocities in the source regions and consequently as the velocity increases with pressure ratio (fig. 179) the noise sources appear to be displaced downstream.

4.6.3 NOISE-SOURCE DISTRIBUTION VARIATION WITH NOZZLE TUBE NUMBER

It has been pointed out in previous discussions that tube number is one of the key variables in a multielement-nozzle noise signature. By holding the nozzle-array area ratio and jet gas conditions constant and varying tube number from 7 through 61, the results shown in figure 180 were obtained. The results from a R/C nozzle are also included for comparison purposes. The general trend is again for the premerged jet noise band peaks to correlate with the tip of the supersonic core. If the results are normalized with respect to the unsuppressed R/C nozzle, they show a progressive shift of the noise sources closer to the nozzle exit plane as the tube number is increased. This comes about for two reasons; first the elemental jet diameter decreases with increasing tube number, and secondly, the spacing between adjacent jets decreases causing the individual jets to mix-out sooner and thus affecting noise source characteristics. Figure 180 shows very little change in the high frequency source locations between the 37- and 61-tube nozzles. This is thought to be due to a lack of resolution in this particular noise-source measurement and analysis technique which prevents accurate source determinations to be made very close to the nozzle exit plane so that most of the test data tends to become asymptotic to X/D = 1.2.

Postmerged jet, low frequency noise characteristics of multitube nozzles have been shown in previous discussions to be independent of tube number variations, and the results in figure 180 generally tend to confirm this. The 7-tube nozzle results appear to deviate slightly from the other nozzles at the low frequencies but this is thought to be associated with data repeatability when trying to determine the peak value of a relatively flat, broad source distribution. The flow-profile results in figure 181 tend to further substantiate the low frequency noise characteristics with varying tube number because it clearly shows how both the 7- and 61-element jets mix out to achieve very similar velocity profiles in the postmerged jet noise-source region.

4.6.4 NOISE-SOURCE DISTRIBUTION VARIATION WITH NOZZLE AREA RATIO

The multitube-nozzle area ratio is the other major geometric variable affecting jet noise. Far-field noise analysis has shown AR to mainly affect the low frequency postmerged jet noise. Noise-source location results for a 37-tube nozzle series of varying area ratios are shown in

figure 182. Based on noise-source characteristics discussed in preceding sections, the premerged, high frequency sources should correlate with the elemental supersonic core tip. Figure 182 shows this to be generally true for the smaller area ratios (AR $\leq$ 3.3). For area ratios greater than 3.3, the jet element spacing becomes large and the interior jet cores are not well shielded acoustically by the outer jets. The jet cores in the center of the nozzle cluster appear to be stretched, showing an apparent displacement of noise sources in the downstream direction.

As expected, the postmerged jet, low frequency noise sources are shown in figure 182 to be very sensitive to AR change. The mixing rates of multielement jets are quite different for different area ratios as shown by the flow profiles in figure 183. A larger AR nozzle with accompanying larger jet spacing is able to entrain more ambient air to the center of the jet cluster to more rapidly mix the jet flows and achieve lower mean velocities in the postmerged jet noise-source region.

4.6.5 NORMALIZATION OF NOISE-SOURCE DISTRIBUTION RESULTS FOR REGULAR ARRAY NOZZLES

The jet noise-source location results have been discussed in terms of various nozzle geometric and gas parameters. It is clear from these discussions that for multitube nozzles the noise sources fall into two categories of premerged or postmerged jet noise sources. The source characteristics of each region are quite different and are governed by different nozzle parameters, hence they are best analyzed separately.

The premerged jet noise-sources are primarily associated with the supersonic core tip of the elemental jets. Nozzle AR, or elemental jet-spacing ratio appears to be a second order effect. An empirical test data collapse has been obtained for all of the premerged jet noise frequencies as shown in figure 184. The data covers supersonic jet velocities for nozzle pressure ratios between 2.0 and 4.0 and jet temperatures between 550^{o}F and 1150^{o}F. Since premerged jet noise is related to individual elemental jet characteristics it is not surprising that the R/C nozzle data also normalizes with the multitube data. It should be reemphasized that this normalization procedure is limited to symmetrical close-packed arrays of multitube nozzles.

The postmerged jet noise sources have been shown to be primarily a function of nozzle AR and jet velocity. An empirical collapse of the test data has been obtained for nozzle-exit gas conditions ranging over pressure ratio from 2.0 to 4.0 and jet temperature of 550^{o}F and 1150^{o}F as shown in figure 185. Postmerged jet noise-source locations of course, will not correlate with round convergent jet data as premerged jet sources did in figure 184.

4.6.6 NOISE-SOURCE DISTRIBUTION CHARACTERISTICS OF IRREGULAR NOZZLE ARRAYS

The noise source characteristics of close-packed arrays have been discussed in section 4.5.1 through 4.5.5. Many deviations from a close-packed array are possible, but only two examples will be examined here; the radial array and the composite array of a nozzle containing tubes, a flow annulus and a centerbody.

The radial-array nozzle results are compared with the close-packed arrays in figure 186. There does not appear to be any significant effect on the premerged jet noise characteristics. The

postmerged jet, low frequency sources are stretched out further downstream for the radial array. The flow-profile results in figure 187 show that although ventilation in the outer rows of tubes is improved, the higher density of primary flow in the center of the cluster of jets is not well ventilated, maintaining a high velocity core for a long distance downstream.

The 42-tube-annulus-centerbody nozzle was a duplicate of the 61-tube, AR 3.3 nozzle as far as the nozzle peripheral dimensions were concerned. Therefore, it is not surprising to see that the premerged jet high frequency noise-source characteristics in figure 188 are identical. The reason for the differences in the postmerged jet low frequency source locations can be seen in figure 189 of the flow profiles. Although the flow from the outer row of tubes was mixing at the same rate for both nozzles, the annulus flow in the center of the composite nozzle was attaching to the centerbody and thus failed to mix with the ambient air.

The 42-tube-annulus nozzle thus shows very large centerline velocities in the postmerged jet noise region leading to a stretched-out source volume.

4.6.7 NOISE-SOURCE DISTRIBUTION VARIATION WITH HARDWALL EJECTORS

In the preceeding discussions that noise distribution characteristics of a number of multitube nozzle configurations have been established. A selected number of these nozzles were subsequently fitted with a series of hardwall ejectors and the resultant changes in their respective noise distribution characteristics were observed.

In the test program, ejector lengths were held constant at $L/D_E = 2.0$, while their diameters were varied to obtain different ejector area ratios (2.6, 3.1, and 3.7). Jet conditions at the nozzle exit were the same as for the bare multitube-nozzle series (NPR = 3.0 and $T_T = 1150^{\circ}F$).

Generally, the effect of an ejector installation on a multitube suppressor is to displace the sources downstream without necessarily changing the shape of the curve. Figure 190 shows the source-location results of four bare-suppressor nozzles and the downstream shift of the sources when an ejector is installed. The similarity in the curves in the presence of an ejector, particularly in the mid- to high frequencies implies that similar acoustic generation mechanisms exist in the premerging region. The ejector shields these high frequency sources and delays their appearance for approximately one ejector-length as is evidenced in the four cases of figure 190. The source distribution curves also show that the low frequency, jet noise-source locations of the bare suppressor versus the ejector cases approach one another.

Flow profiles and centerline velocities (fig. 191) indicate that at a given axial station in the postmerged jet region of a multitube flow, with and without an ejector, the geometry and gas conditions are very similar and hence, account for the similar source locations that are observed.

The greatest ejector effect on source locations is the one observed between tight and loose ejectors on the very high frequencies. These sources are seen to shift or bulge further downstream when the ejector is tight. Figure 190b shows this high frequency source shift when the loose 3.7 AR ejector is compared to a 3.1 AR ejector. Figures 190c and 190d also show that a high frequency, downstream bulge is present. This tight-ejector phenomena is best explained by observing in figures 191 and 192, the ejector-exit flow profiles which indicate a high velocity spike at the ejector lip. This is conceivably due to flow attachment to the ejector wall. As a

result of this flow attachment in a tight ejector, the higher velocities at the ejector lip are responsible for a new shear region generating additional high frequency noise sources which are additive to those radiating from inside the ejector. Consequently, the second high frequency jet noise-source region shows up as the bulge in the source-location curves in figure 190. For loose ejectors the mixing process is not as efficient and the high lip-exit velocities are not observed and no additional source regions are created.

4.7 FLIGHT EFFECTS ON JET NOISE SUPPRESSION

The use of a modified 9- by 9-ft low-speed wind tunnel for determining jet noise flight effects is being pursued at The Boeing Company. Comparisons with flight test results have shown that meaningful flight-effects information can be obtained with this technique. Because of the acoustic near-field nature of measurement, absolute noise levels are difficult to record accurately between hardware configuration changes. Therefore, the results presented in this section were used only to develop incremental changes with flight velocity. The flight increments measured in the wind tunnel were then applied to acoustic far-field data to generate accurate absolute noise levels.

This section presents the results of the wind tunnel flight effects noise tests for a baseline R/C nozzle and a reference 37-tube suppressor nozzle with and without ejector shrouds.

4.7.1 BASELINE ROUND CONVERGENT NOZZLE

Acoustic near-field spectra measured under static conditions in the wind tunnel are compared with far-field spectra measured in the HNTF for nozzle pressure ratios of 2.0, 3.0 and 4.0. The comparison in figure 193 and 194 is made after the respective data have been extrapolated to a common 100-ft sideline. Because of the distributed nature of jet noise sources it is somewhat meaningless to compare the near-field spectra on an angle basis that is normally referenced to the nozzle exit plane. Therefore, in all this work the comparisons are made for the peak-noise spectra regardless of angle. The near- and far-field peak-noise spectra compare reasonably well and indicate that the near-field jet noise peaks at an angle closer to the jet axis. This is an expected result due to the downstream location of important jet-noise sources. The above comparison was made to establish confidence in the validity of taking what amounts to near-field data and extrapolating it to the far-field and then treating this data as being representative of normal far-field measurements.

Jet noise flight effects for the baseline R/C nozzle are shown in figures 195 through 200. The peak-noise spectra comparisons of figure 195 and 196 include flight spectra at the indicated ideal and relative jet velocities and static spectra having ideal jet velocities that match the flight ideal and relative jet velocities. As shown the static and flight spectra match reasonably well at equal relative velocity. It is noted that the flight spectra were corrected for Doppler frequency effects by shifting all calculated SPL values to the next lower 1/3-octave band. This accounts for source motion past a stationary observer that is not inherent to a wind tunnel test.

The curves of OASPL and PNL versus relative jet velocity (fig. 197) show that peak jet noise is significantly reduced by flight. Further, the flight noise level can be estimated by applying the relative velocity principle to the static data (interpolate static data at flight relative

velocity). The slope of the OASPL/velocity curve varies with jet velocity, however, in the subsonic to sonic region the relationship follows a V_J^8 to V_J^9 characteristic.

The flight effect at angles closer to the inlet is a strong function of nozzle pressure ratio. Figures 198 through 200 show the results for a near-field angle of 130°. At these angles the low frequency part of the spectrum contains facility burner noise and hence those frequencies have been cut out from the analysis. Previous near/far-field comparisons show that this angle is equivalent to a far-field angle of 100° to 110°, again due to the source-location effect. At pressure ratio 2.0 the flight spectra compare favorably with the static spectra at equal relative velocity (fig. 198). At pressure ratio 3.0 and 4.0 (fig. 198 and 199) the flight effect is considerably different from the pressure ratio 2.0 case and is due to the presence of shock noise. The near-field data includes both screech and broadband shock noise. As indicated the screech frequency is reduced slightly by external velocity and if anything is higher in level. The broadband level appears to be reduced slightly but this is likely due to the jet noise component being reduced.

The comparison of static and flight OASPL and PNL versus relative velocity (fig. 200) shows that the pressure ratio 2.0 flight noise level is consistent with relative velocity. The pressure ratio 3.0 and 4.0 flight noise levels are obviously not predictable using relative velocity. It is very difficult to directly relate the observed near-field flight effect to far-field for this situation. The 130° near-field data has a jet noise component representative of a low far-field angle (100°) while the shock noise component may be more representative of a different far field angle (130° or less) depending upon source location and radiating characteristics of this noise source. Consequently each source (jet and shock) must be evaluated independently.

In order to assess a far-field flight effect it is necessary to isolate the jet and shock noise components (fig. 201). This may be done by the use of jet noise prediction techniques. The jet noise component will be reduced in flight and can be estimated by applying the relative velocity principle. Based on this test it is recommended that the shock noise component remain unchanged by flight velocity. The two sources are then added to define the predicted flight noise level for the particular angle of interest.

4.7.2 MULTITUBE NOZZLE

Acoustic near-field spectra measured under static conditions in the wind tunnel are compared in figure 202 with near- and far-field spectra measured in the HNTF at nozzle pressure ratios of 2.0 and 3.0. The spectra are representative of the peak noise in each case. The low frequency part of the wind tunnel spectra containing burner noise has been removed. The high frequency premerged jet noise dominates the peak noise levels of this nozzle and the near-field spectra appear to correlate well between the two facilities. The comparison with the far-field spectra does not appear as good at the postmerged jet noise low frequencies as it does at the higher premerged jet noise frequencies. But this is expected because the near-field spectra should show a lower noise level in the postmerged jet frequency range (50 Hz to 200 Hz) for the 130° angle due to the downstream source location of this noise component. The premerged jet mixing noise is generated close to the nozzle exit plane and for this reason the premerged jet mixing noise radiates more like a point source and near- and far-field signals are essentially the same for a given angle. It is concluded that the near-field wind tunnel signal is representative of the far-field if noise-source locations are properly accounted for. Premerged jet mixing noise flight effects may be related directly on an angle to

angle basis. Postmerged jet mixing noise flight effects can only be evaluated by analysis of wind tunnel data not influenced by burner noise. This occurs at angles near the jet axis where burner noise radiation is weak and postmerged jet mixing noise is prominent.

Jet noise flight effects for the 37-tube suppressor nozzle are provided in figures 203 through 207. Static and flight peak noise spectra comparisons are shown in figure 203 for PR 4.0. The flight spectra compare reasonably well with static spectra at equal relative velocity. The experimental results of section 4.5.4 show that the premerged jet mixing noise of a multi-tube suppressor is dominated by the outer row of tubes. For this nozzle configuration, the entrained velocity around the outer tubes is probably rather low during static conditions. Consequently external flow will decrease the relative velocity of the outer tubes and therefore substantially reduce the mixing noise of these elements. If it is assumed that the outer jets undergo a full relative-velocity effect ($V_{J1} - V_\infty$), then the flight noise reduction follows a slope greater than the static data. This is possible because the static data reflect not only a changing primary jet velocity but a different flow structure due to the changing pressure ratio.

Static and flight OASPL and PNL directivity comparisons are shown in figures 204, 205 and 206, for pressure ratios 2.0, 3.0 and 4.0. At PR 2.0 the flight reduction of OASPL and PNL is consistent with static data at equal primary relative velocity for all of the angles shown. The peak flight noise angle is relatively unchanged for OASPL but appears to shift slightly toward the inlet for PNL (3^o to 4^o).

At pressure ratios 3.0 and 4.0 the flight reduction of OASPL and PNL exceeds the static predicted values at angles above 120^o. The reason for this is that the peak premerged jet mixing noise flight reduction is greater than the static throttle curve would predict (fig. 208). At angles less than 120^o the flight noise reduction becomes progressively less. This is thought to be the result of premerged jet shock noise that appears to be prominent in the near-field spectra at low angles. The far-field spectra do not appear to reflect this component, consequently it may be a highly directive noise source that either does not radiate strongly to the far-field (bow-shock phenomena) or radiates at an angle less than 90^o (not measured in the far field). On this basis it is expected that the far-field noise levels will be reduced during flight at all angles above 90^o consistent with the wind tunnel results above 120^o.

The curve of peak OASPL and PNL versus relative velocity in figure 207 indicates that the relative velocity simulation of flight noise reduction will provide a good estimate at PR 2.0 and a somewhat conservative estimate at PR 3.0 and 4.0. The slope of this curve and the resultant flight effect is dominated by the premerged jet mixing noise. The flight effect on postmerged jet mixing noise is obscured at the lower angles due to burner-noise performance. The postmerged jet mixing-noise flight effect is evaluated in figure 209 and is considered to be representative of all angles. A frequency of 100 Hz was selected as a near-peak postmerged jet mixing frequency and is consistent with the Strouhal relationship for the mixed jet. The velocity chosen for comparison is the relative velocity of the merged jet as obtained from downstream velocity profile measurements. As indicated the flight noise level compares reasonably well with the static value at equal relative velocity. This is consistent with flight effects for the uniform flow R/C baseline nozzle.

4.7.3 MULTITUBE NOZZLES WITH HARDWALL EJECTORS

Acoustic near-field spectra measured under static conditions in the wind tunnel are compared in figure 210 with near- and far-field spectra measured in the HNTF. The comparisons are made for peak noise at PR = 4.0 for a loose ejector (AR = 3.7). Similar spectrum comparison with an AR = 3.1 ejector could not be made because of microphone calibration errors discovered after the test. Again, the premerged jet high frequency noise compares reasonably well with normal far-field measurements and justifies the wind tunnel technique for interpreting flight effects.

Jet noise flight effects for the 37-tube nozzle with an AR = 3.1 ejector shroud at lower pressure ratios are shown in figures 211 through 214. This configuration is referred to as having a tight fitting shroud since the shroud and tube array have essentially the same effective AR. Static and flight peak noise spectra are compared in figure 211 for PR 3.0. The reduction of premerged jet mixing noise due to external flow is seen to be quite small. Internal pressure measurements indicate that entrained air velocities surrounding the outer row of tubes is substantial during static operation (the order of 500 ft/sec). With the tunnel on the entrained velocity increases only slightly (on the order of +20 ft/sec for a tunnel velocity of 280 ft/sec). Thus the premerged jet mixing noise that is dominated by the outer-tube relative velocity is essentially unaffected by external flow. A slight decrease in frequency due to Doppler effects is favorable to aft quadrant PNL reduction during flight and is accounted for in the analysis.

Static and flight OASPL and PNL directivity comparisons are provided in figures 212 and 213 for PR = 2.0 and 3.0 operation. As shown, there is a moderate peak-noise reduction at PR = 2.0 but no reduction at PR = 3.0. The flight noise reduction increases at angles near the jet axis and is due to the prominence of postmerged jet noise in this region that is being reduced by the external flow.

Static and flight OASPL and PNL are compared as a function of primary relative velocity in figure 214. This plot shows that the use of relative velocity does not provide a good estimate of inflight noise. The best approach would be to correct static spectra at each angle as follows:

1. Reduce the low frequency postmerged jet mixing noise by interpolating static data as a function of mixed-flow relative velocity.

2. Leave the premerged jet noise levels unchanged.

3. Apply a Doppler frequency shift as a function of flight velocity and angle.

4. Calculate the flight noise level using the corrected spectra. It is noted that a convenient method to account for Doppler frequency shift is to calculate PNL for no frequency shift and a full 1/3-octave-band shift. The desired value at each angle may then be interpolated depending upon the extent of the actual frequency shift at each angle.

Jet noise flight effects for the 37-tube nozzle with an AR = 3.7 ejector shroud are illustrated in figure 215. In contrast to the AR = 3.1 shroud, this configuration is considered to be a relatively loose fitting shroud. Static and flight spectra comparisons are shown in figure 215

for PR = 4.0. The reduction of premerged jet mixing noise is greater than that of the tight-fitting AR = 3.1 shroud (fig. 211), but less than that of the 37-tube nozzle without shroud (fig. 203). Internal pressure measurements for this nozzle indicate that there is a significant increase in outer-tube relative velocity due to external flow. The increase is of the order of 100 ft/sec for a tunnel velocity of 280 ft/sec. The reduction of premerged jet mixing noise is in general agreement with a change in velocity of this magnitude as illustrated in figure 216.

It is interesting to note that the change in premerged jet mixing noise with power setting (pressure ratio) is less for the shrouded configuration than the unshrouded. Internal pressure measurements for the shrouded nozzle indicate that the outer-tube relative velocity change with PR is significantly less than the change in primary velocity. For example the PR = 2.0 premerged jet mixing noise was reduced by about 3.5 dB by throttling from 1870 ft/sec to 1650 ft/sec. The actual change in outer-tube relative velocity is estimated at 160 ft/sec for the throttling increment of 220 ft/sec. Using a V^8 relationship and an estimated internal relative velocity of 1550 ft/sec the reduction in noise level is 3.8 dB for 160 ft/sec and 5.3 for 220 ft/sec. The 3.8 dB compares well with the measured 3.5 dB. The unshrouded nozzle spectra showed a premerged jet mixing noise reduction of about 5 dB for a throttling delta velocity of 280 ft/sec. The V^8 relationship calculates a reduction of 5.6 dB assuming a negligible entrained air velocity around the outer tubes. This tends to indicate that premerged jet mixing noise does respond to outer-tube relative velocity.

Static and flight OASPL and PNL directivity comparisons are shown in figures 217, 218 and 219 for PR = 2.0, 3.0 and 4.0. These curves show that the flight noise levels compare reasonably well with static data at equal primary relative velocity for all angles. The low angle noise is dominated by premerged jet mixing noise while the angles near the jet axis are dominated by postmerged jet mixing noise. Although the outer tubes experience a moderate change in relative velocity (100 ft/sec) due to external flow the effect on jet mixing noise is significant in comparison with the throttling noise reduction. The postmerged jet mixing noise is reduced by airplane velocity in accordance with relative velocity of the mixed jet.

The curve of peak OASPL and PNL versus primary relative velocity (fig. 220) also shows that the flight values can be estimated by interpolating the static data at flight relative velocity. The approach for a loose ejector would require that static spectra be adjusted as follows:

1. Reduce the low frequency postmerged jet mixing noise by interpolating static data as a function of mixed flow relative velocity.

2. Reduce premerged jet mixing noise in accordance with outer tube relative velocity change using a V^8 relationship.

3. Apply a Doppler frequency shift as a function of flight velocity and angle.

4. Calculate the flight noise level using the corrected spectra.

4.7.4 JET NOISE SUPPRESSION WITH FLIGHT EFFECTS

The acoustic flight effects determined from the wind tunnel tests and discussed in the previous sections were applied to the far-field, static test data measured in the HNTF. In that way the

peak jet noise suppression characteristics could be extrapolated to flight. The following summarizes the flight effects as they were applied to the different configurations assuming a flight velocity of 300 ft/sec.

- *Baseline R/C nozzle:* Use the relative velocity relationship therefore interpolate static data at flight V_R to establish flight PNL.

- *37-tube nozzle without shroud:* Use the relative velocity relationship as described above.

- *37-tube nozzle with area ratio 3.7 shroud:* Use the relative velocity relationship as described above.

- *37-tube nozzle with area ratio 3.1 shroud:* Create a flight spectrum assuming a merged-jet relative velocity procedure for postmerged jet noise and no reduction of premerged jet mixing noise. Calculate flight peak PNL using corrected spectra for no Doppler shift and 1/3-octave-band Doppler shift. Interpolate between the two PNL values to account for the expected amount of Doppler shift at the peak angle.

The analysis was done for pressure ratios 3.0 and 4.0 with a primary gas total temperature of 1150°F. The resulting far-field static and flight peak PNL values are shown in the table below for the four nozzles. The static and flight PNL suppressor levels are tabulated as are the changes in suppression due to flight. The flight spectra for the configuration with an AR 3.1 shroud is shown in figure 221. The low frequency level was established by interpolating the static data at $V_{R\ post} = V_{J\ mix} - V_{\infty}$. The high frequency noise level was broken into premerged jet mixing noise and postmerged jet mixing noise. The premerged jet noise remained unchanged while postmerged noise was reduced in the same manner as the low frequency. The two noise levels were recombined to produce the estimated level shown in figure 221.

The results in the table below show the changes in suppression in going from static to flight conditions. At PR = 4.0 a slight gain in suppression is indicated for the 37-tube nozzle and 37-tube nozzle with AR = 3.7 shroud. This is the result of the small change in noise level experienced by the R/C nozzle at high jet velocity. As the pressure ratio is reduced, a significant loss of suppression occurs in flight for each suppressor. The loss is greater for the shrouded configurations than the unshrouded configuration.

STATIC AND FLIGHT PNL FOR REFERENCE CONICAL AND 37-TUBE NOZZLE WITH AND WITHOUT SHROUDS

Nozzle	PR	θ	Static PNL PNdB	Flight PNL PNdB	Static suppression PNdB	Flight suppression PNdB	Flight Δsuppression PNdB
Ref. conical Nozzle	4.0	130°	118.0	114.4			
	3.0	130°	115.3	109.5			
37-Tube (Ref)	4.0	130°	104.9	100.4	13.1	14.0	+0.9
	3.0	110°	101.2	97.0	14.1	12.5	-1.6
37-Tube + AR 3.1 shroud	4.0	110°	104.1	100.8	13.9	13.6	-0.3
	3.0	110°	101.4	99.5	13.9	10.0	-3.9
37-Tube + AR 3.7 shroud	4.0	110°	105.2	101.0	12.8	13.4	+0.6
	3.0	110°	101.6	99.3	13.7	10.2	-3.5

Note: 2128-ft sideline
1000-ft altitude
T_T = 1150°F

5.0 ACOUSTICALLY LINED EJECTORS

The mechanisms of high velocity jet noise suppression with multitube nozzles and hardwall ejectors have been described in section 4.0. It has been shown that the characteristics of a multielement nozzle are such that a large portion of the acoustic energy occurs in the high frequency part of the spectrum (premerging jet noise), as compared to a R/C nozzle of the same flow area. Secondly, these premerged jet noise sources are located relatively close to the nozzle exit plane providing the opportunity for the use of acoustically lined ejectors to further attenuate this component of jet noise. Extensive studies using acoustically lined ejectors for jet noise absorption have been conducted and reported in reference 5. The major objectives of that program (ref. 5) were to experimentally evaluate the application of conventional duct-lining design procedures and scaling relationships to the design of acoustically lined ejectors for jet noise suppression. It was found that the basic design procedure for acoustically lined ducts with airflow could be used as a first approximation for the determination of the lining tuned-frequency and noise attenuation relationships in ejectors. Measured lined-ejector sound power insertion loss, however, was always lower than predicted for the following two main reasons:

- The acoustic sources are distributed within the ejector and are not located upstream of the ejector entrance as the lining prediction procedures normally assume.

- Noise generated downstream of the ejector exit plane, which cannot be attenuated by the lining, may have prevented the true measurement of lining attenuation.

It was concluded in reference 5, that an accurate prediction of lining sound power insertion loss requires the quantitative description of the acoustic source distribution in the ejector together with a knowledge of the way in which acoustic energy propagates through the temperature and velocity gradients inside the ejector.

The work conducted for this program report was essentially an extension of that carried out in reference 5. It consisted of further experimental evaluations of acoustic linings in ejectors, improvements to the semi-emperical lining impedance model with grazing flow and analytical studies to determine the impact of noise-source distribution effects and flow gradient effects on lining attenuation in ejectors.

5.1 TEST PROGRAM RESULTS

Two kinds of acoustically lined ejector tests were conducted in this program. The first was a direct extension of the work of reference 5 and included the use of the same test hardware and the same single-layer acoustic linings. The second series of tests were done in support of the model scale suppressor nozzle system described in volume 6 and consisted mainly of double-layer acoustic lining tests. The results are described below.

5.1.1 SINGLE-LAYER ACOUSTIC LININGS

To complete the work that was undertaken in reference 5, the following single-layer acoustic lining tests were run:

- Using a mix of two lining depths to achieve an increased bandwidth of noise absorption.
- Changing the location of the lining in the ejector to determine most efficient placement of lining.
- Investigate the effect of ejector axial placement on lining efficiency.

The use of distributed single-layer linings has been suggested as a method of increasing the attenuation bandwidth, i.e., making them appear as broadband liners. The technique was to line the upstream half of the ejector with a lining tuned to high frequencies and the downstream half with a lining tuned to lower frequencies, much along the lines of the noise source distribution trends. The results are shown in figure 222 and include constant depth linings of 0.55 inch and 1.0 inch for comparison. The effect of the distributed linings can best be seen at the lower nozzle pressure ratio (PR = 1.4) because the results for the higher pressure ratio are obscured by the high jet-noise levels generated beyond the ejector's exit plane. Figure 222 shows that in principle, the distributed lining concept is feasible and that it will give a broader bandwidth coverage than a given single-layer lining. The amount of improvement attainable can not be presently quantified and will be highly sensitive to the skill of the designer in knowing the flow environment and noise sources inside the ejector and the effect of the noise sources beyond the ejector.

It is commonly accepted that the noise sources in a jet are distributed over a large volume in the axial direction. Assuming convection of the acoustic energy by the flow inside the ejector, the acoustic lining near the exit should be exposed to more jet noise than the lining at the upstream end and consequently should have the potential for absorbing higher jet noise levels. This hypothesis was investigated by alternately lining the upstream half and then the downstream half of the ejector and comparing the results with the fully-lined configuration as shown in figure 223. Again the results at the higher nozzle pressure ratio tend to be obscured by the exterior jet noise levels, but the lower pressure ratio case clearly shows that the same acoustic lining in the downstream half of the ejector can absorb more of the jet noise than in the upstream half. In the PR = 4.0 example, where the jet noise downstream of the ejector is a limiting factor to the amount of jet noise absorption that can be observed from the total system, the second-half-lined configuration provides as much absorption as the fully-lined case. This indicates that in designing acoustic linings the potential for jet noise absorption by a given area of lining should be balanced against the level of the downstream jet noise sources in order to avoid unnecessary lining weight and cost penalties in a given suppressor system.

Finally, the effect of the ejector-inlet opening relative to the nozzle exit plane was investigated from the point of view of noise leakage to the far field, as well as overall ejector positioning relative to the jet noise sources. Tests were run with an ejector in three axial locations relative to the nozzle exit plane as shown in figure 224. When the ejector was in the downstream position it was found that some high frequency noise was radiating from the ejector inlet to the far field, especially at angles close to 90^{o} from the jet axis. This was determined by using an acoustic baffle across the ejector inlet and observing the results as shown in figure 225. Noise radiation from the ejector inlet can affect the acoustic lining effectiveness as observed in the far field for the total suppressor system. The results in figure 224 show that at low nozzle pressure ratios (PR = 1.4) when the premerged jet noise sources are close to the nozzle exit plane and the ejector inlet, noise leakage from the inlet reduces lining effectiveness when the

ejector is in the downstream location. Conversely, at supercritical nozzle pressure ratios (PR = 4.0) the premerged jet noise sources are much further downstream so that moving the lined-ejector axially to enclose more of the premerged jet noise sources more than offsets the noise leakage from the ejector inlet.

The above examples illustrate the importance of having a detailed knowledge of lined ejector characteristics in combination with jet noise-source location information and the radiation paths to the far-field observer.

5.1.2 DOUBLE-LAYER ACOUSTIC LININGS

Acoustic lining theory indicates that multiple-layer tuned linings will absorb sound over a broader bandwidth of frequencies than a single-layer tuned lining. It has been found in practice that a double-layer lining design makes a good compromise between the added complexity, weight and cost of multiple-layer linings and the improvements in acoustic energy absorption. Two sets of double-layer perforated plate acoustic linings were fabricated to support the model-scale suppressor system program described in volume X.

(i) Lining no. 1:

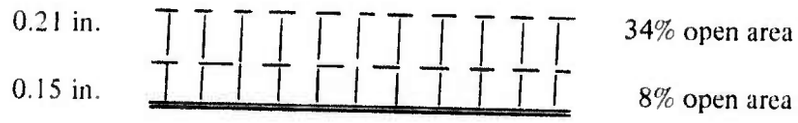

(ii) Lining no. 2:

Lining no. 2 was also fabricated and evaluated full scale on a turbojet engine as described in volume X.

Lining no. 1 was used initially to evaluate the broadband aspects of double-layer designs by comparing it against an equivalent single-layer configuration. The resultant sound-power insertion-loss spectra are shown in figure 226 for a range of nozzle gas conditions. It can be seen that for a given lined-ejector length the double-layer configuration does exhibit broader bandwidth characteristics. Increasing the ejector length naturally increases the insertion loss levels, both as a result of increased lining area as well as enclosure of more jet noise sources within the large ejector. The sound pressure attenuation spectra at various angles from the jet axis are difficult to analyze because of the complex relationships between the radiation characteristics of ejectors and the masking effect of the jet noise sources beyond the ejector exit plane. Examples of measured lining attenuation directivity results are shown in figure 227 to illustrate these difficulties.

Both linings no. 1 and no. 2 were used subsequently to support the final model scale suppressor system (LNHP-2, -3, and -4) evaluation described in volume X. Lining no. 2 was designed as a variant of lining no. 1 to see if similar trends of changes in absorption and tuning would be observed as for single-layer linings reported in reference 5.

Typical results of sound-power insertion-loss spectra are shown in figure 228 for lining no. 2 with the LNHP-2 suppressor system. Variation of power insertion loss with nozzle pressure ratio (jet velocity) can be seen. The double-layer lining was designed to give an approximately flat response between 6.3 and 12.5 kHz which experimentally could only be observed at the lower pressure ratio (PR = 2.0). For the design nozzle PR of 3.0 the broadband nature of the lining is obscured by the postmerged jet noise sources downstream of the ejector. These curves also show that the ultrasonic frequencies from deep within the ejector are absorbed more efficiently than the midfrequencies that occur closer to the ejector exit plane.

Both linings no. 1 and no. 2 were tested with the LNHP-2 suppressor system and their relative characteristics are shown in figure 229. The results indicate that the impedance characteristics of lining no. 1 are closer than lining no. 2 to the optimum required for the particular ejector environment. An increase of about 25% in the sound power insertion loss is observed across the midfrequencies of the spectrum.

As mentioned earlier, the jet noise absorption characteristics of a given lined ejector will be dependent of the noise-source location and flow-gradient properties inside the ejector. These vary with nozzle velocity (power setting) or they can also vary by changing the basic nozzles. In this program an $L/D_E = 2$ ejector with lining no. 1 was tested with the three LNHP series of nozzles and the results are shown in figure 230. The three nozzles had different area ratios, tube sizes and numbers (vol. X), so that both source locations and flow gradients in the ejectors were affected. Consequently the same lined ejector showed different jet noise absorption characteristics. The very complex nature of jet noise absorption by lined ejectors is further illustrated by the directivity patterns in figures 231 and 233. These results are difficult to interpret except for some very generalized observations. As discussed in section 4.2.3, the premerged jet noise from multitube nozzles and ejectors is refracted to and tends to dominate the noise at angles between 90^o and 120^o. At angles between 130^o and the jet axis the dominant noise sources are from the postmerged jet beyond the ejector exit plane and very little of the energy from inside the ejector is directed to those angles. The beam patterns in figures 231 through 233 reflect that hypothesis by showing reduced attenuation levels at angles close to the jet axis. Secondly, high frequency jet noise radiation from ejectors has exhibited a very strong directivity peak at or near 110^o which invariably shows up in lining attenuation beam patterns as an attenuation minimum. This phenomenon is not well understood at present and deserves further study.

5.1.3 FULL SCALE DOUBLE-LAYER ACOUSTIC LININGS

Full scale double-layer acoustic linings were designed and fabricated to support the full scale suppressor-demonstrator program reported in volume X. The full-scale suppressor was five (5) times the LNHP-2 model suppressor's size (linear dimensions), so that the model scale lining depth was also scaled by a factor of five. In other words the full scale lining was tuned

to have a flat frequency response between 1.25 and 2.5 kHz. The full scale lining was also fabricated using perforated plates and honeycomb spacers as follows:

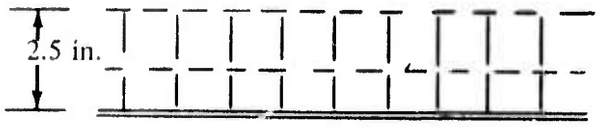

The full scale, acoustically lined ejector was evaluated by first testing a fully lined configuration, and following with a second configuration where the alternate flat panels in the 24-sided ejector were hardwall (i.e., 50% acoustically lined). The latter configuration was representative of a practical SST ejector design where the variable-area secondary nozzle requirement would prevent 100% lining of the ejector. The resultant sound-power insertion-loss curves for the above two configurations are shown in figure 234. These results show that the 50%-lined ejector suffers a penalty in the high frequency absorption as compared to the fully lined case. The fully lined ejector behaves in a similar way to the model scale counterpart in figure 228 when analyzed as a function of nozzle pressure ratio. Increasing the nozzle pressure ratio tends to degrade the overall lining effectiveness.

Lined ejector scaling comparisons are made in figures 235 and 236. Model scale data was selected that most closely duplicated the J-58 engine test conditions of jet temperature and nozzle pressure ratio. The sound-power insertion-loss spectra in figure 235 compare very well when the model scale tuning frequency is displaced by the scaling factor of 5. There appear to be significant differences in the very high frequency absorption characteristics, but these are of secondary importance, when compared to the primary design frequencies which usually lie in the most sensitive annoyance (PNL) range. The very high frequency characteristics shown in figure 235 are thought to be highly dependent of flow profiles in the ejector and they are most difficult to scale in such tests as these. The beam-pattern comparisons in figure 236 show good agreement between the scaled data at angles between 90^{o} 110 110^{o} from the engine inlet axis. At angles closer to the jet axis the full-scale tests achieved higher attenuation levels than the model scale. However, the noise at these angles has little impact on the overall suppressor performance as shown in volume X.

5.2 ACOUSTIC IMPEDANCE OF PERFORATED PLATE LININGS IN THE PRESENCE OF GRAZING FLOW

Acoustic linings in the walls of an ejector shroud are used to absorb the jet noise that is generated inside and which propagates along the ejector with the jet flow. The acoustic linings are exposed to a high-velocity, grazing flow along the surface which has a very large effect on the impedance of the acoustic material. The impedance, in turn, determines the absorption characteristics of the liners. Therefore, the accuracy of acoustic lining attenuation prediction procedures depend very heavily on the accuracy of the lining impedance values in the ejector environment. The current practice is to use semi-empirical mathematical models of the impedance in lining attenuation prediction procedures. Such a mathematical model is given in reference 27. The model has been derived largely from experimental work.

Additional experimental work was conducted under this contract to extend the experimental data base and hence improve the semi-empirical impedance model of reference 27. The experimental evaulations were limited to perforated plates which at the present time are the only practical lining materials for the ejector environment.

5.2.1 EXPERIMENTAL TECHNIQUE

The experimental technique used was the two-pressure method of determining the complex impedance and is based on measuring the sound pressure difference and phase difference across the resonator aperture. Figure 237 shows part of the test section of the facility and the location of the microphones. The acoustic pressure on the surface of the lining is given by p_1 and at the bottom of the cavity by p_2. If the cavity is assumed to have a circular cross-section, the acoustic pressure in the cavity can be written in the form:

$$p_{cav.} = C\, Jn\,(k_r^{(m)} r) \left[e^{-ik_x^{(m,n)} x} + Re^{ik_x^{(m,n)} x} \right] e^{i(n\phi + \omega t)}, \qquad (18)$$

where C is a constant related to the modes of propagation, while R is another constant that can be evaluated. Only plane waves can propagate in the cavity at frequencies below 22,000 Hz for a core of 0.95-cm diameter since higher order modes are cutoff, as shown below for the second lowest mode:

$$\left[\frac{\partial p}{\partial r}\right]_{r = r_o} = 0 \qquad J_1 (k_r^{(m)} r_o) = 0$$

$$k_r^{(1)} r_o = 0 \qquad k_r^{(1)} = 0 \;:\; \text{plane wave}$$

$$k_r^{(2)} r_o = 3.84 \rightarrow f = 22{,}000 \text{ Hz}$$

The equivalent electric circuit of the acoustic panel of figure 237 is depicted below:

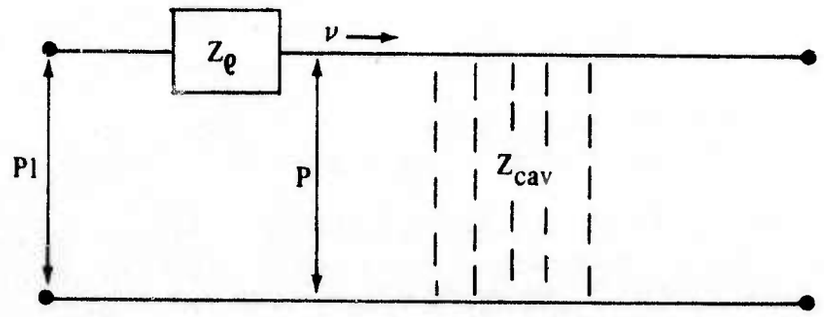

Z_{cav} is known

Z_e is unknown

Then:

$$p_{cav} = p_o (e^{-ikx} + Re^{ikx}) e^{i\omega t} \tag{19}$$

at x = d (bottom of cavity)

$$\frac{\delta p}{\delta x} = 0$$

hence,

$$p_{cav} = p_o \left[e^{-ikx} + e^{ik(x - 2d)}\right] e^{i\omega t} \tag{20}$$

$$p = p_o (1 + e^{-2id}) e^{i\omega t} \tag{21}$$

$$p_2 = 2p_o e^{i(\omega t - kd)} \tag{22}$$

From the circuit,

$$Z_e = \frac{p_1 - p}{v} \tag{23}$$

but

$$v = \frac{p}{Z_{cav}} \tag{24}$$

Z_{cav} is the entrance impedance of a tube of length d. It can be obtained from the formulas above, for x = 0:

$$Z_{cav} = i\rho c \cot (kd) \tag{25}$$

From equations 21, 22, 23, 24 and 25

$$\frac{Z_e}{\rho c} = \frac{p_1 - p_2 \cos (kd)}{ip_2 \sin (kd)} \tag{26}$$

Assuming,

$$\frac{p_1}{p_2} = r\exp(i\phi) \tag{27}$$

$$\frac{Z_e}{\rho c} = \frac{re^{i(\phi - \pi/2)}}{\sin (kd)} + i \cot (kd) \tag{28}$$

Hence,

$$\mathrm{Re}\,(Z_e/\rho c) = \frac{R}{\rho c} = \frac{r \sin \phi}{\sin (kd)} \tag{29}$$

$$\mathrm{Im}\,(Z_e/\rho c) = \frac{X}{\rho c} = \frac{-r \cos \phi}{\sin (kd)} + \cot (kd) \tag{30}$$

is the ratio of the sound pressures at the upper side of the acoustic facing and the bottom of the cavity. ϕ is the phase difference between p_1 and p_2. When p_1 and p_2 are given in decibels, r is expressed by

$$r = 10^{\log_{10}(p_1/p_2)} = e^{.115\ \mathrm{dB}} \tag{31}$$

where $\mathrm{dB} = 20 \log_{10} (p_1/p_2)$

Equations 29, 30, and 31 are the basic expressions used in the test data analysis.

The test facility used consisted of a wooden duct approximately 150 cm long attached to an air supply. The test section was 15.25 cm long with a cross-section of 7.5 cm by 7.5 cm. The boundary layer on the test sample was controlled by means of suction just upstream of the acoustic panel. A variable speed driven siren was used as the sound source and was positioned above the test sample as shown in figure 237.

The maximum sound pressure level that was achieved in this facility was approximately 165 dB. Two microphone arrays were used to obtain sound pressure and phase information. The array flush with the acoustic facing consisted of three microphones while the array at the bottom of the cavity had two. The time-dependent outputs of the microphones in each array were added together and averaged. Arrays of microphones were used to reduce the effects of possible acoustic facing irregularities. Total temperature was also measured in the free-stream flow, at the lining surface and at the bottom of the cavity. The boundary layer profile was measured with a total pressure rake.

5.2.2 ANALYSIS OF TEST RESULTS

The normalized outputs of the two sets of microphones were analyzed on a narrow band basis (20 or 200 Hz bandwidth) to reject noise-floor and distortion interference. The phase and SPL difference results were plotted on line, on X-Y plotters.

Four samples of perforated-sheet linings were tested for the following 8 frequencies of 500, 630, 800, 1000, 1250, 1600, 2000 and 2500 Hz. The lining specifications are given in the following table.

Material type	% open area	Hole dia. (cm)	Plate thickness (cm)	D.C. flow resistance (rayls)	
				at 20 cm/sec	at 100 cm/sec
Plate A	41	.0914	.0635	0.37	0.85
Plate B	33	.0914	.0635	0.81	1.57
Plate C	23	.0406	.0406	1.6	3.74
Plate D	24	.0914	.0635	1.06	3.04

The tests were conducted at grazing flow Mach numbers of 0.2 and 0.4. For the Mach number 0.4 tests two boundary-layer thicknesses were used and designated as thin and thick.

The test results in the form of normalized flow resistance ($R/\rho c$) versus particle velocity (V_P) through the lining surface are presented in figures 238 through 249.

A *least-square fit* curve has been drawn through each set of test data. The test data was compared with similar data published in reference 27. It was concluded that the M = 0.2 results obtained in this test series were too high. The M = 0.4 results, however, were considered to be accurate enough to use them to modify the semi-empirical flow resistance model given in reference 27. The revised flow resistance model for perforated plate linings in the presence of grazing flow is given below with the curves also being shown in figures 238 through 249. The normalized flow resistance is given by:

$$\frac{R}{\rho c} = .75(RVC) + .5\sqrt{.25(RVC)^2 + 4R_g^2} + (RVA) + (RMI), \qquad (32)$$

where

RVC = the steady flow viscous component

$$= \frac{.03\, t\, \theta^2}{\lambda\, \sigma\, (\theta + .416)}$$

RVA = the fluctuating flow viscous component

$$= \frac{3.83 \times 10^{-5}}{\sigma} (1 - \sigma + t/d) \sqrt{\frac{f\, \theta^{3/2}}{\lambda\, (\theta + .416)}}$$

RMI = inertia effects

$$= 1.138 \frac{(1 - \sigma^2)}{\sigma^{2.1}} M_{pe}^{-(.51\, t/d + S_N)}$$

$$S_N = \frac{1.8 f t \sigma}{M_p c}$$

R_g = grazing flow effects

$$= .1667 M_o \sqrt{\frac{1 - \sigma^2}{\sigma^{2.1}}} \; e^{-(.507 t/d)}$$

The experimentally obtained values for the reactive component of the impedance with grazing flow were not accurate enough to warrant any changes to the existing function which is reproduced below:

$$\frac{X}{\rho c} = \frac{2\pi f}{\sigma c} \left[t + .85 d(1 - .7\sqrt{\sigma}) e^{-(8.65 M_o^2 + .819 M_o)} \right] , \qquad (33)$$

This limited test series has demonstrated that the two-pressure method can be used to obtain consistent results for the resistance of acoustic linings in the presence of grazing flow. There appear to be some unresolved problems at low values of grazing-flow Mach number, ($M \leq 0.2$), which should be investigated further. However, for ejector and jet noise applications higher Mach numbers ($M \geq .4$) are more typical where also better accuracy was attained.

This test series also showed the need for further improvements in the experimental techniques so that data for reactance in the presence of grazing flow could be obtained. Similarly the whole impedance data base should be extended by further experiments to higher-grazing Mach numbers ($M > .45$).

5.3 NOISE SOURCE LOCATION EFFECTS ON THE ATTENUATION IN ACOUSTICALLY LINED DUCTS

The current prediction procedures for sound attenuation in lined ducts assume that the sound is generated by an unspecified source distribution located upstream of the region of interest, figure 250a. This approach has been found to be valid for fan noise studies when predicting the sound attenuation by lined ducts.

In a jet, however, the noise sources are distributed in the entire jet volume which, in part, is shrouded by the ejector-suppressor (fig. 250b). It has been demonstrated experimentally (ref. 5) that the same analysis can not be used to predict the noise reduction by ejector-suppressors. Therefore it is necessary to develop an analysis of noise attenuation by lined ducts where the noise sources are distributed inside the lined-duct segment.

Many researchers, references 28 and 32 among others, have treated the problem of obtaining the attenuation in ducts without considering sources inside the region of interest. Ko (ref. 29) and Mungur and Gladwell (ref. 30) have assumed that the lined duct is infinitely long and they obtain the total pressure by superposition of modes. In order to get the attenuation Ko had to assume that the modal coefficients were all the same. He could not define these coefficients unless a specific noise source or source distribution was assumed.

No attenuation spectra were presented in reference 30. Kurze and Allen (ref. 31) presented attenuation spectra but they considered only one mode (least attenuated). Kapur, Cummings and Mungur (ref. 32) considered a more difficult problem, not amenable to a theoretical solution, which had to be solved using a numerical procedure. They did not present attenuation spectra.

Rice (ref. 28) and Lansing and Zorumski (ref. 33) assumed a pressure distribution at the entrance and at the exit of the lined section of the duct. They obtained an expression for the acoustic field inside the lined-duct region and matched this expression to the assumed pressure distribution at both ends. In this manner, the pressure field was completely defined and no additional assumptions were necessary for obtaining the attenuation.

Lansing and Zorumski (ref. 33) also considered sources inside the duct, but no systematic analysis of location effects on the attenuation are presented. Tester (refs. 34 and 35) has constructed a solution for the pressure field generated by a source (monopole) for an infinitely long, lined duct, but he was not concerned about the effect of source location on the sound attenuation.

The work presented in this section concerns the effects of source location on the sound attenuation by lined ducts when the sources lie inside region of interest (fig. 251). As indicated before, this type of problem arises when a lined duct shrouds a jet, i.e., in the use of ejector-suppressors for reducing jet noise.

The source location effects will be analyzed for a two-dimensional channel (fig. 251) where the coordinate z lies along the direction of sound propagation while x is the other coordinate. ξ and η are the nondimensional coordinates. Currently used procedures assume that the duct is infinitely long and that it is lined throughout its entire length; this assumption facilitates the determination of the solution since reflection from the duct ends or from changes in the wall admittance are neglected.

In the problem treated in this section, the sources will be assumed to exist inside the lined segment, and the analysis will be carried out for an infinitely long, lined duct and for uniform flow (no boundary layer). Flow gradient effects will be analyzed separately and described in section 5.4. A further simplifying assumption will be the use of a solution of a rectangular duct geometry to represent a cylindrical ejector. Viscosity effects will also be neglected.

After obtaining the pressure field for a single source, the solution will be extended to source distributions. When source distributions are considered, the manner in which the sources pulsate with respect to one another greatly affects the composite pressure. This will be accounted for by a weighting function (source distribution function) in the definition of the composite pressure field. Two kinds of solutions will be presented: (a) when the weighting function is a prescribed function of source location, and (b) when the weighting function is a random function of the variables mentioned above. Since jet noise is mostly generated by quadrupoles and, in some cases, dipoles, the pressure field generated by these sources will also be obtained.

The technique used to solve the distributed source problem is based on the work presented in references 36, 37 and 38.

The first part of this section gives a detailed analysis of the procedure required to determine the pressure field of monopoles. In the second part the basic differential equations that give the pressure fields for dipoles and quadrupoles are obtained. Some of the mathematical details not required to understand the basic procedure can be found in appendix A.

5.3.1 MONOPOLE NOISE SOURCES

A two-dimensional channel with uniform flow is assumed for this study. The duct will have a zero boundary layer.

The fundamental differential equation is:

$$\frac{\partial^2 p}{\partial \xi^2} + (1 - M_o)\frac{\partial^2 p}{\partial \eta^2} - 2 i s \frac{\partial p}{\partial \eta} + s^2 p = A h^2 \delta(\eta - \eta_s)\, \delta(\xi - \xi_s) , \qquad (34)$$

where

$$\xi = x/h, \quad \eta = z/h, \quad s = \frac{2 \pi f h}{c} ,$$

ξ_s and η_s are the source coordinates.

M_o is the Mach number of the steady flow, f is the frequency, c is the speed of sound and the source strength is assumed proportional to $Ae^{i\omega t}$. The time dependence has been taken to be of the form $e^{i\omega t}$.

Let:

$$p(\xi, \eta) = \sum_{m=0}^{\infty} \epsilon_m \tilde{p}_m(\eta) \cos(m \pi \xi) \qquad (35)$$

where

$$\epsilon_m = \begin{cases} 1, & m = 0 \\ 2, & m \neq 0 \end{cases}$$

so that:

$$\tilde{p}_m = \int_0^1 p(\xi, \eta) \cos(m \pi \xi)\, d\xi \qquad (36)$$

Also,

$$\int \frac{\partial^2 p}{\partial \xi^2} \cos(m\pi\xi)\, d\xi = (-1)^m \left(\frac{\partial p}{\partial \xi}\right)_{\xi=1} - \left(\frac{\partial p}{\partial \xi}\right)_{\xi=0} - (m\pi)^2 \tilde{p}_m \qquad (37)$$

As shown in appendix A, the boundary conditions must be written in the following form:

$$\left(\frac{\partial p}{\partial \xi}\right)_{\xi=\xi_\nu} = i(-1)^\nu s Y_\nu \left(p - 2i \frac{M_o}{s} \frac{\partial p}{\partial \eta} - \frac{M_o^2}{s^2} \frac{\partial^2 p}{\partial \eta^2} \right)_\nu \qquad (38)$$

where,

$$\nu = \begin{cases} 1, \xi = 0 \\ 2, \xi = 1 \end{cases}$$

and Y_ν are the nondimensional admittances. As in references 37 and 38, the boundary conditions are replaced by unknown velocity source distributions $f_\nu(\eta)$, so that:

$$\left(\frac{\partial p}{\partial \xi}\right)_{\xi=\xi_\nu} = f_\nu(\eta) \qquad (39)$$

The pressure field inside the duct is obtained as a function of $f_\nu(\eta)$; after this, the conditions are imposed which allow us to determine the unknowns, $f_\nu(\eta)$ and thus the pressure field. This method can be used not only when the admittances Y_ν are constant but also when they are known functions of η; the only problem is that the algebra becomes more cumbersome.

The finite Fourier transform, equations 36 and 37, is applied to equation 34; the latter becomes:

$$(1 - M_o) \frac{d^2 \tilde{p}_m}{d\eta^2} - 2is M_o \frac{d\tilde{p}_m}{d\eta} + s^2 \left[1 - \left(\frac{m\pi}{s}\right)^2\right] \tilde{p}_m = f_1(\eta) + (-1)^{m+1} f_2(\eta) + Ah^2 \delta(\eta - \eta_s) \cos(m\pi\xi_s) \qquad (40)$$

Let us define the Fourier integral of $\tilde{p}_m(\eta)$ as follows (ref. 39):

$$\bar{p}_m(\sigma) = \frac{1}{\sqrt{2\pi}} \int_{-\infty}^{\infty} \tilde{p}_m(\eta)\, e^{i\sigma\eta}\, d\eta \qquad (41)$$

Equation 38 is rewritten in the following form:

$$f_\nu(\eta) = i\,(-1)^\nu\, s\, Y_\nu \left(p - 2i \frac{M_o}{s} \frac{\partial p}{\partial \eta} - \frac{M_o^2}{s^2} \frac{\partial^2 p}{\partial \eta^2} \right)_\nu \tag{42}$$

Then, equations 40 and 42 become after the application of the Fourier integral:

$$-\left[(1 - M_o^2)\sigma^2 + 2\sigma s M_o - s^2 + (m\pi)^2\right] \bar{P}_m = F_1(\sigma) + (-1)^{m+1} F_2(\sigma) + A' e^{i\sigma\eta_s} \cos(m\pi\xi_s) , \tag{43}$$

$$F_\nu(\sigma) = i(-1)^\nu s Y_\nu \left(1 - \sigma \frac{M_o}{s}\right)^2 \bar{P}_\nu(\sigma) , \tag{44}$$

From equation 43, obtain:

$$\bar{P}_m(\sigma) = \frac{F_1(\sigma) + (-1)^{m+1} F_2(\sigma) + A' e^{i\sigma\eta_s} \cos(m\pi\xi)}{s^2 - (1 - M_o^2)\sigma^2 - 2\sigma s M_o - (m\pi)^2} \tag{45}$$

On the other hand, by performing the appropriate operations on equation 35, it can be transformed into:

$$\bar{P}_\nu(\sigma) = \sum_{m=0}^{\infty} \epsilon_m \bar{P}_m(\sigma) (-1)^{(\nu-1)m} \tag{46}$$

It should be understood in equation 46 that when $\nu = 1$, $(-1)^{(\nu-1)m} = 1$, whatever the value of m.

Hence, from equations 44 and 46 the basic set of expressions is obtained:

$$F_\nu(\sigma) = (-1)^\nu i s Y_\nu \left(1 - \frac{\sigma M_o}{s}\right)^2 \times \sum_{m=0}^{\infty} (-1)^{(\nu-1)m} \epsilon_m \frac{F_1(\sigma) + (-1)^{m+1} F_2(\sigma) + A' e^{i\sigma\eta_s} \cos(m\pi\xi_s)}{s^2 - (1 - M_o^2)\sigma^2 - 2\sigma s M_o - (m\pi)^2} \tag{47}$$

$$\nu = 1, 2$$

From the nonhomogeneous system of algebraic equation 47, the functions $F_\nu(\sigma)$ can be determined.

$$F_1(\sigma) = s\,A'\,Y_1'\,e^{i\sigma\eta_s}\,\frac{s\,Y_2'\,S_1\,S_2 - i\,S_3\,(1 - i\,s\,Y_2'\,S_4)}{D} \tag{48-a}$$

$$F_2(\sigma) = s\,A'Y_2'\,e^{i\sigma\eta_s}\,\frac{i\,S_2\,(1 - i\,s\,Y_1'\,S_4) - s\,Y_1'\,S_1\,S_3}{D} \tag{48-b}$$

where:

$$Y_\nu' = Y_\nu\left(1 - \frac{\sigma\,Mo}{s}\right)^2 \tag{49}$$

$$S_1 = \sum_{m=0}^{\infty} (-1)^m\,\epsilon_m/R_m \tag{50-a}$$

$$S_2 = \sum_{m=0}^{\infty} (-1)^m\,\frac{\epsilon_m \cos(m\,\pi\,\xi_s)}{R_m} \tag{50-b}$$

$$S_3 = \sum_{m=0}^{\infty} \frac{\epsilon_m \cos(m\,\pi\,\xi_s)}{R_m} \tag{50-c}$$

$$S_4 = \sum_{m=0}^{\infty} \epsilon_m/R_m \tag{50-d}$$

$$R_m = s^2 - (1 - M_o^2)\,\sigma^2 - 2\,s\,\sigma\,M_o - (m\,\pi)^2 \tag{51}$$

$$D = (1 - i\,s\,Y_1'\,S_4)(1 - i\,s\,Y_2'\,S_4) + s^2\,Y_1'\,Y_2'\,S_1^2 \tag{52}$$

The solution for $p(\xi, \eta)$ is given by the expression:

$$p(\xi,\eta) = \sum_{m=0}^{\infty} \frac{\epsilon_m \cos(m\,\pi\,\xi)}{\sqrt{2\,\pi}} \int_{-\infty}^{+\infty} \overline{P}_m(\sigma)\,e^{-i\sigma\eta}\,d\sigma \tag{53}$$

where $\bar{P}_m(\sigma)$ is obtained from equations 46 and 48:

$$\bar{P}_m(\sigma) = \frac{A' e^{i\sigma\eta_s}}{R_m} \left[\frac{Y_1 \, s Y_2' S_1 S_2 - i S_3 (1 - i s Y_2' S_4)}{D} \right.$$

$$\left. + (-1)^{m+1} Y_2' \frac{i S_2 (1 - i s Y_1' S_4) - s Y_1' S_3 S_1}{D} + \cos(m \pi \xi) \right], \qquad (54)$$

The pressure field $p(\xi, \eta)$ can be written in the form:

$$p(\xi, \eta) = \sum_{m=0}^{\infty} \frac{\in \cos(m\pi \xi)}{\sqrt{2\pi}} \cdot 2\pi i \sum_{J=1}^{\infty} \text{Residues} \qquad (55)$$

The integral in equation 53 has been evaluated in appendix B.

Equation 55 represents the pressure field of a monopole source not only for a duct with hard walls but also for a lined duct. The interesting feature of the solution given by equation 55 is the use of the eigenfunctions $\cos(m \pi \xi)$ that constitute a complete set and are orthogonal. This last property simplifies the evaluation of the total acoustic energy flux.

5.3.2 DIPOLE AND QUADRUPOLE NOISE SOURCES

In order to determine the pressure field generated by dipoles and quadrupoles some changes must be introduced to the right-hand side of equation 34. The pressure field of a dipole is obtained from:

$$\mathcal{L}[p] = A h^2 \, \underset{\sim}{e} \cdot \nabla_s [\delta(\eta - \eta_s) \delta(\xi - \xi_s)] \qquad (56)$$

where $\mathcal{L}[p]$ represents the left-hand side of equation 34 and $\underset{\sim}{e}$ gives the orientation of the dipole (fig. 251).

Equation 56 can be written in the form:

$$\mathcal{L}[p] = A h^2 \left[\cos\theta_d \, \delta(\eta - \eta_s) \frac{d}{d\xi_s} \delta(\xi - \xi_s) + \sin\theta_d \, \delta(\xi - \xi_s) \frac{d}{d\eta_s} \delta(\eta - \eta_s) \right], \qquad (57)$$

This is the basic differential equation that gives the pressure field of a dipole.

The presence of a quadrupole is indicated by the appearance of second derivatives or products of first derivatives in the right-hand side of equation 34. A quadrupole is generated by the appropriate combination of three or four monopoles (fig. 251). Extending what was done for the dipole, the following is obtained:

$$\mathcal{L}[p] = A h^2 \Big[\cos\theta_1 \cos\theta_2 \, \delta(\eta - \eta_s) \frac{d^2}{d\xi_s^2} \, \delta(\xi - \xi_s)$$

$$+ \sin(\theta_1 + \theta_2) \frac{d}{d\eta_s} \, \delta(\eta - \eta_s) \frac{d}{d\xi_s} \, \delta(\xi - \xi_s)$$

$$+ \sin\theta_1 \sin\theta_2 \, \delta(\xi - \xi_s) \frac{d^2}{d\eta_s^2} \, \delta(\eta - \eta_s) \Big] \qquad (58)$$

The angles θ_1 and θ_2 are interchangeable.

The right-hand side of equation 58 represents a combination of lateral and longitudinal quadrupoles giving rise to what Ribner calls oblique quadrupoles (ref. 40). Terms of the types

$$T_{11} \, \delta(\eta - \eta_s) \frac{d^2}{d\xi^2} \, \delta(\xi - \xi_s) \quad \text{and} \quad T_{22} \, \delta(\xi - \xi_s) \frac{d^2}{d\eta_s^2} \, \delta(\eta - \eta_s) \, , \qquad (59)$$

correspond to longitudinal (or axial) quadrupoles (ref. 41) that can be constructed from three monopoles or two dipoles (Morse and Ingard, ref. 42).

The terms

$$T_{12} \frac{d}{d\xi_s} \delta(\xi - \xi_s) \frac{d}{d\eta_s} \delta(\eta - \eta_s) \quad \text{and} \quad T_{21} \frac{d}{d\xi_s} \delta(\xi - \xi_s) \frac{d}{d\eta_s} \delta(\eta - \eta_s) \, , \qquad (60)$$

correspond to lateral (or tesseral) quadrupoles that are constructed from two dipoles.

Since the right-hand side of equation 58 was obtained from two dipoles oriented in a specific manner the quantities T_{IJ} have known values given by sines and cosines. However, in general this is not so. In practical applications the orientation and location of the dipoles generating the quadrupoles are random. This implies that T_{IJ} will be random functions of location and in order to perform numerical evaluations the bounds of the quantities T_{IJ} must be known.

From equations 57 and 58, by following the same procedure used for monopoles, the pressure field for dipoles and quadrupoles is obtained. The solution is similar to equation 55 with a different value for the residues. These results can be found in appendix B.

5.3.3 CALCULATION OF ATTENUATION

When no sources are present inside the lined segment, the acoustic intensity in the η -direction is given by:

$$I_\eta = \frac{\rho_o c_o M_o}{4}(uu^* + ww^*) + \frac{pp^* M_o}{4\rho_o c_o} + \frac{1}{4}(pw^* + p^*w) \qquad (61)$$

The acoustic energy flux is obtained by integrating over the duct cross-section.

$$Q = h \int_0^1 I_\eta \, d\xi \qquad (62)$$

Since a two-dimensional channel is being investigated, the Q given by equation 57 is the acoustic energy flux per unit length in the direction perpendicular to ξ and η. There are other formulas, references 45, 46 and 47, that express the energy flux under fewer constraints than those of equation 61, but they are not needed for the problem treated here.

The evaluation of u, w and p can be found in appendices B and C.

Formula (C-6) of appendix C expresses the acoustic energy flux. The attenuation in decibels is given by:

$$\text{Att.} = 10 \log_{10} [Q(\eta_o)/Q(\eta_L)] \qquad (63)$$

where

$Q(\eta_o)$ is the energy flux at $\eta = \eta_o$

$Q(\eta_L)$ is the energy flux at $\eta = \eta_L$

$\eta_L > \eta_o$

Equation 63 has been used to predict the attenuation of fan noise by lined ducts with good results. The attenuation of jet noise by a lined ejector must be evaluated using a different formula, although, similar to expression 63.

A lined ejector shrouds only part of the jet (fig. 252). The lower graph of this figure shows the far-field relative PWL per unit of axial length as a function of axial distance, the frequency being the parameter.

For any frequency, part of the acoustic energy is generated outside the ejector creating an effective floor to the attenuation that could be achieved with that particular lined ejector.

The acoustic energies E_i and E_o generated inside and outside, respectively, of the ejector can be obtained from figure 252 by numerical integrations.

The effective attenuation that could be achieved is given by the formula below:

$$\text{Att.}_{\text{eff.}} = 10 \log_{10} \frac{E_i + E_o}{E_i' + E_o} \tag{64}$$

where:

E_i is the residual acoustic energy inside the ejector after attenuation.

The expression above can be rewritten in the form:

$$\text{Att.}_{\text{eff.}} = 10 \left[\log_{10} (E_i/E_i') - \log_{10} \frac{1 + (E_i/E_i')(E_o/E_i)}{1 + (E_o/E_i)} \right], \tag{65}$$

If the assumption is made that equation 63 is equivalent to:

$$\text{Att.} = 10 \log_{10} (E_i/E_i') \tag{66}$$

Then, E_i/E_i' can be determined; in this way, all quantities in equation 65 are known.

What was said above is useful provided that E_i is given experimentally. E_i' must be evaluated analytically. If the attenuation is given experimentally, E_i can be easily obtained.

On the other hand, the purpose of this work is to develop the ability to predict attenuations by assuming some source distributions. In this context, both E_i and E_i' must be evaluated analytically. It is simple to define the acoustic energy flux E_i' leaving the lined ejector, since the composite pressure and particle velocities can be evaluated at the exit without difficulties; they will give the composite effect of all sources at the exit. However, it has not been possible to find a similar expression for E_i since the sources are distributed inside the ejector.

In order to circumvent this problem, drastic assumptions were made concerning the manner in which the sources pulsate with respect to one another. It was considered that the sources are uncorrelated in the η -direction, i.e., the total energy flux E_i is given by the sum of each source flux evaluated at an η very close to each source. In a similar fashion, E_i' was obtained as the sum of the fluxes that the sources produce at the exit plane of the ejector. However, the sources lying on the same cross-section were assumed to be correlated (though not necessarily in phase). Equation C-13 of appendix C synthesizes the above statement.

Another manner of evaluating E_i and E_i' gives rise to the concept of insertion loss. In this case E_i is the total energy flux at the exit of a hard walled duct while E_i' is the flux existing at the exit of the same duct with soft walls. Then:

$$\text{Insertion loss} = 10 \log_{10} (E_i^{(h)}/E_i') \tag{67}$$

However, this method gave results that had, in some cases, no physical meaning (negative values for the insertion loss). The sources lying closest to the duct exit had a disproportionately large overall effect on the acoustic energy flux. Also, the insertion loss as a function of frequency did not look correct in most of the examples tried. The reasons for this behavior are not understood. Because of these problems, the concept of insertion loss was not used.

When only one source is involved, its location with respect to η is irrelevant because the duct analyzed is lined throughout its entire length, which is infinite, and therefore it is possible to change the origin of the η-coordinate. The analysis shown below refers to the location effects of the single source with respect to the ξ-coordinate.

Conversely, when a source distribution is considered, the functional dependence of the source location with respect to η is an important parameter in defining the attenuation.

In the case having a finite number of sources, equation C-10 (appendix C) gives the composite pressure:

$$p_\omega(\xi, \eta) = Ah^2 i \sum_{m=0}^{\infty} \epsilon_m \cos(m\pi\xi) \sum_{j=1}^{J} \sum_{n=1}^{N} \alpha_n T_{m,j}^{(n)} \tag{68}$$

where $T_{m,j}^{(n)}$ is given by equation C-7 of appendix C.

The composite pressure given by a generalized source distribution function $H(\xi_s, \eta_s, \omega)$ is expressed by equation D-6 of appendix D:

$$p_\omega(\xi, \eta) = \int_{\eta_s^{(1)}}^{\eta_s^{(2)}} \int_0^1 H(\xi_s, \eta_s, \omega)\, \Gamma(\xi, \eta; \xi_s, \eta_s)\, d\xi_s\, d\eta_s \tag{69}$$

where $\Gamma(\xi, \eta; \xi_s, \eta_s)$ is expressed by D-5 of appendix D.

α_n and $H(\xi_s, \eta_s, \omega)$ have similar roles in the above expressions.

α_n has the role of a weighting factor in defining the composite pressure. It can be a function of n and frequency. The location of a source, given by n, may affect the weight it has on the total pressure. The pair ξ_s, η_s in $H(\xi, \eta_s, \omega)$ has the same role when a generalized source distribution is considered.

The effect due to source location can be included as a component in the weighting function α_n.

It could happen that identical sources do not pulsate in phase. Then,

$$p_{\omega}(\xi, \eta) = Ah^2 i \sum_{m=0}^{\infty} \epsilon_m \cos(m\pi\xi) \sum_{j=1}^{J} \sum_{n=1}^{N} e^{-i\omega t_n} T_{m,j}^{(n)} \qquad (70)$$

where t_n are the time differentials with respect to some specified initial time. In this manner, phase differences are created among the components of the composite pressure which can be accounted as part of the weighting function α_n. In general, the phase differences will be functions of frequency.

All the results shown in this section were obtained using expression 66. E_i and E_i' were obtained analytically.

5.3.3.1 Single Monopole

A lining optimized for a narrow frequency band according to equation A-20 of reference 44 was chosen for all the studies made. The lining characteristics and flow parameters are:

Mach number 0.50 (exhaust mode)
Speed of Sound = 34,000 cm/s
Nondimensional, lined length L/h = 3.333
Impedance of acoustic facing = 1.05 (1 + i f/15)
Cavity depth = 1.92 cm, duct height = 30 cm

In figure 253, three spectra corresponding to three dissimilar source locations in the duct were plotted together with the spectrum obtained from equation A-20 of reference 44. The spectra corresponding to other source locations lie in between the ones plotted. Reference 44 assumed that the root mean square of the pressure amplitudes of all modes were the same. The modes of the reference mentioned above are associated with the poles in the present work.

It can be seen from these results that the source location has a strong effect on the attenuation. The source located closest to the lining gives rise to a broader spectrum than the ones corresponding to sources located farther away from the wall; also, the peak attenuations of the spectra of these sources are lower than the peak of the attenuation curve corresponding to the source located nearest to the wall. This means that the lining will be more efficient when the noise sources are closer to the wall.

The spectrum obtained from reference 44 lies in between the spectra corresponding to the isolated sources. This result would indicate that a set of sources could generate that spectrum.

One interesting feature of all the spectra plotted is that the location of the peaks in the attenuation curves do not vary much; they lie inside a 2/3-octave-band range.

5.3.3.2 Distributed Monopoles

Appendix D gives the pressure generated by a generalized distribution function $H(\xi_s, \eta_s, \omega)$. Unfortunately, experimentally obtained source distribution data are limited. The investigation of source locations in a jet as a function of frequency is just beginning to produce some results (sec. 4.5).

If a finite number of sound sources whose locations are well defined are considered, a question arises about the values the weighting function α_n should have. As will be shown later, the value of this function is of paramount importance in obtaining meaningful predictions for the attenuation when source distributions are concerned.

In order to analyze the effects of source distribution, very simple configurations of five and ten monopoles were studied, and also an array of monopoles was analyzed. Four cases were investigated; one where the weighting function α_n was a constant (uniform weight), and three where the weighting function was not a constant (non-uniform weight), as shown below:

(a) Uniform weight. In this instance the α_n have the same constant value. Five sources were located at:

$$\xi_s = \left[1 + 3(n - 1) + (n - .95)^2 + .35\right] /h \tag{71}$$

$$\eta_s = \eta/h \tag{72}$$

Also, a ten-source configuration was analyzed with the coordinates

$$\xi_s = \left[1 + 3(n - 1) + (n - .95)^2 + .35\right] /(3.7h) \tag{73}$$

$$\eta_s = \eta/2h \tag{74}$$

The location of the sources is sketched below:

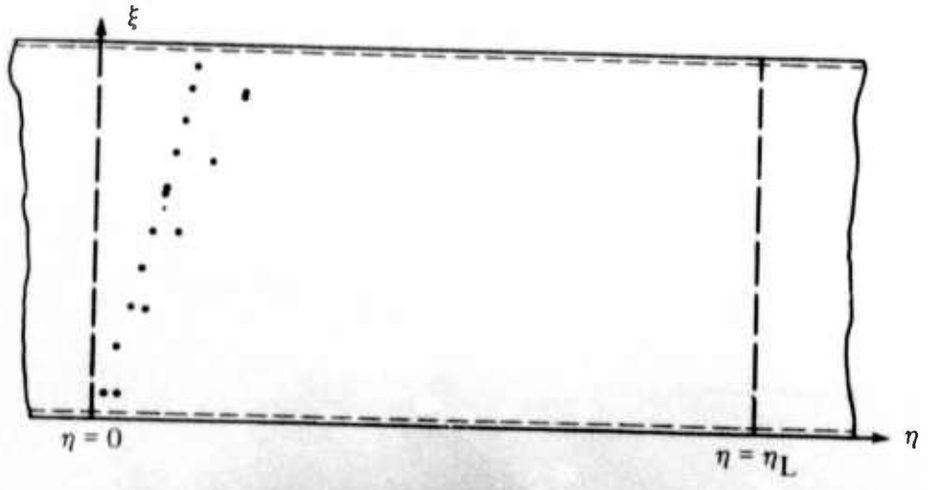

Figures 255 and 256 show the attenuation spectra of the ten- and five-sources configurations, respectively.

(b) Instead of assuming that the α_n were constant, different values which were functions of n, but independent of ω, were assigned to them, so that:

$$\alpha_n = -2.5\ n^2 + 15\ n - 12.5 \tag{75}$$

for both five- and ten-sources configurations. This function α_n gives low weights to sources corresponding to n = 1 and n = 5. The coordinates ξ_s and η_s of the sources were the same as in the previous case.

The attenuation spectra were plotted in figures 254 and 255.

(c) Here, α_n was made a function of n and f, as follows:

$$\alpha_n = \begin{cases} .10(nf)^2 - 10(nf) + 65, \text{ 5-sources configuration} \\ -.792(nf)^2 + 21.8(nf) - 48.5, \text{ 10-sources configuration} \end{cases} \tag{76}$$

where the frequency f is given in kHz. The first α_n above gives the lowest weights to nf = 7 and nf = 8, while the second one has the lowest values at nf = 25. The coordinates ξ_s and η_s were the same as in (a) and (b).

These attenuation spectra are also shown in figures 254 and 255.

The functions α_n chosen above are not representative of any known physical problem and, most likely, if other functions had been selected the results would have been different. Nevertheless, it is expected that the main conclusions to be derived below still hold. It can be seen from figure 253, where all the results for the configurations with ten sources have been plotted, that the curves corresponding to the α_n, which are independent of ω, are similar, although the one for constant α_n lies below the others. The curve corresponding to α_n, also a function of frequency, has a second peak higher than the first (about 3 dB). Larger differences in the spectra corresponding to the configurations with five sources can be seen in figure 255. It is obvious that the shape of the attenuation curve will depend upon the weight assigned to each source, i.e., if sources lying closest to the wall have the largest weight, the composite spectra will be similar to the ones of those sources taken alone. This is so because no phase difference has been given to the sources (there is only one source per cross-section). The results show the importance of the weighting function α_n in defining the attenuation.

(d) In this case monopole arrays were considered, one for each frequency. All frequencies were represented in each cross-section which was defined by η_s. This meant that the number of arrays per cross-section was equal to the number of frequencies chosen.

Ten values for η_s were selected.

(e) Each array contained twenty monopoles randomly distributed as a function of ξ_s. The ξ_s and η_s are given as follows:

$$\xi_s = U(n) \tag{77}$$

$$\eta_s = \eta_L/2\ell \qquad \ell = 1, 2, \ldots, 10 \tag{78}$$

where:

U(n) is given by a random number generator

and η_L is the nondimensional lined length.

The location of the sources is sketched below:

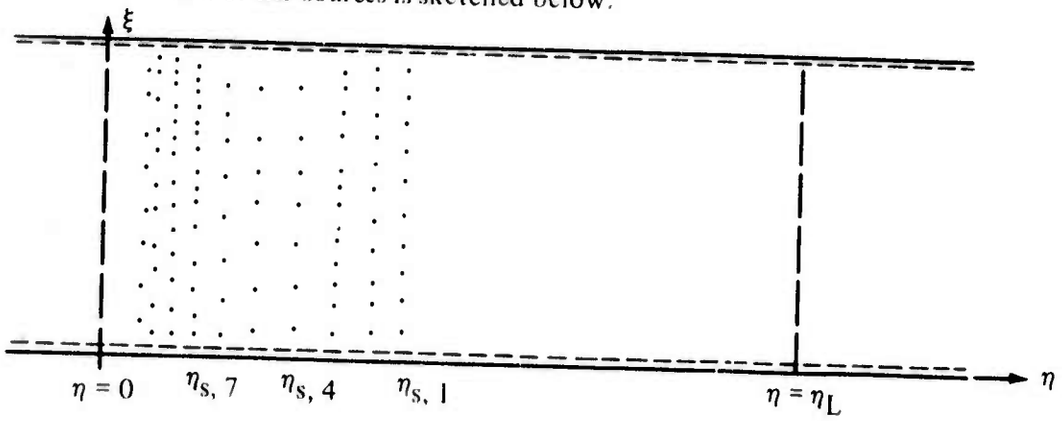

In this sketch,

$$\eta_{s,\ell} = \eta_L/2\ell, (\ell = 1, 2, \ldots, 10)$$

The random number generator is a computer program that gives a set of numbers based on the normal or uniform distribution as requested. In this problem the U(n) were selected in such a way that the probability density function is:

$$\frac{1}{d\sqrt{2\pi}}\, e^{-[U(n) - .50]^2/(2d^2)} \tag{79}$$

where d is defined as follows:

$$d = 1/6 = 0.1666$$

Then the probability that a source lies between ξ_1 and ξ_2 is given by:

$$\frac{1}{d\sqrt{2\pi}} \int_{\xi_1}^{\xi_s} e^{-(\xi_s - .50)^2/(2d^2)} \, d\xi_s \tag{80}$$

The U(n) have been chosen in such a way that the most likely location for a source is near the duct center where $\xi = .50$. This choice may or may not be in agreement with what actually happens in a jet where the sources might be clustered away from the axis but maintaining axial symmetry.

Two dissimilar expressions for α_n were used in this case. They are:

$$\alpha_n = e^{16.2\,(.50 - \xi_s)^2 + i\,\Omega} \tag{81}$$

$$\alpha_n = e^{i\,\Omega} \tag{82}$$

The first α_n above was chosen in such a way that it has the lowest values when the sources are close to the walls, while it has the highest magnitude for sources located near the duct axis. The second α_n is a function of n only by way of Ω.

The phase Ω is defined according to:

$$\Omega = 2\pi V(n) \tag{83}$$

where V(n) were given by the random number generator. A uniform distribution was assumed for the V(n).

The attenuation spectra corresponding to the weighting functions expressed above are shown in figure 256 together with the spectrum obtained applying the analysis of reference 44.

The spectra corresponding to the α_n above show striking differences, especially at the peaks. At the same time, these attenuation spectra are quite dissimilar with the one obtained using the approach of reference 44. This could simply mean that the lining used is not optimum for the particular geometrical configuration and source distribution considered.

5.3.3.3 Single Dipole

Two configurations were analyzed for dipoles, namely (a) $\theta_d = \pi/2$ and (b) $\theta_d = 0$.

Results for three source locations of configuration (a) are shown in figure 257 while three representative spectra of (b) are shown in figure 258. It can be seen from the figures that the differences between the cases (a) and (b) are large. When the dipole axis is oriented parallel to the duct axis, $\theta_d = \pi/2$, the location effects are similar to those of the monopole;

i.e., the closer the source to the wall the higher the attenuation. Also, the attenuation spectra are close (but not equal) to those of the monopoles. When the dipole axis is oriented normal to the duct walls $\theta_d = 0$ the effects of source position follow a different pattern since the farther the source is from the wall the higher the attenuation, and the peak values of the spectra are, for some locations 50% higher than those of case (a).

5.3.3.4 Single Quadrupole

Three configurations were analyzed for quadrupoles, (a) $\theta_1 = \theta_2 = 0$ (b) $\theta_1 = 0$, $\theta_2 = \pi/2$ and (c) $\theta_1 = \theta_2 = \pi/2$. The spectra corresponding to these three configurations are shown in figures 259, 260 and 261 respectively. As in the case of dipoles the differences among them are very large.

The spectra corresponding to longitudinal quadrupoles, generated by monopoles lying along the ξ-direction $\theta_1 = \theta_2 = 0$, do not show large changes when the single quadrupole moves from the duct center towards the wall. The main result is the large attenuation.

The results for the lateral quadrupole show proportionally larger changes than in the previous configuration when the source moves from the wall towards the center of the duct.

The spectra corresponding to the other longitudinal quadrupoles, generated by monopoles lying along the η-direction $\theta_1 = \theta_2 = \pi/2$ show a behavior similar to that of dipoles oriented in the same direction. In this instance the attenuation increases when the source gets closer to the duct walls and there is a definite shift of the peaks of the attenuation spectra towards the lower frequencies when the source moves away from the walls.

5.3.3.5 Distribution of Dipoles and Quadrupoles

In this configuration, arrays of dipoles and quadrupoles were considered.

The distribution of the sources followed the same pattern as in (d) of subsection 5.3.3.2. The weighting factor α_n used was:

$$\alpha_n = \exp(i\Omega) \tag{84}$$

where

$$\Omega = 2\pi V(n) \tag{85}$$

V(n) was given by a random number generator and it followed a uniform distribution.

The dipole angles θ_d and the quadrupole angles θ_1 and θ_2 were also obtained from the random number generator and as V(n) they followed the uniform distribution.

The spectra corresponding to this case are shown in figure 262.

The spectrum corresponding to the monopoles was the same as one of the curves shown in figure 256. The results shown in figure 262 indicate that the dipoles give significantly

more attenuation than the monopoles, and quadrupoles more attenuation than the dipoles.

The curves shown in figure 262 correspond to one random case based on random numbers for source position, phase, θ_d, θ_1 and θ_2. If a different set of random values had been assigned, then the spectra corresponding to each type of source would change. By using the Monte Carlo technique it is possible to determine the mean of a very large number of spectra, obtained by changing the random numbers assigned to the quantities mentioned above. This was not tried because of the very large amount of computing time required. From a few samples done it seems that the spectra do not change much going from one set of random numbers to another. The important point is that there are differences between spectra of one type of source and those of another.

5.4 VELOCITY, TEMPERATURE AND DENSITY GRADIENT EFFECTS ON SOUND ATTENUATION IN DUCTS

Past studies of sound attenuation by acoustically-lined ducts in the presence of a mean flow have assumed a uniform flow profile across the duct with no gradients present. In an ejector surrounding a jet flow the temperature and velocity varies in both radial and axial directions as shown by some typical examples in section 4.5. In order to make lined ducts analyses more realistic it has become necessary to investigate flow gradient effects. In the following study only radial-flow gradients were investigated.

It has been shown by many investigators (refs. 48 through 51) that velocity gradients affect the eigenvalues and hence the attenuation. Similar effects for temperature gradients are shown in reference 52. Beckemeyer, in reference 53, shows that density (temperature) gradients localized inside boundary layers adjacent to duct walls can have a significant effect on single modes. In none of the previous references, however, has a systematic presentation been made of the effects of flow gradients on the attenuation spectra.

In this section the fundamental differential equation is solved using the Runge-Kutta and Adams-Bashforth techniques to obtain the propagation-constants. Later the attenuation spectra are evaluated by using two dissimilar methods. The effects of two examples of velocity profiles and one temperature profile are investigated.

5.4.1 BASIC EQUATIONS AND NUMERICAL TECHNIQUES

Figure 263 depicts the geometry of the problem. The basic differential equation from reference 52 is:

$$\frac{d^2p}{d\xi^2} + \left[\frac{2\mu_z \dfrac{d(QM)}{d\xi}}{1-(QM)\mu_z} + \frac{\dfrac{dQ}{d\xi}}{Q}\right]\frac{dp}{d\xi} + s^2\left[\left(\frac{1-\mu_z QM}{Q}\right)^2 - \mu^2{}_z\right]p = 0, \qquad (86)$$

where

$$\xi = x/\frac{h}{2}$$

$$s = k_\infty h/2$$

$$\mu_z = k_z/k_\infty$$

$$Q = \frac{c}{c_\infty} = \sqrt{T/T_\infty}$$

M is the Mach number.

c is the local speed of sound.

Equation 86 also includes the effects of density gradients, given by the term

$$\frac{1}{Q} \cdot \frac{dQ}{d\xi}$$

Equation 86 is based on the following assumptions: (a) viscosity effects are neglected, (b) heat transfer effects are neglected, and (c) mean pressure is uniform throughout.

Only the case where opposite duct walls have equal admittances has been solved. The following procedure can be extended to the case of dissimilar admittances.

The determination of the eigenvalues is done using the Runge-Kutta technique that furnishes starting values. The differential equation 86 can be written in the form:

$$\frac{dY}{d\xi} = -g_1 Y - g_2 P = F \tag{87}$$

$$Y = \frac{dP}{d\xi} \tag{88}$$

$$g_1 = \frac{2\mu_z \frac{d(QM)}{d\xi}}{1 - (QM)\mu_z} + \frac{1}{Q} \cdot \frac{dQ}{d\xi} \tag{89-a}$$

$$g_2 = s^2 \left[\left(\frac{1 - \mu_z QM}{Q} \right)^2 - \mu_z^2 \right] \tag{89-b}$$

The following parameters are used in this method.

$$m_1(j) = \delta F(j) \tag{90}$$

$$m_2(j) = \delta \left\{ g_1(j + 1/2) \left[Y(j) + \frac{m_1(j)}{2} \right] + g_2(j + 1/2) \left[P(j) + .5\delta Y(j) \right] \right\}, \tag{91}$$

$$m_3(j) = \delta \left\{ g_1(j + 1/2) \left[Y(j) + \frac{m_2(j)}{2} \right] + g_2(j + 1/2) \left[P(j) + .5\delta Y(j) + .25\delta m_1(j) \right] \right\} , \quad (92)$$

$$m_4(j) = \delta \left\{ g_1(j + 1) \left[Y(j) + m_3(j) \right] + g_2(j + 1) \left[P(j) + \delta Y(j) + .5 m_2(j)\delta \right] \right\} , \quad (93)$$

$$P(j + 1) = P(j) + \delta \left[Y(j) + (m_1(j) + m_2(j) + m_3(j))/6 \right] , \quad (94)$$

$$Y(j + 1) = Y(j) + \left[m_1(j) + 2m_2(j) + 2m_3(j) + m_4(j) \right] /6, \quad (95)$$

In the expressions above δ is the step size, j is index associated with the point in the finite difference scheme. The quantities $g_1(j + \frac{1}{2})$ and $g_2(j + \frac{1}{2})$ mean that g_1 and g_2 are evaluated between j and j + 1 by performing a simple averaging.

The Runge-Kutta method could give large errors if used alone. After obtaining values of P and Y for the first five points, P and Y for the sixth point is given by (Adams-Bashforth technique):

$$P(j) = P(j-1) + DP(j-1) \quad (96)$$

$$Y(j) = Y(j-1) + DY(j-1) \quad (97)$$

where:

$$DP(k) = \delta \left\{ Y(k) + .5DY(k - 1) + \frac{5}{12} DY^2(k - 2) + \frac{3}{8} DY^3(k - 3) + \frac{251}{720} DP^4(k - 4) \right\} , \quad (98)$$

$$DY(k) = \delta \left\{ F(k) + .5DPY(k - 1) + \frac{5}{12} DPY^2(k - 2, + \frac{3}{8} DPY^3(K - 3) + \frac{251}{720} DPY^4(k - 4) \right\} , \quad (99)$$

$$DPY(k) = F(k + 1) - F(k), \quad (100)$$

Even with these formulas that improve the accuracy of the Runge-Kutta technique, it is difficult to get more than five good modes at the higher frequencies such as when fh/c is >4. In order to maintain accuracy, the step size must be reduced but the computational time increases accordingly.

Methods of this kind using backward differences are generally referred to as Adams-Bashforth methods. These methods belong to the more general predictor-corrector techniques described in reference 54.

The use of backward differences improves the accuracy of the solution but they tend to enhance small perturbations that may arise in the process of finding the solution. If occurrences of this type happen, the solution cannot be obtained because some of the quantities needed in the numerical process become infinite. However, situations of this kind are not common and they generally happen at high fh/c when the starting points for the solution are not close enough to the final value.

The numerical scheme starts at the duct axis proceeding toward the lined wall. It is unlikely that the first try for the eigenvalue will give the solution. The Newton-Raphson method is used to determine the eigenvalues:

$$(\mu_z)_{NEW} = (\mu_z)_{OLD} - \frac{F(\mu_z)}{dF/d\mu_z} \tag{101}$$

In general, the starting values for μ_z are very important. Since opposite walls have linings of equal admittance the solution for p can be split into even and odd modes. For the even modes p has the following value at the axis:

$$p_{\xi=0} = 1 \quad \text{(imaginary part = 0)} \tag{102}$$

Also, for even modes,

$$\left(\frac{dp}{d\xi}\right)_{\xi=0} = 0 \tag{103}$$

For odd modes,

$$(p)_{\xi=0} = 0 \quad \text{(Real and imaginary components are zero)} \tag{104}$$

while

$$\left(\frac{dp}{d\xi}\right)_{\xi=0} = s\sqrt{\left(\frac{1-\mu_z Q(0)M(0)}{Q(0)}\right)^2 - \mu_z^2} \tag{105}$$

In the last expression Q(0) and M(0) stand for Q and M at $\xi = 0$.

The procedure outlined above requires an initial guess for μ_z which would be the first $(\mu_z)_{old}$ in the entire sequence of iterations. This very first value for μ_z can be obtained from prediction programs that do not consider flow profiles. The importance of this initial guess cannot be stressed enough since the Newton-Raphson method is, in many cases, very sensitive to the value assigned to the first $(\mu_z)_{old}$, otherwise the iterative process does not converge.

5.4.2 CALCULATION OF ATTENUATION

The determination of the attenuation in the case of uniform flow parameters requires that some assumptions be made concerning the mode amplitudes. The easiest assumption is to consider all these mode amplitudes equal. This has proven to be a reasonable assumption since the results tend to agree with experimental flow duct data.

If gradients are considered, the solution is usually obtained by following a numerical procedure and some way must be found to make meaningful comparisons of the attenuation spectra corresponding to uniform and nonuniform flow parameters, i.e., if a numerical approach is used to solve the uniform case, the attenuation should be the same as that following a purely theoretical procedure (closed-form solution). Since the pressure, or the first pressure derivative (depending on type of mode), at the duct center (starting point) can have any value, a procedure has to be constructed that would allow comparison with uniform flow results, regardless of the values assigned to the pressure and first derivative at the starting point.

The following assumption makes this comparison possible: the acoustic energy flux of each mode n is normalized with respect to

$$N_{n,n} = \int_0^1 p_n \, p_n^* \, d\xi \tag{106}$$

where p_n is the pressure of the n-mode.

As in references 49, 50, and 55, the contribution to the acoustic energy flux of the terms arising from crossproducts is assumed zero. This is not a bad assumption since it can be shown that if a random distribution of phases is assumed to exist between the modes, the average contribution of the cross terms to the energy flux is zero.

5.4.2.1 Blokhintsev's Equation

A generalized version of the Blokhintsev equation, valid when the temperature at infinity (reference temperature) is not the same as the local temperature, can be obtained by following the procedure shown in reference 55. Equation A-19 of reference 55 has been used in the past to determine the attenuation.

The acoustic energy flux, according to Blokhintsev, when the local and reference temperatures are not the same, is the following:

$$E^{(b)} = \sum_n \sum_m E^{(b)}_{n,m} = \frac{1}{4\rho_\infty c_\infty} \sum_{n=0}^{\infty} \sum_{m=0}^{\infty} \left\{ Q^3 M \left[\frac{Y_n Y^*_m}{(ZN)_n (ZN)^*_m s^2} + \right. \right. \tag{107}$$

$$\left. \left. \frac{\mu_{z,n} \mu^*_{z,m} P_n P^*_m}{(ZN)_n (ZN)^*_m} \right] + P_n P^*_m QM + Q \left[\frac{P_n P^*_m \mu_{z,m}}{(ZN)^*_m} + \frac{P^*_m P_n \mu_{z,n}}{(ZN)_n} \right] \right\},$$

The total acoustic energy flux, normalized with respect to $N_{n,m}$ is given by:

$$E^{(b)}_t = \sum_n \sum_m \frac{\frac{h}{2} \int_0^1 E^{(b)}_{n,m} \, d\xi}{N_{n,m}} \tag{108}$$

In equation 107 P represents the pressure, $Y = \frac{dP}{d\xi}$ and

$$ZN = 1 - \mu_z QM \tag{109}$$

Equation 106 has been obtained assuming no-shear, and no temperature or density gradients. However, when performing the integration equation 107, each point (or strip) has a different value for Q and M. In this manner, Blokhintsev's formula can be extended to problems having gradients.

5.4.2.2 Möhring's Equation

Some investigators (ref. 56 and 57) have obtained expressions for the acoustic energy flux that account for gradients. The expression used in this work was given by Möhring (ref. 56).

$$E^{(m)} = \sum_n \sum_m E^{(m)}_{n,m} = \frac{1}{2 c_\infty \rho_\infty} \sum_{n=0}^{\infty} \sum_{m=0}^{\infty} \in_{n,m} \left\{ \frac{-Q^2}{s^2 (ZN)^2_n (ZN)^{*2}_m} \cdot \frac{d(QM)}{d\xi} \cdot \right.$$

$$\left. \left(P_n Y^*_m + P_m Y_n \right) + \left[2QM + Q^2 \left(\mu^*_{z,n} + \mu_{z,m} \right) (1 - M^2) \right] \cdot \frac{P_n P^*_m}{(ZN)_n (ZN)^*_m} \right\}, \tag{110}$$

$$\epsilon_{n,m} = \begin{cases} 1, & n \neq m \\ 1/2, & n = m \end{cases}$$

The total acoustic energy flux, according to Möhring, normalized with respect to $N_{n,m}$, is given by the expression

$$E_t^{(m)} = \frac{h}{2} \sum_n \sum_m \int_0^1 \frac{E_{n,m}^{(m)}}{N_{n,m}} \, d\xi \qquad (111)$$

P and Y include the z-dependence.

The integration in expression 111 must be carefully done for the limiting case where the shear layer thickness tends to zero. In this instance there is a nonvarnishing contribution from the first term of expression 110.

This contribution is expressed by:

$$I = \frac{Q^2 M_o}{2 s \rho_\infty c_\infty} \, Re \left\{ \sum_n \sum_m \epsilon_{n,m} \left[\frac{i \eta^*}{1 - \mu_{z,n} Q M_o} - \frac{i \eta}{1 - \mu_{z,m}^* Q M_o} \right] \right\}, \qquad (112)$$

This result was obtained by taking Q constant across the duct.

The attenuation is given by the usual expression:

$$\text{Att.} = 10 \log_{10} [E(0)/E(L)] \qquad (113)$$

where E(0) corresponds to conditions at z = 0
and E(L) represents the flux at z = L.

Two Mach number and one temperature profile were investigated.

(a) This Mach number profile is expressed by:

$$M = M_o \frac{[(1 - \xi)^\alpha - \alpha(1 - \xi)]}{1 - \alpha} \qquad (114)$$

$$\alpha < 1$$

The expression above can give a set of profiles by varying α. When $\alpha = 0$ the plug-flow case is obtained. Figure 264 depicts this set of profiles.

$$\frac{dM}{d\xi} = -\alpha M_o \quad \frac{\left[(1-\xi)^{\alpha-1} - 1\right]}{1-\xi} \tag{115}$$

at $\xi = 0$ (duct-axis) $\frac{dM}{d\xi} = 0$

The average Mach number of expression 114 obtained by integrating from $\xi = 1$ to $\xi = 0$, is

$$M_{av} = \frac{M_o}{2} \quad \frac{2+\alpha}{1+\alpha} \tag{116}$$

(b) The second set of profiles is obtained from the following expression:

$$M = M_o \cdot \frac{z^\sigma + \sigma\left[c(\sigma)z^2 + d(\sigma)z^3\right]}{1 + \sigma(c(\sigma) + d(\sigma)} \tag{117}$$

$$\sigma < 1$$

where

$$z = 1 - \xi$$

By varying σ a set of profiles is obtained (fig. 265). These profiles have a hump.

$$c(\sigma) = \frac{z_1^2 - z_1^\sigma - 1}{2z_1\ (1 - z_1)} \tag{118}$$

$$d(\sigma) = \frac{-(1 + 2c(\sigma))}{3} \tag{119}$$

where $z_1 = 1 - \xi_1$ gives the location of the hump (fig. 266). The average Mach number is given by

$$M_{av} = \left[\frac{\frac{1}{\sigma+1} + c(\sigma)\frac{\sigma}{3} + d(\sigma)\frac{\sigma}{4}}{1 + \sigma(c(\sigma) + d(\sigma))}\right] M_o \tag{120}$$

When $\sigma = 0$, the plug-flow profile is obtained. M_o is the Mach number at the duct center. One important characteristic of both profiles is that when ξ is close to 1 they behave like profiles of turbulent boundary layer.

The profile chosen for the Q is the following:

$$Q = \xi^2 + (1 - \xi^2)\,\beta \tag{121}$$

By changing β from 1 to higher values, a set of profiles can be obtained (fig. 267).

$$\frac{dQ}{d\xi} = 2\xi(1 - \beta) \tag{122}$$

which is zero at the axis.

When $\beta = 1$, the plug-flow profile is recovered.

5.4.3 DISCUSSION OF RESULTS

Several numerical samples have been evaluated using the above analysis techniques. In all cases a fixed duct geometry and acoustic lining was employed:

Duct height	=	12.7 cm
Lining length	=	25.4 cm
Mach number at duct center	=	variable
Temperature at duct center	=	1060 K

The following double-layer perforated plate lining was assumed:

Outer layer - Open Area = 0.35, Hole Diam = 0.15865 cm, thickness = 0.0508 cm, Particle Mach number = 0.02, Mach number used to compute the impedance = 0.40, pressure ratio = 0.90, temperature ratio = 2.40, speed of sound = 66,000 cm/s, core depth = 0.846 cm, temp. ratio air cavity to air duct = 0.75

Inner layer - Open area = 0.05, hole diam. = 0.15865 cm, thickness = 0.0508 cm, Particle Mach number = 0.008, Mach number used to evaluate the impedance = 0, pressure ratio = 0.90, temperature ratio = 1.60, core depth = 0.424 cm, temp. ratio air cavity to air duct = 0.90, blockage in both cases = 0.95

Although two dissimilar methods were used to obtain the acoustic energy flux, namely, Blokhintsev's and Möhrings, it was found that both gave similar attenuations, as shown in figure 267. In the subsequent discussions results obtained by using Blokhintsev's formula only will be used.

The effect of the first Mach number profile on attenuation in a lined duct are shown in figures 268 and 269. In figure 268 the Mach number on the axis was kept constant while the average Mach number was allowed to vary. In figure 269 the average Mach number was kept constant while the value on the axis was allowed to vary. Both cases gave very similar results which indicate that as the profile becomes more rounded, i.e., increasing value of α (fig. 269), the position of the peak in the spectrum shifts towards lower frequencies with an accompanying increase in attenuation level.

The effect of a humped Mach number profile (fig. 265) on attenuation in a lined duct is shown in figures 270 and 271. Again the Mach number on the axis was kept constant in figure 270, and the average Mach number constant in figure 271. In figure 270 where the average Mach number varied there is a small change in low-frequency attenuation with hardly any changes in peak values. In figure 271 where the Mach number on the axis varied the changes were even less significant.

The effect of a temperature profile on attenuation in a lined duct with constant average duct Mach numbers is shown in figure 272. The tendency is for the attenuation peak to shift to a lower frequency and increasing in level as compared to the uniform profile case.

The above examples are a very limited set of results that need to be extended to cover a much broader range of cases in order to provide some quantitative conclusions to the flow profile effects. The computational techniques used are very time and budget consuming so that the work could not be carried beyond that discussed above. The results obtained this far have been summarized in figure 273 for all the flow profiles studied to demonstrate the significance of taking into account flow profiles in lined-duct attenuation calculations.

6.0 CONCLUSIONS

Jet noise suppression, a major problem in the development of quiet airplane systems, has experienced a substantial technology advance as described in this report. Fundamental technology development has lead to a better understanding of nozzle aerodynamics, noise generation and noise transmission processes. This newly acquired knowledge was applied in the design of a full scale suppressor system demonstrator which is described in volume X. The full scale test results confirmed the veracity of the acoustic design technology employed.

The multitube-nozzle parametric test program provided far-field jet noise data which, together with jet noise-source location and flow-profile data, enabled identification of prime noise sources in the flow. The characteristics of these noise sources have been identified. It has been concluded that the double-peaked far-field noise spectrum of a multitube nozzle is composed of the output of several different noise generating mechanisms.

At low frequencies, postmerged jet-mixing turbulence noise,and facility engine core noise is dominant, while at high frequencies elemental jet-mixing turbulence noise, shock (or screech) noise, and spiral-mode flow-instability noise dominate.

Multitube-nozzle postmerged-jet noise radiates from a region which has flow characteristics similar to a simple jet. The postmerged jet core diameter is approximately equal to the multitube-array diameter. The gas conditions in the postmerged jet core are equal to the average flow conditions (P_T, T_T, and V_J) in a round jet which has expanded to a diameter equal to the multitube-array diameter. The fully-expanded-flow area ratio is an important consideration when considering postmerged jet core gas conditions.

The postmerged jet noise peak frequency is related to the Strouhal number relationship where the dimension term is equal to the multitube-nozzle array diameter and the velocity term is equal to the postmerged jet, potential core velocity. The postmerged jet, core velocity profile affects peak PNL values when this source of noise is dominant. A flat profile attained by proper tube distribution, e.g., close-packed-array arrangement, yields lower PNL values. A postmerged jet core velocity profile which peaks in the center, e.g., radial-array arrangement of tubes, results in higher PNL values. This is due to a change in the direction of postmerged jet noise frequencies away from the jet axis. The postmerged jet noise power levels were not affected significantly by postmerged jet core velocity profile shape, however.

Multitube suppressor nozzles provide reduced noise levels in the low frequency portion of the jet noise spectrum. This is due to the low jet velocity inherent with the postmerged jet region. This situation makes facility (or engine) upstream generated noise, e.g., core noise, an important consideration when determining multitube nozzle effectiveness in suppressing jet noise. Care should be exercised to provide a quiet burner system in a test facility used for jet noise research purposes. In this test program the facility's core noise was apparent in a few one-third-octave bands.

The elemental jet mixing turbulence noise is generated in the premerged jet region. The outer row of jets in the multitube nozzles' efflux effectively shields noise generated by the inner jets. About 4 to 5 dB of additional suppression of premerged jet noise was realized with the

61-tube nozzle beyond that expected from geometric shielding concepts. It has been postulated that this additional suppression is due to acoustic or flow mutual-coupling between adjacent elemental jets. The premerged jet noise peak-frequency is related to the Strouhal number relationship modified by fully-expanded flow area, total temperature and number of tubes.

Shock noise, or screech tones in the multitube-nozzle jet were observed, especially at ambient flow conditions. The tone frequency was a function of the tube diameter and nozzle pressure ratio. This phenomenon is not expected to occur under the hotter supersonic gas conditions common to contemporary jet engines.

A new source of multitube-nozzle supersonic jet high frequency noise was identified. This noise is apparently generated by spiral-mode flow-instability at nozzle PR $\geq$ 2.5. The frequency of this noise mechanism agrees with theory, being a function of tube diameter, Mach number and jet velocity. The noise is primarily directed at 90^{o} to the jet axis. Noise level is a function of the number of tubes in a nozzle array, exit area, and nozzle pressure ratio. Spiral-mode flow-instability can influence peak PNL as well as EPNL values.

Of all the multitube-nozzle geometric parameters tested, only two were found to be dominant acoustically. Tube number determined the premerged noise levels, while the array's area ratio determined the postmerged noise levels. Tube arrangement and flow radial distribution were found to be second order effects.

Hardwall ejectors surrounding multijet flows were found to provide additional jet noise suppression. An ejector induces additional secondary flow between the jet elements causing some noise reduction due to a relative velocity effect. It is also postulated that under favorable geometric conditions, noise reflections from the ejector wall back to the source region may be affecting the noise generation process, reducing the sound output. Fully-mixed ejector configurations were found to also reduce postmerged jet noise, probably due to a lowering of the kinetic energy in the postmerged jet. Ejectors, generally, were shown to have a very distinctive radiation characteristic, causing the premerged jet noise to peak at approximately 110^{o} from the engine inlet.

Multitube-nozzle jets were shown to have inherent jet noise shielding properties associated with the premerged jet noise. In addition, it was shown that high temperature, low velocity flow in the outer row of jets was a very effective acoustic shield against the noise generated by the central cluster of jets.

Acoustical linings in the ejectors were another means of increasing the premerged jet noise suppression. The linings have to be tuned to the noise frequencies generated inside the ejector. Similarly the lining impedance has to be optimized for the flow and noise environment inside the ejector. The overall lining effectiveness, from the far-field noise point of view, is determined by the relative level of the noise floor of the jet noise generated beyond the ejector exit plane. Analytical studies showed that noise-source distribution and flow-profile characteristics inside the ejector are also important in determining the lining effectiveness.

The acoustic characteristics of a jet noise suppressor system are a composite of the above noise mechanisms. Secondly, the suppressor system is invariably evaluated on the subjective PNL scale. This means that the properties of the above noise components have to be weighted according to the annoyance scale and properly balanced relative to each other, as described in volume X, in order to achieve maximum jet noise suppression.

The effect of forward velocity (flight) on jet noise suppression with multitube nozzles and ejectors was studied in a low-speed wind tunnel. It was concluded from the wind tunnel studies that the peak noise from an unsuppressed R/C nozzle varied simply as the relative velocity. Multitube nozzles without ejectors also radiated peak noise simply as a function of relative velocity. Presence of ejectors in the suppressor system degraded the premerged jet noise suppression in flight beyond the relative velocity effect. The amount of degradation was a function of ejector diameter; loose fitting ejectors suffered less loss than tight fitting configurations. The postmerged jet peak noise, however, was unaffected and followed the relative velocity function.

Until very recently, the normal course of action was to optimize the acoustic characteristics of suppressor systems for their static performance and then take whatever flight penalty there was when the design was tested in flight. The forward velocity studies on jet noise conducted in this program, now enable the designer to take flight effects into account at an earlier stage in the design process.

A parallel propulsion performance technology program (vol. IV) has achieved similar advances in the basic understanding of suppressor nozzle system performance mechanisms. A coordinated effort between noise and propulsion staffs enabled these advances in technology to be incorporated into the full scale suppressor system demonstrator described in volume X.

7.0 RECOMMENDATIONS

The planned systematic approach used in this program to investigate high-velocity jet noise suppression mechanisms has paid off by giving better insight into multitube nozzle aerodynamics, noise generation and noise transmission processes. As a natural follow-on to this work, a similar program should be conducted to study jet noise suppression at subsonic velocities. Such a program should not necessarily be restricted to multitube nozzles alone, because the best suppressor concept for low velocity jet noise suppression has not been established as yet. The tubular nozzle concept, however, should be pursued to some length, because studies in this program have shown a promising trend. At lower jet velocities smaller area ratio nozzle arrays ($AR < 3.0$) are better jet noise suppressors than large area ratio arrays which is the reverse of the high velocity case. This is an encouraging trend because from the point of view of flight hardware design, smaller area ratio nozzles are more practical.

The multielement-jet noise studies established the similarity in flow structure and noise characteristics between the postmerged jet noise component and an equivalent simple jet. This work should be continued to establish firmly the quantitative relationships between the postmerged jet and the simple jet. In order to finalize this work, flow turbulence effects should be studied and accounted for.

This program has shown that jet noise shielding with low velocity, peripheral flows has suppression potential. Jet noise shielding studies should be continued to develop a quantitative base to this technology in order that rational design concepts could be initiated. Dual-flow (turbofan) and multicycle engines are natural future candidates for the application of the gas-shielding/jet-noise suppression concept.

Hardwall ejectors coupled to multitube nozzles were shown to exhibit a hitherto unrecognized noise suppression mechanism, where the reflected noise from the ejector wall appeared to influence the jet noise generating efficiency. This hypothesis should be explored further. It should be first verified and then quantified so that full use of this jet noise suppression mechanism could be used in future applications.

The multitube nozzle concept has been considered only for its jet noise suppression characteristics. A large area ratio multitube nozzle introduces an area change (acoustic impedance change) in the engine's exhaust duct system. Consequently the engine internal (core) noise propagating through this system will experience some transmission loss, as was observed in some of the model scale test configurations. Therefore, from the point of view of engine core noise reduction, this aspect of suppressor nozzle installations should be looked into, so that all the benefits are extracted in the final analysis.

Jet noise suppression technology is firmly established in terms of static evaluation and analysis. The most important application of jet noise suppression, however, is under flight conditions where the relative velocity effects modify the statically observed results. A low-speed wind tunnel was used successfully to study these effects on multitube-nozzle ejector systems. A great deal more work is necessary in the area of flight effects on jet noise generation, radiation and suppression to establish the necessary confidence in applying the static jet noise technology.

PRECEDING PAGE BLANK-NOT FILMED

Analytical studies were undertaken to investigate noise-source location and flow-profile effects on jet noise absorption in acoustically lined ejectors. The techniques of solution of these analytical problems proved to be more cumbersome and time consuming than originally envisaged. Efforts should be made to streamline the methods of solution so that a wider range of cases could be studied, leading to a quantitative understanding and improvement in this technology area.

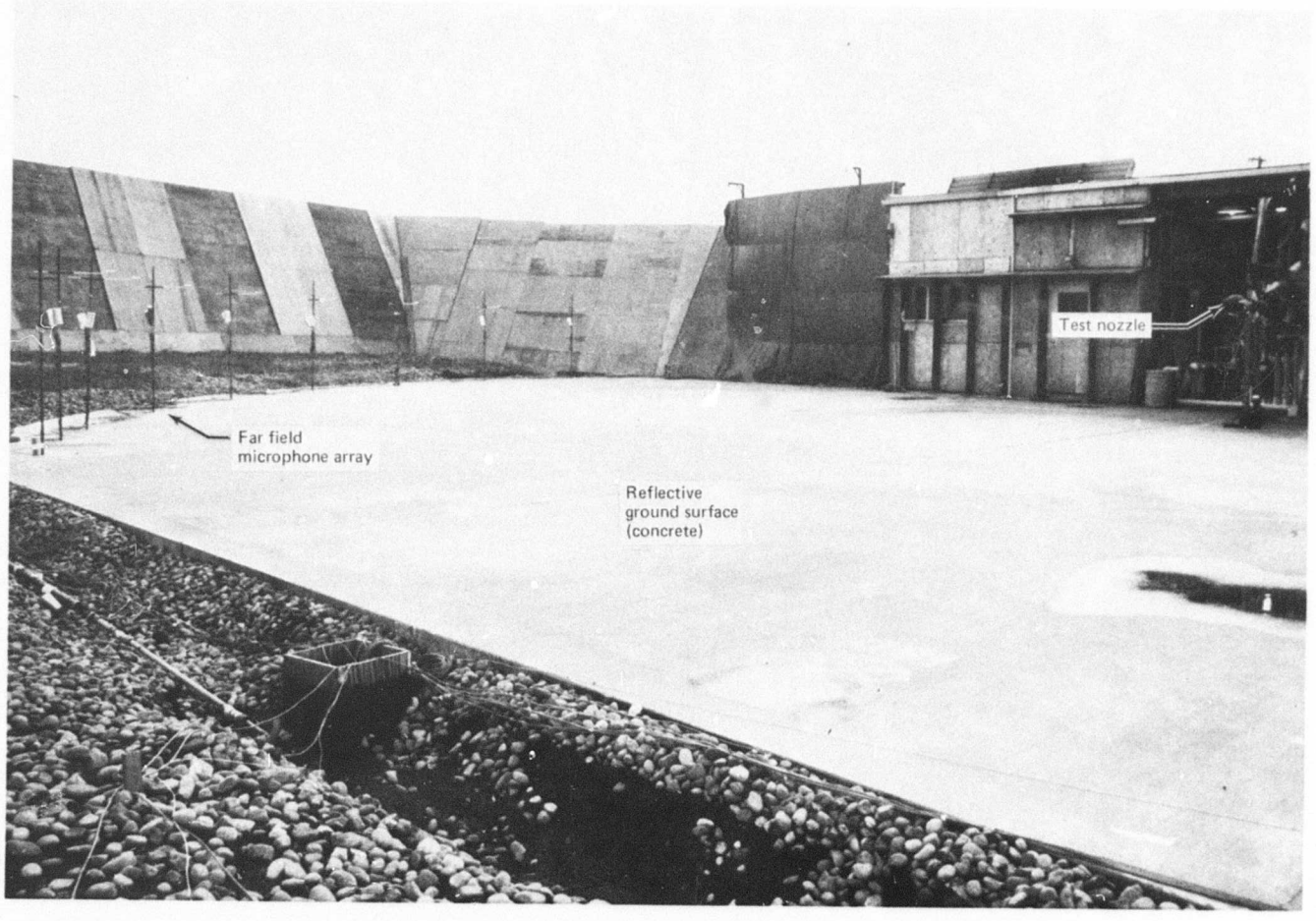

Figure 1. — Acoustic Arena Hot Nozzle Test Facility (HNTF)

Figure 2. — HNTF Microphone Installations

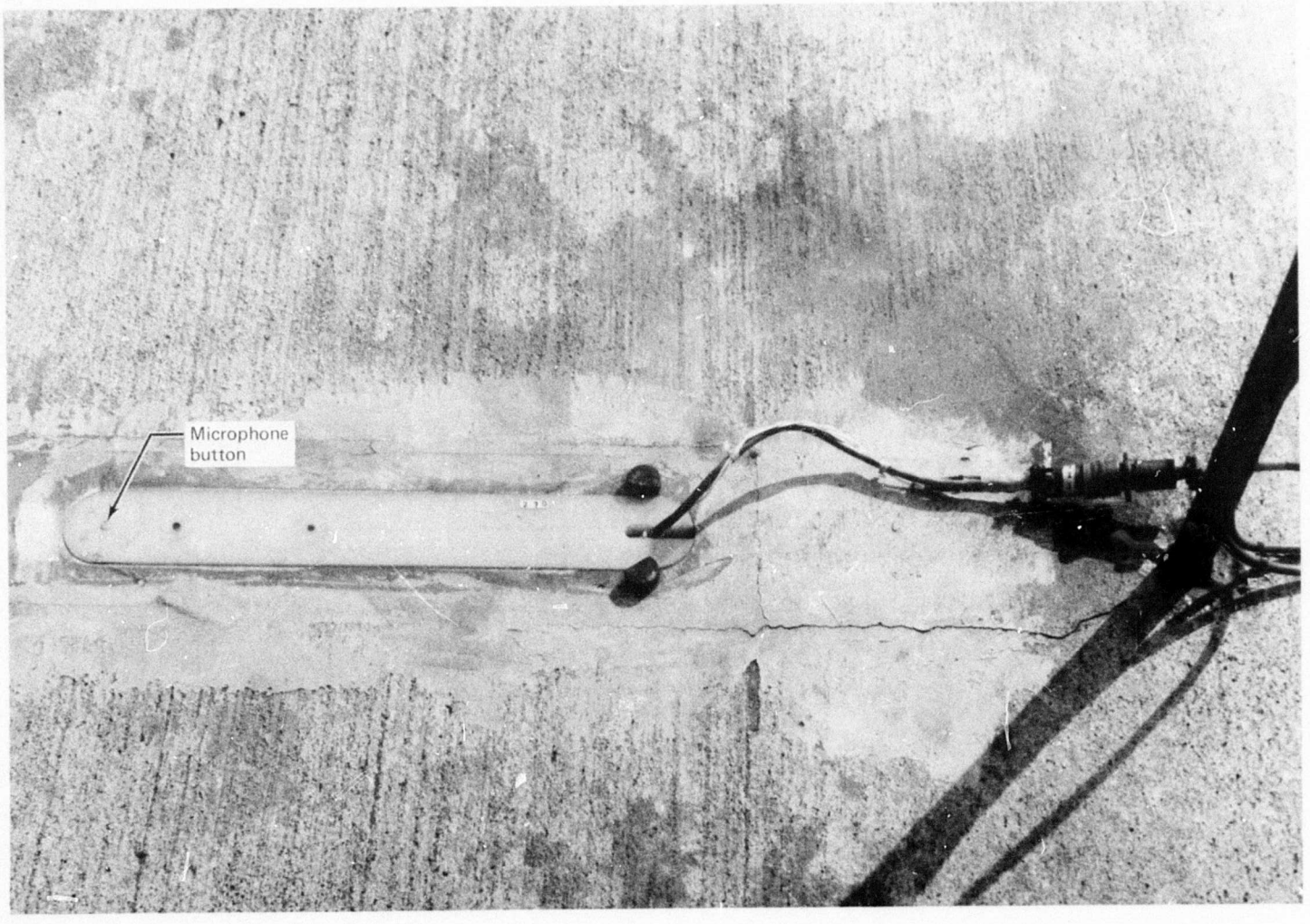

Figure 3. — HNTF Ground Microphone Installation

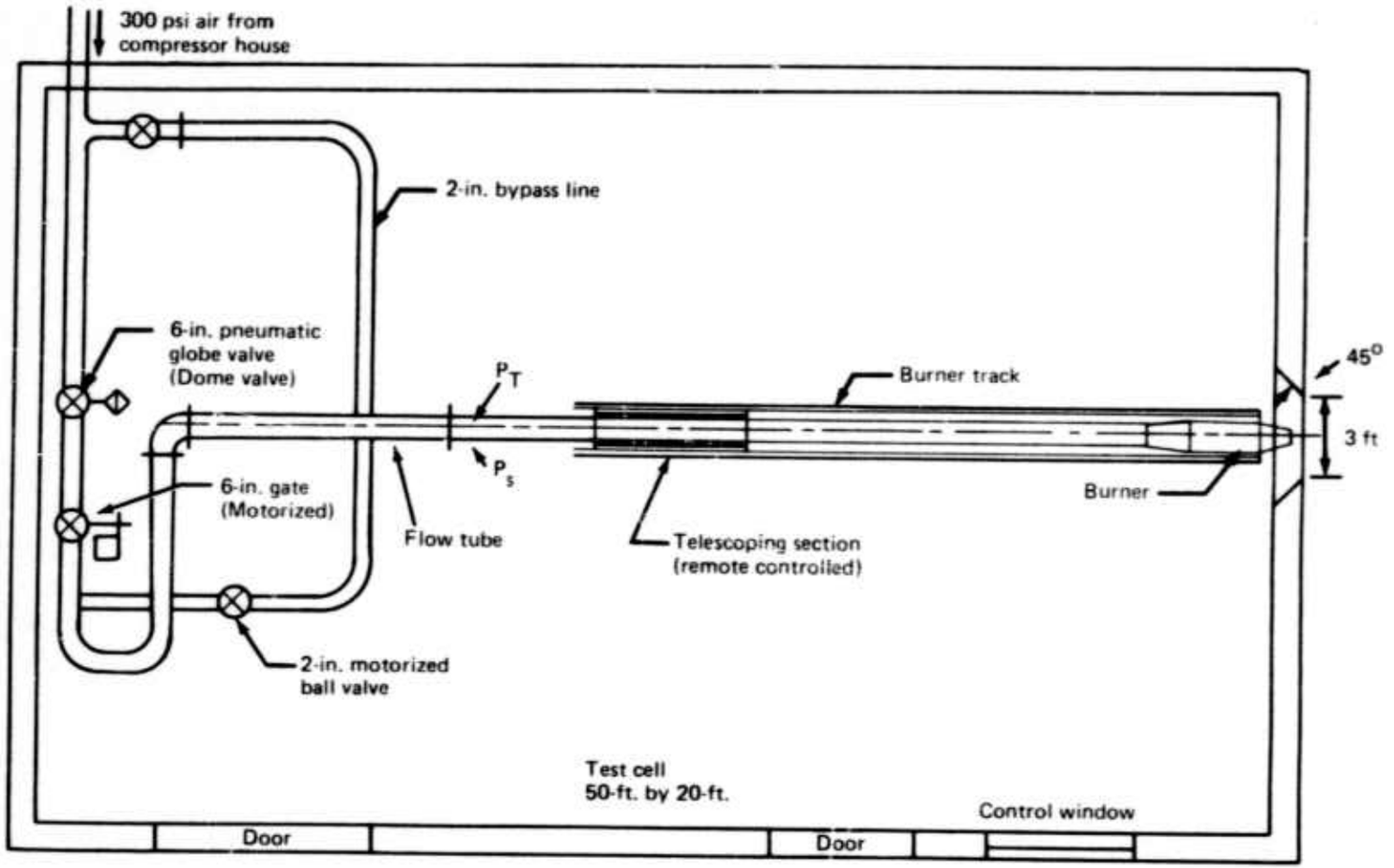

Figure 4. — Schematic of Test Cell Showing Retractable Burner

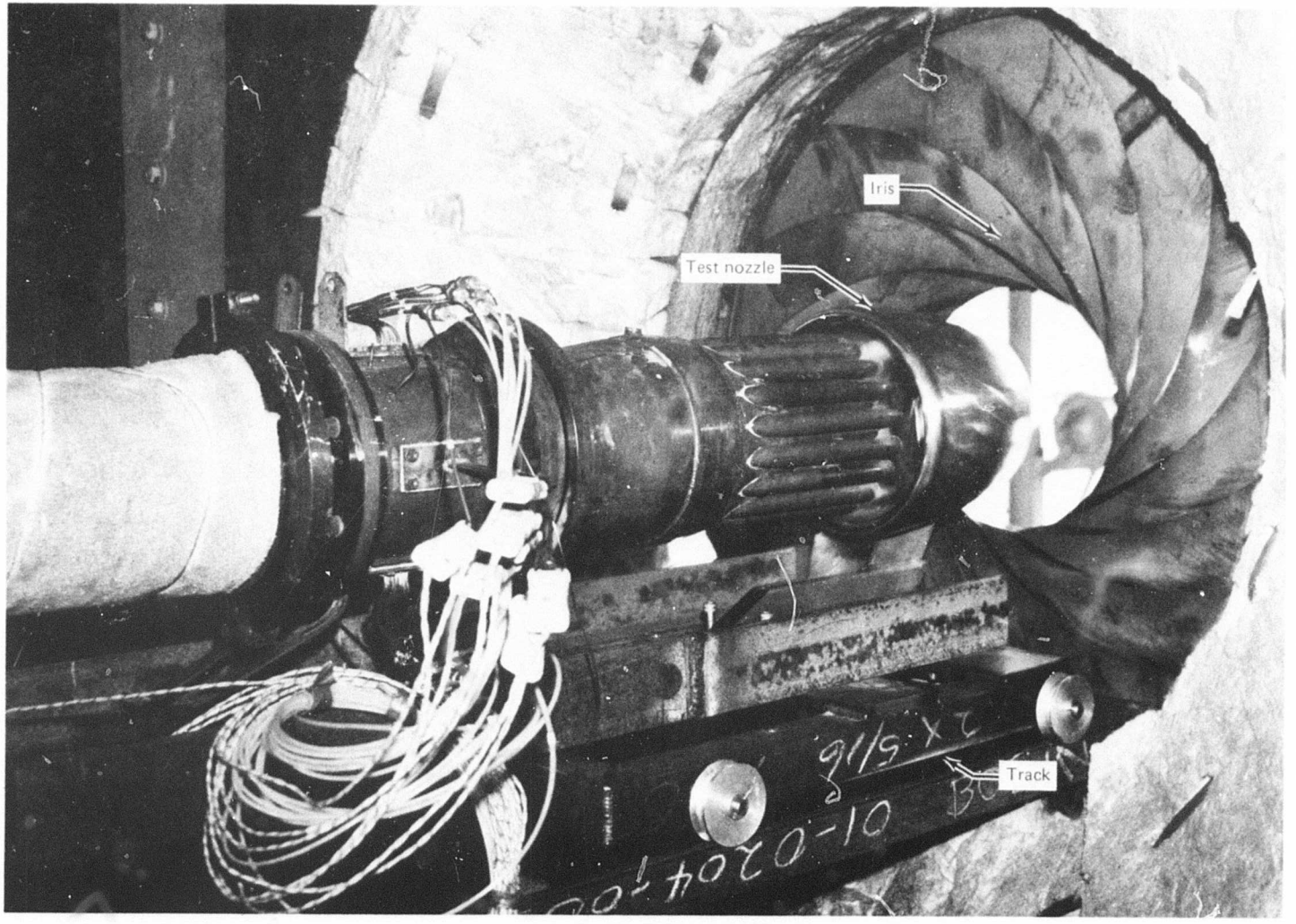

Figure 5. — Interior View of Wall Isolation Facility

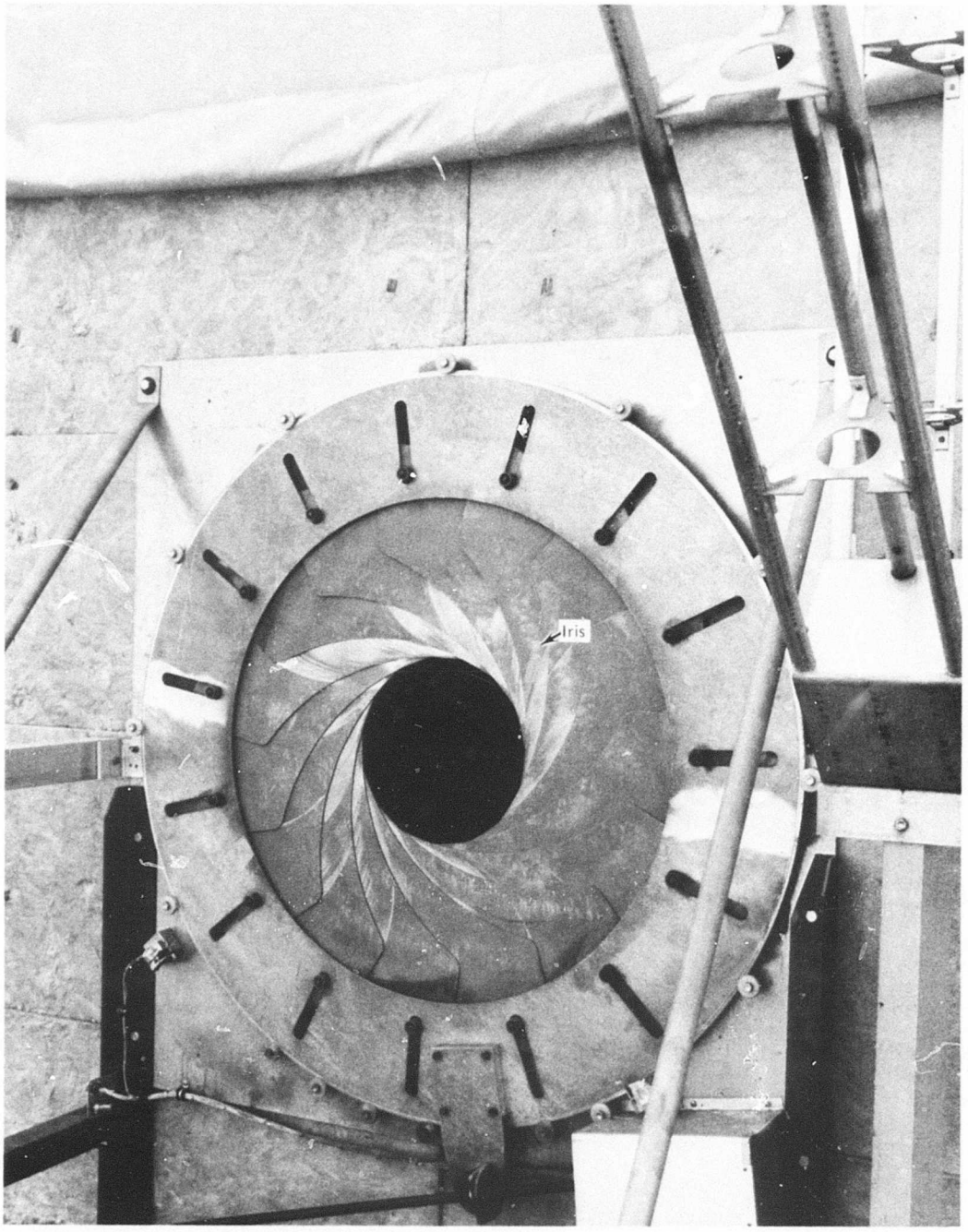

Figure 6. — Exterior View of Wall Isolation Facility

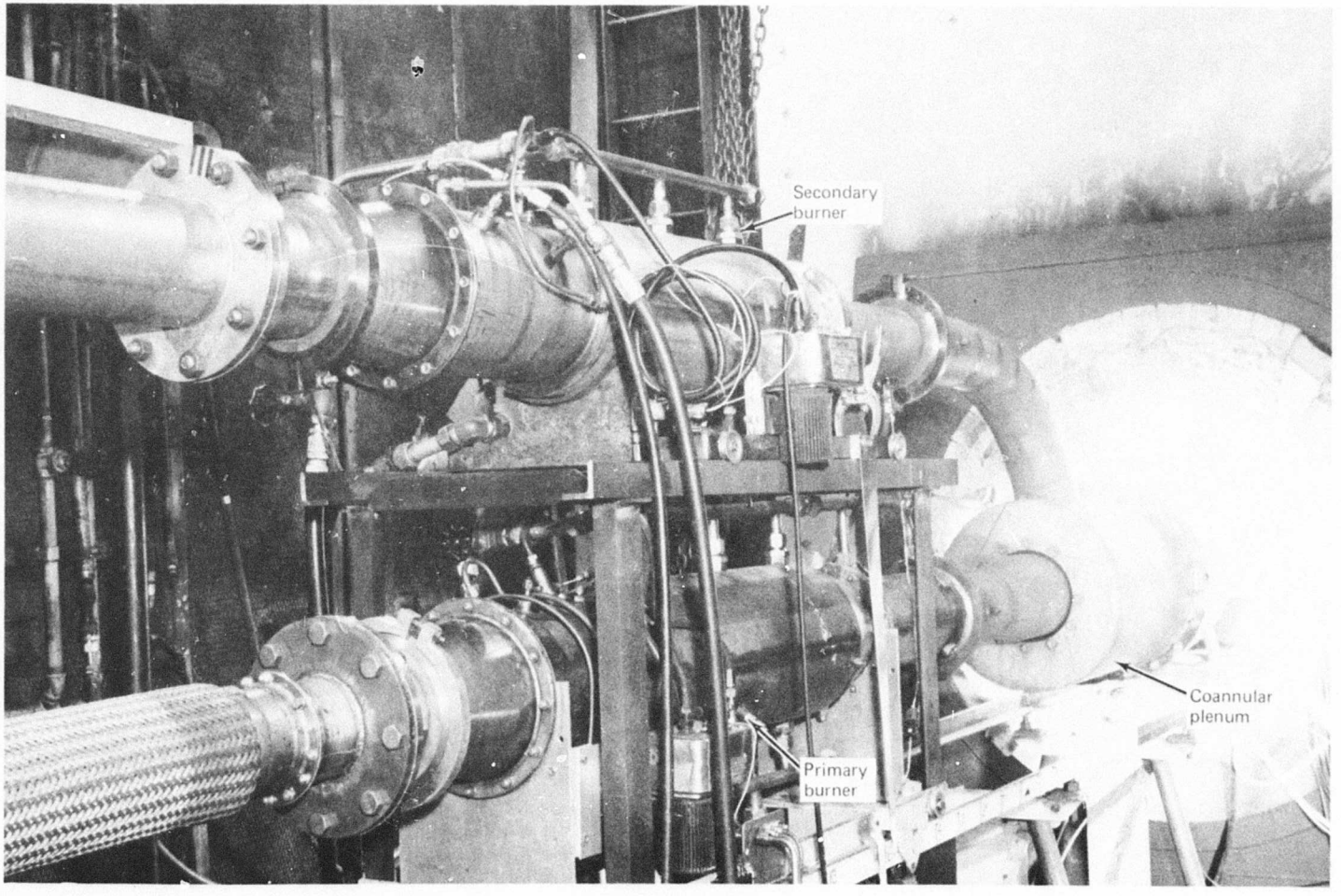

Figure 7. — Dual Burner/Flow Setup

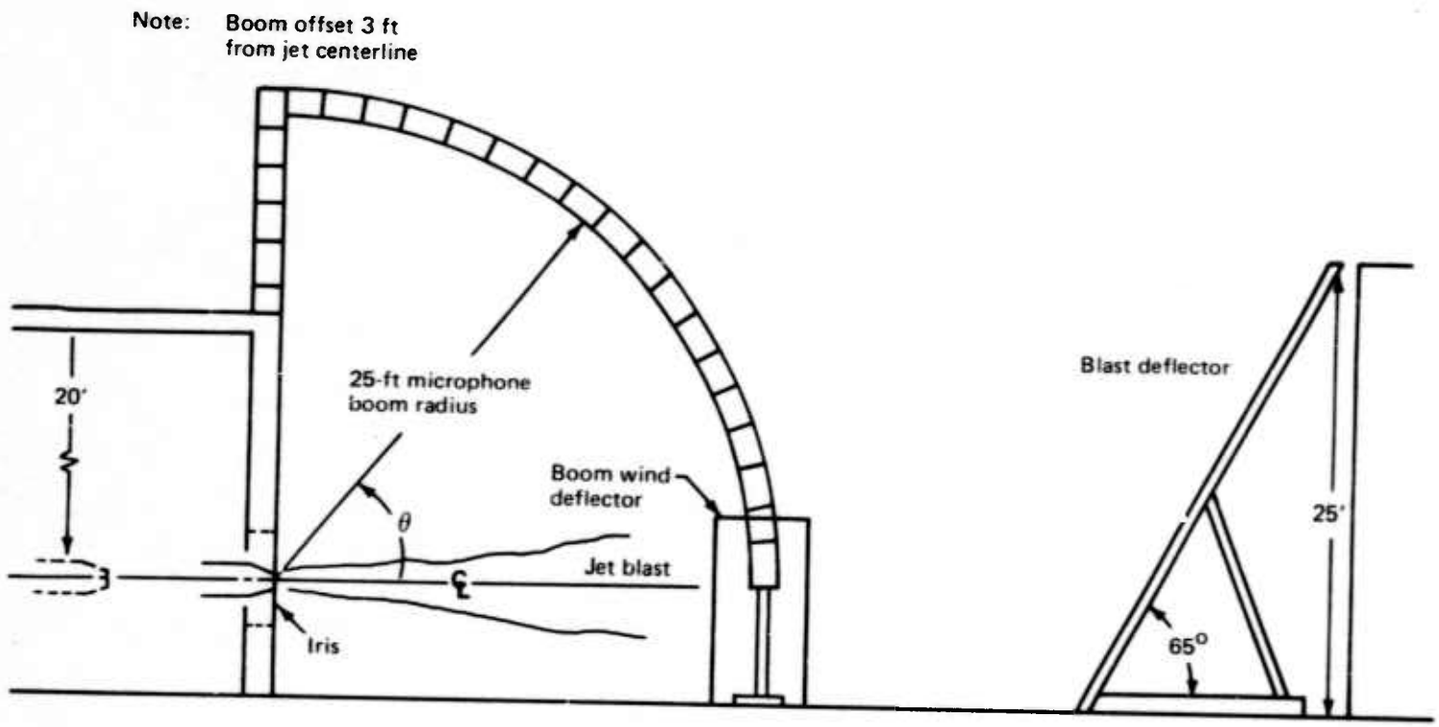

Figure 8. — Schematic of Test Arena

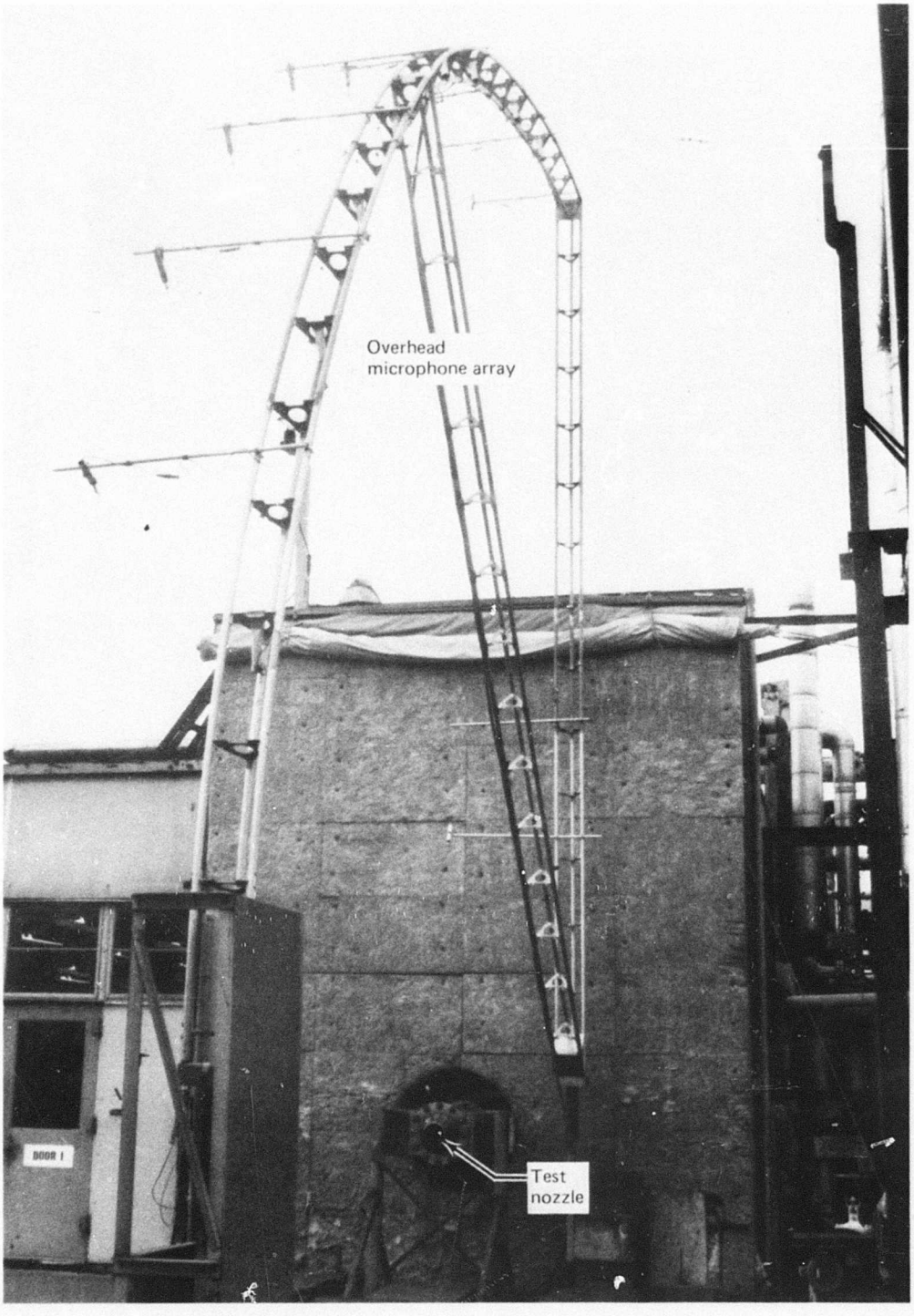

Figure 9. — Wall Isolation Facility Acoustic Arena

Figure 10. — Jet Noise Test Installation in the 9 ft by 9 ft Wind Tunnel

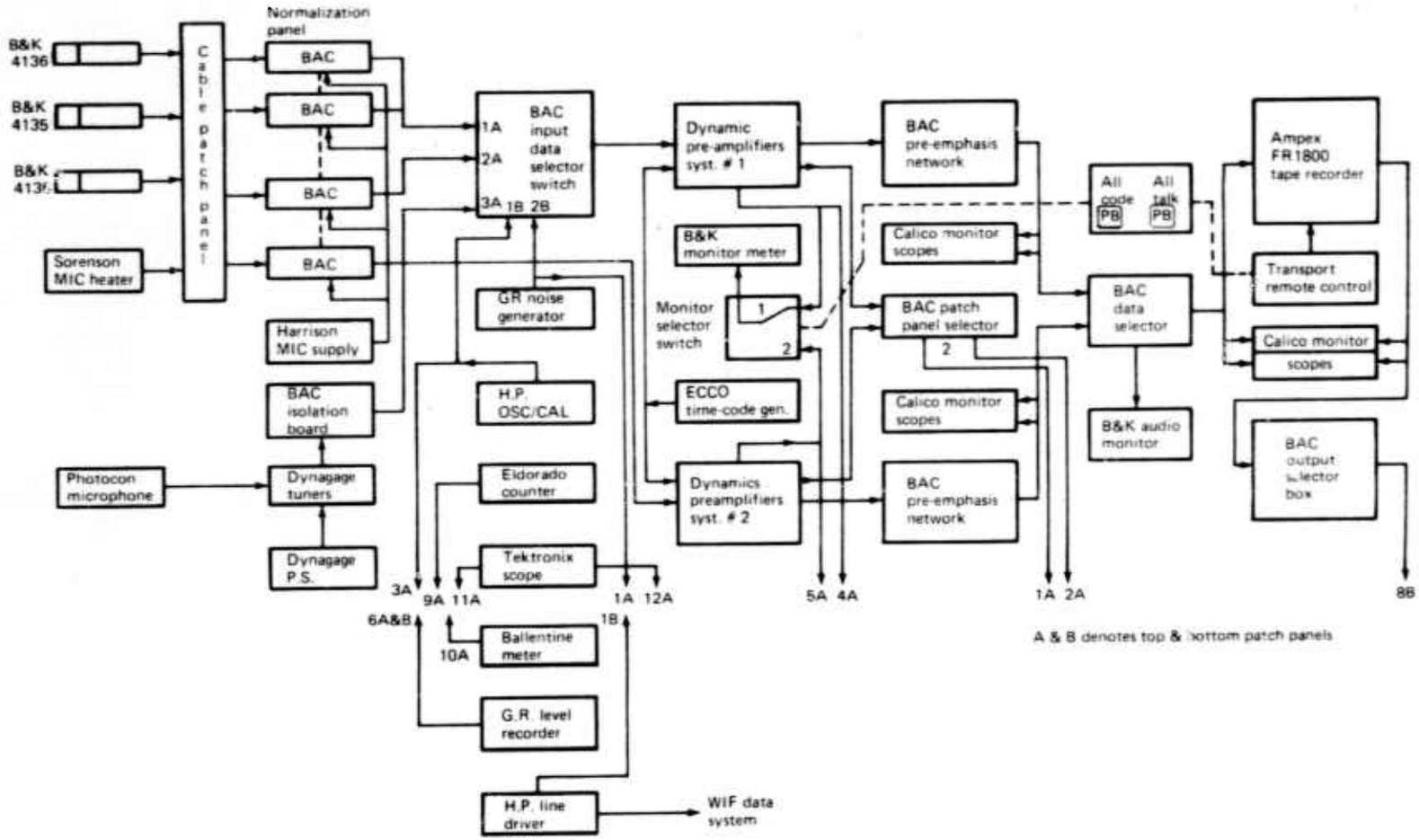

Figure 11. — Block Diagram, Acoustics Data Acquisition System, HNTF, North Boeing Field

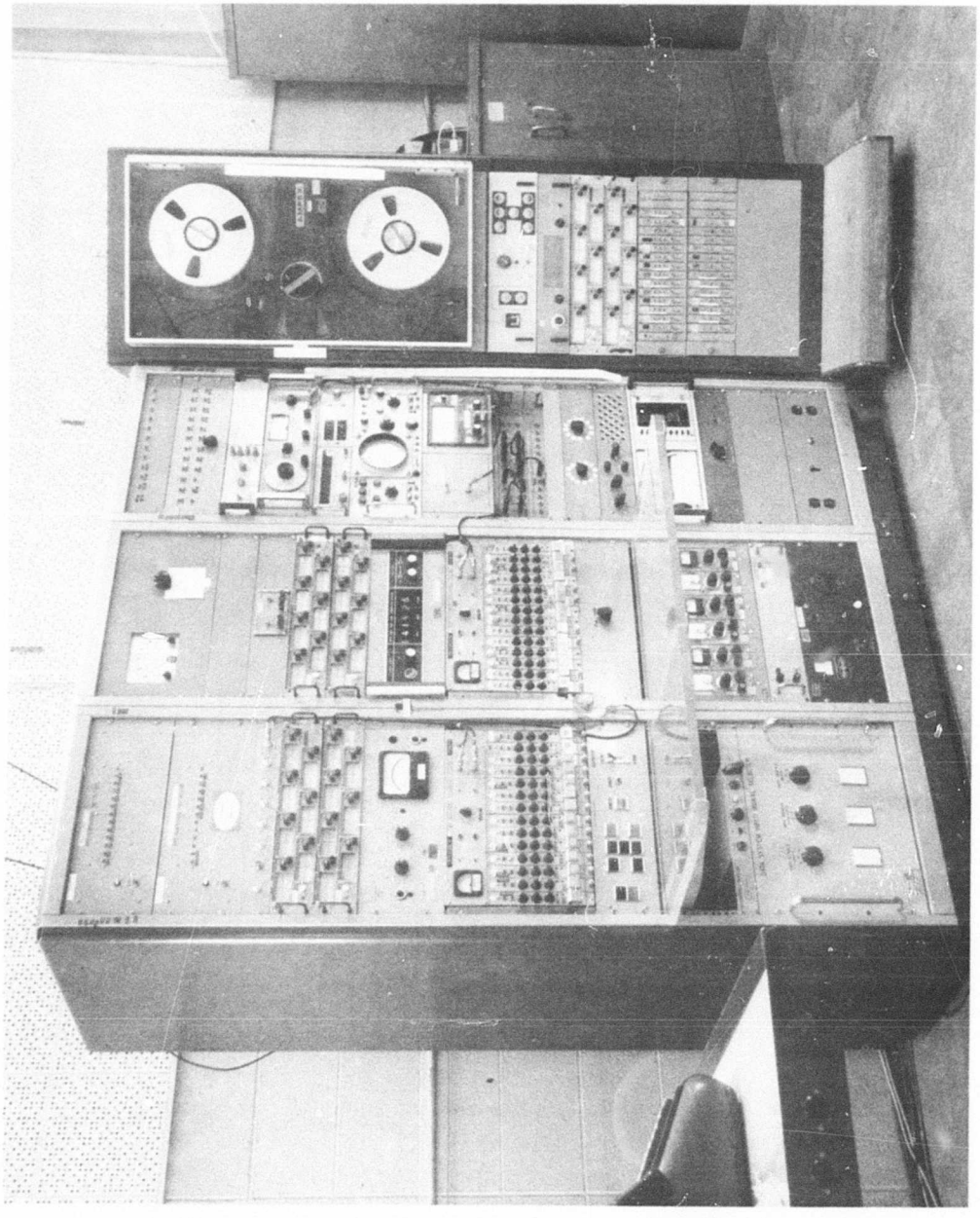

Figure 12. — Acoustic Data Acquisition System

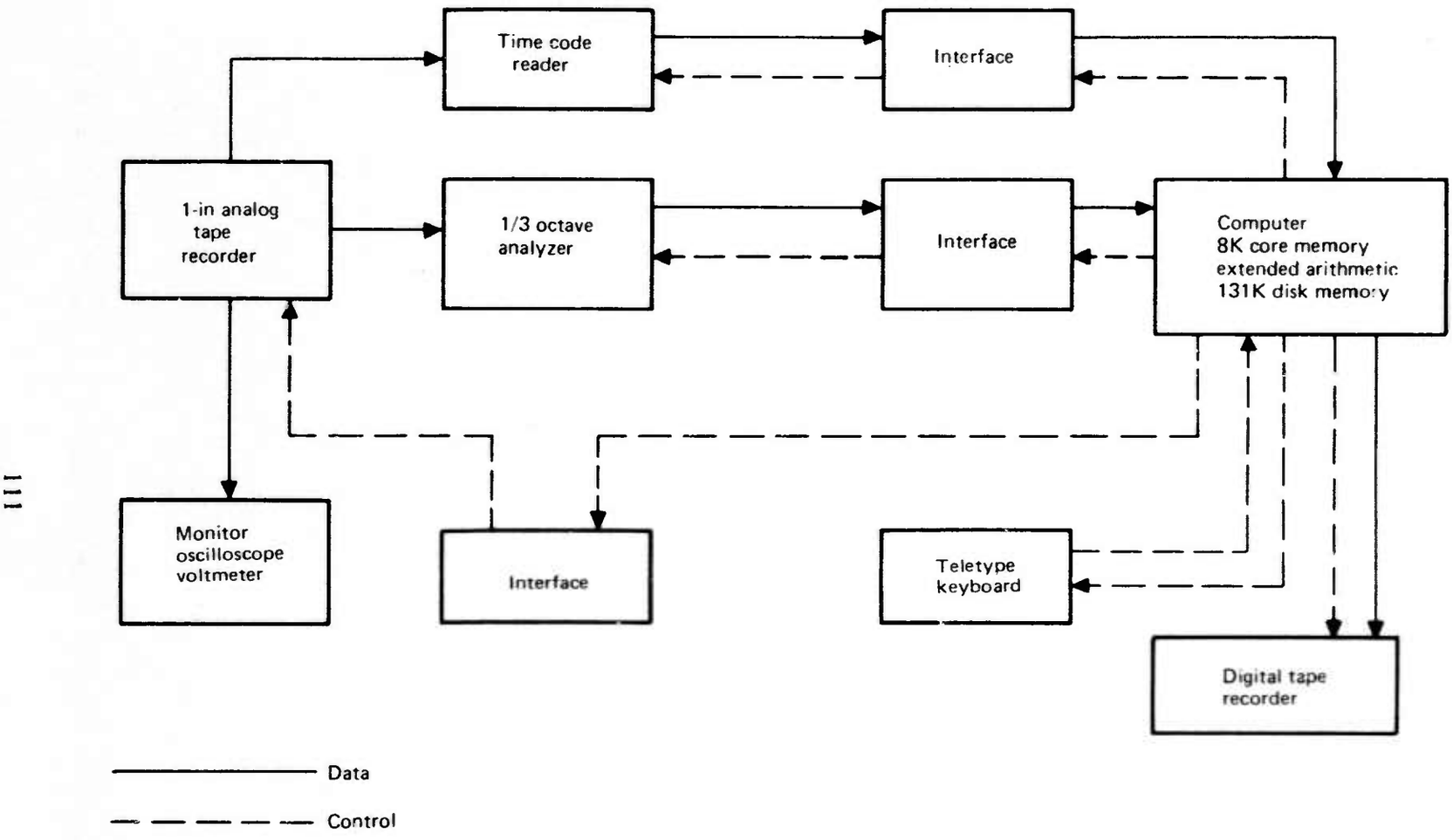

Figure 13. — Block diagram Acoustic Data Reduction System

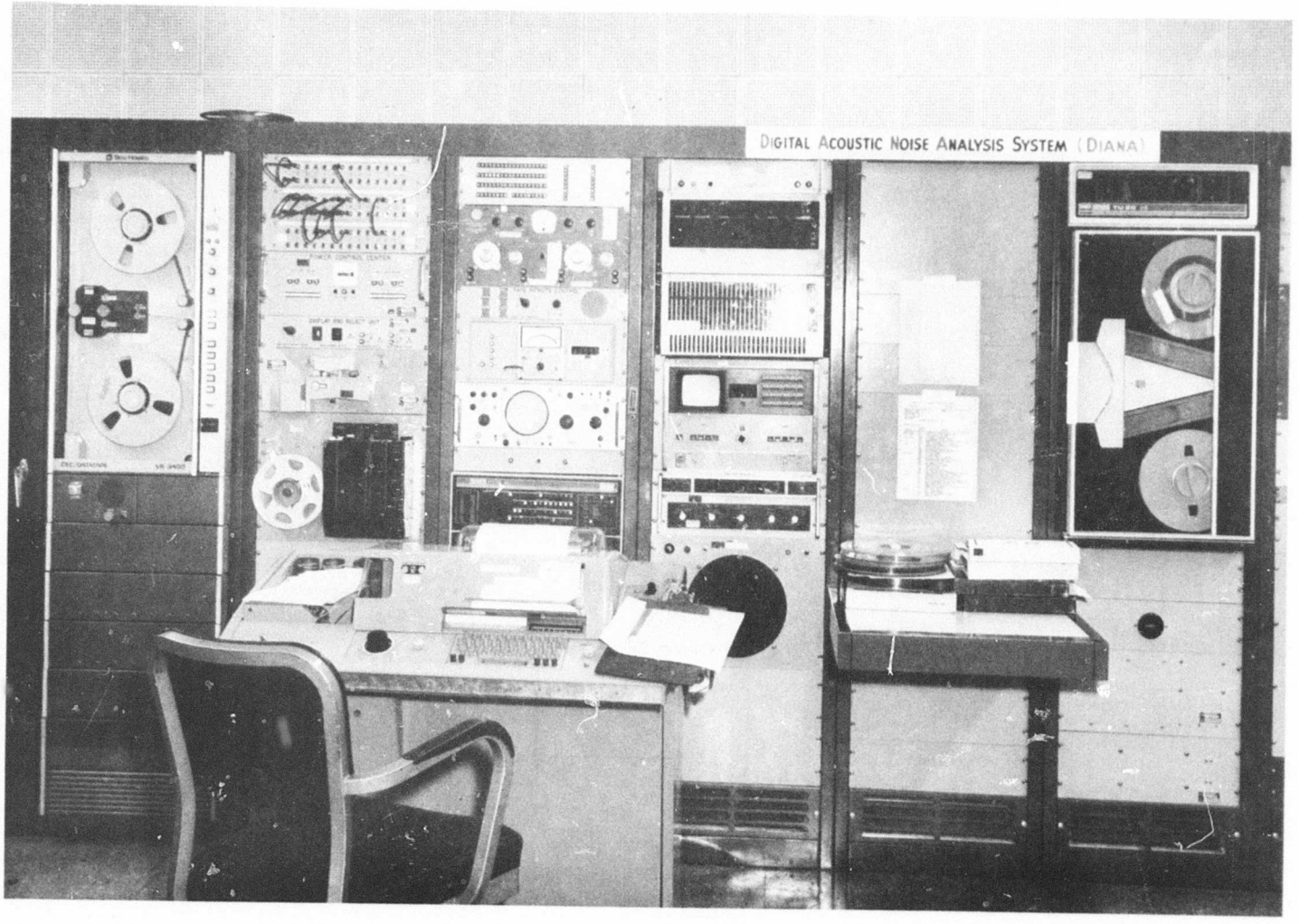

Figure 14. — Acoustic Data Reduction System

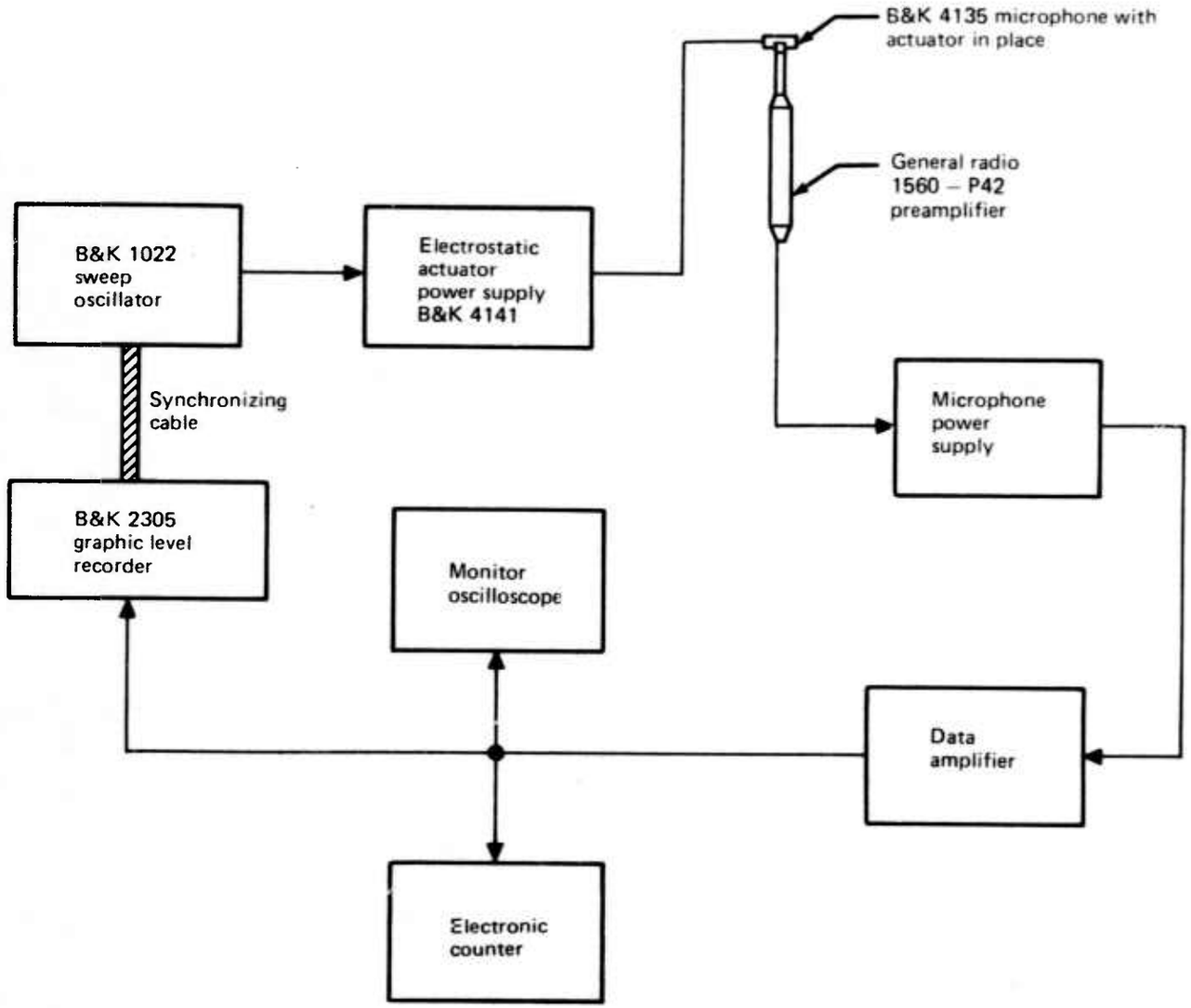

Figure 15. — Electrostatic Actuator Calibration of Data Microphone System

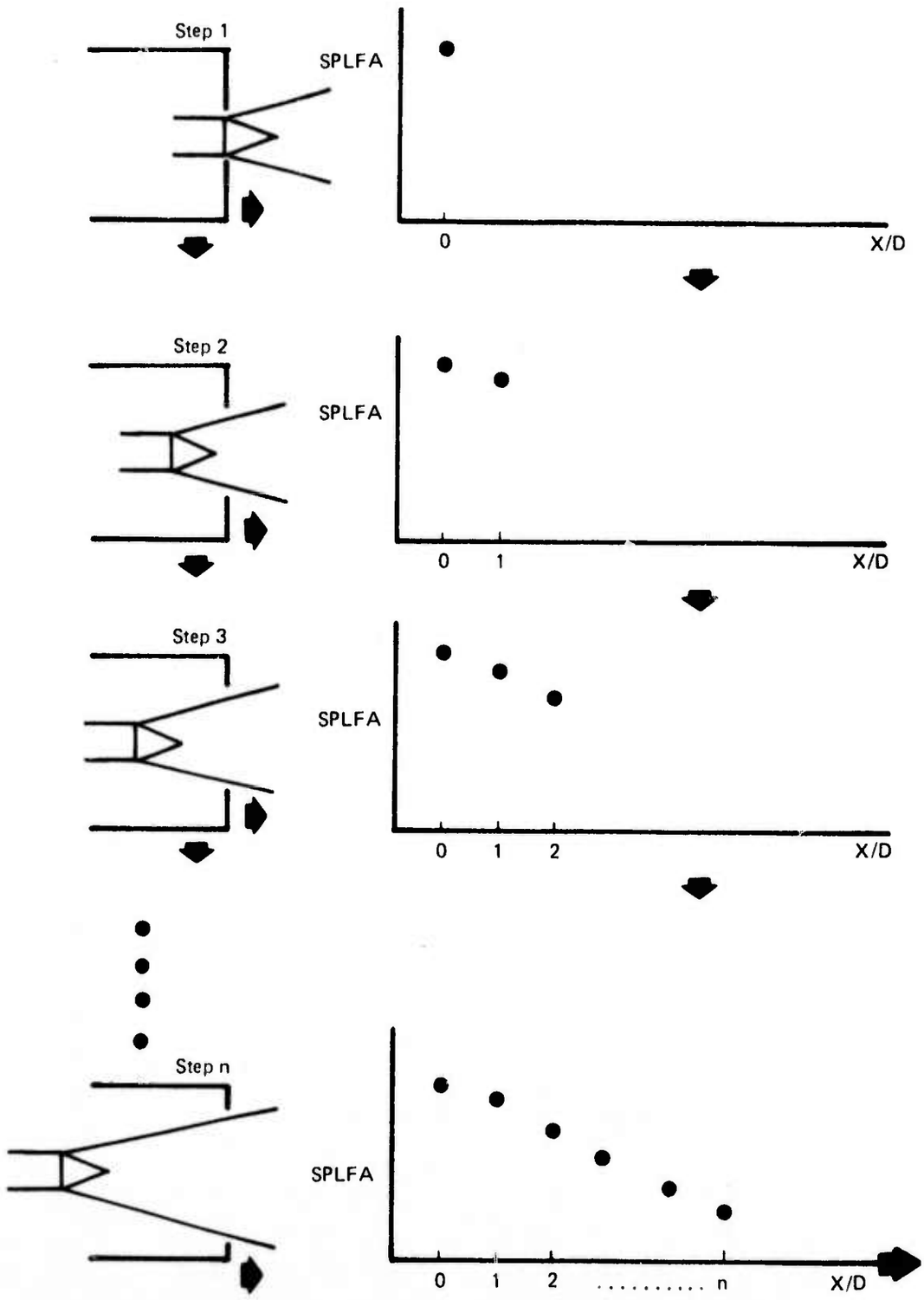

Figure 16. — Schematic of the Measurement Steps Involved in Obtaining a Source Distribution

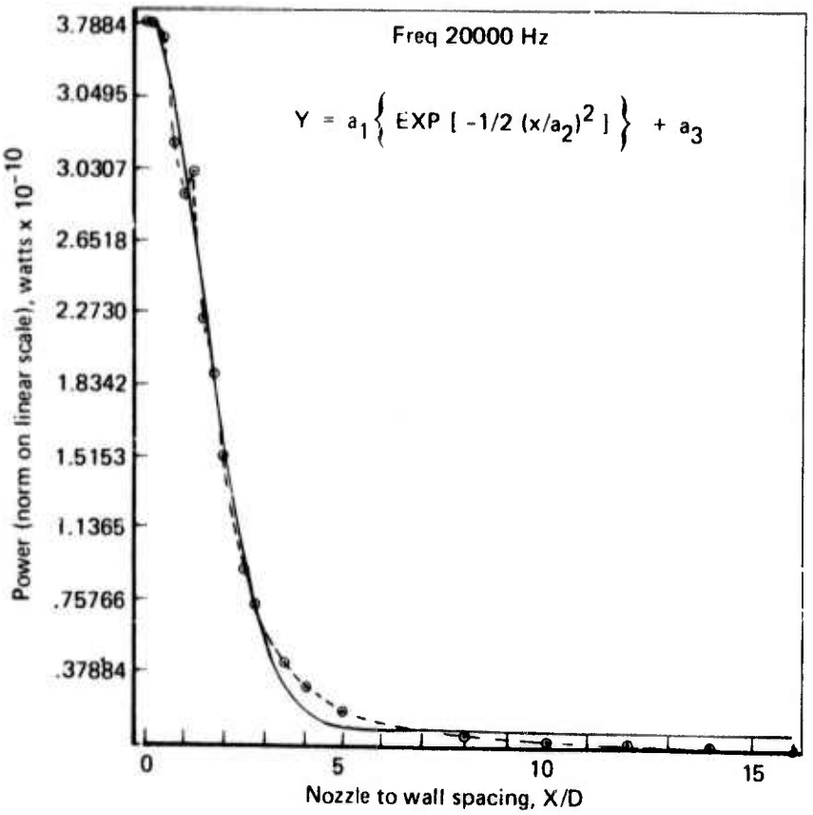

Figure 17. — Curve Fit of Linearized Sound Power Data

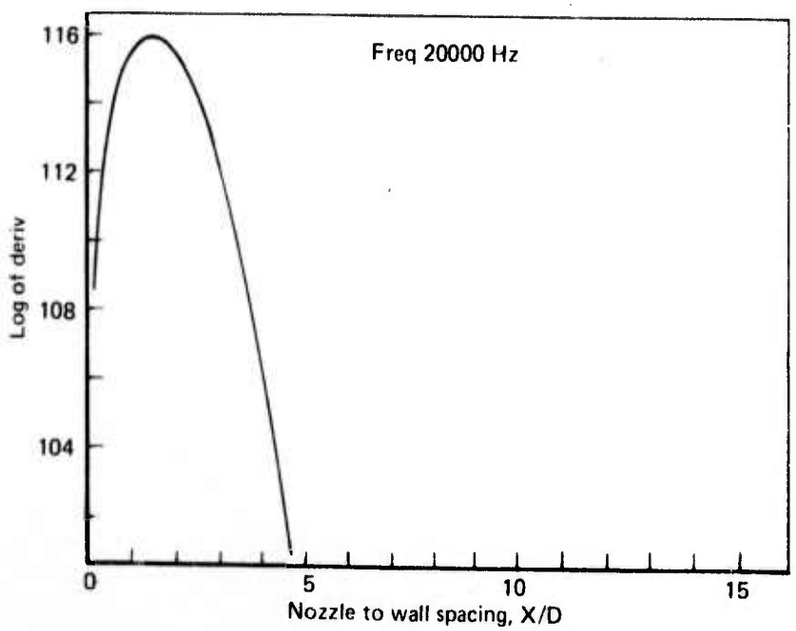

Figure 18. — Axial Source Distribution

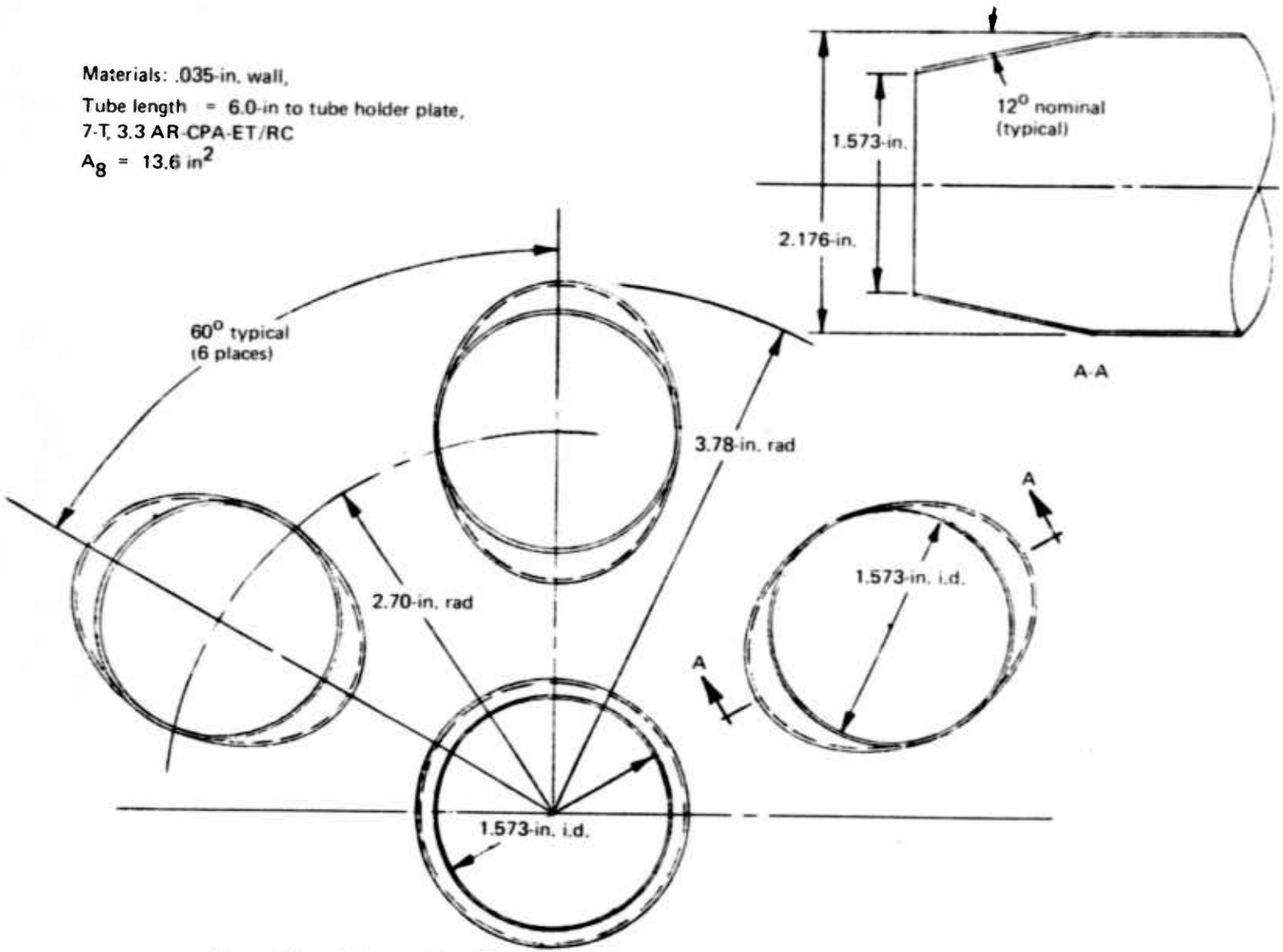

Figure 19. — Schematic of 7-Tube AR 3.3 Elliptical-Tube Nozzle

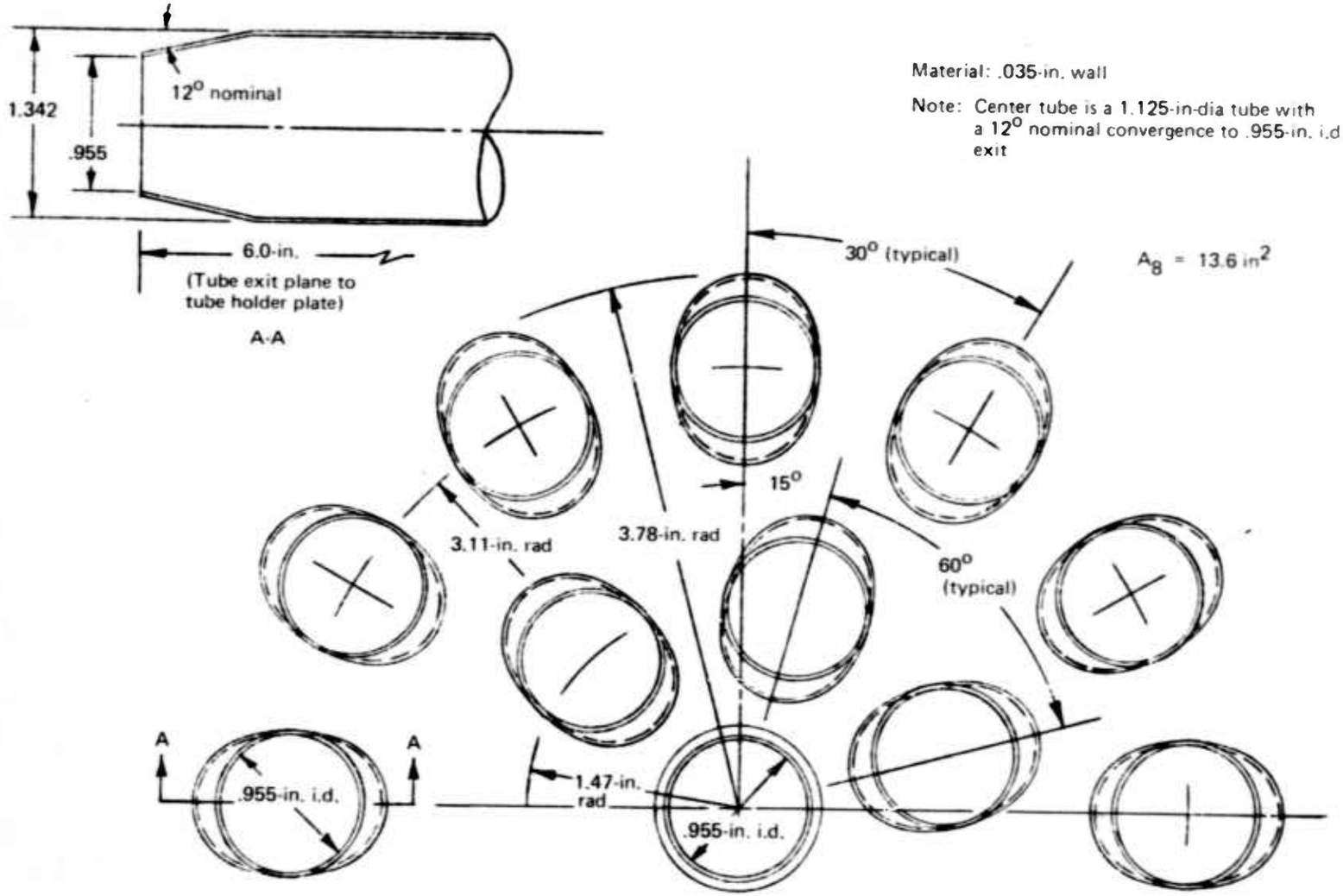

Figure 20. — Schematic of 19-Tube, AR 3.3 Elliptical-Tube Close-Array Nozzle

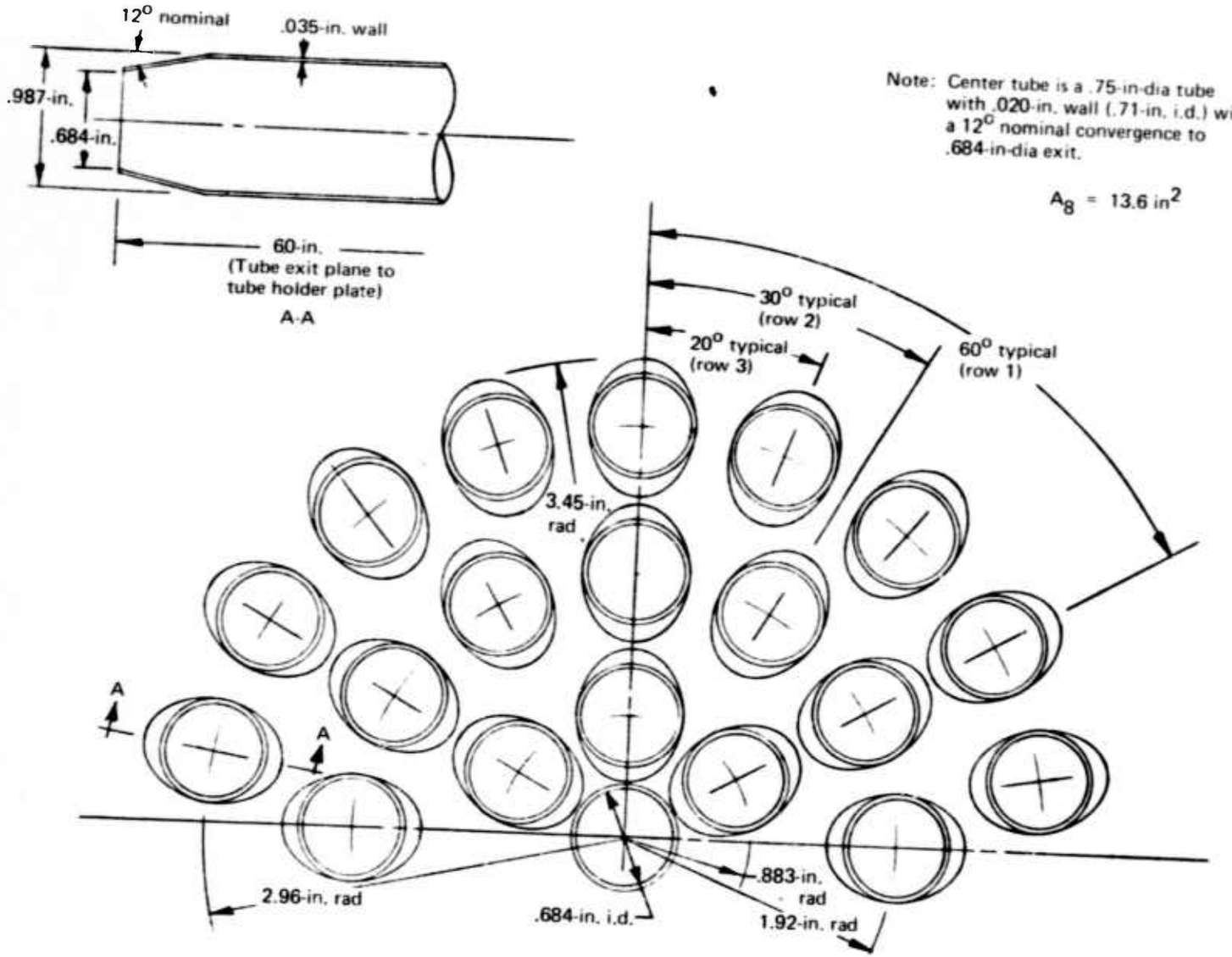

Figure 21. — Schematic of 37-Tube, AR 2.75 Elliptical-Tube Close-Array Nozzle

Area ratio	R_1	R_2	R_3	R_{MAX}
3.3	1.058	2.172	3.286	3.78
4.5	1.268	2.592	3.917	4.41
6.0	1.498	3.052	4.607	5.10

Note: Center tube is a .875-in-dia tube with 12° nominal convergence to .684-in i.d. exit.

Material: .035-in wall.

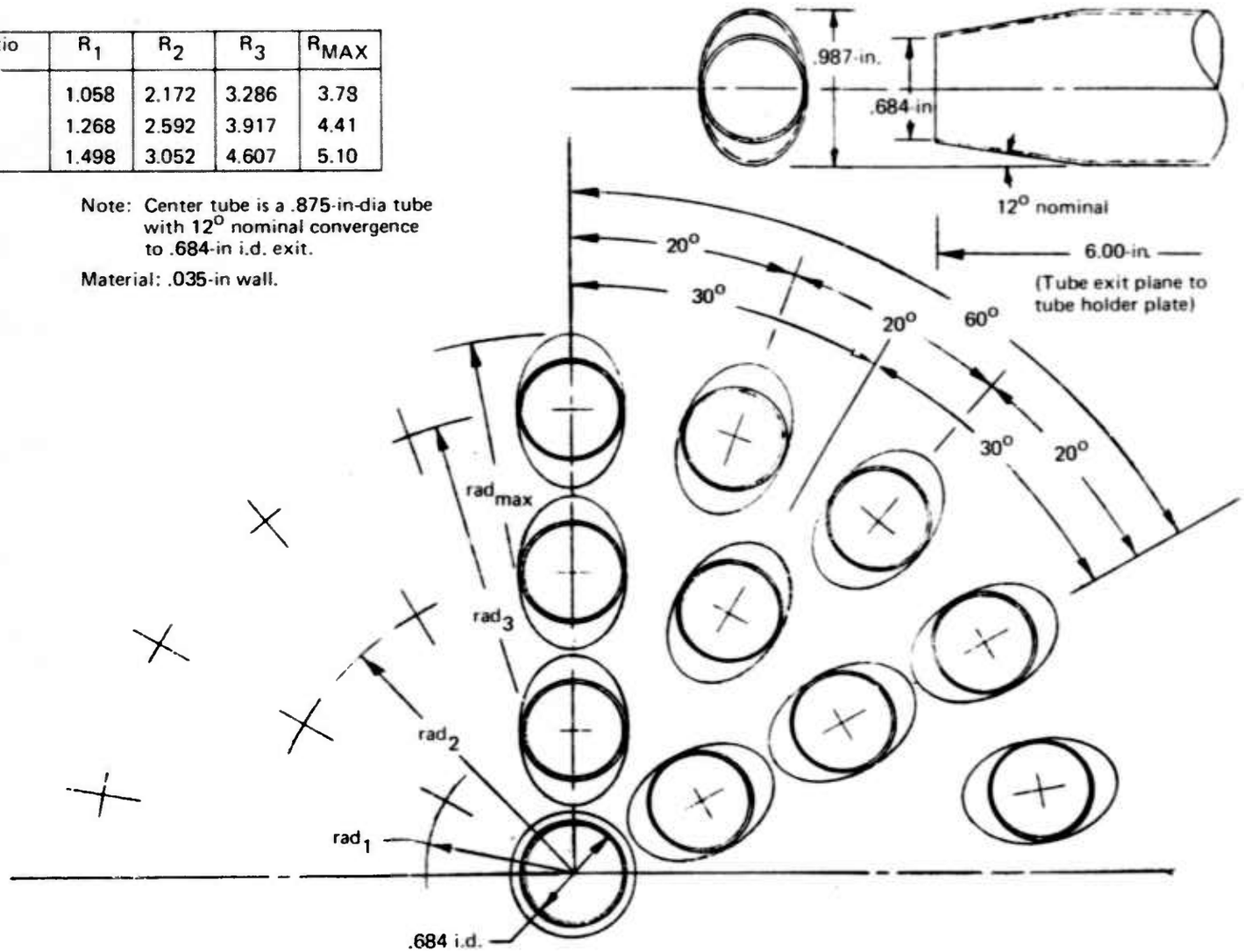

Figure 22. — Schematic of 37-Tube, AR 3.3, 4.5, 6.0 Elliptical-Tube Close-Array Nozzles

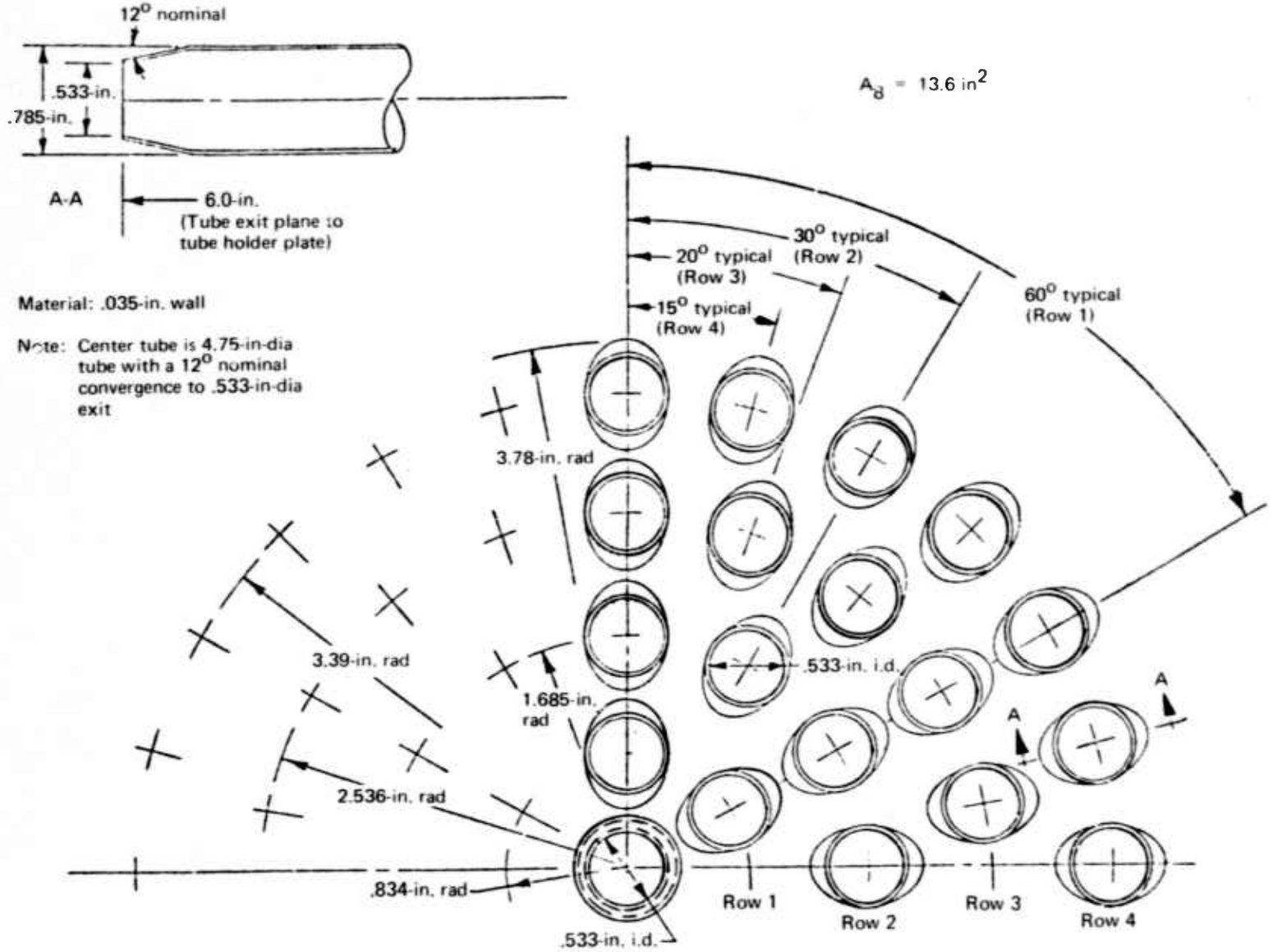

Figure 23. — Schematic of 61-Tube, AR 3.3 Elliptical-Tube Close-Array Nozzle

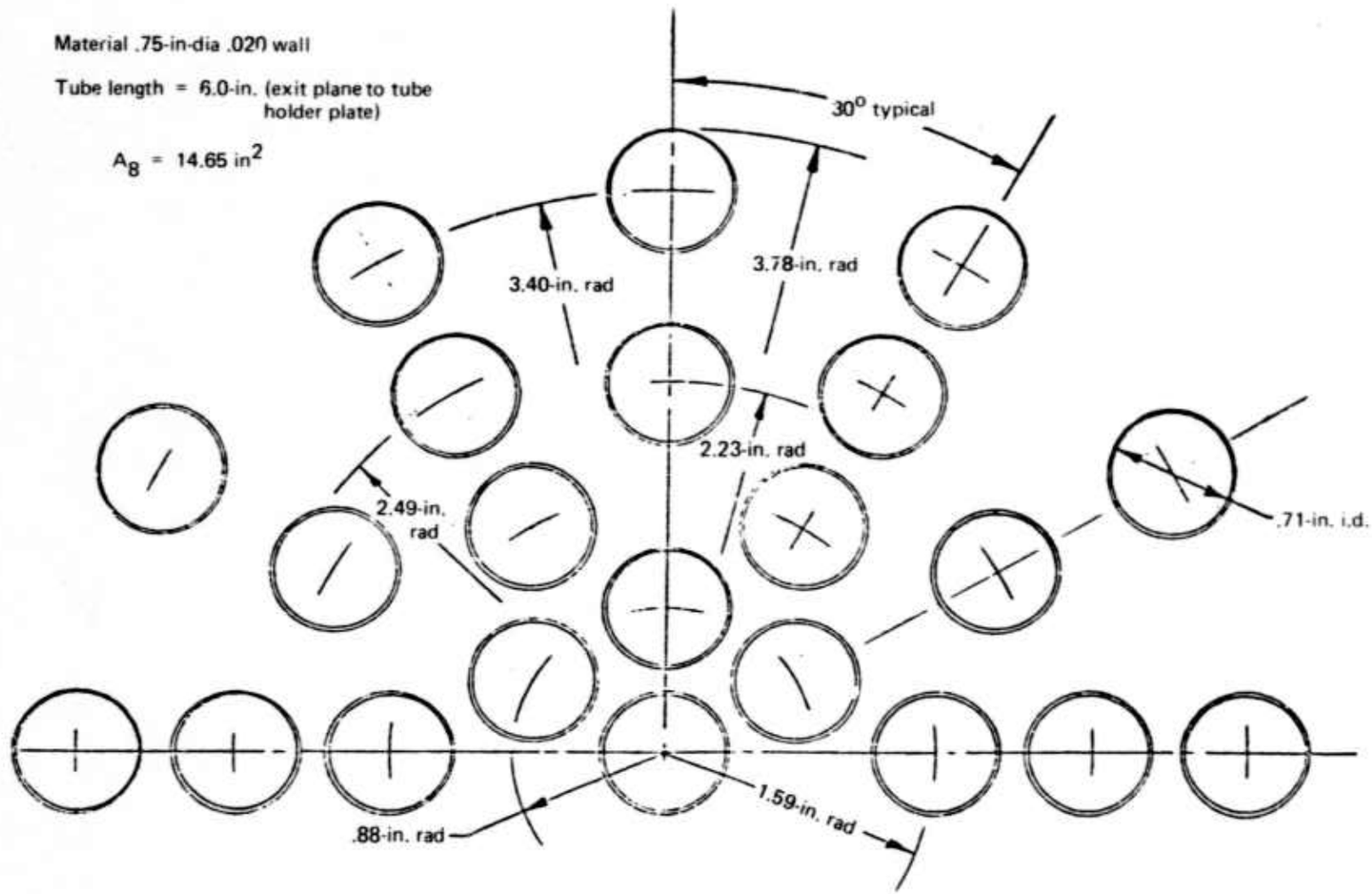

Figure 24. — Schematic of 37-Tube, AR 3.3 Straight-Tube Radial-Array Nozzle

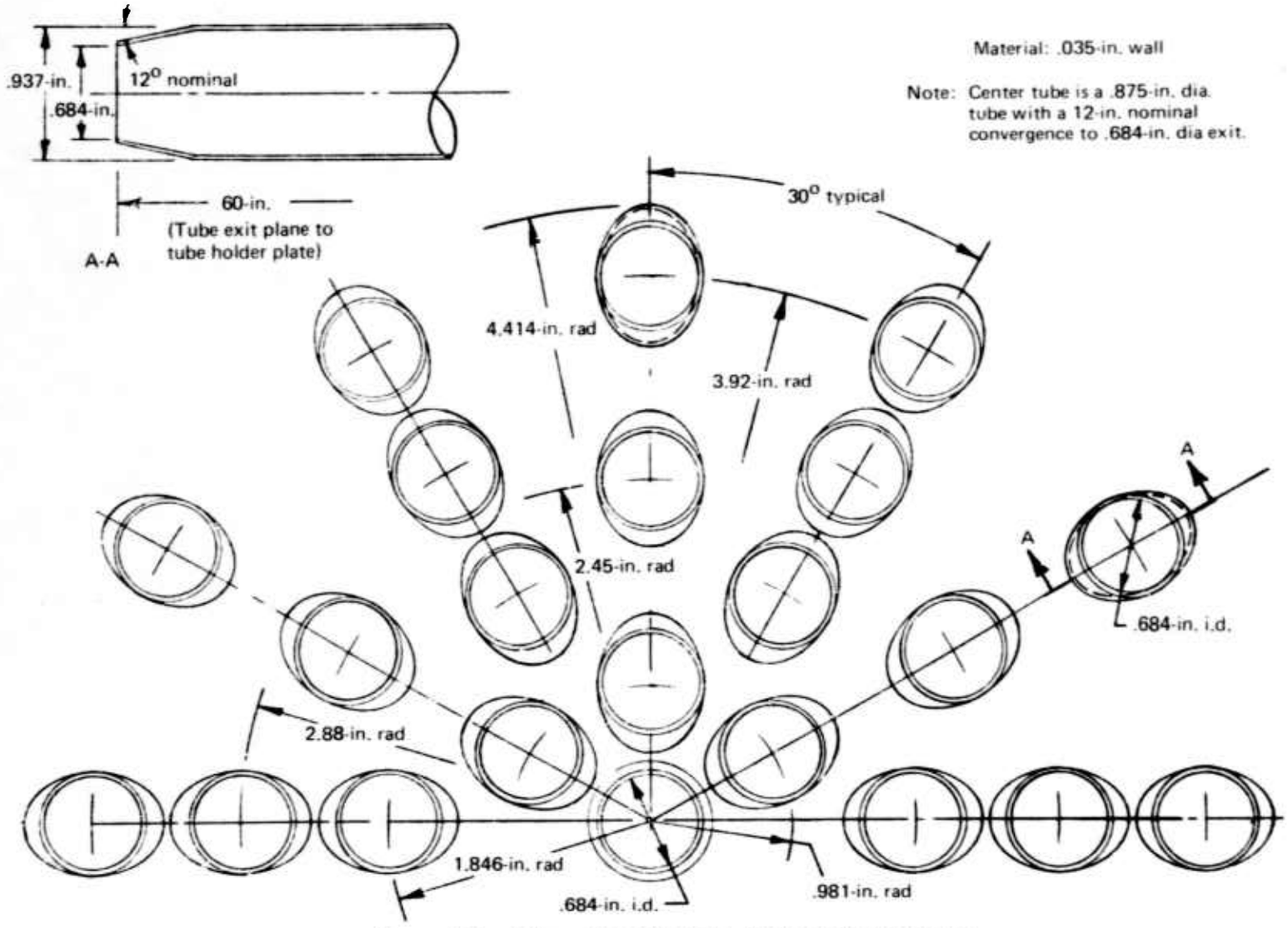

Figure 25. — Schematic of 37-Tube AR 4.5 Elliptical-Tube Radial-Array Nozzle

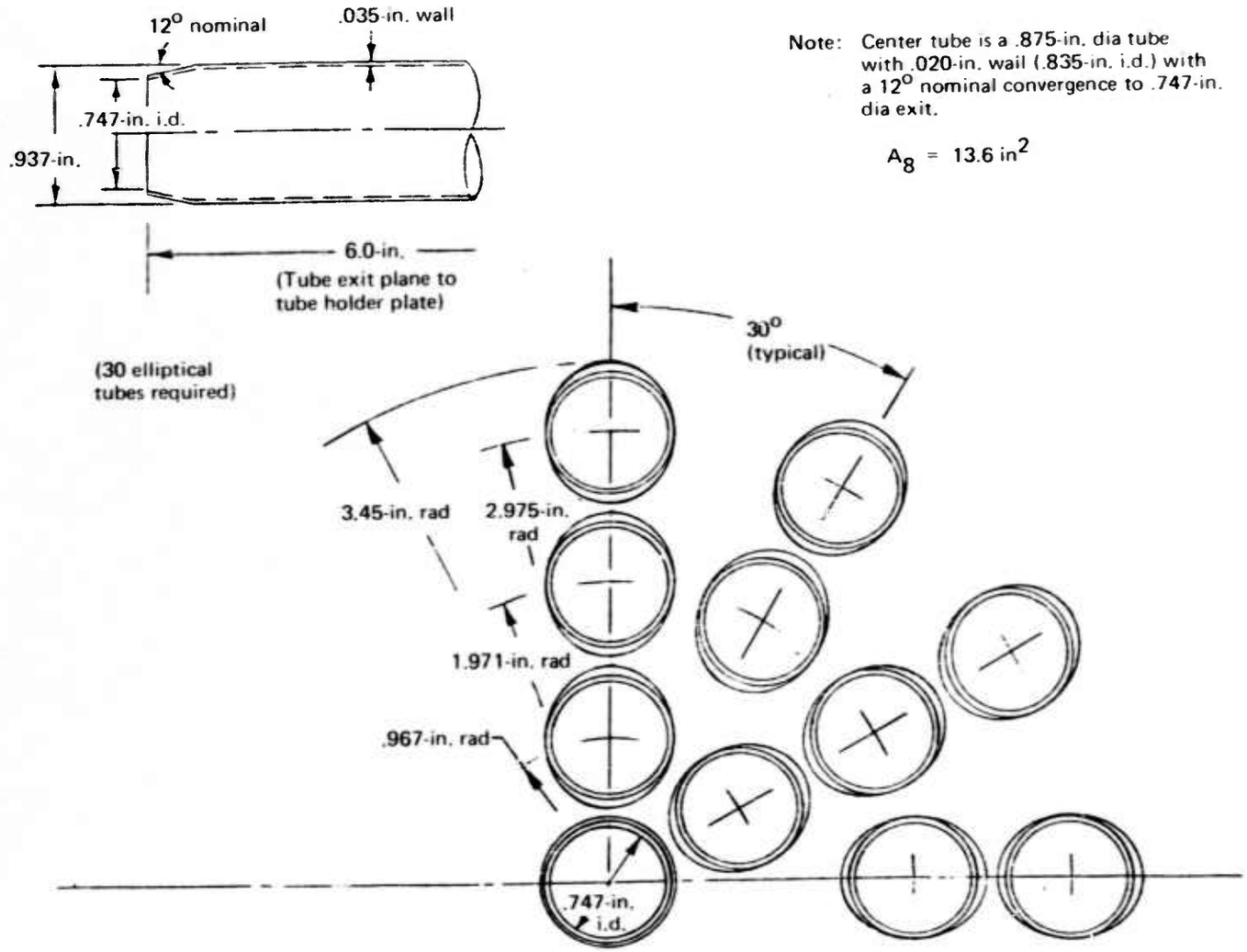

Note: Center tube is a .875-in. dia tube with .020-in. wall (.835-in. i.d.) with a 12° nominal convergence to .747-in. dia exit.

$A_8 = 13.6\ in^2$

Figure 26. — Schematic of 31-Tube, AR 2.75 Elliptical-Tube Radial-Array Nozzle

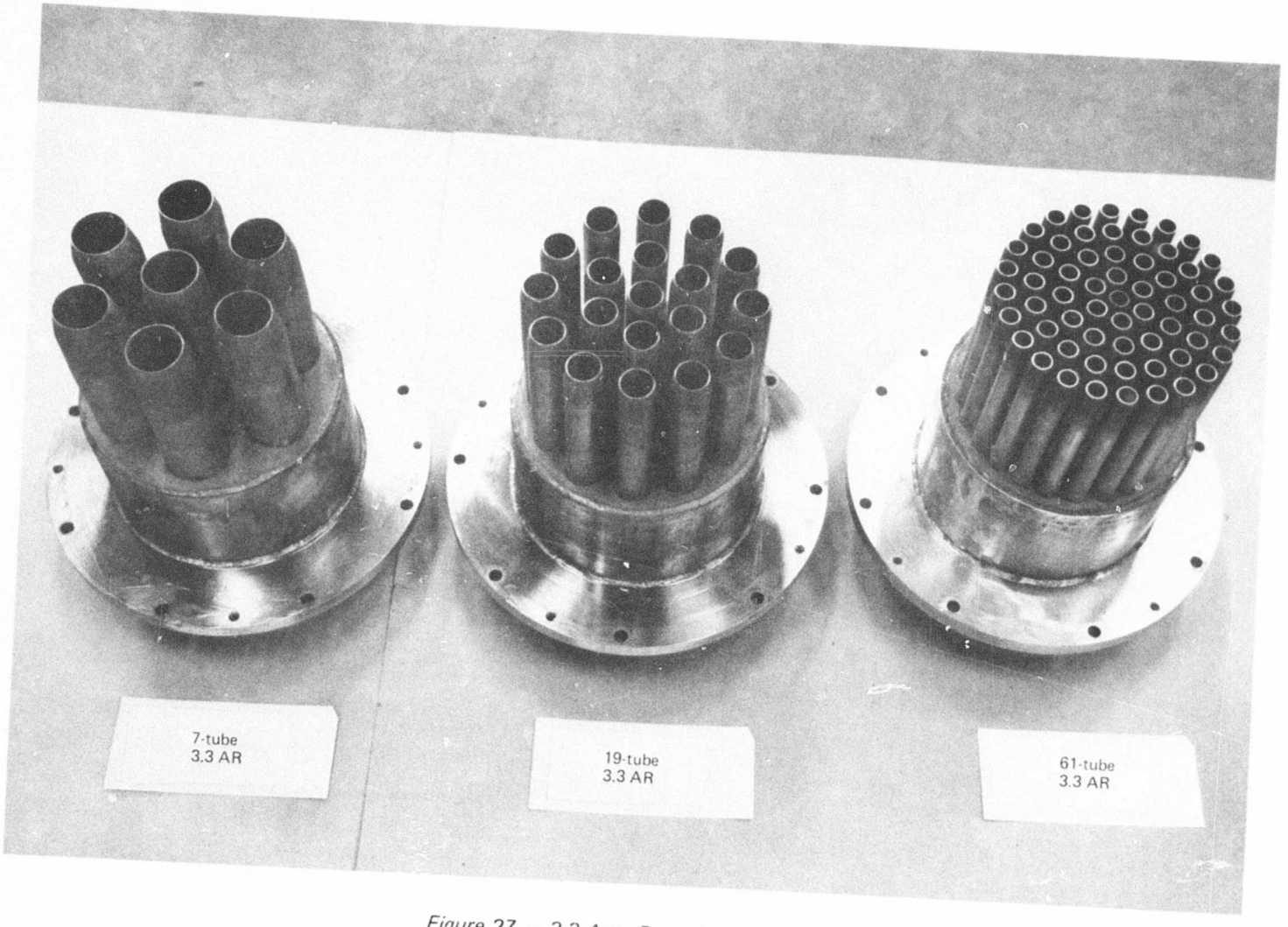

Figure 27. — 3.3 Area Ratio Multitube Nozzles

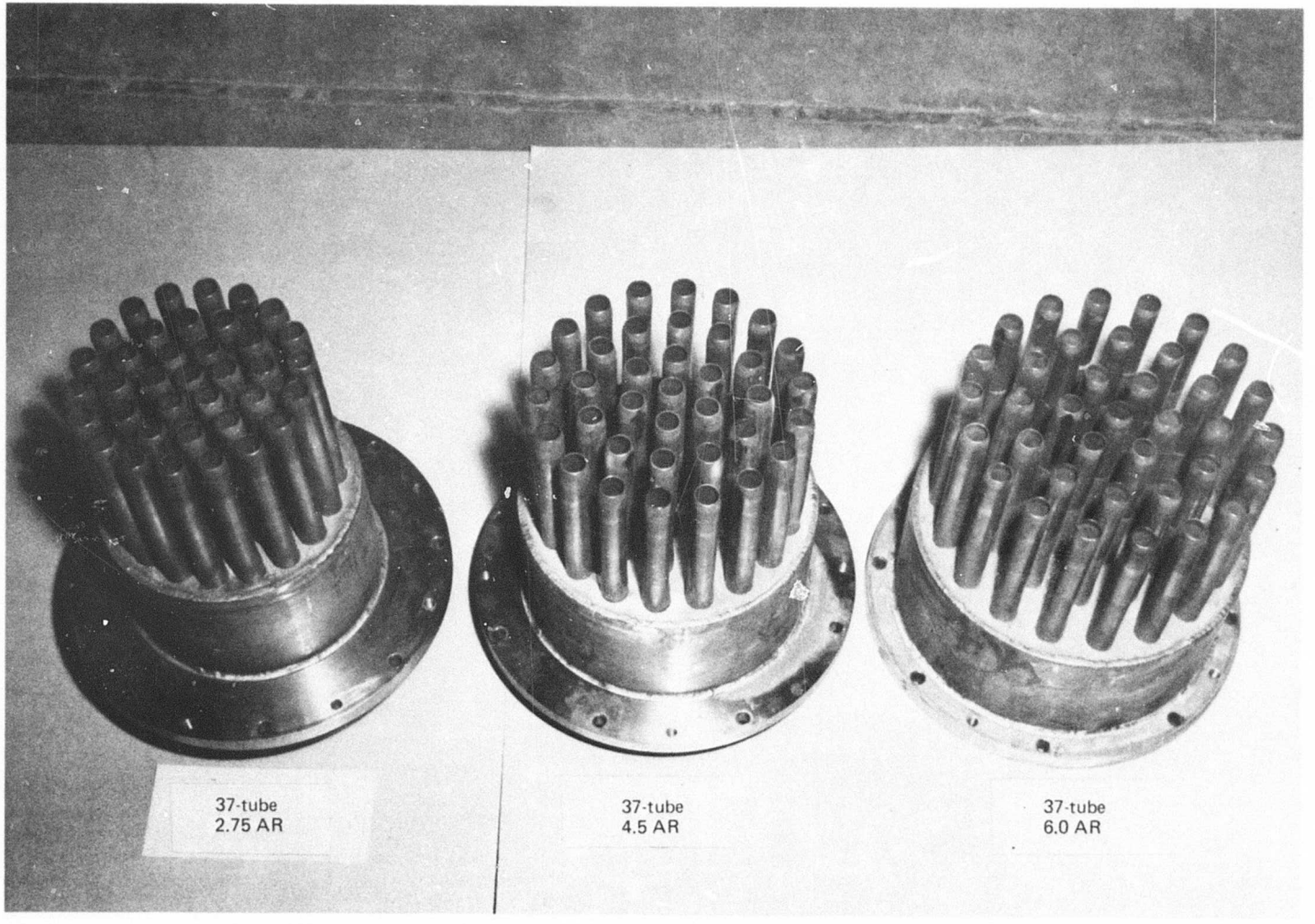

Figure 28. — 37-Element Multitube Nozzles

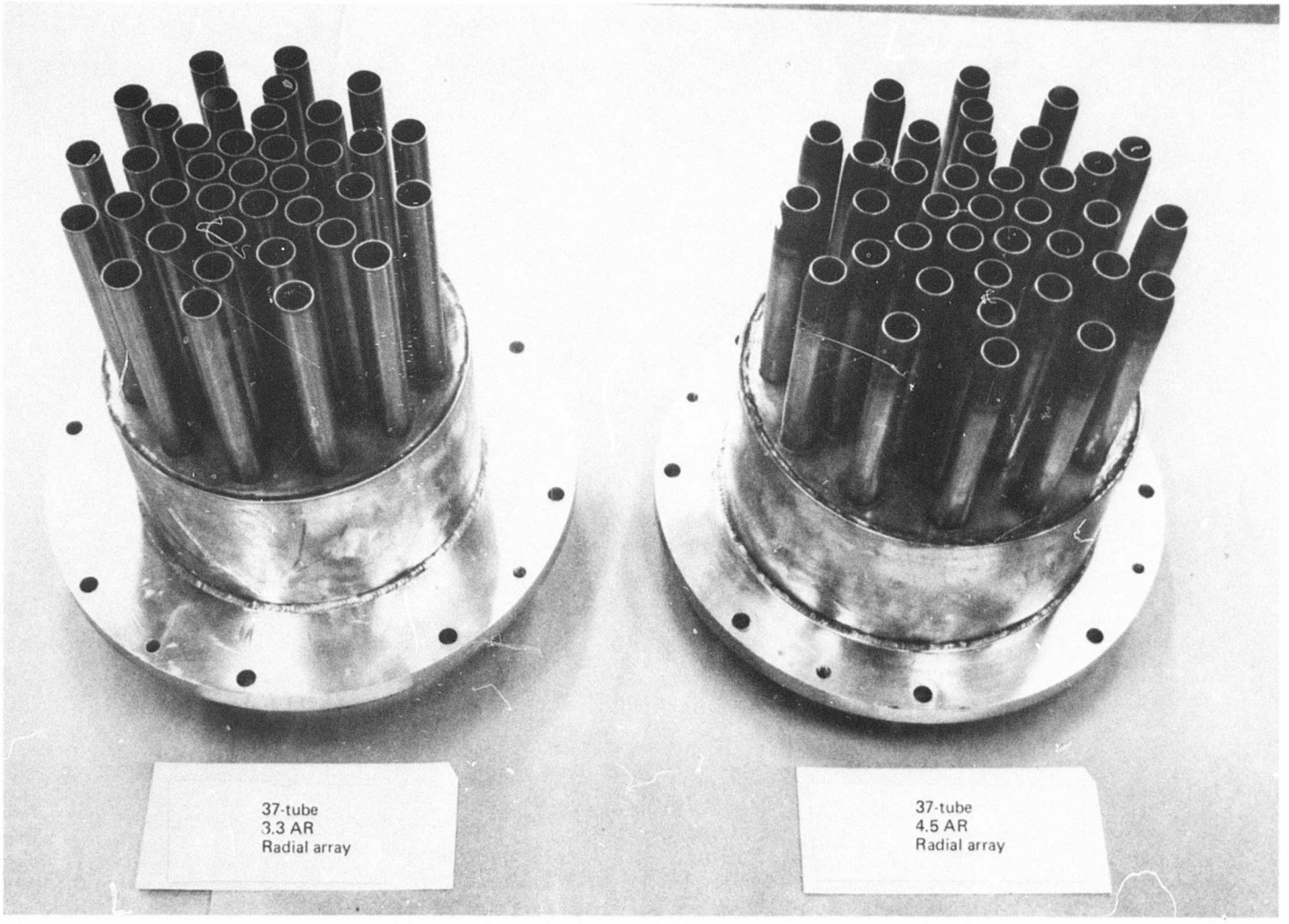

Figure 29. — Radial Array Multitube Nozzles

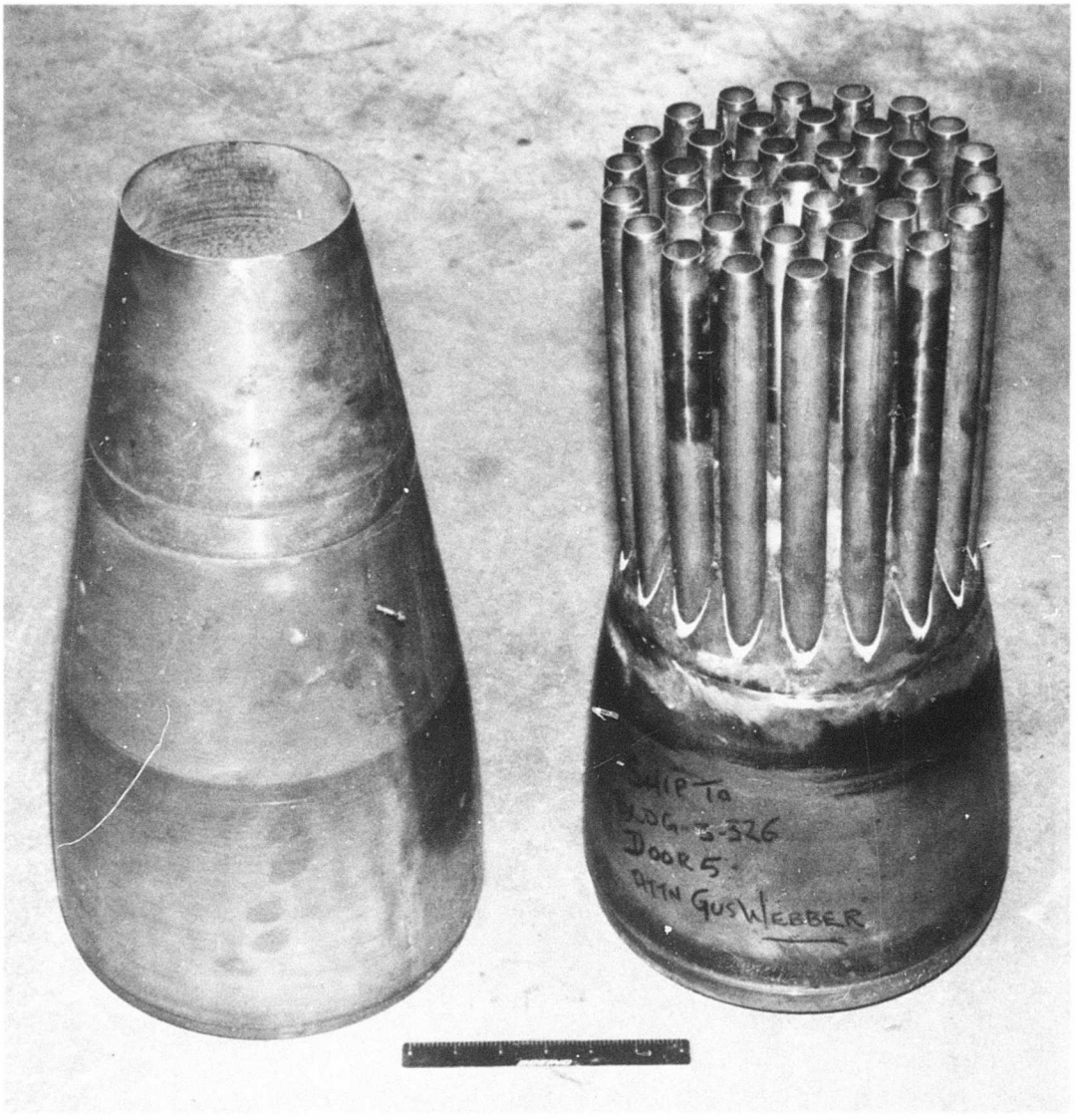

Figure 30. — Reference Conical and Multitube Nozzles

Figure 31. — Hardwall Ejectors

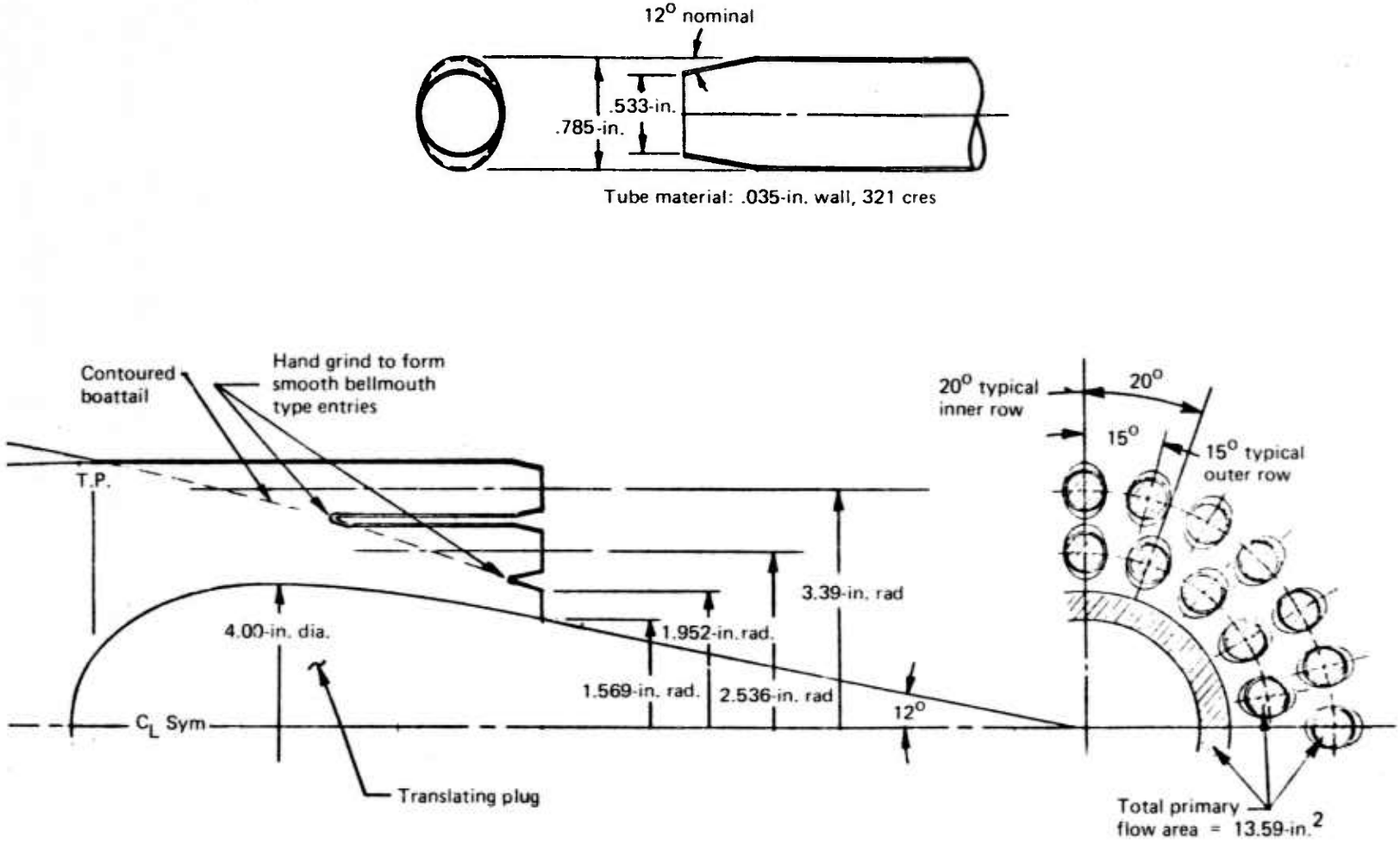

Figure 32. — Schematic of 42-tube, 3.3AR-CPA-ET/RC Nozzle (0.383-in. Wide Annulus)

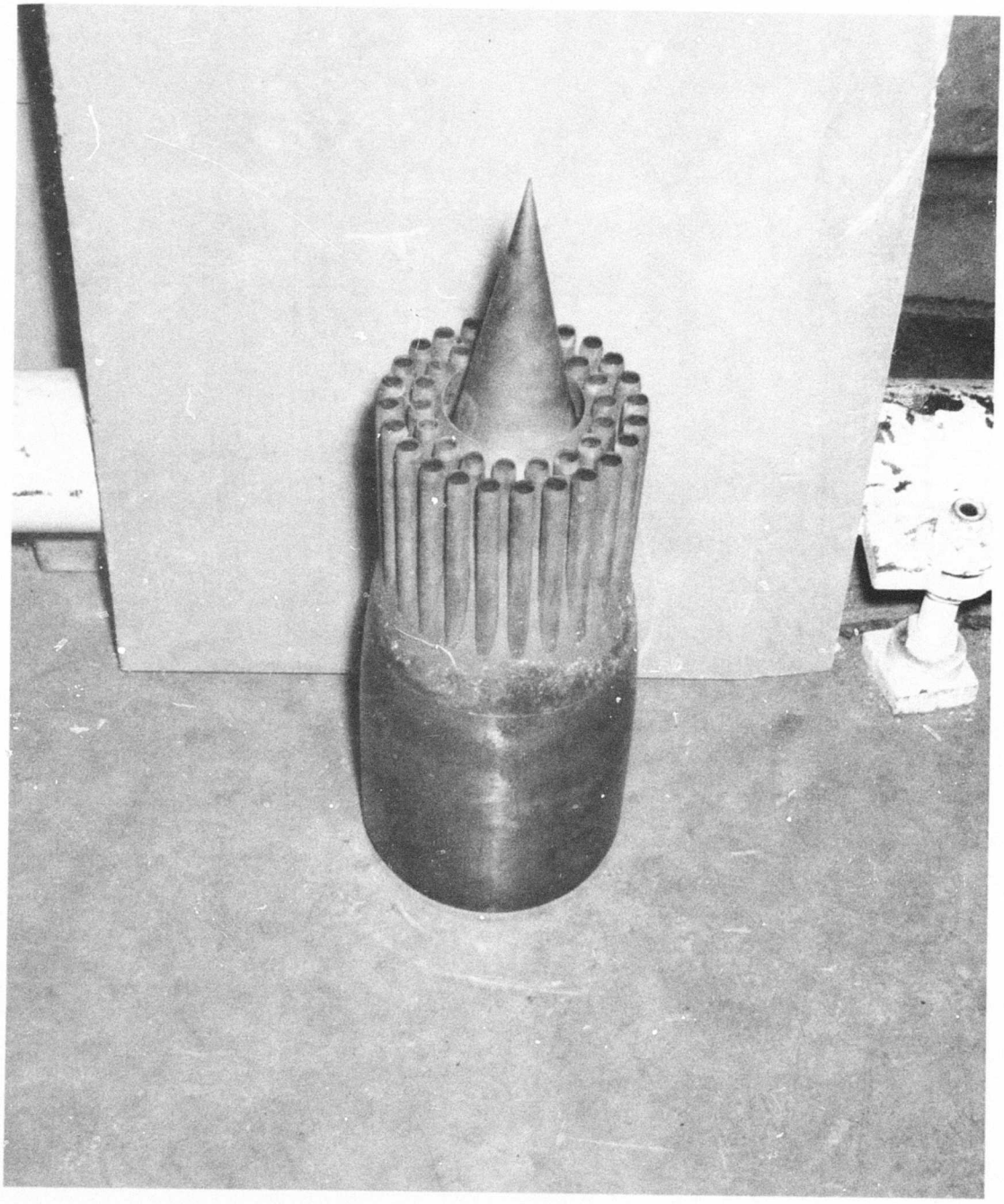

Figure 33. — 42-T/Annulus, 3.3 AR-CPA-ET/RC (0.383-in.-Wide Annulus)

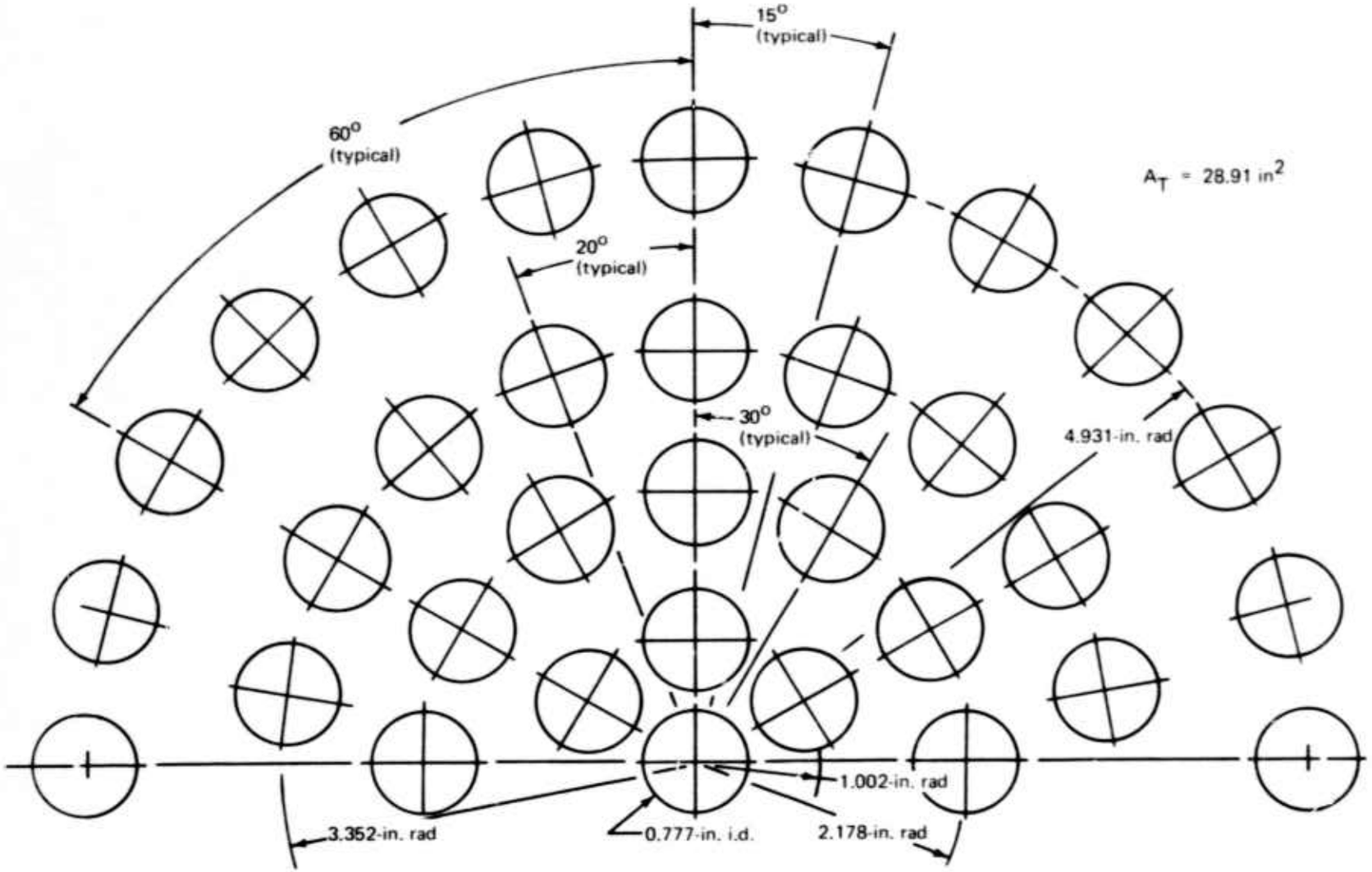

Figure 34. — 61-Tube, AR 3.07 Nozzle Exit Flow Pattern

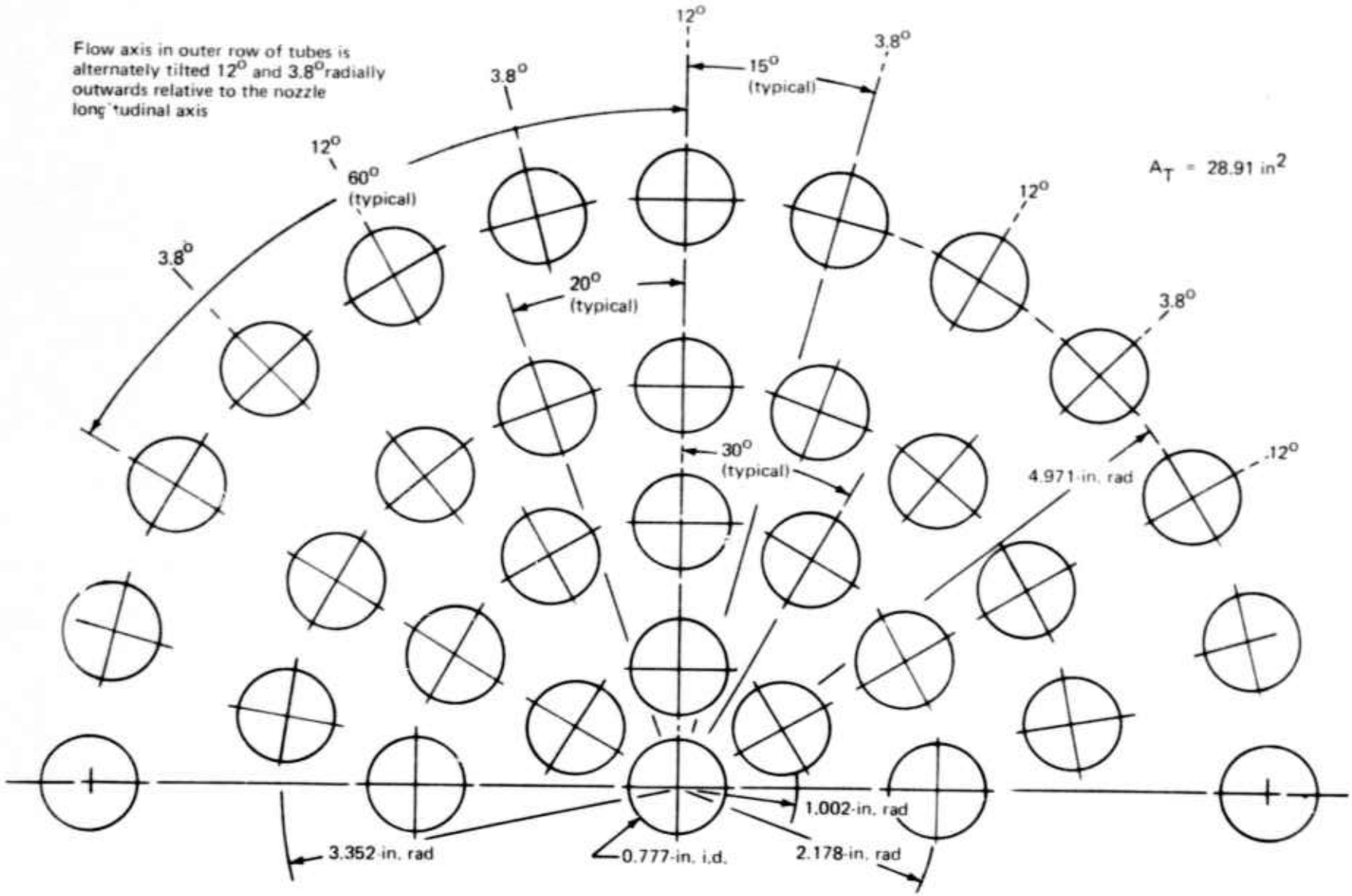

Figure 35. — 61-Tube, AR 3.07 Nozzle Exit Flow Pattern (With Tilted Outer Row of Tubes)

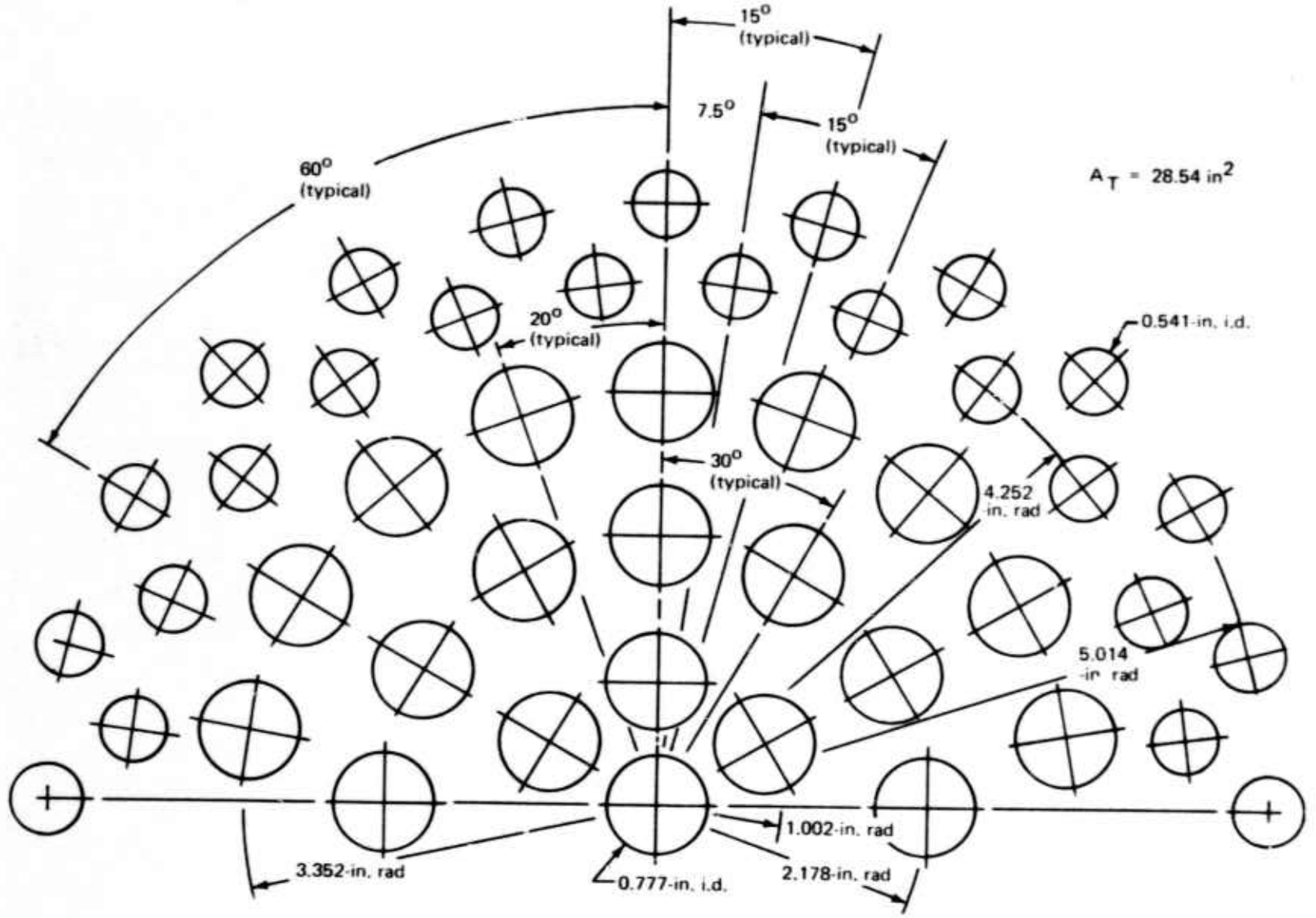

Figure 36. — 85-Tube, AR 3.07 Nozzle Exit Flow Pattern

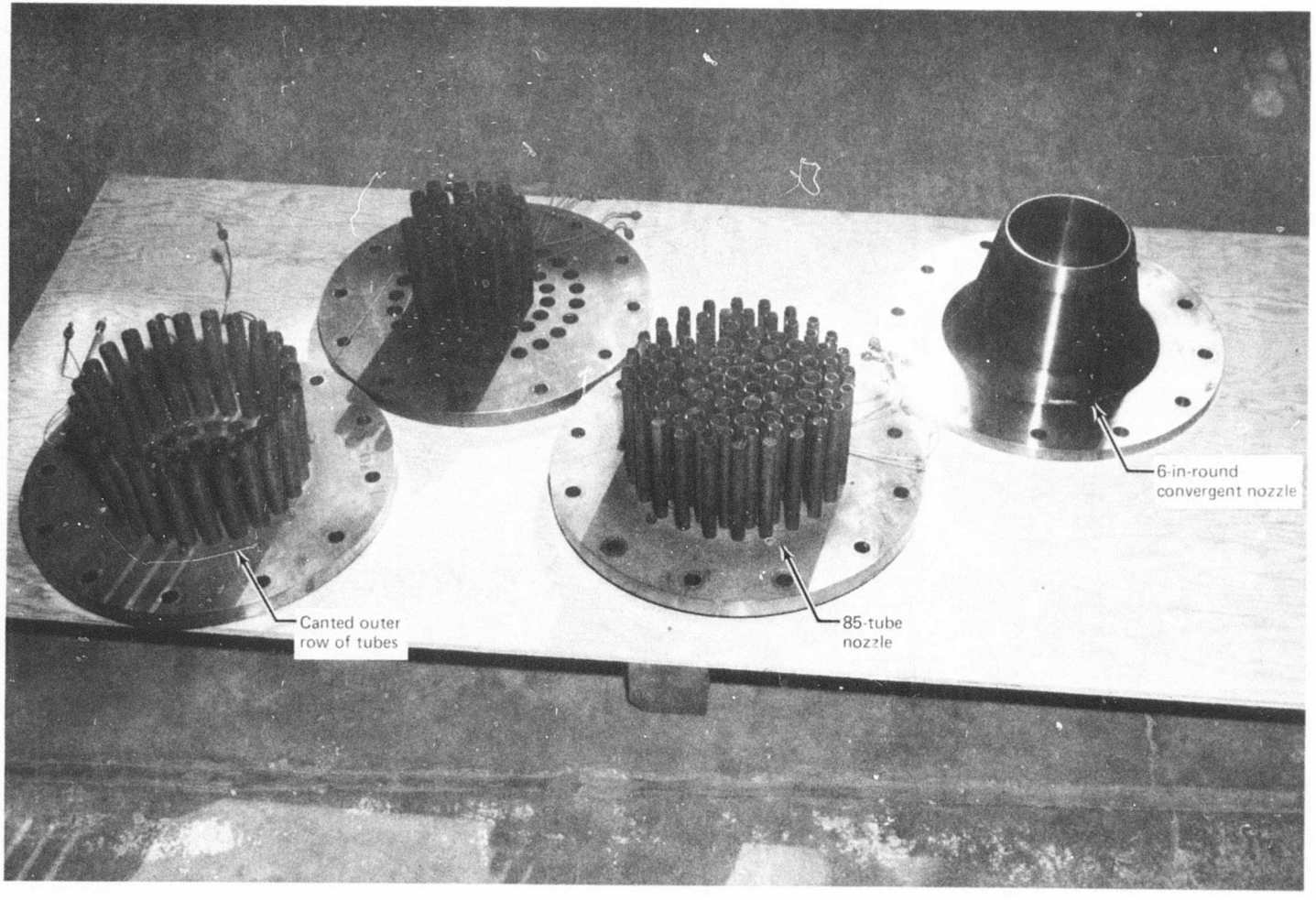

Figure 37. — Irregular Array Nozzles

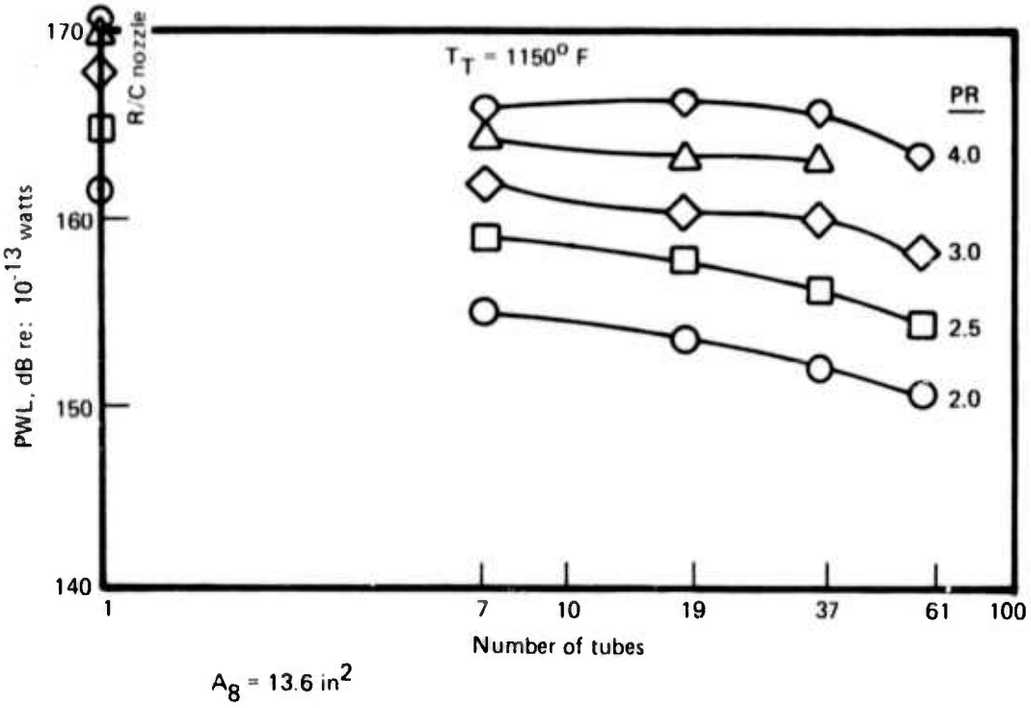

Figure 38. — Multitube 3.3 AR Nozzle, Total Jet Noise Power Levels

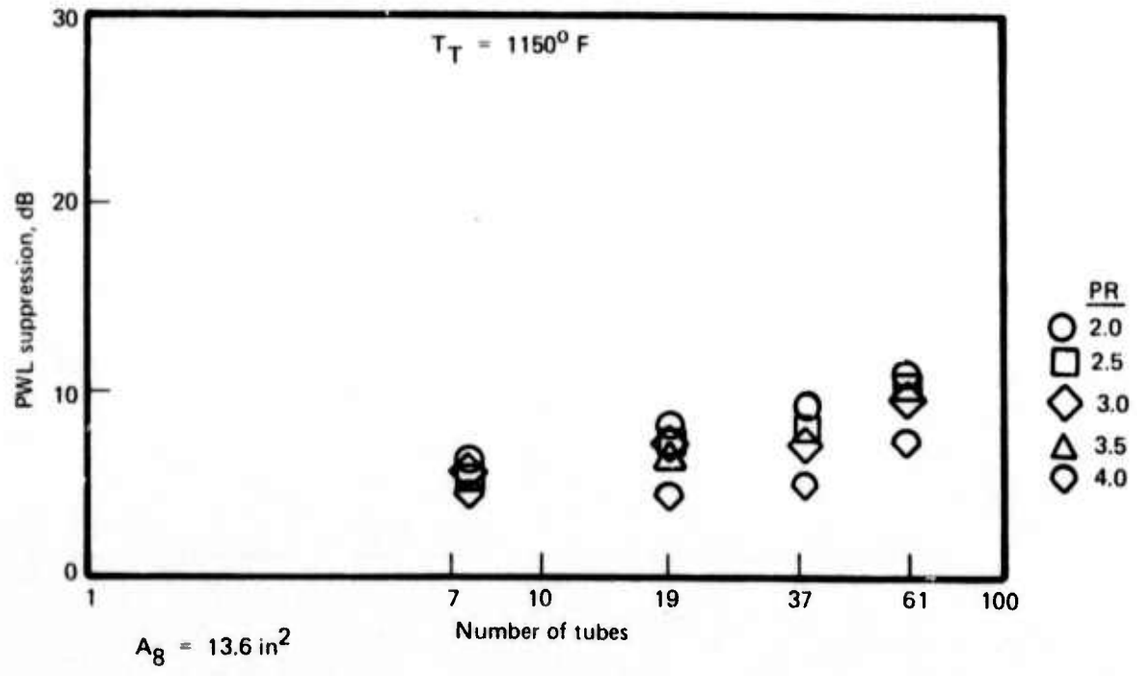

Figure 39. — Multitube Nozzle 3.3 AR, Total Jet Noise Power Suppression

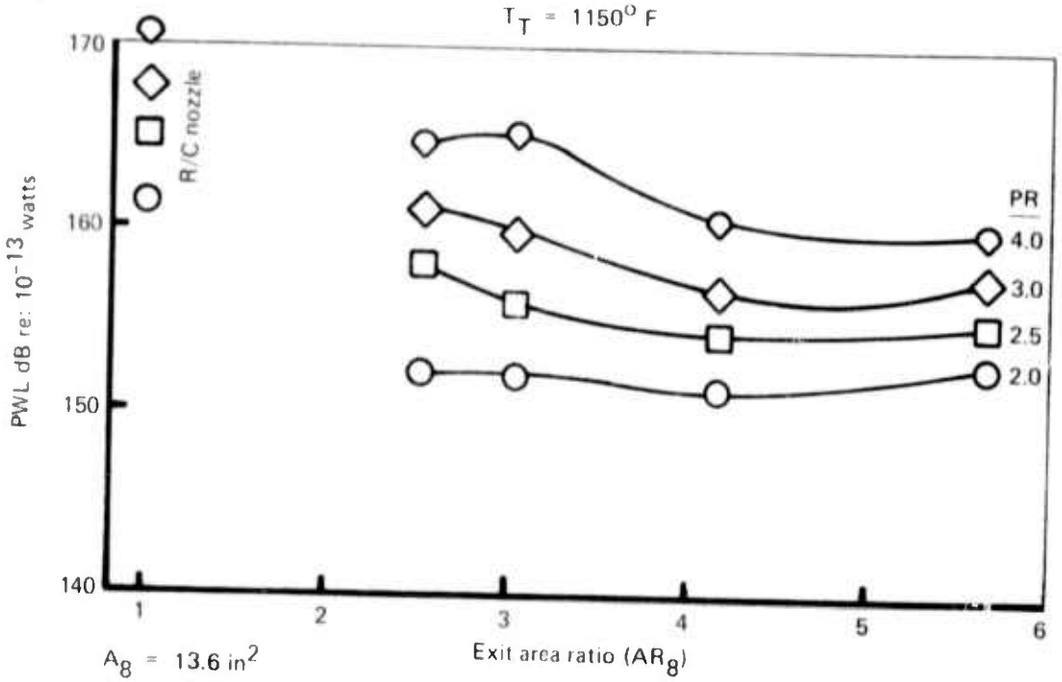

Figure 40. — Total Jet Noise Power Levels for Close-Packed Array, 37-Tube Nozzles With Various Area Ratios

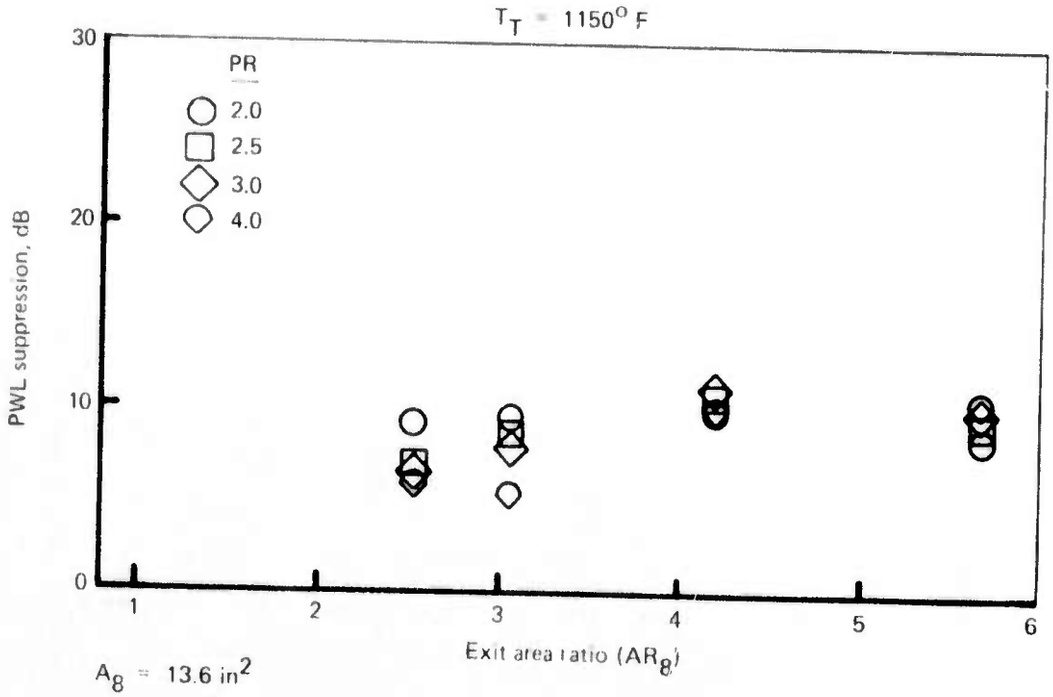

Figure 41. —Total Jet Noise Power Suppression for Close-Packed Array, 37-Tube Nozzles With Various Area Ratios

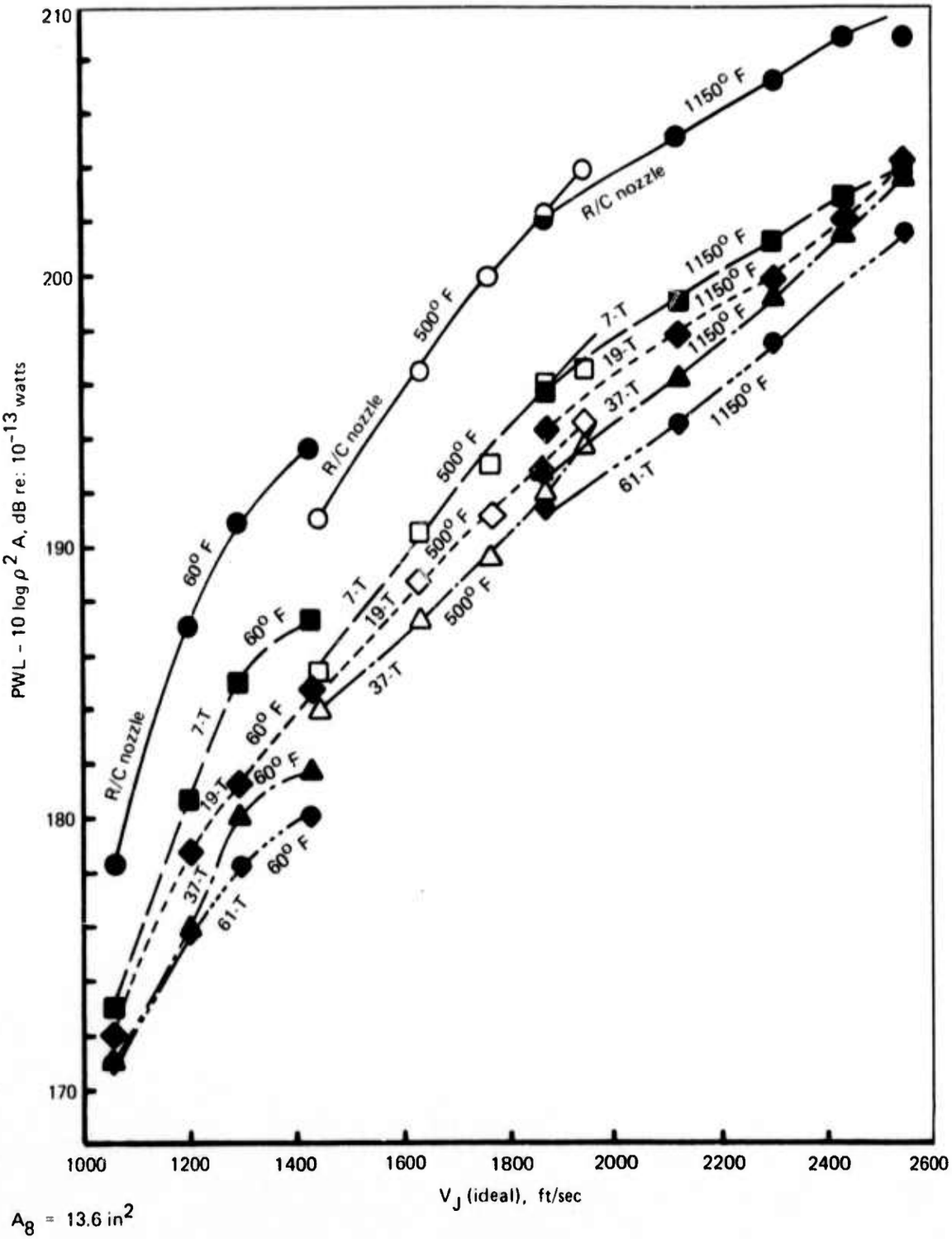

Figure 42. — Normalized Total Jet Noise Power Levels for Area Ratio 3.3, Close-Packed Array Multitube Nozzles

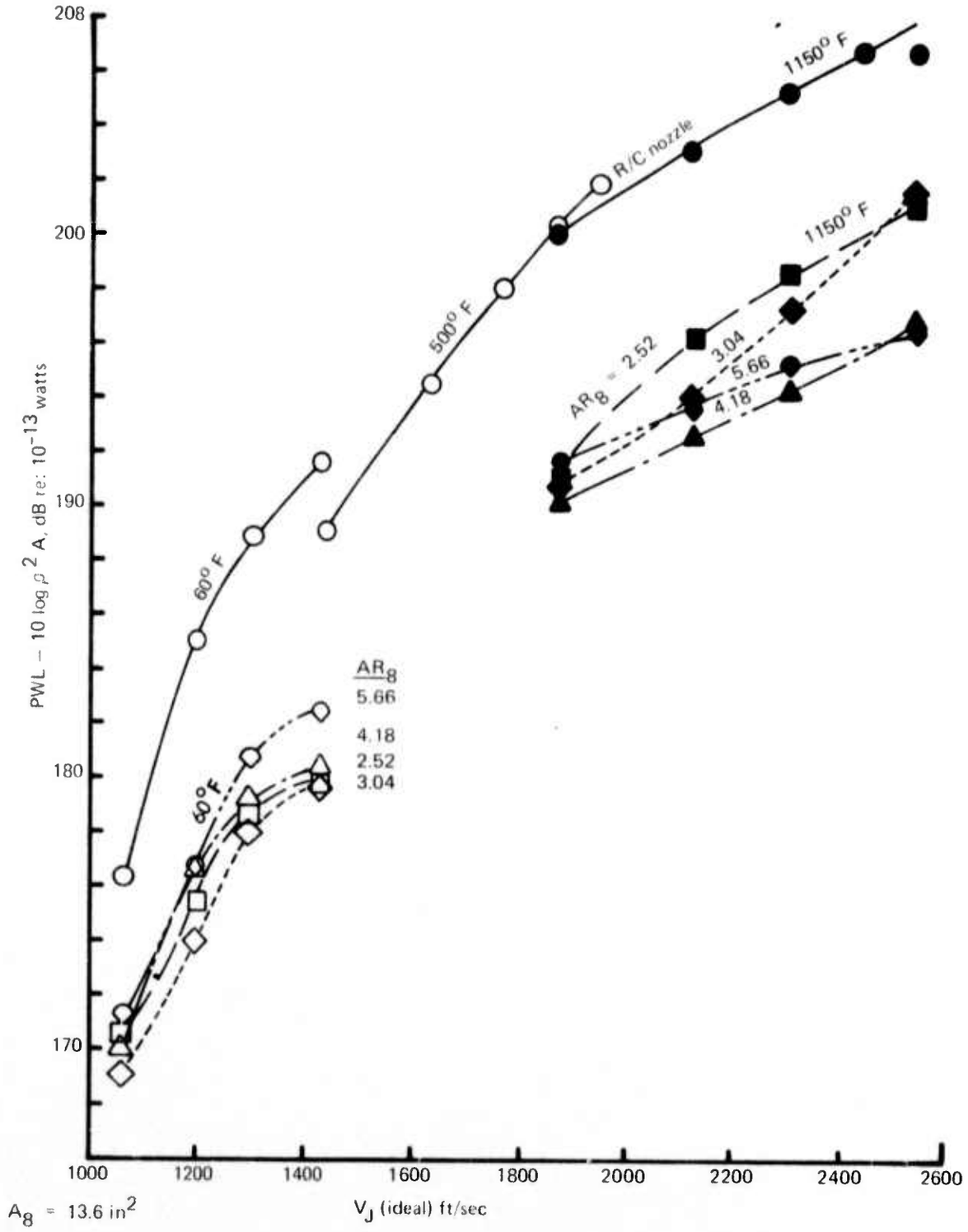

Figure 43. — Normalized Total Jet Noise Power Levels for Close-Packed Array, 37-Tube Nozzles

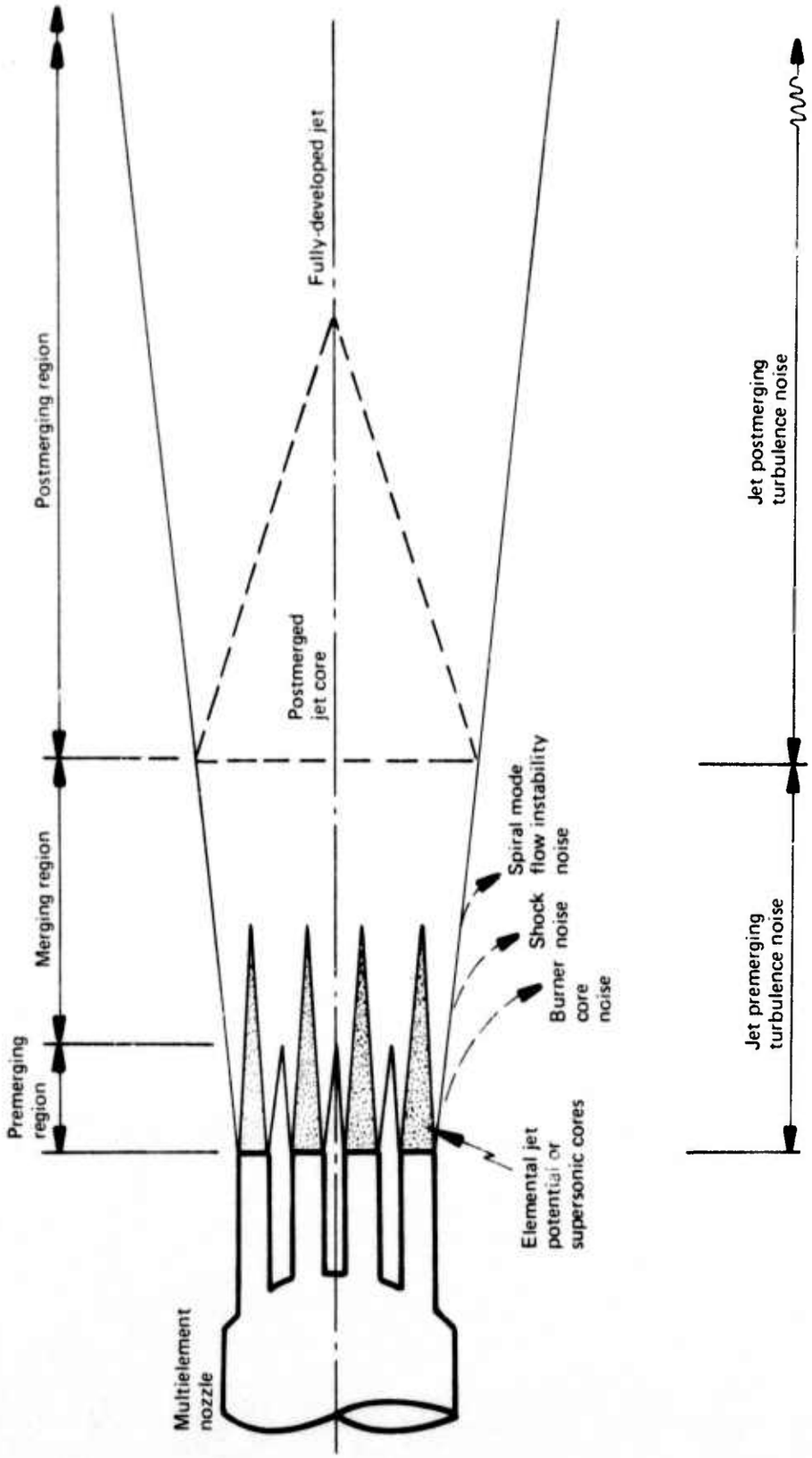

Figure 44. — Multielement Jet Nomenclature

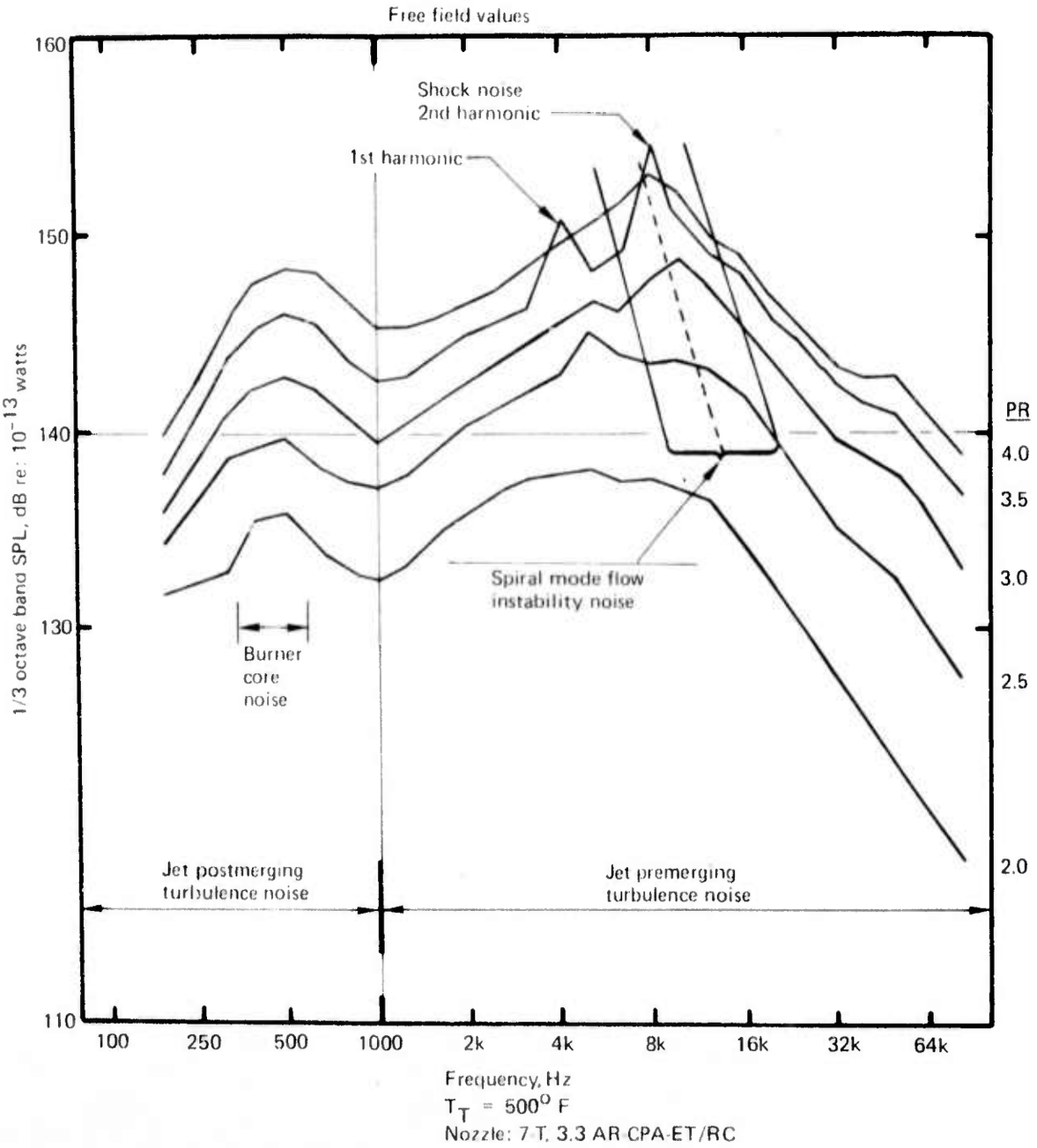

Figure 45. — Composite Jet Noise Power Spectra for the 7-Tube, 3.3 AR Nozzle

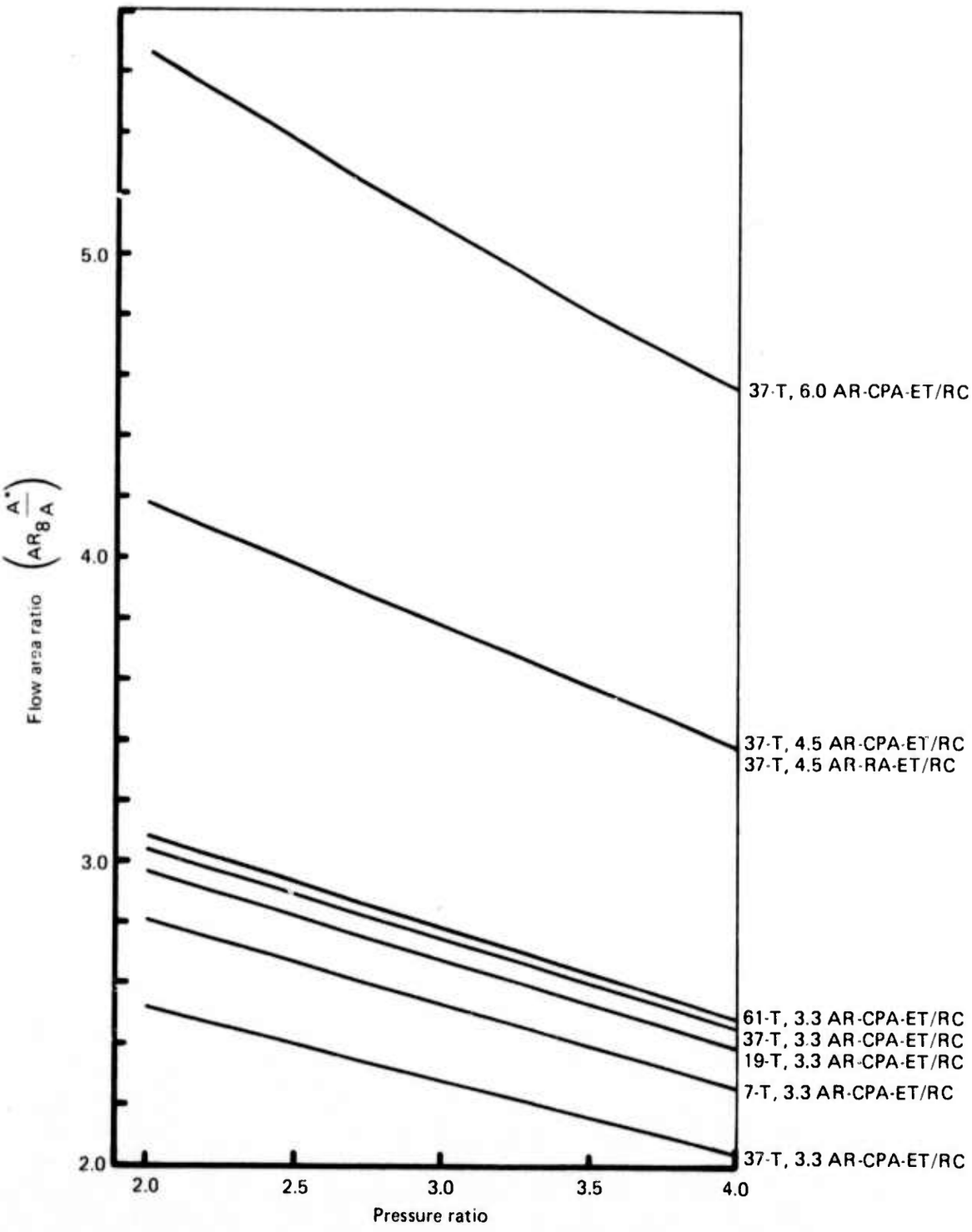

Figure 46. — Multitube Nozzle Flow Area Ratios as a Function of Pressure Ratio

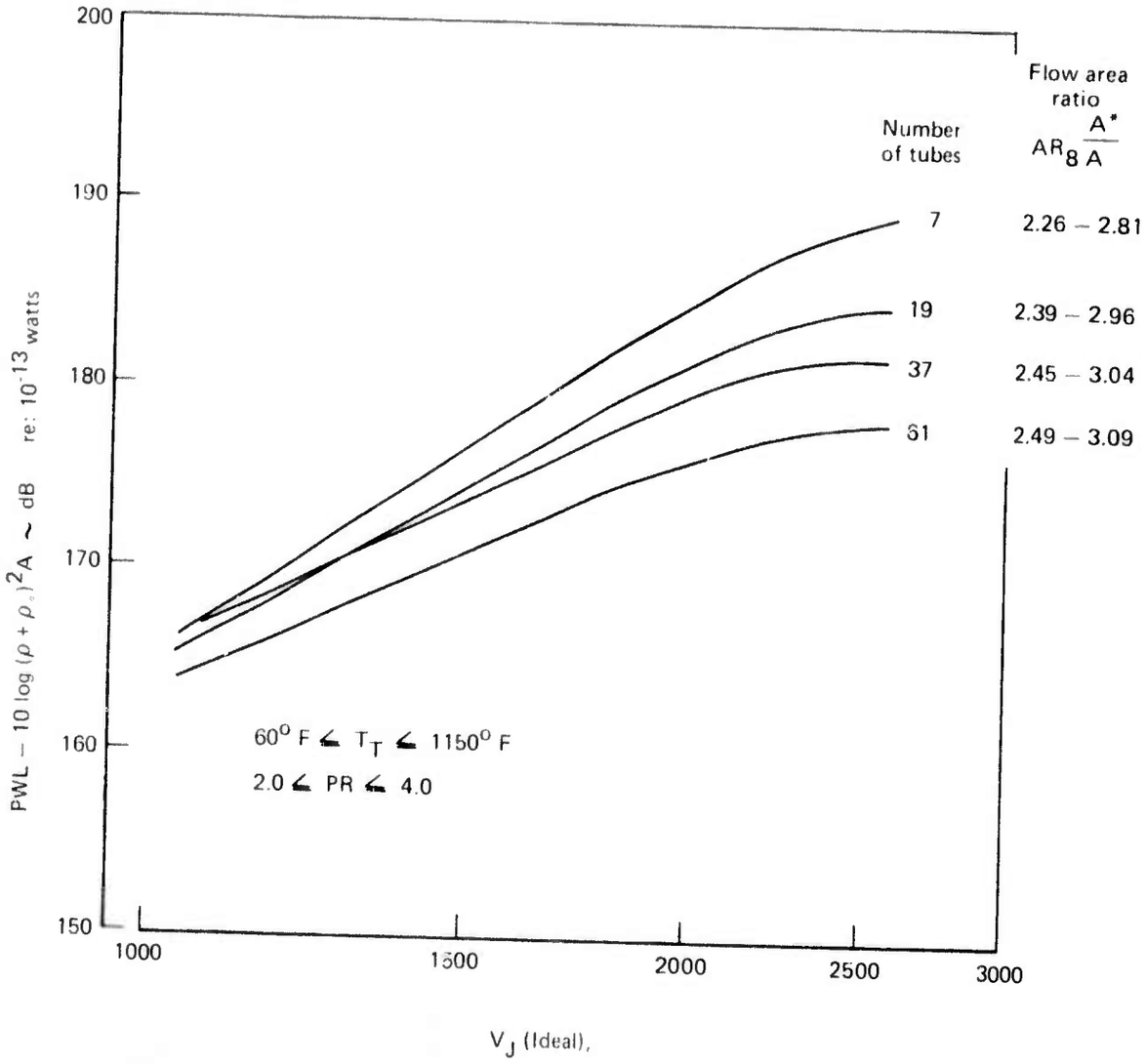

Figure 47. — Normalized Premerged Jet Noise Power Levels for 3 3 Area Ratio Nozzles

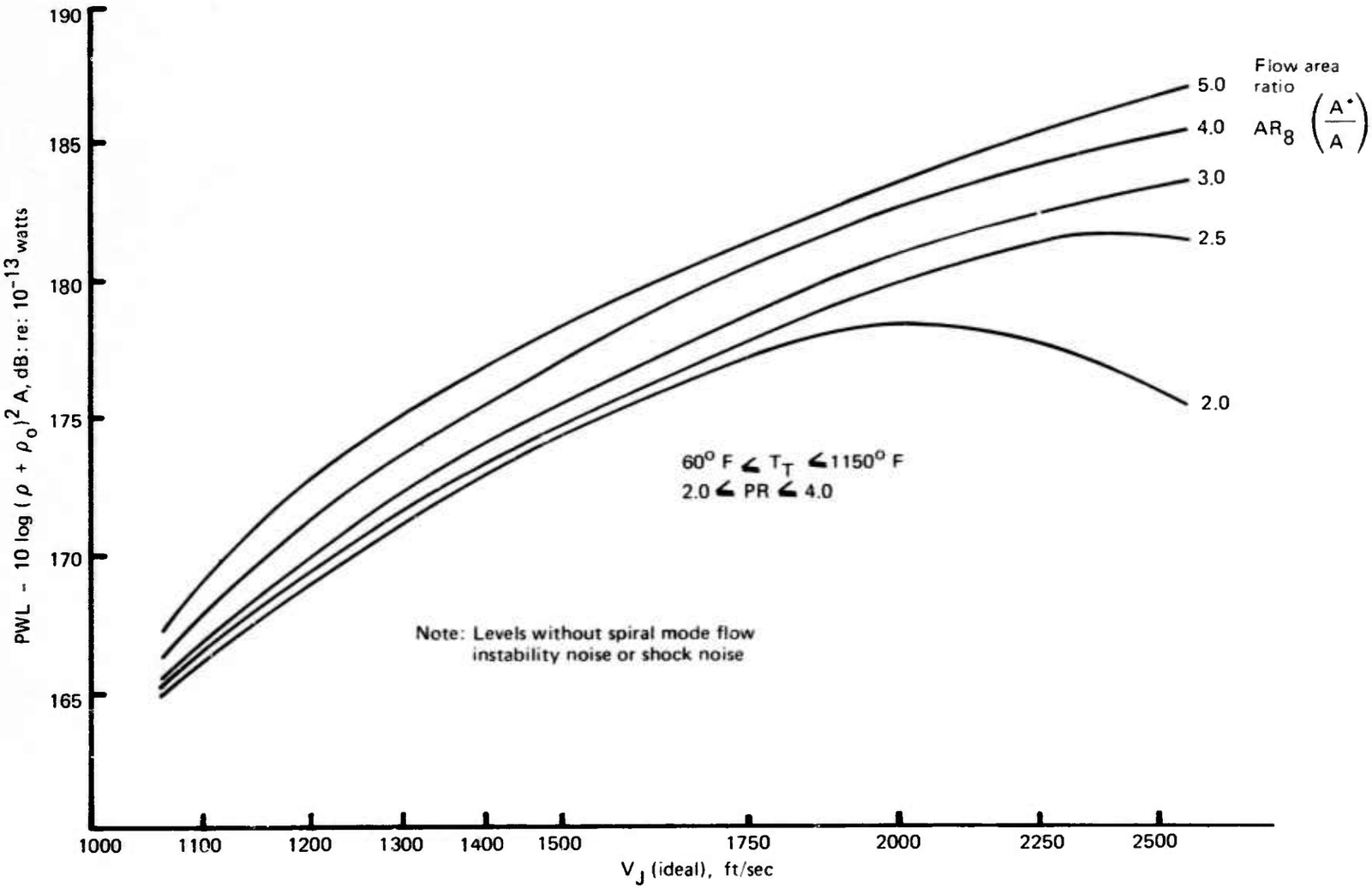

Figure 48. — 37-Tube Nozzle Premerged Jet Noise Power Levels

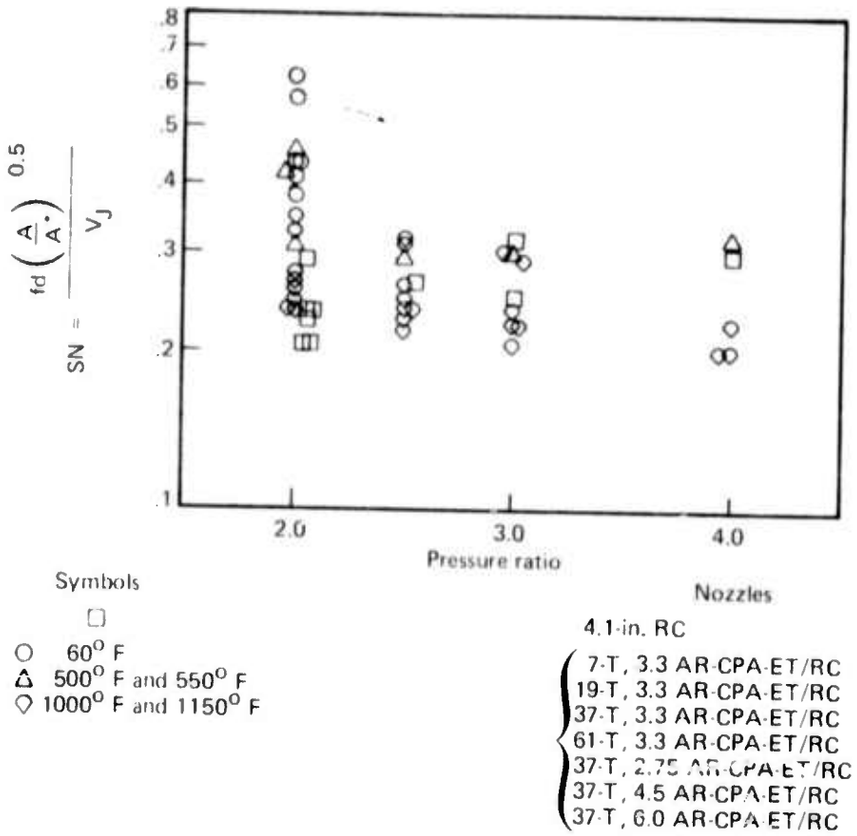

Figure 49. — Multitube Nozzle Premerged Jet Noise Peak-Frequency Strouhal Number Relationship

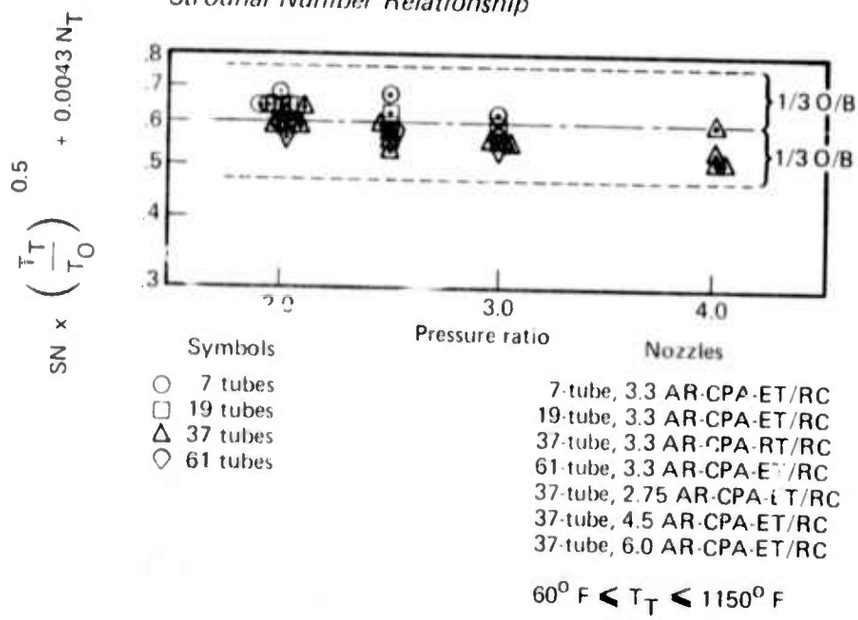

Figure 50. — Multitube Nozzle Premerged Jet Noise Peak-Frequency Strouhal Number Relationship with Temperature and Number of Tubes Correction

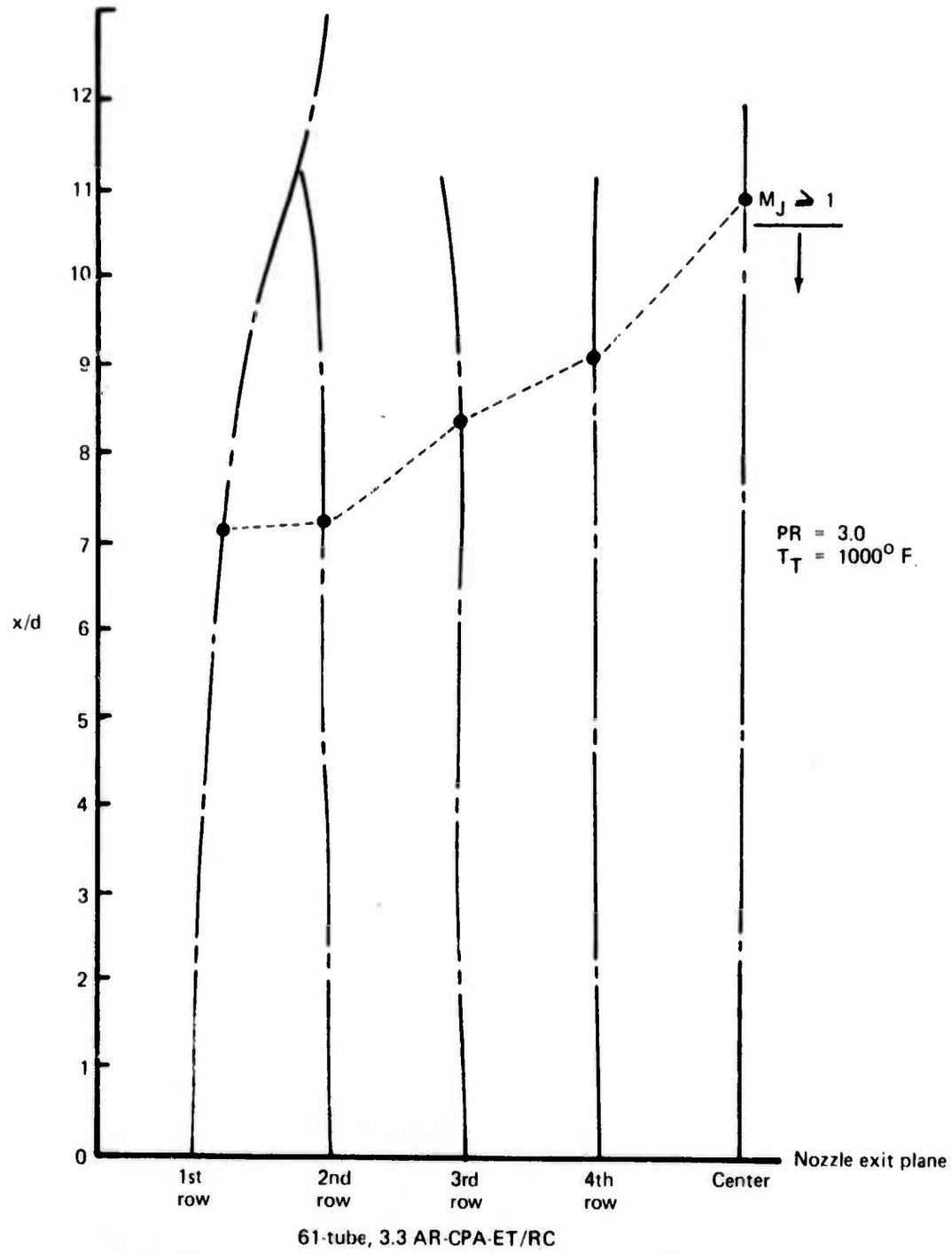

Figure 51. — 61-Tube, 3.3 AR Elemental Jets Flow Axes

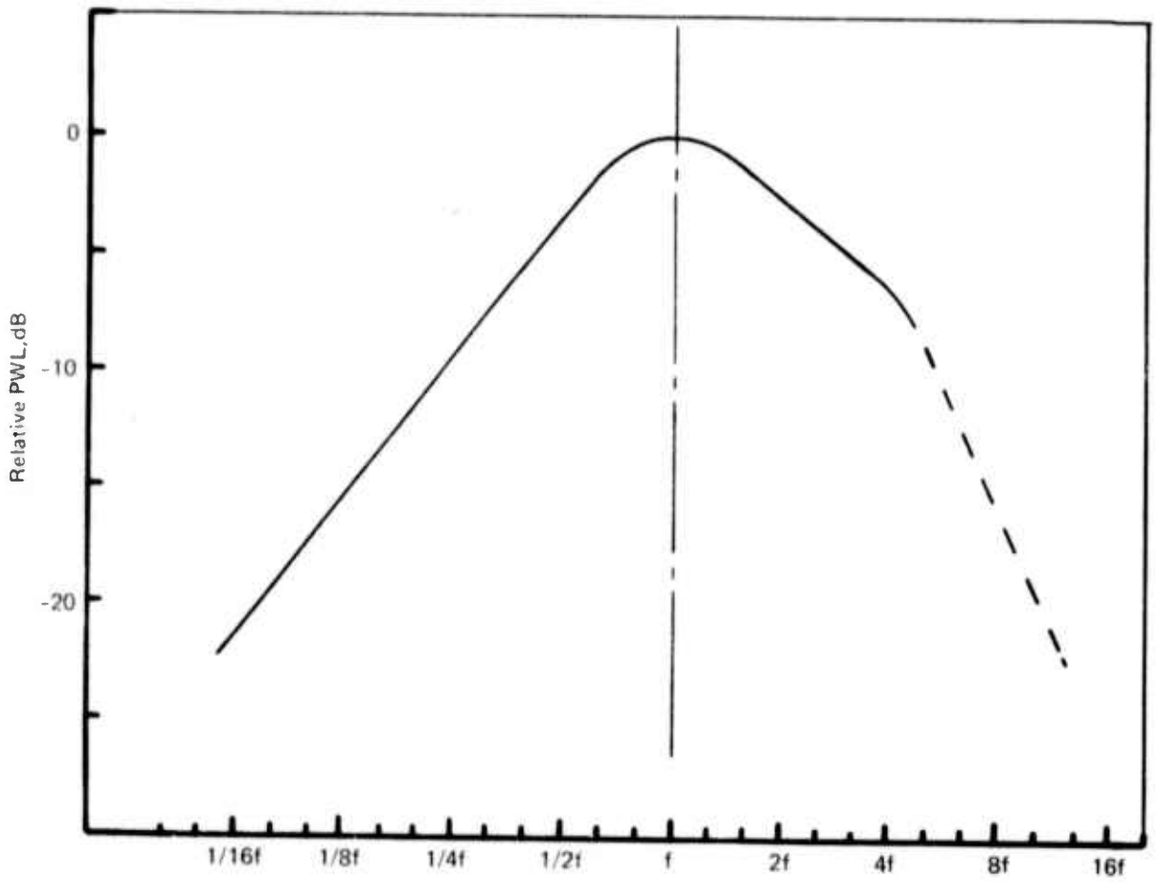

$$f \simeq \frac{(0.6 - 0.0043\, N_T)\ V_J}{d\left(\frac{A}{A^*}\right)^{0.5} \left(\frac{T_T}{T_0}\right)^{0.5}} \quad \text{, for } M_J \geq 1$$

Figure 52. — Estimated Multitube Nozzle, Premerged Jet Noise PWL 1/3 Octave Band, Spectrum Shape

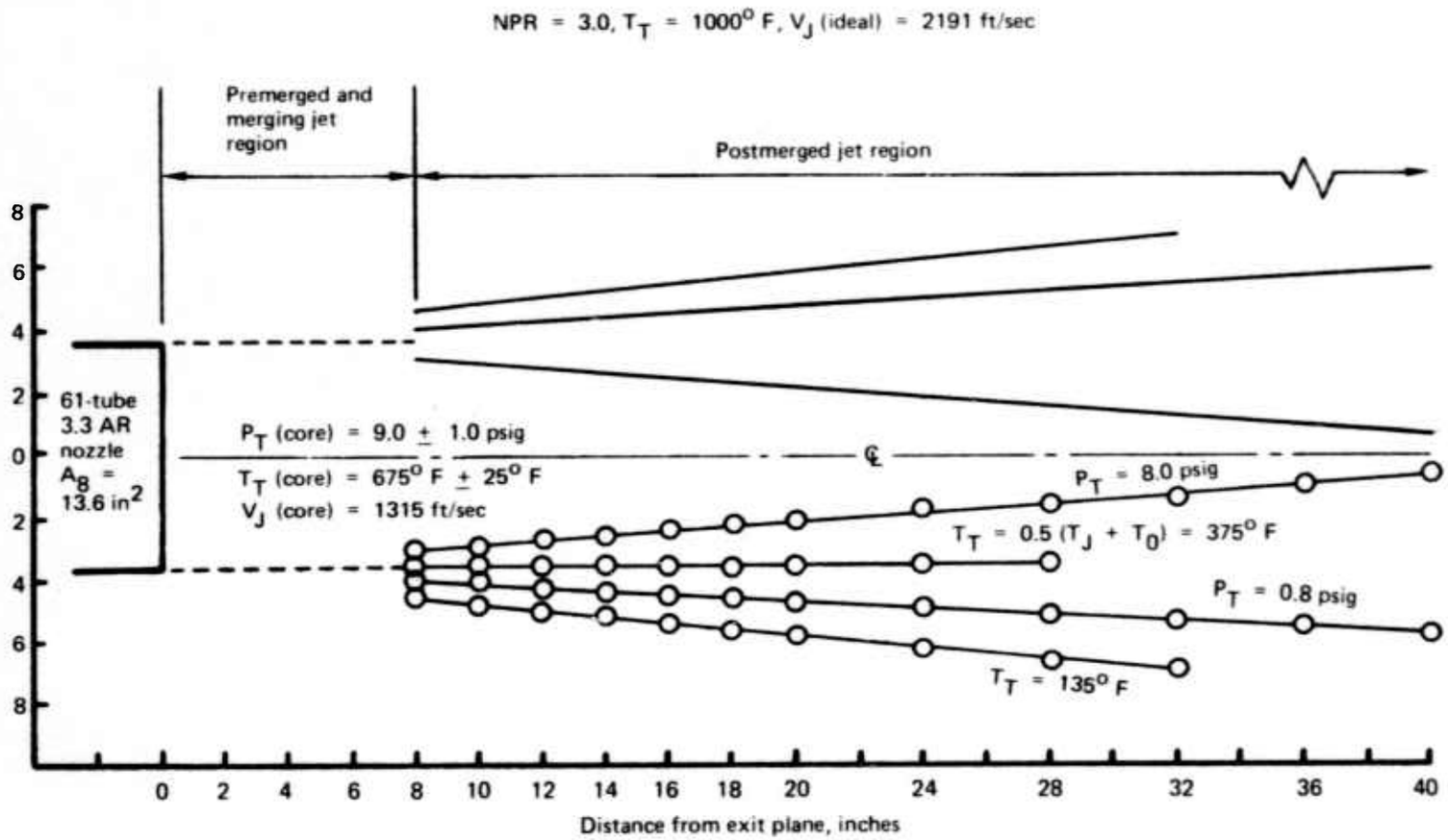

Figure 53. — Measured 61-Tube, 3.3 Area Ratio Nozzle, Postmerged Jet Flow Conditions

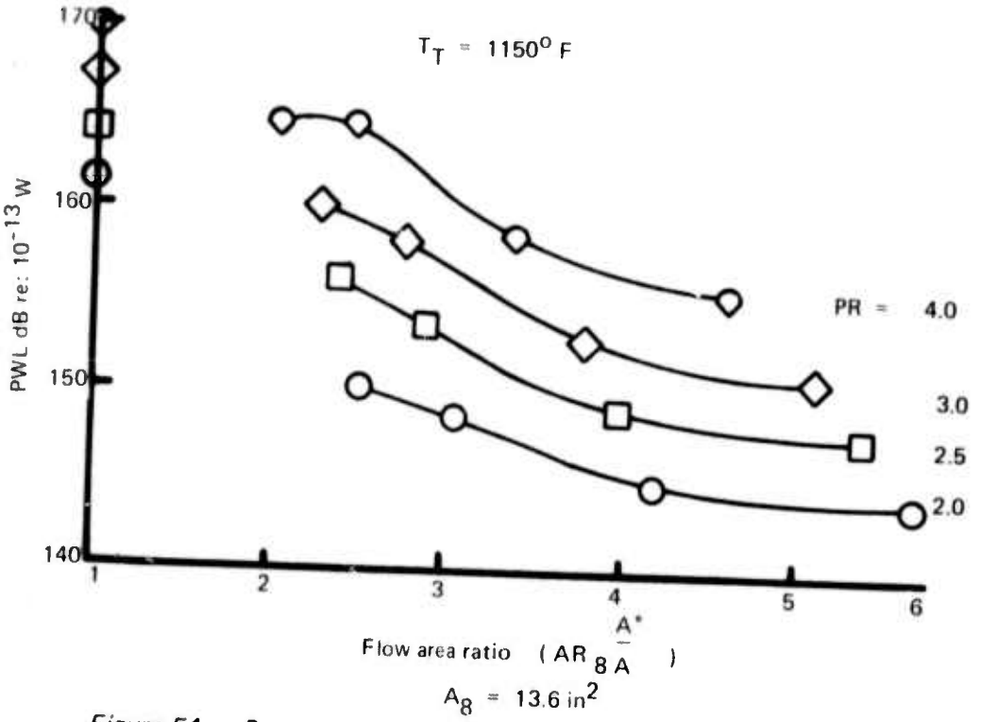

Figure 54. — Postmerged Jet Noise Power Levels for Close-Packed Array, 37-Tube Nozzles

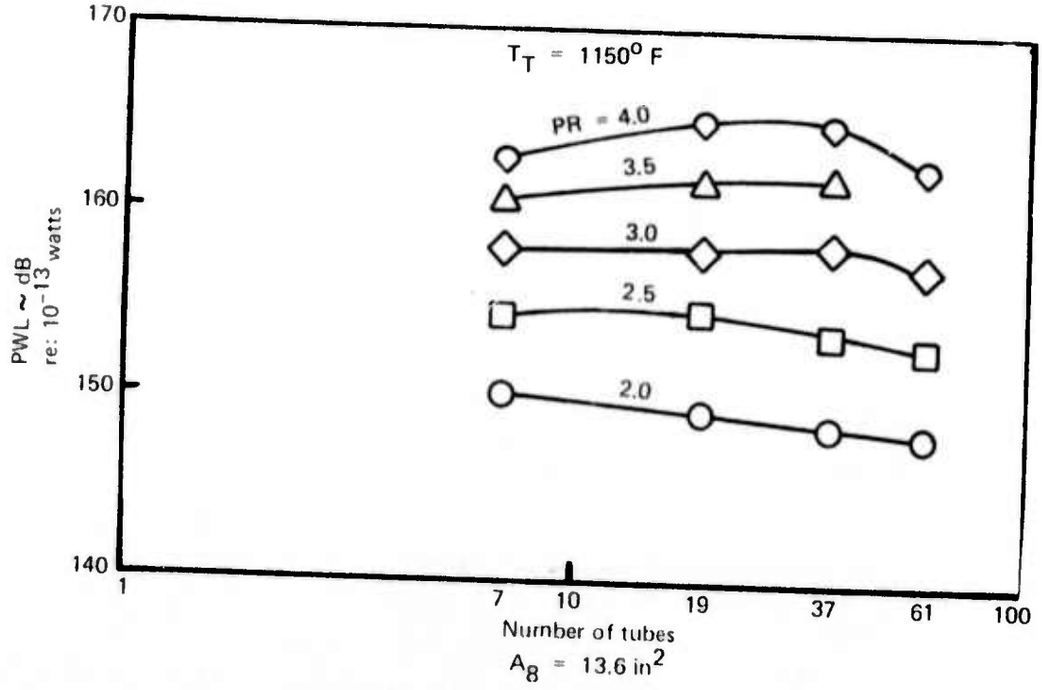

Figure 55. — Postmerged Jet Noise Power Levels for Area Ratio 3.3 CPA Multitube Nozzles

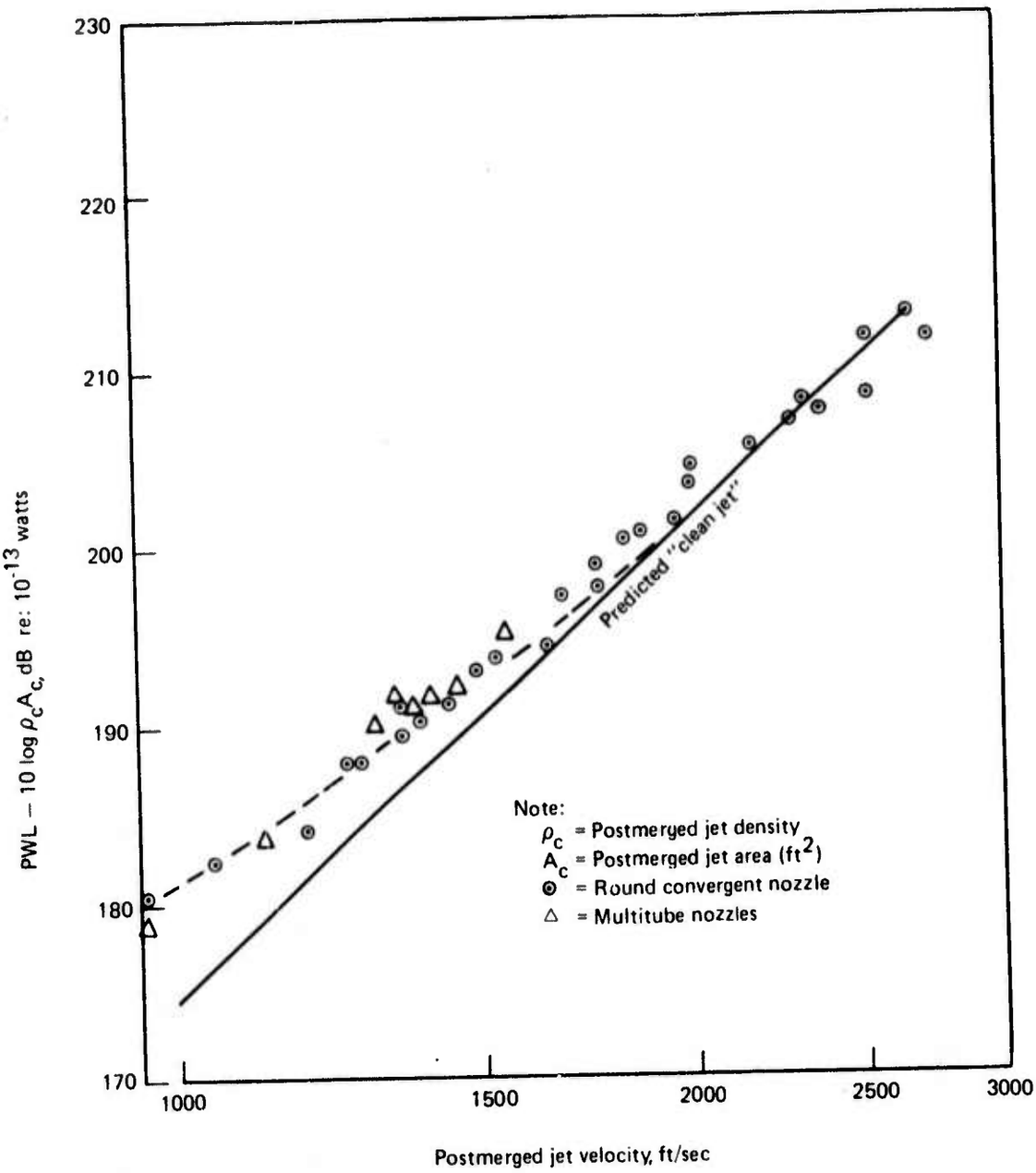

Figure 56. — Normalized Postmerged Jet Noise Power Levels

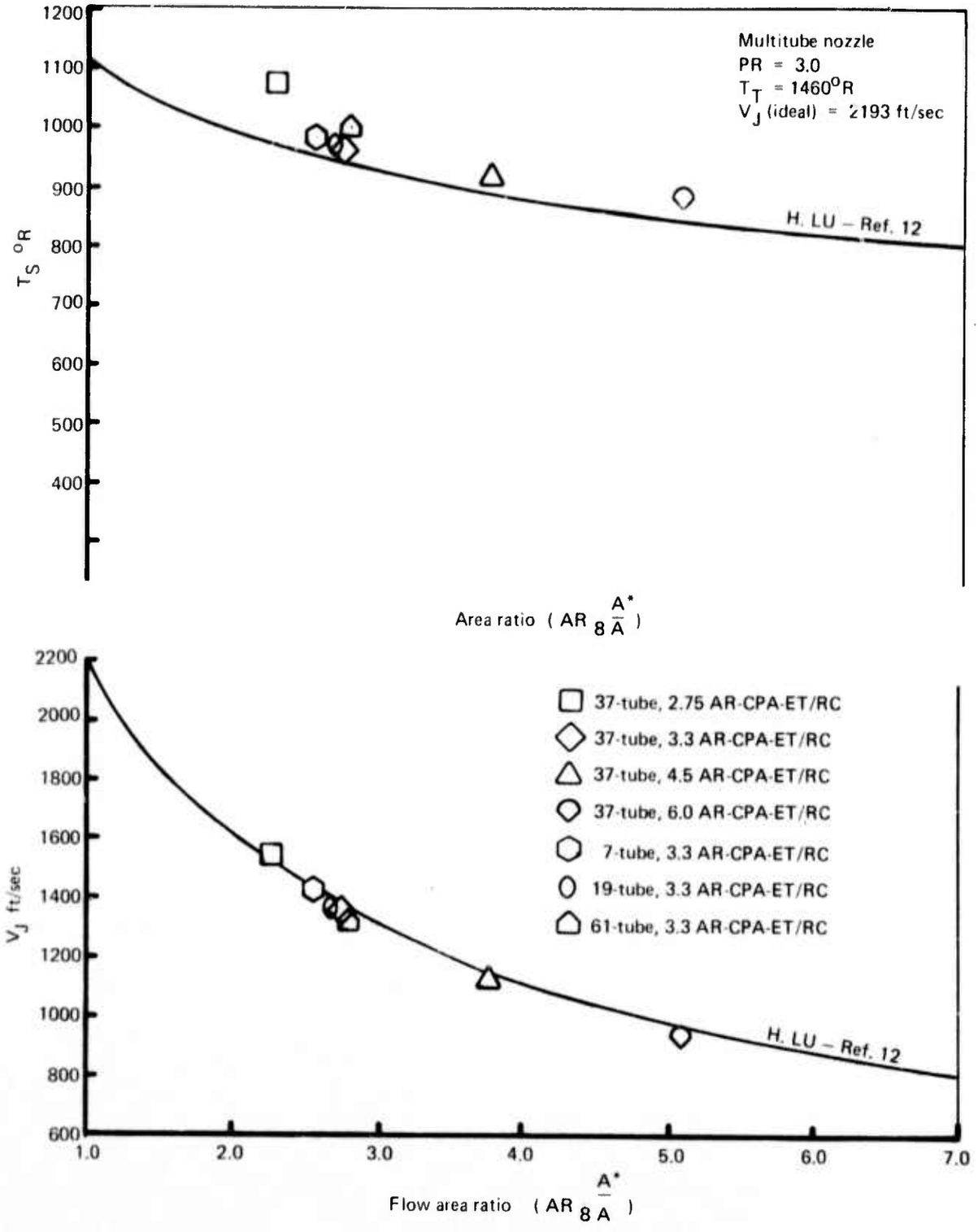

Figure 57. — Predicted and Measured Postmerged Jet Core Gas Conditions for Multitube Nozzles

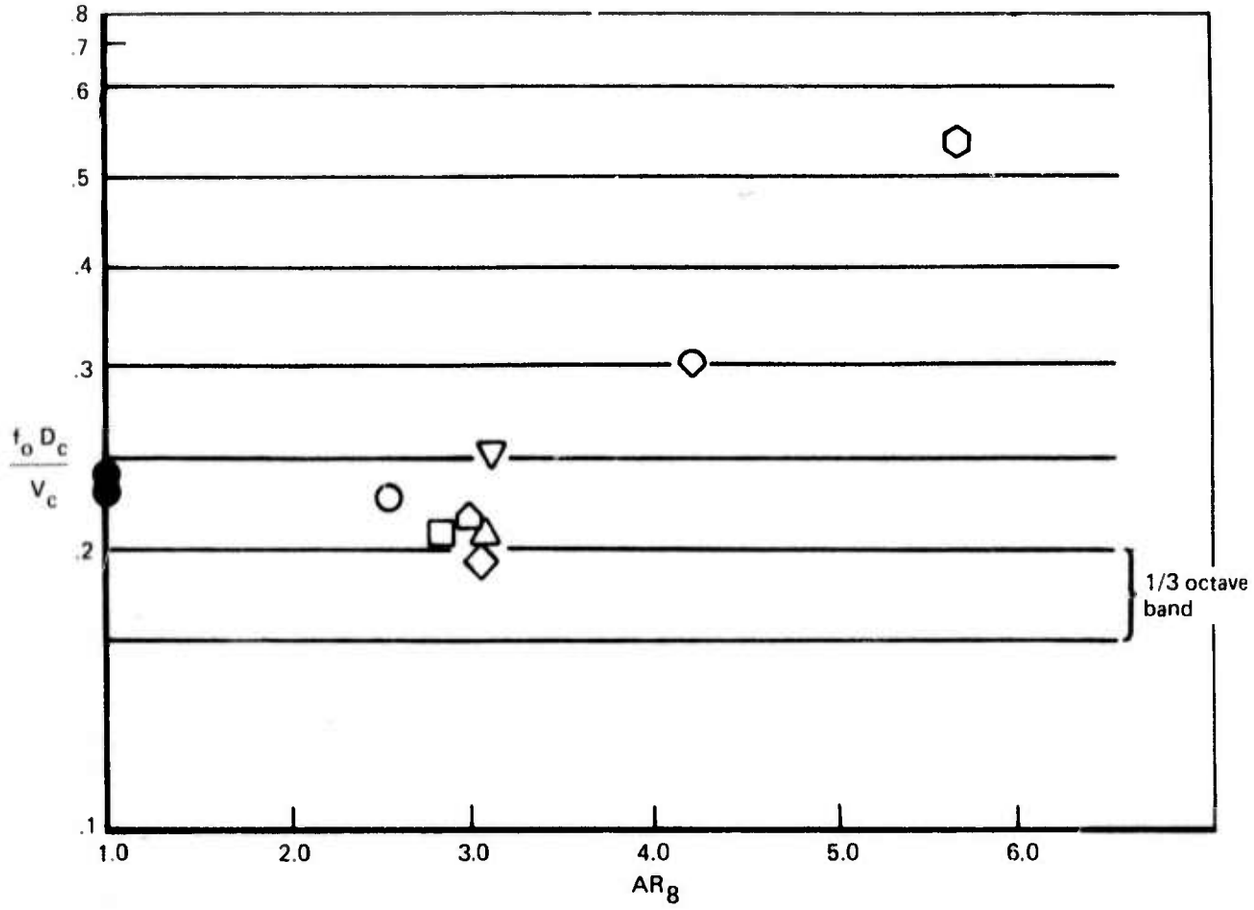

- ● 4.1-in-RC nozzle T_T = 500° F, PR = 2.0
- ○ 37-tube, 2.75 AR-CPA-ET/RC
- △ 37-tube, 3.3 AR-CPA-RT/RC
- ◇ 37-tube, 4.5 AR-CPA-ET/RC
- ⬡ 37-tube, 6.0 AR-CPA-ET/RC
- □ 7-tube, 3.3 AR-CPA-ET/RC
- ⌂ 19-tube, 3.3 AR-CPA-ET/RC
- ▽ 61-tube, 3.3 AR-CPA-ET/RC
- ◇ 37-tube, 3.3 AR-RA-RT/NC

Multitube nozzle conditions
T_T = 1150° F, PR = 3.0, V_J = 2303 ft/sec

f_o ; postmerged jet peak frequency, 1/3 octave band PWL

D_C ; postmerged jet core diameter, $\left(\frac{4 A_8 \times AR_8}{\pi}\right)^{1/2}$, in feet

V_C ; postmerged jet core velocity (measured) ft/sec

AR_8 ; nozzle exit flow area ratio

Figure 58. — Postmerged Jet Peak-Noise Frequency Strouhal Number Relationship

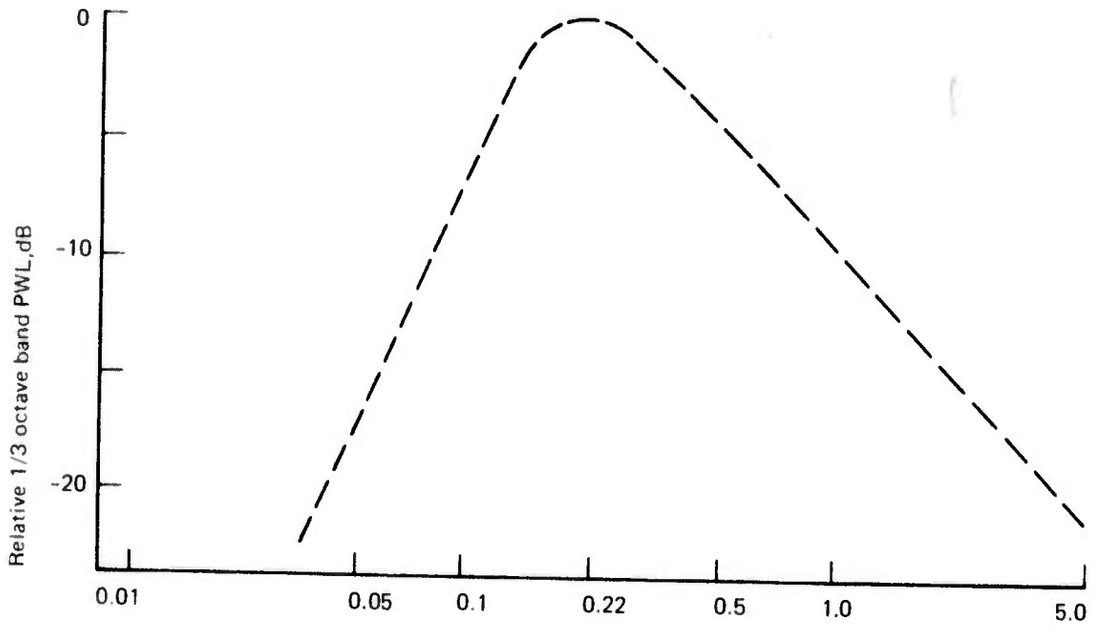

$$D_c = \left(\frac{4 A_8 \times AR_8}{\pi} \right)^{1/2}$$

V_c ; Measured postmerged jet core velocity, ft/sec

Figure 59. — Multitube Nozzle Postmerged Jet Noise Spectrum Shape

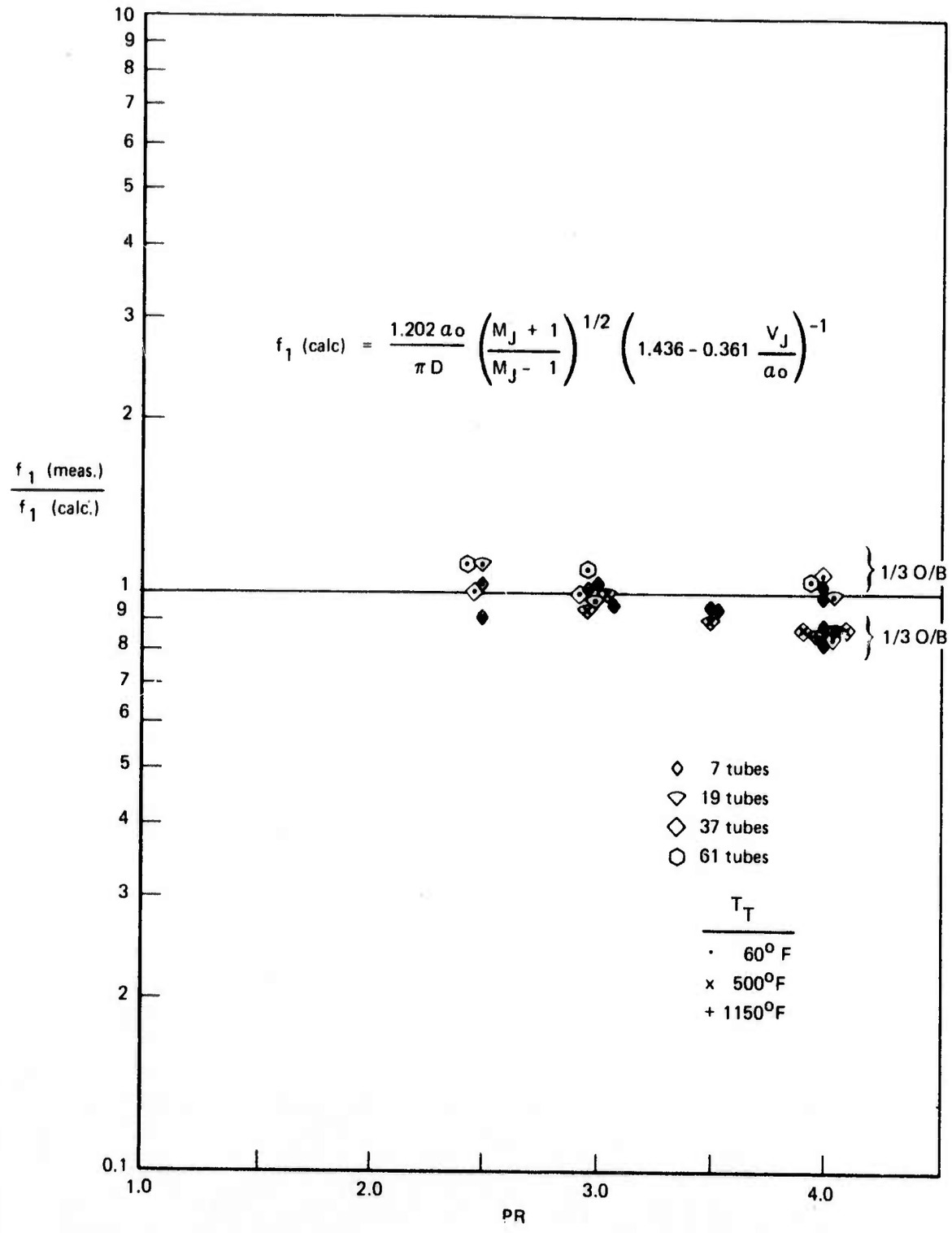

Figure 60. — Multitube Nozzle (Close-Packed Array) 3.3-AR Spiral-Mode Flow-Instability Noise Frequency

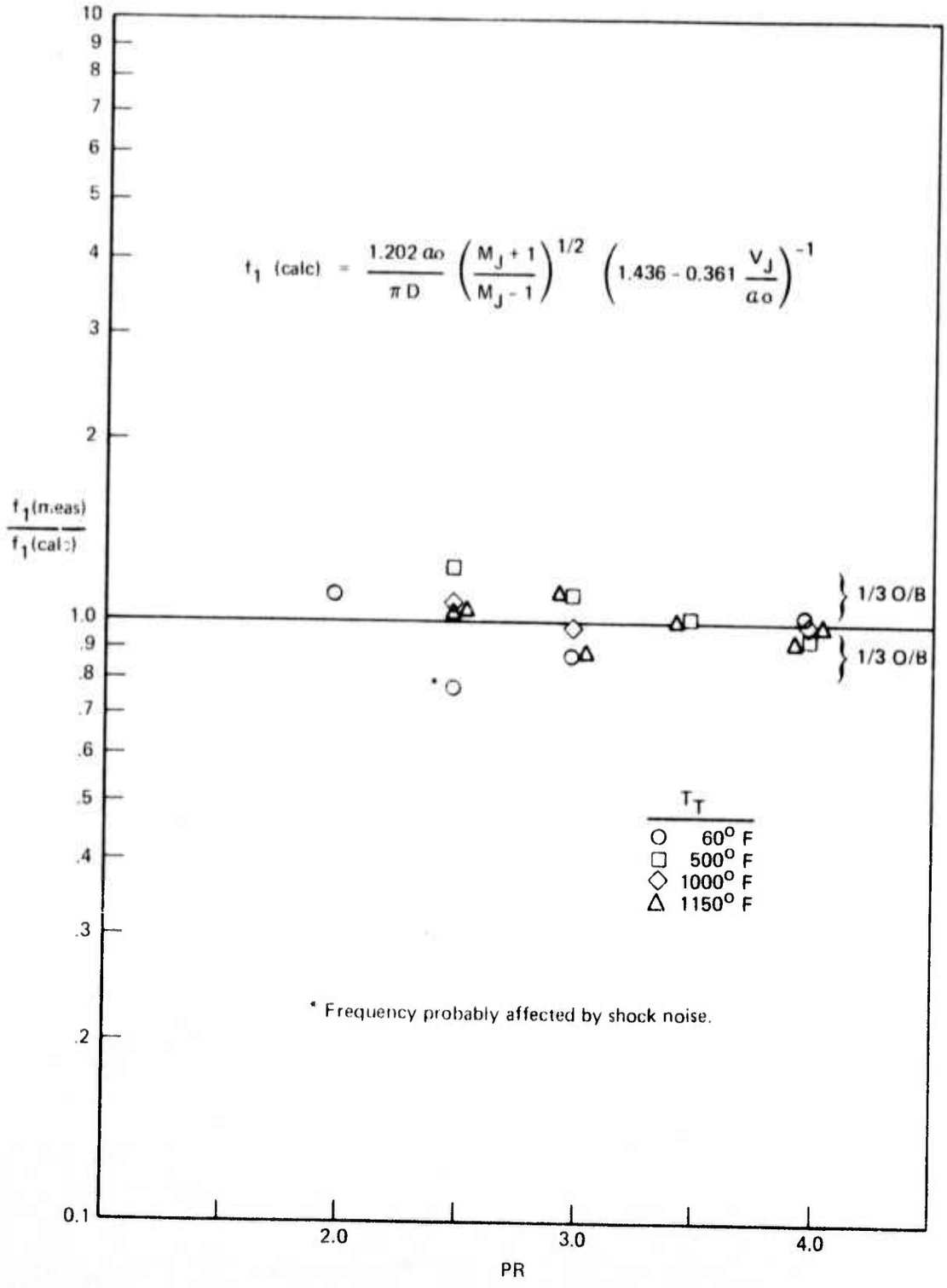

Figure 61. — 4.1-inch R/C Nozzle Spiral-Mode Flow-Instability Noise Frequency

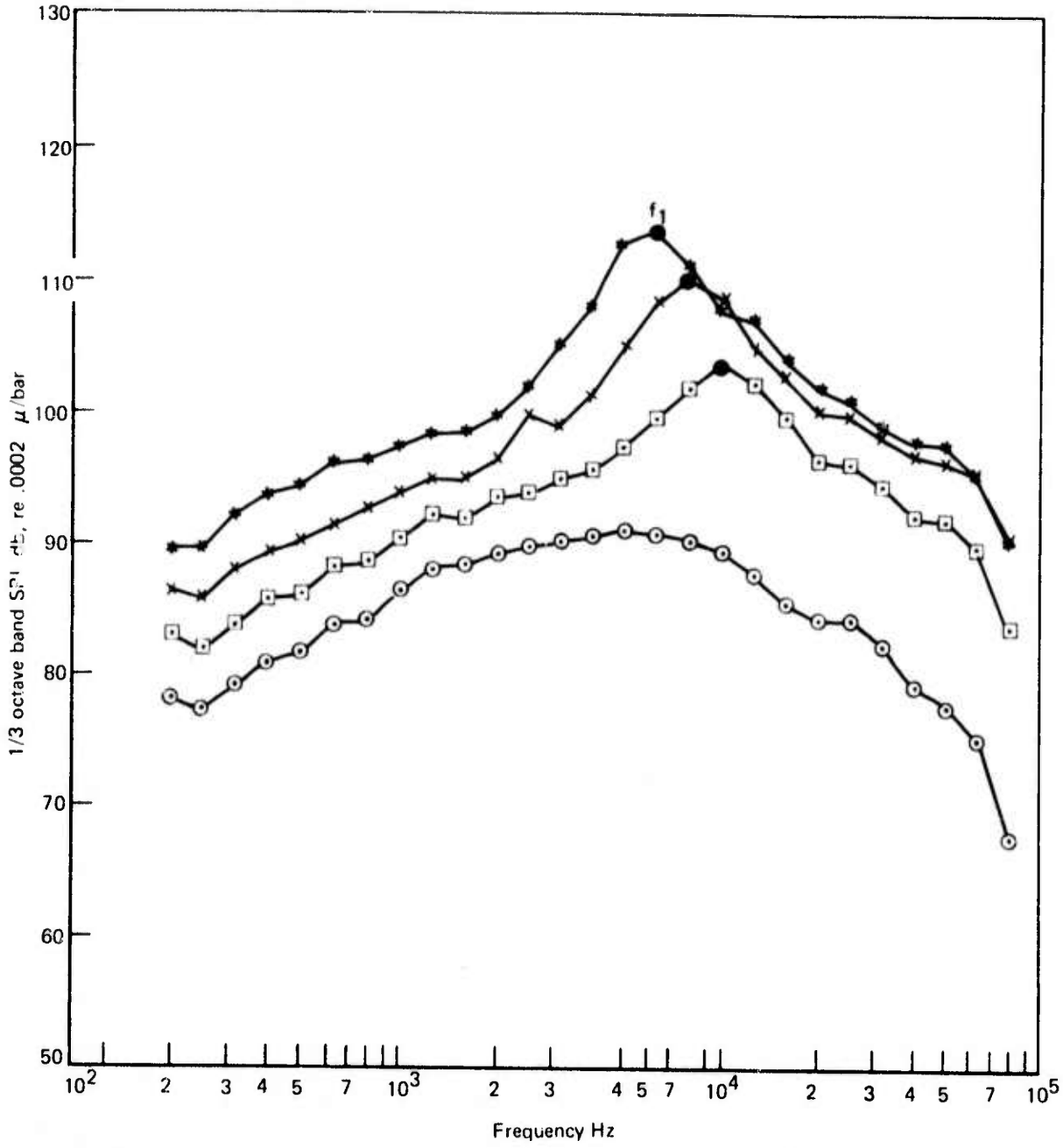

Plot symbol	Pressure ratio	Angle re inlet
⊙	2.000	90°
⊡	2.500	90°
X	3.000	90°
*	4.000	90°

T_T = 520° R

Figure 62. — 7-Tube, 3.3-AR Nozzle Noise Spectra at 90°

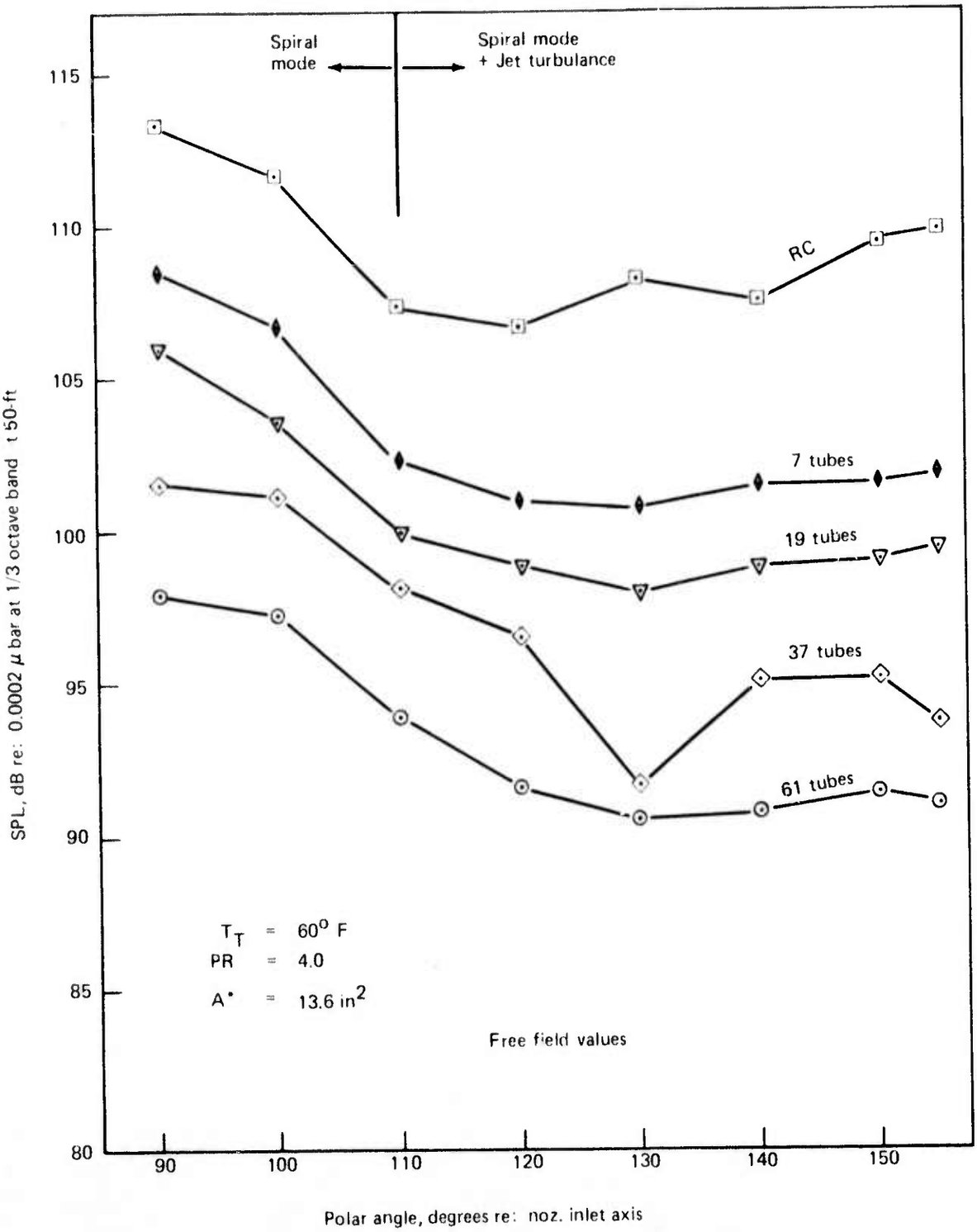

Figure 63. — Spiral-Mode Flow Instability Noise beam Patterns for 1-to-61 Tube Nozzles, 3.3 AR

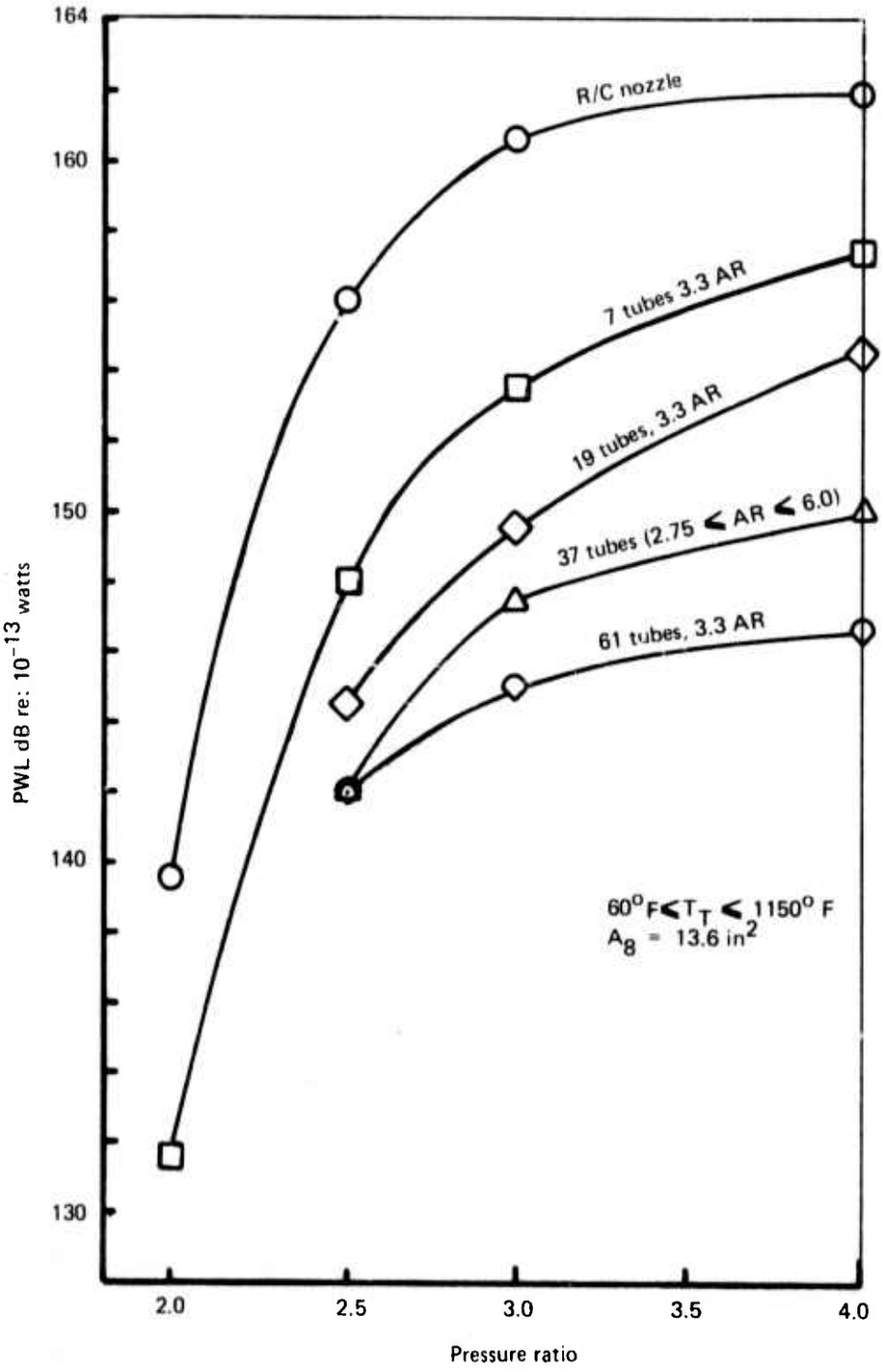

Figure 64. — Approximate Spiral-Mode Flow-Instability Noise Power Levels for 3.3 AR Multitube Nozzles

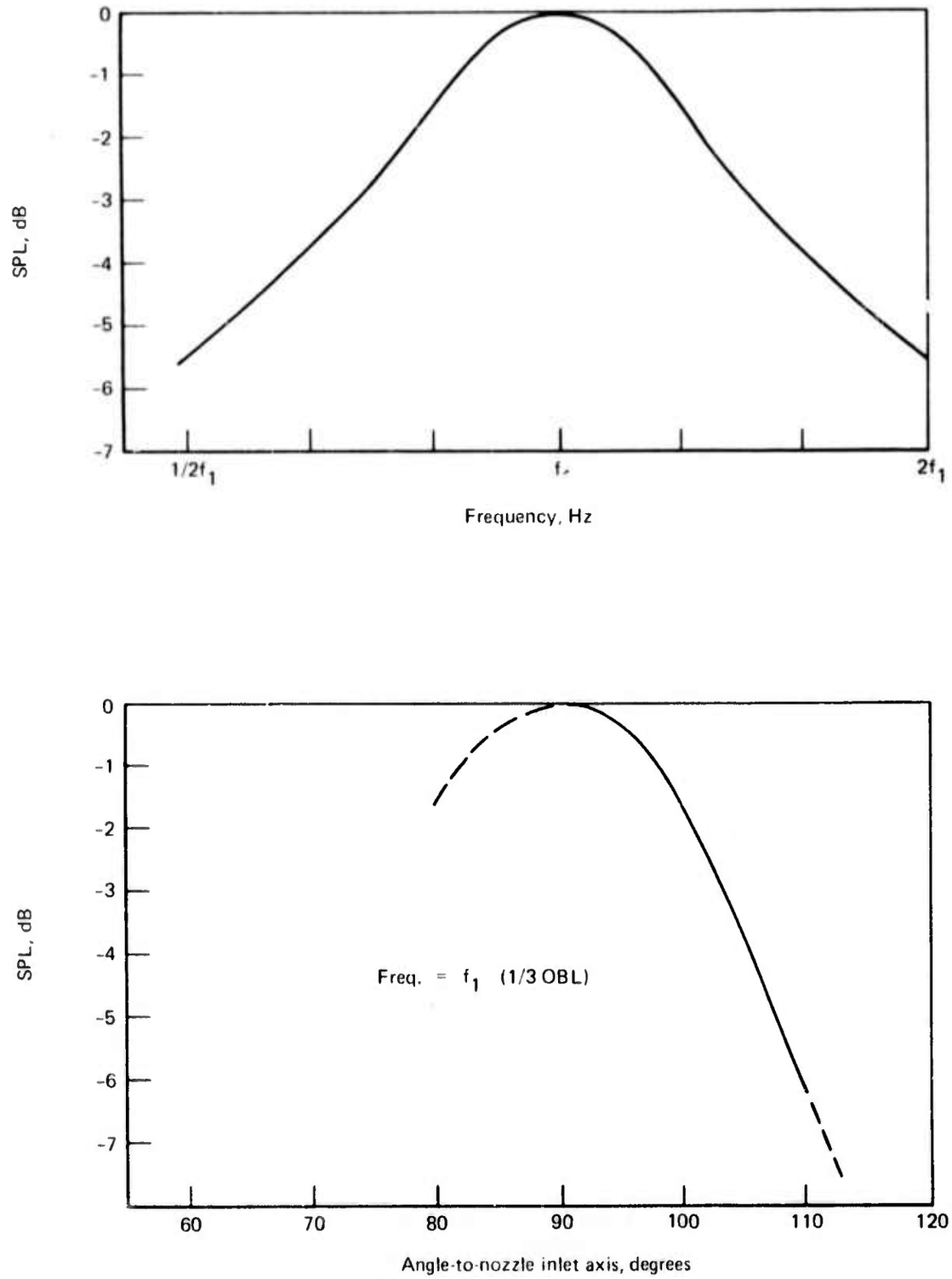

Figure 65. — Estimated Spiral-Mode Flow-Instability Noise Spectrum and Beam Pattern

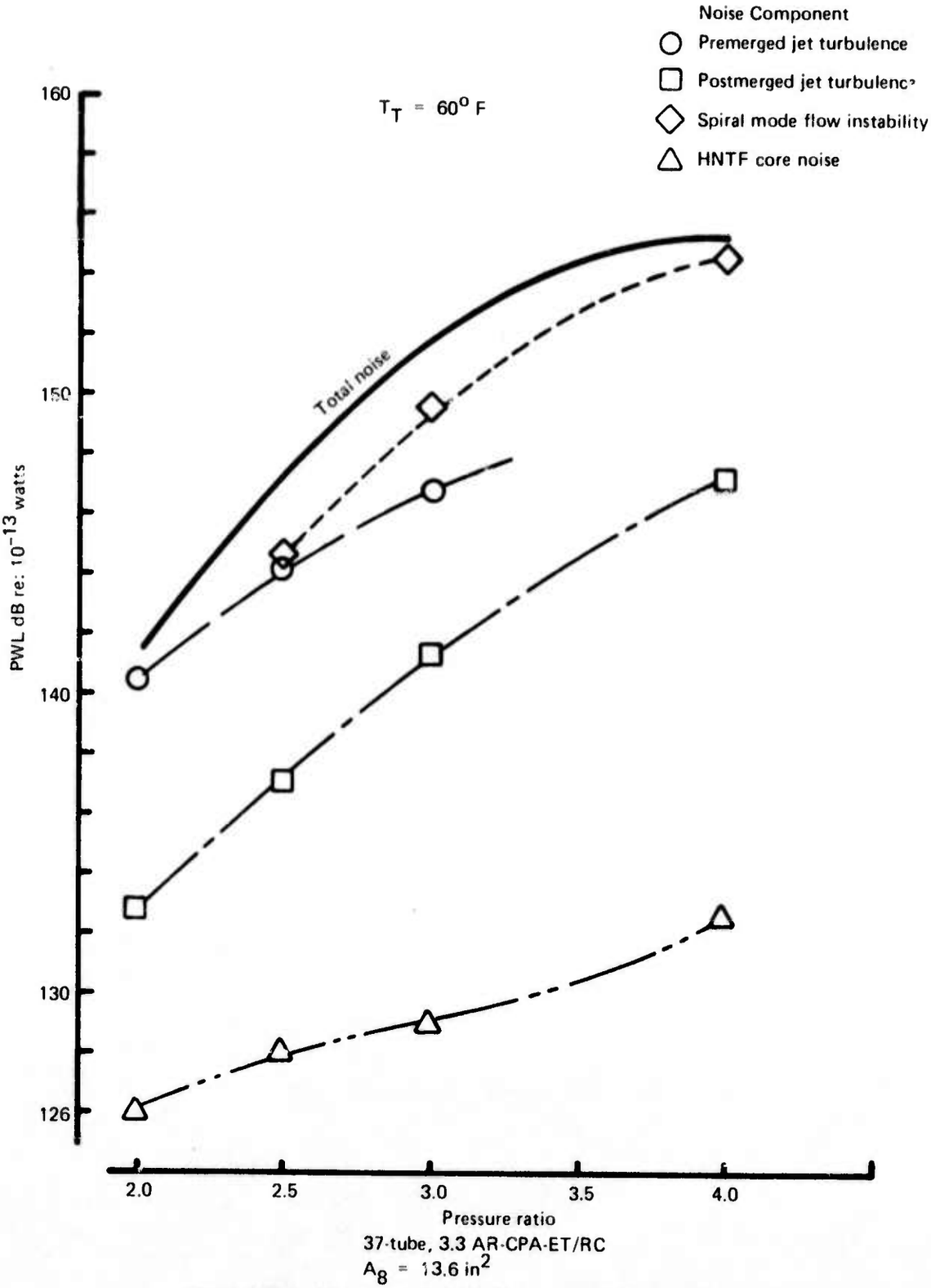

Figure 66. — 37-tube, 3.3 Area Ratio Nozzle Components of Jet Noise at T_T = 60° F

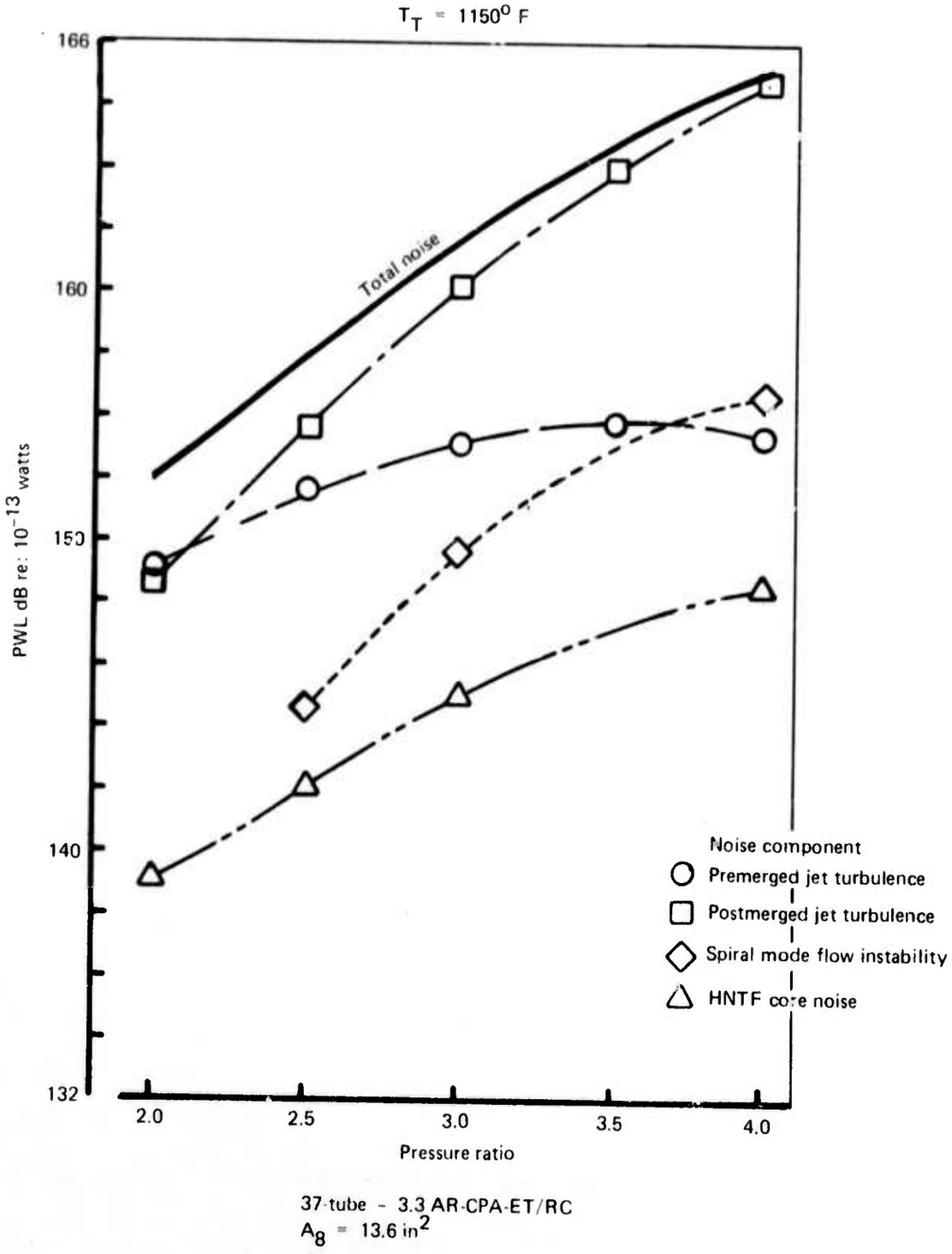

Figure 67. — 37-tube, 3.3 Area Ratio Nozzle Components of Jet Noise at T_T = 1150° F

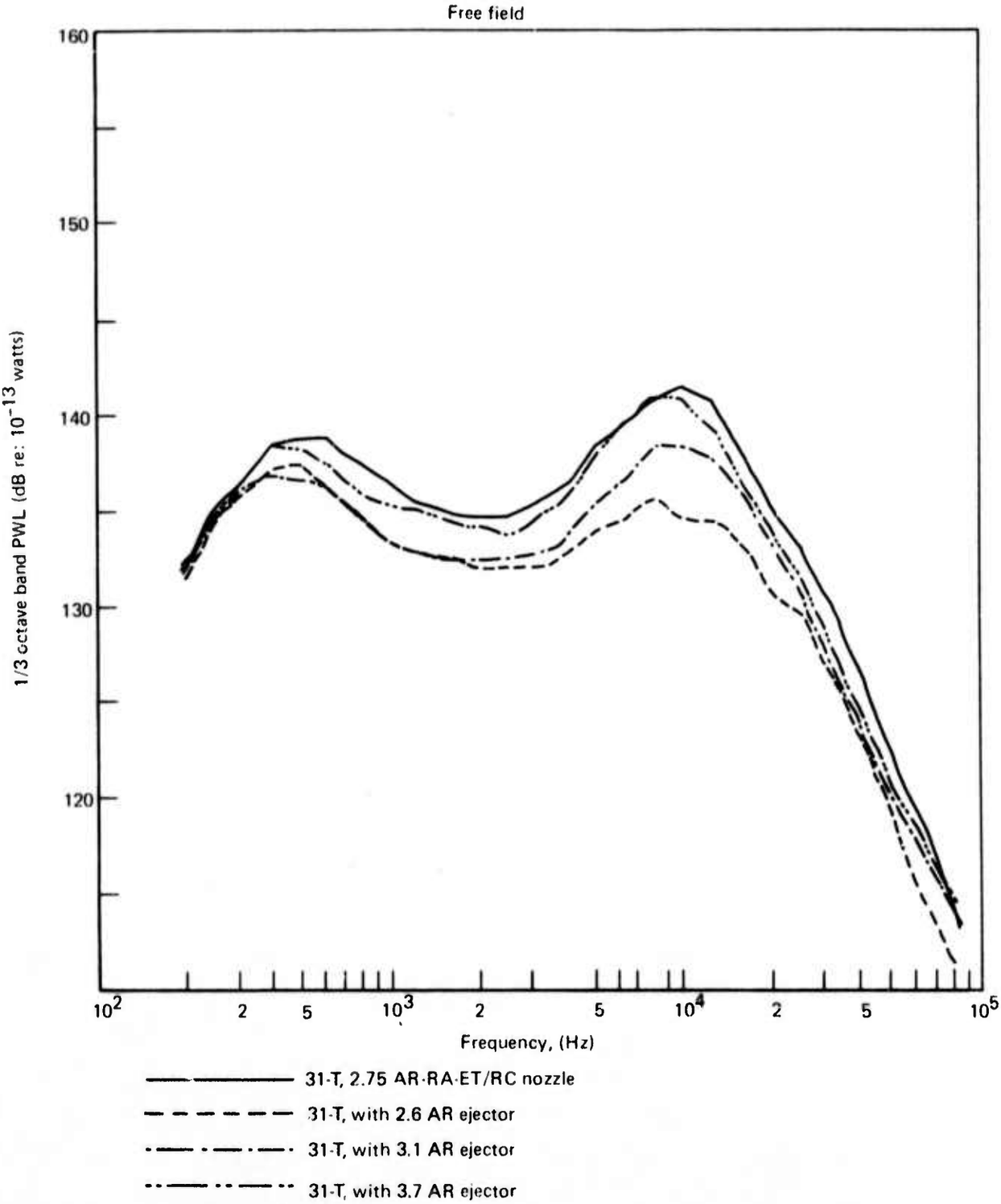

Figure 68. — 31-Tube, 2.75 AR Nozzle With Hardwall Ejectors, Jet Noise Power Spectra (PR = 2.0, T_T = 1150° F)

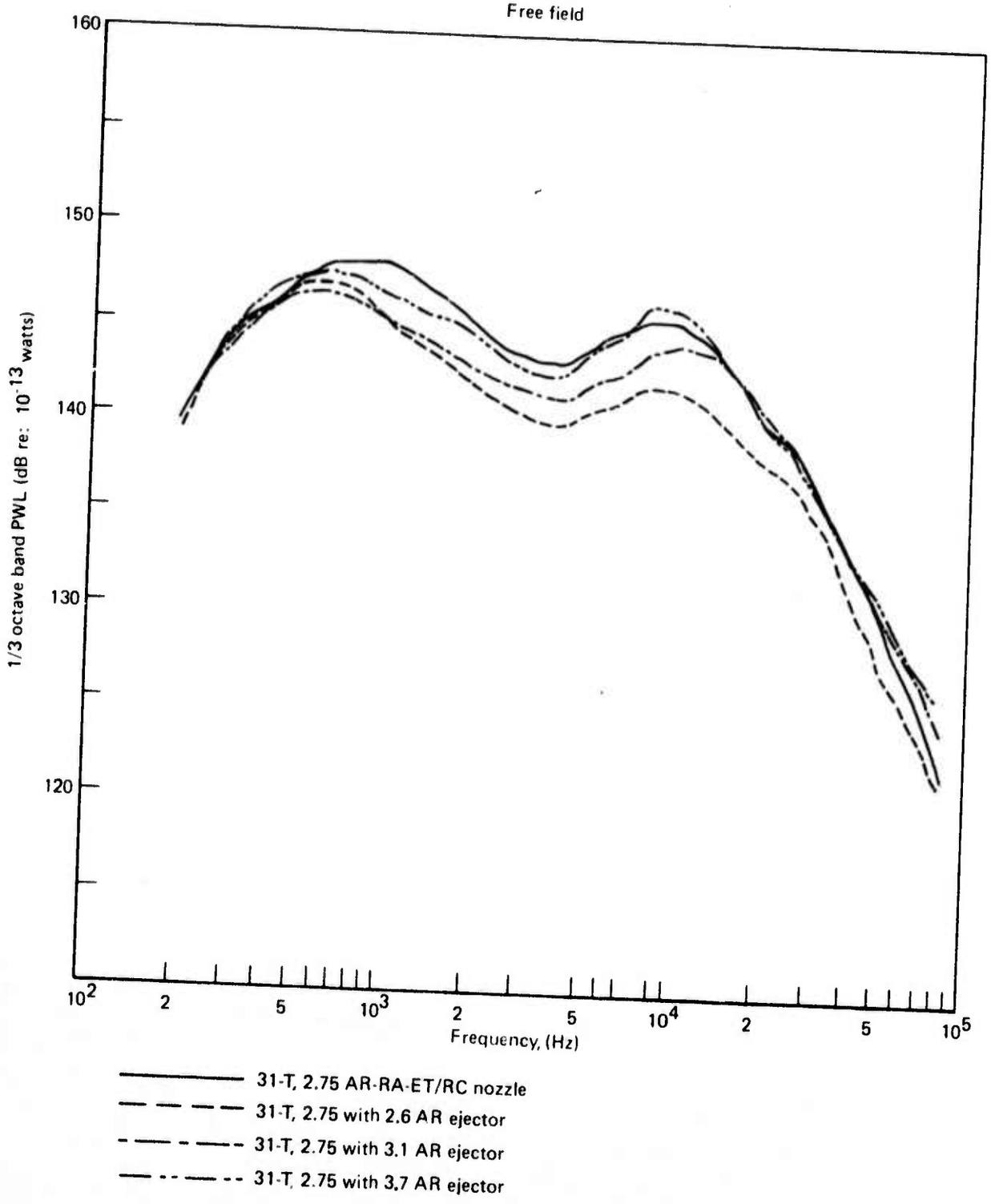

Figure 69. — 31-Tube, 2.75 AR Nozzle With Hardwall Ejectors Jet Noise Power Spectra (PR = 3.0 , T_T = 1150° F)

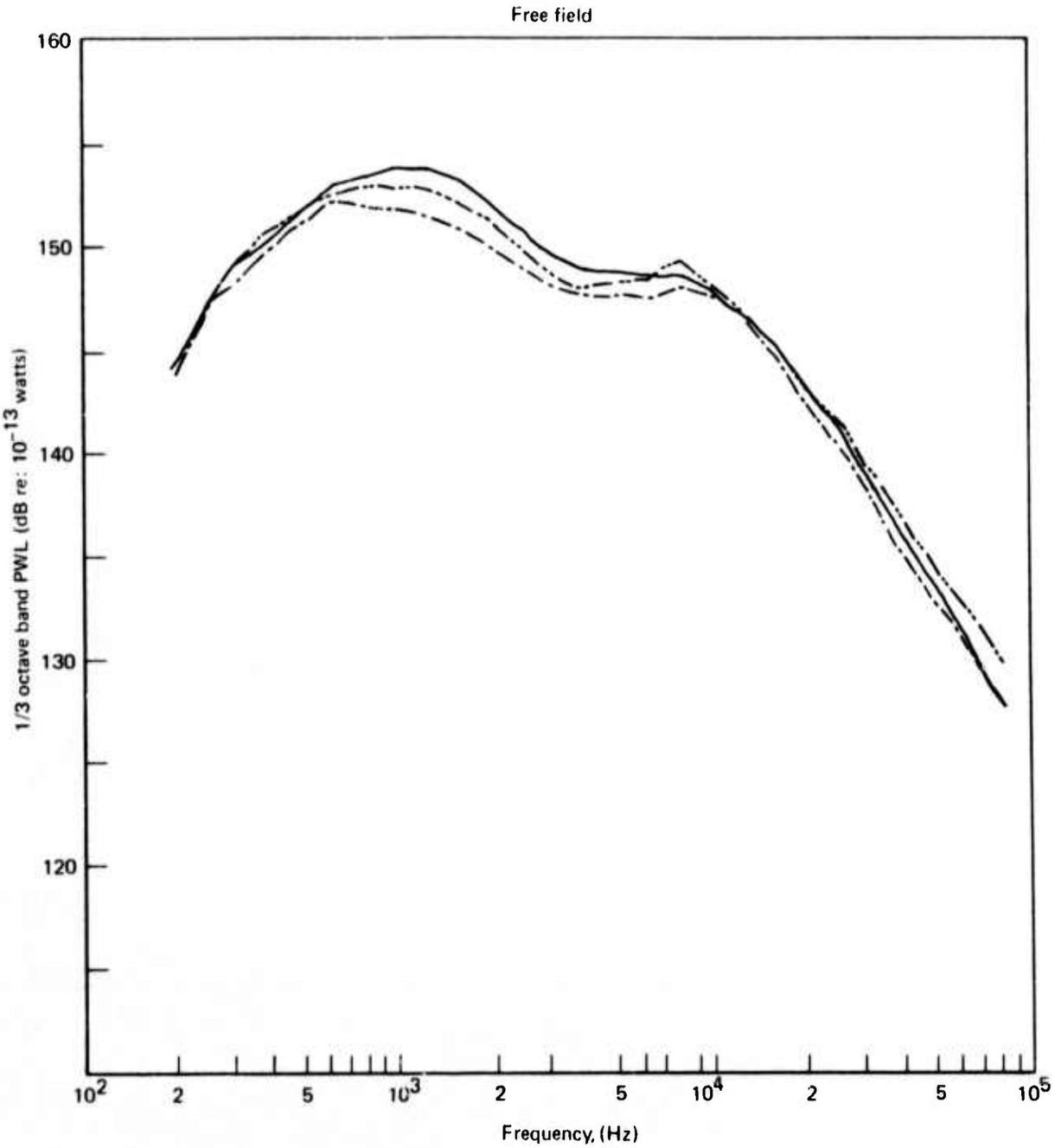

Figure 70. — 31-Tube, 2.75 AR Nozzle With Hardwall Ejectors Jet Noise Power Spectra (PR = 4.0, T_T = 1150° F).

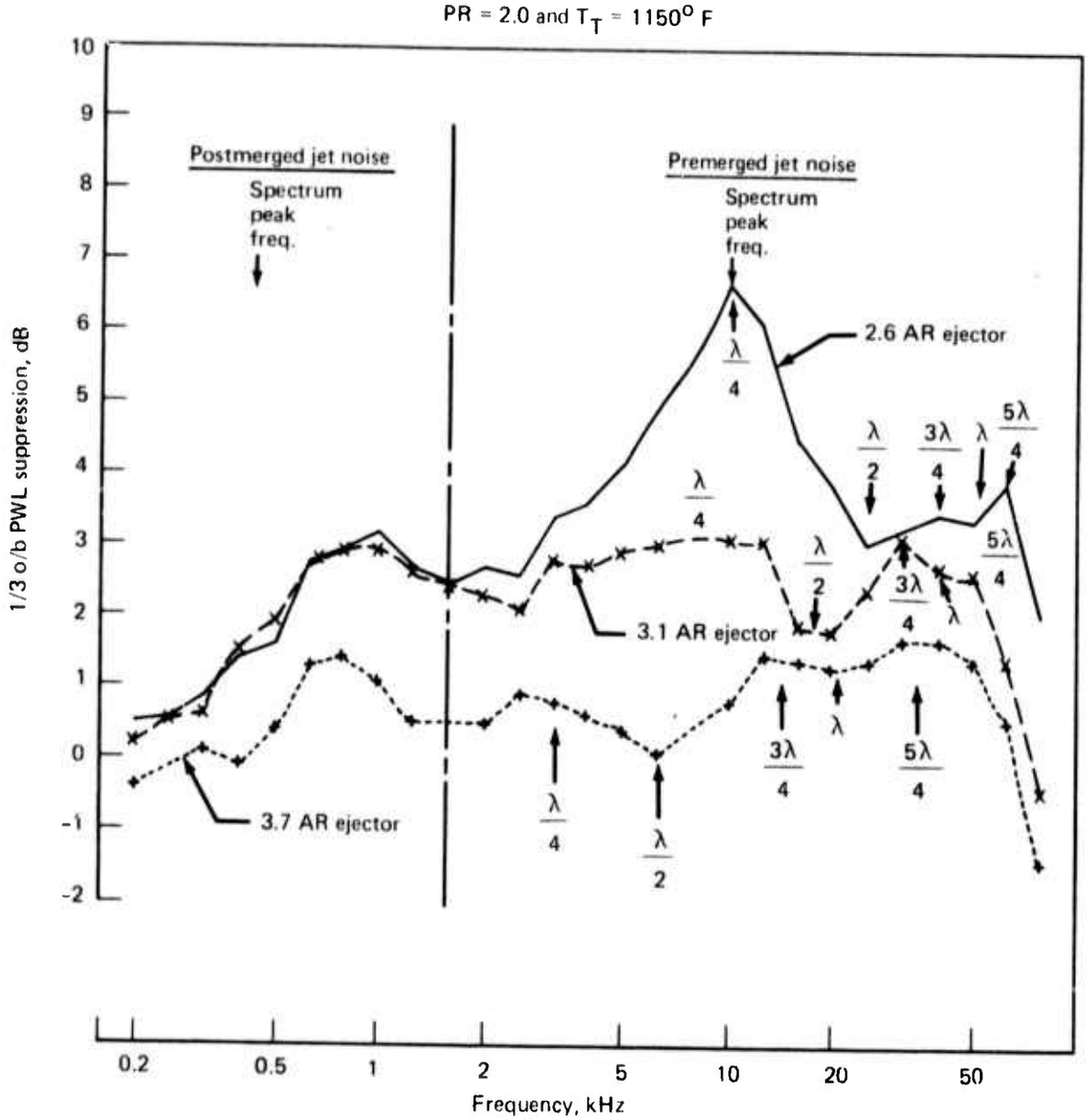

Figure 71. — Jet Noise Suppression Characteristics of Hardwall Ejectors With the 31-Tube 2.75 AR Nozzle

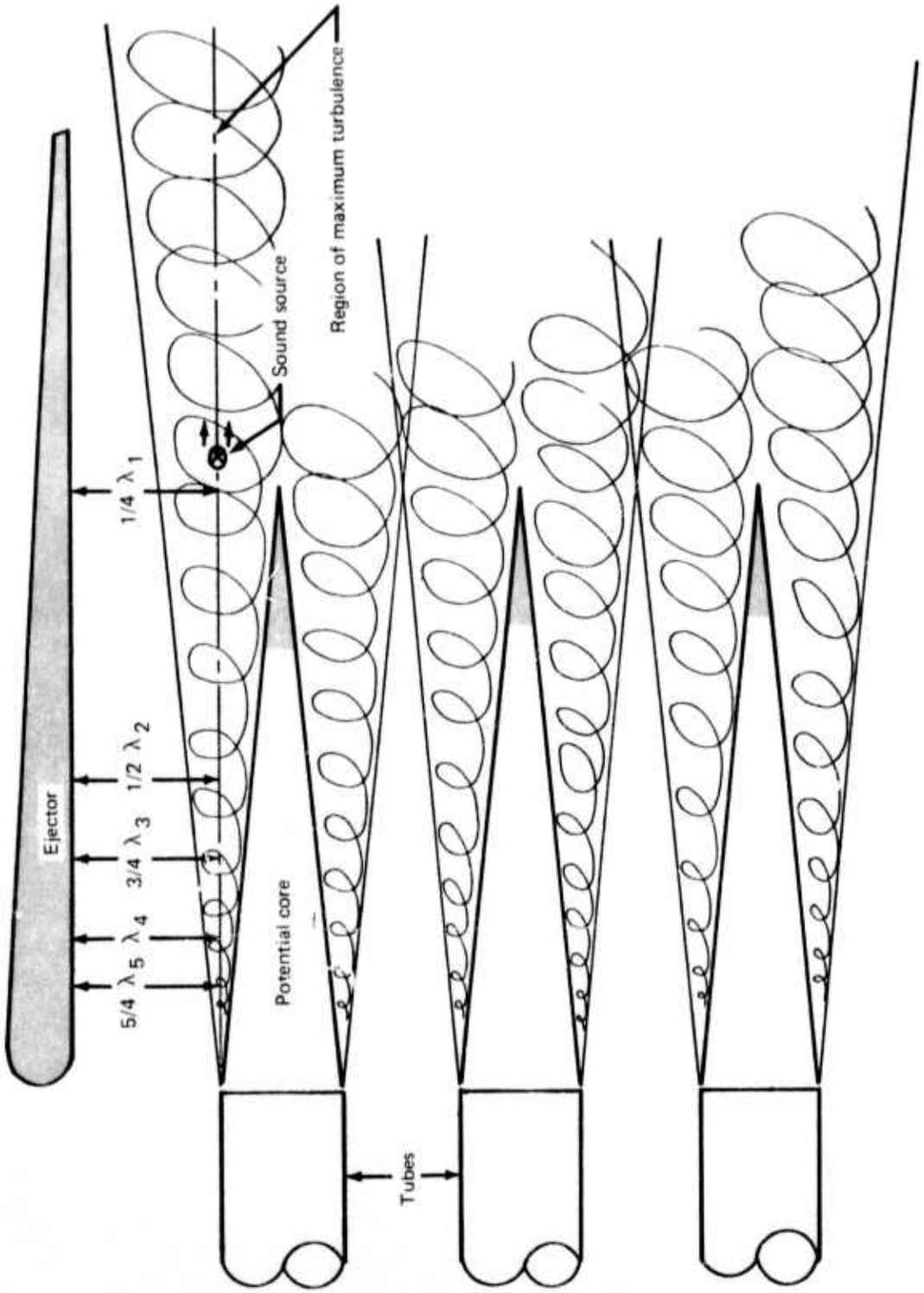

Figure 72. — Schematic of Possible Jet Noise Positive and Negative Feedback Due to the Presence of a Hardwall Ejector

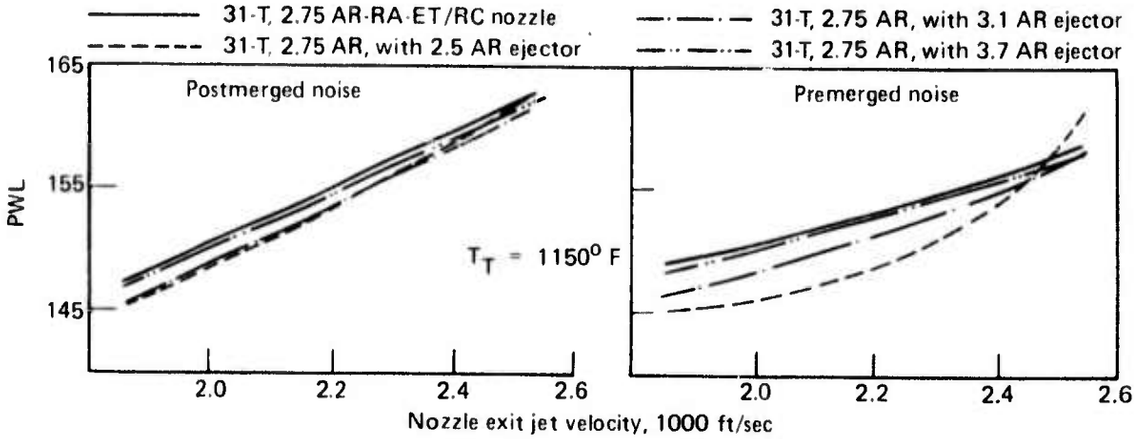

Figure 73. — Postmerged and Premerged Jet Noise Power Levels for 31-Tube Nozzle/Ejector Configurations

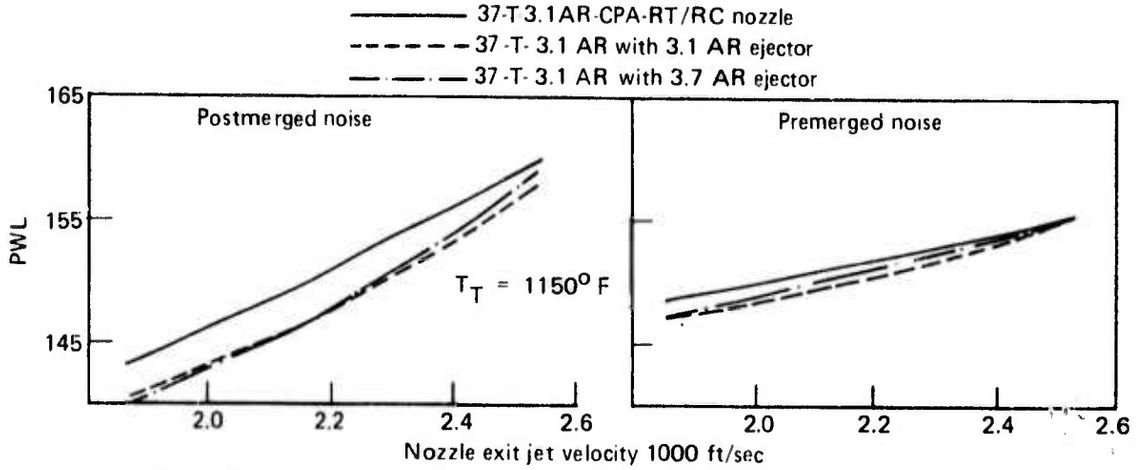

Figure 74. — Postmerged and Premerged Jet Noise Power Levels for 37-Tube Nozzle/Ejector Configurations

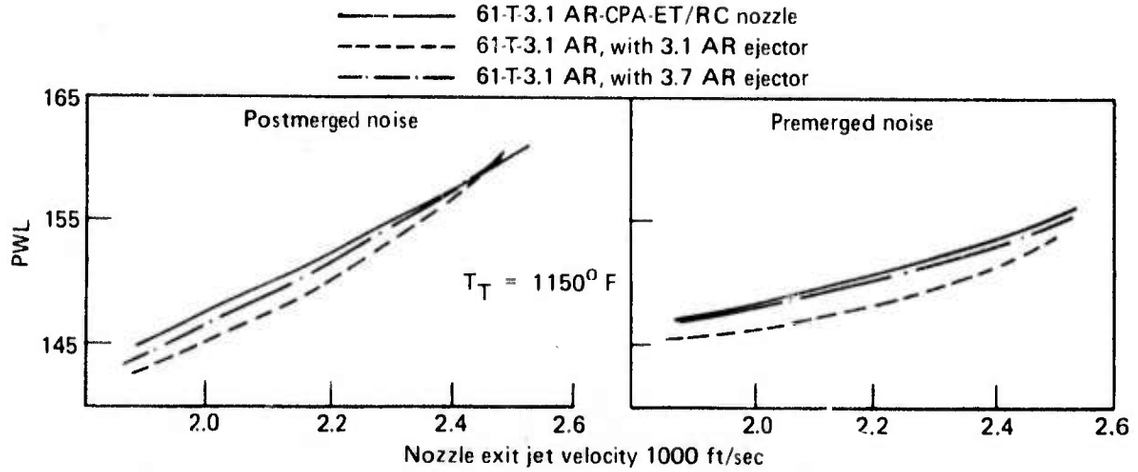

Figure 75. — Postmerged and Premerged Jet Noise Power Levels for 61-Tube Nozzle/Ejector Configurations

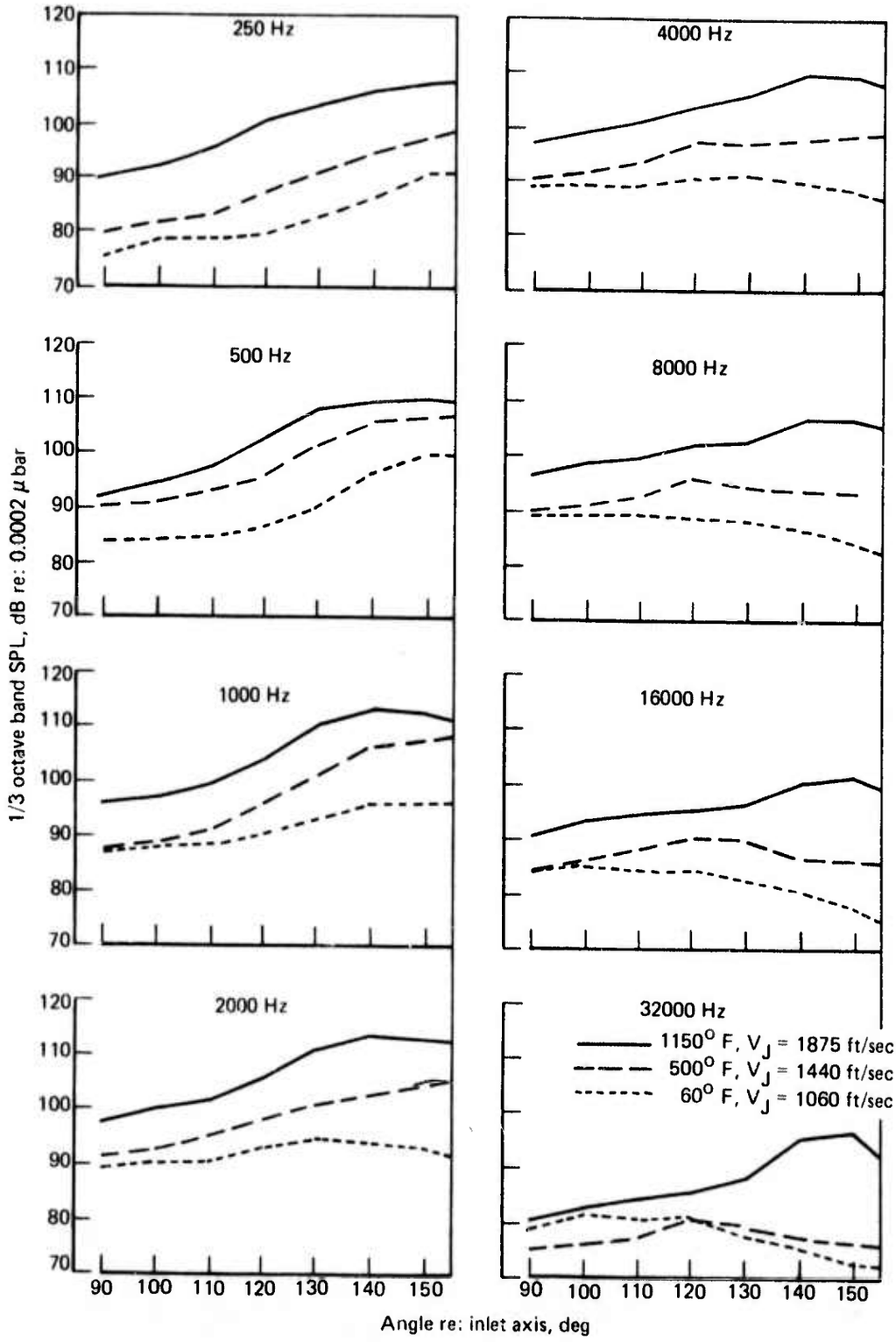

Figure 76. — R/C Nozzle Beam Patterns at PR = 2.0

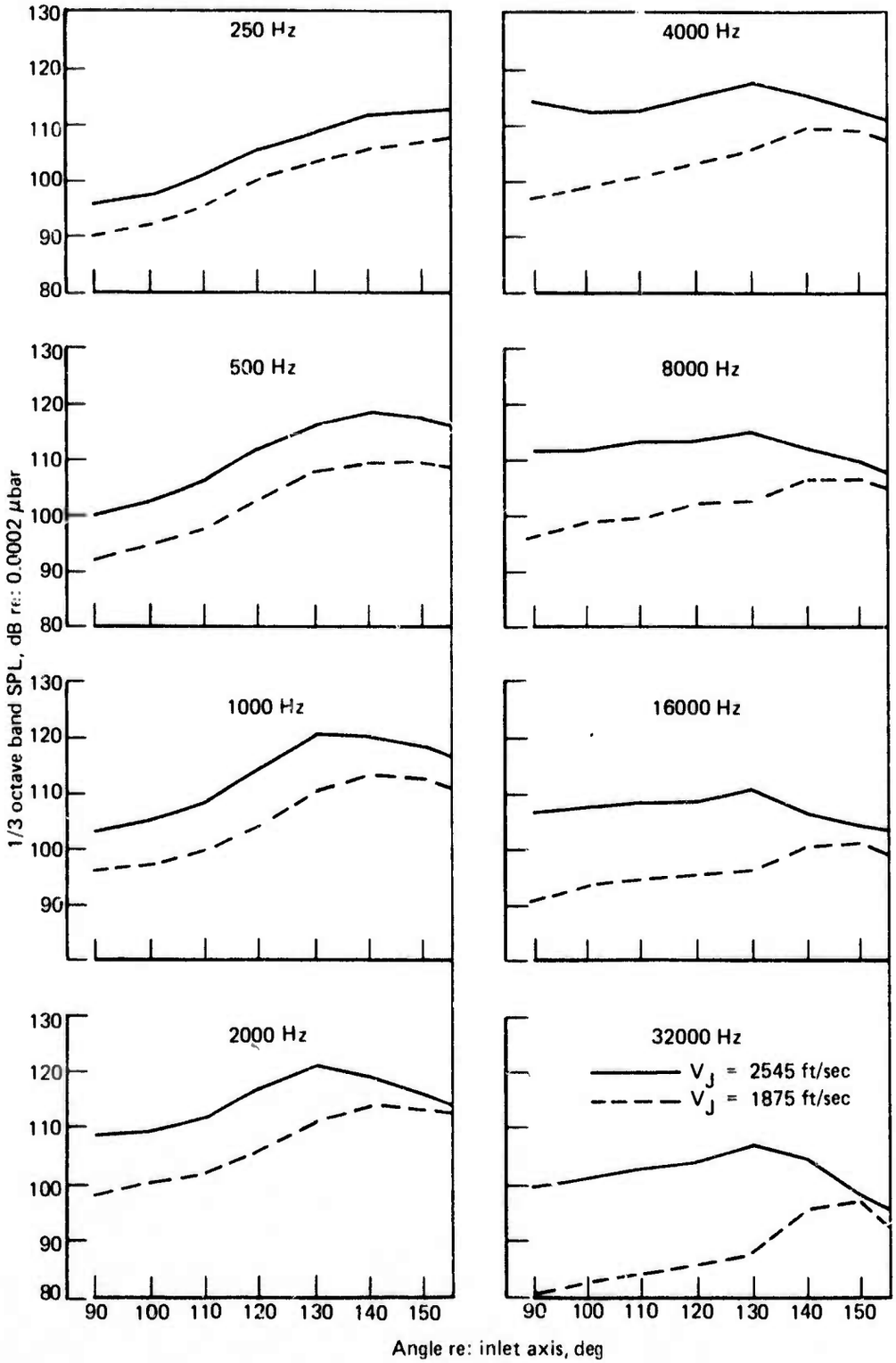

Figure 77. — R/C Nozzle Beam Patterns at 1150° F

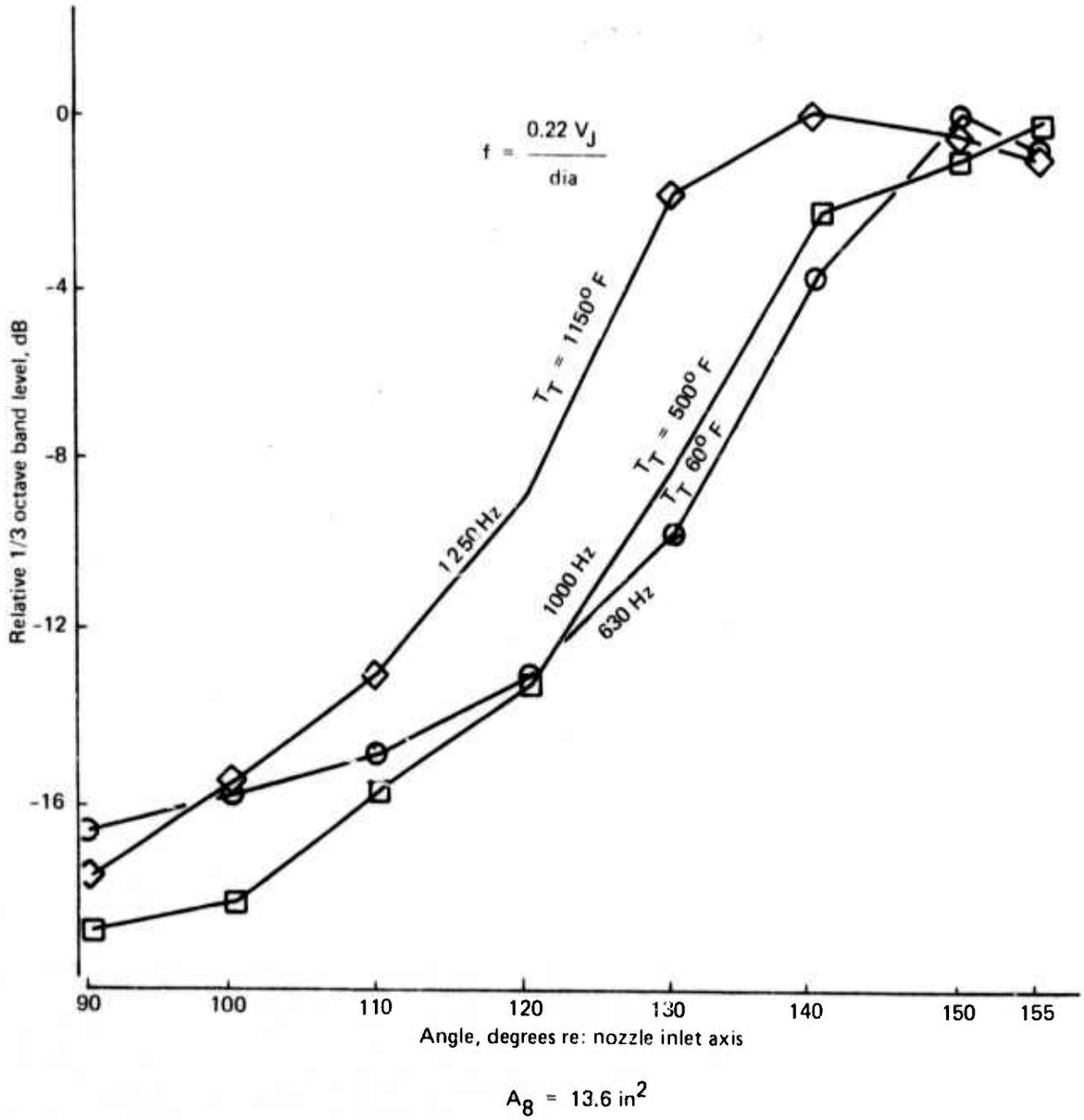

$A_8 = 13.6\ in^2$

Figure 78. — R/C Nozzle Jet Noise Peak-Frequency Beam Patterns (PR = 2.0)

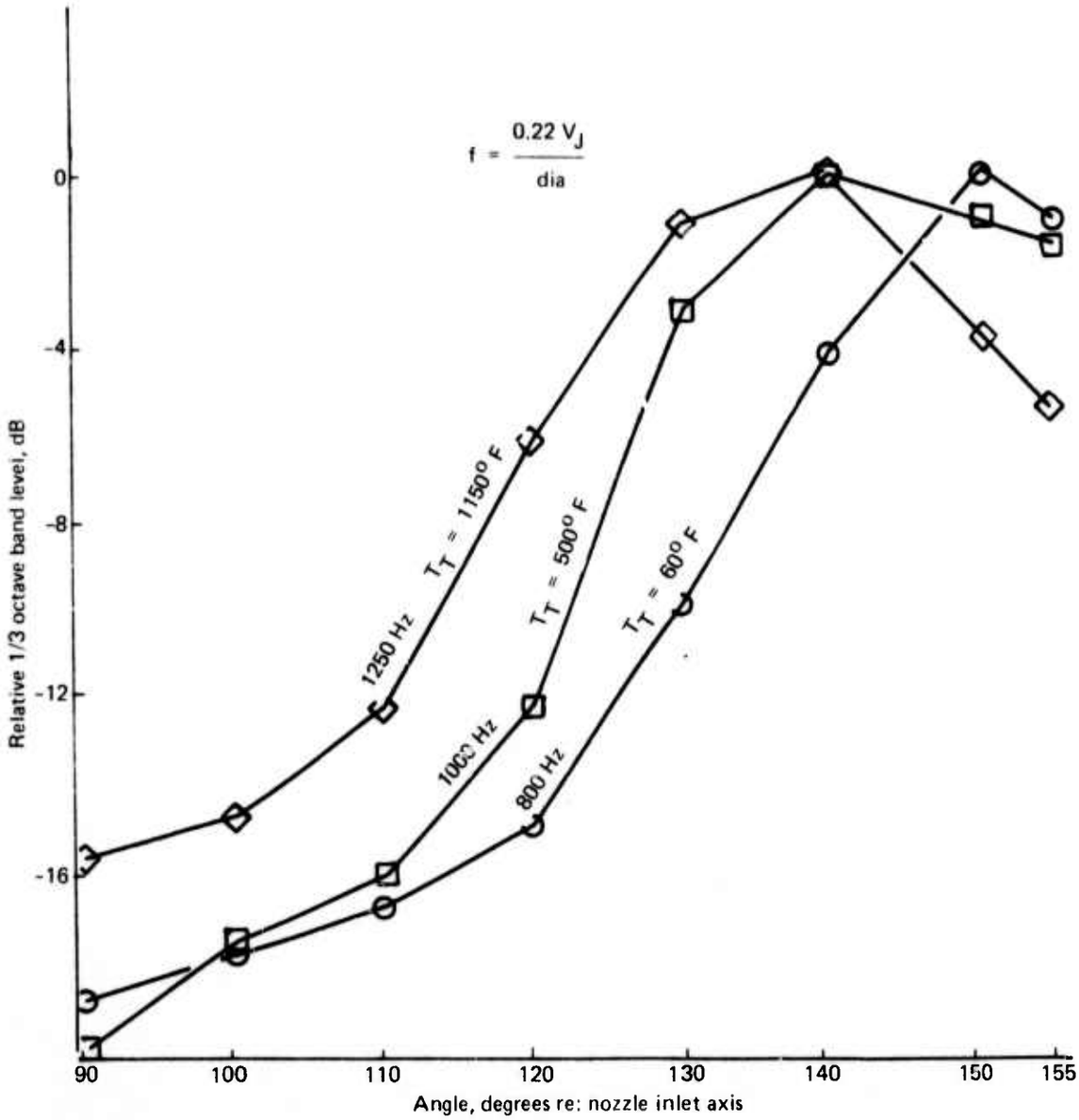

A_8 = 13.6 in^2

Figure 79. — R/C Nozzle Jet Noise Peak-Frequency Beam Patterns (PR = 4.0)

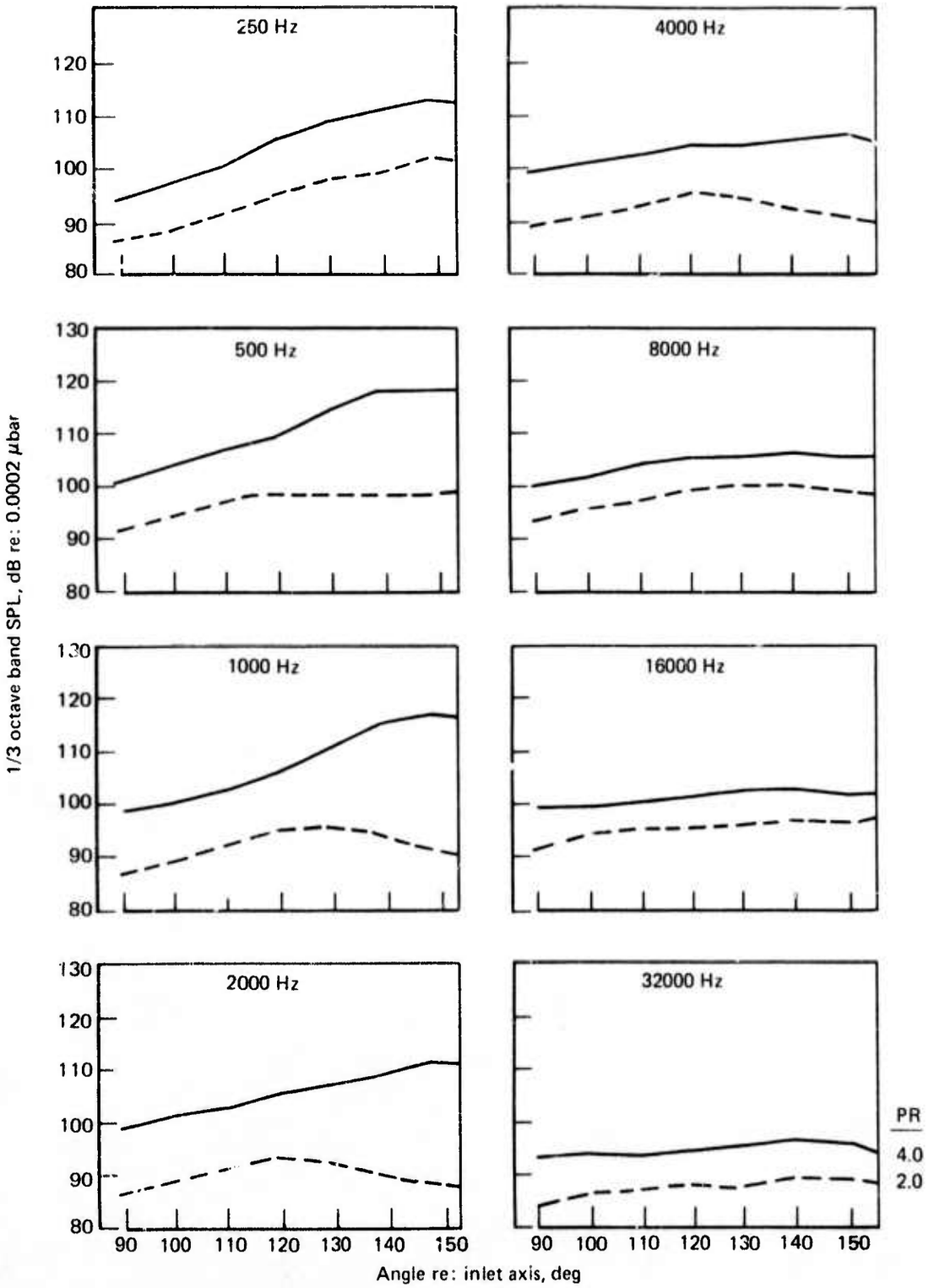

Figure 80. — 37-Tube, 3.3 AR Nozzle Jet Noise 1/3 octave band Beam Patterns. T_T = 1150° F

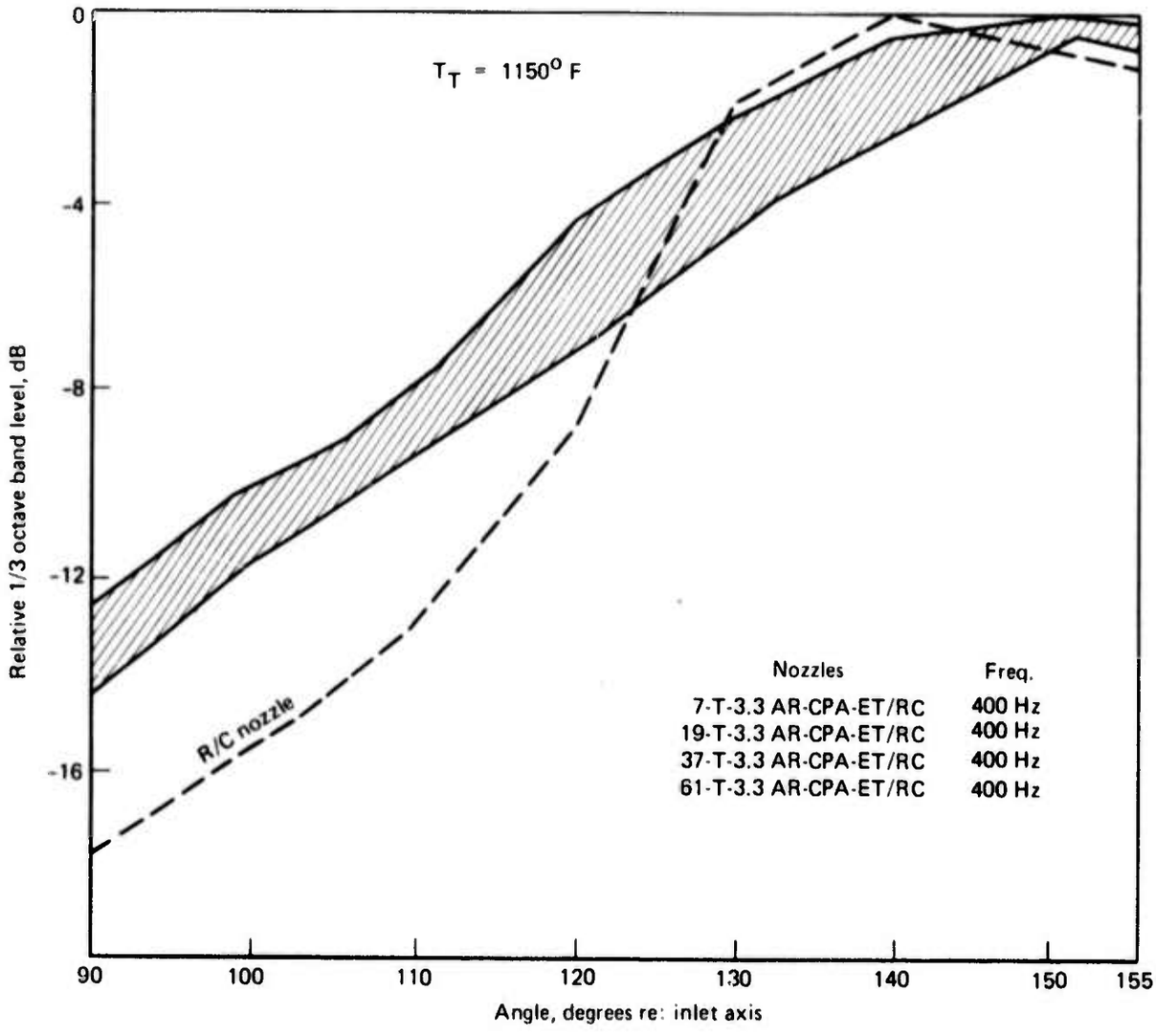

Figure 81. — Multitube Nozzle Postmerged Jet Noise Peak-Frequency Beam Patterns at PR = 2.0

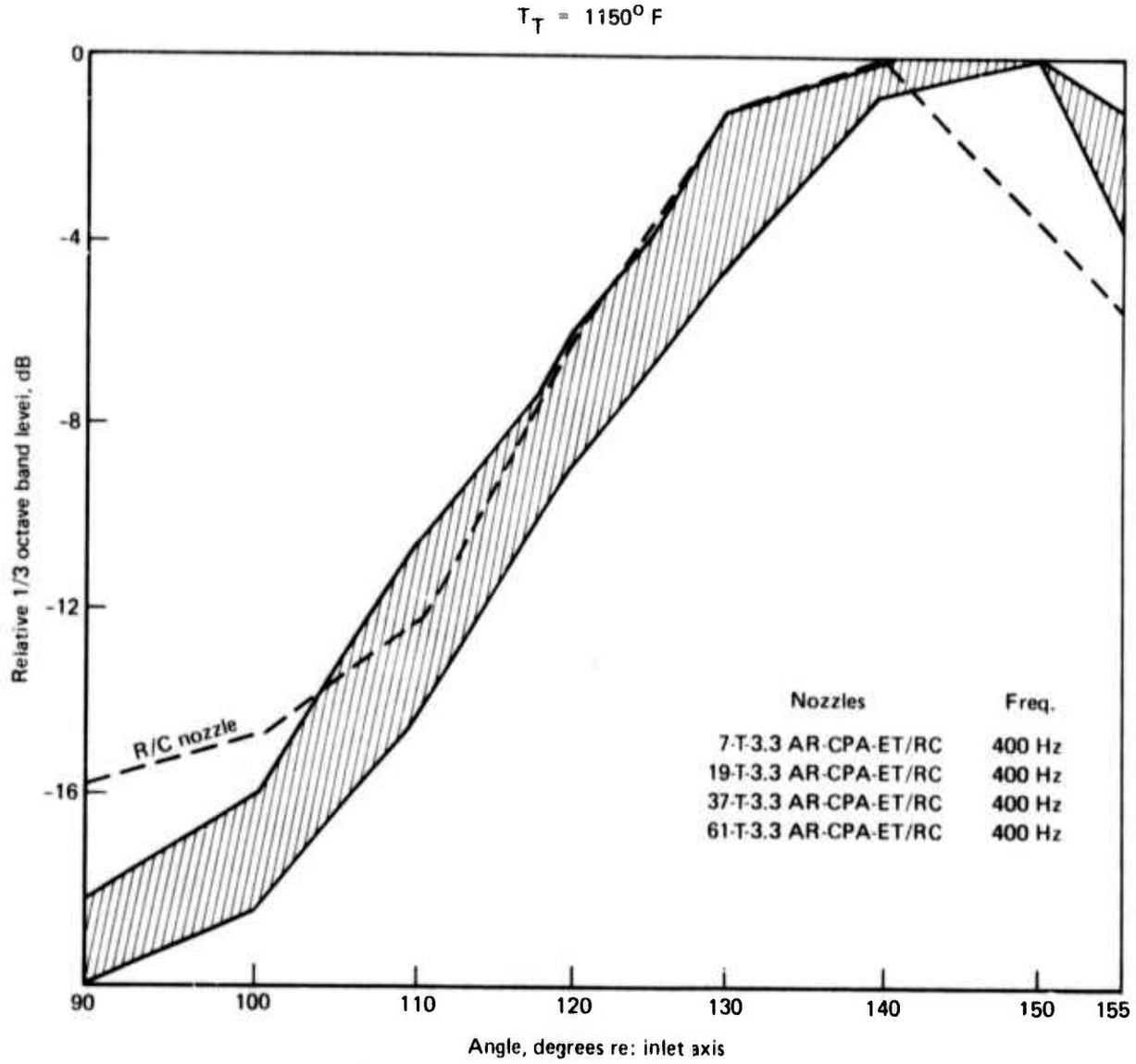

Figure 82. — Multitube Nozzle Postmerged Jet Noise Peak-Frequency Beam Patterns at PR = 4.0

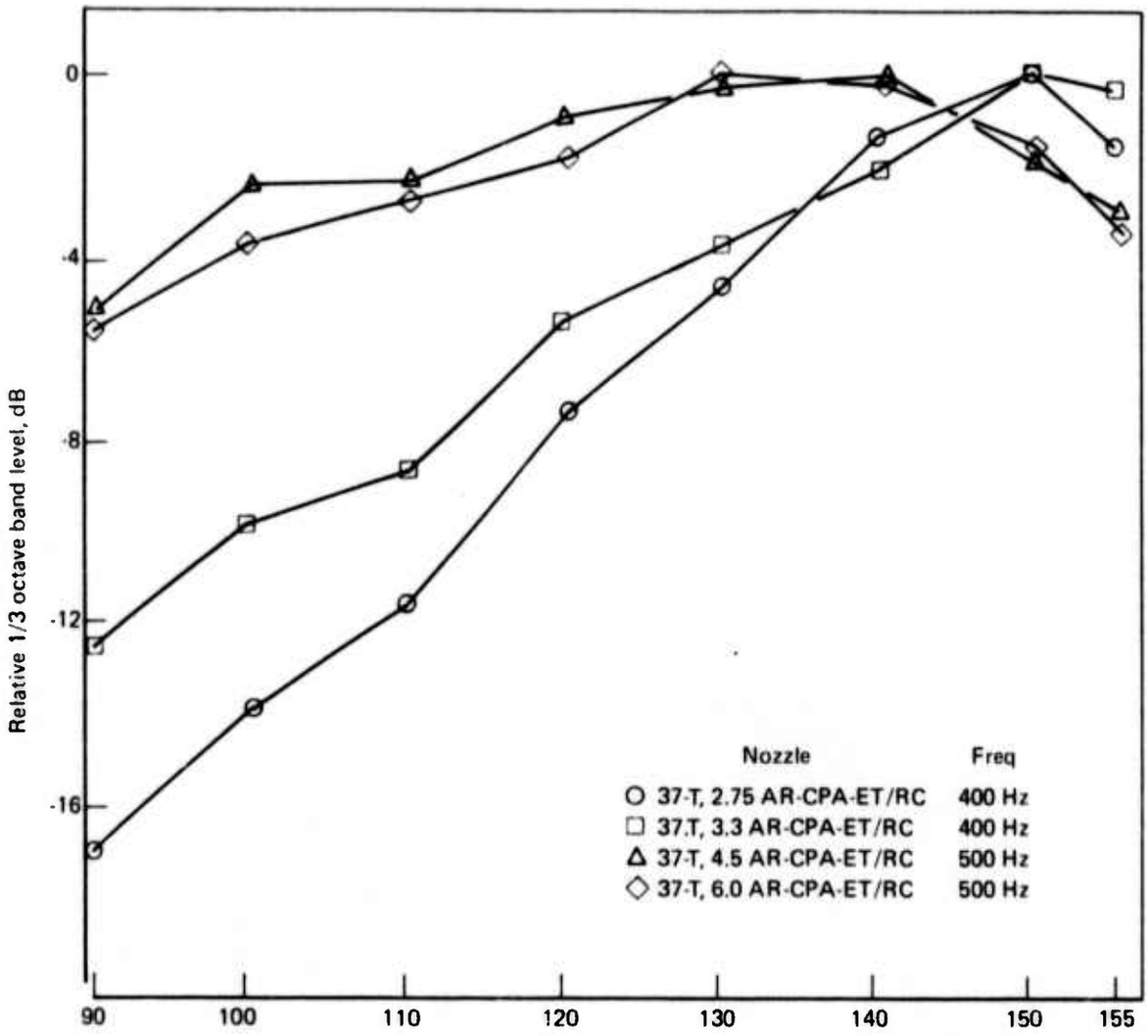

$A_8 = 13.6\ in^2$

Figure 83. — 37-Tube Nozzle Postmerged Jet Noise Peak-Frequency Beam Patterns ($T_T = 1150^o$ F, PR = 2.0)

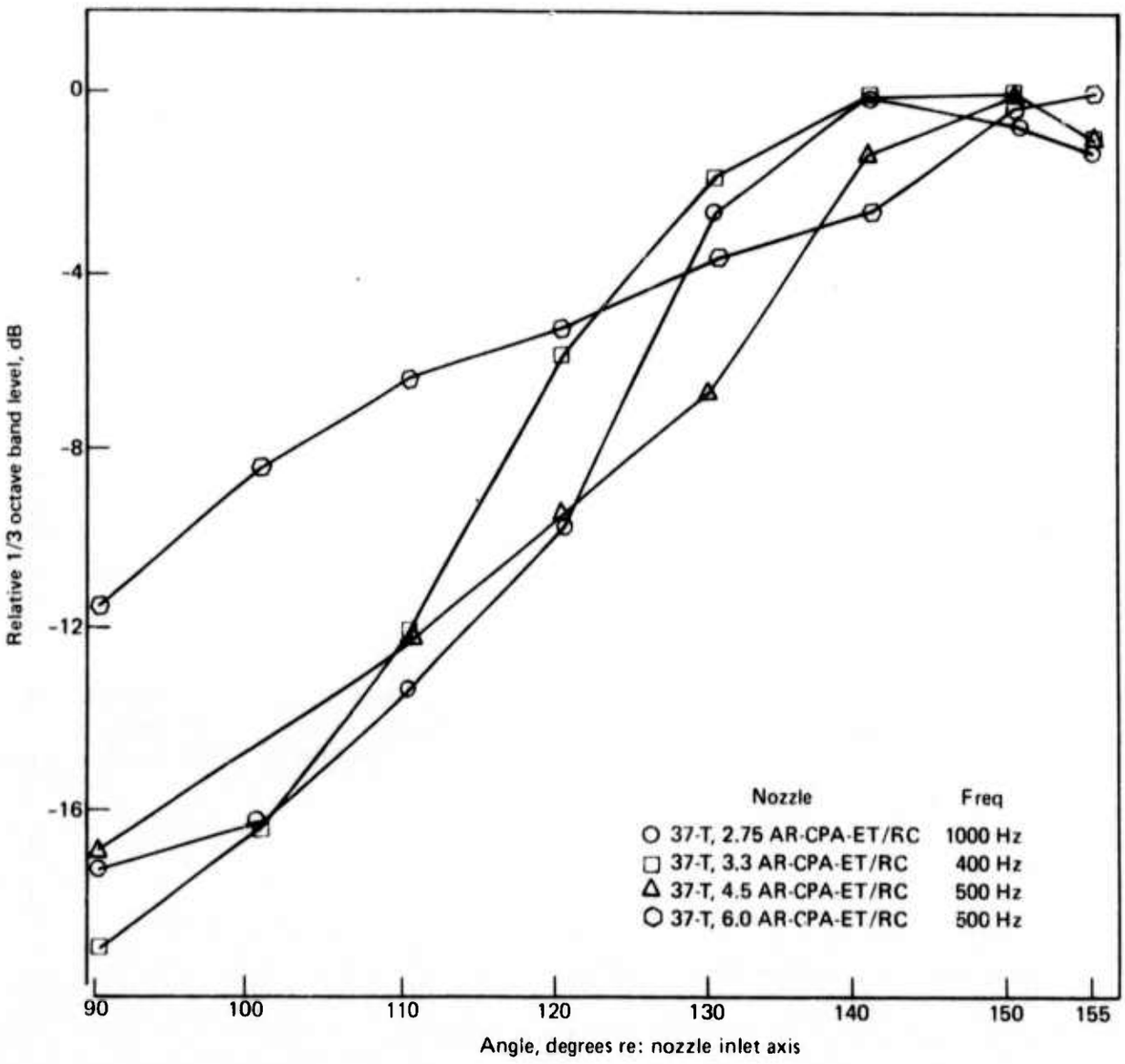

$A_8 = 13.6\ in^2$

Figure 84. — 37-Tube Nozzle Postmerged Jet Noise Peak-Frequency Beam Patterns ($T_T = 1150^o$ F, PR = 4.0)

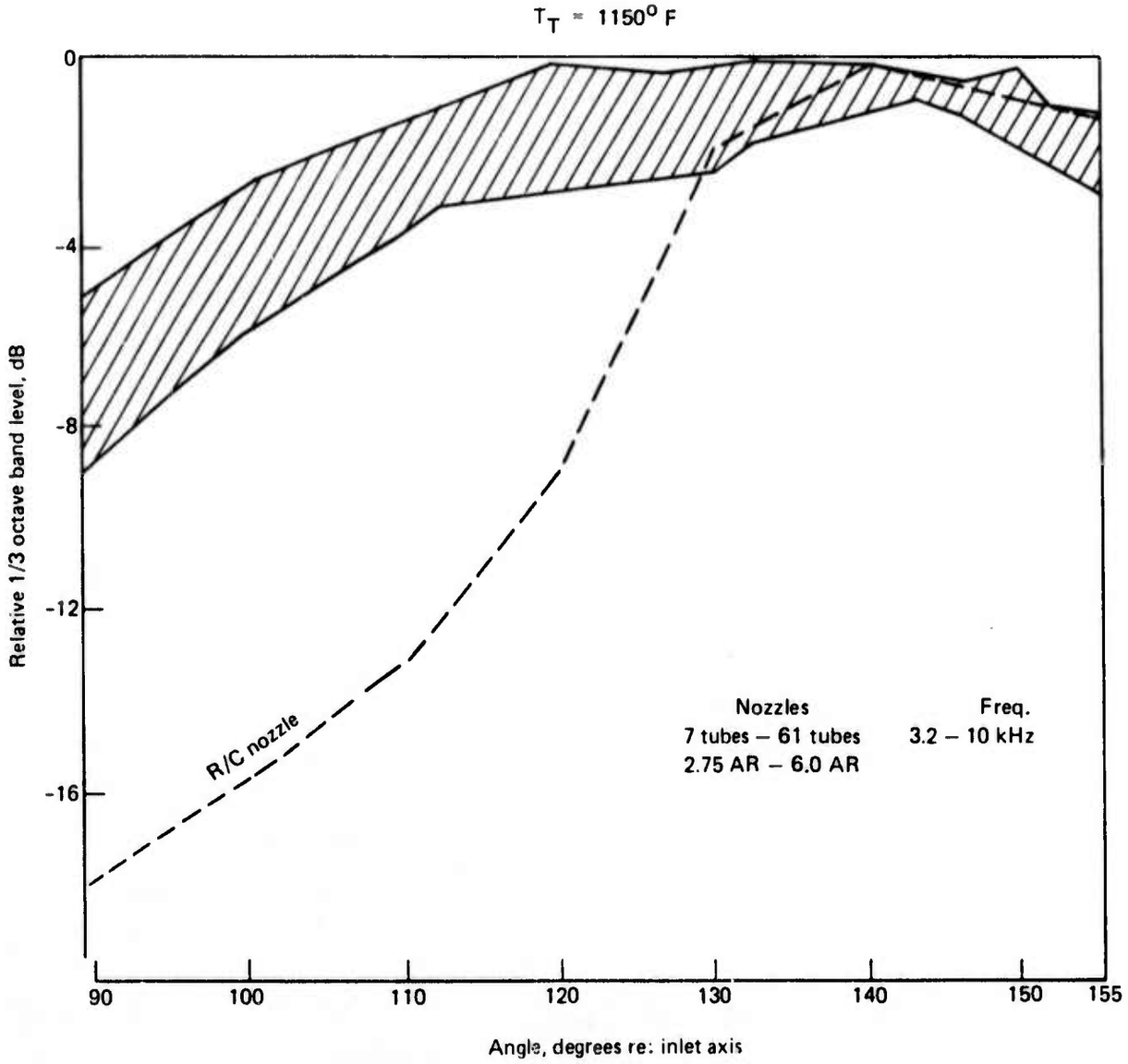

Figure 85. — Multitube Nozzle Premerged Jet Noise Peak-Frequency Beam Patterns at PR = 2.0

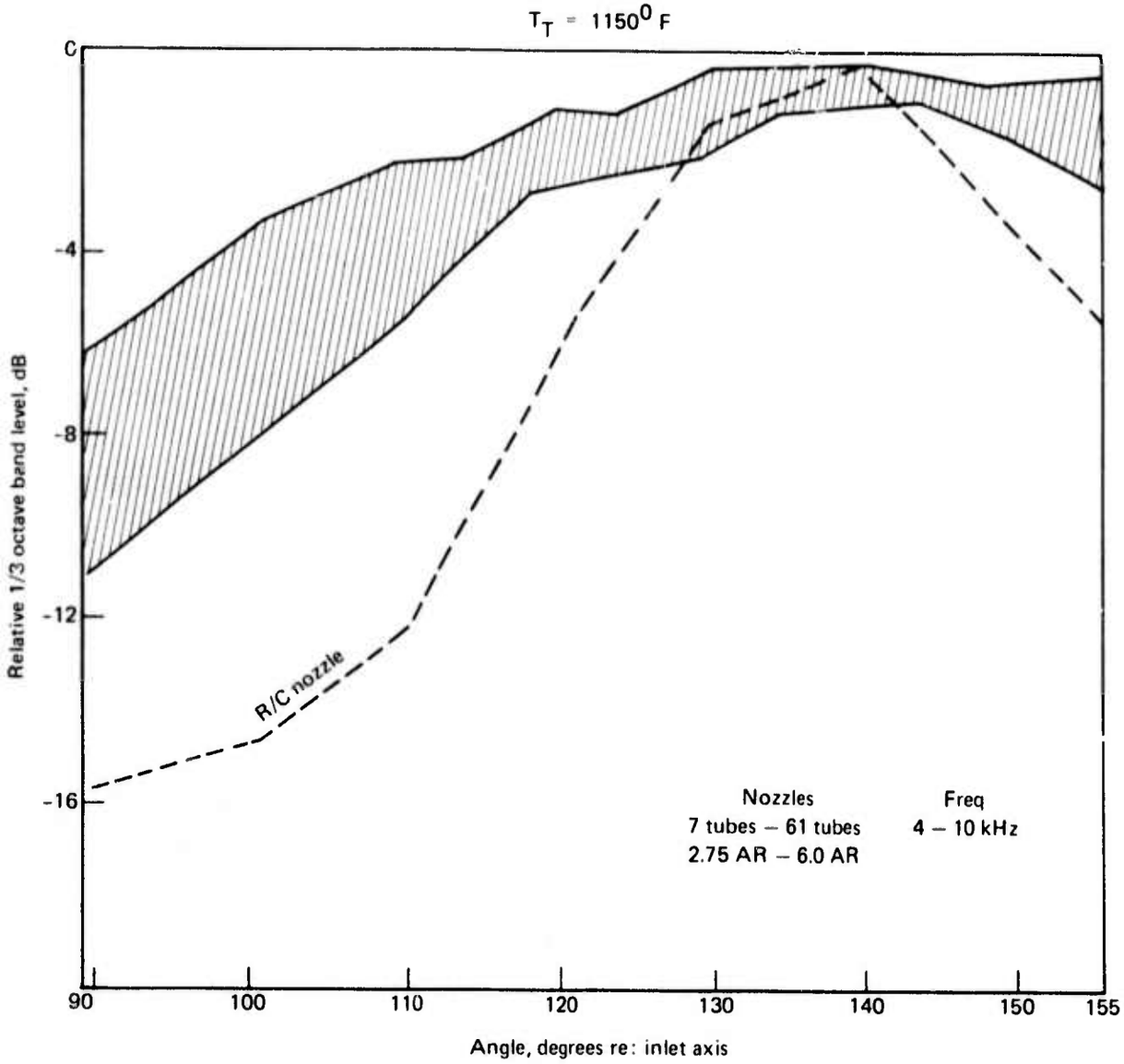

Figure 86. — Multitube Nozzle Premerged Jet Noise Peak-Frequency Beam Patterns at PR = 4.0

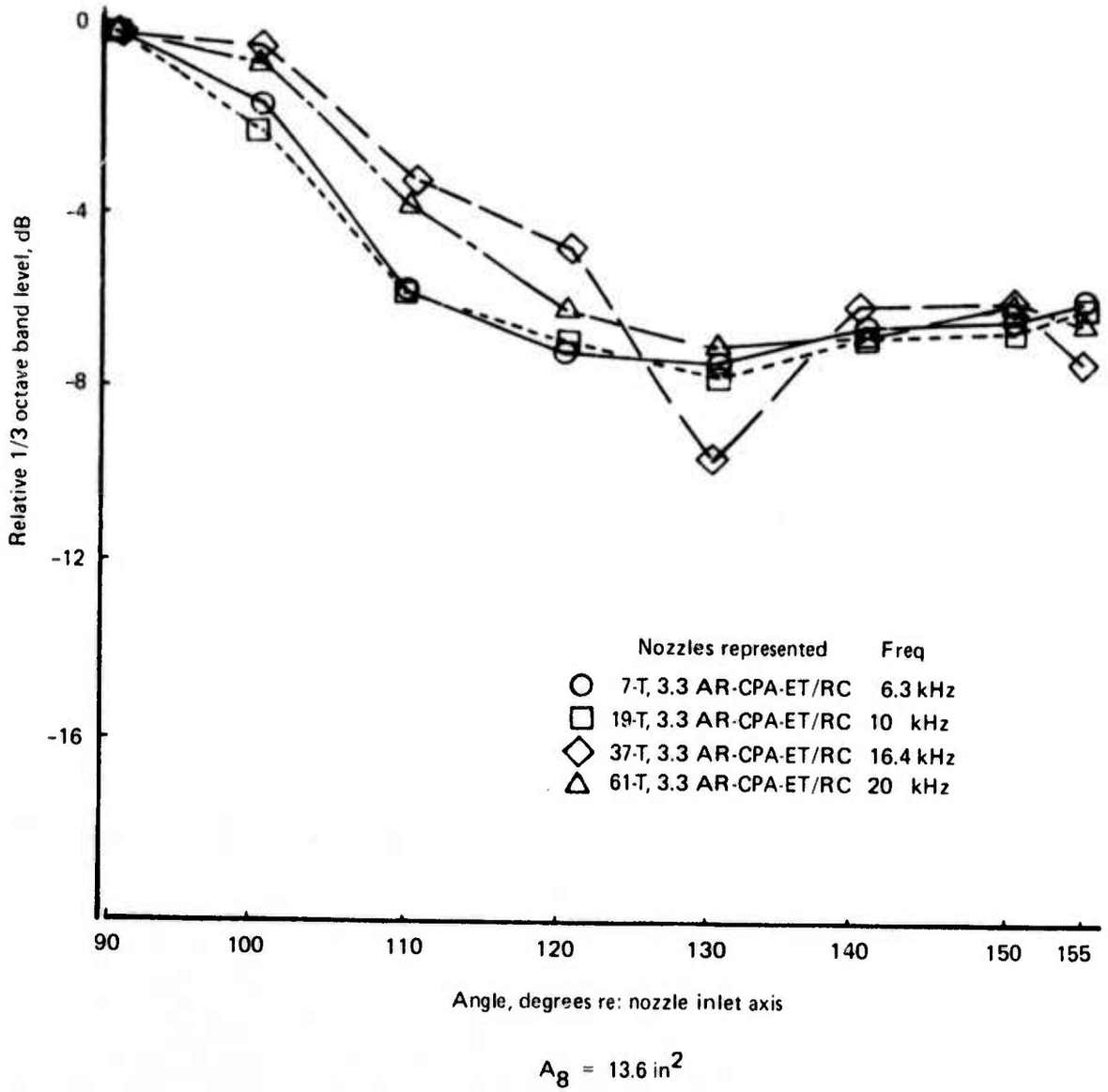

Figure 87. — Multitube Nozzle Spiral-Mode Flow-Instability Jet Noise Peak-Frequency Beam Patterns ($T_T = 60^0$ F, PR = 4.0)

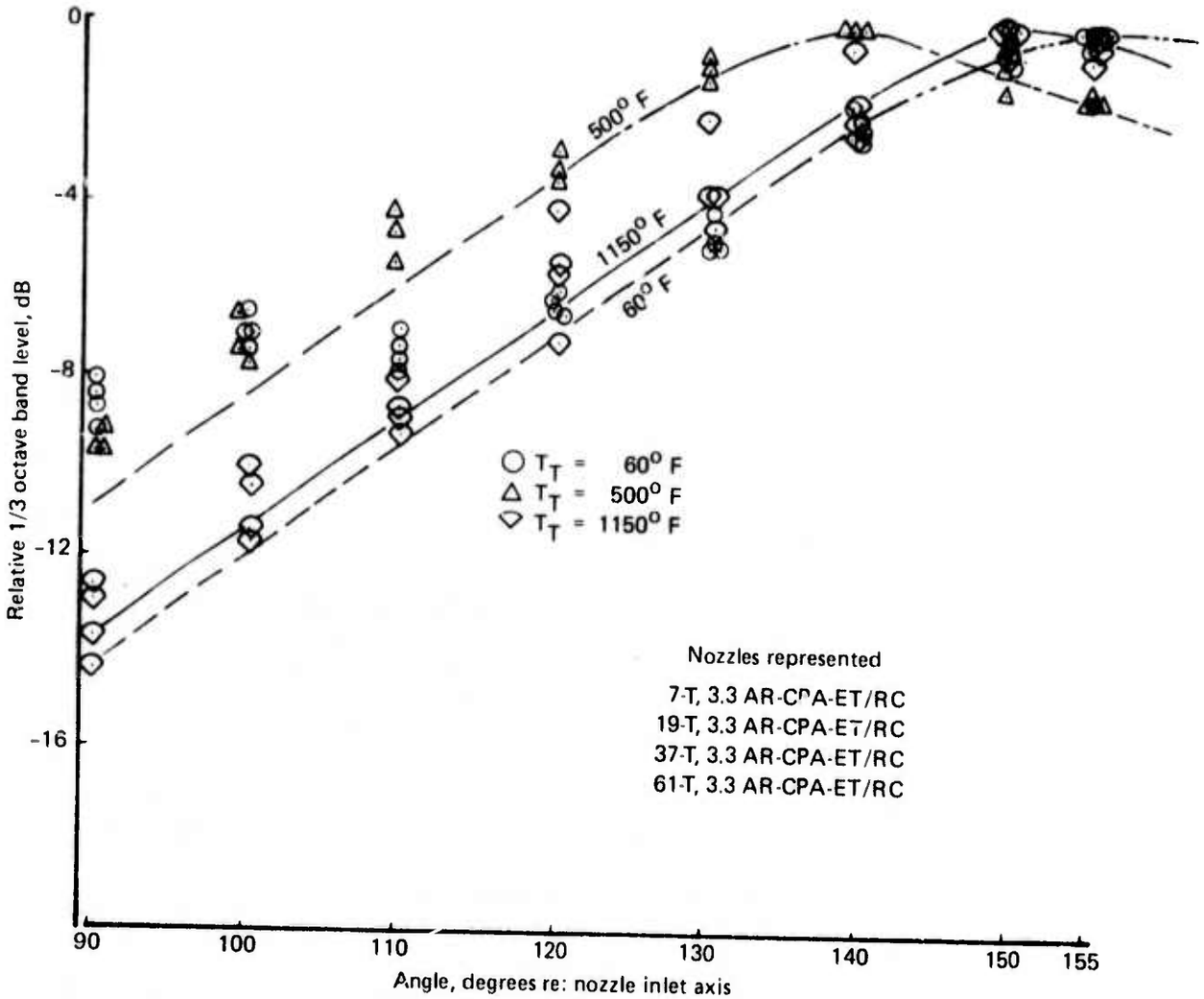

Figure 88. — 3.3 AR Multitube Nozzles Postmerged Jet Noise Peak-Frequency Beam Patterns (PR = 2.0)

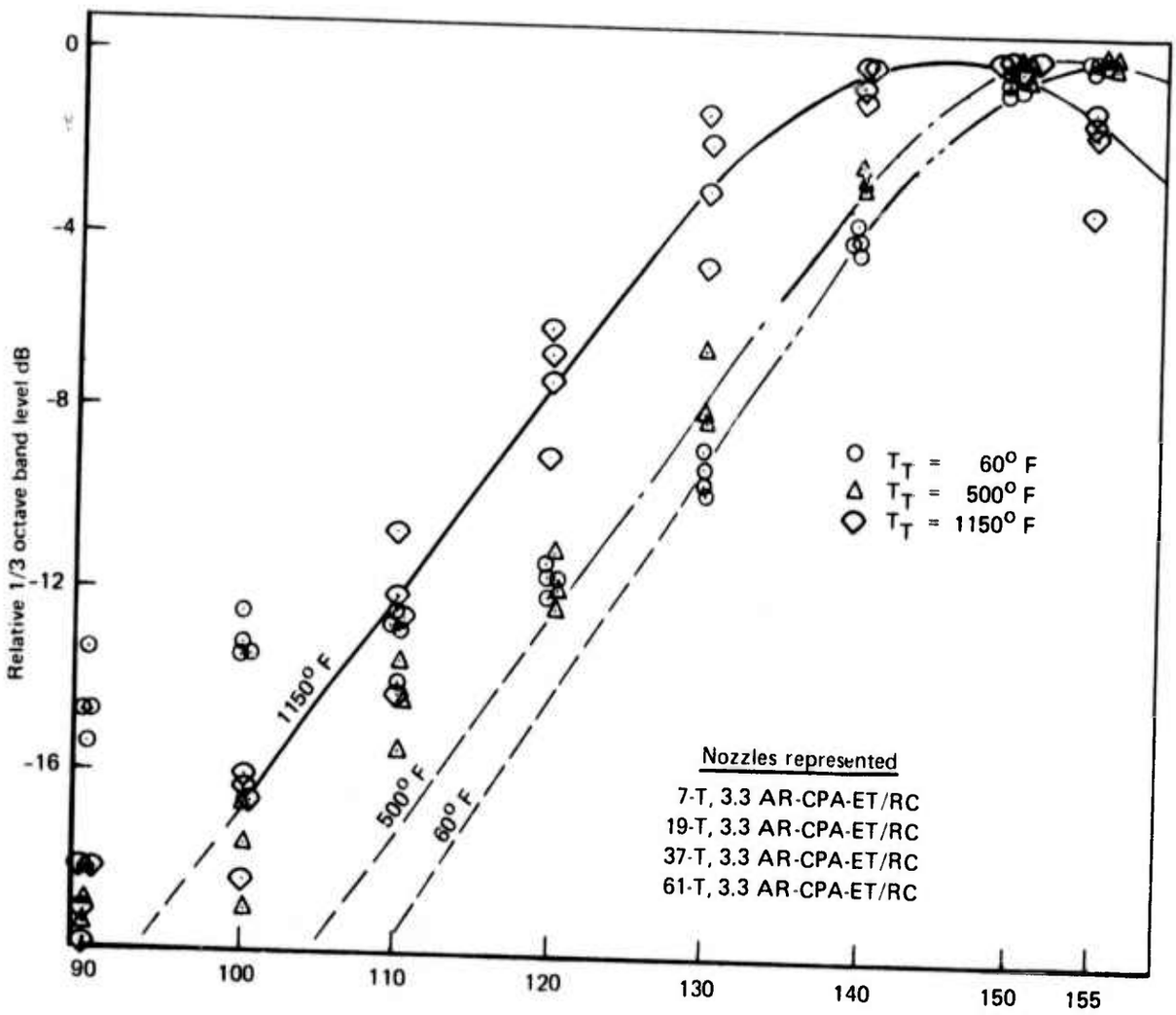

$A_8 = 13.6\ in^2$

Figure 89. — 3.3 AR Multitube Nozzles Postmerged Jet Noise Peak-Frequency Beam Patterns (PR = 4.0)

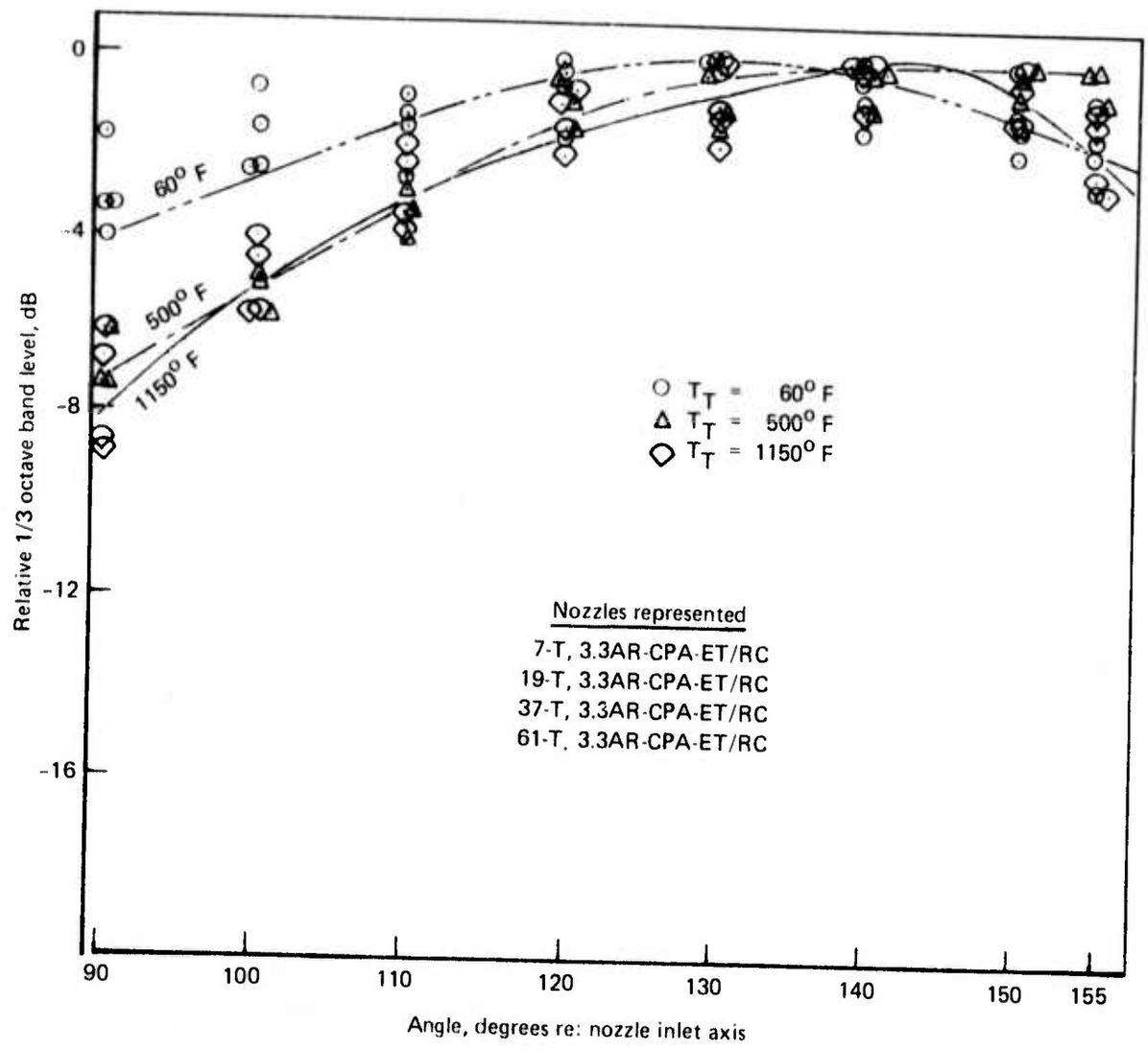

$A_8 = 13.6\ in^2$

Figure 90. — 3.3 Area Ratio Multitube Nozzles Premerged Jet Noise Peak-Frequency Beam Patterns (PR = 2.0)

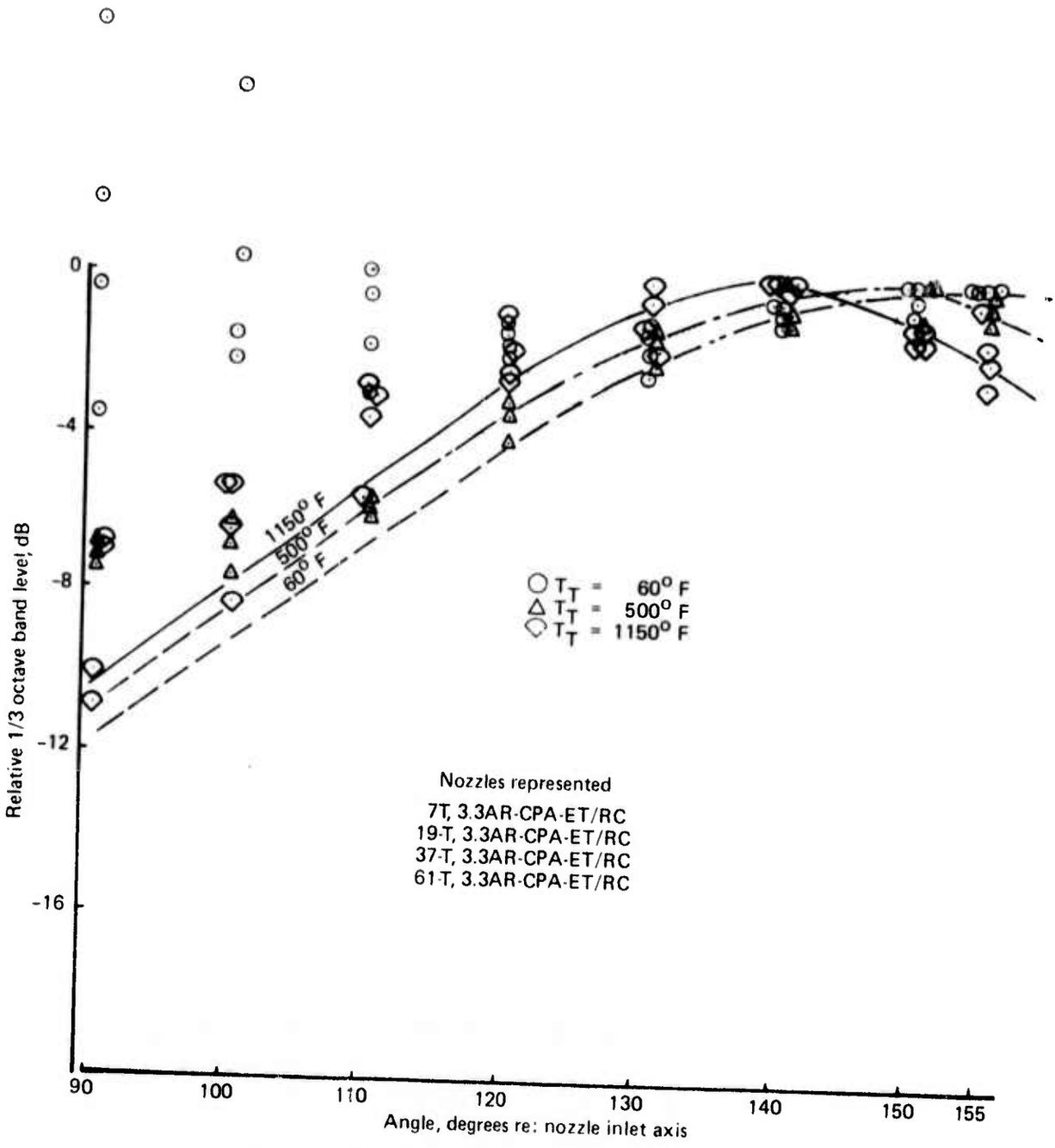

A_8 = 13.6 in^2

Figure 91. — 3.3 AR Multitube Nozzle Premerged Jet Noise Peak-Frequency Beam Patterns (PR = 4.0)

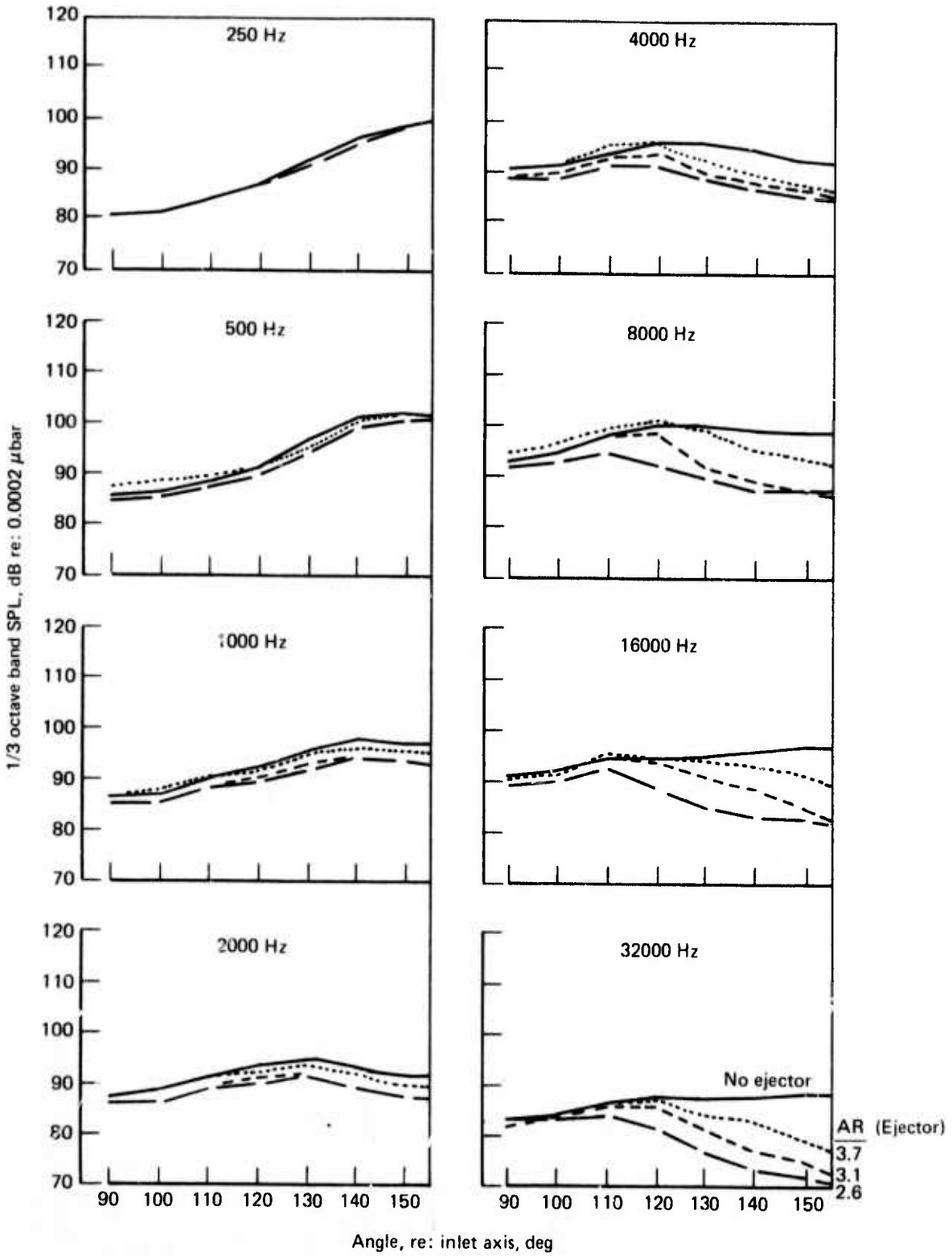

Figure 92. -- 31-Tube Nozzle With Ejectors at PR = 2.0, T_T = 1150° F

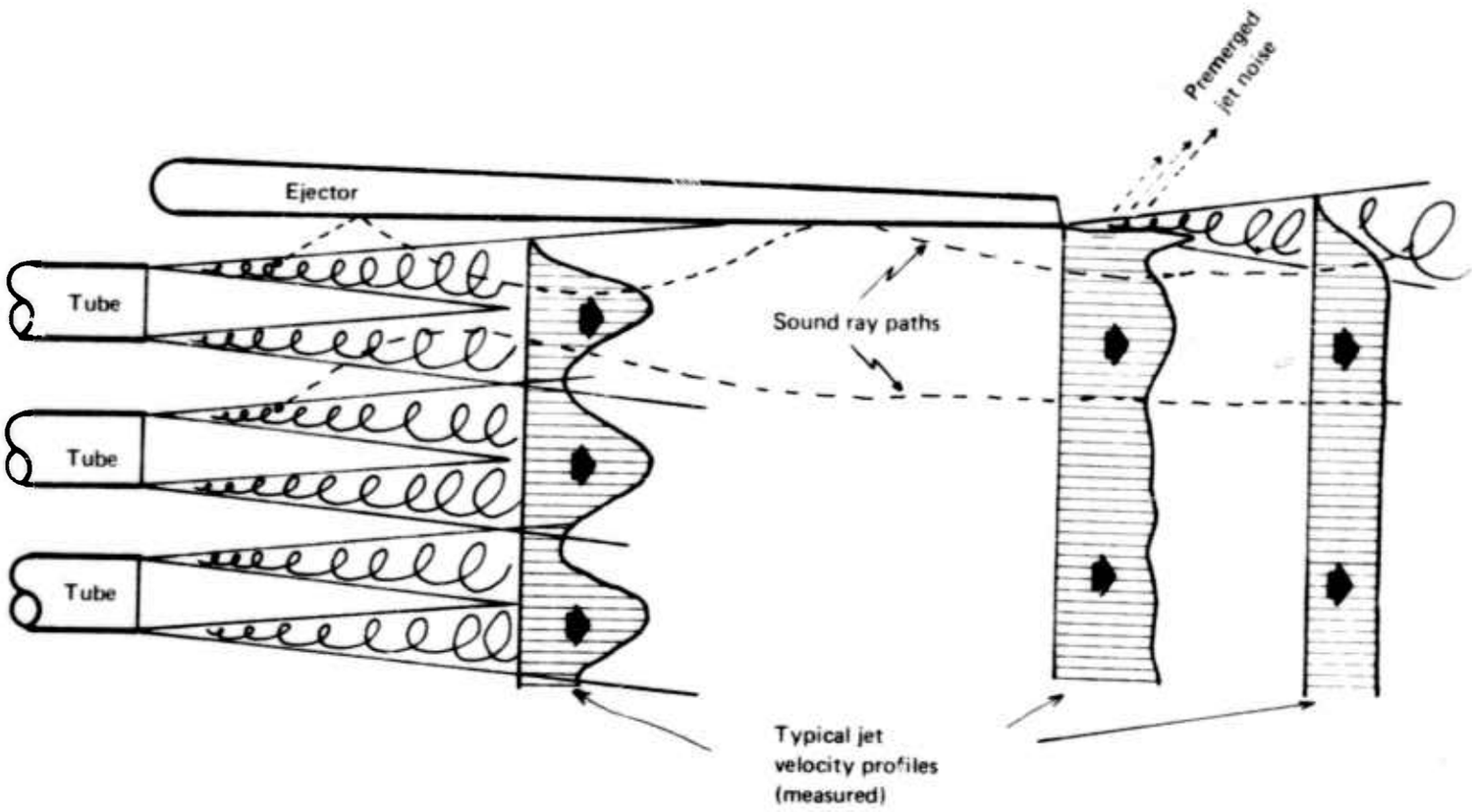

Figure 93. — Schematic of Possible Jet Noise Ray Paths for a Multitube Nozzle With Tight-Fitting Ejector

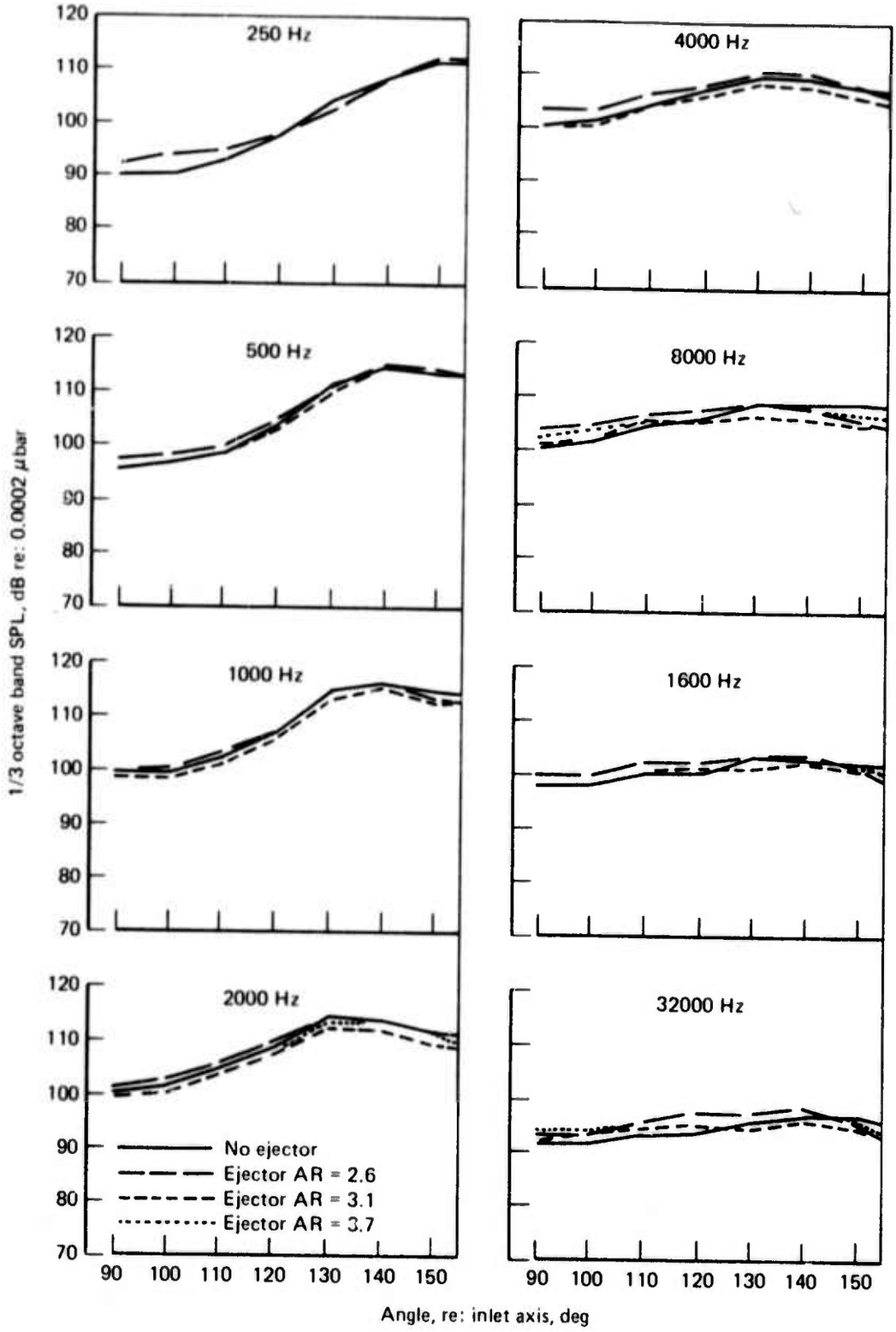

Figure 94. — 31-Tube Nozzle With Ejectors at PR = 4.0, T_T = 1150° F

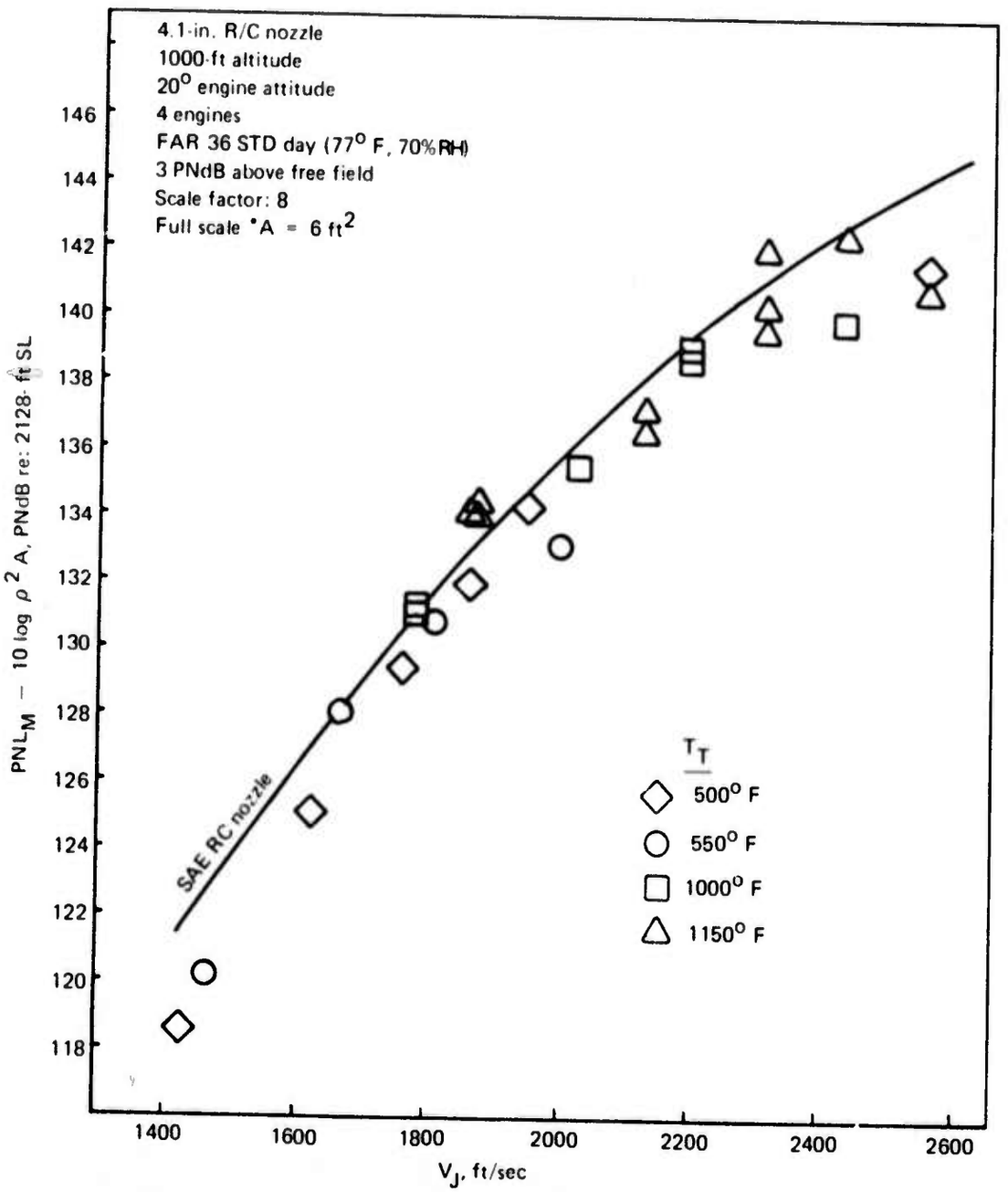

Figure 95. — Baseline Nozzle "Normalized" Peak Perceived Noise Levels

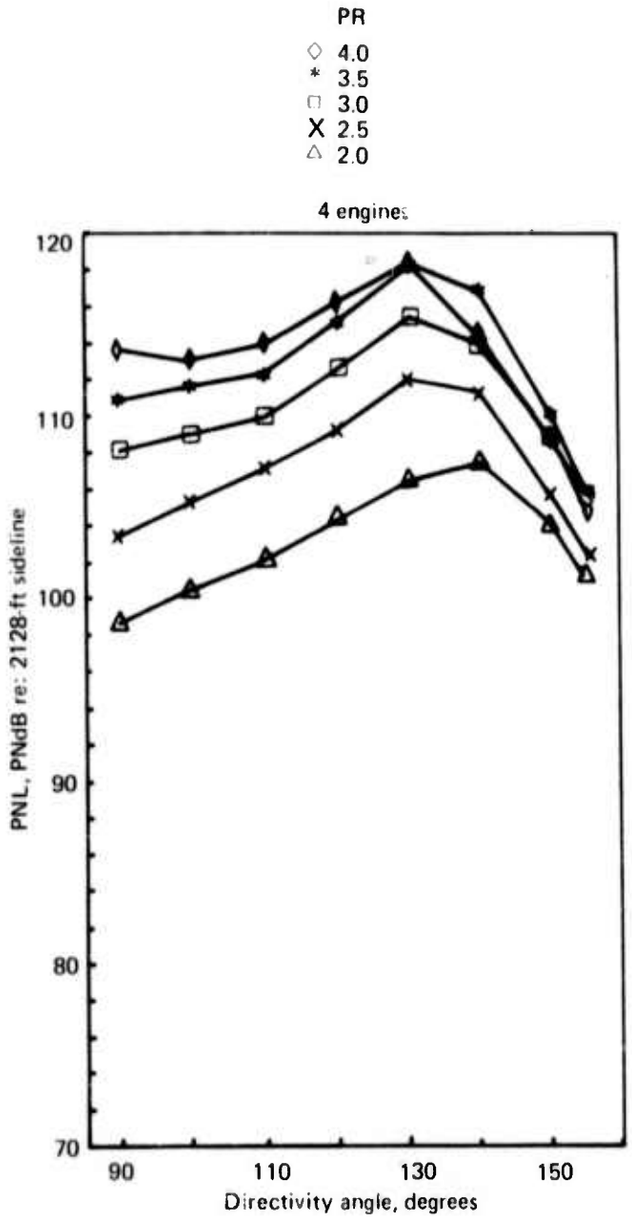

$T_T = 1150^{o}$ F

Figure 96. — R/C Nozzle PNL Beam Patterns

37-TUBES, AR 3.3 CLOSE-PACKED ARRANGEMENT
(ROUND TUBES - CONVERGENT ENDS)

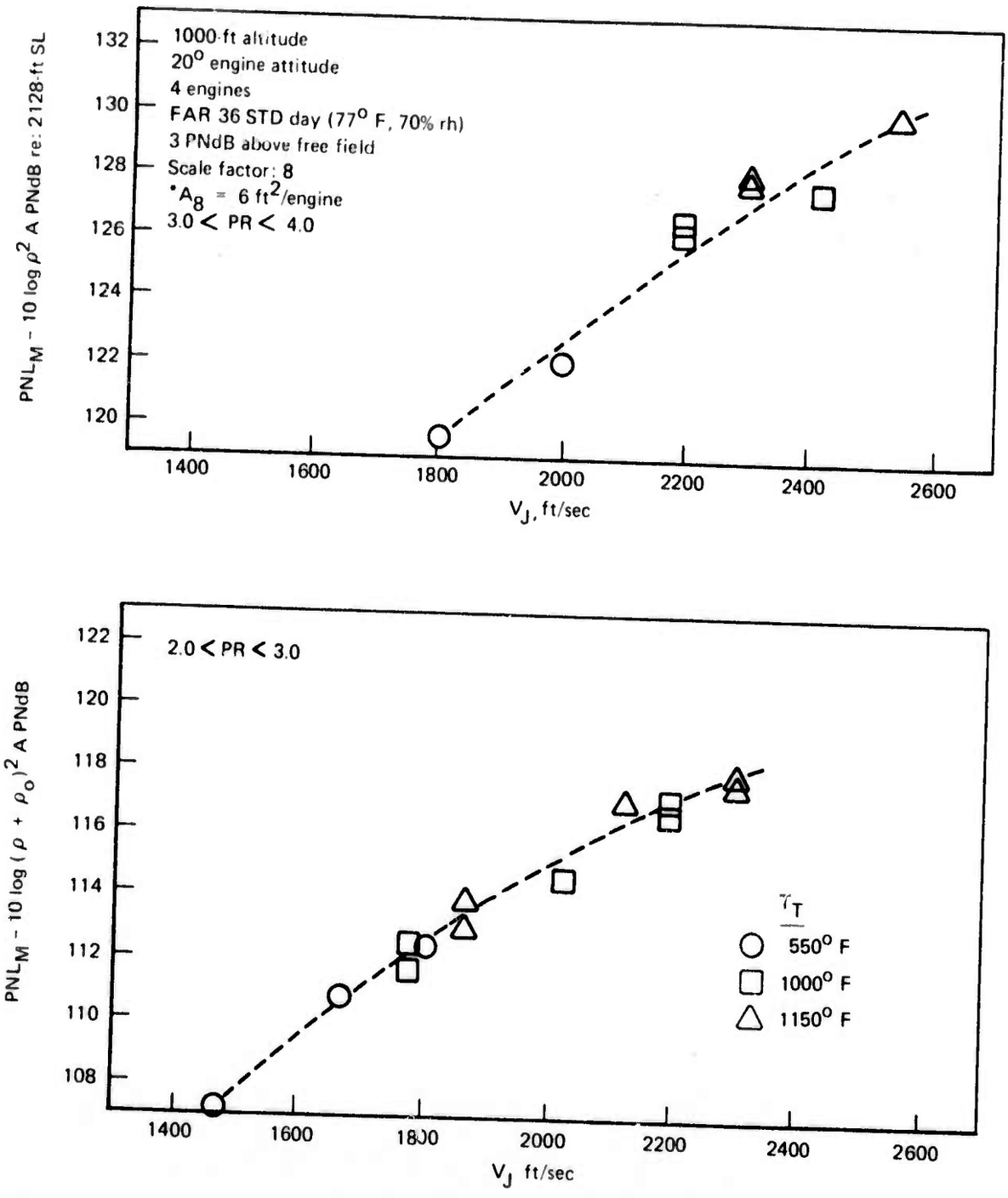

Figure 97. — 37-tube, AR 3.3 Nozzle "Normalized" PNL

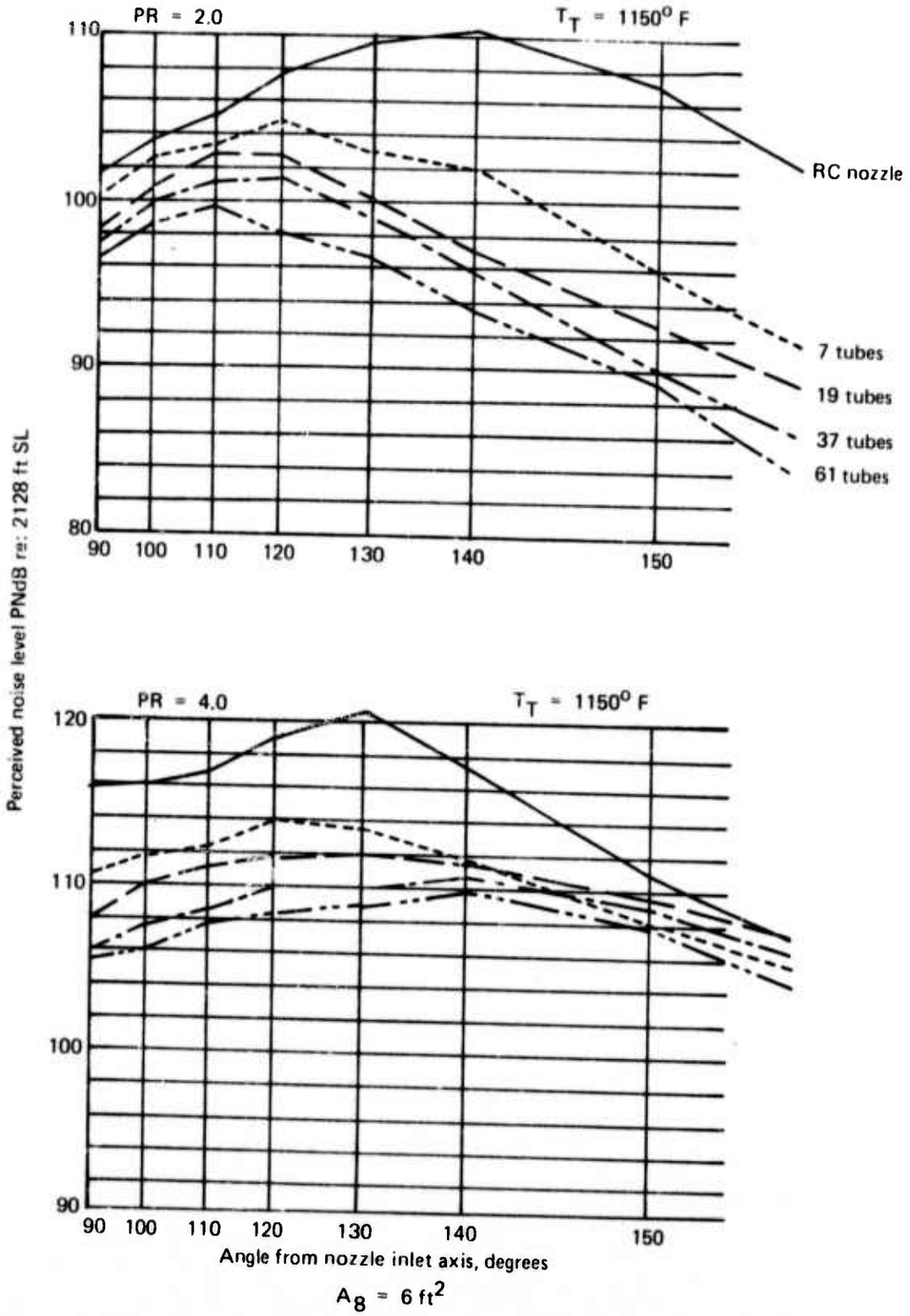

Figure 98. — 3.3 AR Multitube Nozzles PNL Linear Beam Patterns

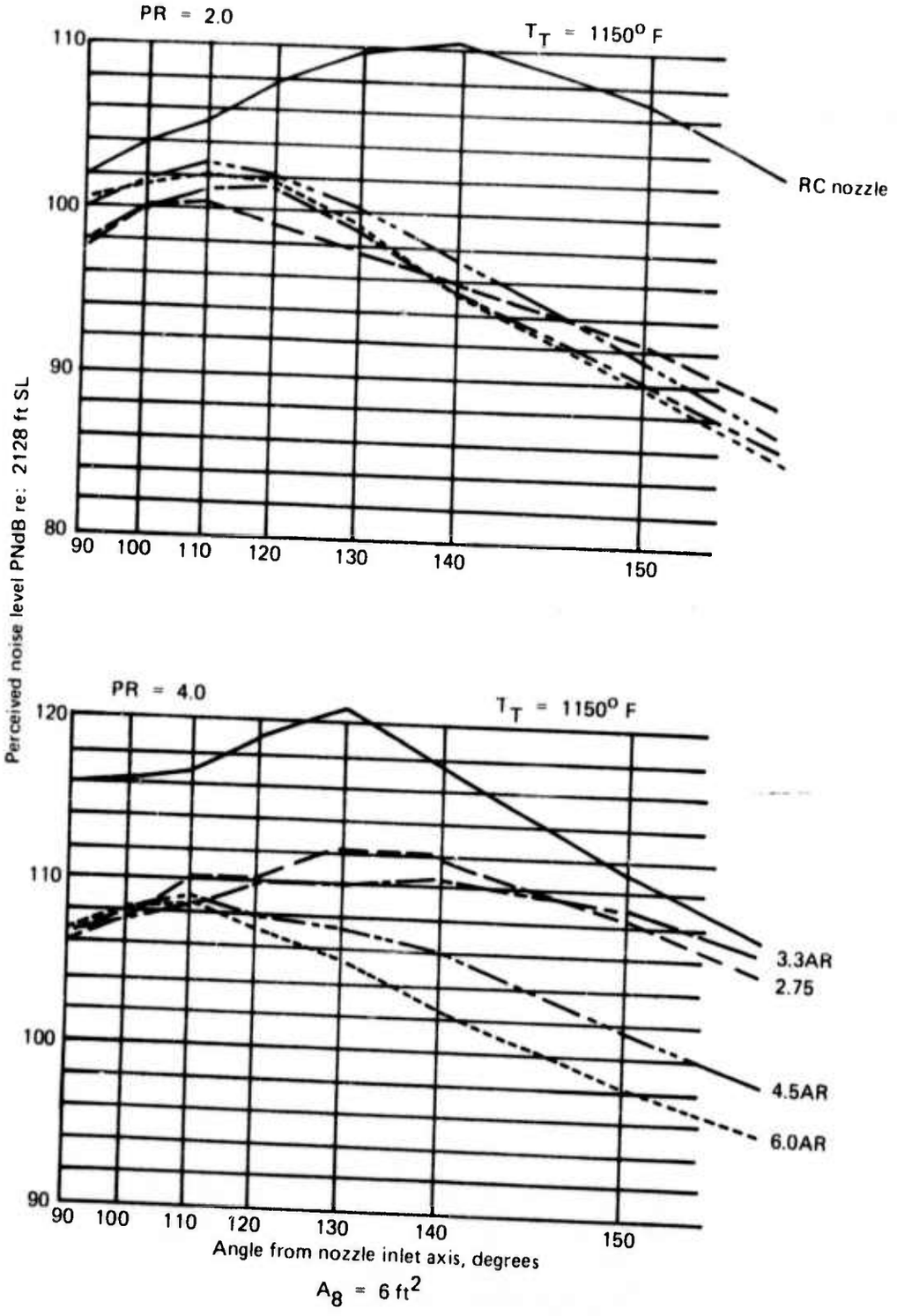

Figure 99. — 37-Tube Nozzles PNL Linear Beam Patterns

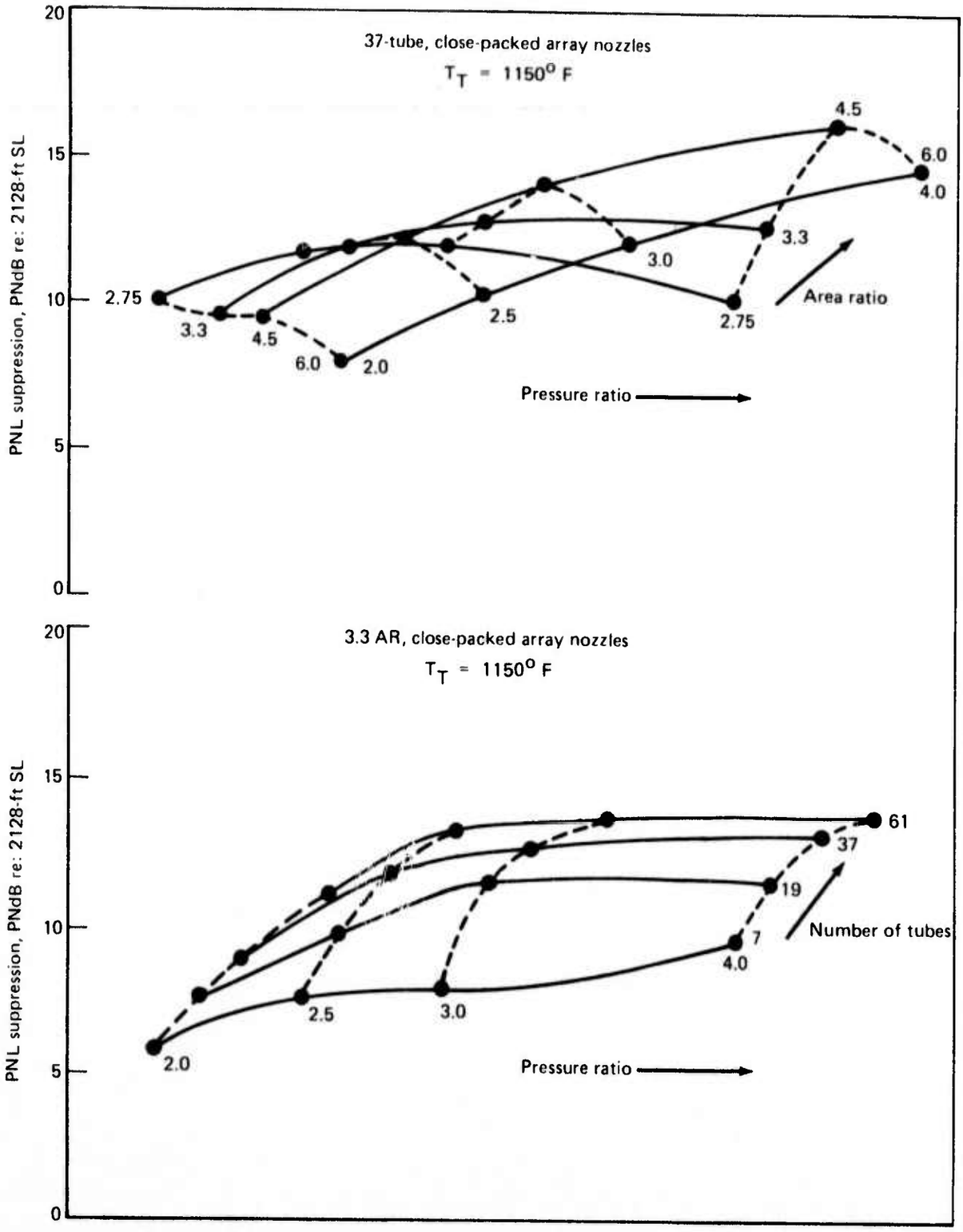

Figure 100. — A Summary of Multitube Nozzle PNL Suppression as a Function of Tube Number and Area Ratio

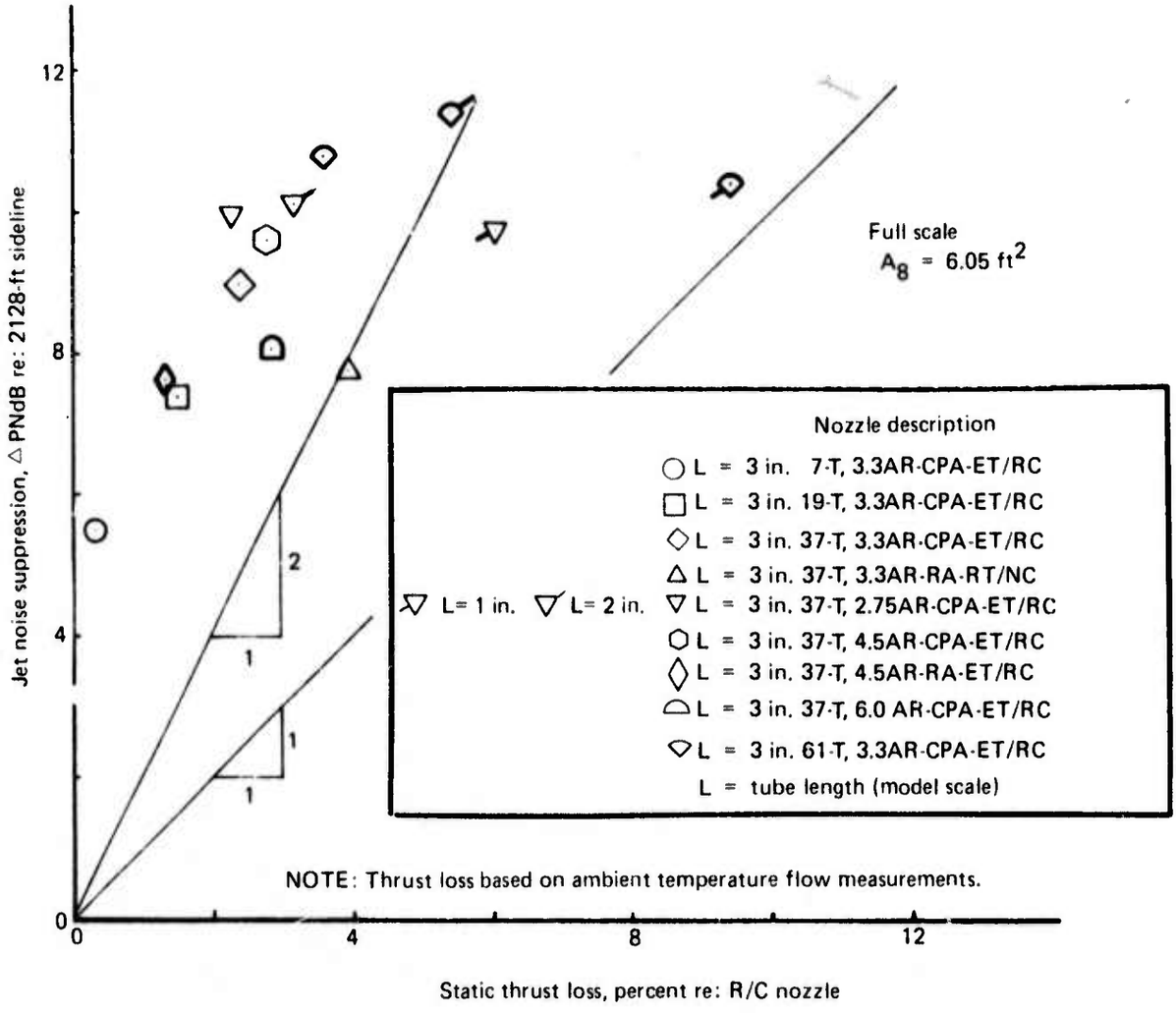

Figure 101. — Multitube Nozzle Acoustic Noise Suppression/Thrust Loss Relationship at (T_T = 1150^o F, PR = 2.0, V_J = 1875 ft/sec)

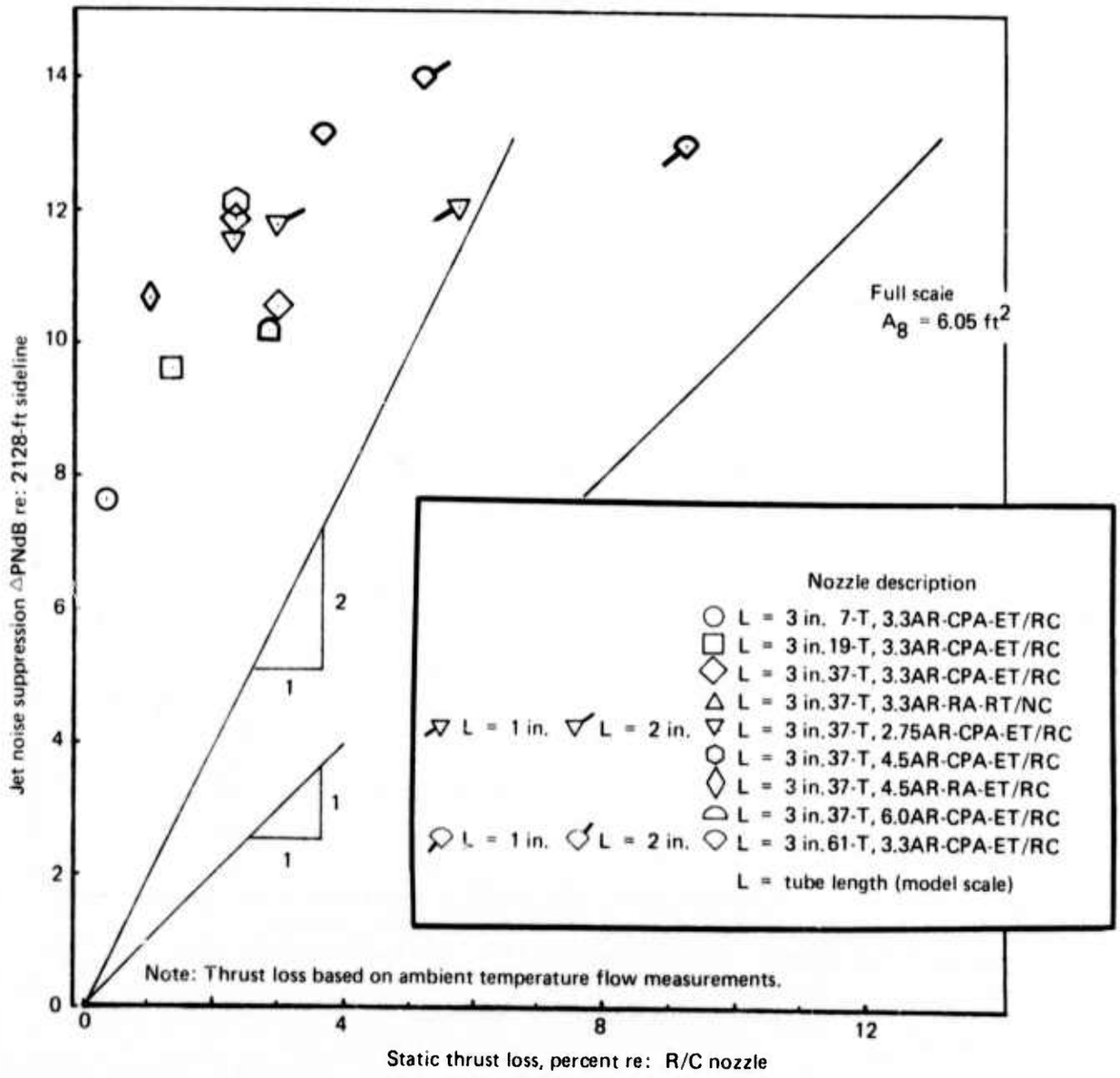

Figure 102. — Multitube Nozzle Acoustic Noise Suppression/Thrust Loss Relationship at (T_T = 1150^0 F, PR = 2.5, V_J = 2126 ft/sec)

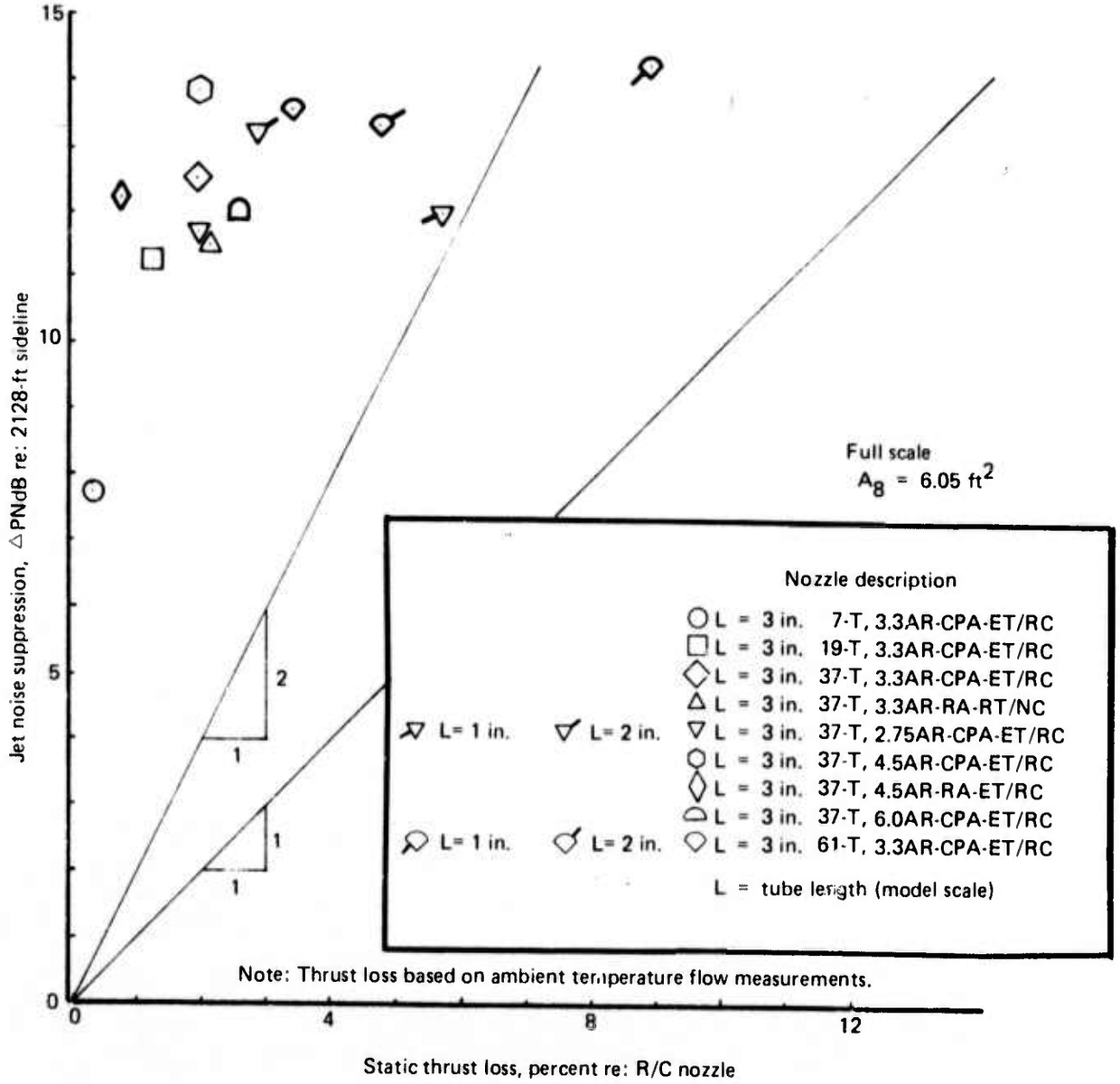

Figure 103. — Multitube Nozzle Acoustic Noise Suppression/Thrust Loss Relationship at (T_T = 1150^0 F, PR = 3.0, V_j = 2303 ft/sec)

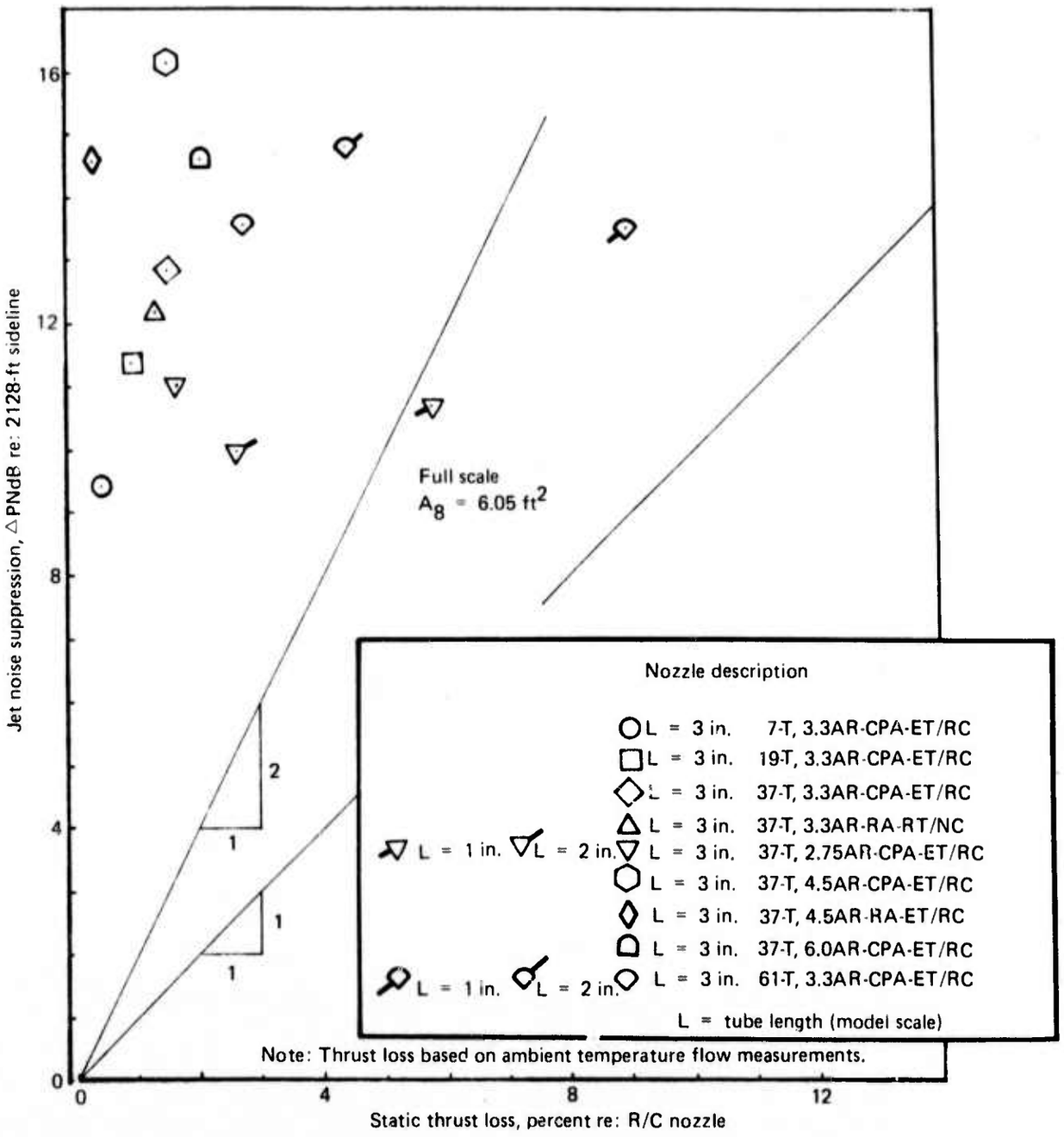

Figure 104. — Multitube Nozzle Acoustic Noise Suppression/Thrust Loss Relationship at (T_T = 1150^0 F, PR = 4.0, V_J = 2544 ft/sec)

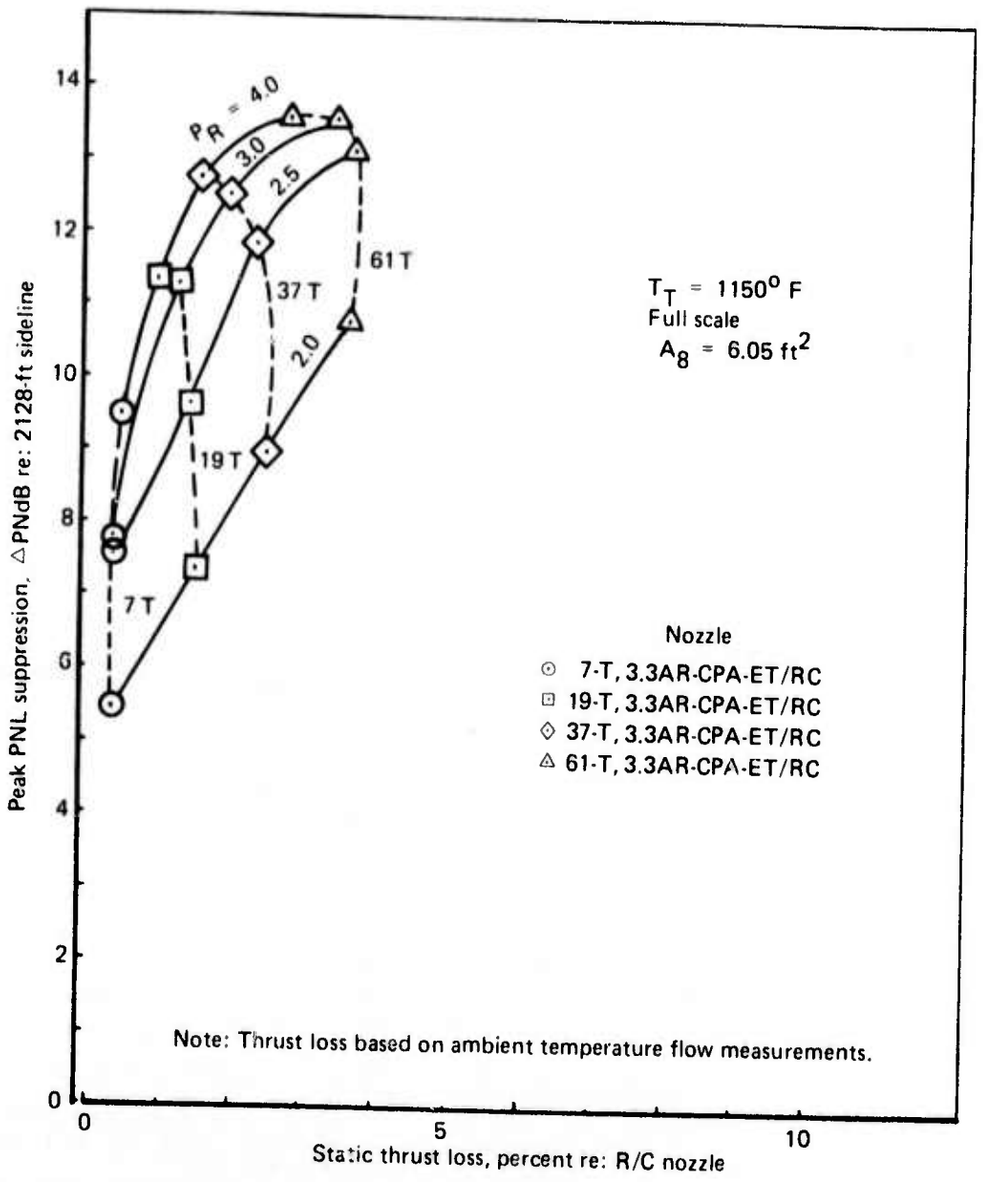

Figure 105. — 3.3 Area Ratio Multitube Nozzles Jet Noise Suppression/Thrust Loss Characteristics

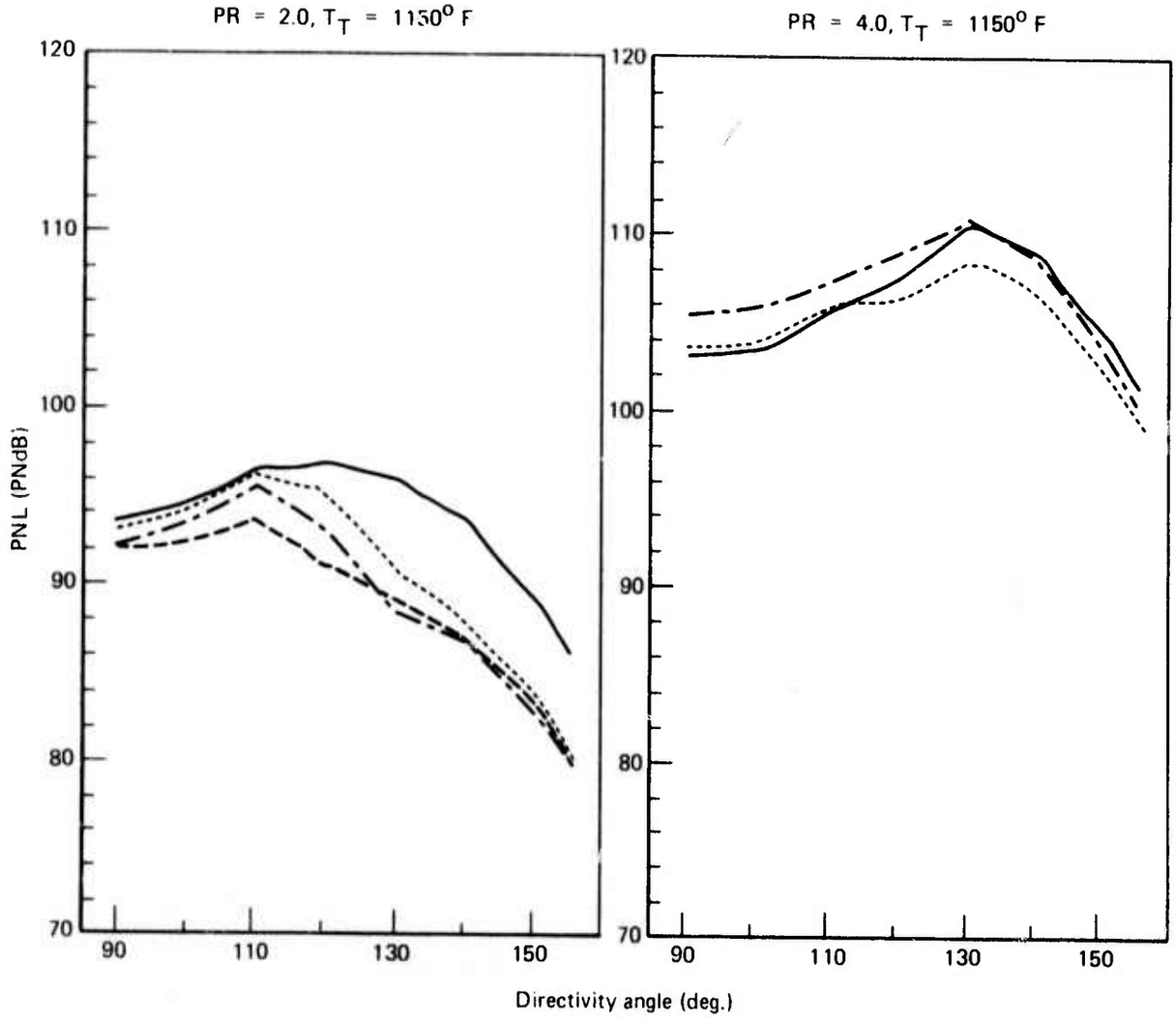

Figure 106. — 31-Tube, 2.75 AR Nozzle With Hardwall Ejectors, 2128-ft Sideline PNL Beam Patterns

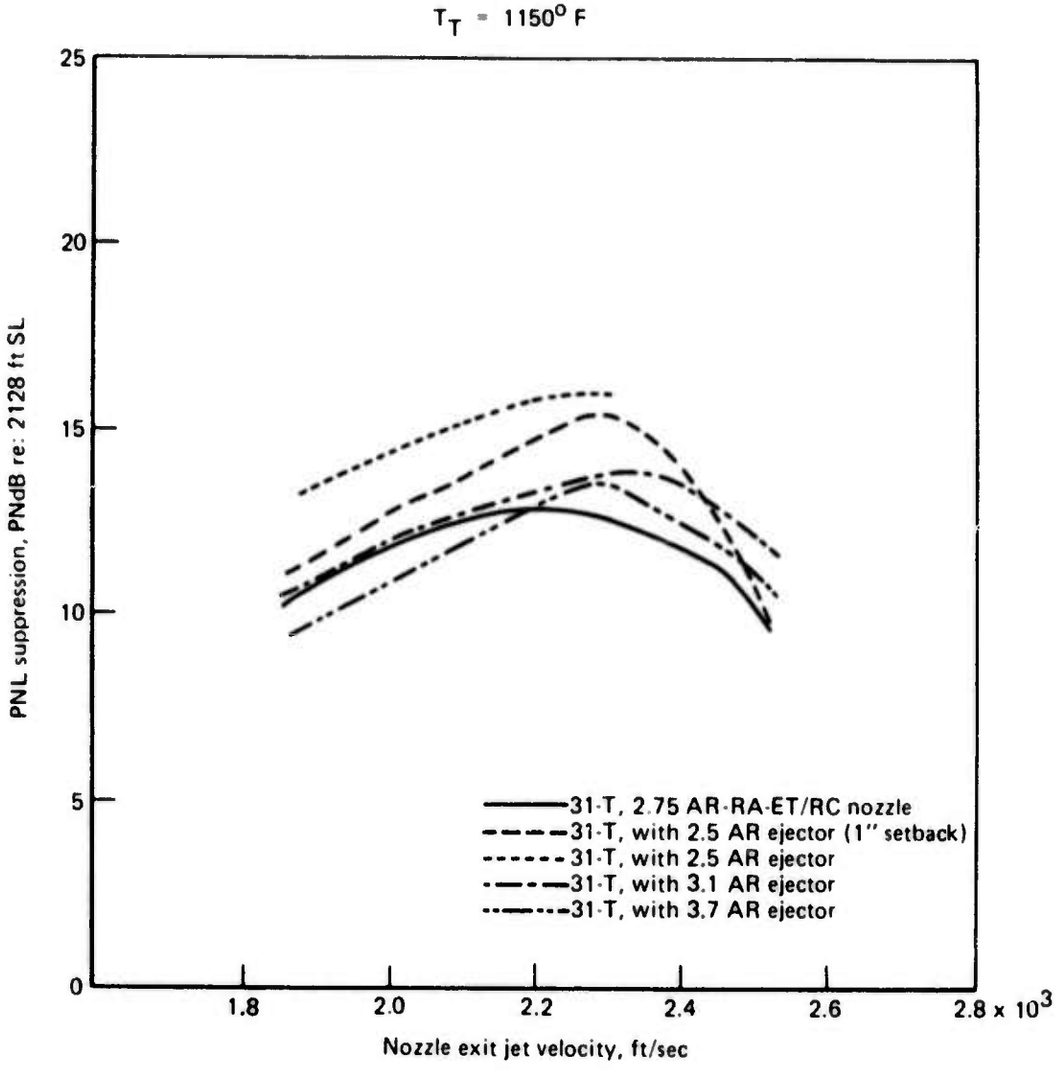

Figure 107. — 31-Tube, 2.75 AR (RA) Nozzle PNL Suppression With and Without Hardwall Ejectors

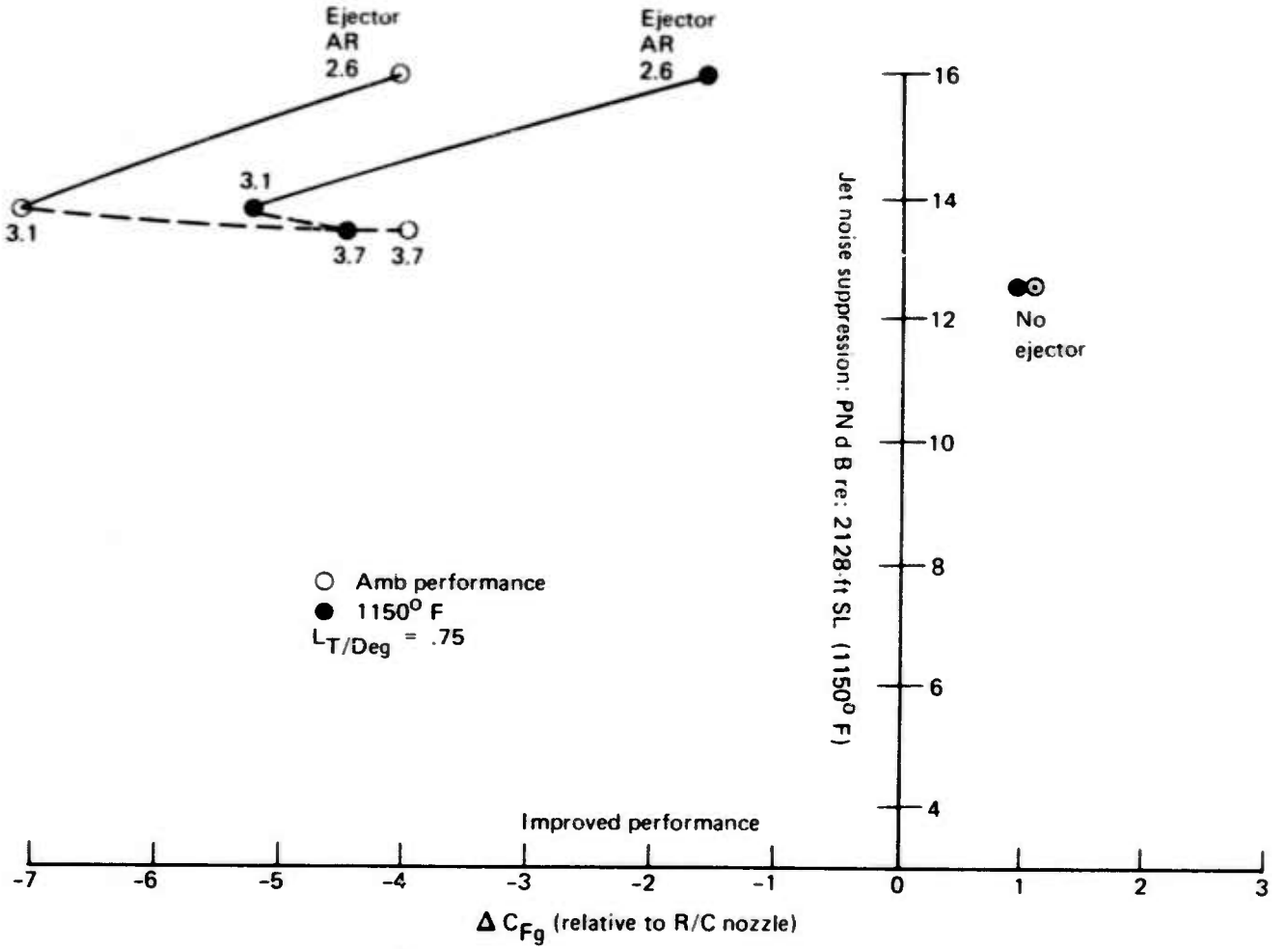

Figure 108. — Multitube Nozzle/Ejector Noise Suppression Versus Thrust Loss Relationships

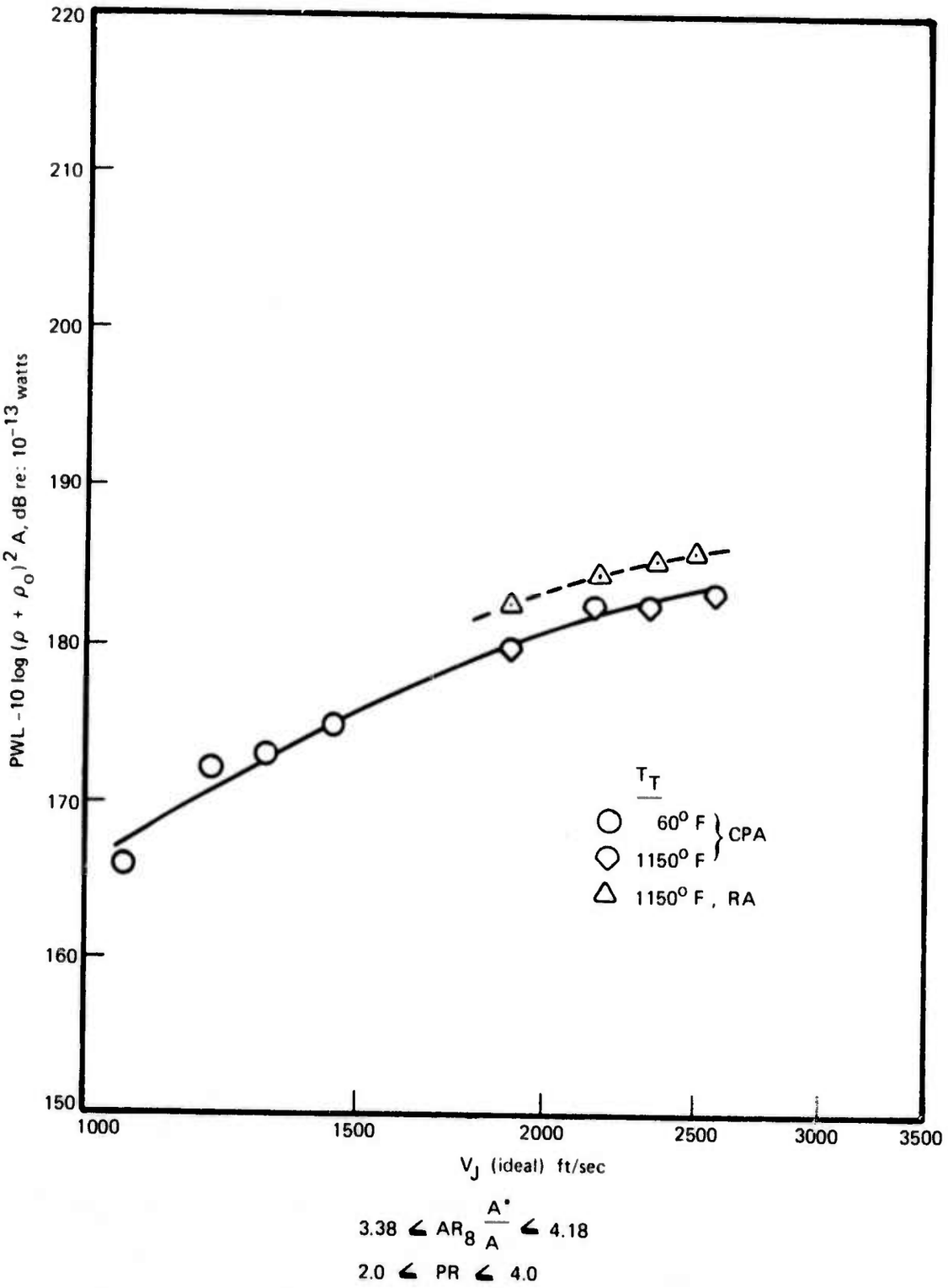

Figure 109. — 37-Tube, 4.5 Area Ratio Nozzle, Premerged Jet Turbulence Noise

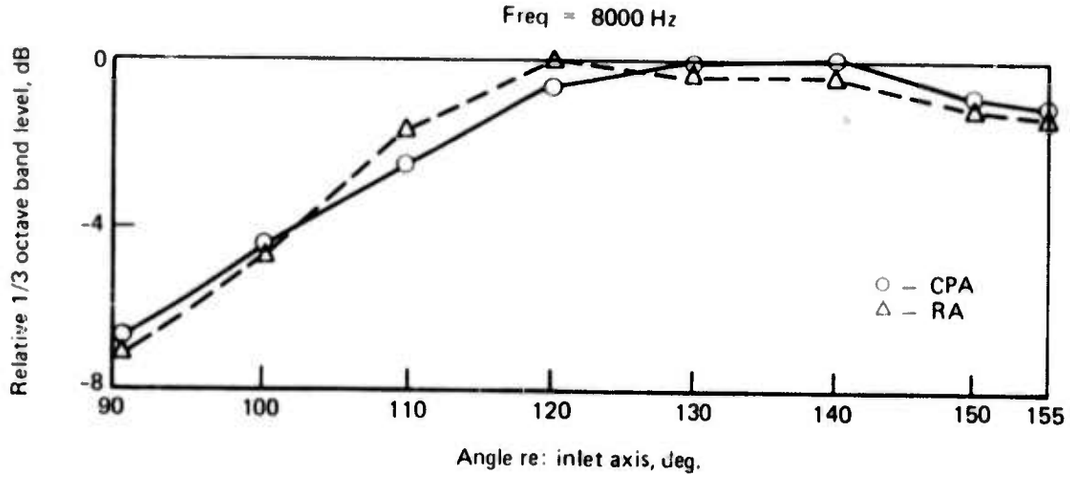

Figure 110. — 37-Tube Nozzle Premerged Jet Noise Peak-Beam Patterns (T_T = 1150° F, PR = 2.0)

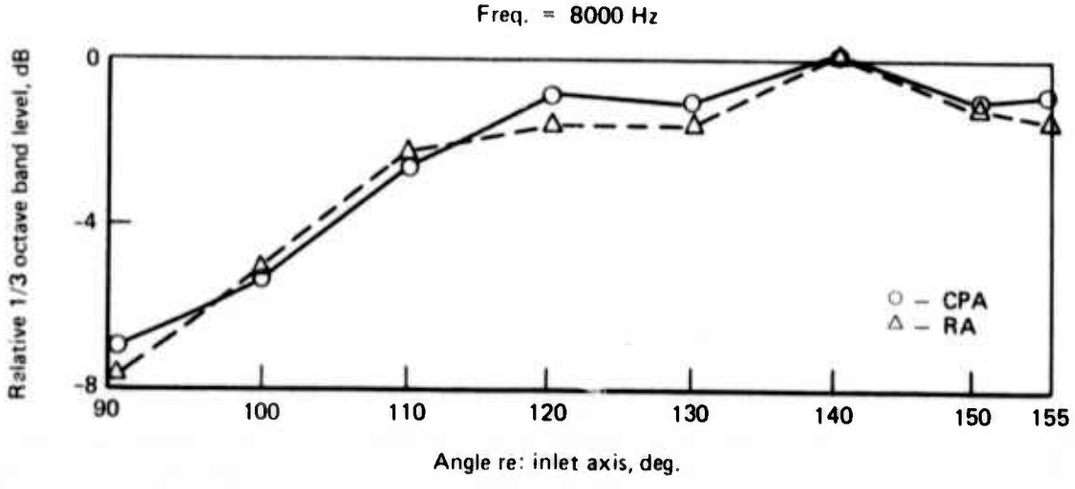

Figure 111. — 37-Tube Nozzle Premerged Jet Noise Peak-Beam Patterns (T_T = 1150° F, PR = 4.0)

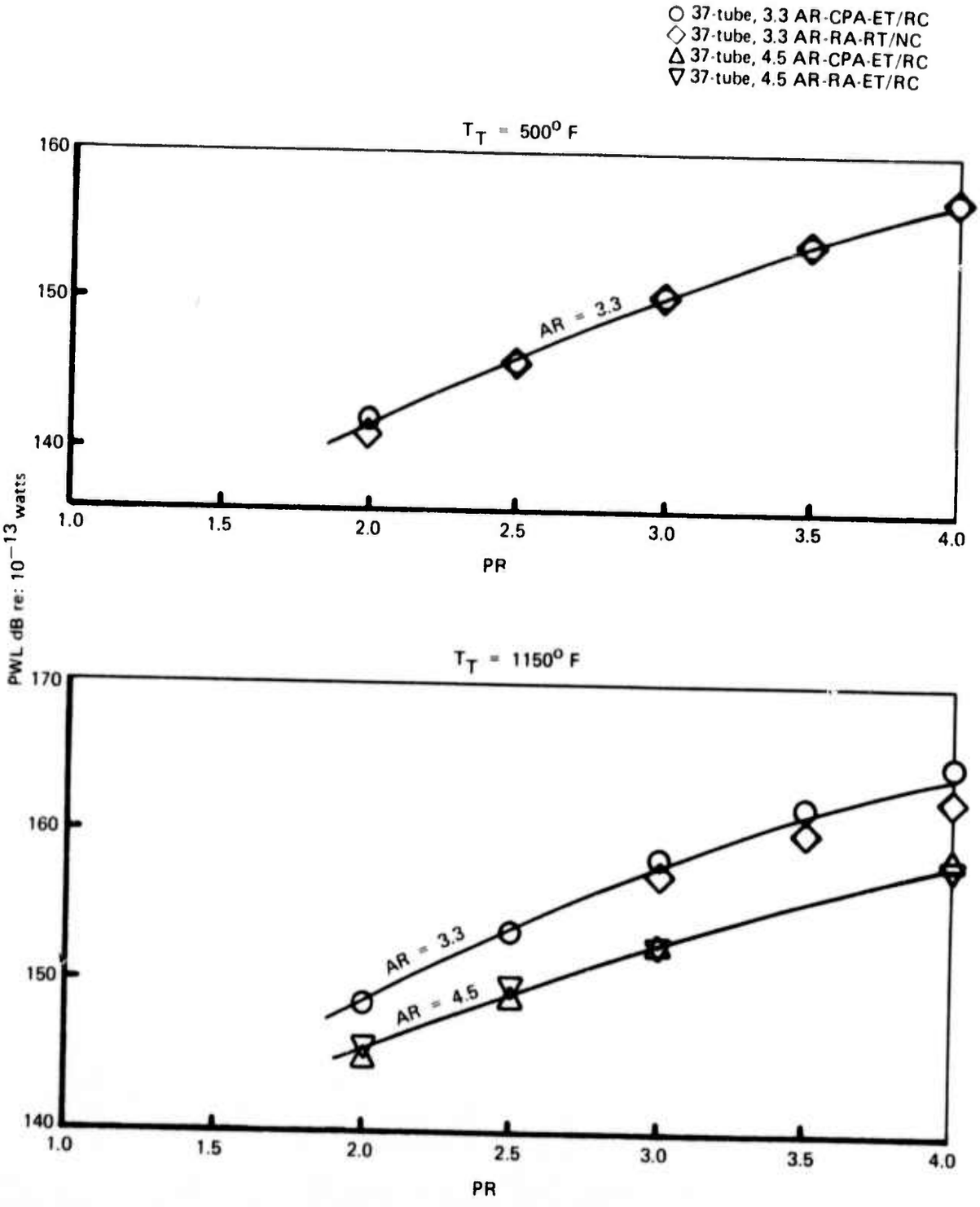

Figure 112. — Postmerged Jet Noise Power Levels from Close-Packed Arrays and Radial-Type Arrays

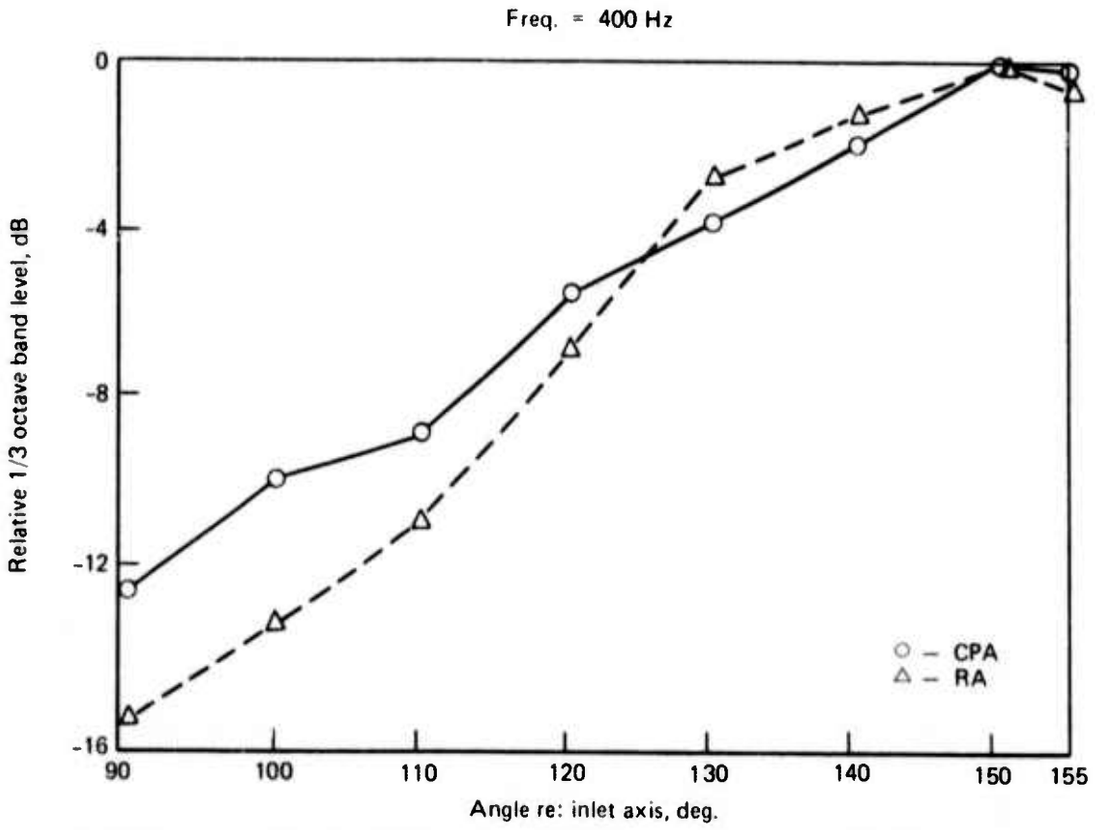

Figure 113. — 37-Tube Nozzle Postmerged Jet Noise Peak-Beam Patterns (T_T = 1150° F, PR = 2.0)

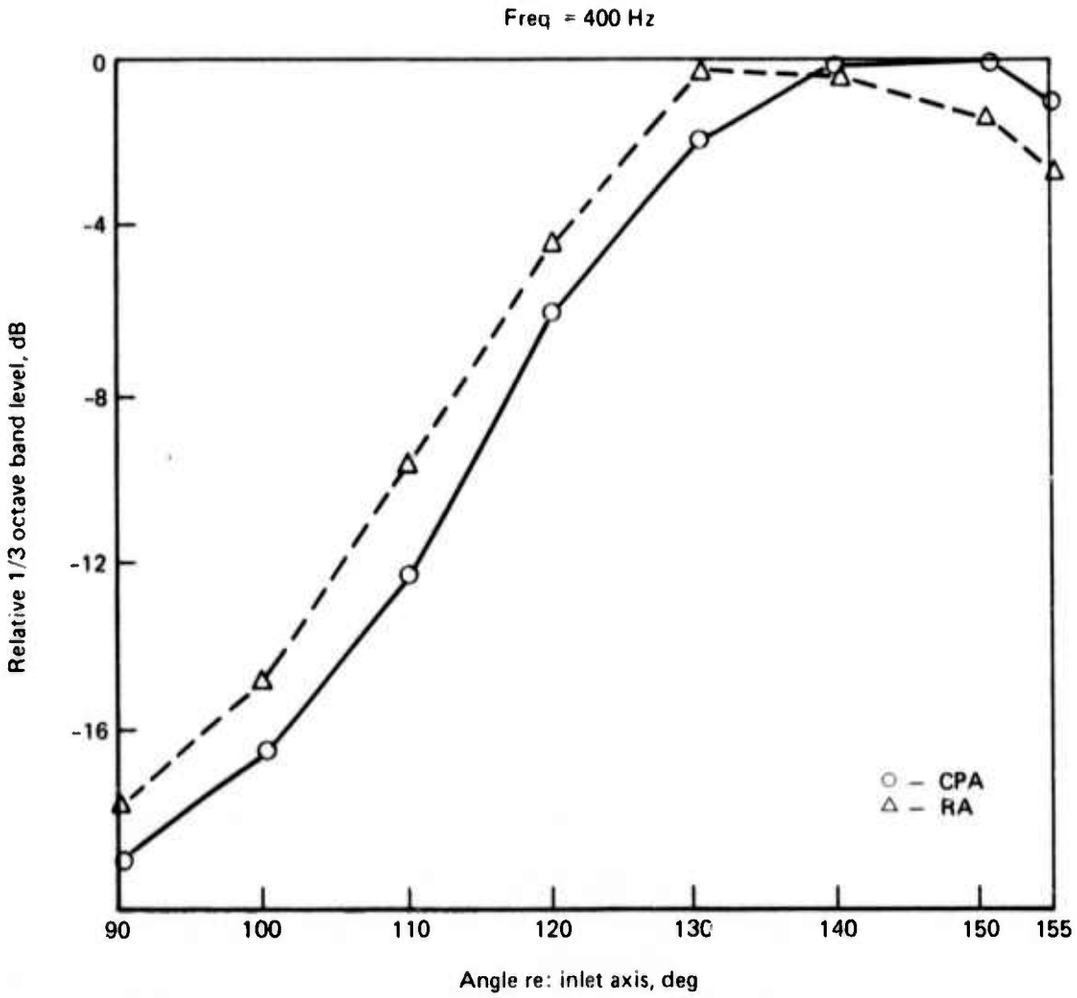

Figure 114. — 37-Tube Nozzle Postmerged Jet noise Peak-Beam Patterns (T_T = 1150° F, PR = 4.0)

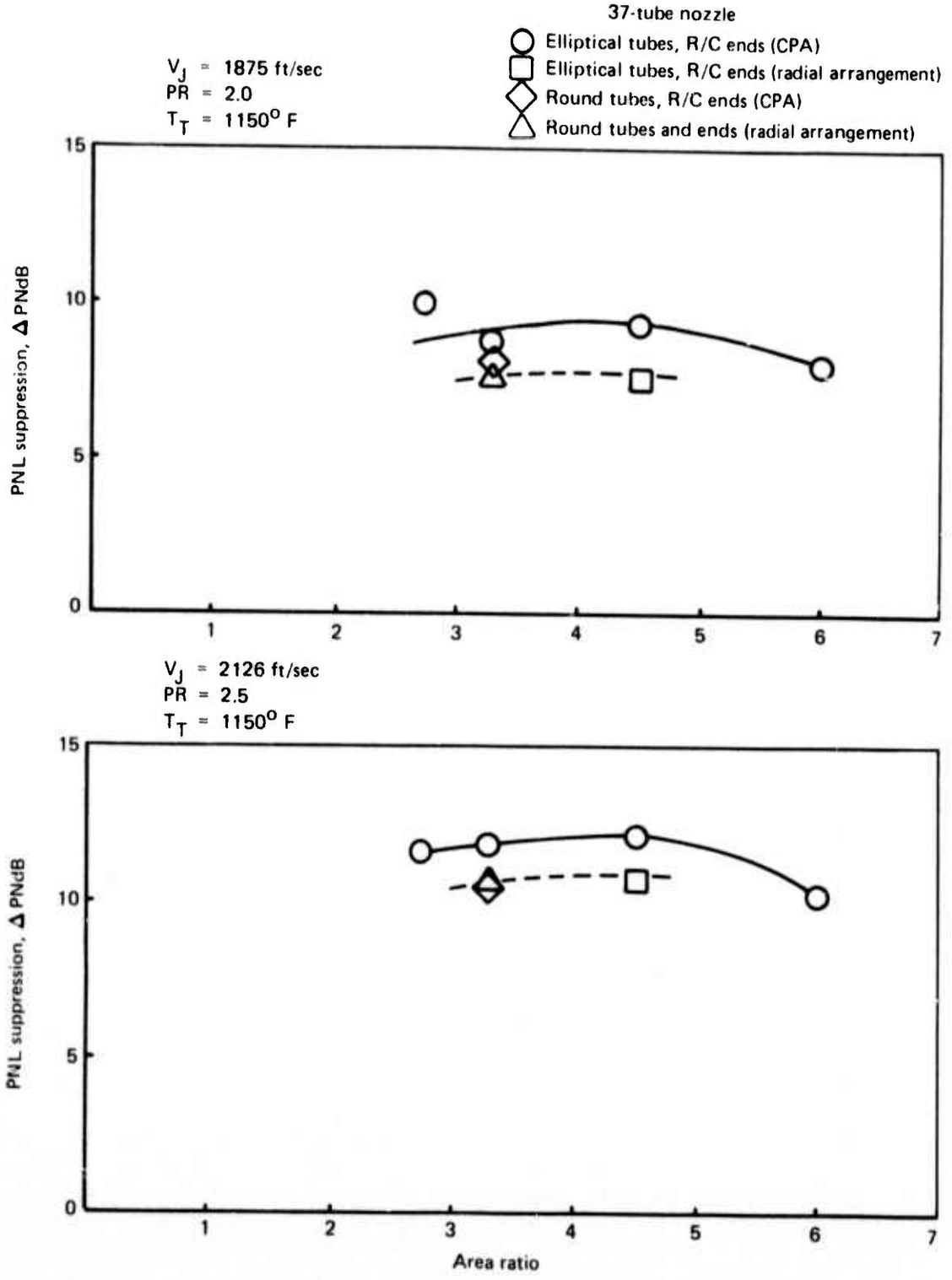

Figure 115. — Effect of Area Ratio on Noise Suppression for 37-Tube Nozzles

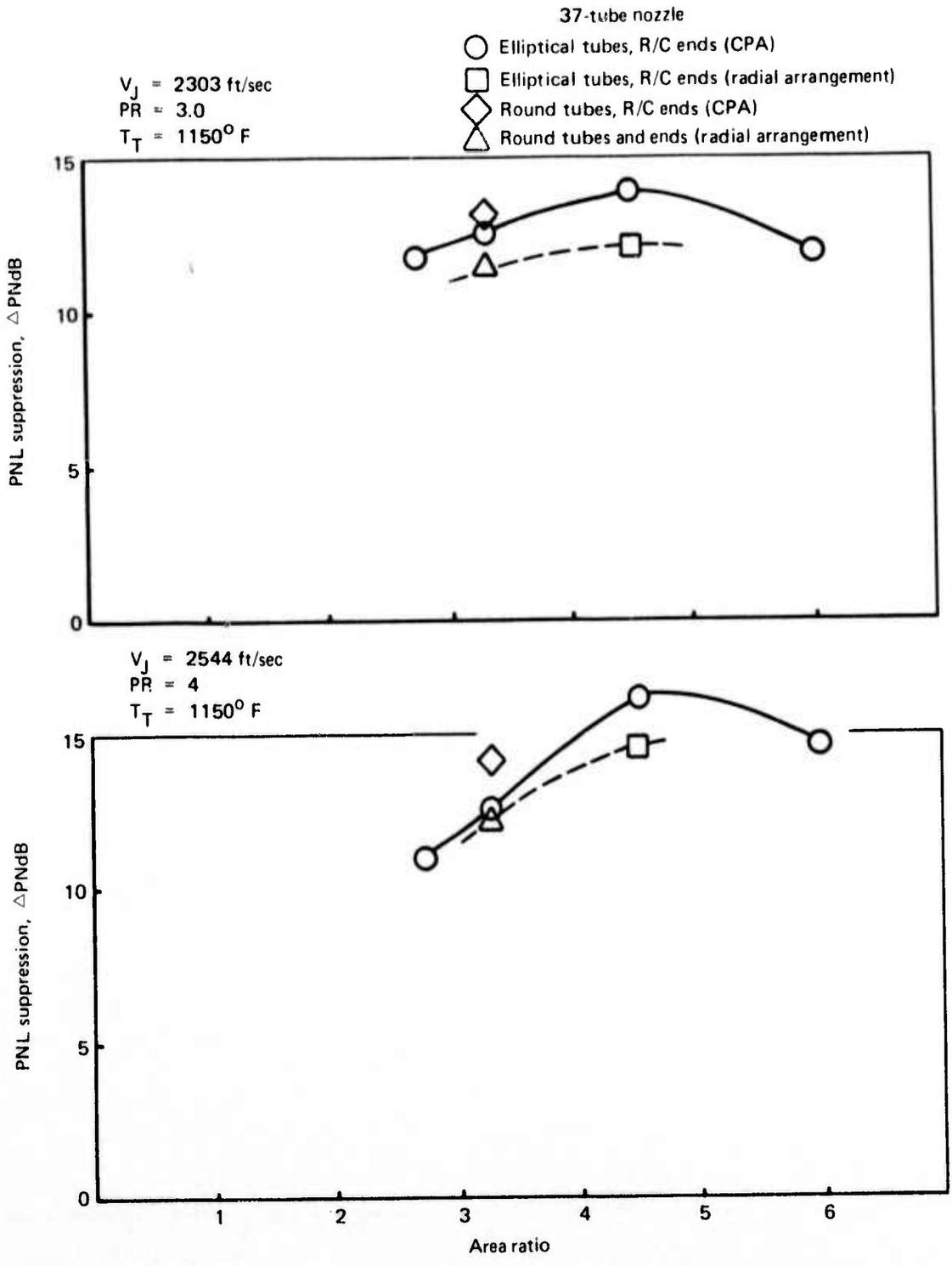

Figure 116. — Effect of Area Ratio on Noise Suppression for 37-Tube Nozzles

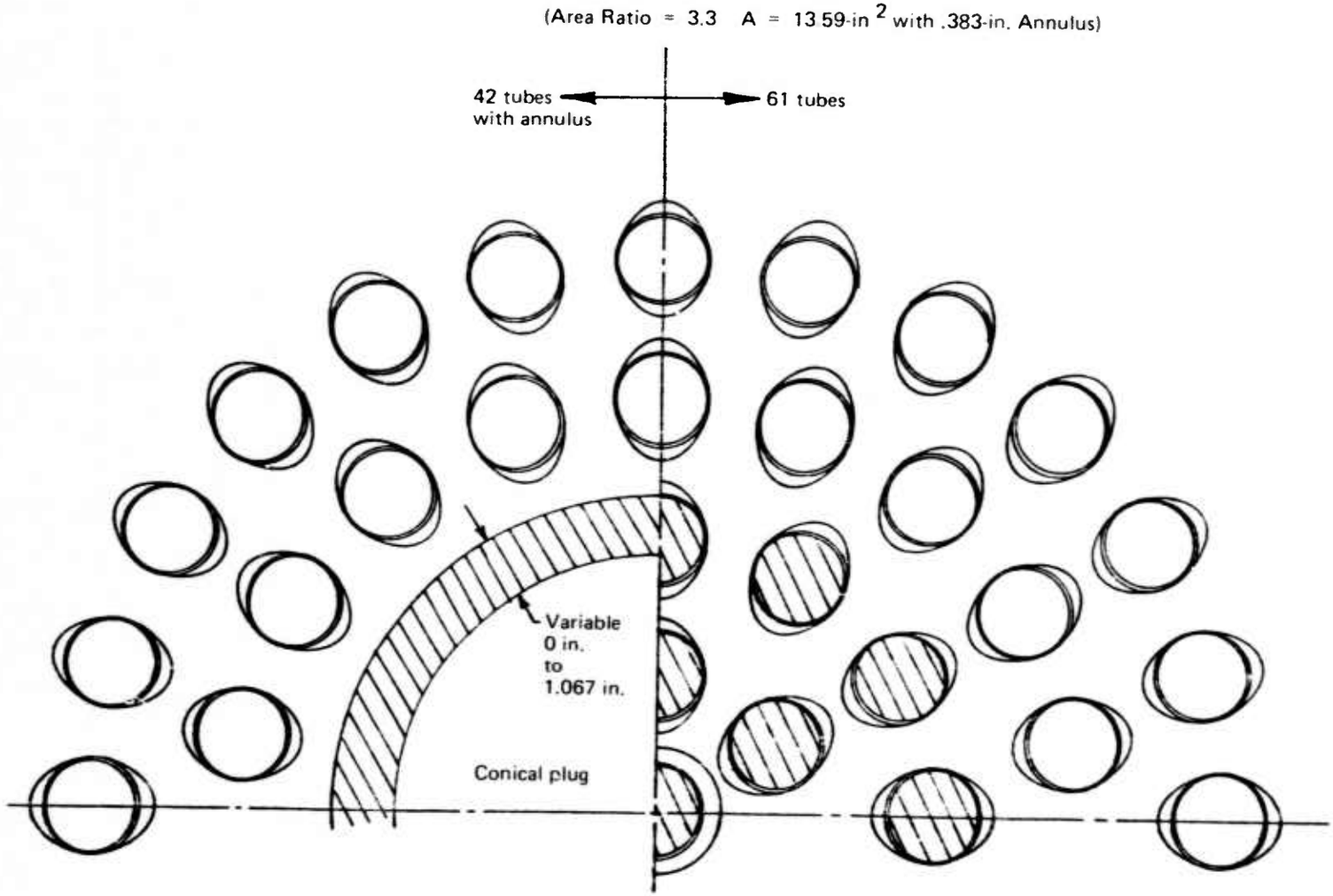

Figure 117. — Comparison of 61-Tube Close-Packed and 42-Tube Close-Packed With Annulus Suppressors

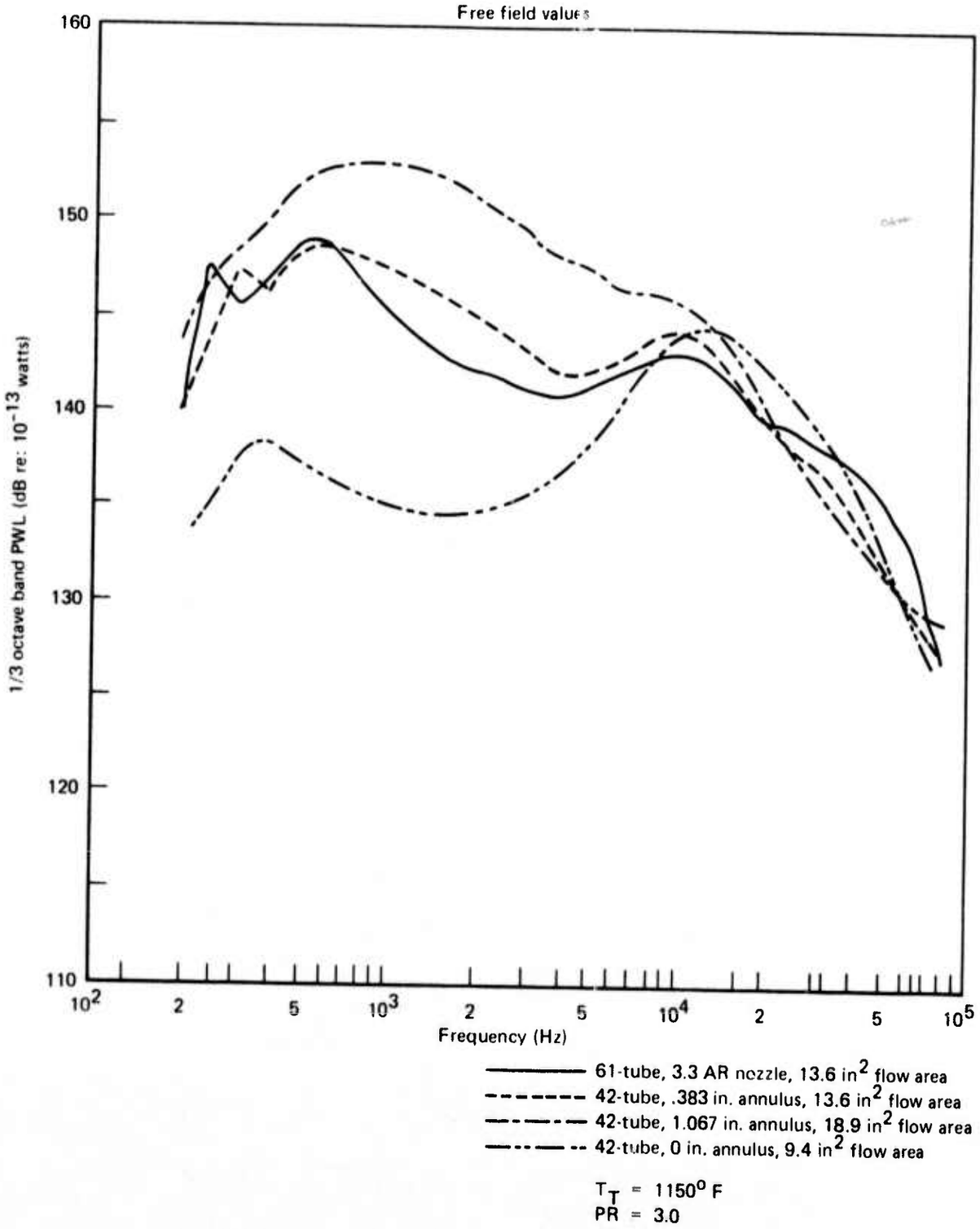

Figure 118. — Comparison of Regular Multitube Nozzle Noise With Multitube/Plug Nozzle Noise Levels

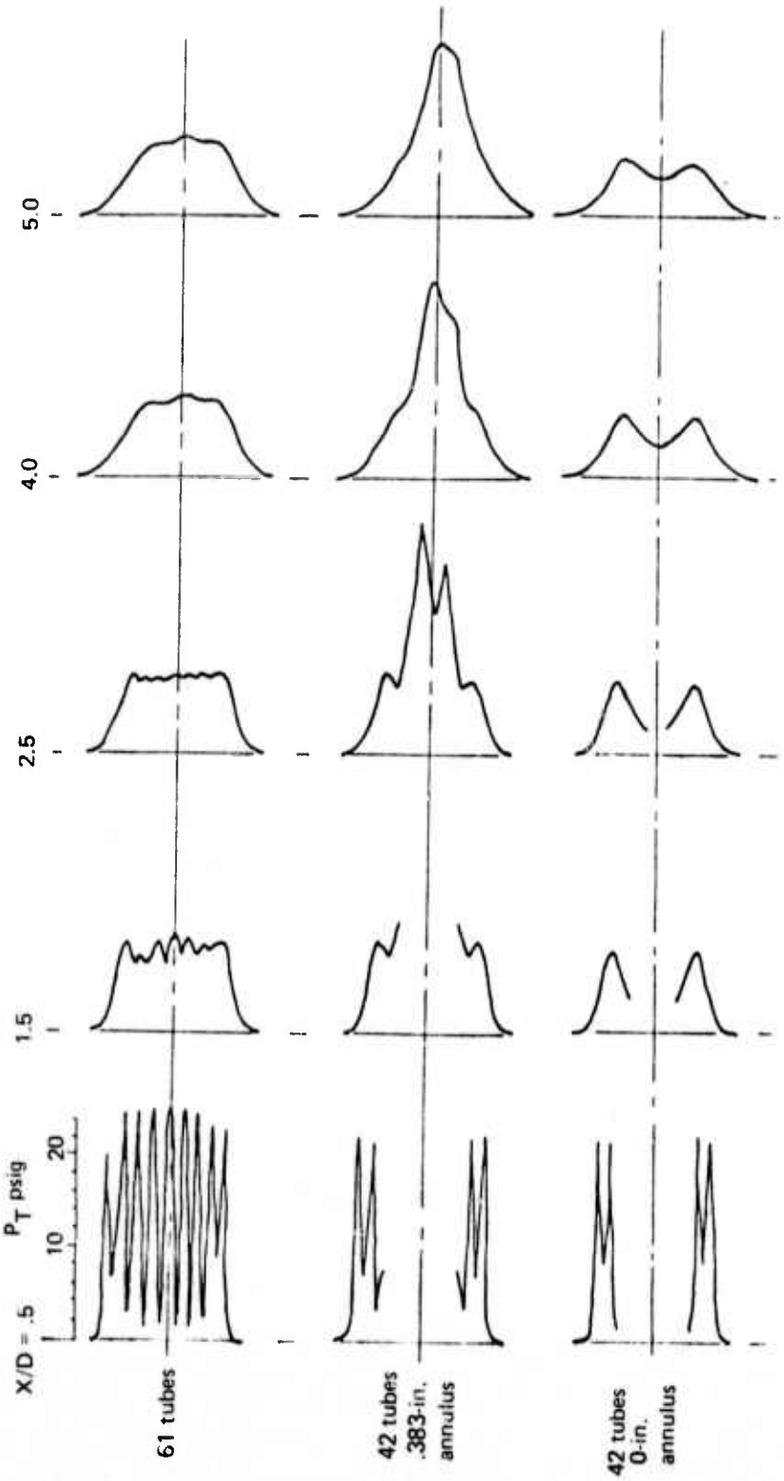

Figure 119. — Total Pressure Profile Comparisons at PR = 3.0, T_T = 1000° F

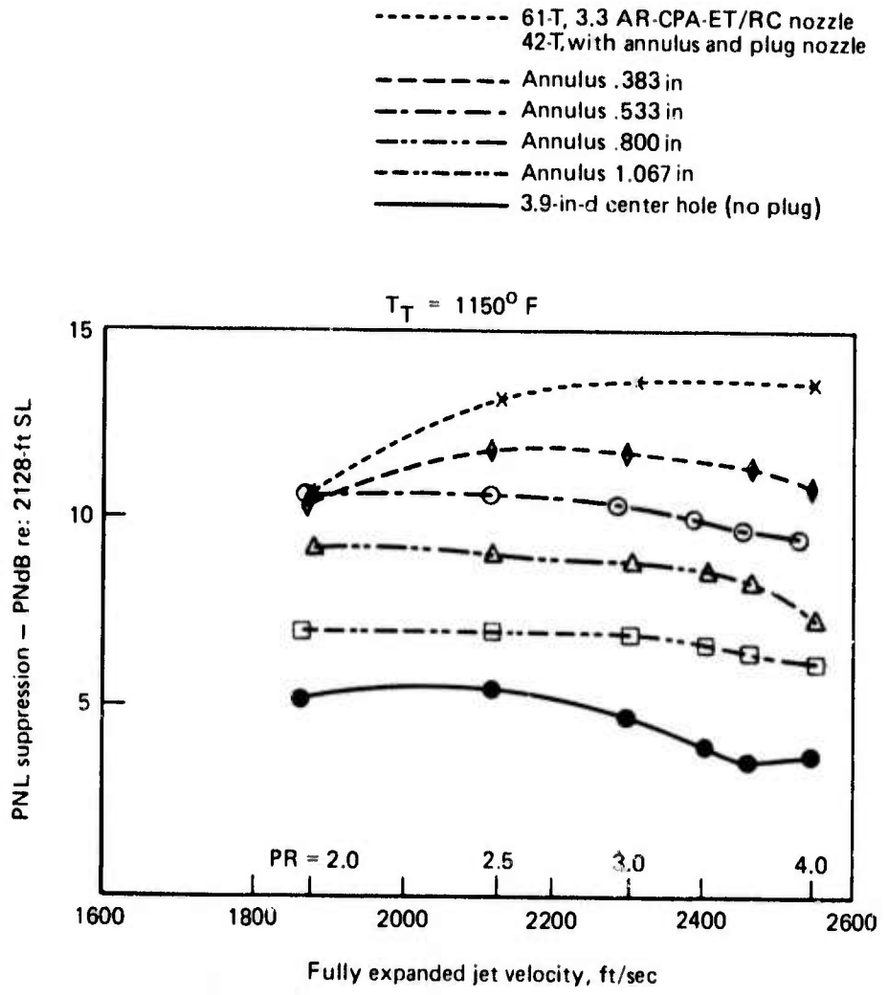

Figure 120. — 42 Tubes with Annulus and Plug, Jet Noise PNL Suppression

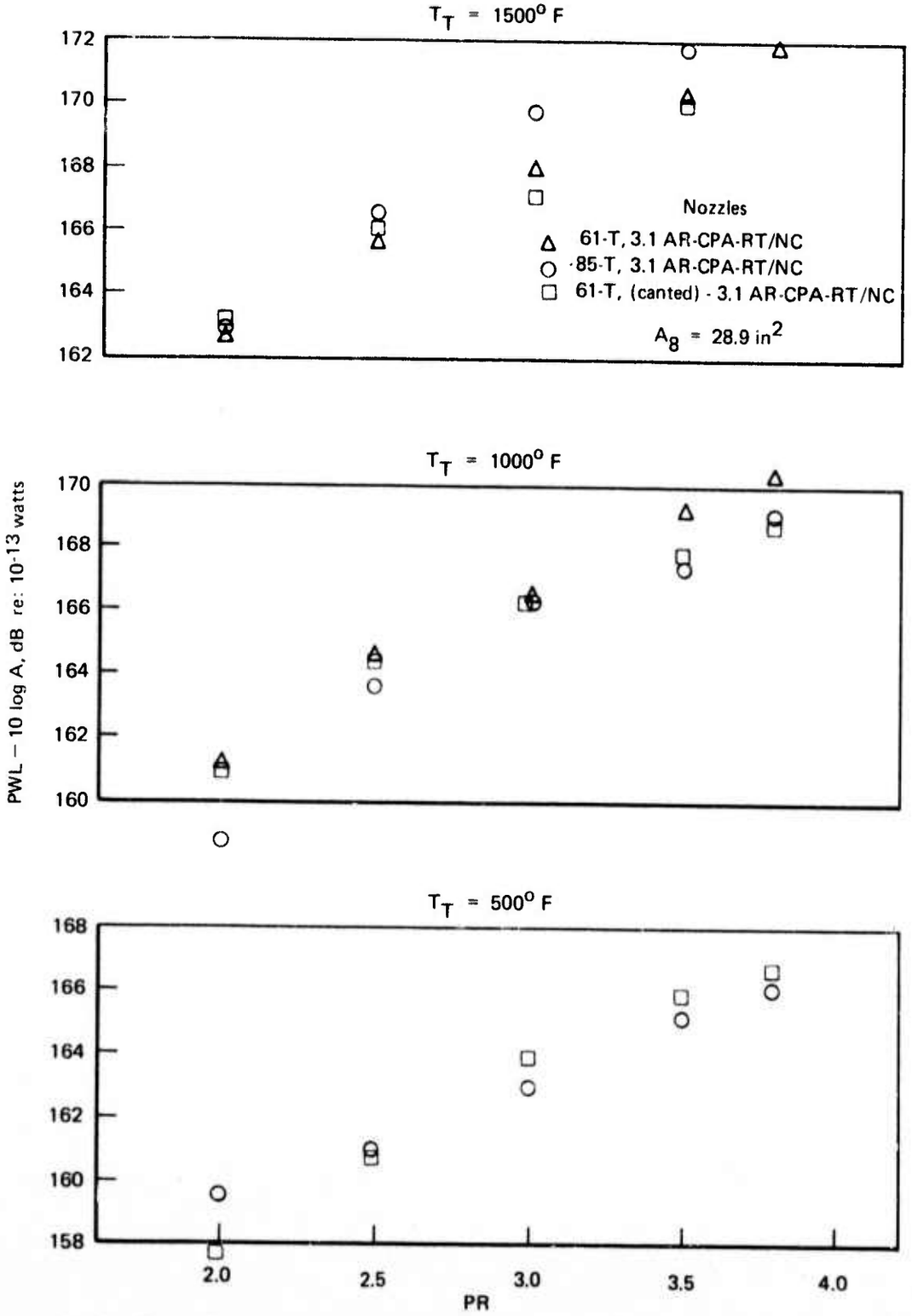

Figure 121. — 3.1 Area Ratio Multitube Nozzle Total Jet Noise Power Levels

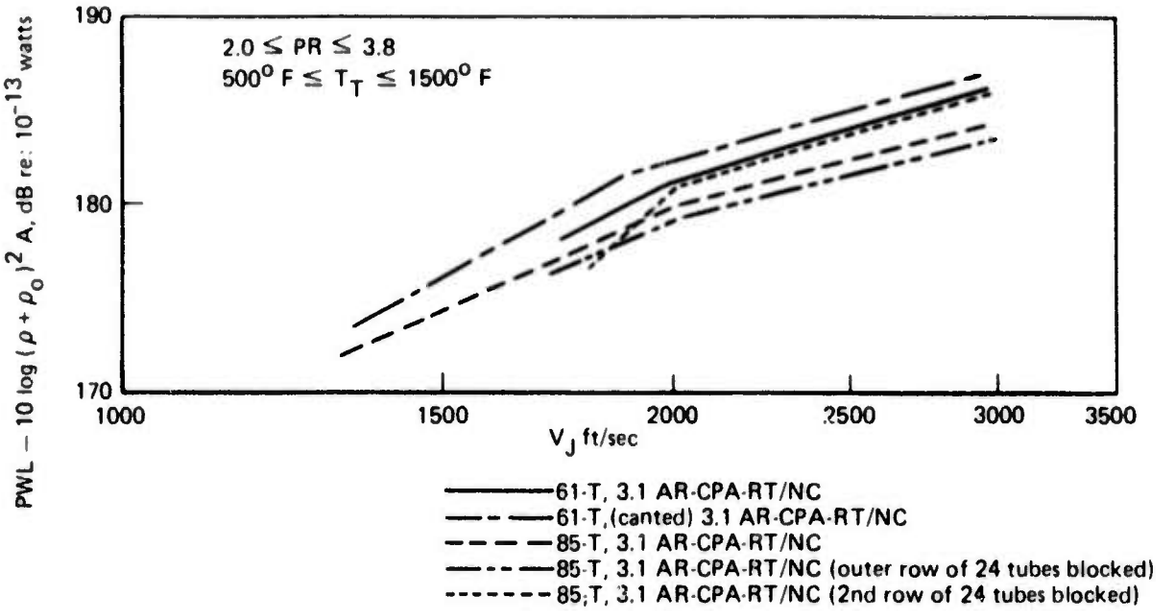

Figure 122. — Multitube Nozzles Premerged Jet Noise Power Level

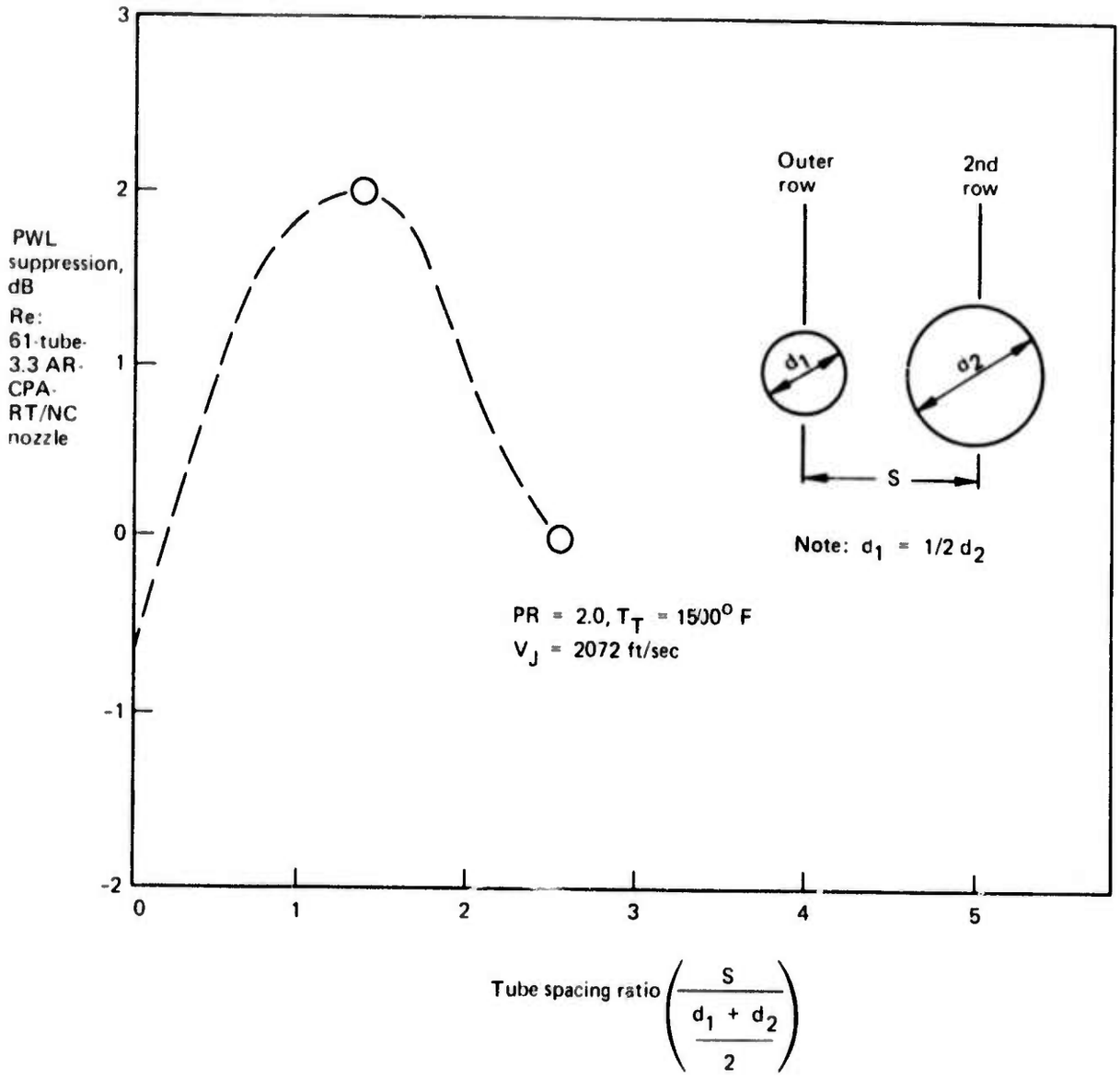

Figure 123. — Premerged Jet Noise Suppression as a Function of Tube Row Spacing Ratio for a 61-Tube Nozzle

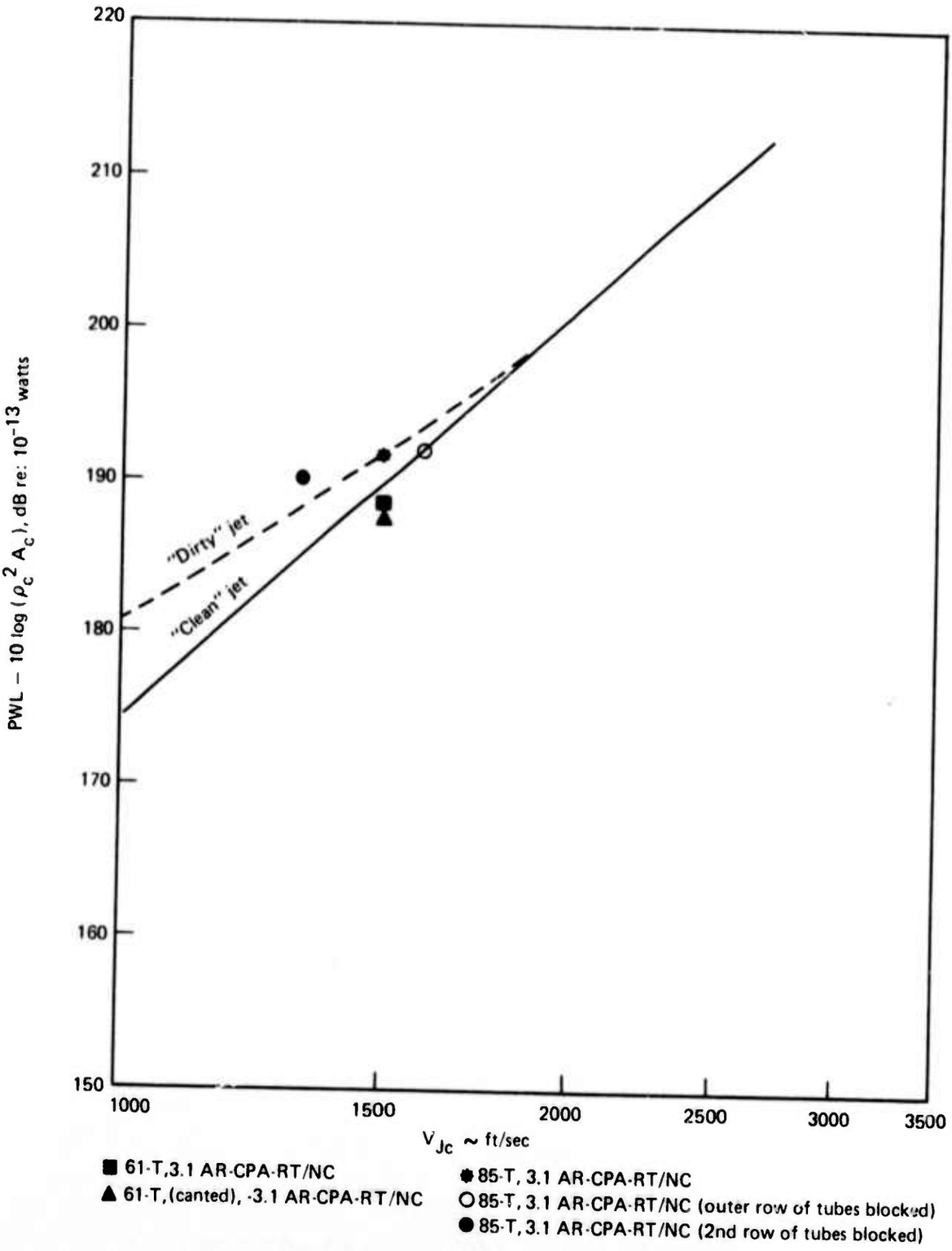

Figure 124. — Normalized Postmerged Jet Noise Power Levels

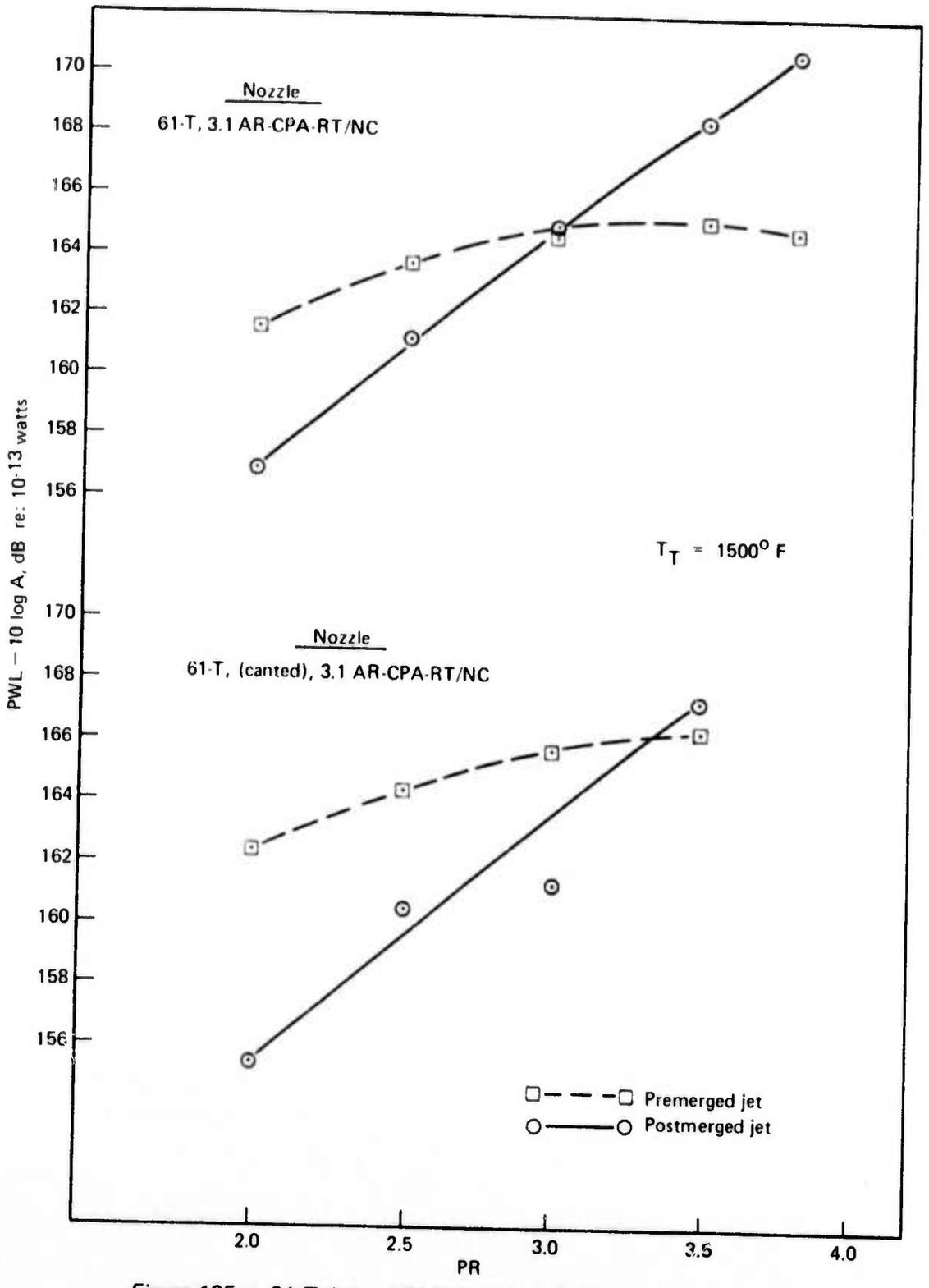

Figure 125. — 61-Tube and 61-Tube (canted) Nozzles Premerged and Postmerged Jet Noise Levels, T_T = 1500° F

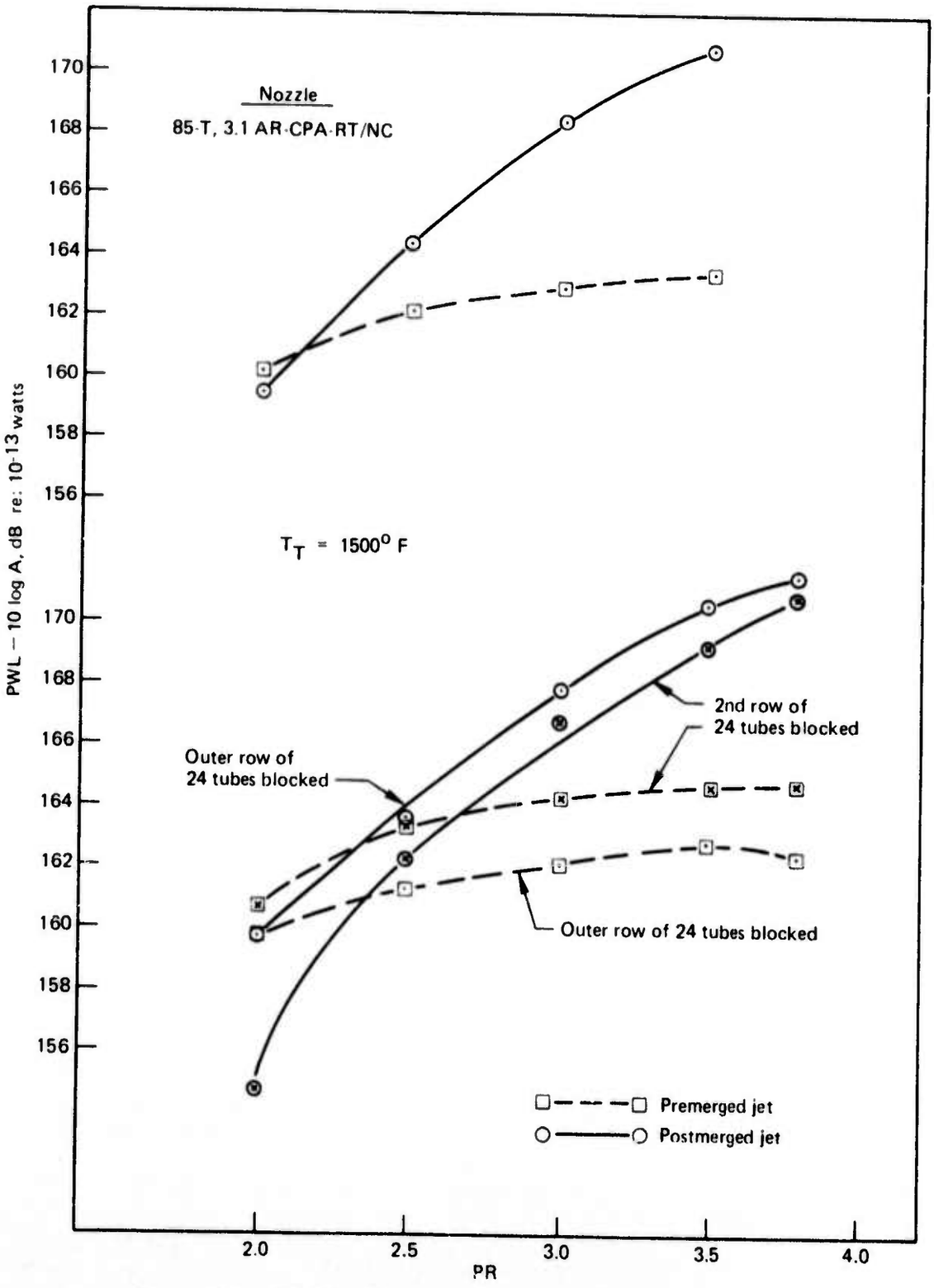

Figure 126. — 85-Tube Nozzle Configurations, Premerged and Postmerged Jet Noise Levels, T_T = 1500° F

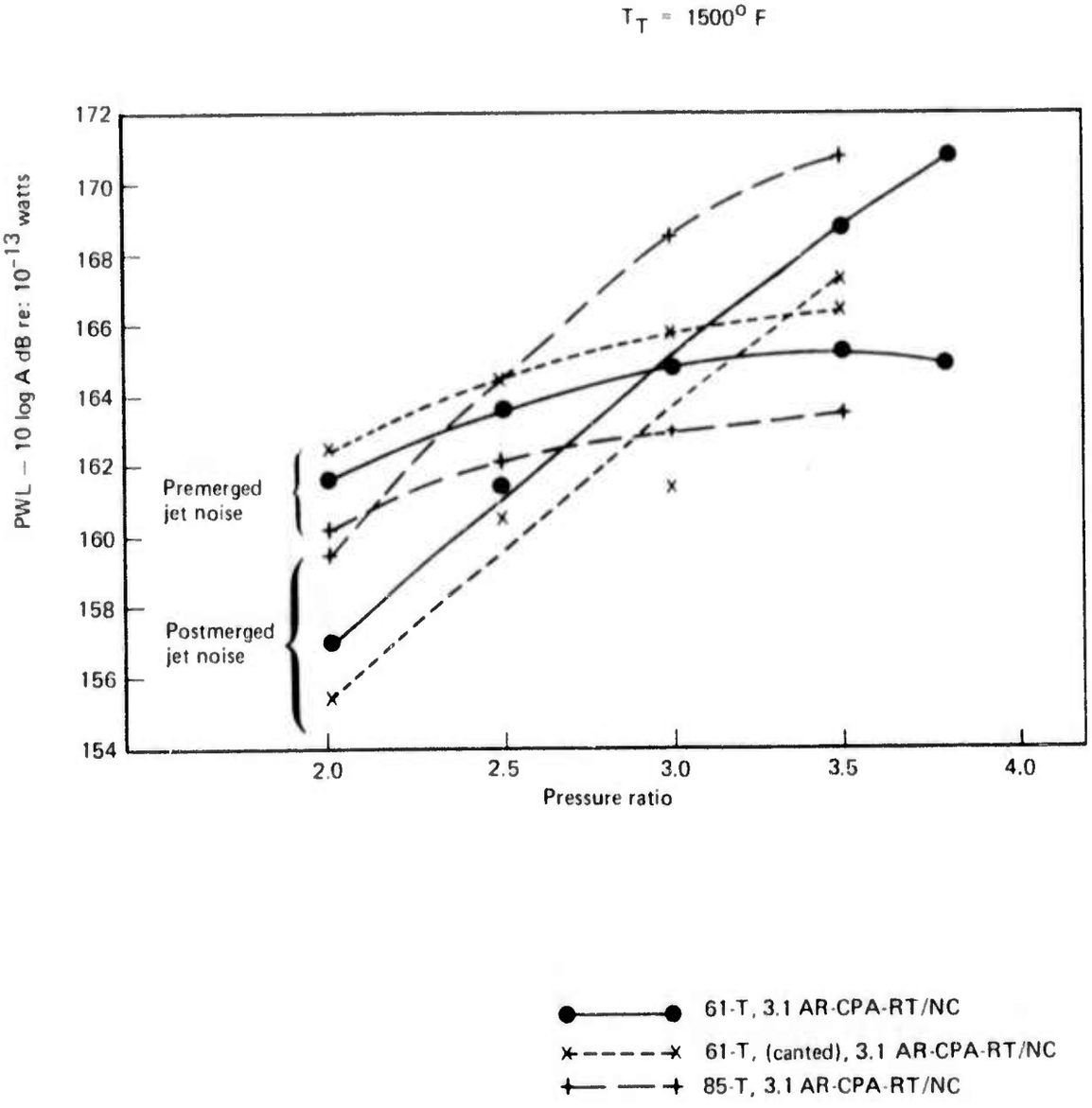

Figure 127. — Multitube Nozzles Premerged and Postmerged Jet Noise Levels, T_T = 1500° F

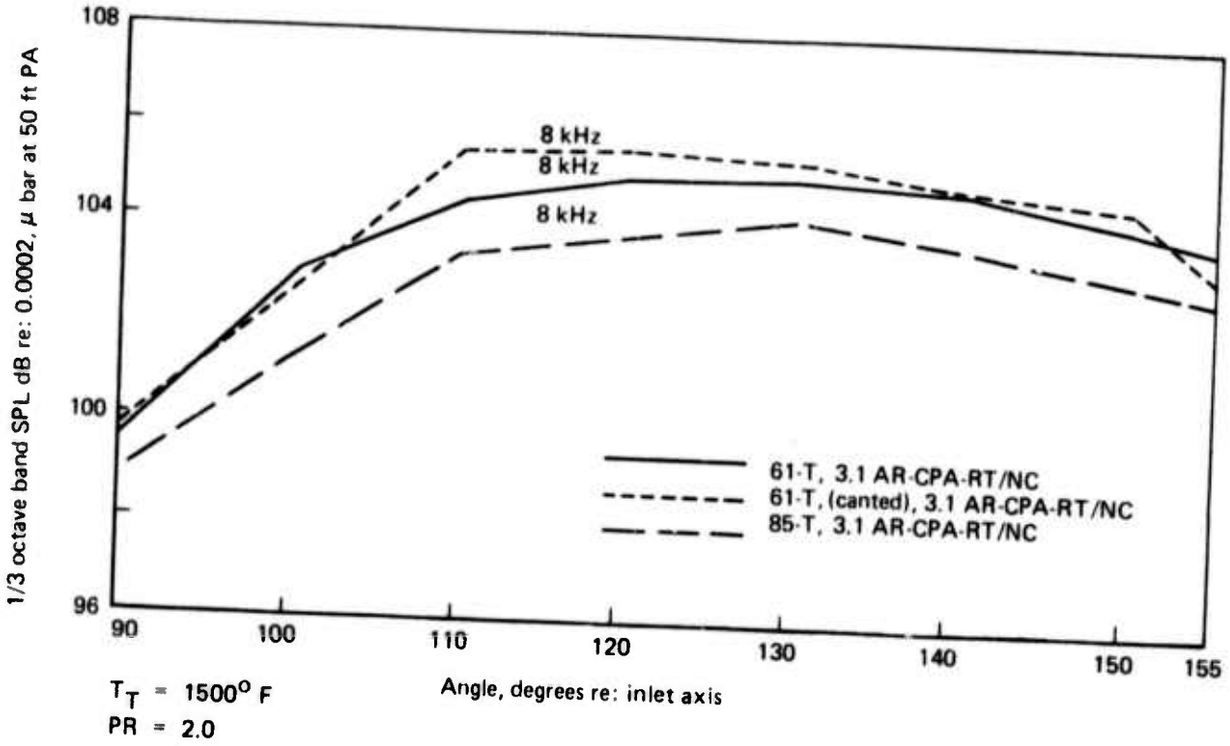

Figure 128. — Multitube Nozzle Premerged Jet Noise Directivity for T_T = 1500° F, PR = 2.0

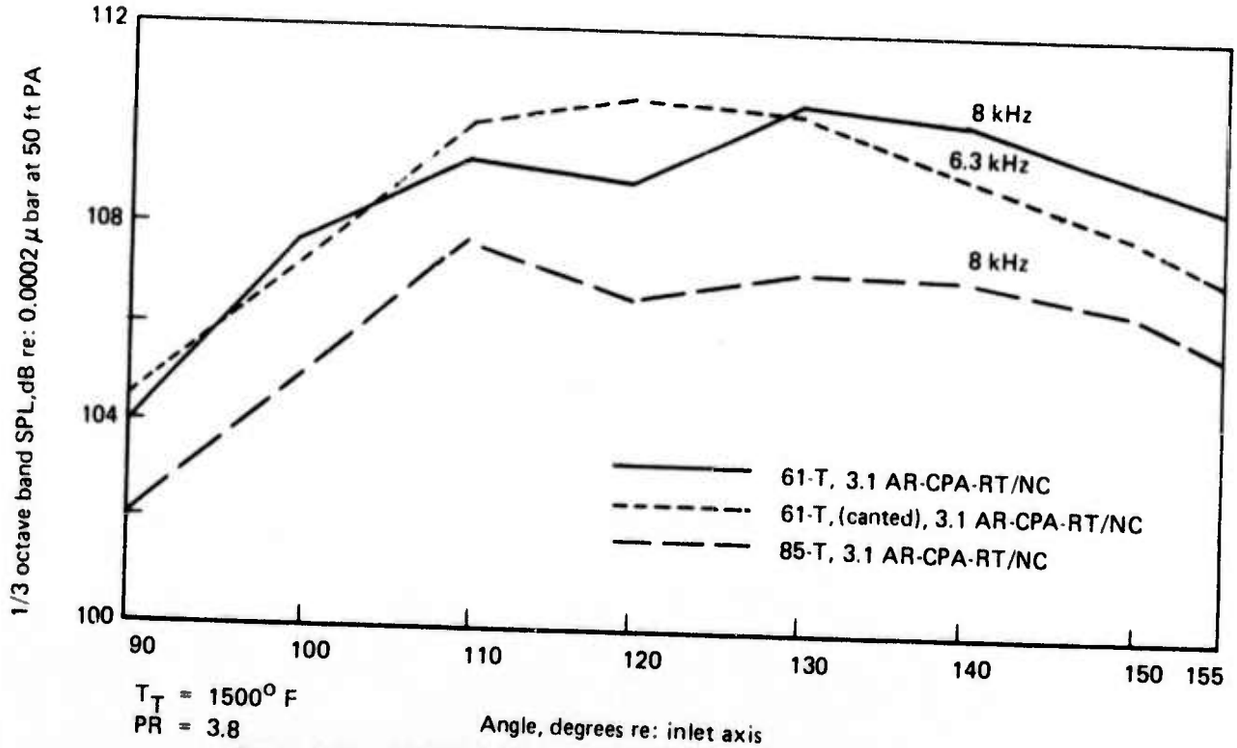

Figure 129. — Multitube Nozzle Premerged Jet Noise Directivity for T_T = 1500° F, PR = 3.8

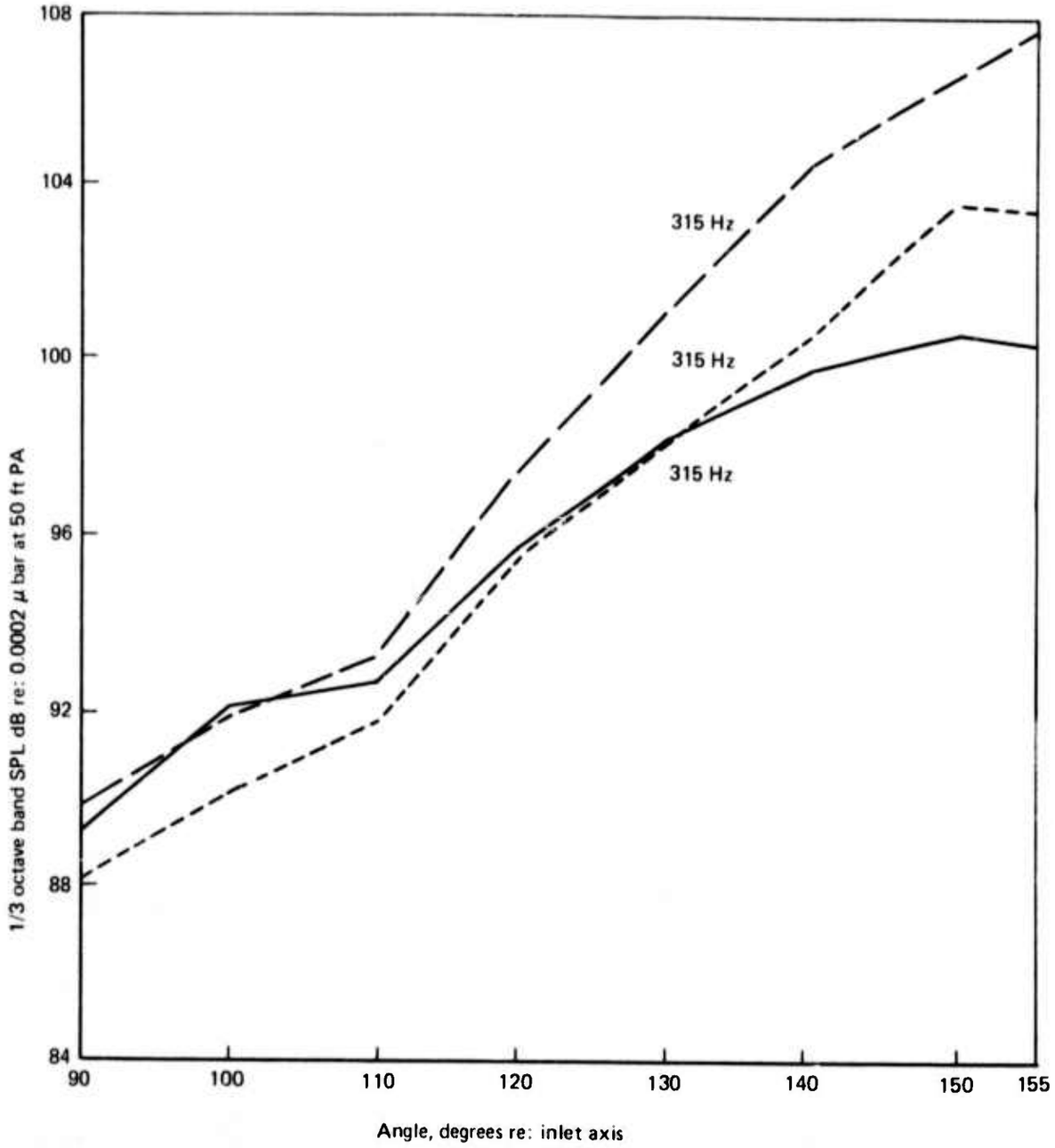

T_T = 1500° F
PR = 2.0

——— 61-T, 3.1 AR-CPA-RT/NC
- - - - - - - 61-T, (canted), 3.1 AR-CPA-RT/NC
— — — 85-T, 3.1 AR-CPA-RT/NC

Figure 130. — Multitube Nozzle Postmerged Jet Noise Directivity for T_T = 1500° F, PR = 2.0

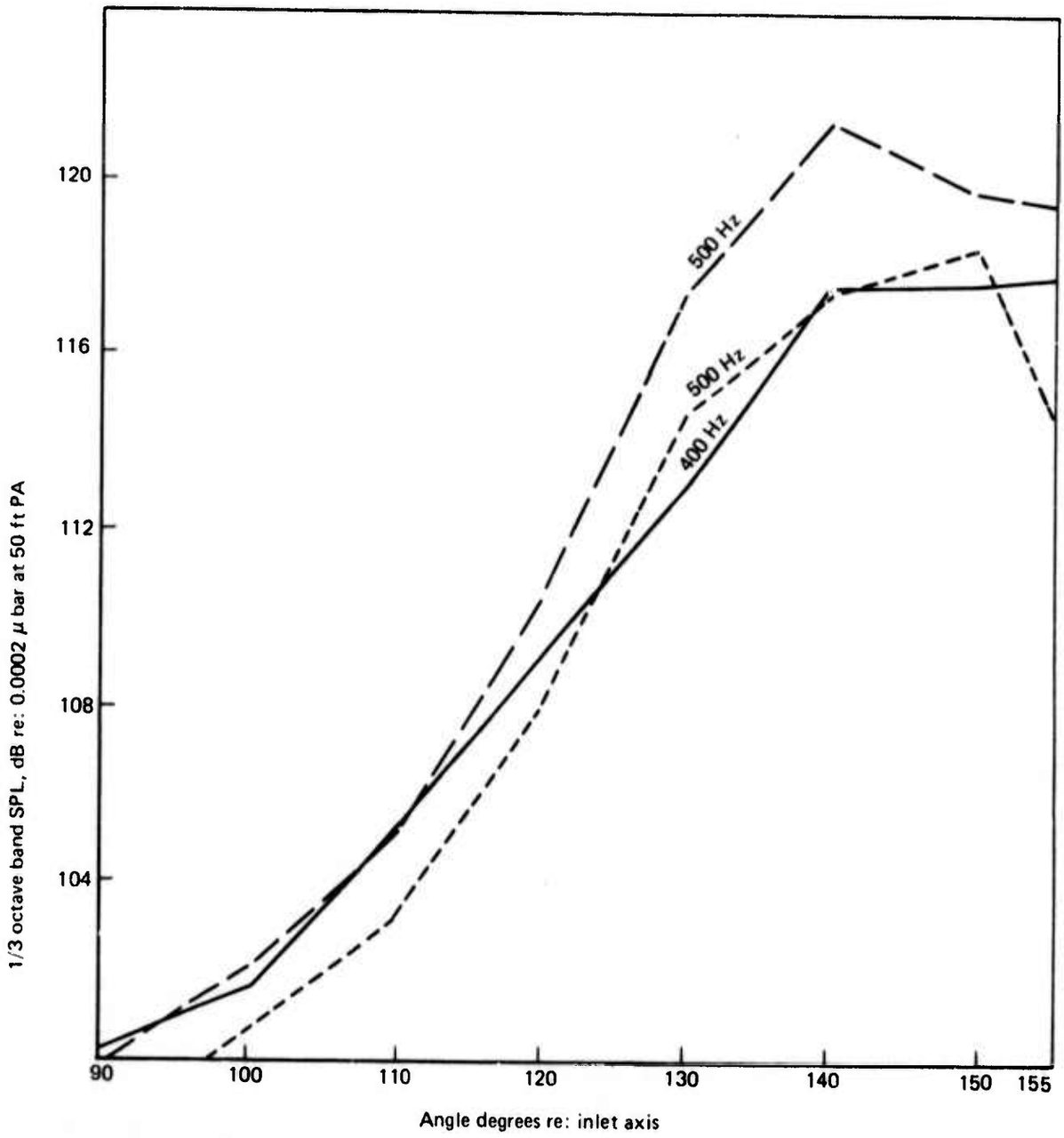

Figure 131. — Multitube Nozzle Postmerged Jet Noise Directivity for T_T = 1500° F, PR = 3.8

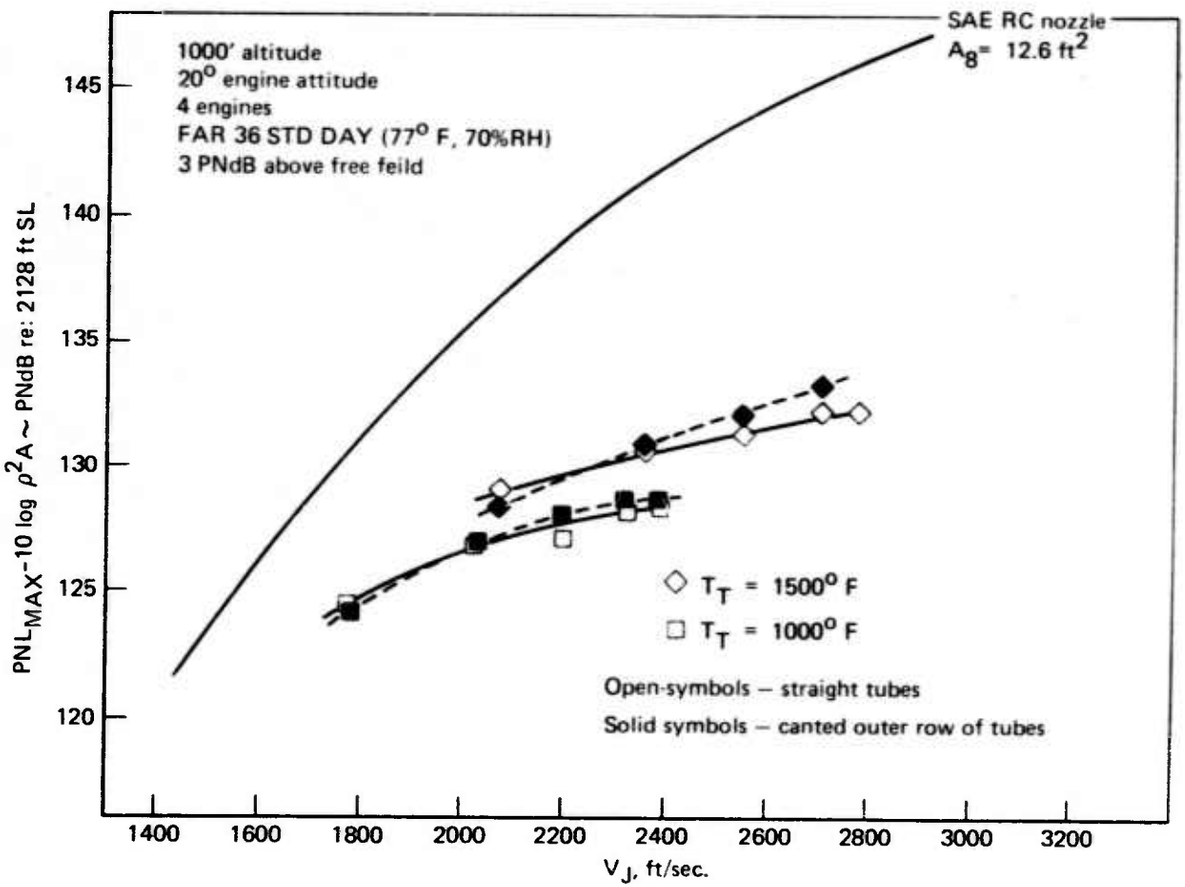

Figure 132. — Normalized 2128-ft Sideline PNL's For 61-Tube, 3.1 AR Nozzle

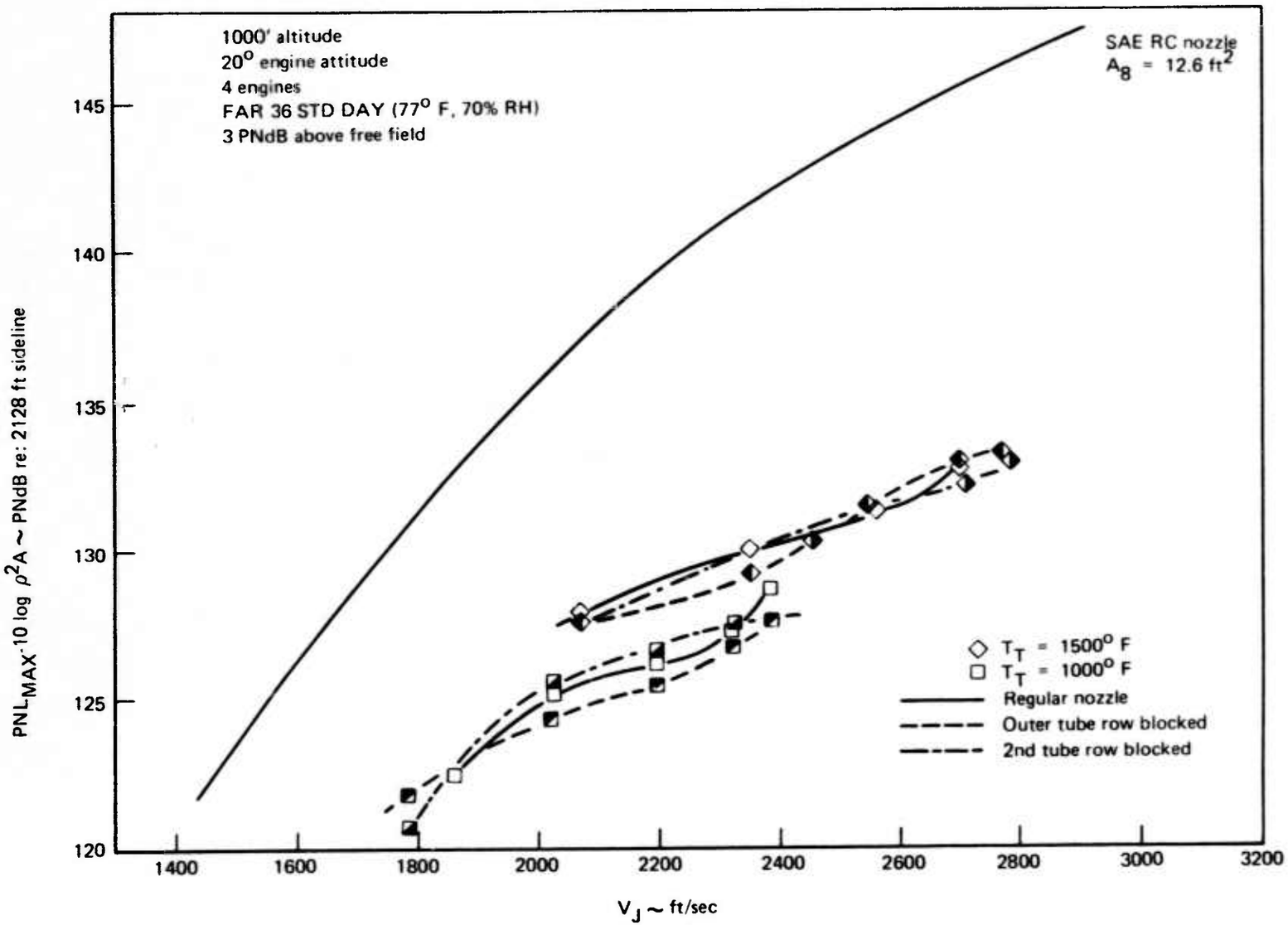

Figure 133. — Normalized 2128-ft Sideline PNL's for 85-Tube, 3.1 AR Nozzle

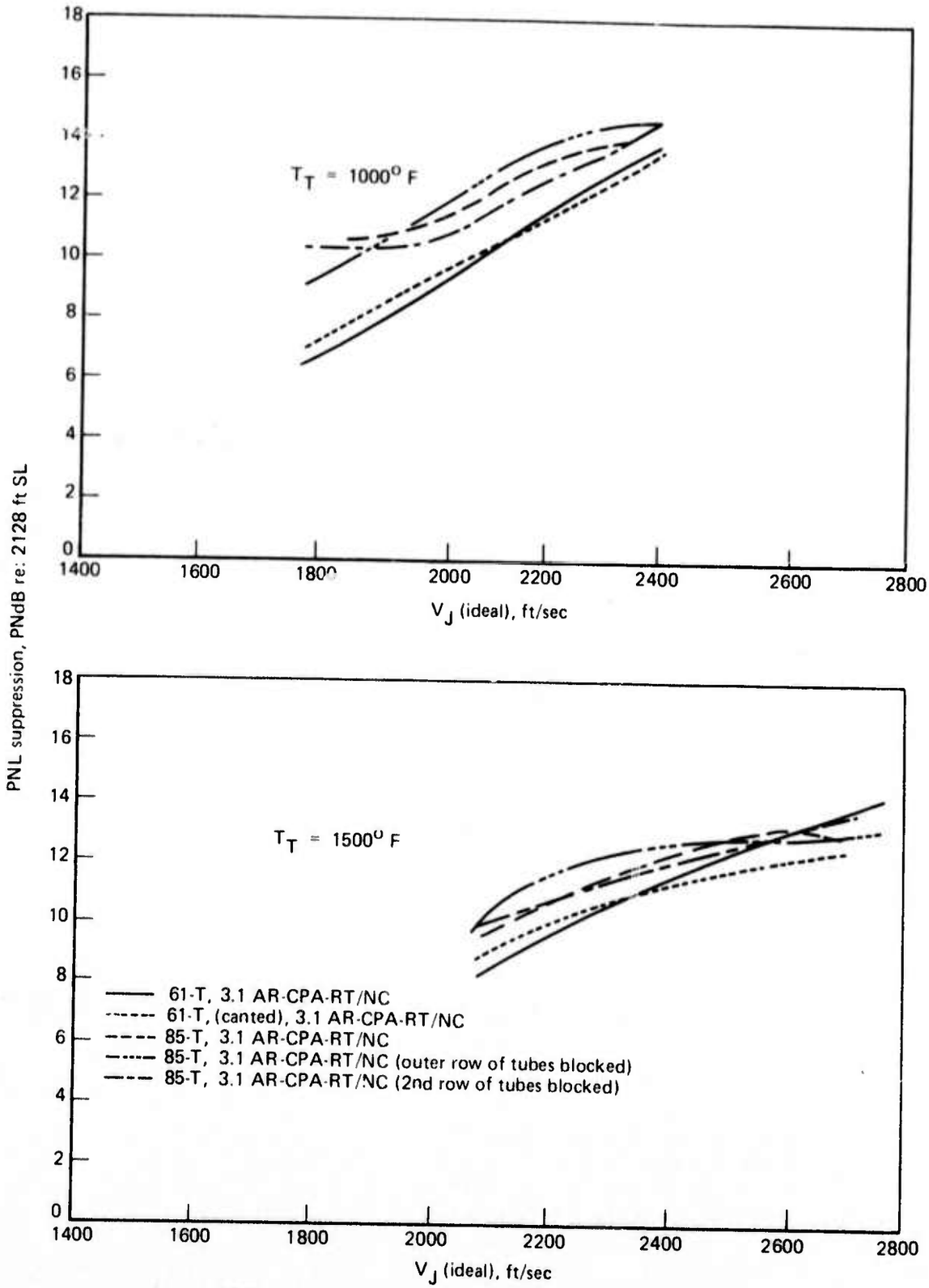

Figure 134. — Sideline Noise Suppression With Irregular Array Nozzles

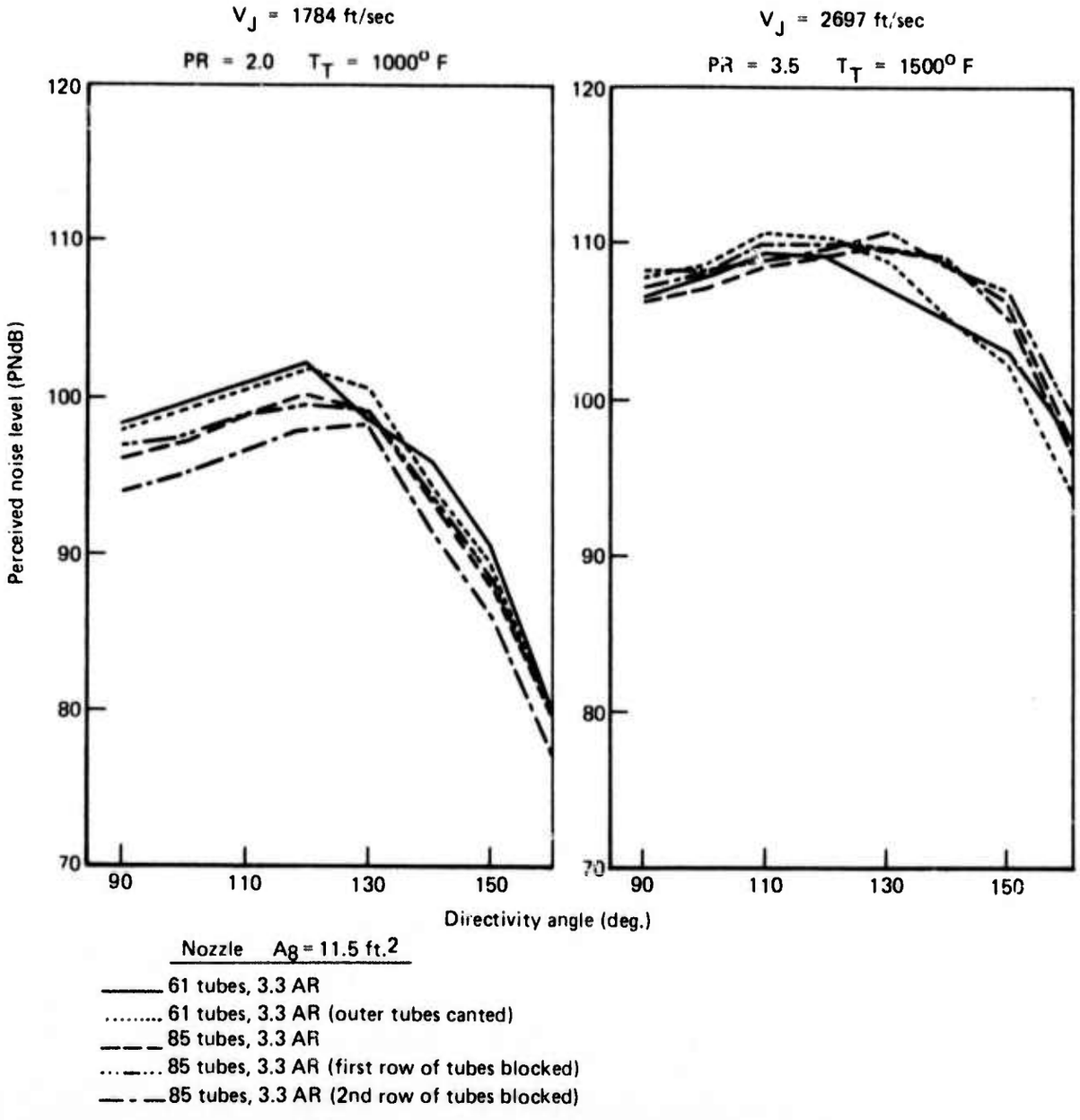

Figure 135. — Multitube Nozzle PNL Beam Patterns

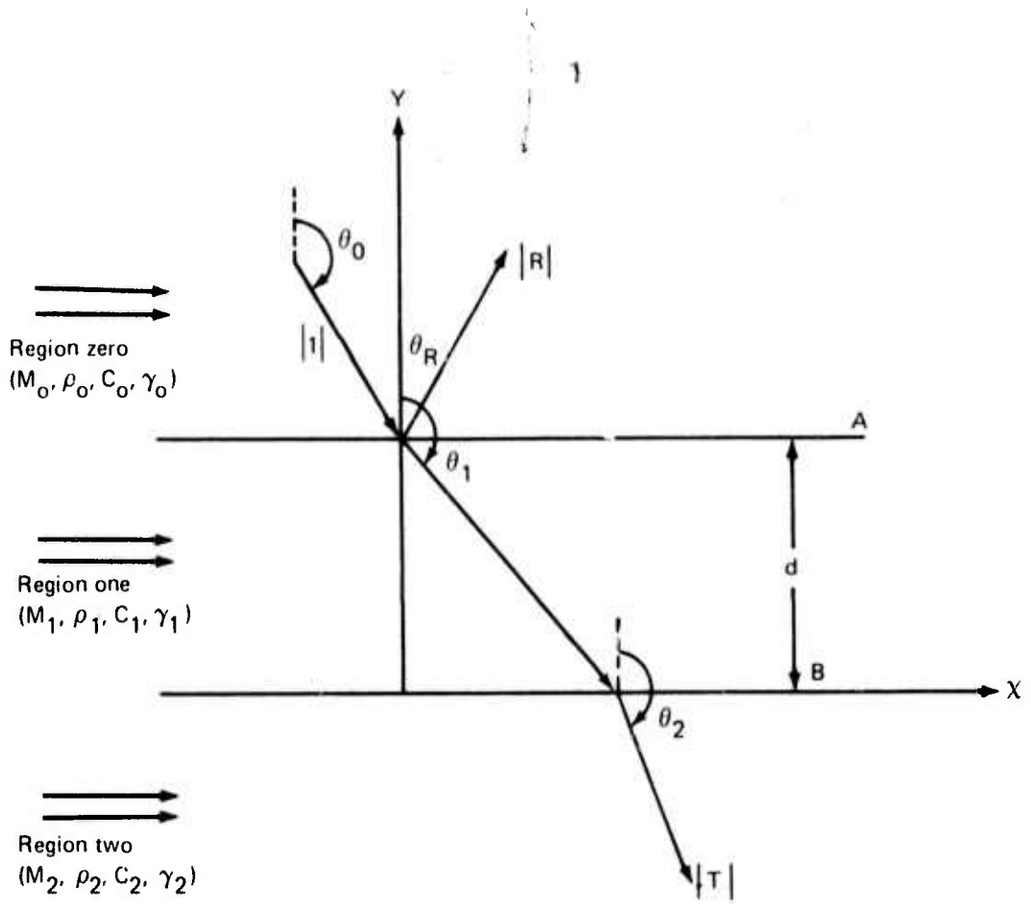

Figure 136. — Three-Layered-Flow, Acoustic Model and Nomenclature

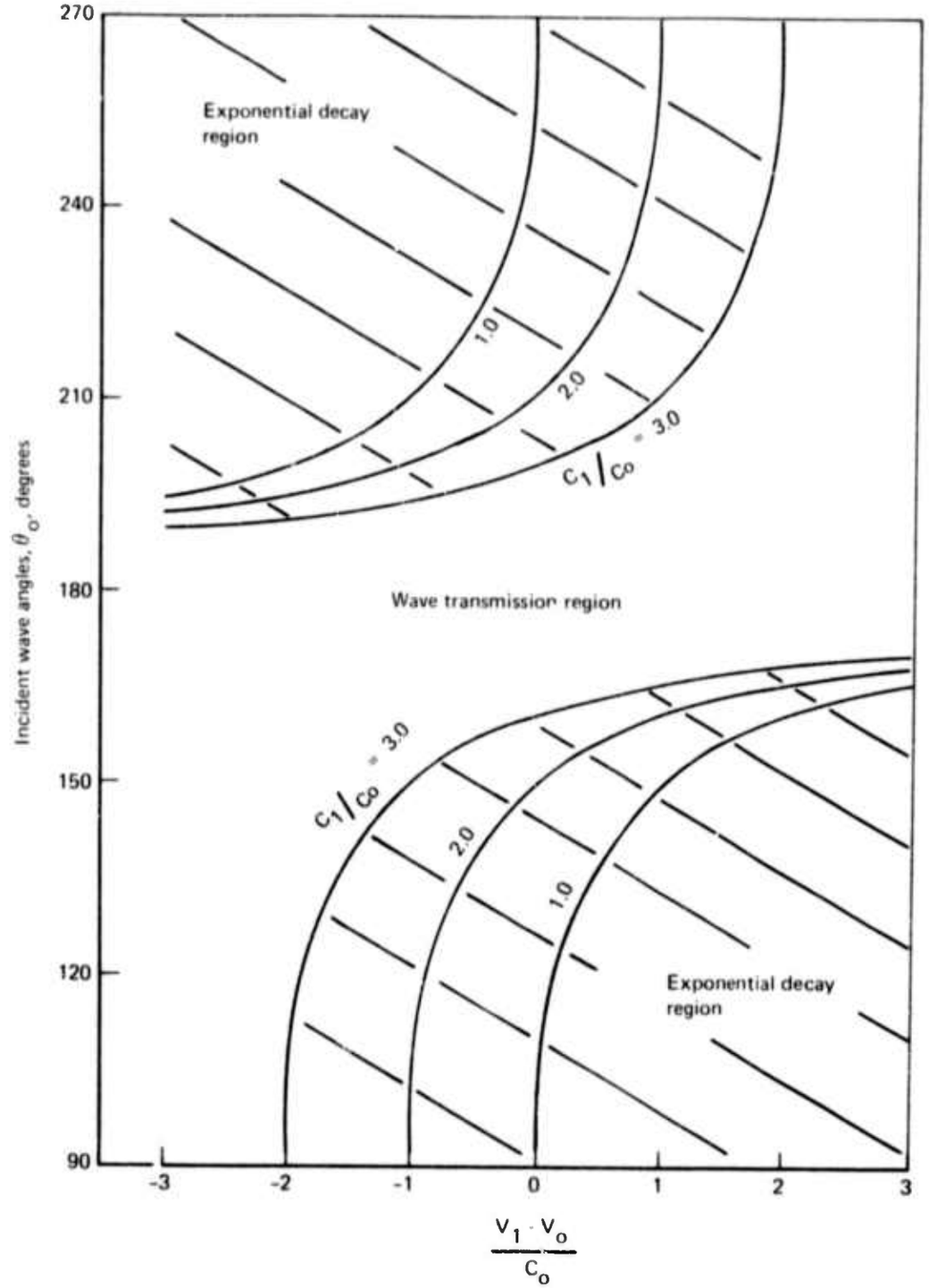

Figure 137. — Cut-Off Angles

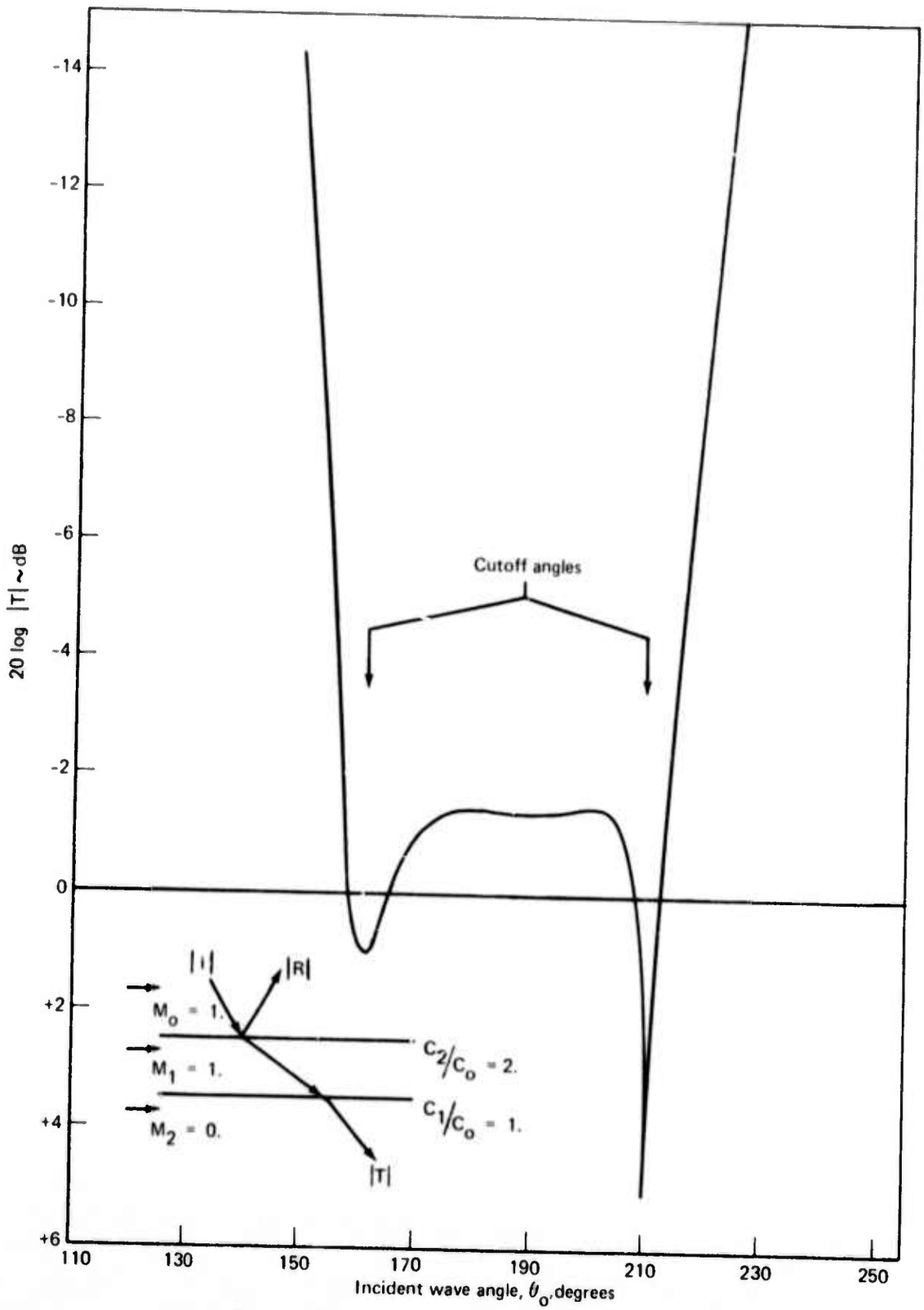

Figure 138. — Transmission Coefficient $K_o d$ = 2.0

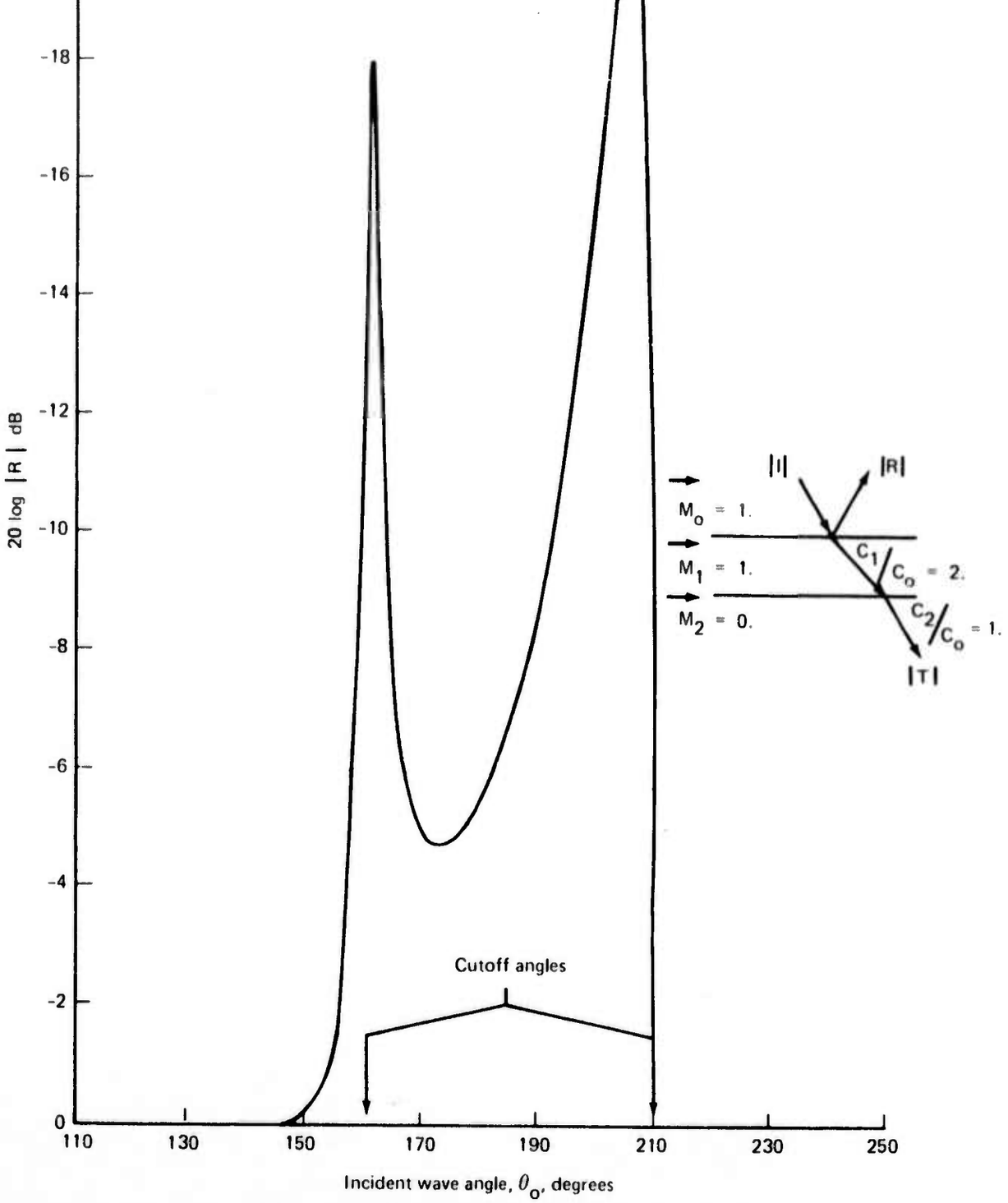

Figure 139. — Reflection Coefficient $K_o d$ = 2.0

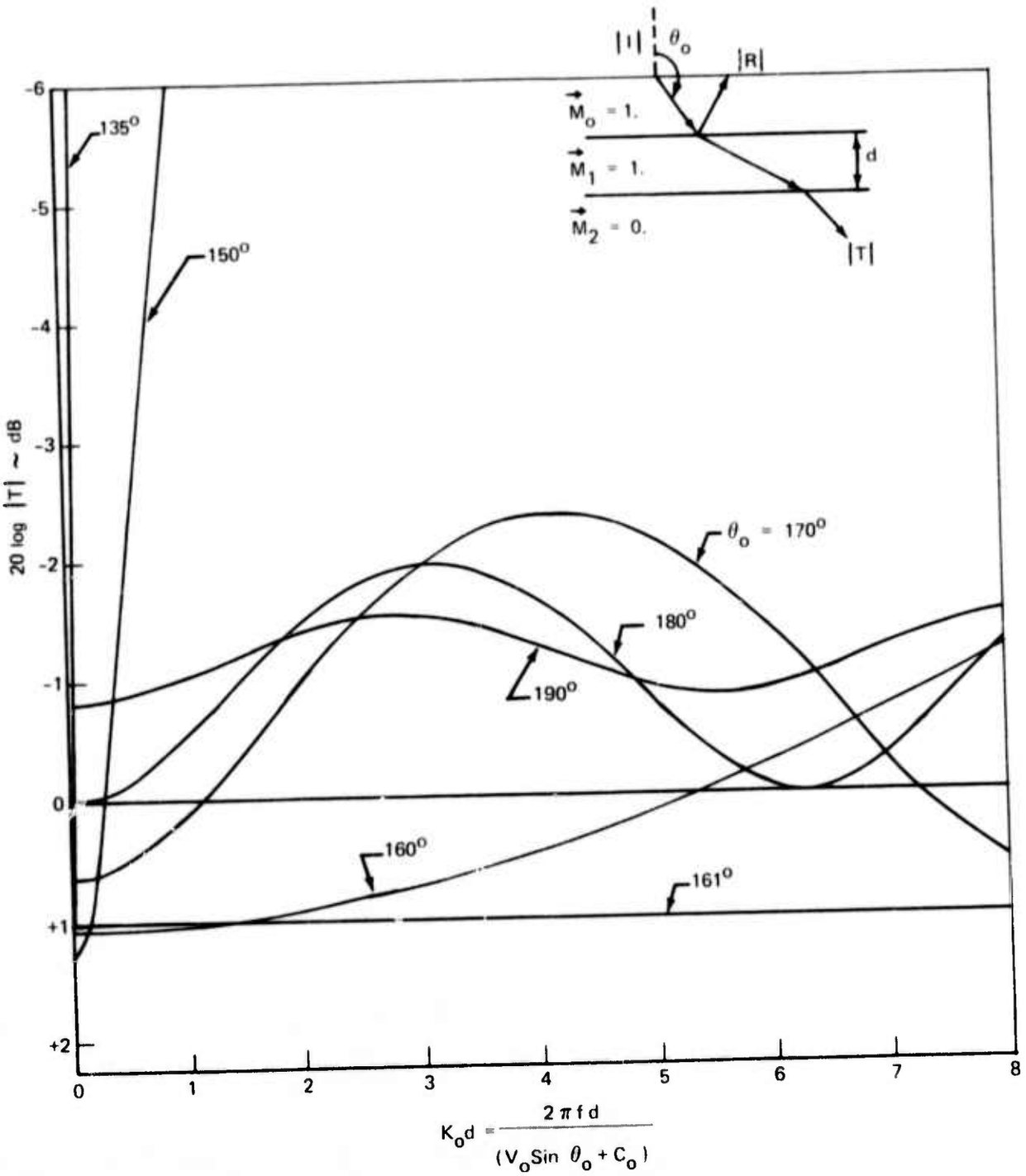

Figure 140. — Transmission Coefficient Spectrum

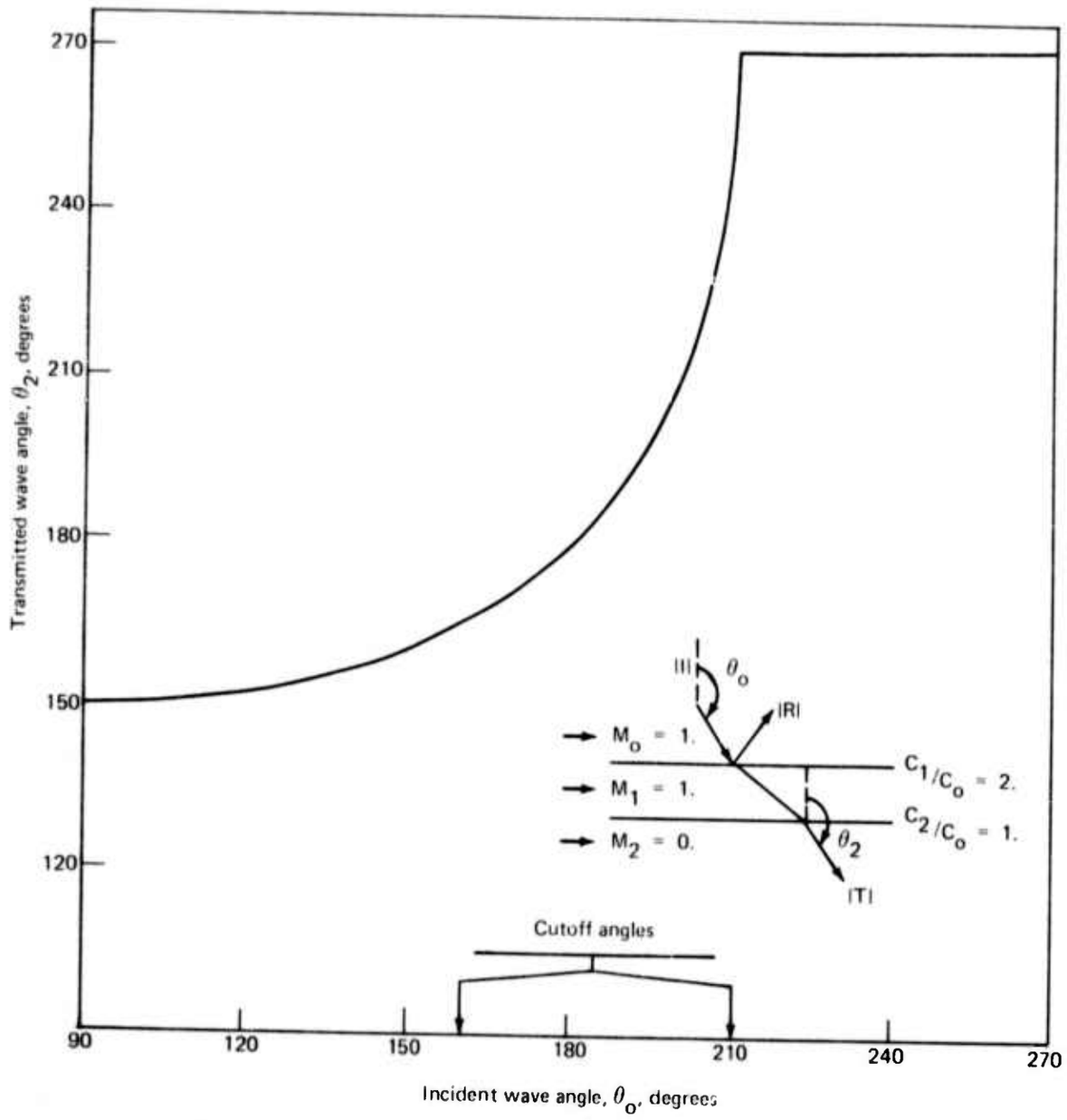

Figure 141. — Spatial Redistribution of the Incident Wave

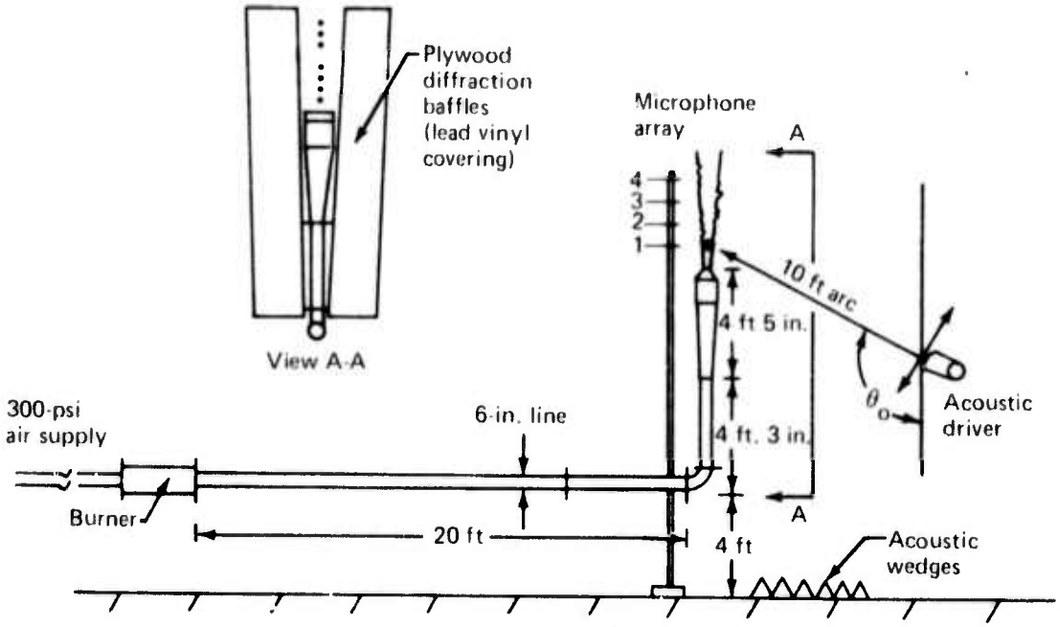

Figure 142. — Jet Noise Shield Test Schematic

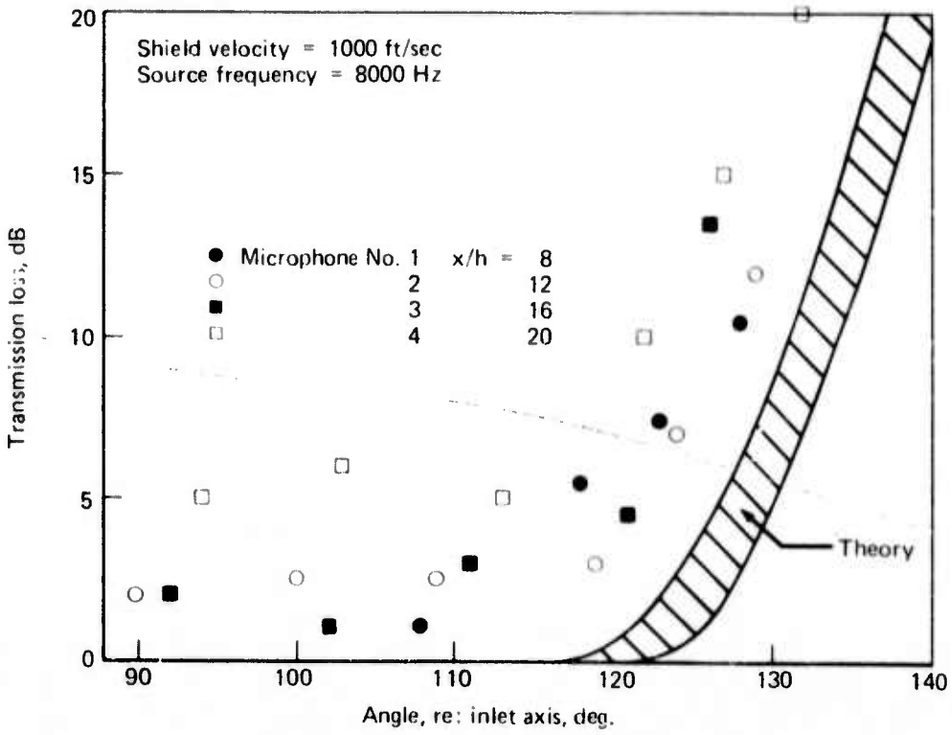

Figure 143. — Tone Source, Measured Transmission Loss

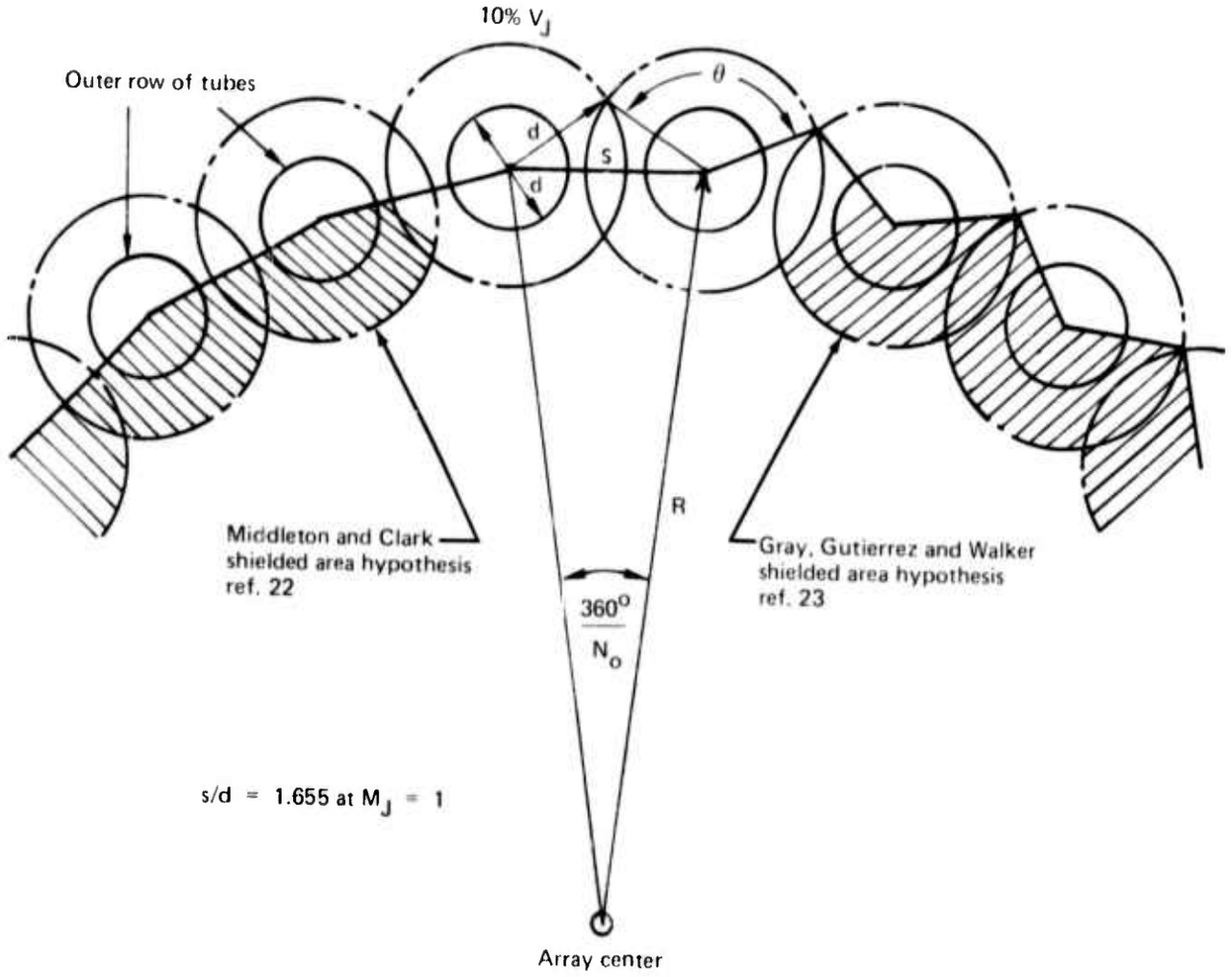

Figure 144. — 24-Tube Annulus Arrangement Shielding Geometry

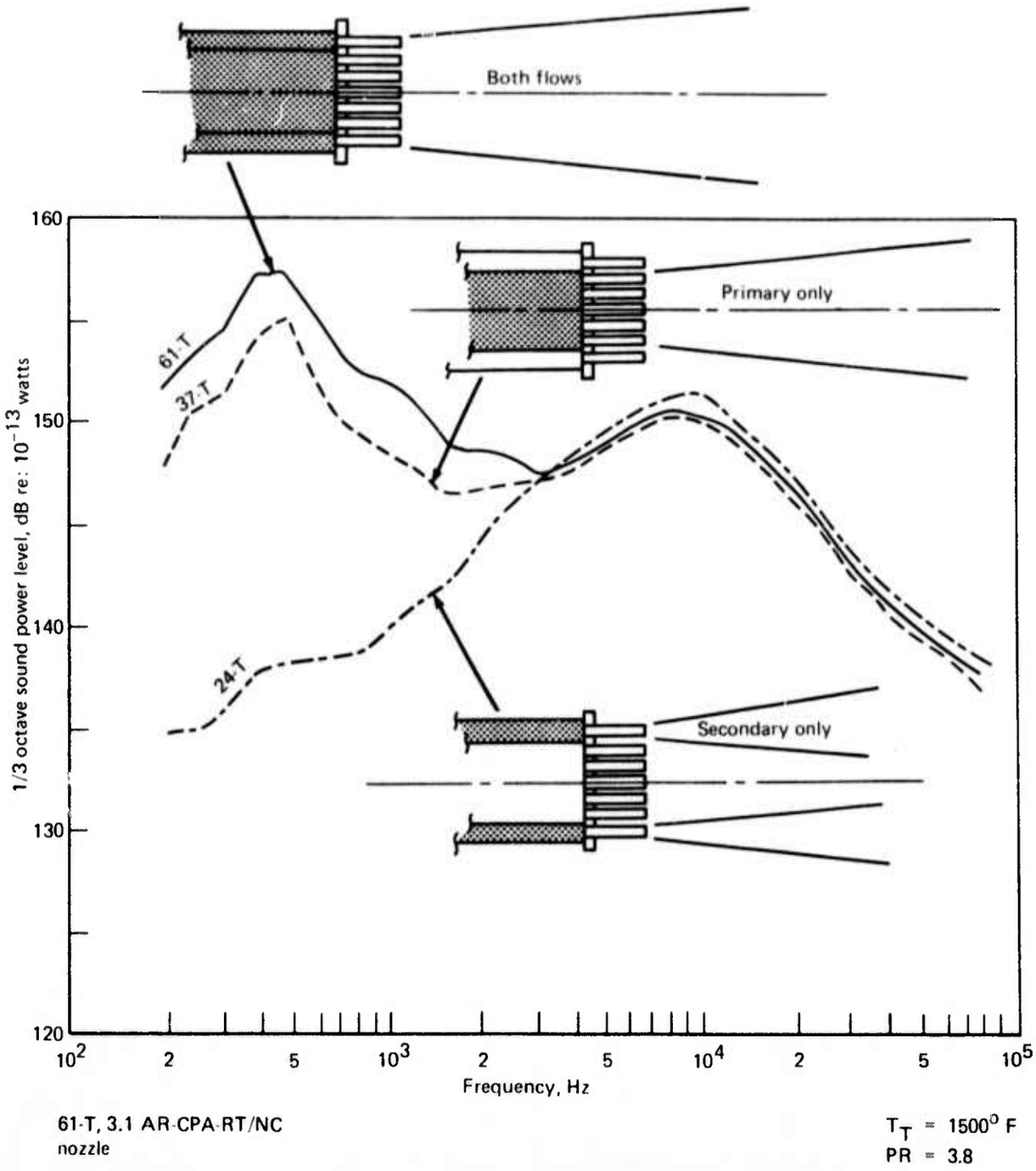

Figure 145. — Multielement Jet Component Noise Levels

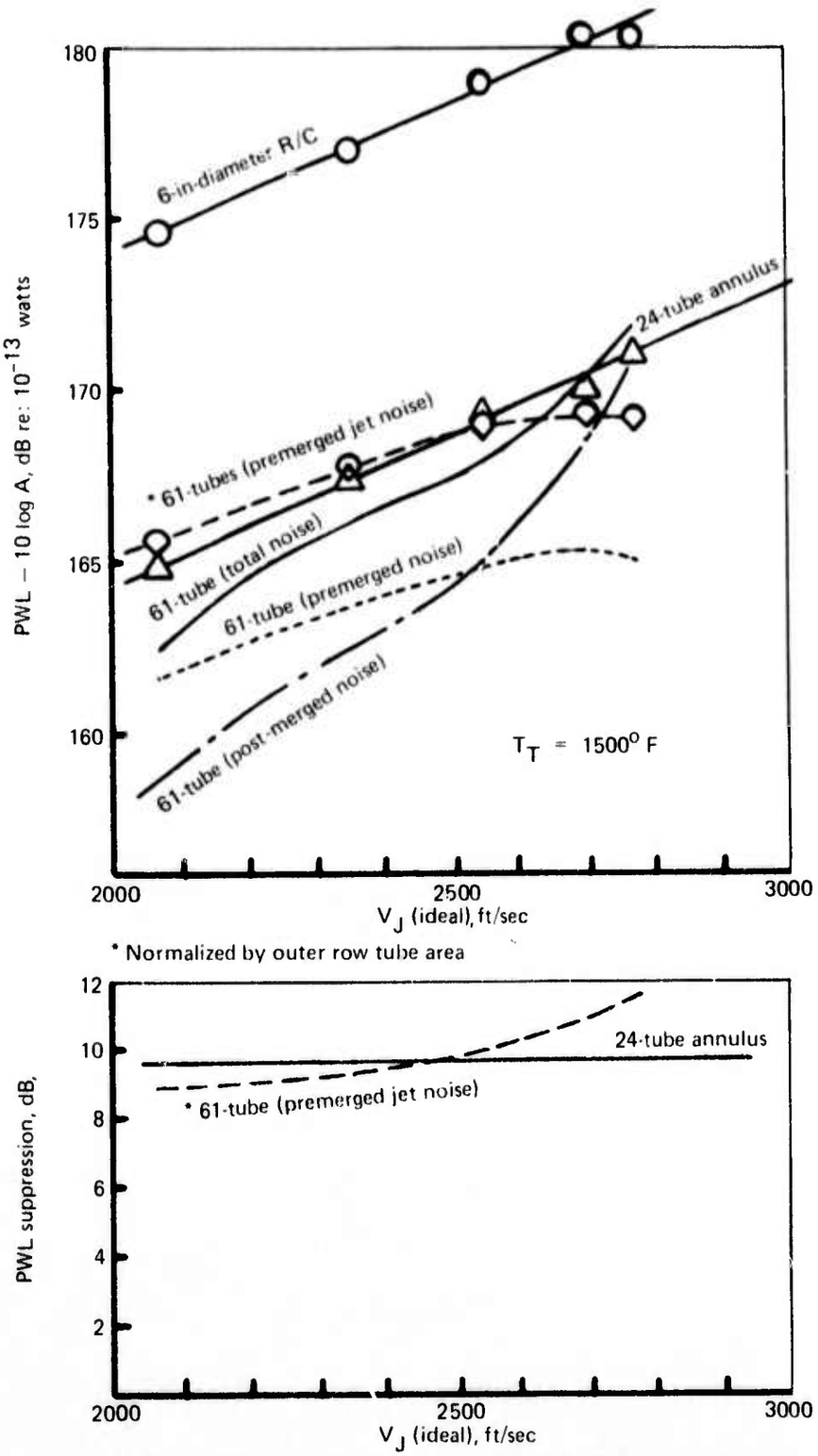

Figure 146. — Premerged Jet Noise Normalized Power Levels for a 61-Tube (CPA) Nozzle and 24-Annulus Tube

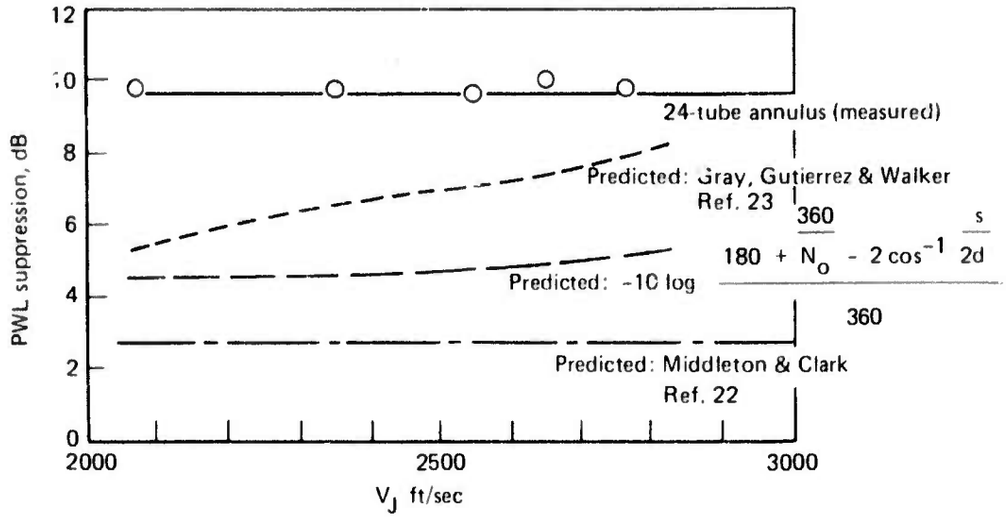

Figure 147. — Premerged Jet Noise Geometric Shielding Suppression Predictions Versus Measured Suppression

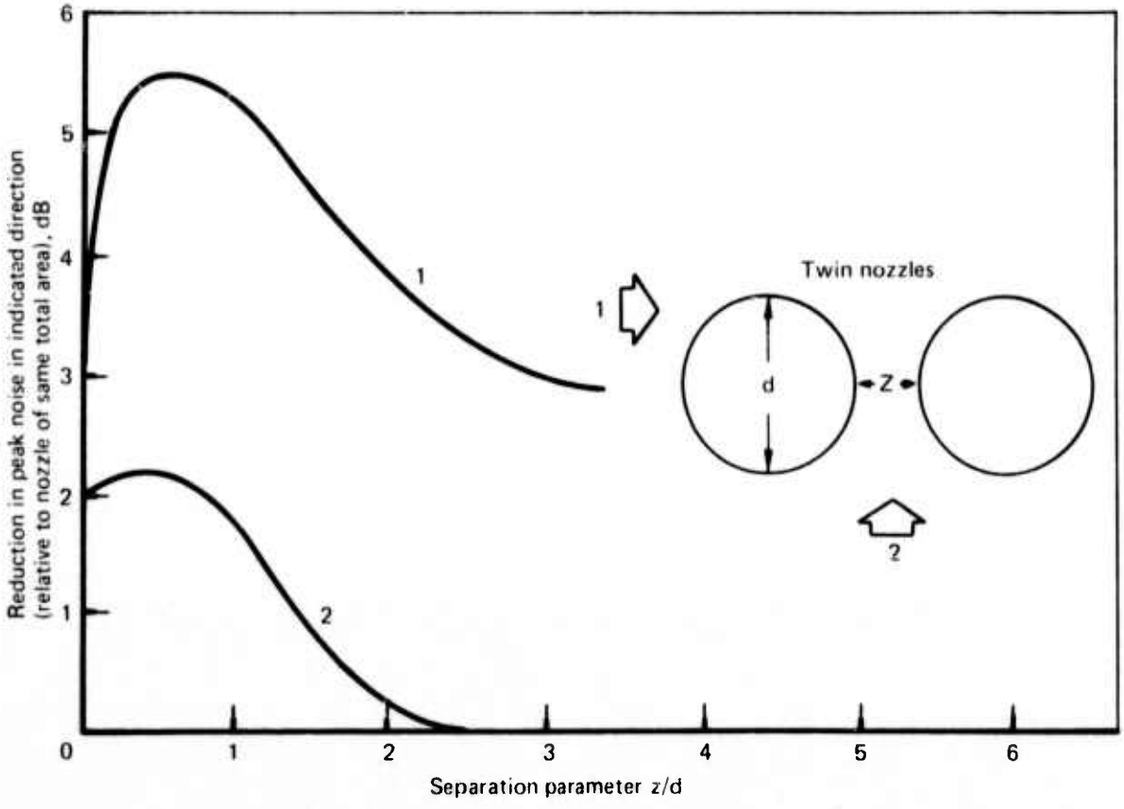

Figure 148. — The Noise Pattern of Two Jets in Proximity

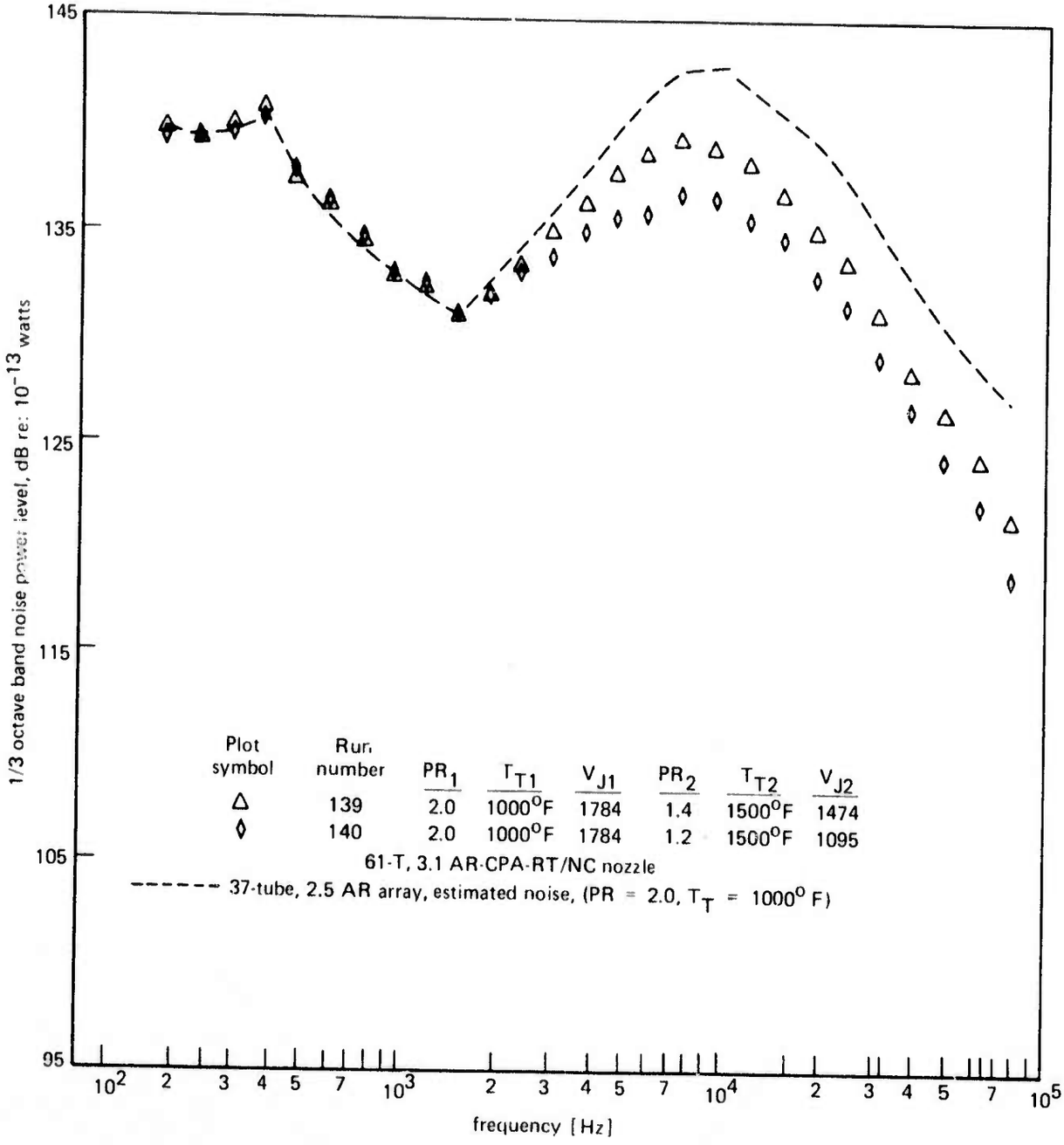

Figure 149. — Dual-Flow Noise Power Spectra for Constant Secondary Flow Total Temperature (Case 1.)

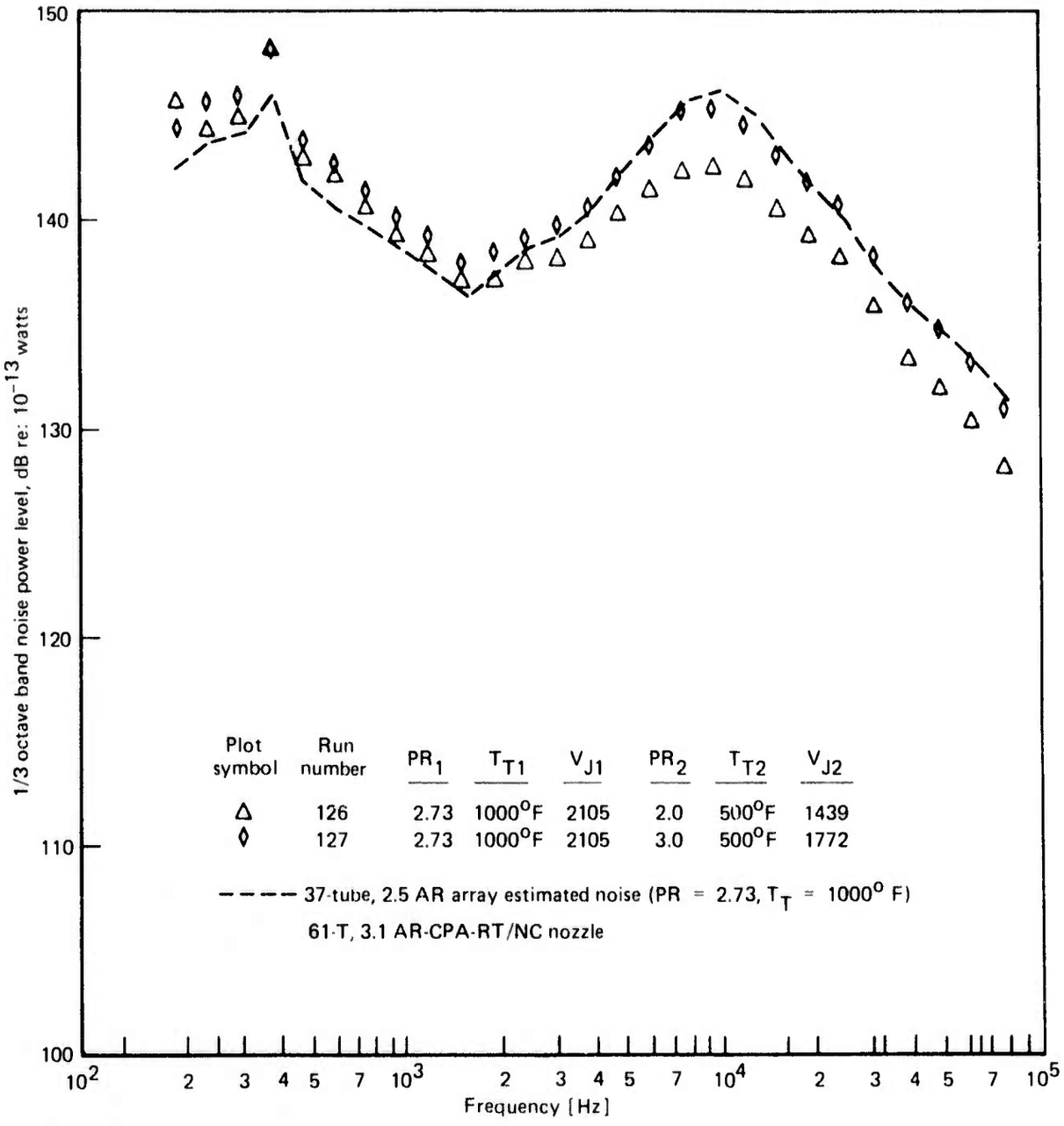

Figure 150. — Dual-Flow Noise Power Spectra for Constant Secondary Flow Total Temperature (Case 2)

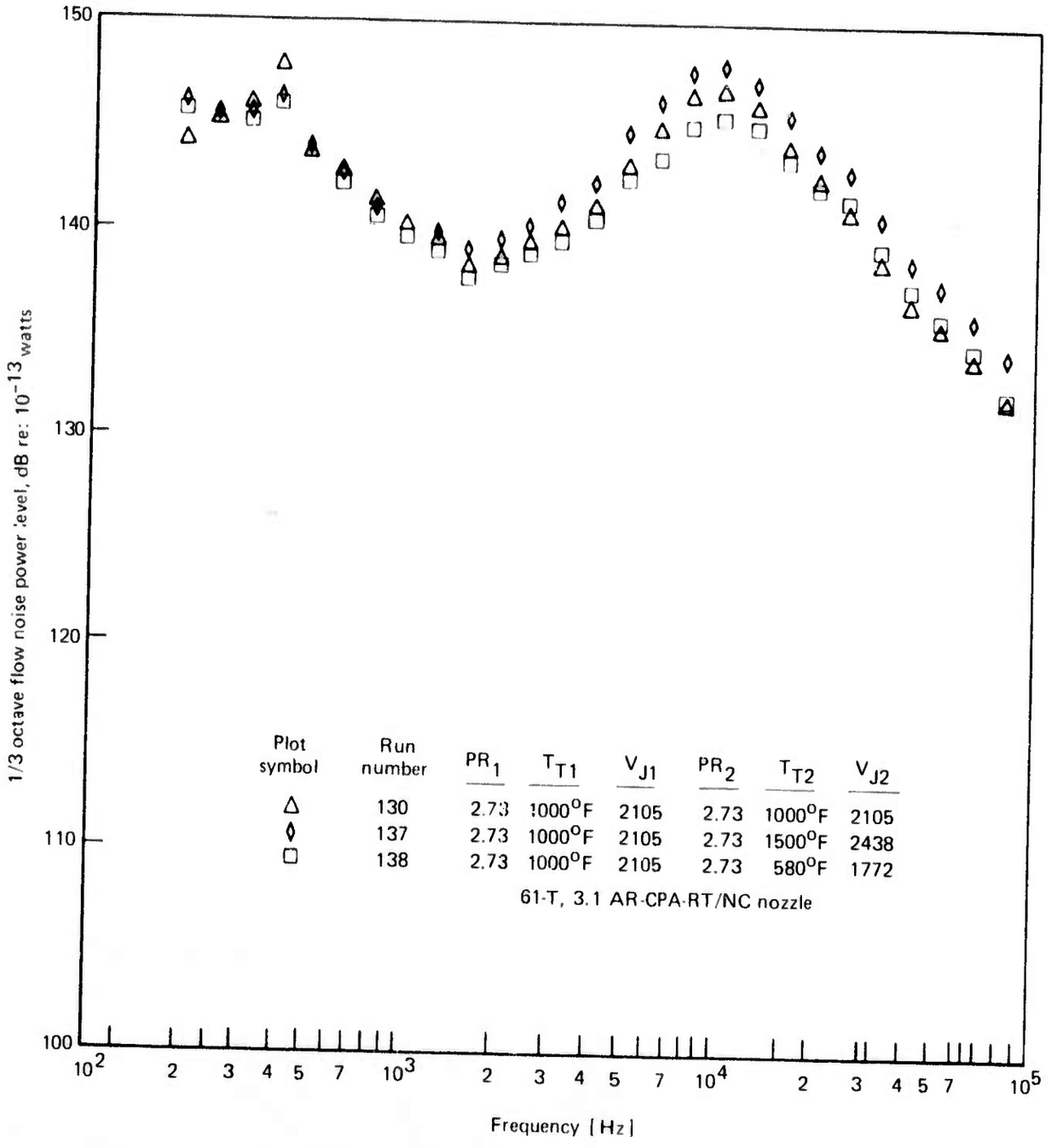

Figure 151. — Dual-Flow Noise Power Spectra For Constant Secondary Flow Pressure Ratio

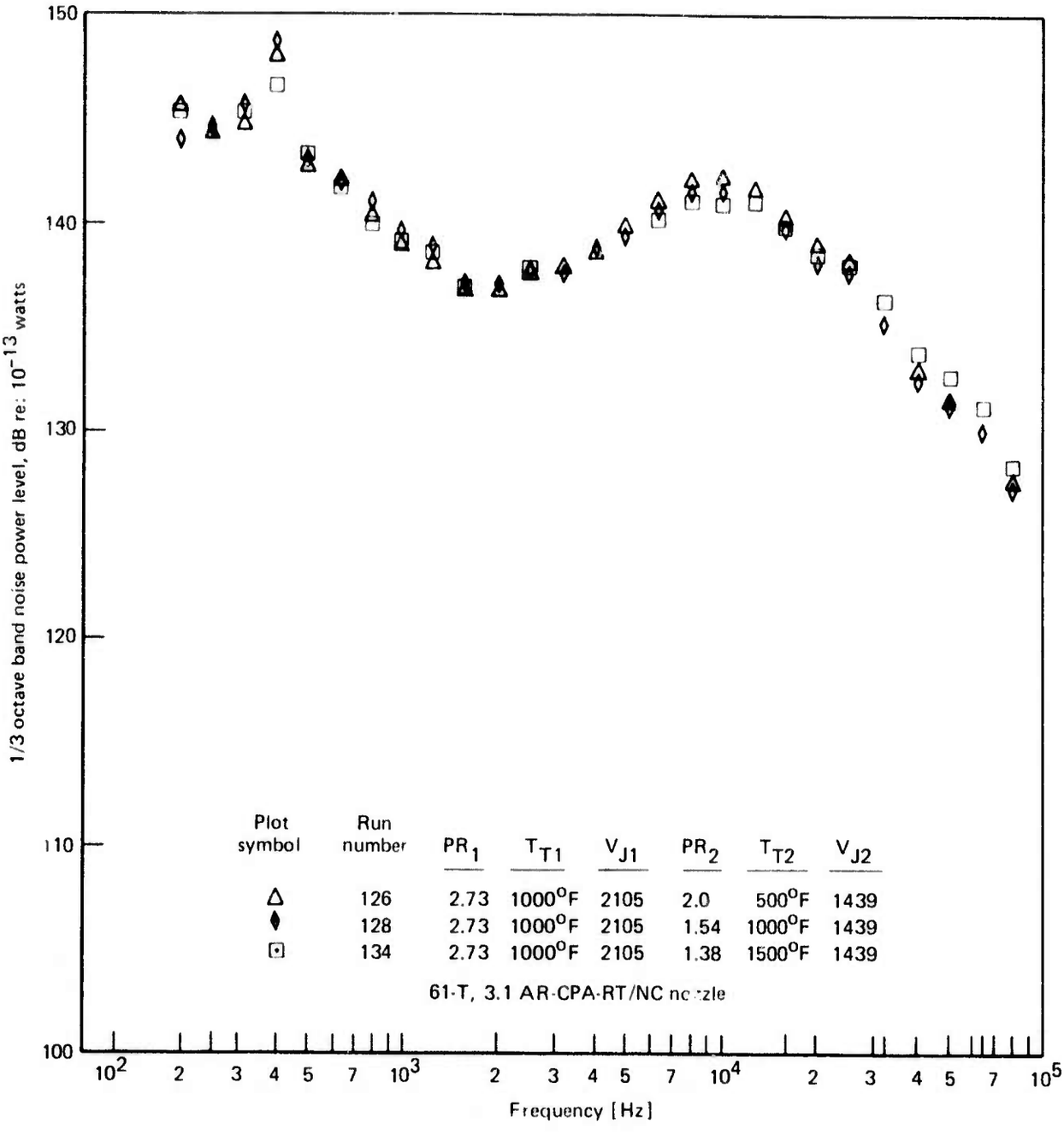

Figure 152. — Dual-Flow Noise Power Spectra for Constant Secondary Flow Jet Velocity (Case 1)

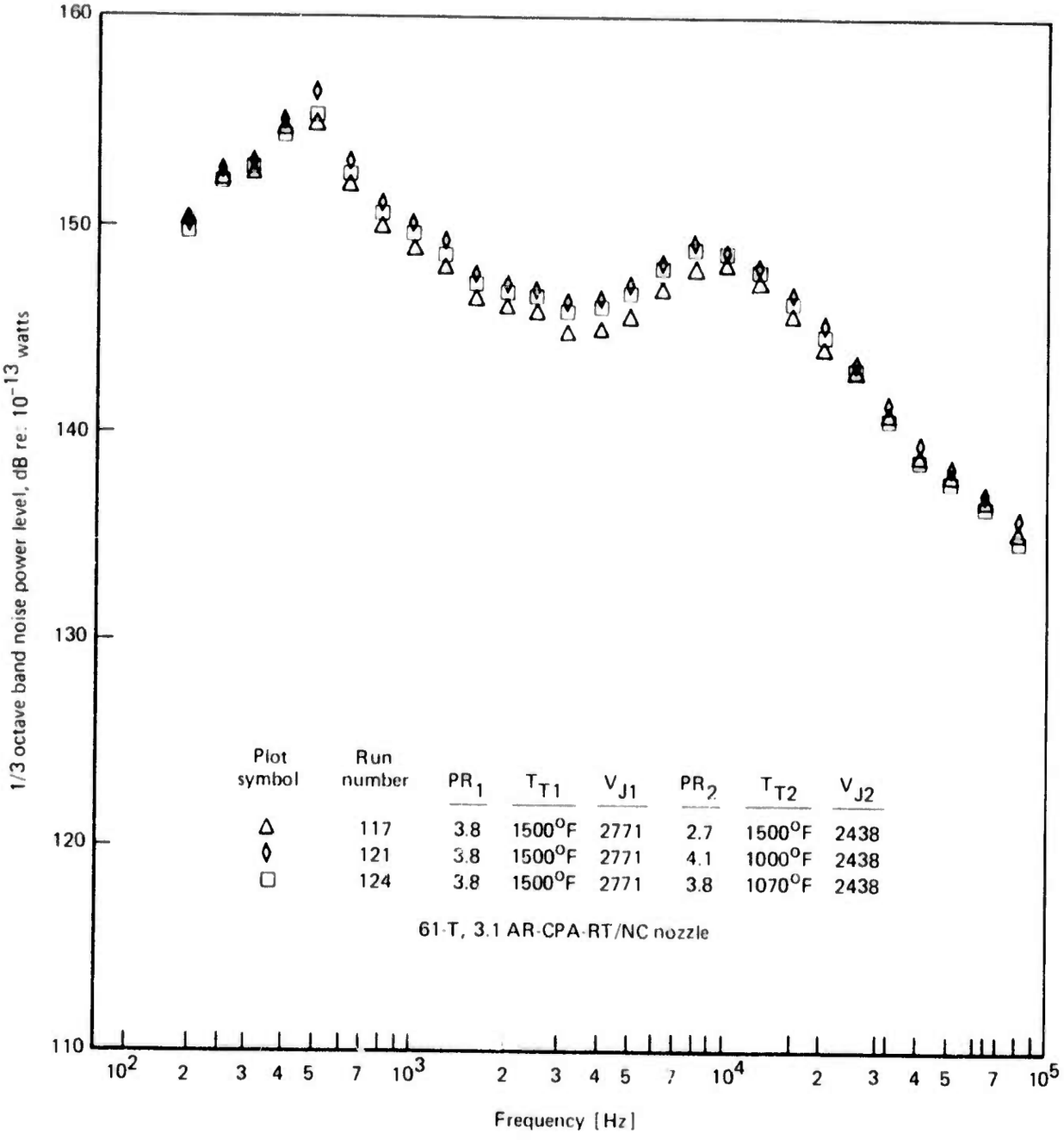

Figure 153. — Dual-Flow Noise Power Spectra for Constant Secondary Flow Jet Velocity (Case 2)

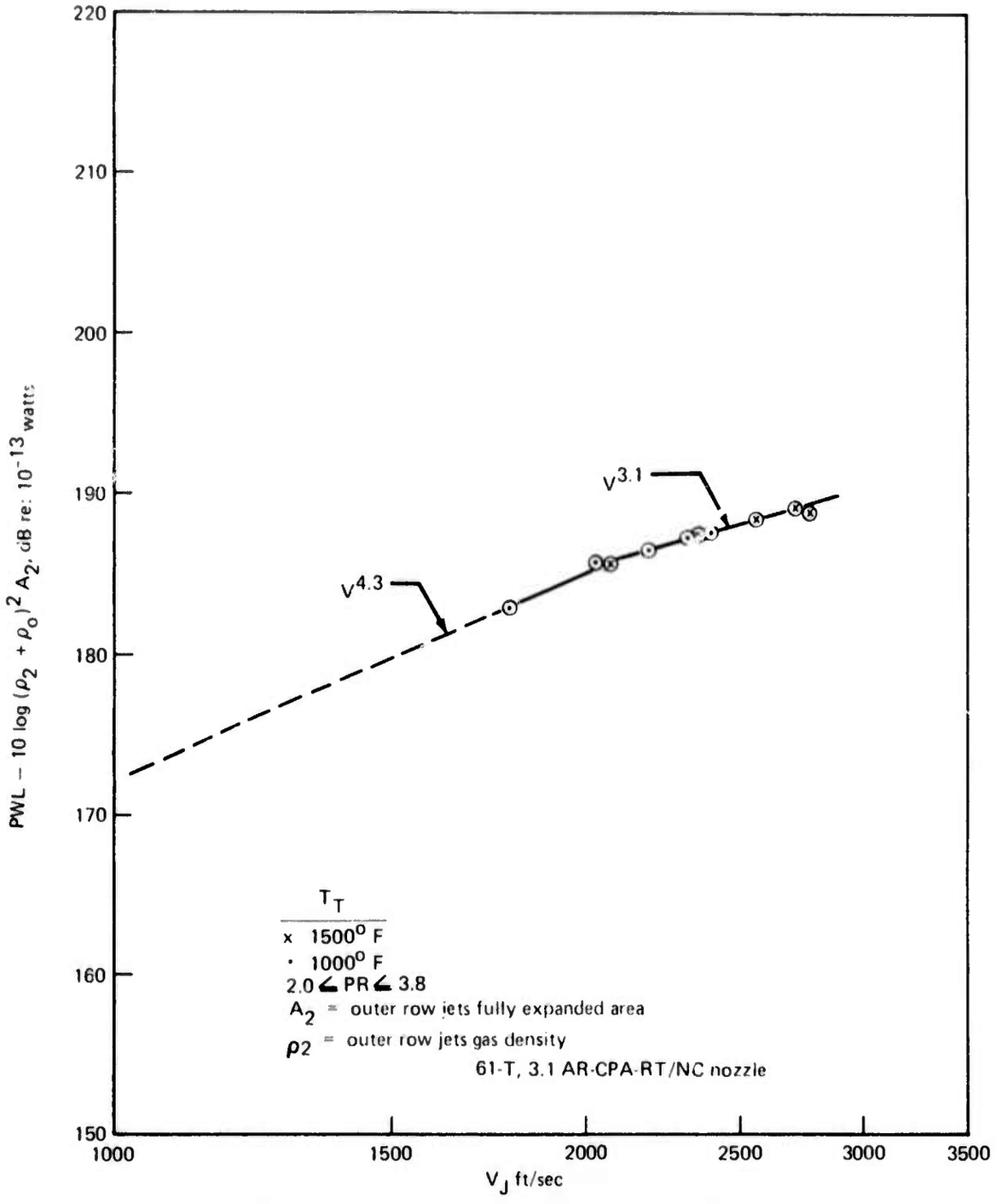

Figure 154. — 61-Tube Nozzle Normalized Premerged Jet Noise Power

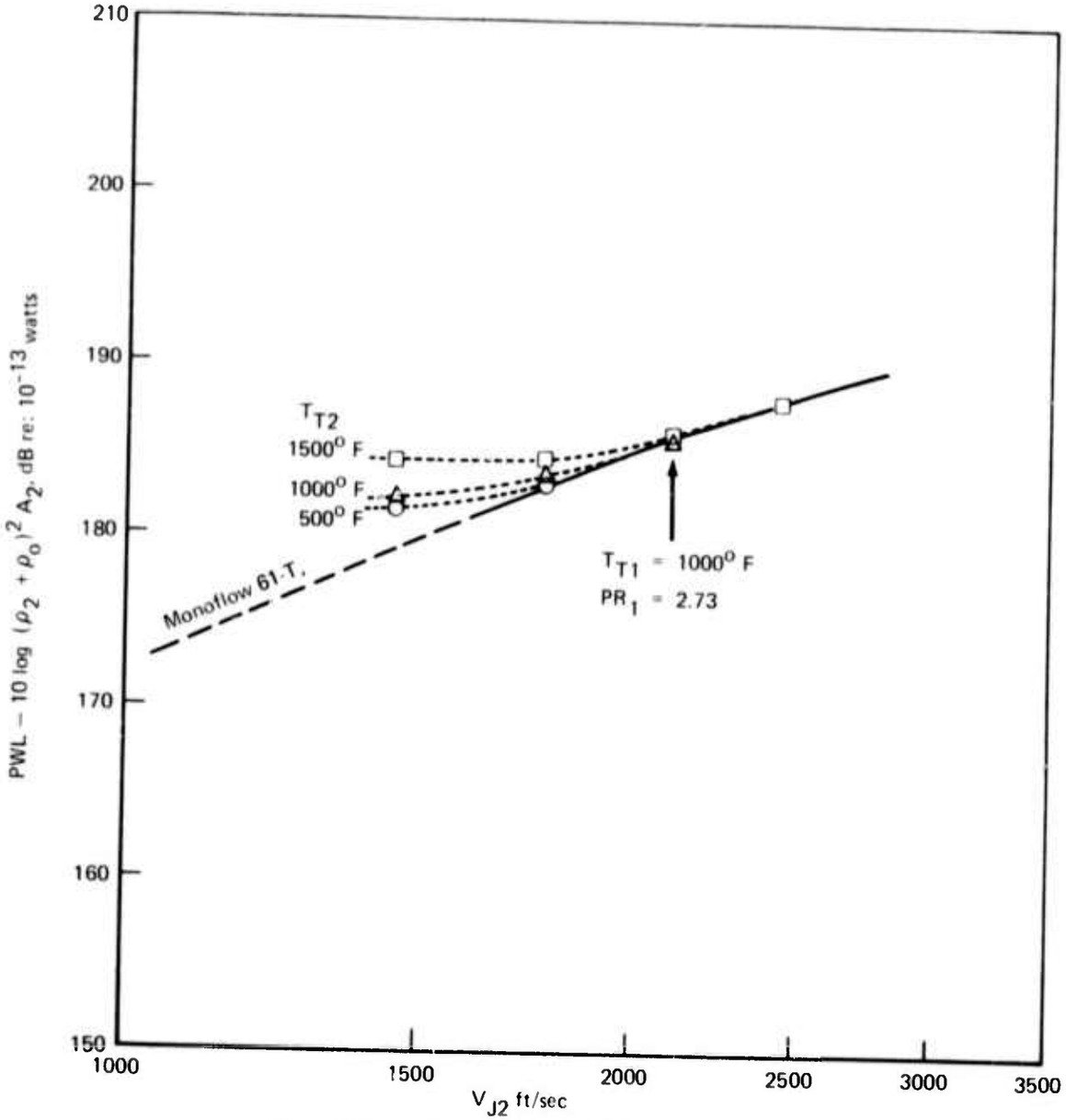

Run	PR_1	T_{T1}	V_{J1}	PR_2	T_{T2}	V_{J2}
126	2.73	1000°F	2105	2.0	500°F	1439
127	2.73	1000°F	2105	3.0	500°F	1772
128	2.73	1000°F	2105	1.54	1000°F	1439
129	2.73	1000°F	2105	1.94	1000°F	1747
130	2.73	1000°F	2105	2.73	1000°F	2105
134	2.73	1000°F	2105	1.38	1500°F	1443
135	2.73	1000°F	2105	1.64	1500°F	1772
136	2.73	1000°F	2105	2.05	1500°F	2105
137	2.73	1000°F	2105	2.7	1500°F	2438

Figure 155. — 61-Tube Nozzle Normalized Dual-Flow Premerged Jet Noise Power

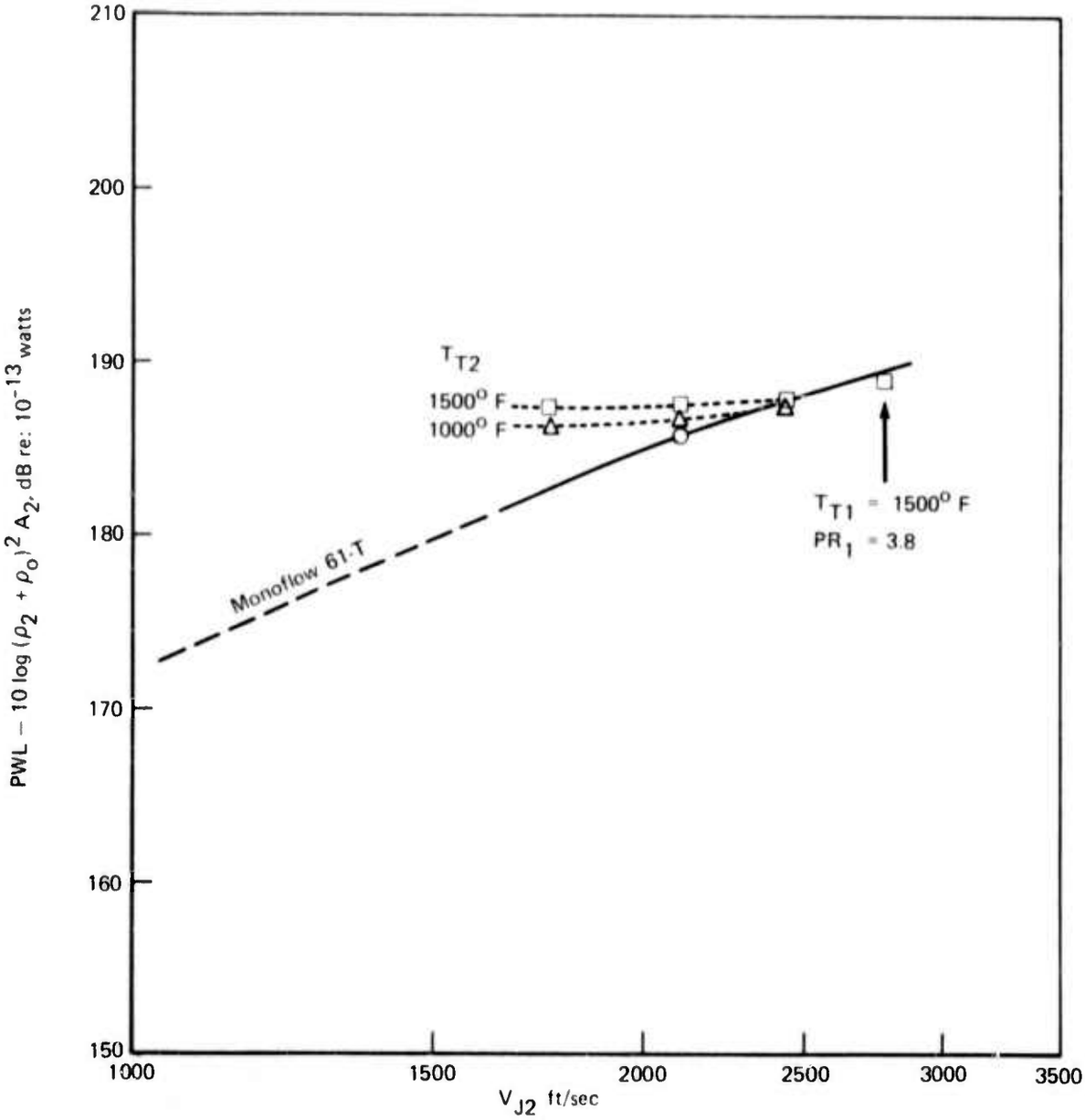

Run	PR_1	T_{T1}	V_{J1}	PR_2	T_{T2}	V_{J2}
115	3.8	1500°F	2771	1.64	1500°F	1772
116	3.8	1500°F	2771	2.05	1500°F	2105
117	3.8	1500°F	2771	2.7	1500°F	2438
118	3.8	1500°F	2771	3.8	1500°F	2771
119	3.8	1500°F	2771	1.98	1000°F	1772
120	3.8	1500°F	2771	2.73	1000°F	2105
121	3.8	1500°F	2771	4.1	1000°F	2438
125	3.8	1500°F	2771	3.8	690°F	2105

Figure 156. — 61-Tube Nozzle Normalized Dual-Flow Premerged Jet Noise Power (Case 2.)

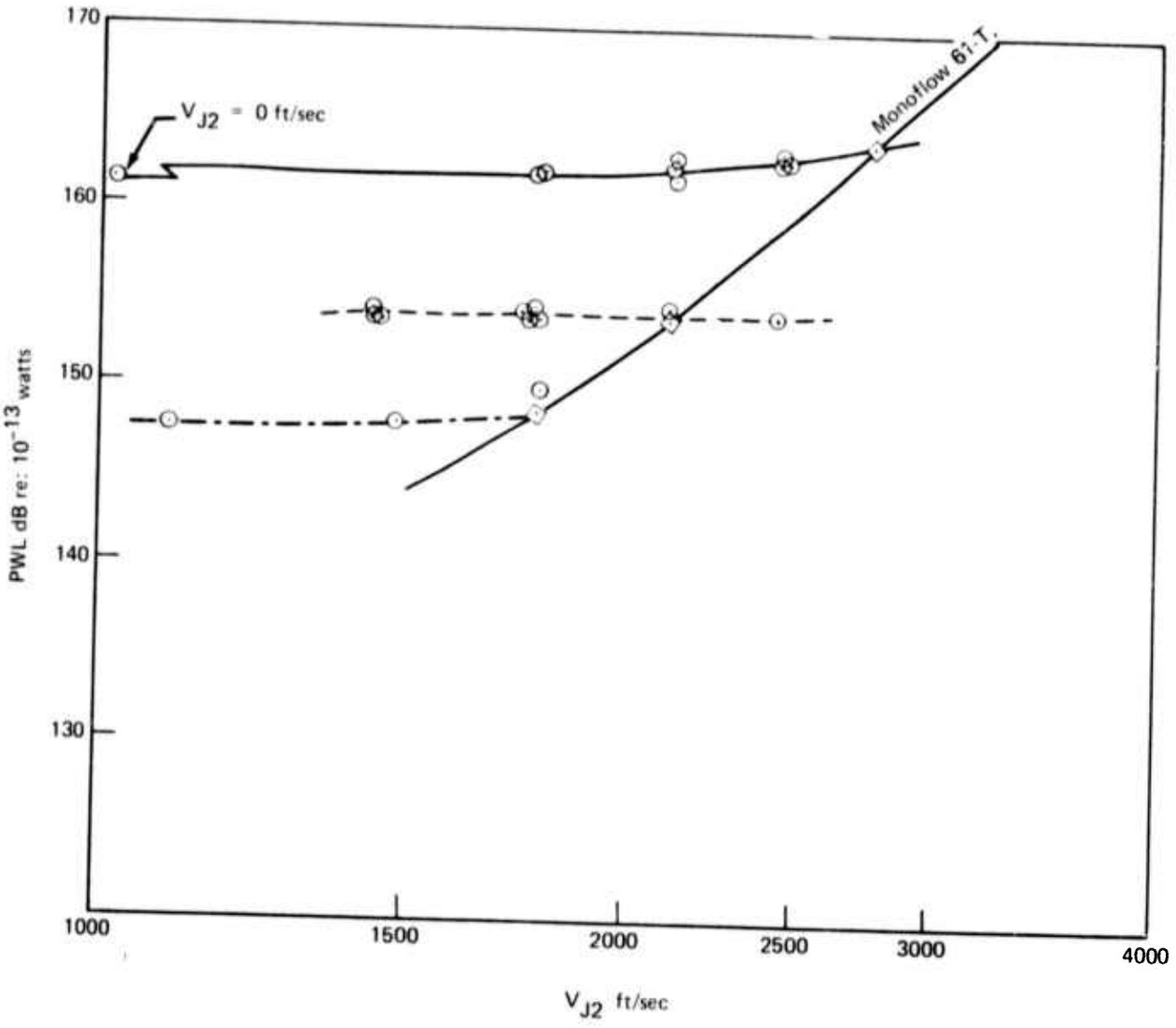

PR_1 = 3.8 T_{T1} = 1500° F V_{J1} = 2771 ft/sec (1.64 ≤ PR_2 ≤ 4.1, 690°F ≤ T_{T2} ≤ 1500°F)

PR_1 = 2.73 T_{T1} = 1000° F V_{J1} = 2105 ft/sec (1.38 ≤ PR_2 ≤ 3.0, 500°F ≤ T_{T2} ≤ 1500°F)

PR_1 = 2.0 T_{T1} = 1000°F V_{J1} = 1784 ft/sec (1.2 ≤ PR_2 ≤ 2.0, 1000°F ≤ T_{T2} ≤ 1500°F)

V_{J1} = V_{J2}

61-tube, 3.1 AR nozzle
Primary flow: inner array of 37 tubes
Secondary flow: outer row of 24 tubes

Figure 157. — Jet Postmerging Noise Power Levels for Dual-Flow Gas Conditions

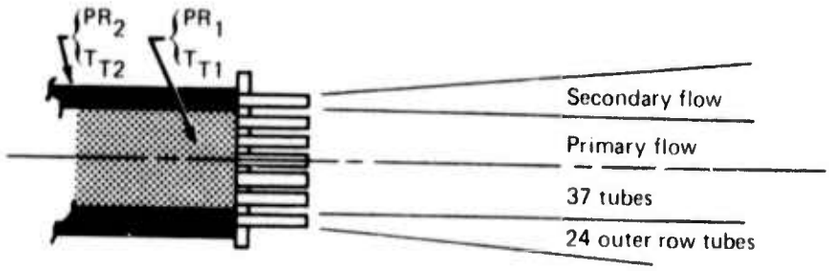

61-T, 3.1 AR-CPA-RT/NC nozzle

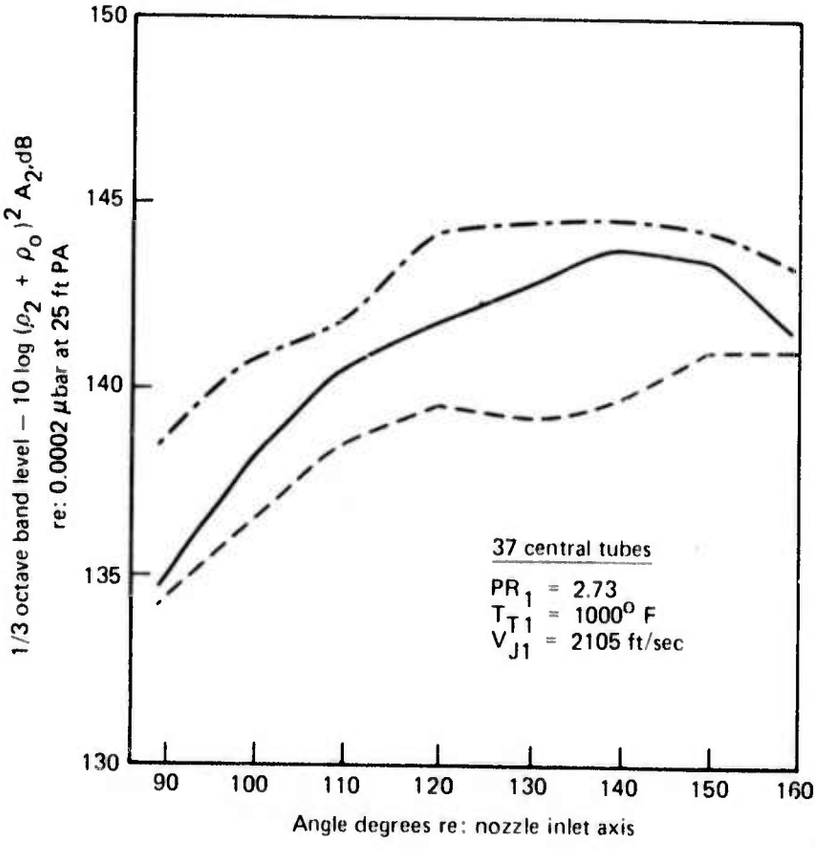

	24 outer row tubes		
	PR_2	T_{T2}	V_{J2}
———	2.73	1000° F	2105 ft/sec
– – – –	2.73	580° F	1772 ft/sec
———	2.73	1500° F	2438 ft/sec

Figure 158. — Dual-Flow Premerging Jet Noise Levels at 10 kHz for Constant PR_2

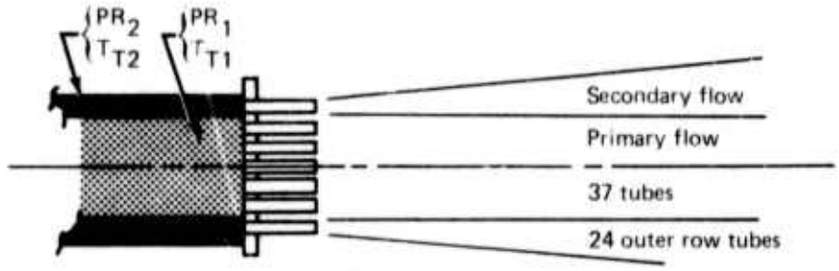

61-T, 3.1 AR-CPA-RT/NC nozzle

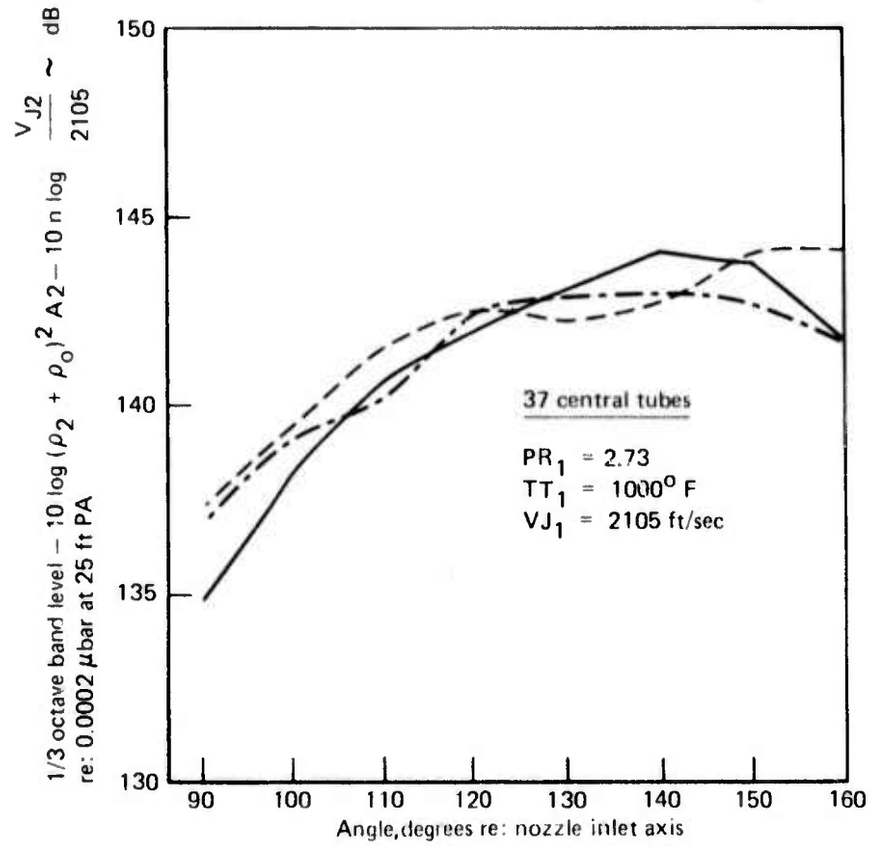

24 outer row tubes

PR	T_{T2}	V_{J2}
2.73	1000° F	2105 ft/sec
2.73	580° F	1772 ft/sec
2.73	1500° F	2438 ft/sec

Note: Velocity exponent (n) = 3.07 for $V_{J2} > 2000$ ft/sec
= 4.27 for $V_{J2} < 2000$ ft/sec

Figure 159. — Normalized Dual-Flow Premerging Jet Noise Levels at 10 kHz for Constant PR_2

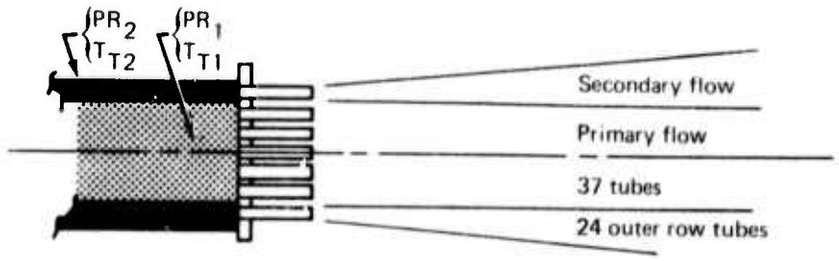

61-T, 3.1 AR-CPA-RT/NC nozzle

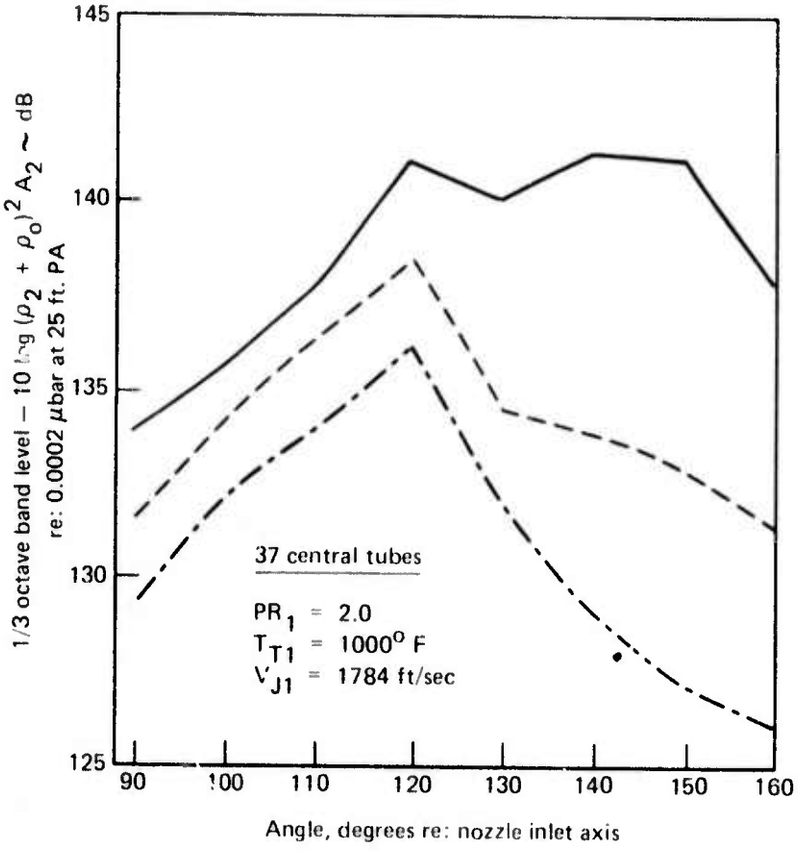

Figure 160. — Dual-Flow Premerging Jet Noise Levels at 8 kHz

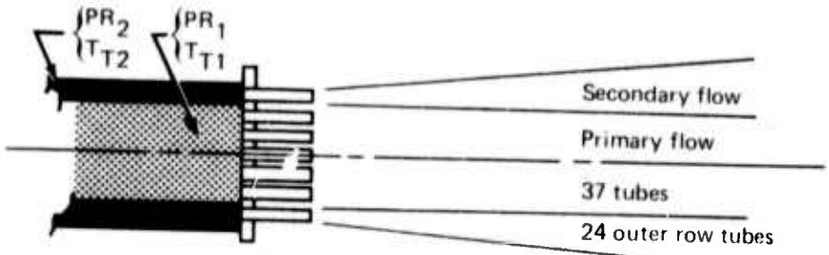

61-T, 3.1 AR-CPA-RT/NC nozzle

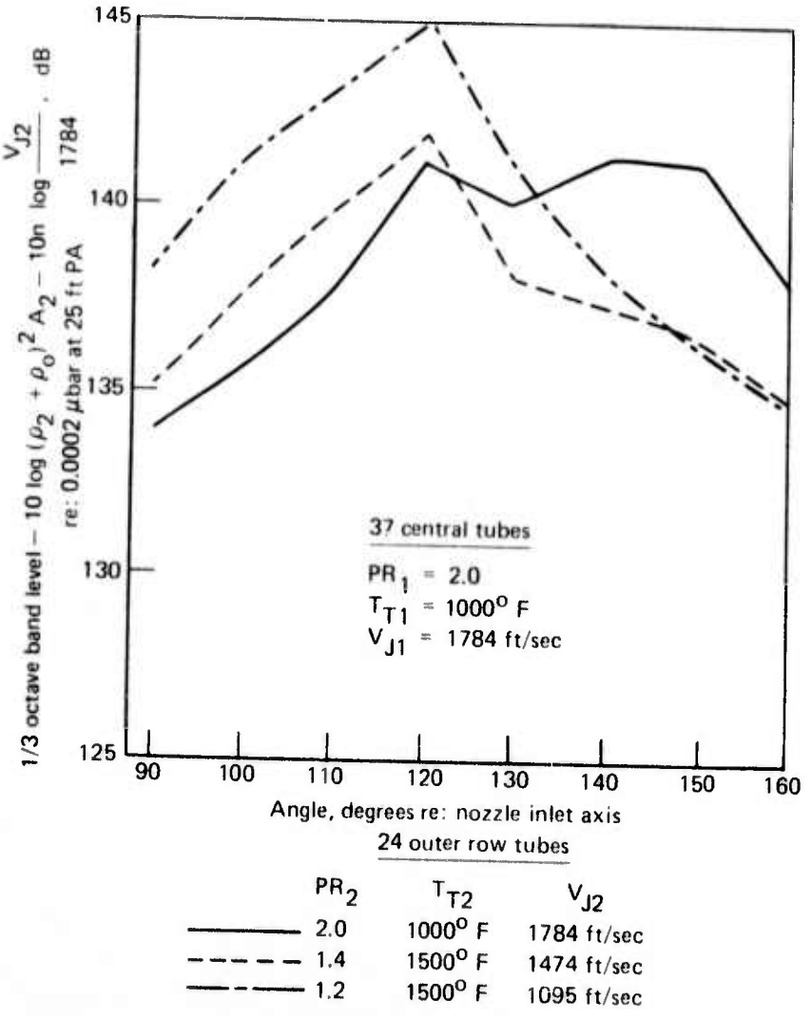

24 outer row tubes

	PR_2	T_{T2}	V_{J2}
———	2.0	1000° F	1784 ft/sec
– – – –	1.4	1500° F	1474 ft/sec
——– – ——–	1.2	1500° F	1095 ft/sec

Note: Velocity exponent (n) = 3.07 for $V_{J2} > 2000$ ft/sec
= 4.27 for $V_{J2} < 2000$ ft/sec

Figure 161. -- Normalized Dual-Flow Premerging Jet Noise Levels at 8 kHz

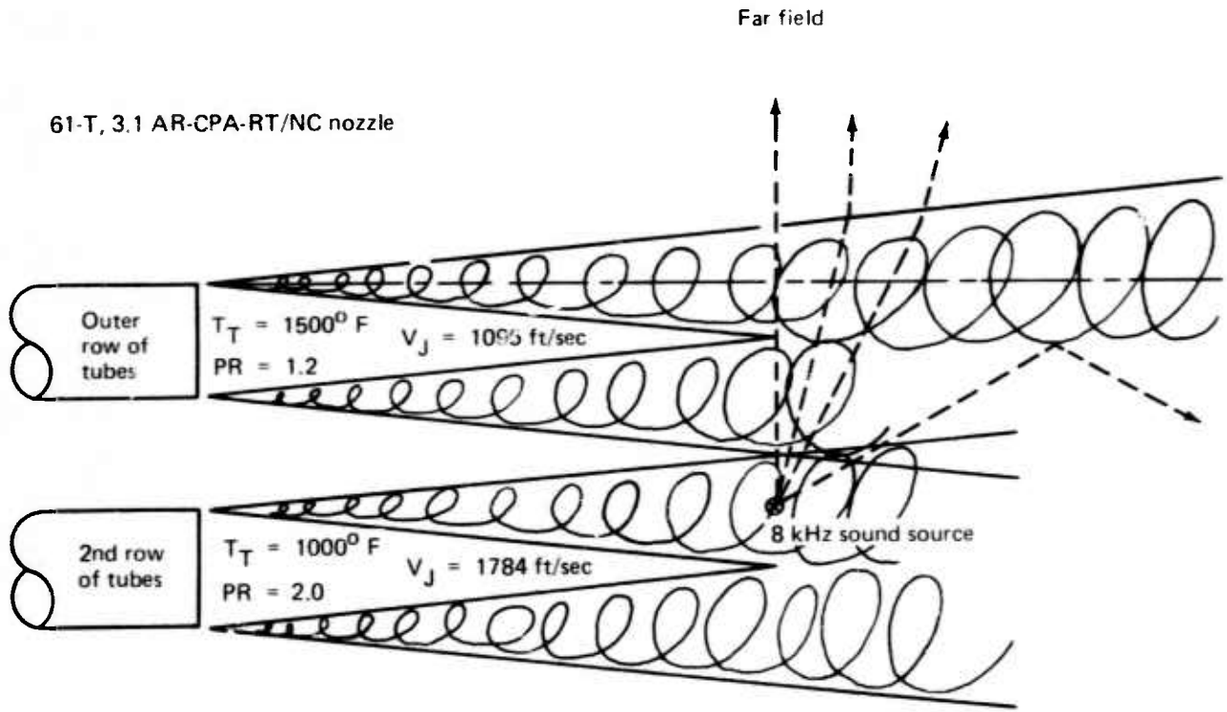

Figure 162. — A Schematic of Propagation Paths of Sound Generated in the Second Row of Jets Premerging Region

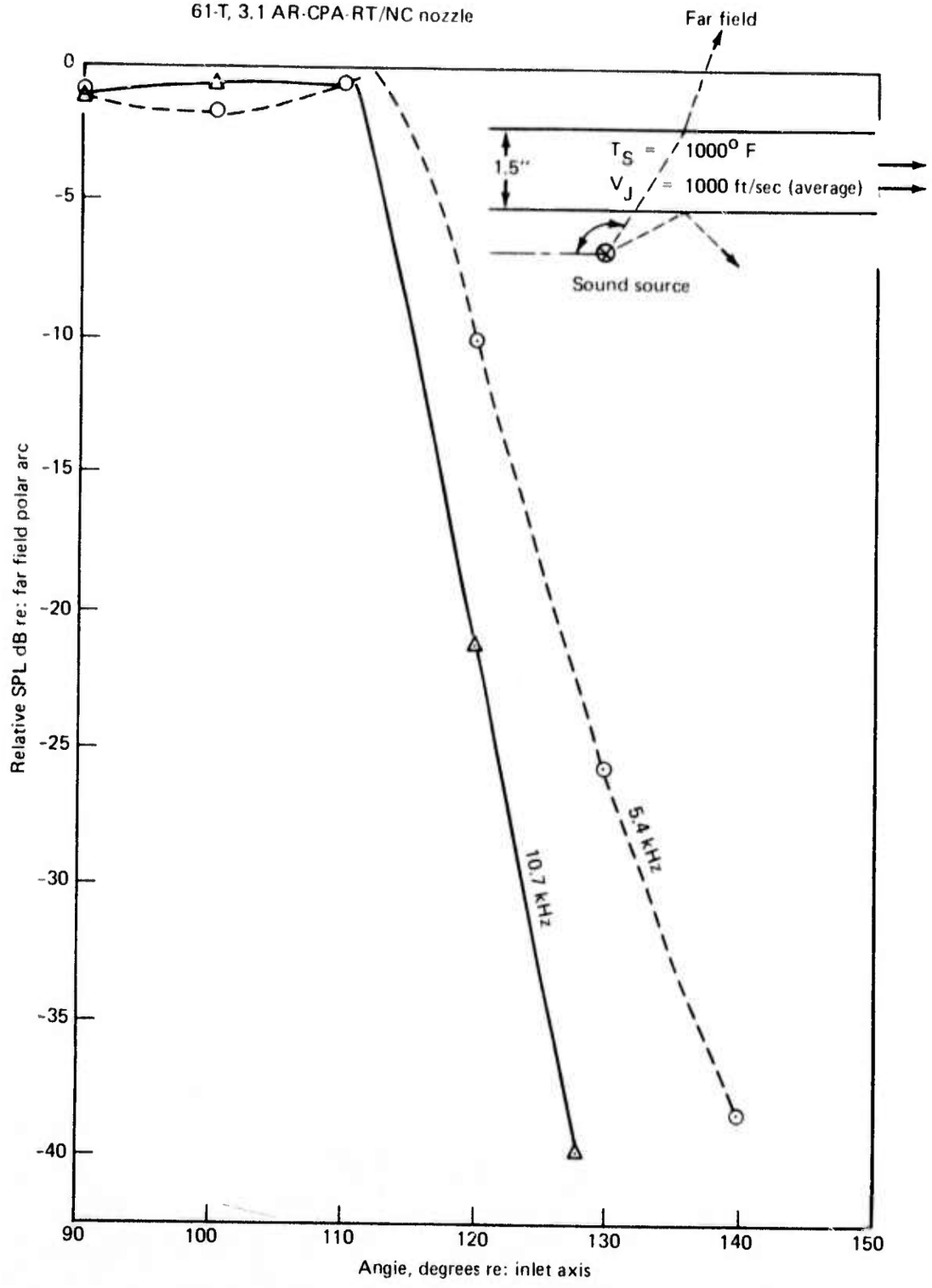

Figure 163. — Theoretical Far-Field Noise Levels with Gas-Flow Shielding

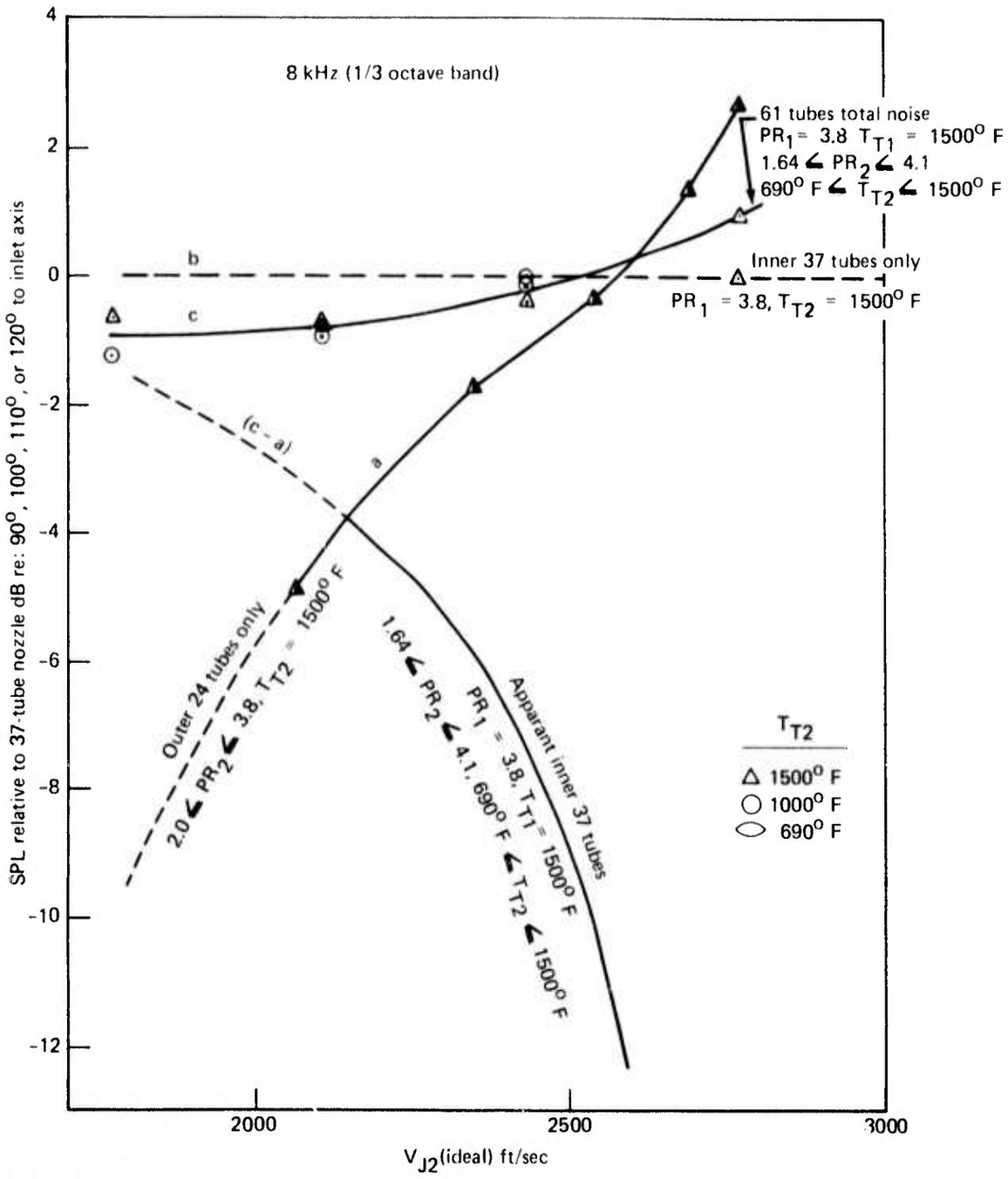

Figure 164. — Relative Peak Premerged Jet Noise Levels for Dual-Flow Conditions

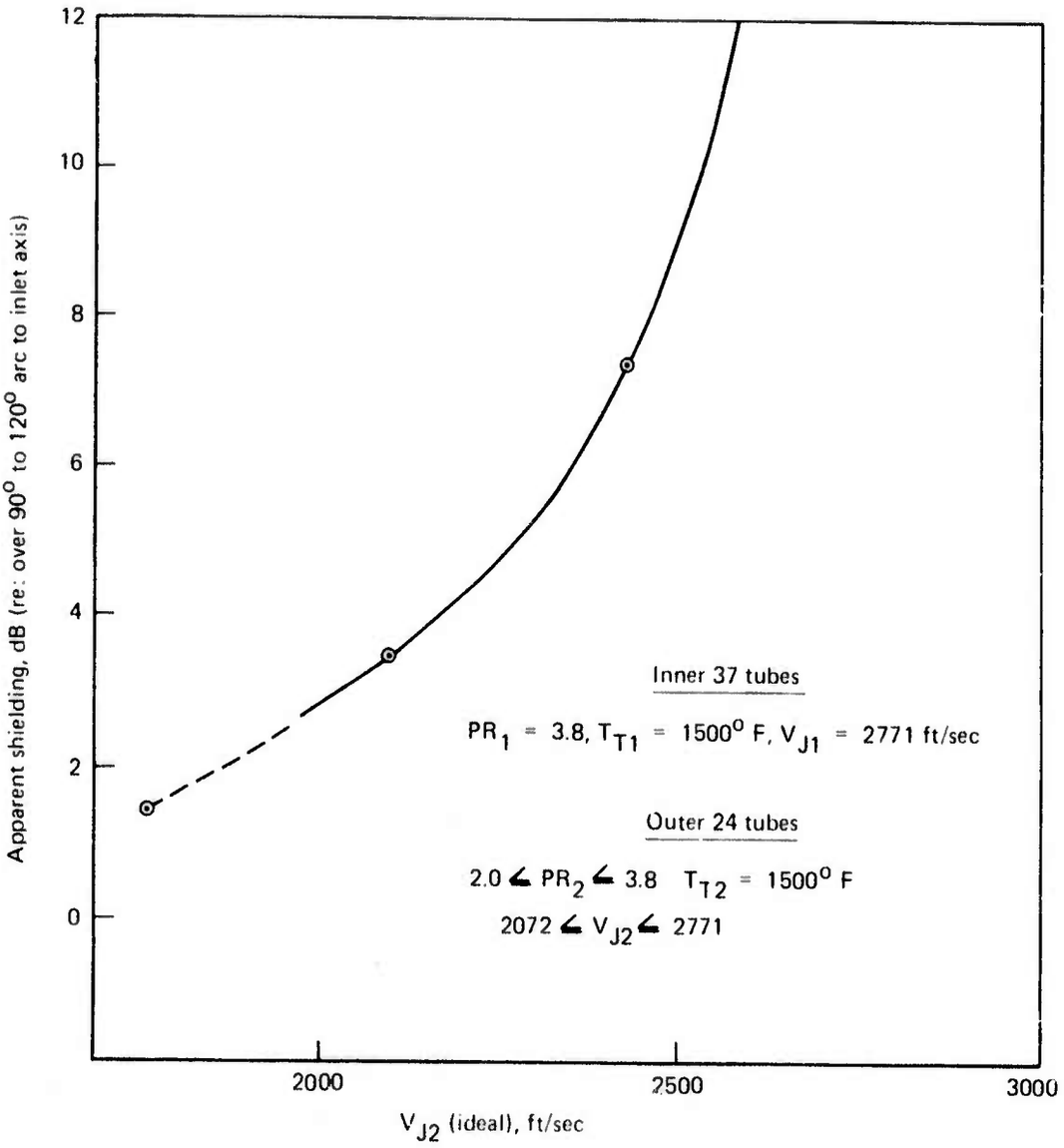

Figure 165. — Apparent Shielding of Premerged Jet Noise for Dual-Flow Conditions

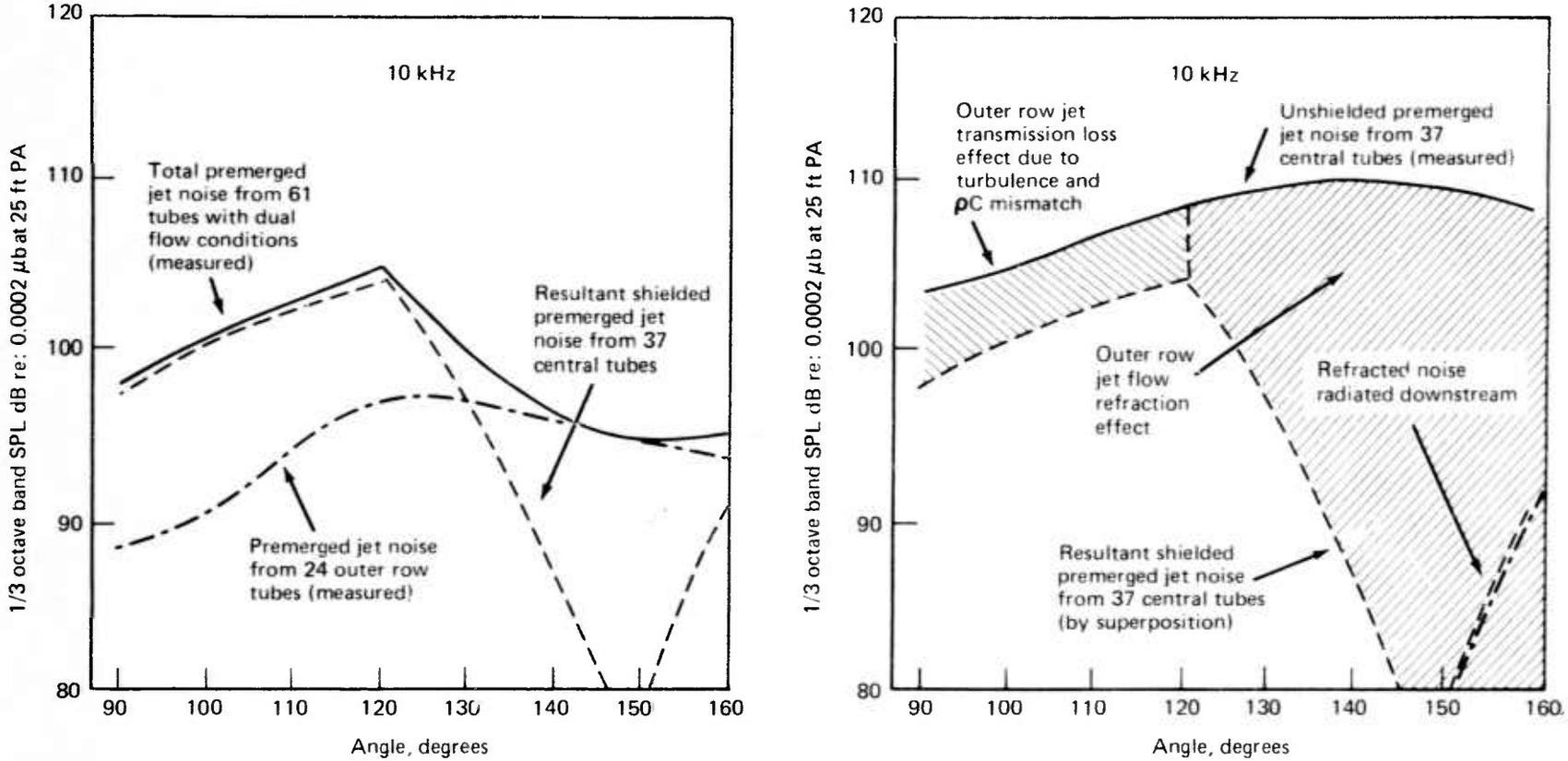

61-T, 3.1 AR-CPA-RT/NC nozzle

37 central tubes	24 outer row tubes
PR_1 = 2.0	PR_2 = 1.2
T_{T1} = 1000° F	T_{T2} = 1500° F
V_{J1} = 1784 ft/sec	V_{J2} = 1095 ft/sec

Figure 166. — Schematic of Dual-Flow Multitube Nozzle Premerged Jet Noise Relationships

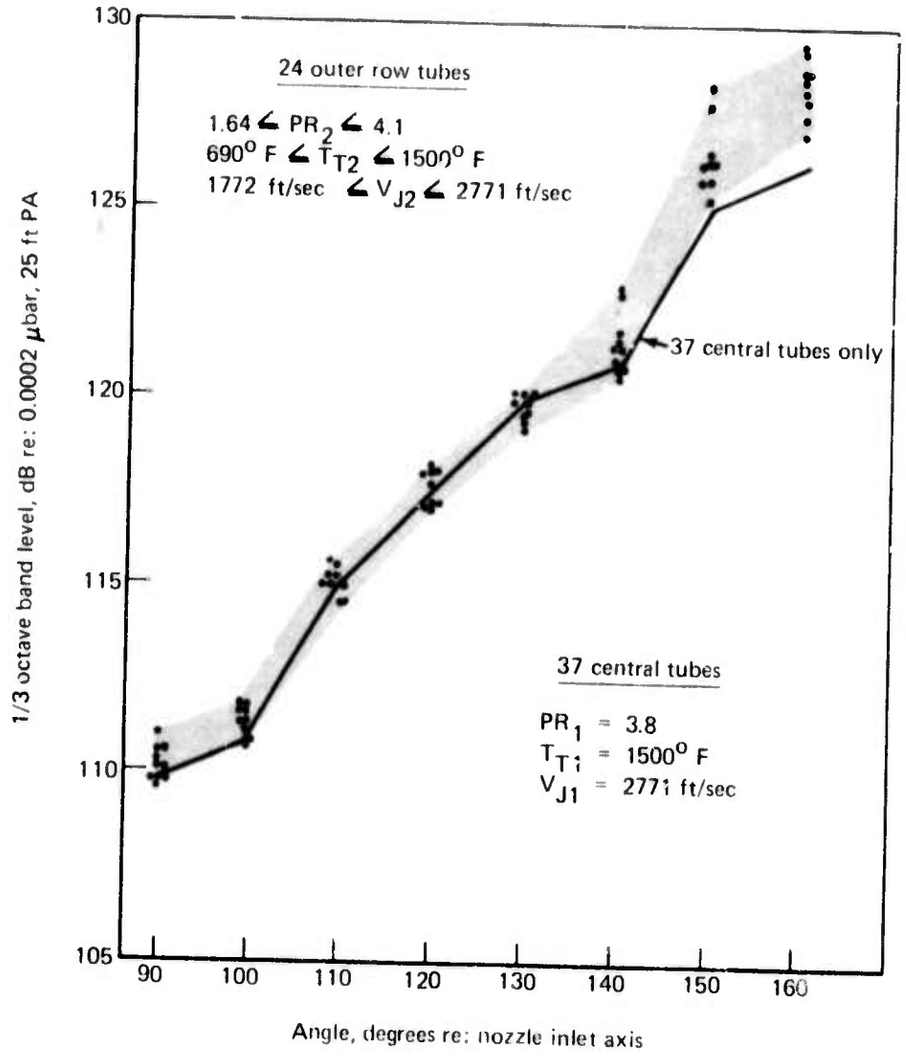

61-T, 3.1 AR-CPA RT/NC nozzle

Figure 167. — Dual-Flow Postmerging Jet Noise Beam Pattern at 500 Hz

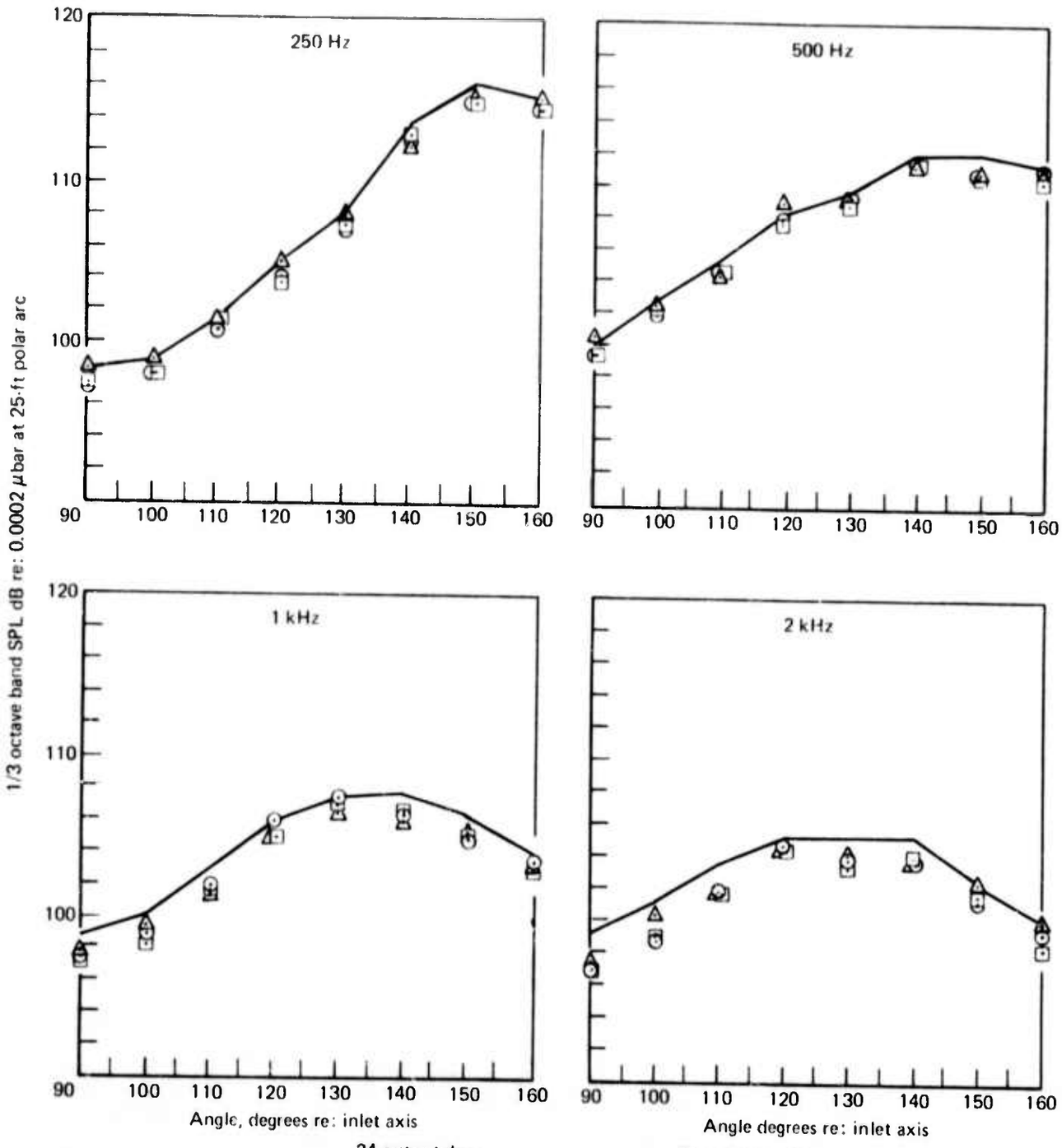

24 outer tubes — 37 central tubes

	PR_2	T_{T2}	V_{J2}	PR_1	T_{T1}	V_{J1}
—	2.73	1000° F	2105 ft/sec	2.73	1000° F	2105 ft/sec
○	1.54	1000° F	1439 ft/sec	2.73	1000° F	2105 ft/sec
□	2.0	500° F	1439 ft/sec	2.73	1000° F	2105 ft/sec
△	1.38	1500° F	1443 ft/sec	2.73	1000° F	2105 ft/sec

Figure 168. — Dual-Flow Postmerged Jet Noise Beam Patterns (250 Hz to 2 kHz)

61-T, 3.1 AR-CPA-RT/NC nozzle

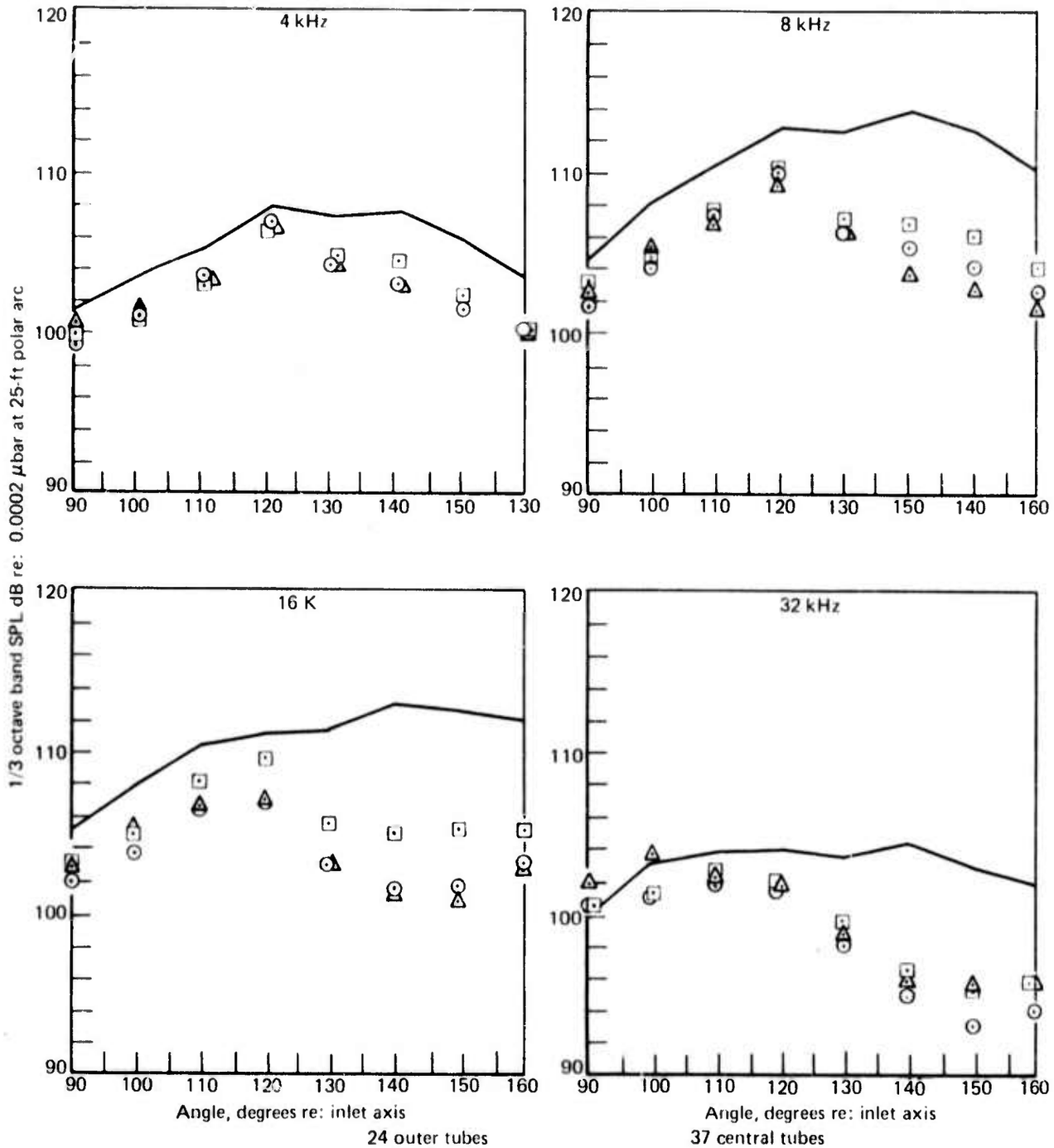

24 outer tubes / 37 central tubes

	PR_2	T_{T2}	V_{J2}	PR_1	T_{T1}	V_{J1}
——	2.73	1000° F	2105 ft/sec	2.73	1000° F	2105 ft/sec
⊙	1.54	1000° F	1439 ft/sec	2.73	1000° F	2105 ft/sec
⊡	2.00	500° F	1439 ft/sec	2.73	1000° F	2105 ft/sec
△	1.38	1500° F	1443 ft/sec	2.73	1000° F	2105 ft/sec

Figure 169. — Dual-Flow Premerged Jet Noise Beam Patterns (4 kHz to 32 kHz)

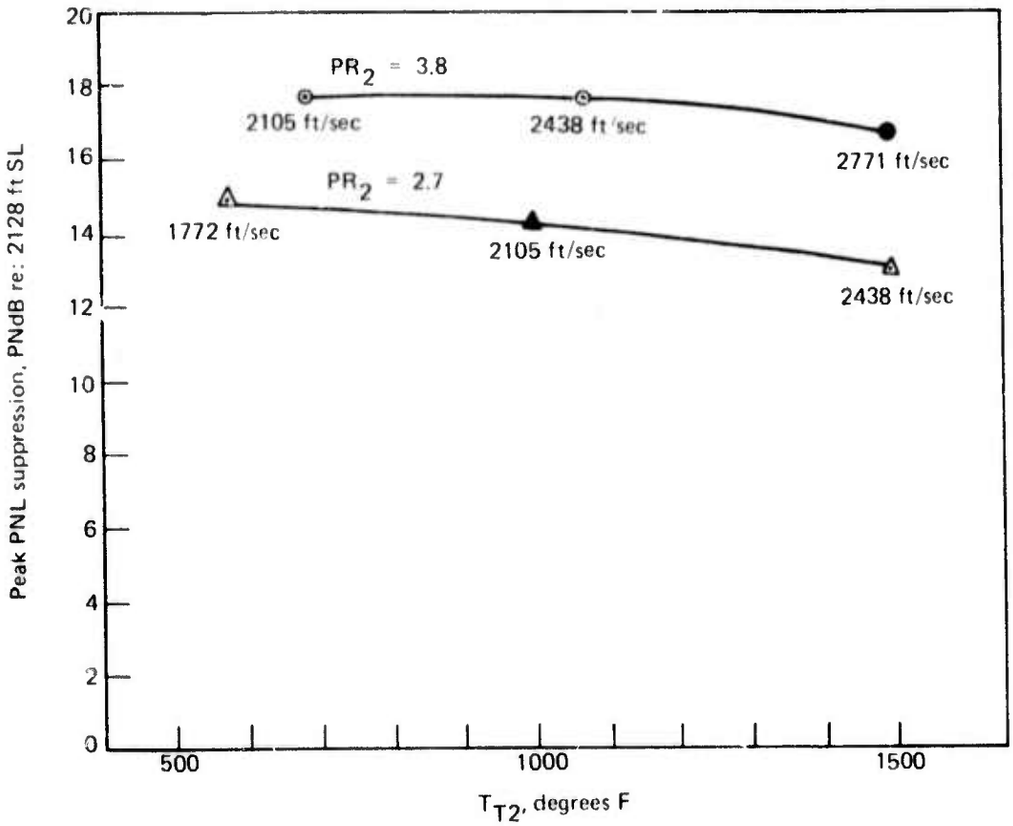

61-T, 3.1 AR-CPA-RT/NC nozzle

37 central tubes

○ T_{T1} = 1500° F, PR_1 = 3.8 V_{J1} = 2771 ft/sec
△ T_{T1} = 1000° F, PR_1 = 2.7 V_{J1} = 2105 ft/sec

Solid symbol — monoflow case

Figure 170. — Dual-Flow Sideline Jet Noise Suppression

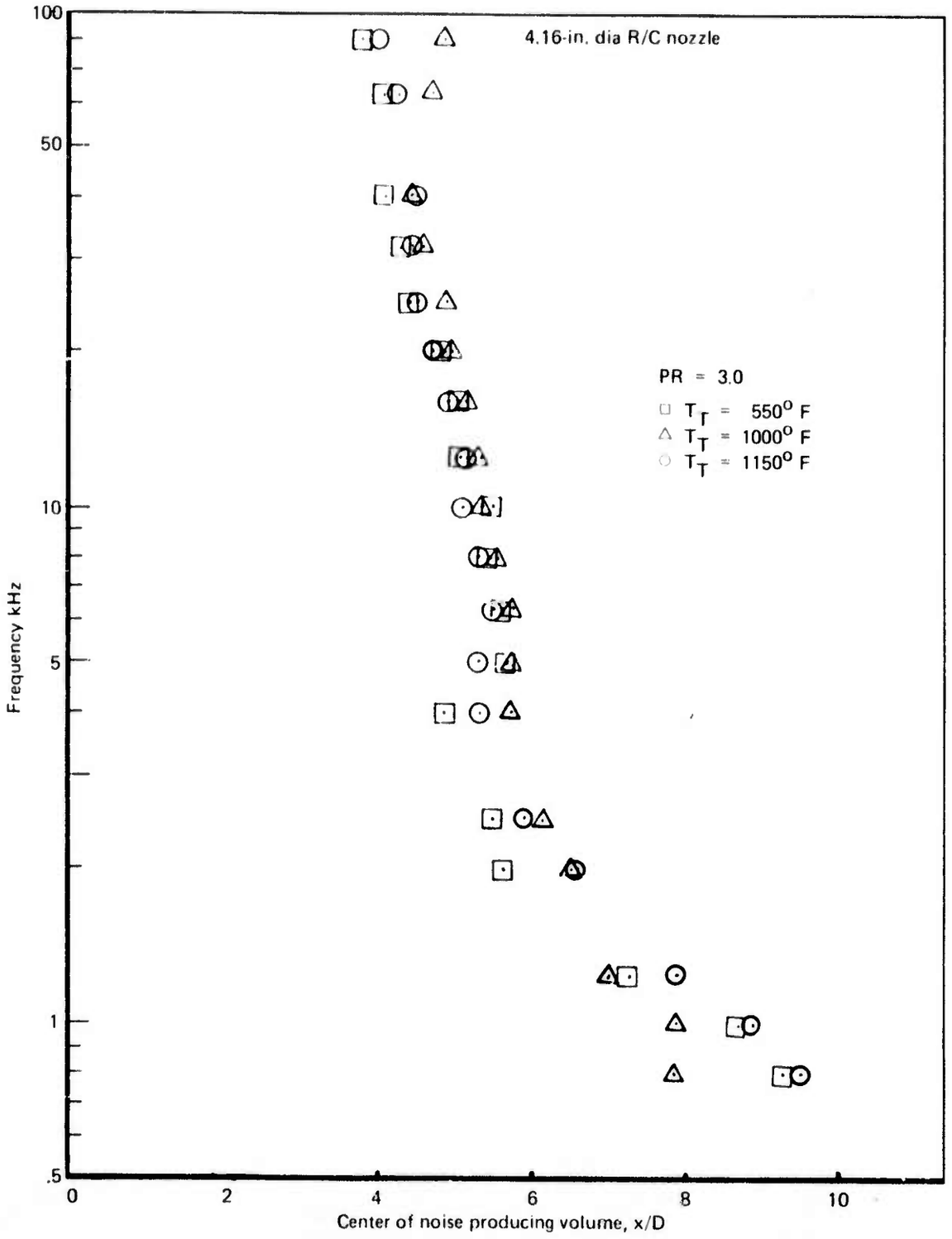

Figure 171. — Apparent Noise Source Location As a Function of Jet Temperature for a Round Convergent Nozzle

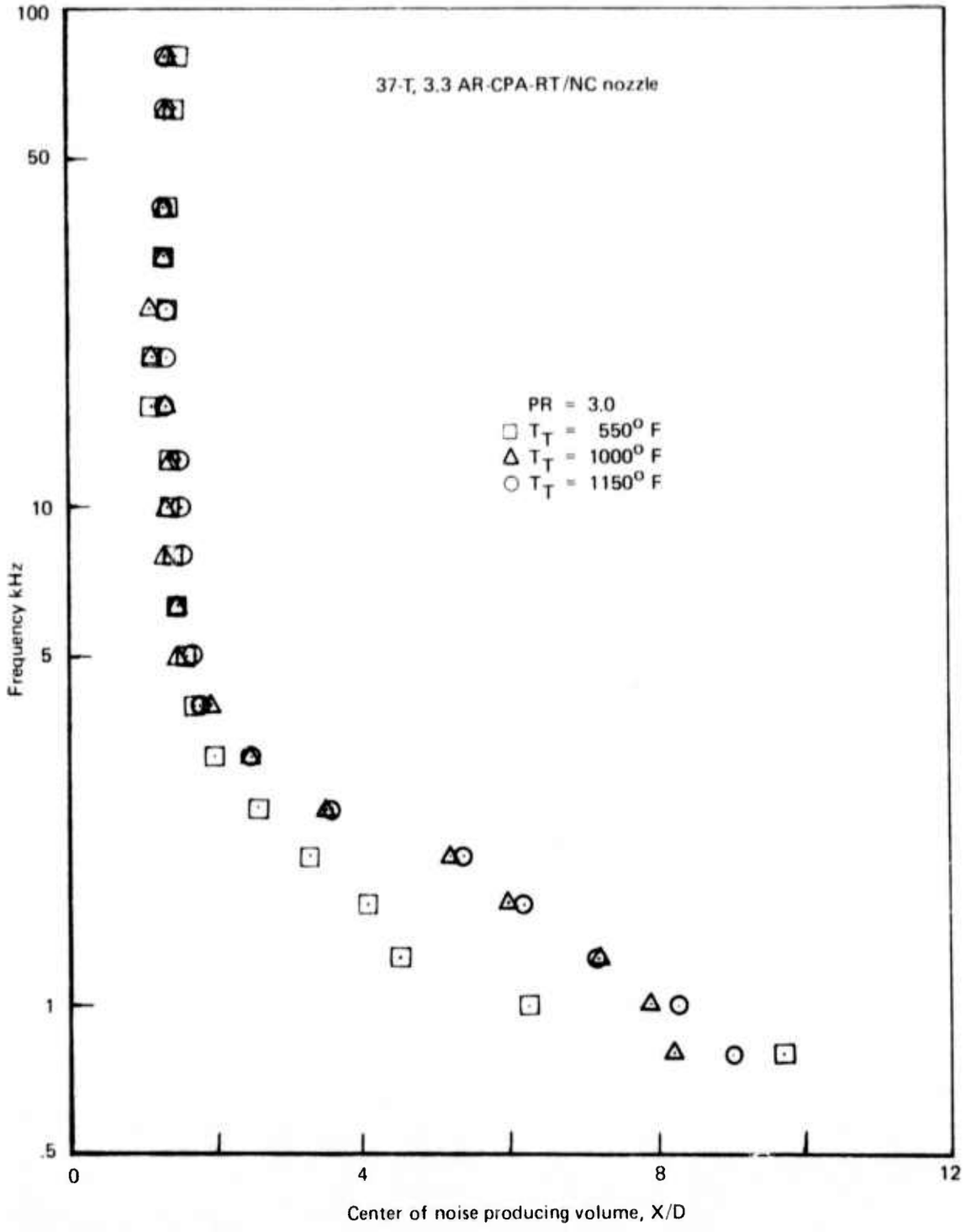

Figure 172. — Apparent Noise Source Location as a Function of Jet Temperature for a Multitube Nozzle

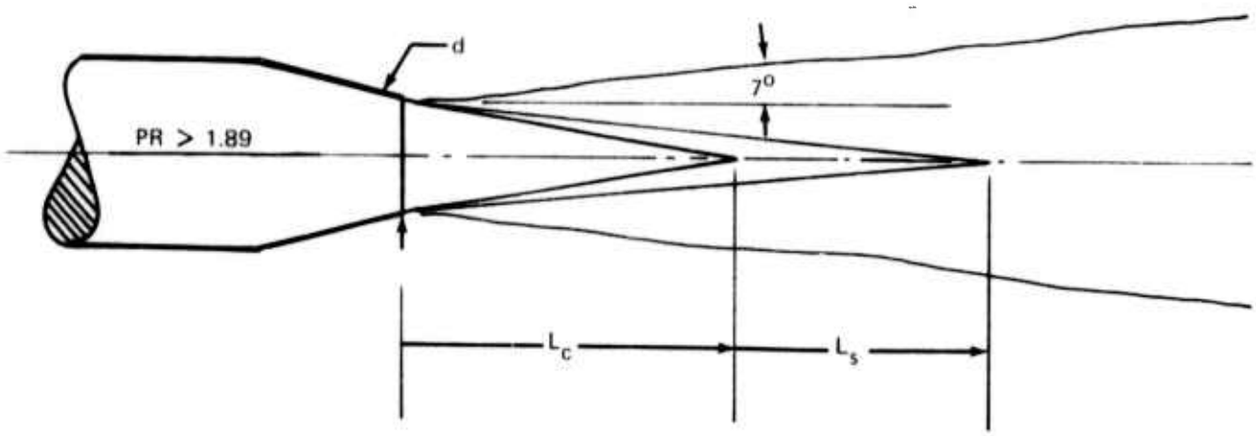

☆ Core length: $L_c = d\,(5.22\,M_j^{0.90} + 0.22)$

☆ Supersonic core length: $L_s = -11.25\,M_j^2 + 48.75\,M_j - 32.5$

★ See reference 13

Figure 173. — Supersonic Jet Geometry Showing Dependence on Jet Mach Number and Tube Diameter

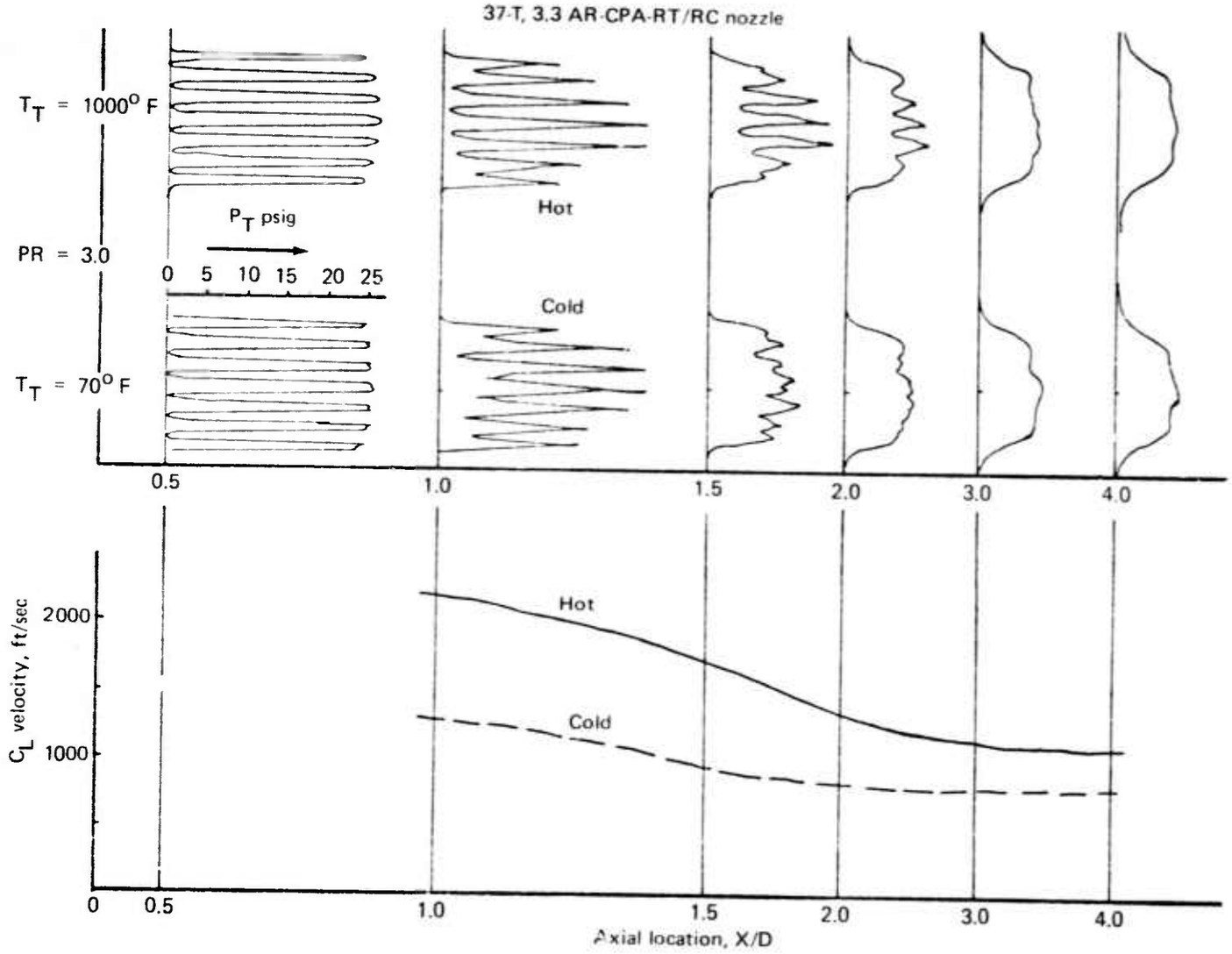

Figure 174. — Comparison of the Total Pressure Profiles and Centerline Velocities of a Multitube Nozzle Operated at a Hot and Cold Temperature

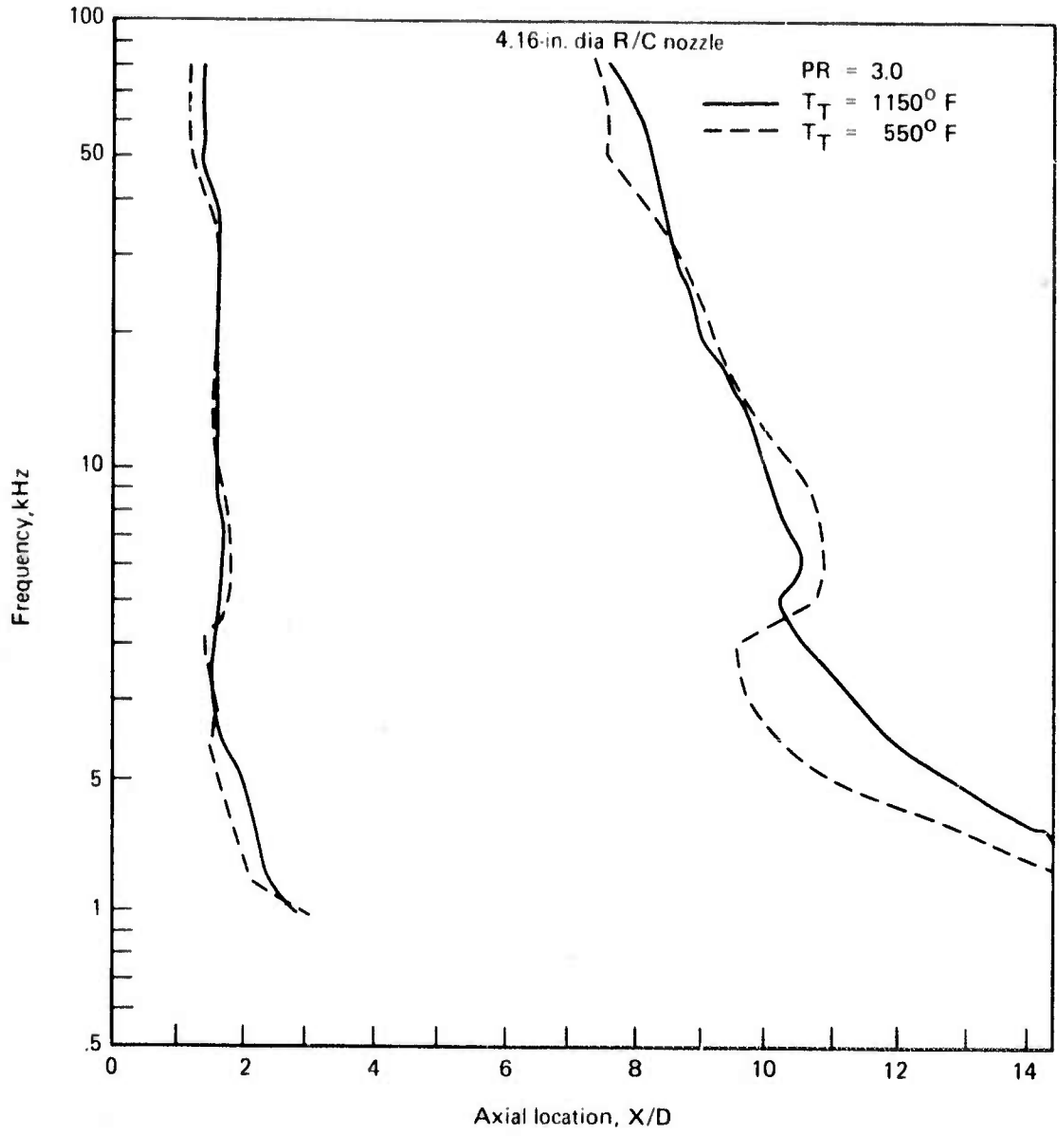

Figure 175. — Peak -3dB Density Distribution as a Function of Jet Temperature

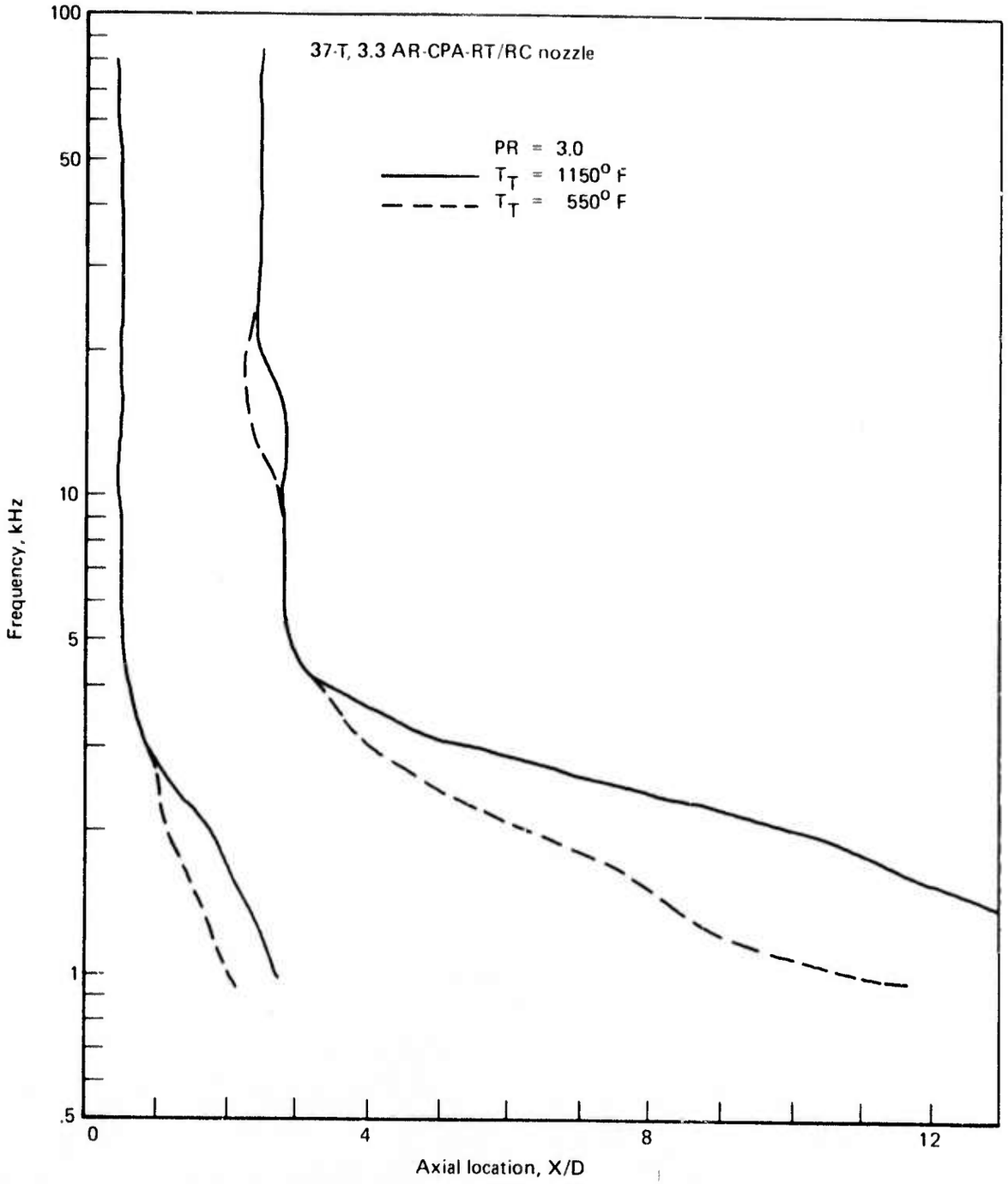

Figure 176. — Peak -3 dB Density Distribution as a Function of Jet Temperature

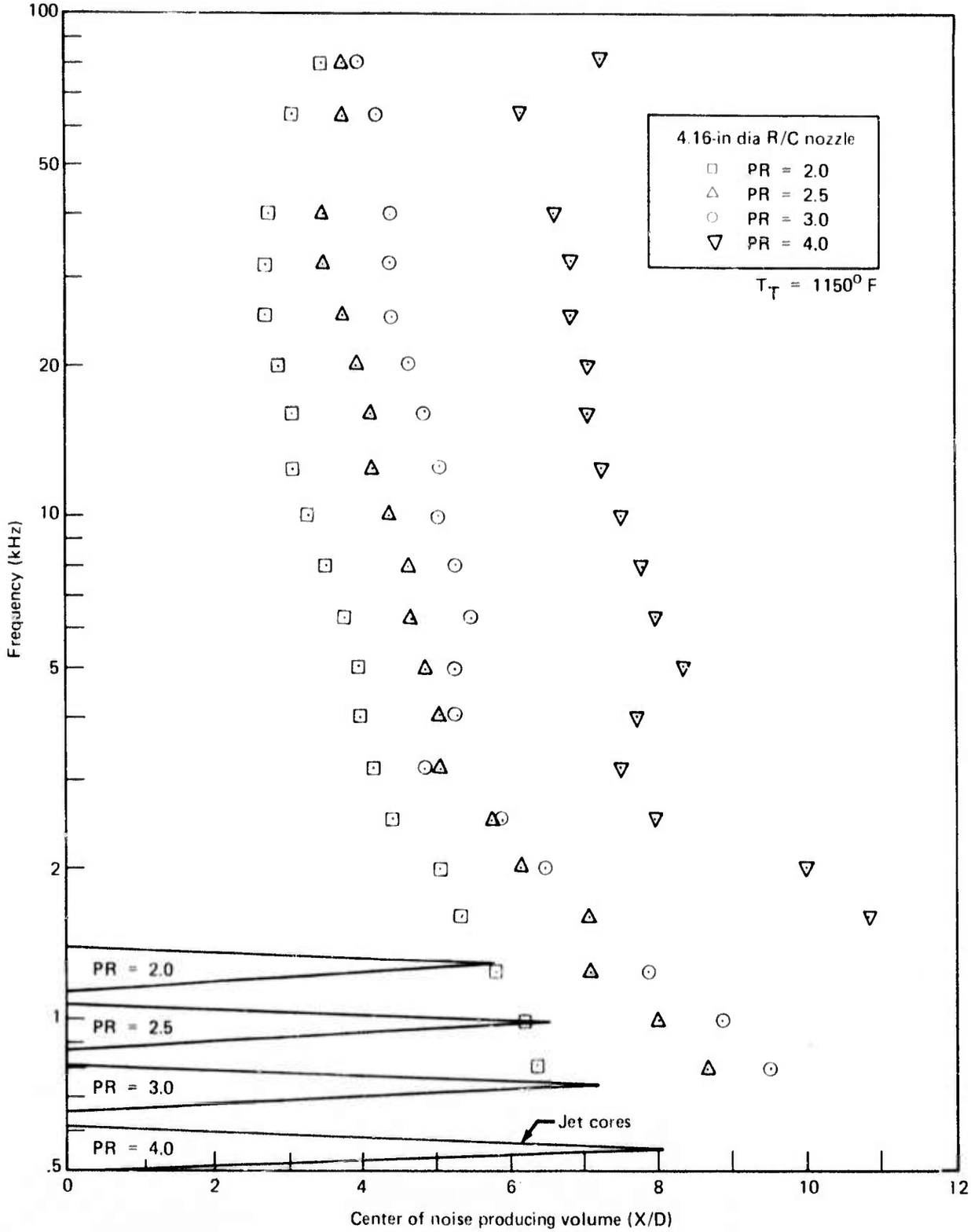

Figure 177. — Apparent Noise Source Location as a Function of Pressure Ratio

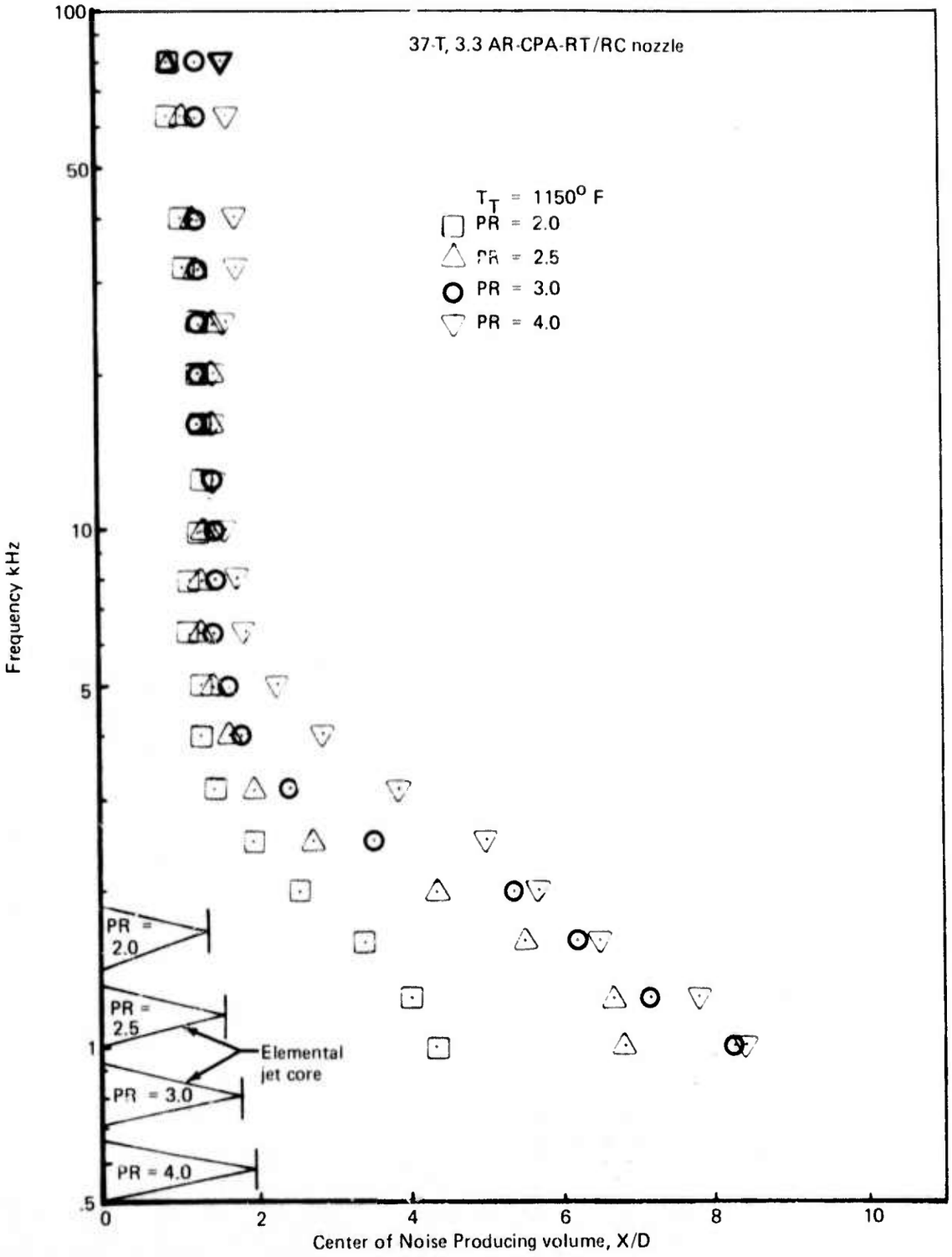

Figure 178. — Apparent Noise Source Location as a Function of Pressure Ratio

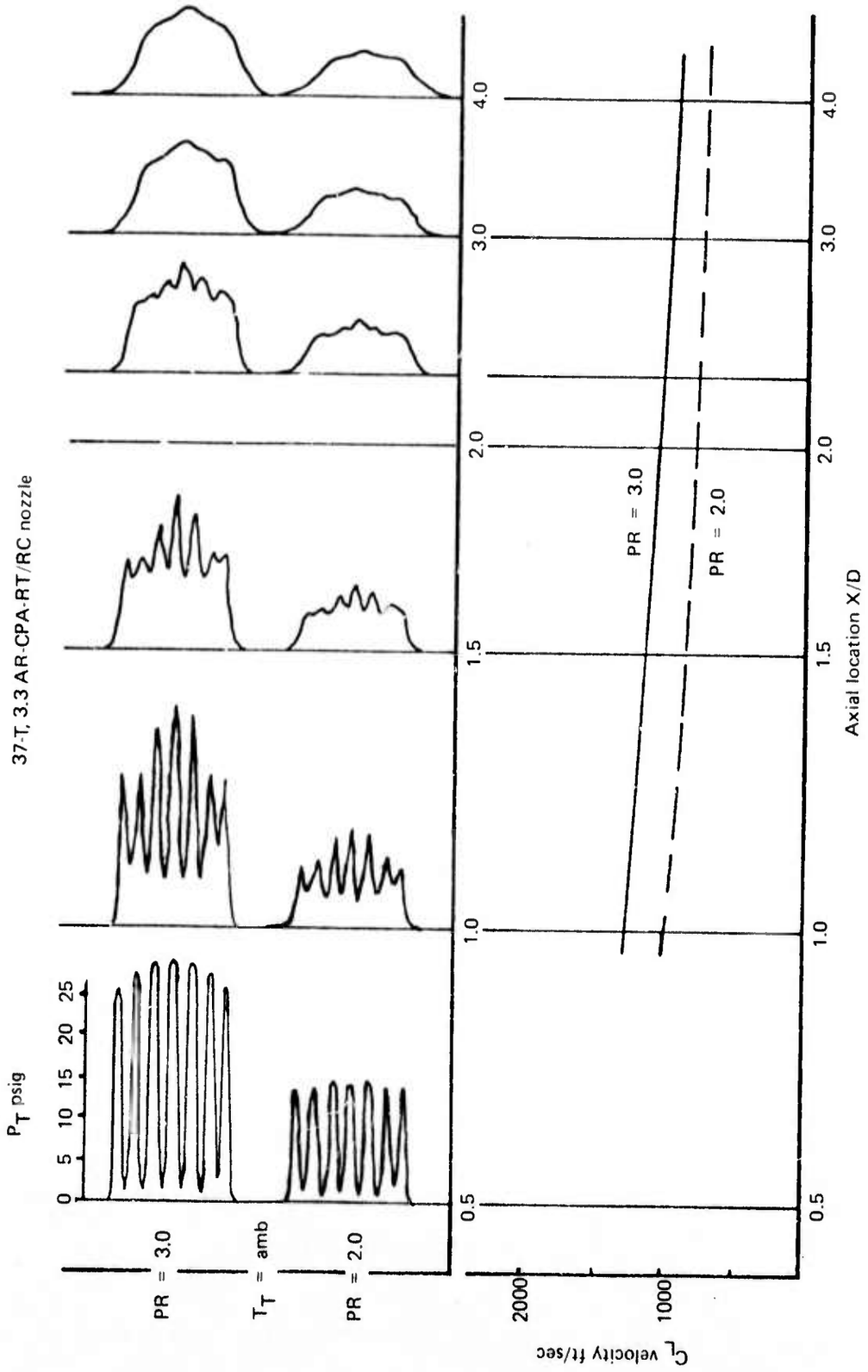

Figure 179. — Comparison of the Total Pressure Profiles and Centerline Velocities of a Multitube Nozzle Operated at Two Pressure Ratios

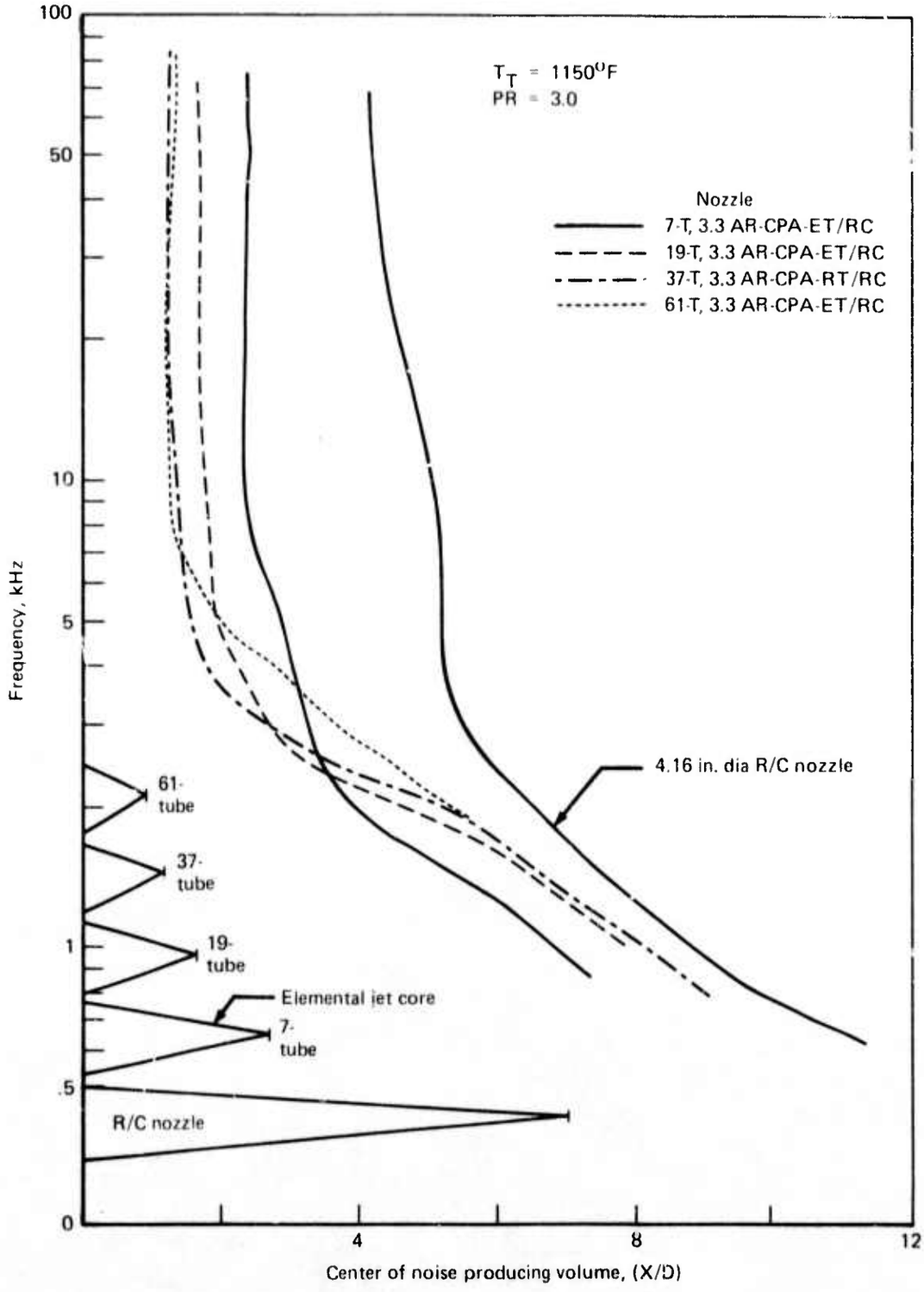

Figure 180.—Apparent Noise Source Location as a Function of Tube Number

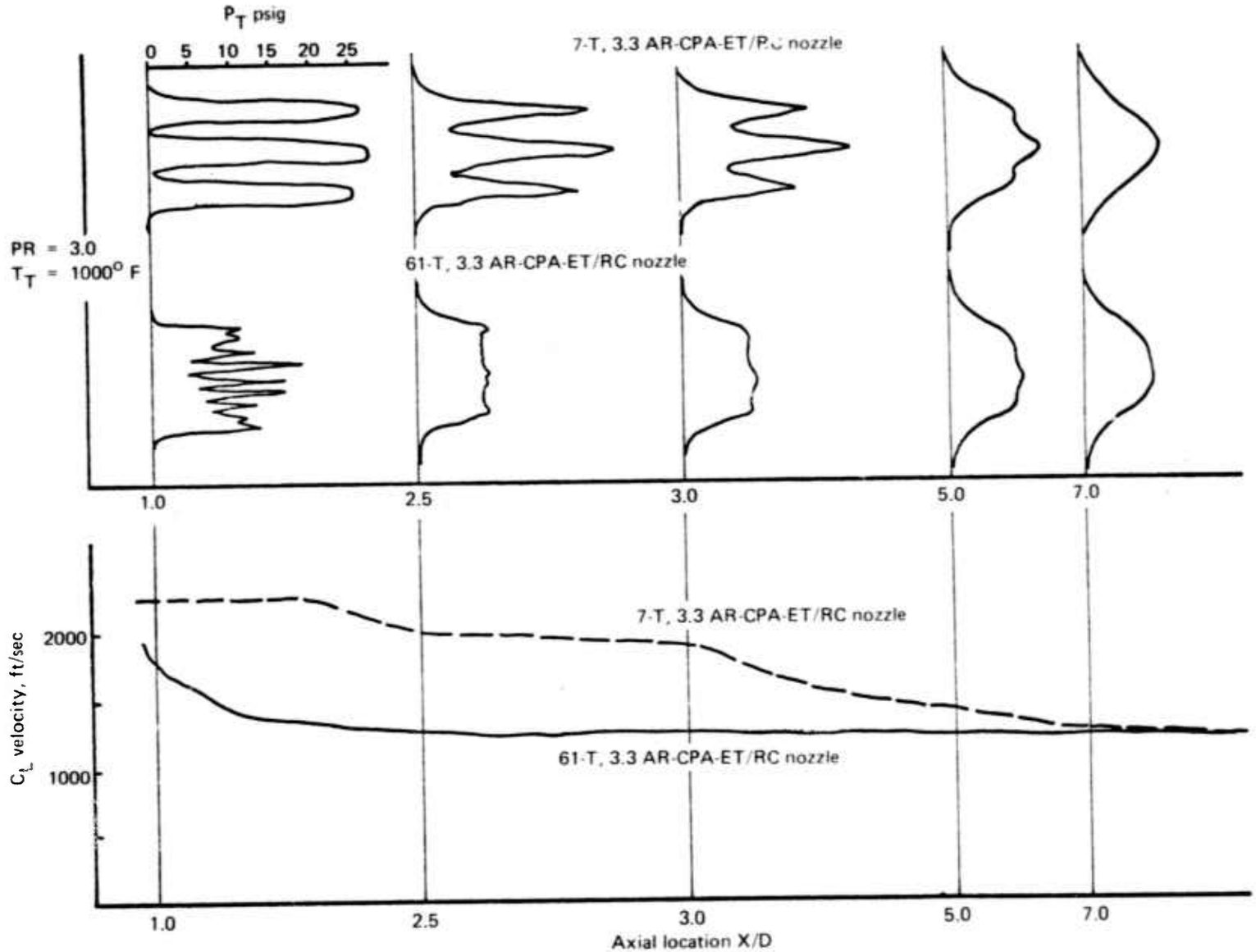

Figure 181. — Comparison of the Total Pressure Profiles and Centerline Velocities of a Multitube Nozzle as a Function of Tube Number

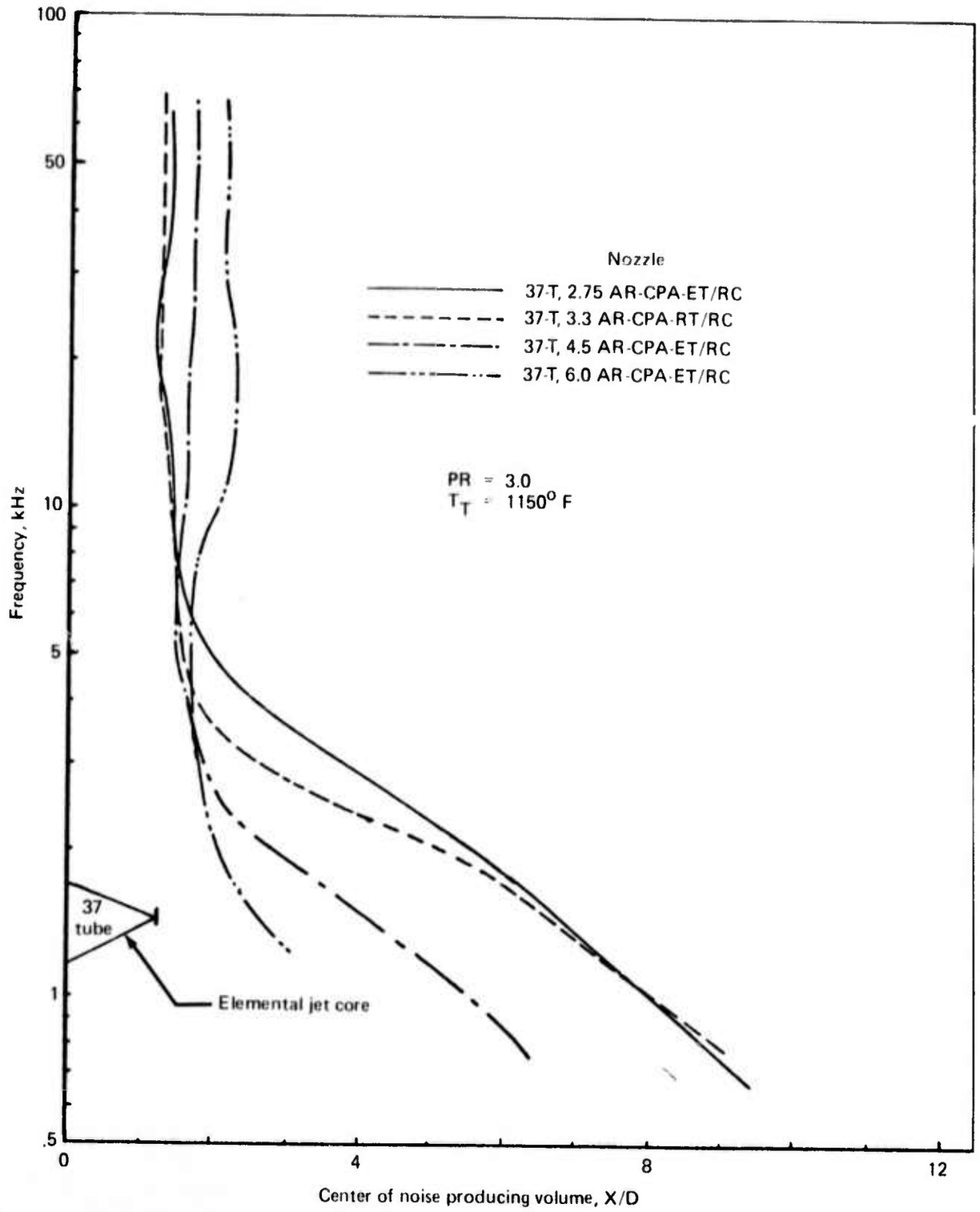

Figure 182. — Apparent Noise-Source Location as a Function of Area Ratio

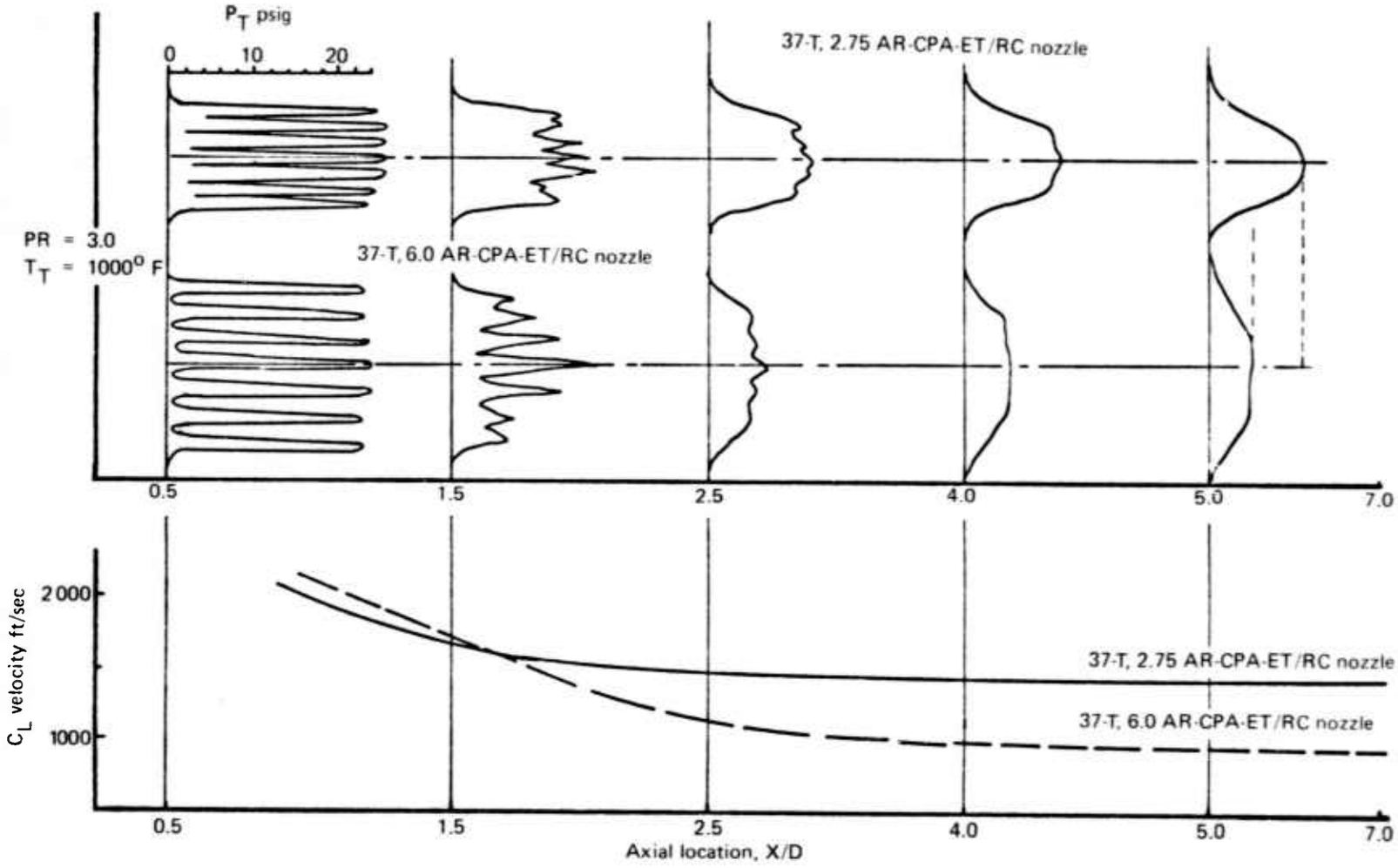

Figure 183. — Comparison of the Total Pressure Profiles and Centerline Velocities of a Multitube Nozzle as a Function of Area Ratio

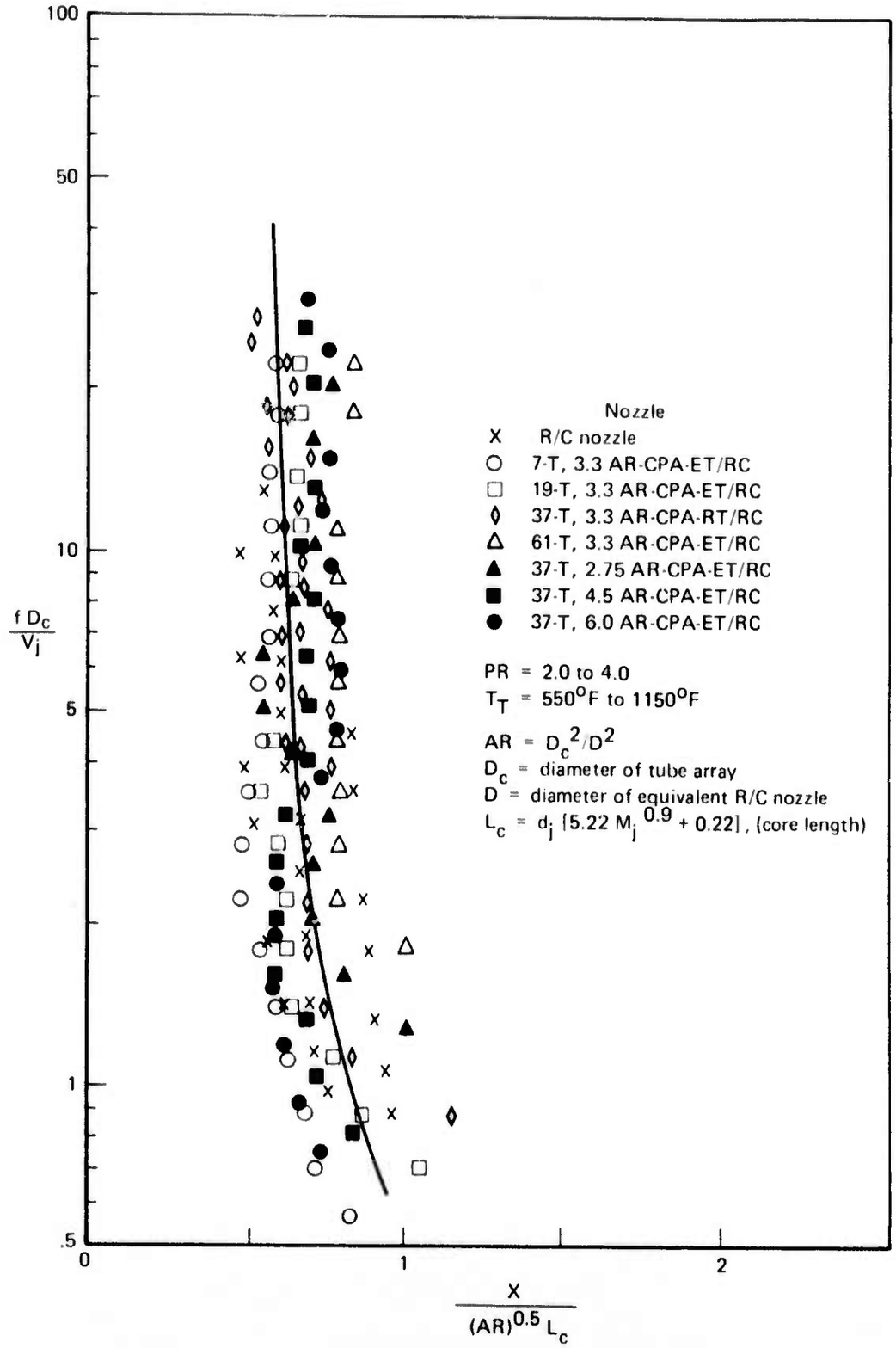

Figure 184.—Normalized Premerged Noise Source Location

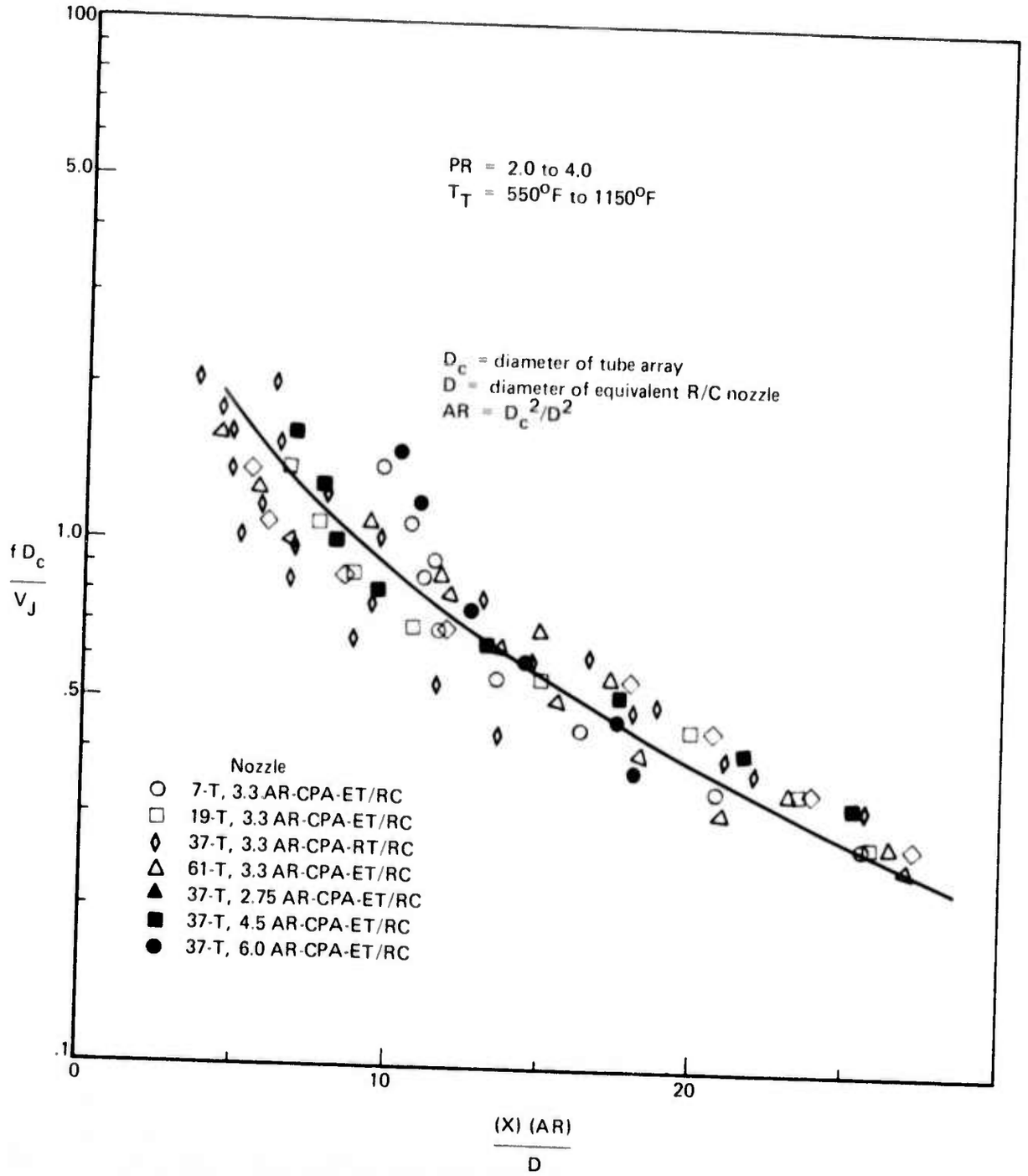

Figure 185.—Normalized Postmerged Noise Source Location

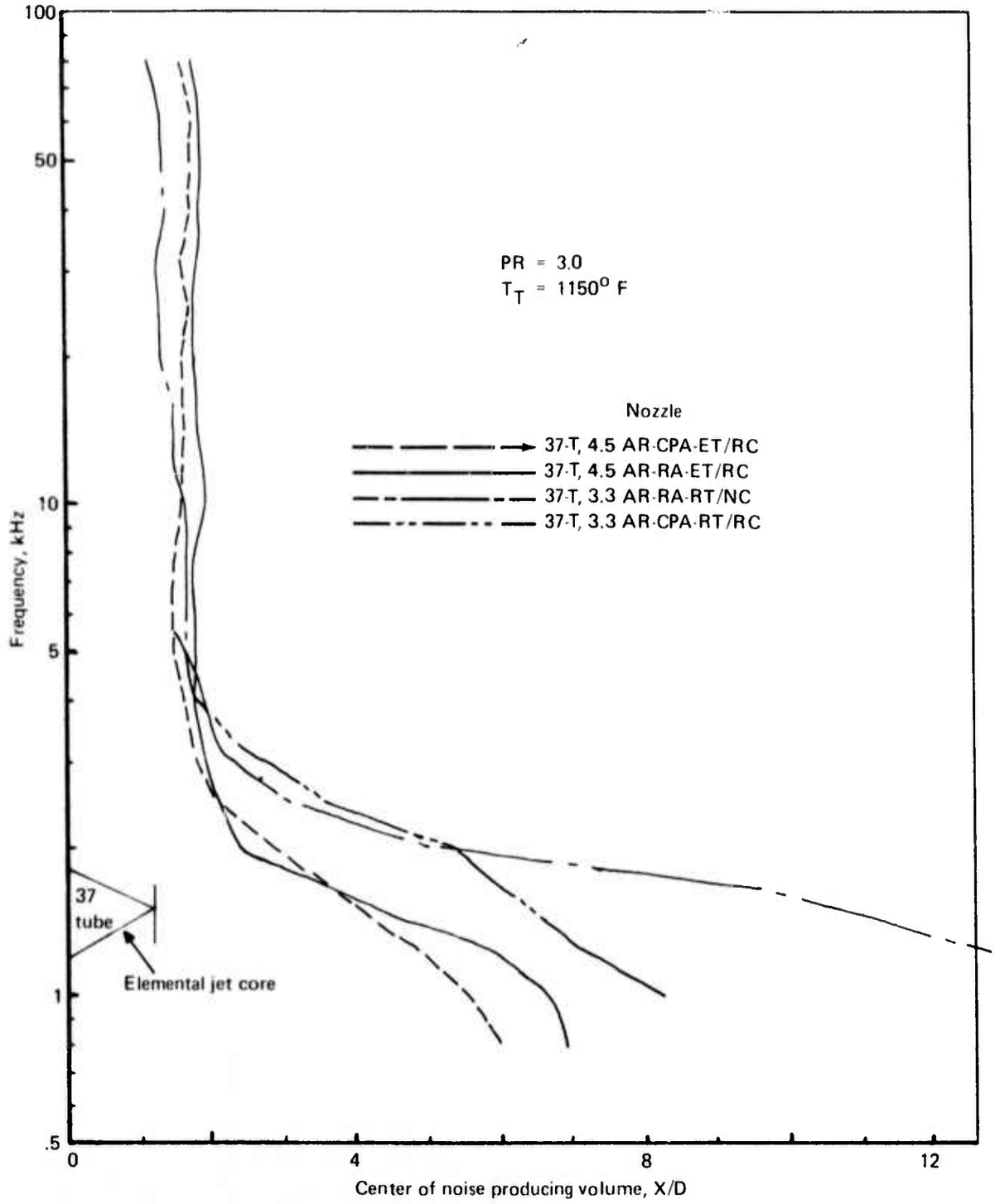

Figure 186. — Apparent Noise Source Location as a Function of Tube Array

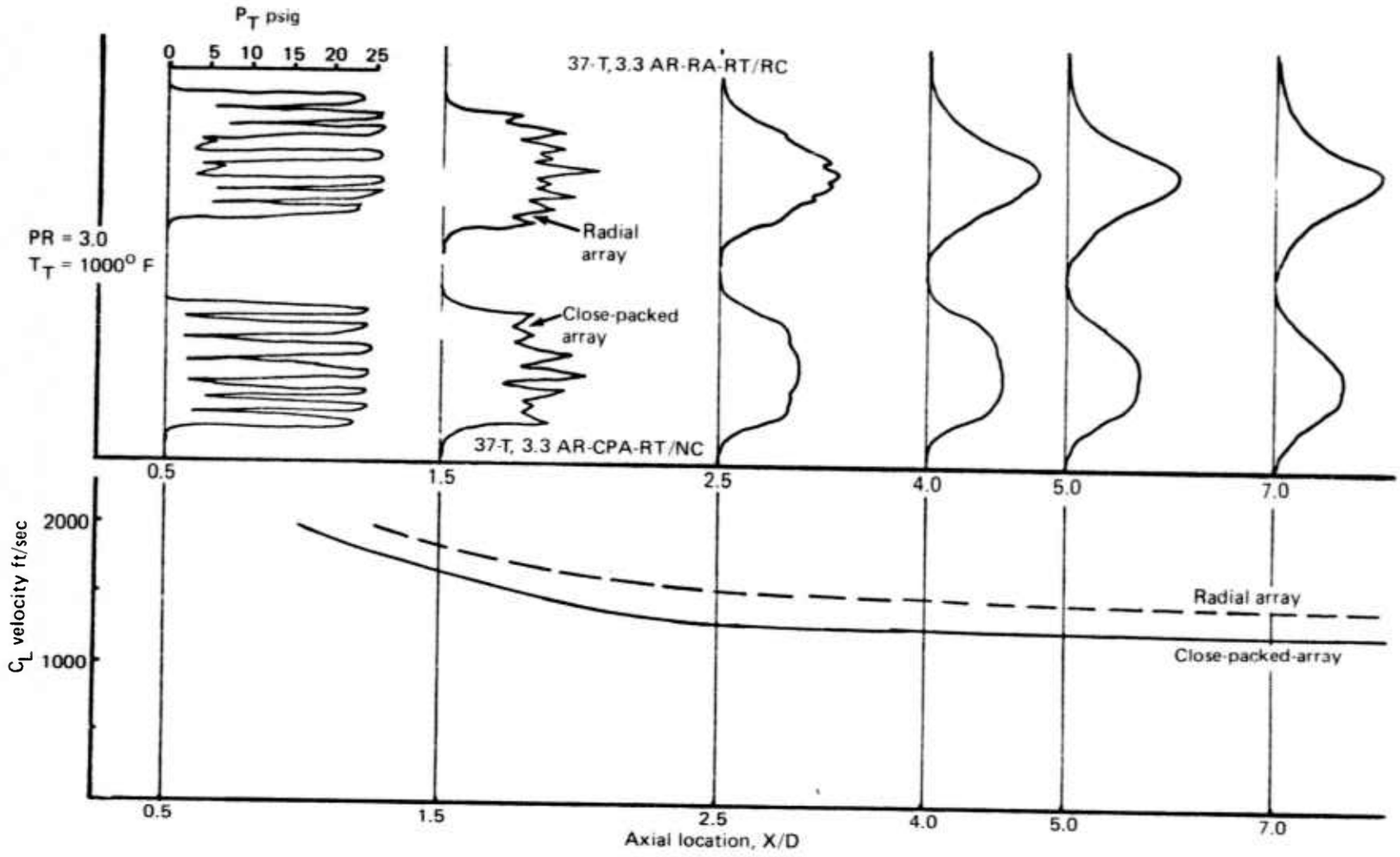

Figure 187. — Comparison of the Total Pressure Profiles and Centerline Velocities of a Multitube Nozzle as a Function of Tube Array

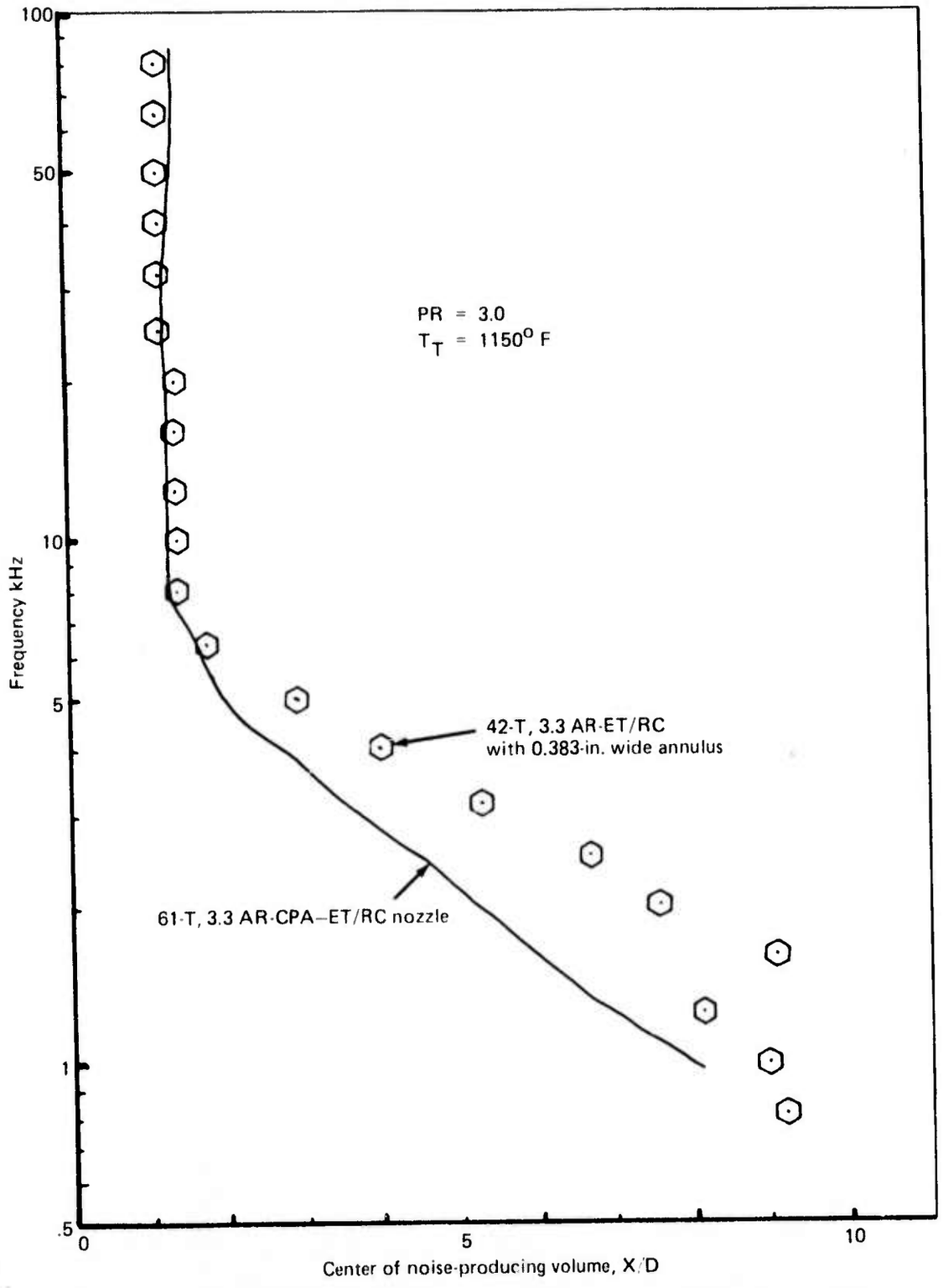

Figure 188. — Apparent Noise-Source Location Comparison of a 61-Tube Nozzle Versus a 42-Tube With 0.383-in. Annulus Nozzle

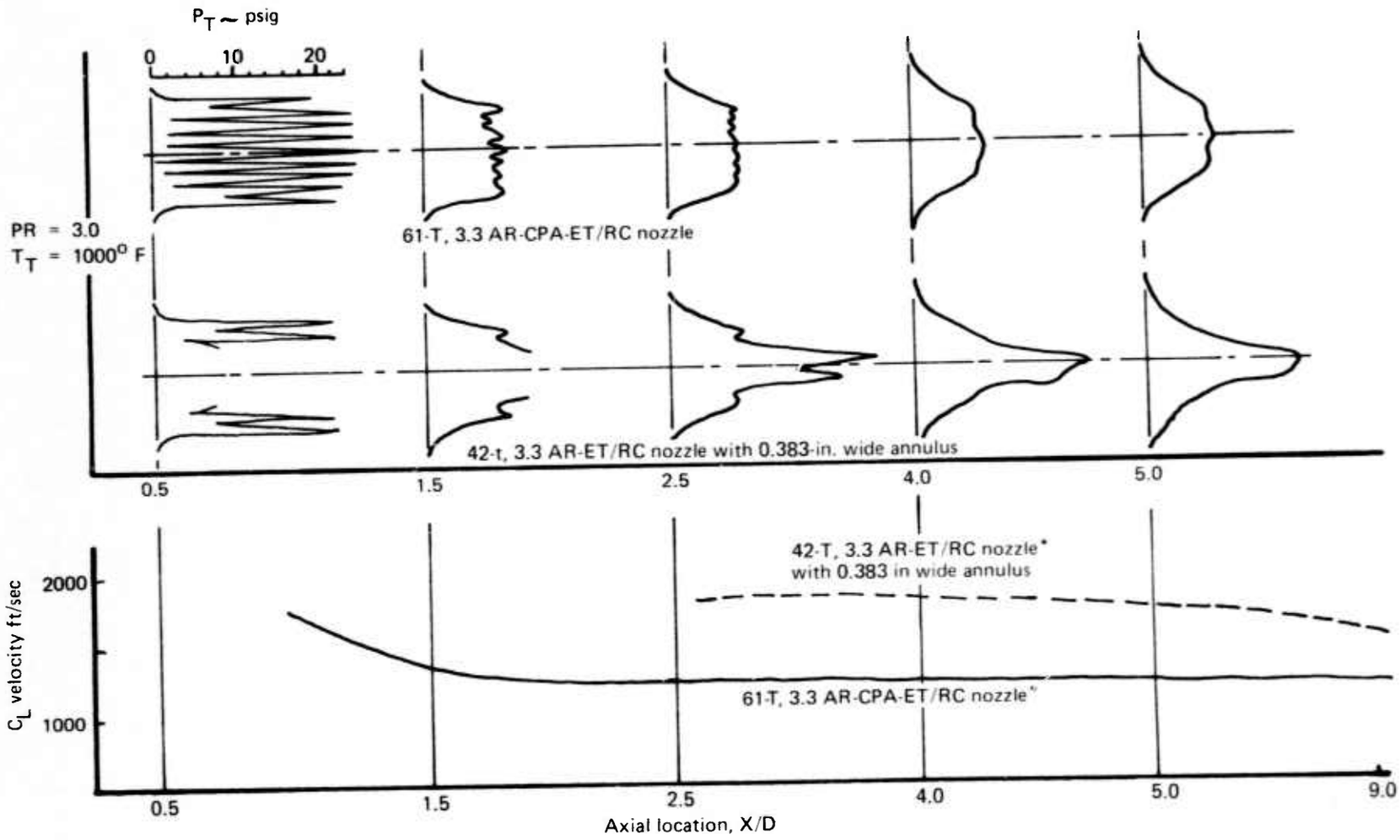

* The outer tubes of both nozzles are identical in size and location

Figure 189.— Comparison of the Total Pressure Profiles and Centerline Velocities of a 61-Tube Nozzle and a 42-Tube Nozzle With 0.383-in. Wide Annulus

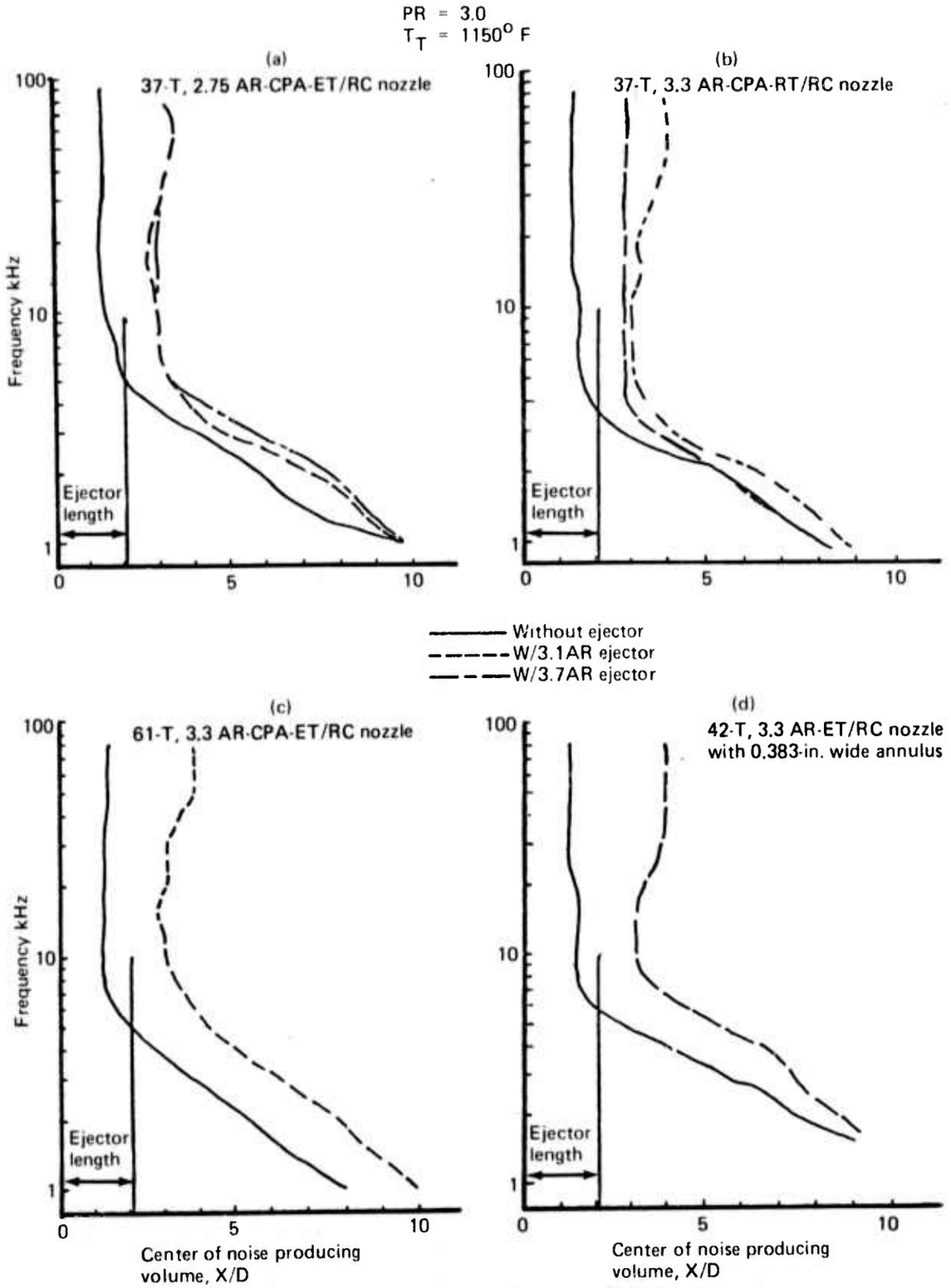

Figure 190. — Apparent Noise-Source Location Shift With Ejector Installation on Four Multitube Configurations

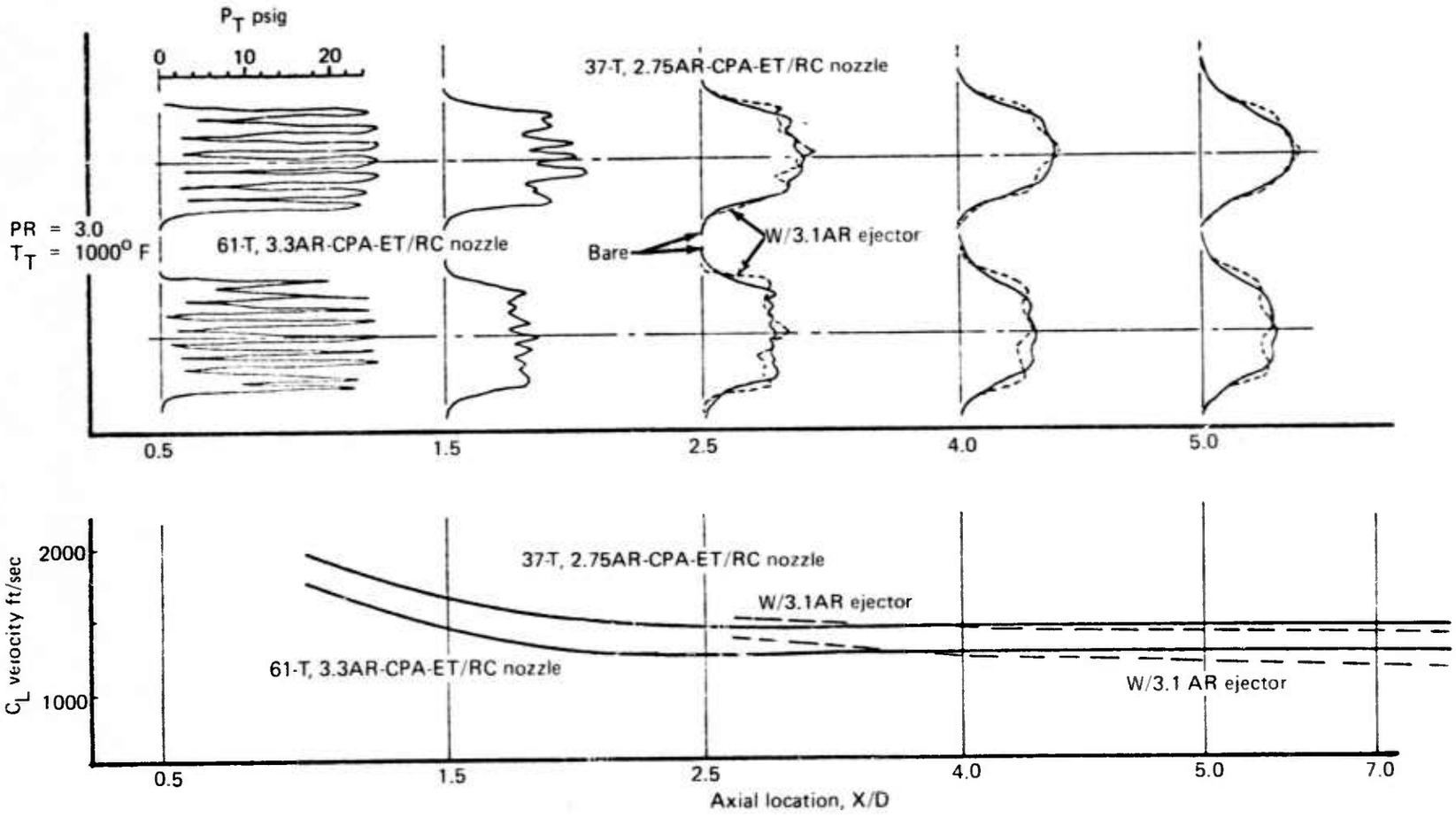

Figure 191. — Comparison of the Total Pressure Profiles and Centerline Velocities of Two Multitube Nozzles Operated With and Without Ejector

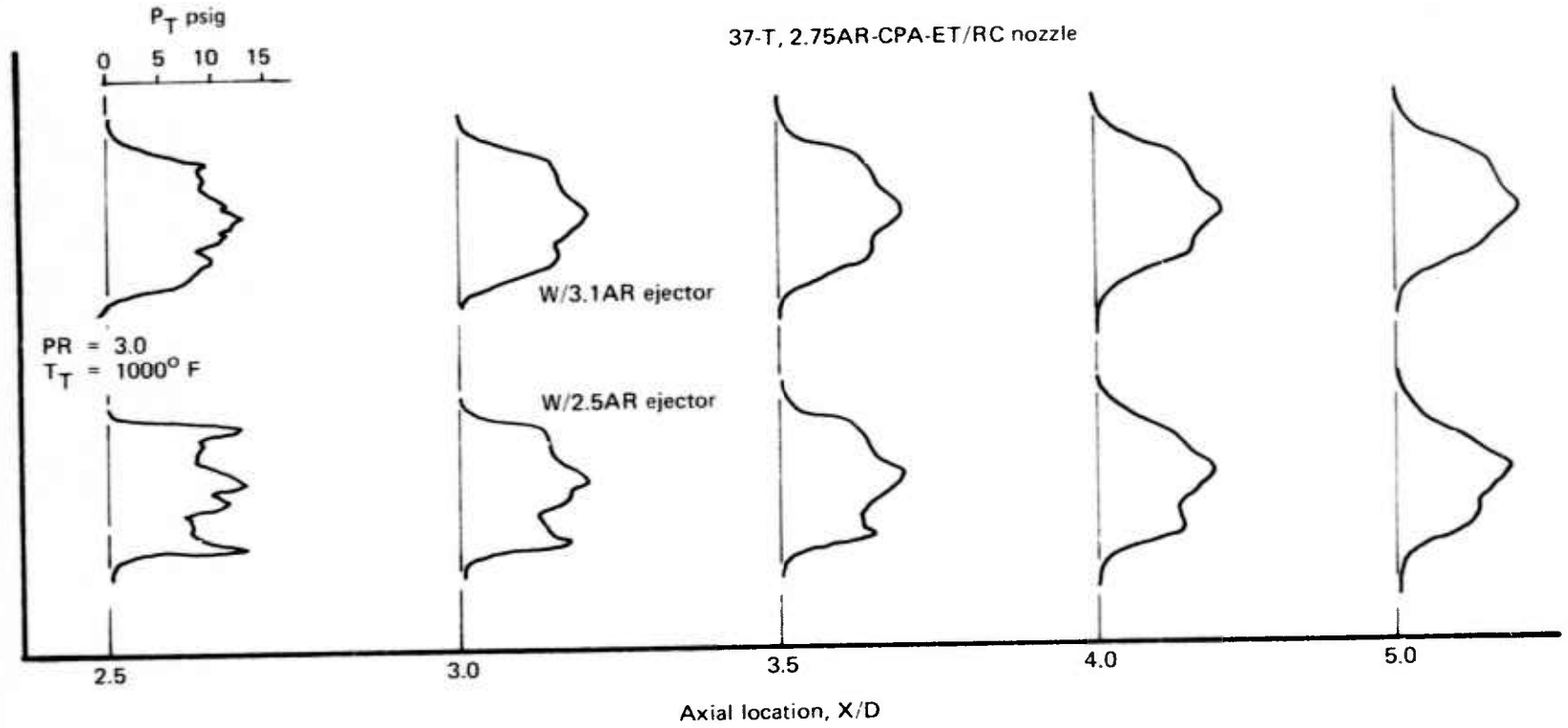

Figure 192.— Comparison of the Total Pressure Profiles of a Multitube Nozzle With a "Tight" (2.5AR EJC) Versus a "Loose" 3.1AR Ejector

NOTE: The wind tunnel absolute noise values shown for this configuration are not directly comparable with other configurations. (Ref. page 50.)

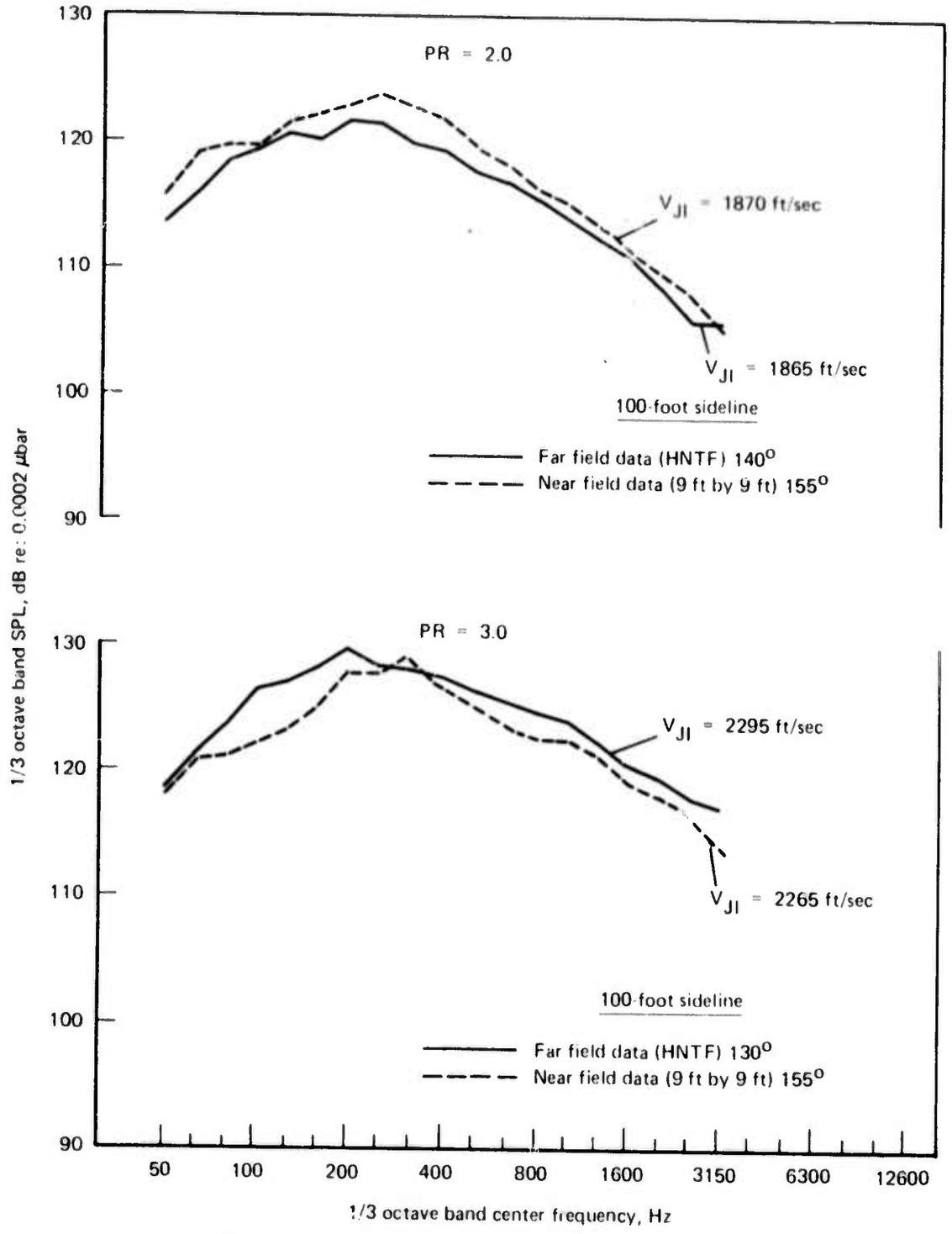

Figure 193.—9 ft by 9 ft Wind Tunnel Noise Test, Comparison of Near- and Far-field Peak Noise Spectra, Reference Conical Nozzle, PR 2 and 3

NOTE: The wind tunnel absolute noise values shown for this configuration are not directly comparable with other configurations. (Ref. page 50.)

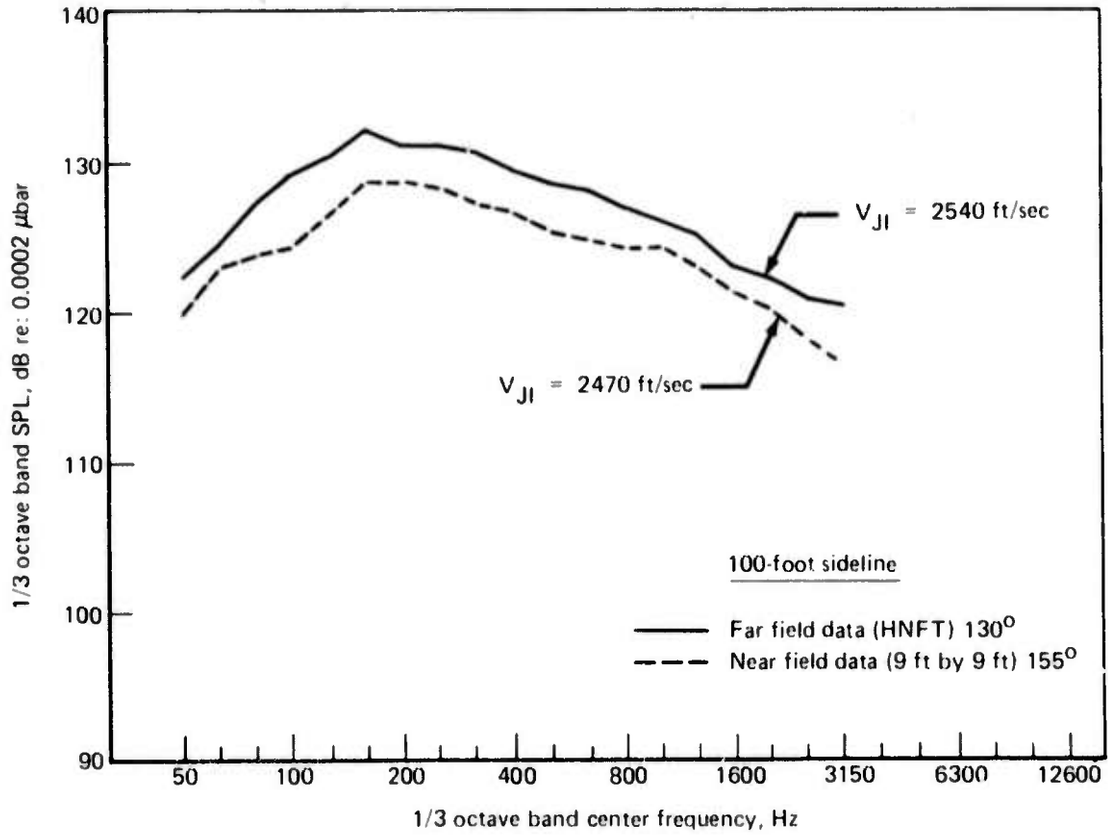

Figure 194.—9 ft by 9 ft Wind Tunnel Noise Test, Comparison of Near- and Far-field Peak Noise Spectra, Reference Conical Nozzle, PR = 4

NOTE: The wind tunnel absolute noise values shown for this configuration are not directly comparable with other configurations. (Ref. page 50.)

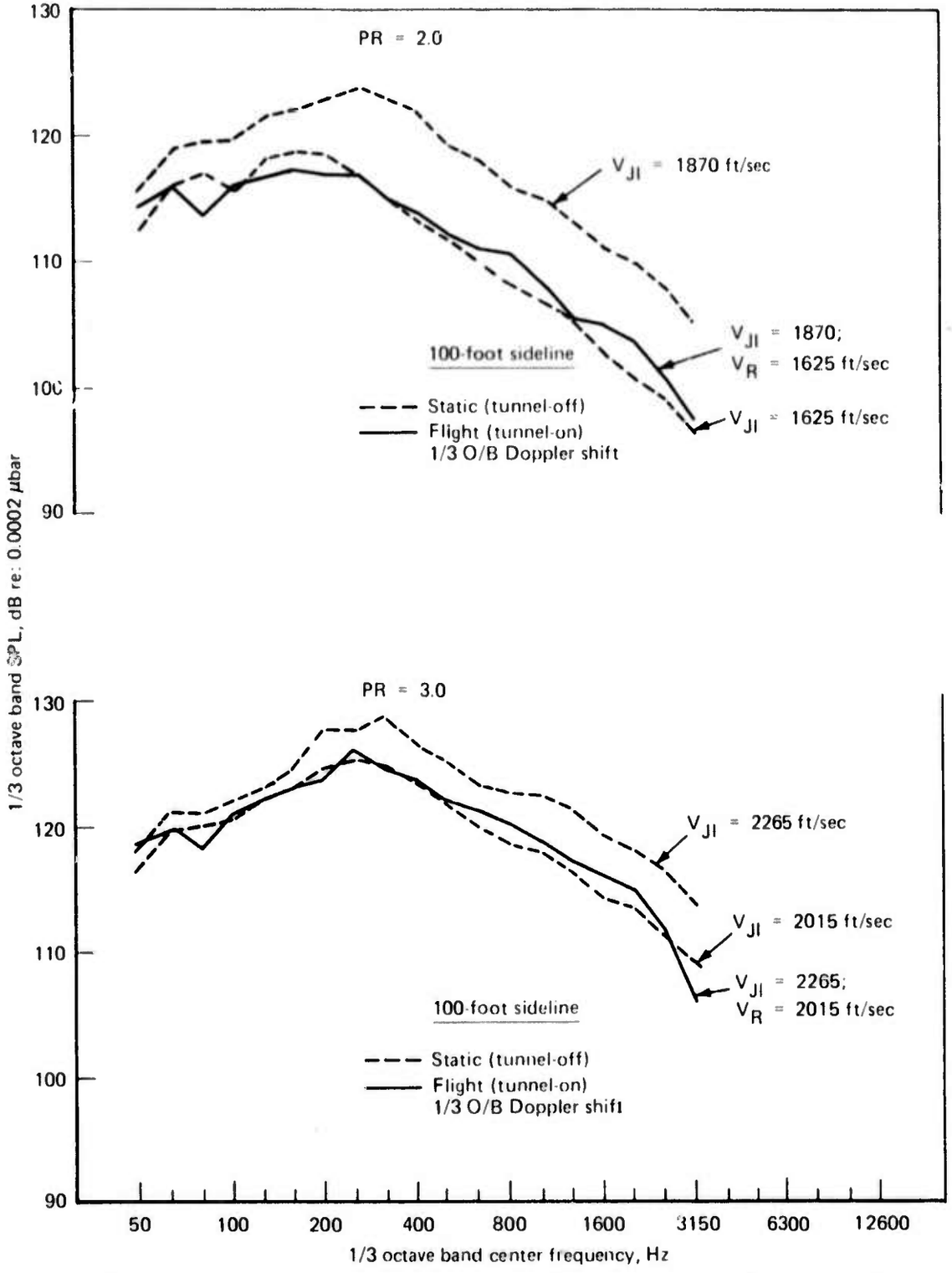

Figure 195.—9 ft by 9 ft Wind Tunnel Noise Test, Comparison of Static and Flight Peak Noise Spectra (155°), Reference Conical Nozzle, PR 2 and 3

NOTE: The wind tunnel absolute noise values shown for this configuration are not directly comparable with other configurations. (Ref. page 50.)

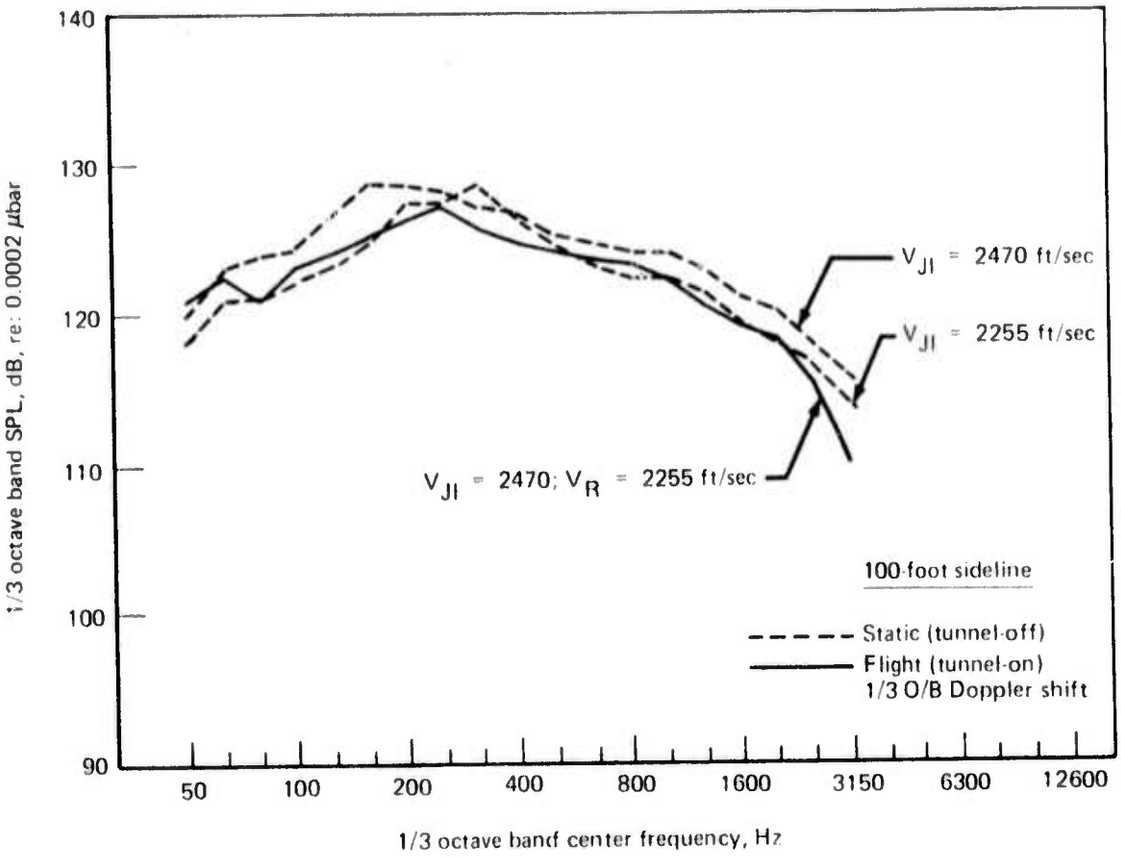

Figure 196.—9 ft by 9 ft Wind Tunnel Noise Test, Comparison of Static and Flight Peak Noise Spectra (160°), Reference Conical Nozzle, PR 4

NOTE: The wind tunnel absolute noise values shown for this configuration are not directly comparable with other configurations. (Ref. page 50.)

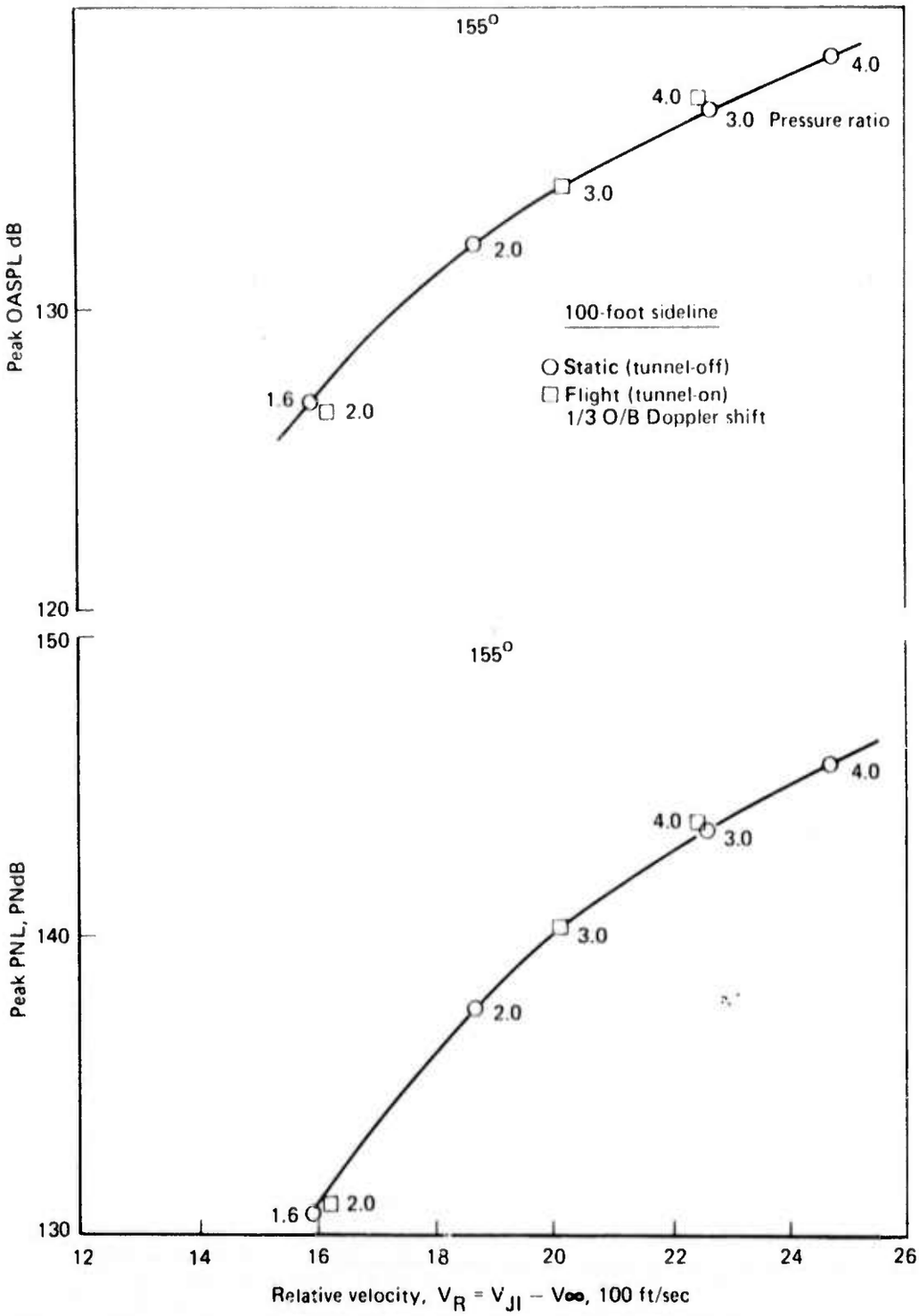

Figure 197.—9 ft by 9 ft Wind Tunnel Noise Test, OASPL and PNL Relative Velocity Relationship, Peak Noise, Reference Conical Nozzle

NOTE: The wind tunnel absolute noise values shown for this configuration are not directly comparable with other configurations. (Ref. page 50.)

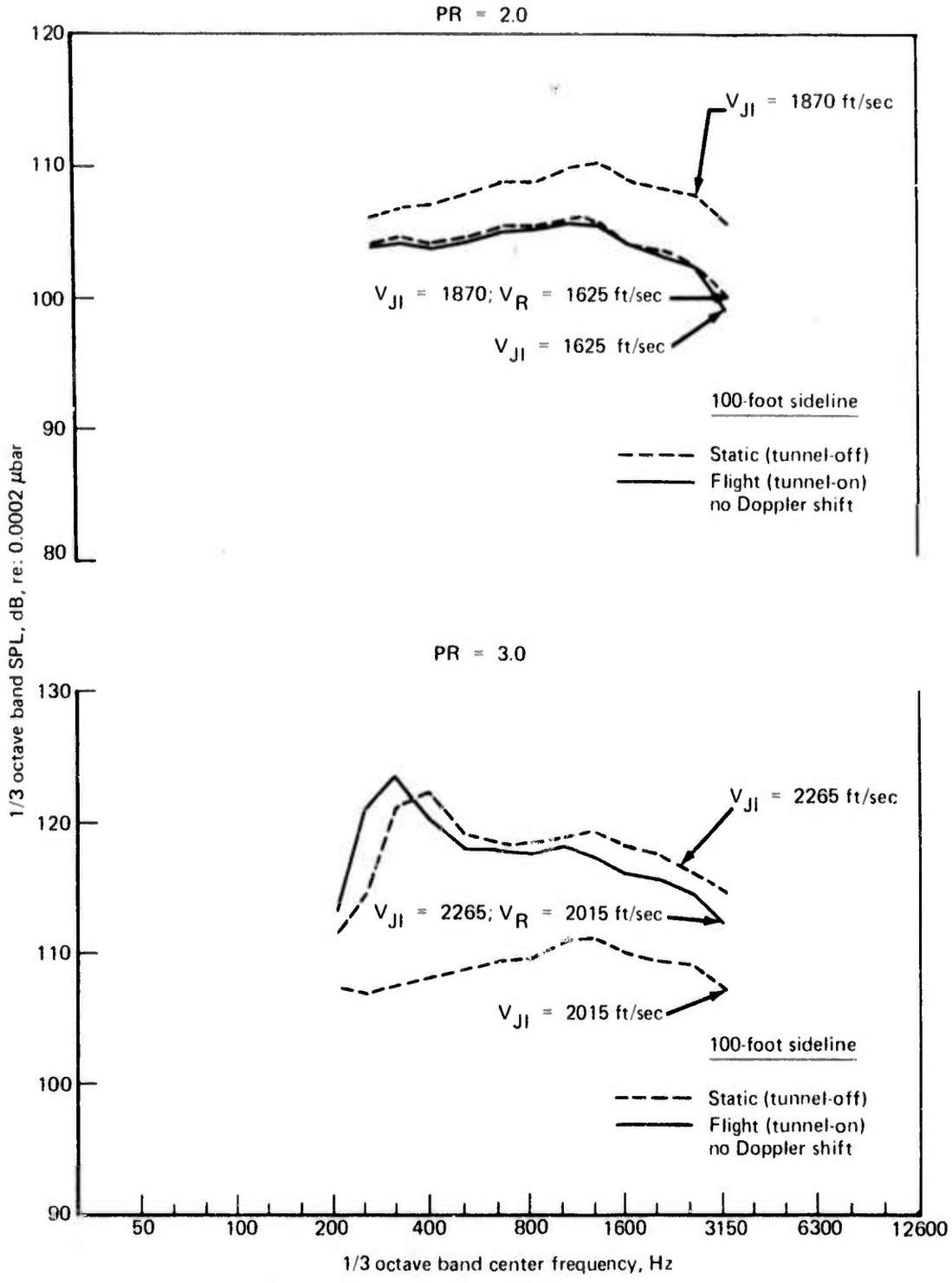

Figure 198.—9 ft by 9 ft Wind Tunnel Noise Test, Comparison of Static and Flight Spectra (130°), Reference Conical Nozzle, PR 2 and 3

NOTE: The wind tunnel absolute noise values shown for this configuration are not directly comparable with other configurations. (Ref. page 50.)

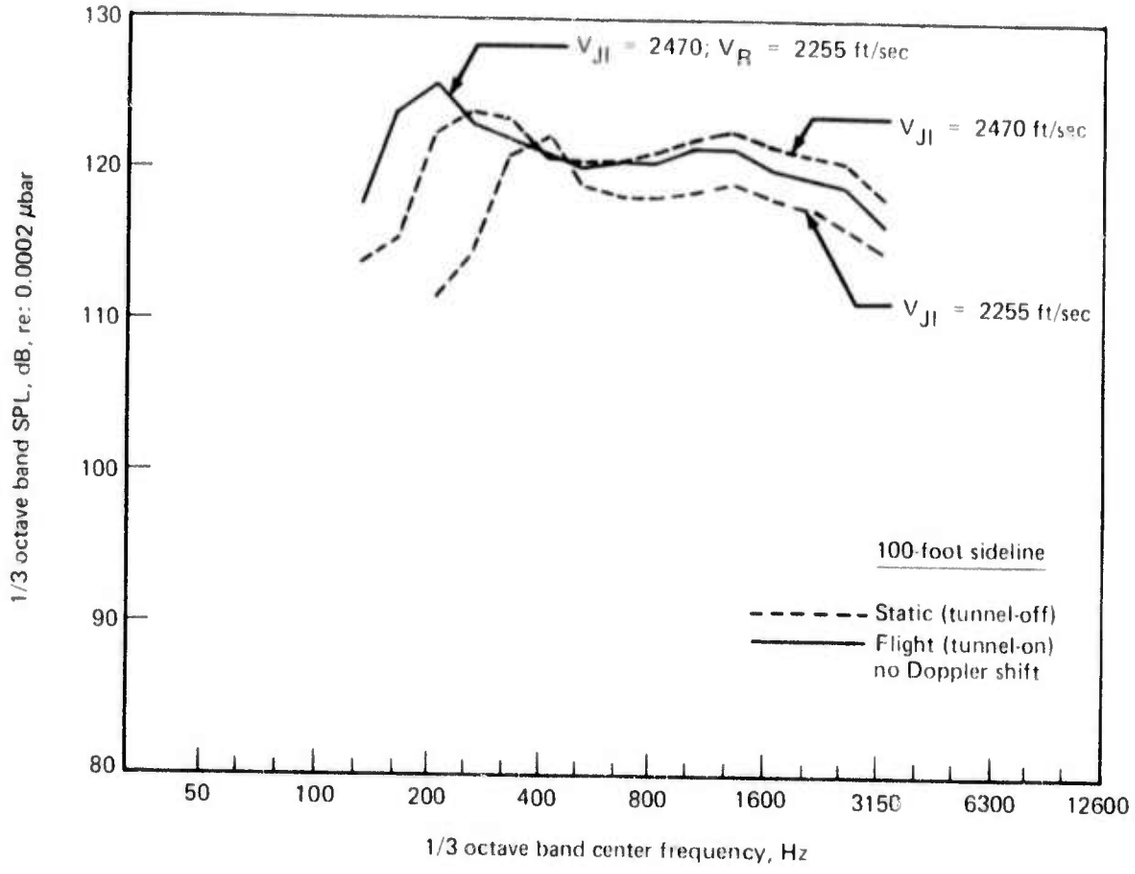

Figure 199.—9 ft by 9 ft Wind Tunnel Noise Test, Comparison of Static and Flight Spectra (130°), Reference Conical Nozzle, PR 4

NOTE: The wind tunnel absolute noise values shown for this configuration are not directly comparable with other configurations. (Ref. page 50.)

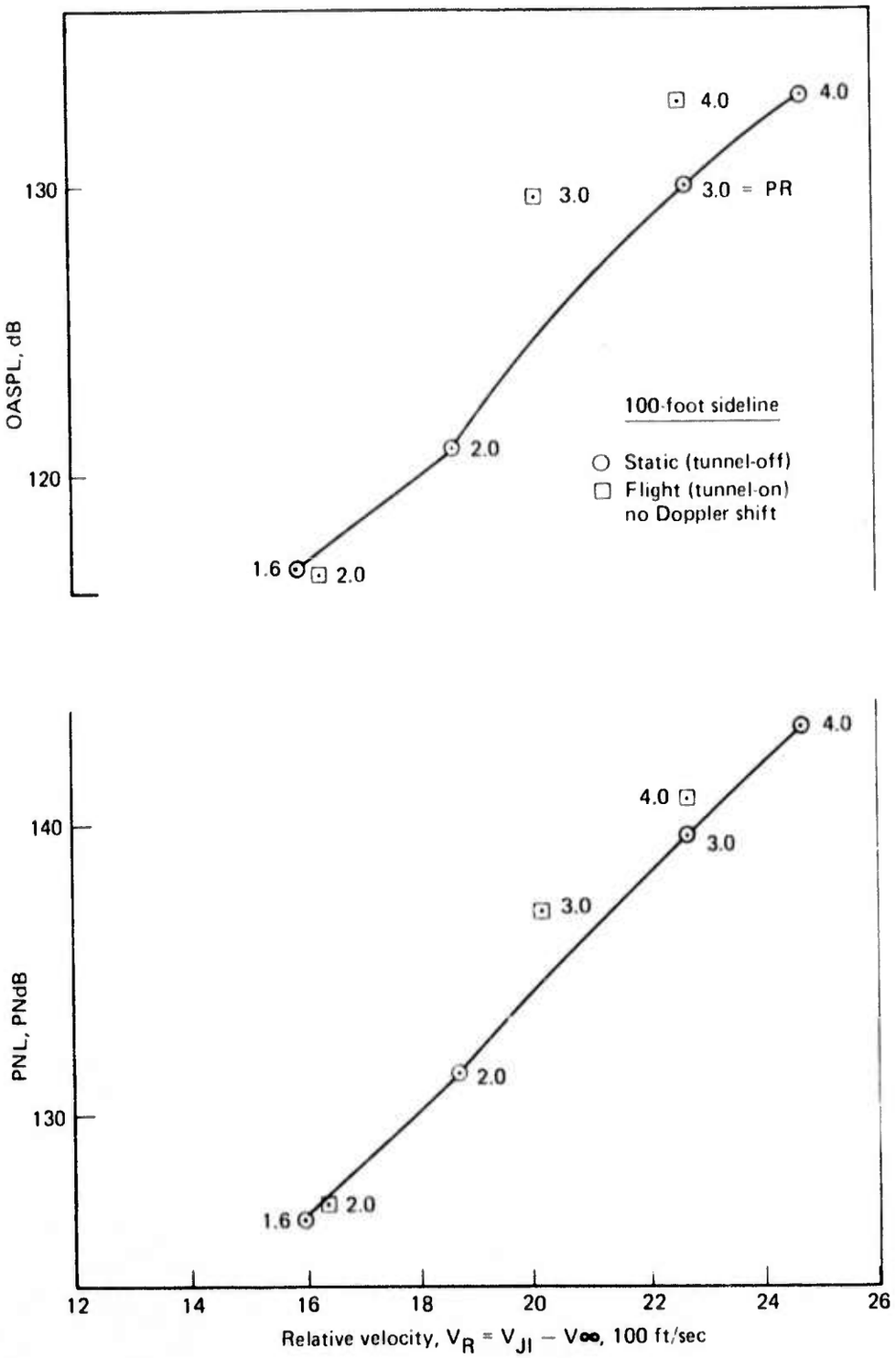

Figure 200.—9 ft by 9 ft Wind Tunnel Noise Test, OASPL and PNL Relative Velocity Relationship at 130°, Reference Conical Nozzle

NOTE: The wind tunnel absolute noise values shown for this configuration are not directly comparable with other configurations. (Ref. page 50.)

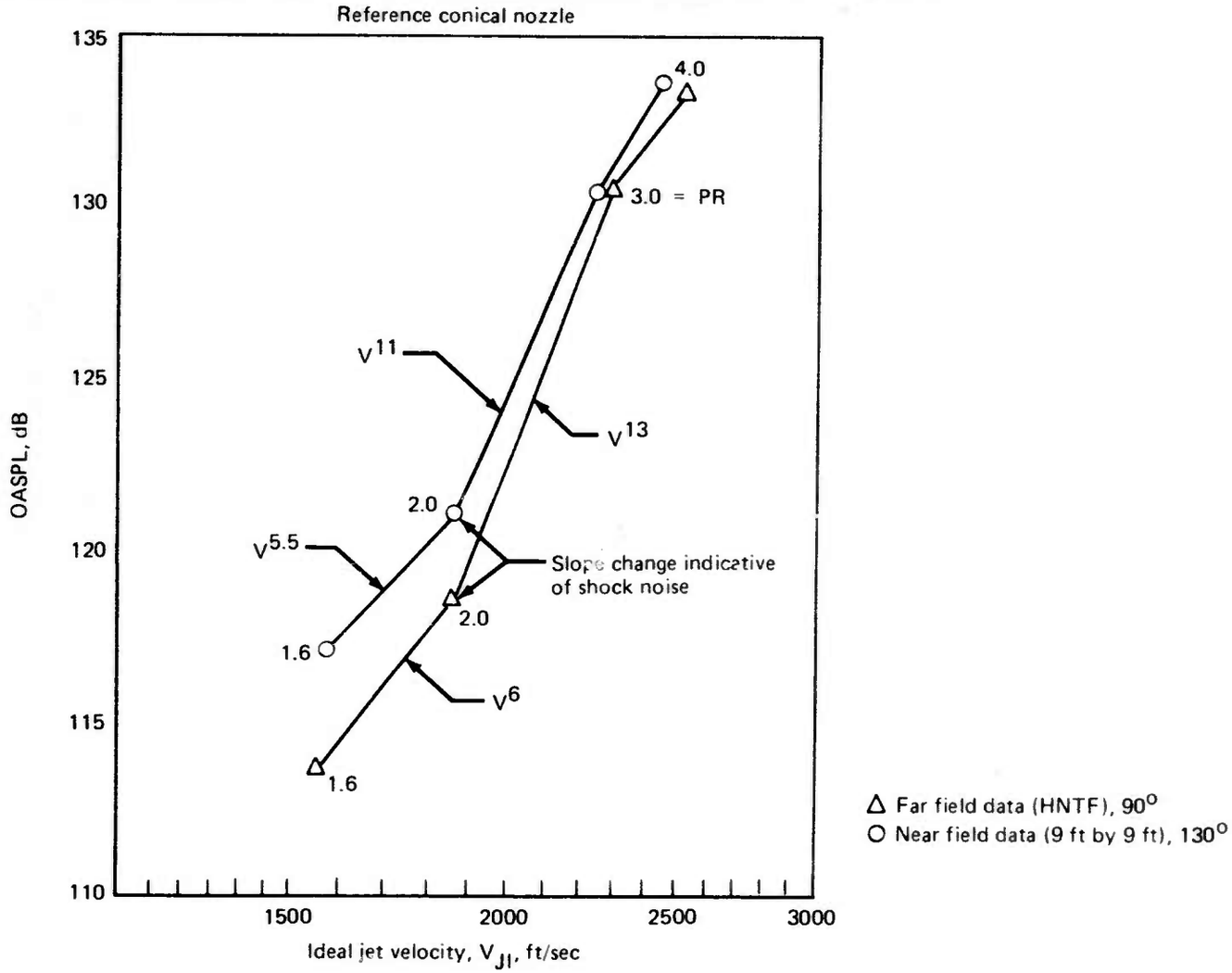

Figure 201.—9 ft by 9 ft Wind Tunnel Test, OASPL/Jet Velocity Relationship at Low-Angle (Shock Noise) Reference Conical Nozzle

NOTE: The wind tunnel absolute noise values shown for this configuration are not directly comparable with other configurations. (Ref. page 50.)

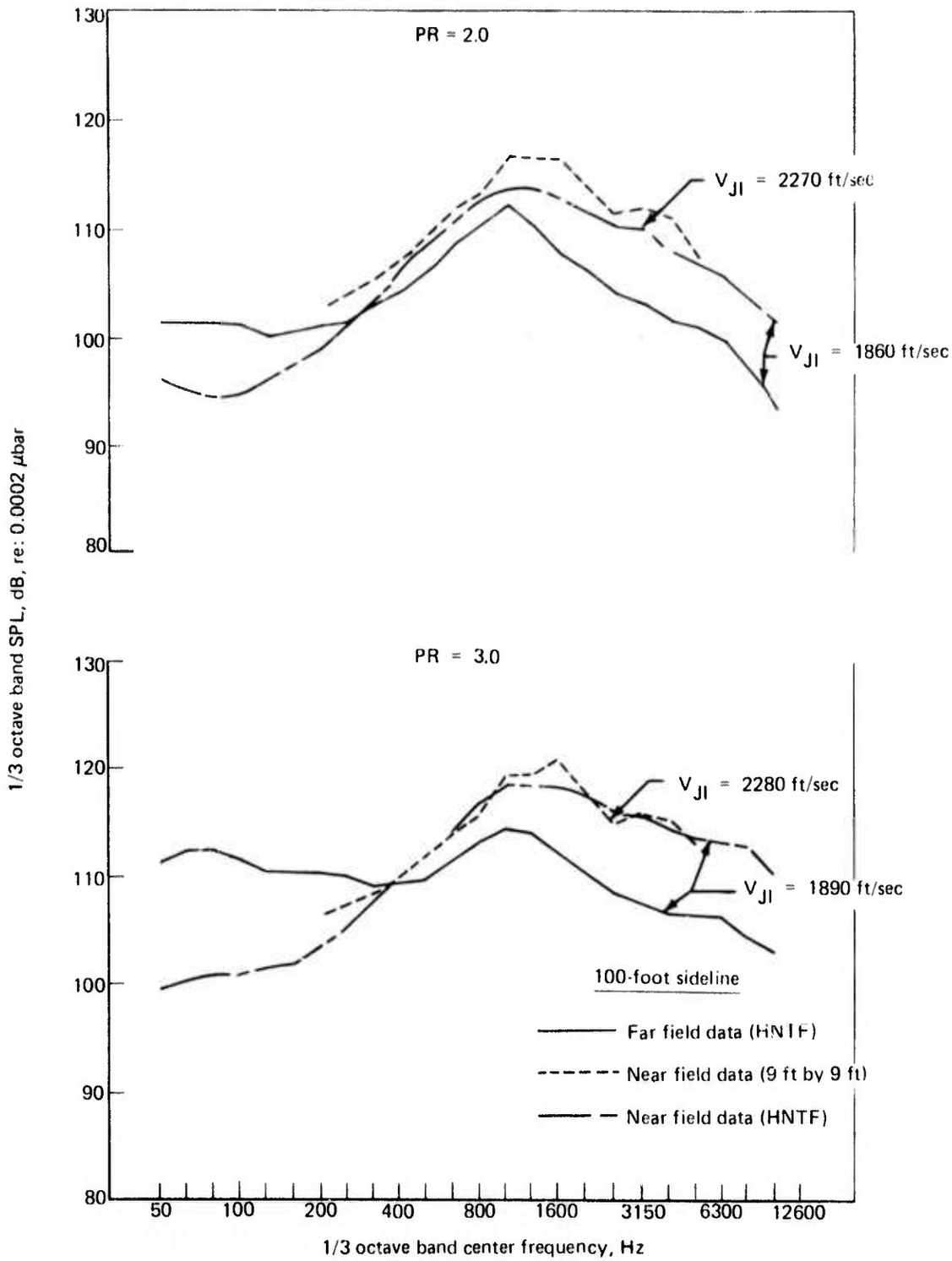

Figure 202.—9 ft by 9 ft Wind Tunnel Noise Test, Comparison of Near- and Far-field Peak Noise Spectra (130°) 37-Tube Nozzle (Ref) Without Shroud, PR 2 and 3

NOTE: The wind tunnel absolute noise values shown for this configuration are not directly comparable with other configurations. (Ref. page 50.)

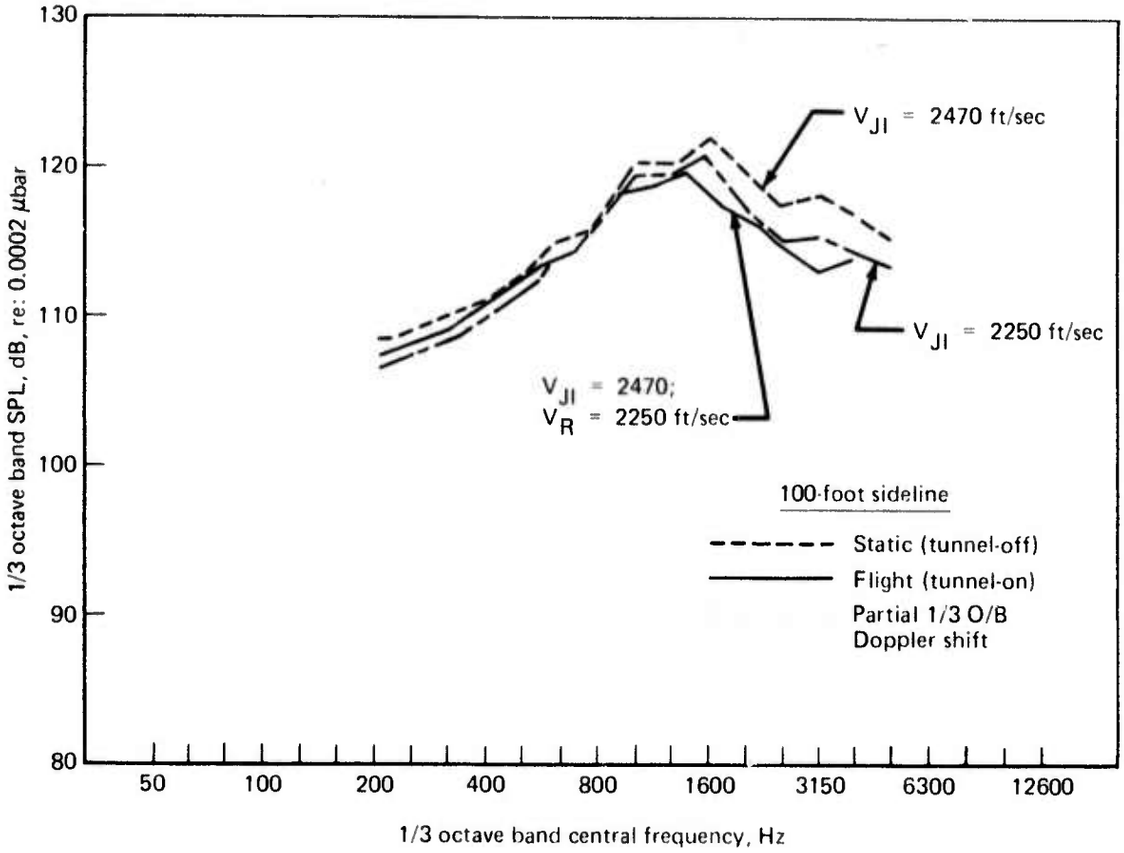

Figure 203.—9 ft by 9 ft Wind Tunnel Noise Test, Comparison of Static and Flight Peak Noise Spectra (130°) 37-Tube Nozzle (Ref) Without Shroud, PR 4

NOTE: The wind tunnel absolute noise values shown for this configuration are not directly comparable with other configurations. (Ref. page 50.)

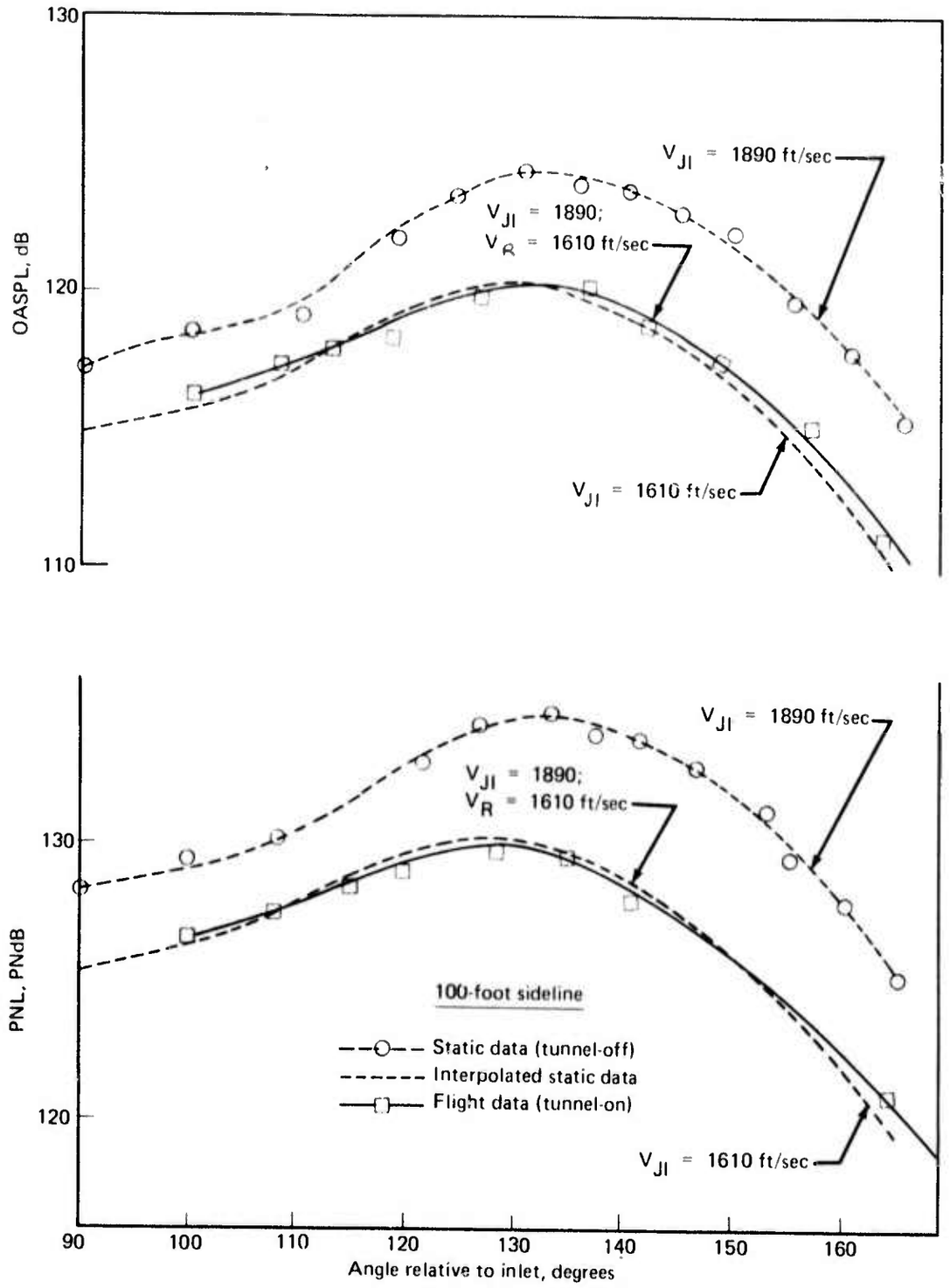

Figure 204.—9 ft by 9 ft Wind Tunnel Noise Test OASPL and PNL Directivity Static versus Flight 37-Tube Nozzle (Ref) Without Shroud, PR 2

NOTE: The wind tunnel absolute noise values shown for this configuration are not directly comparable with other configurations. (Ref. page 50.)

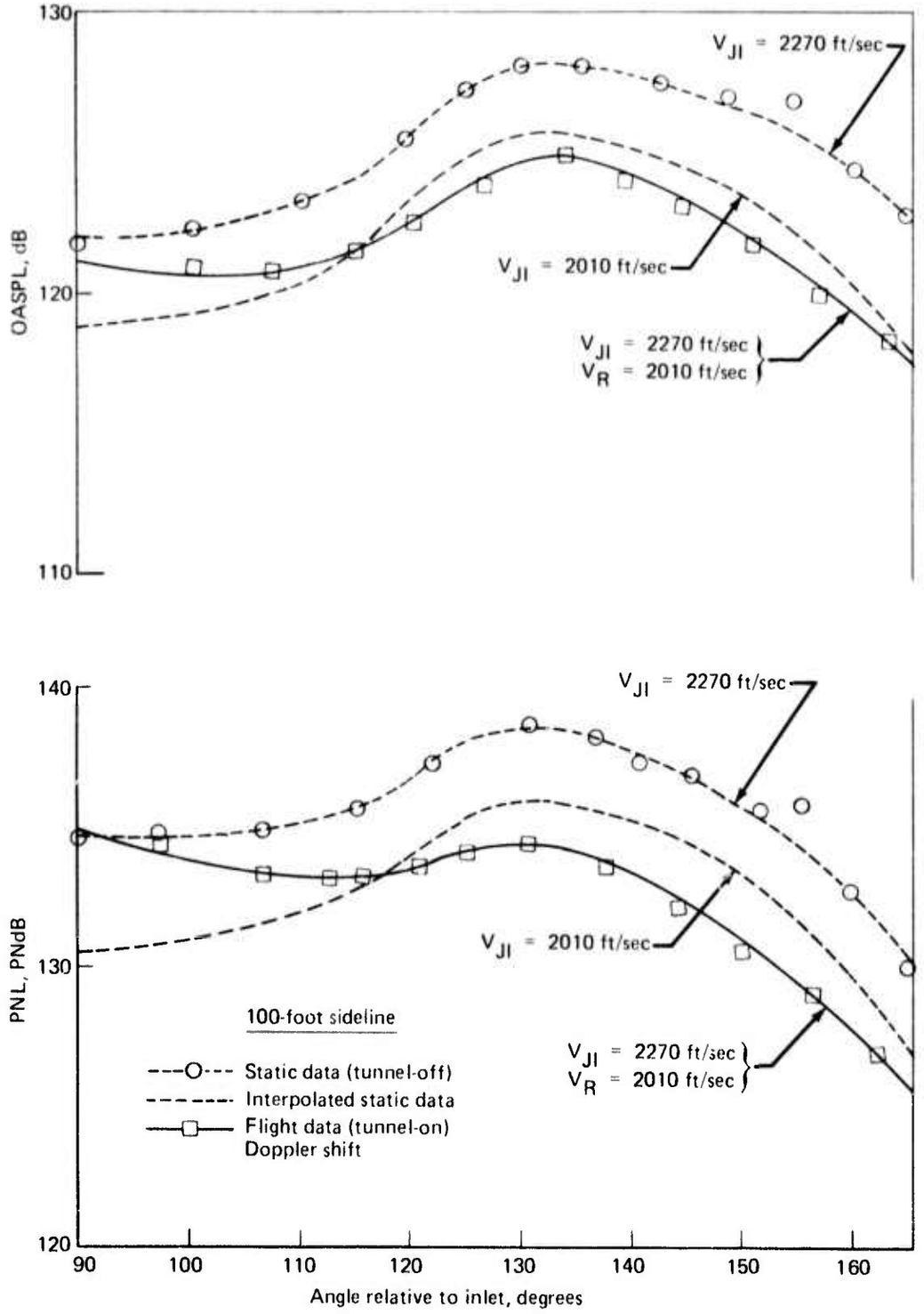

Figure 205.—9 ft by 9 ft Wind Tunnel Noise Test OASPL and PNL Directivity Static versus Flight 37-Tube Nozzle (Ref) Without Shroud, PR 3

NOTE: The wind tunnel absolute noise values shown for this configuration are not directly comparable with other configurations. (Ref. page 50.)

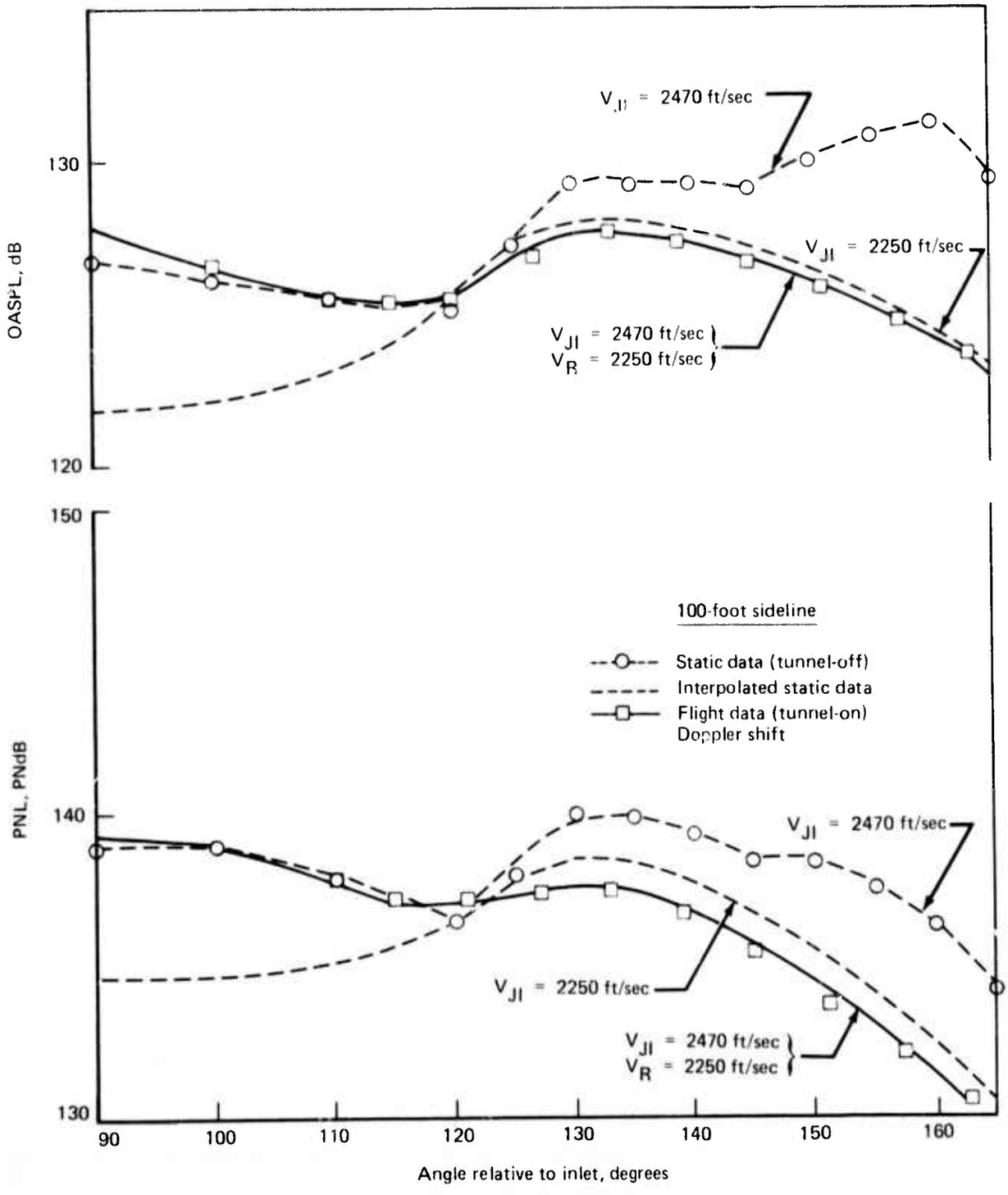

Figure 206.—9 ft by 9 ft Wind Tunnel Noise Test OASPL and PNL Directivity Static versus Flight 37-Tube Nozzle (Ref) Without Shroud, PR 4

NOTE: The wind tunnel absolute noise values shown for this configuration are not directly comparable with other configurations. (Ref. page 50.)

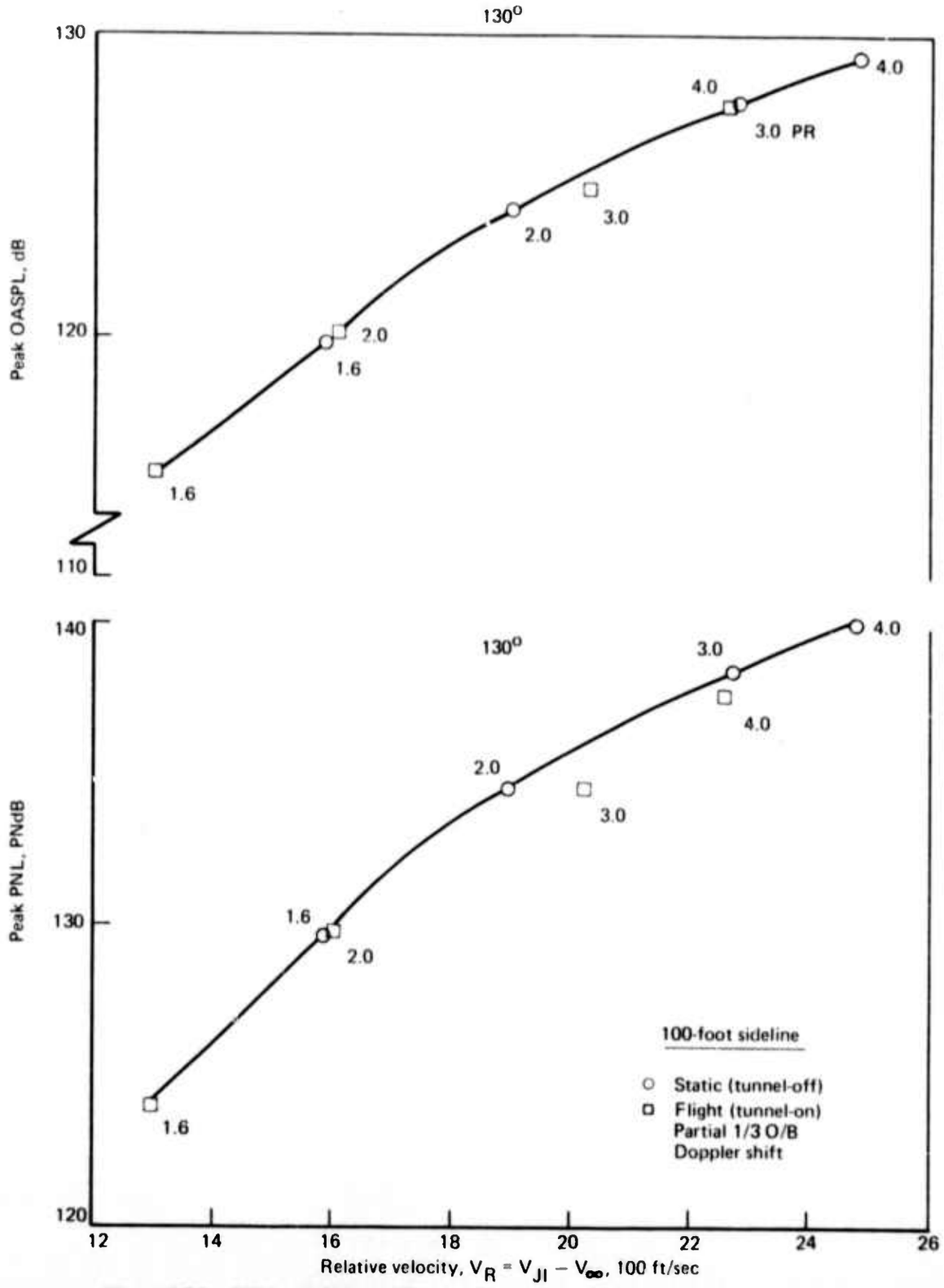

Figure 207.—9 ft by 9 ft Wind Tunnel Noise Test OASPL and PNL Relative Velocity Relationship, Peak Noise 37-Tube Nozzle (Ref) Without Shroud

NOTE: The wind tunnel absolute noise values shown for this configuration are not directly comparable with other configurations. (Ref. page 50.)

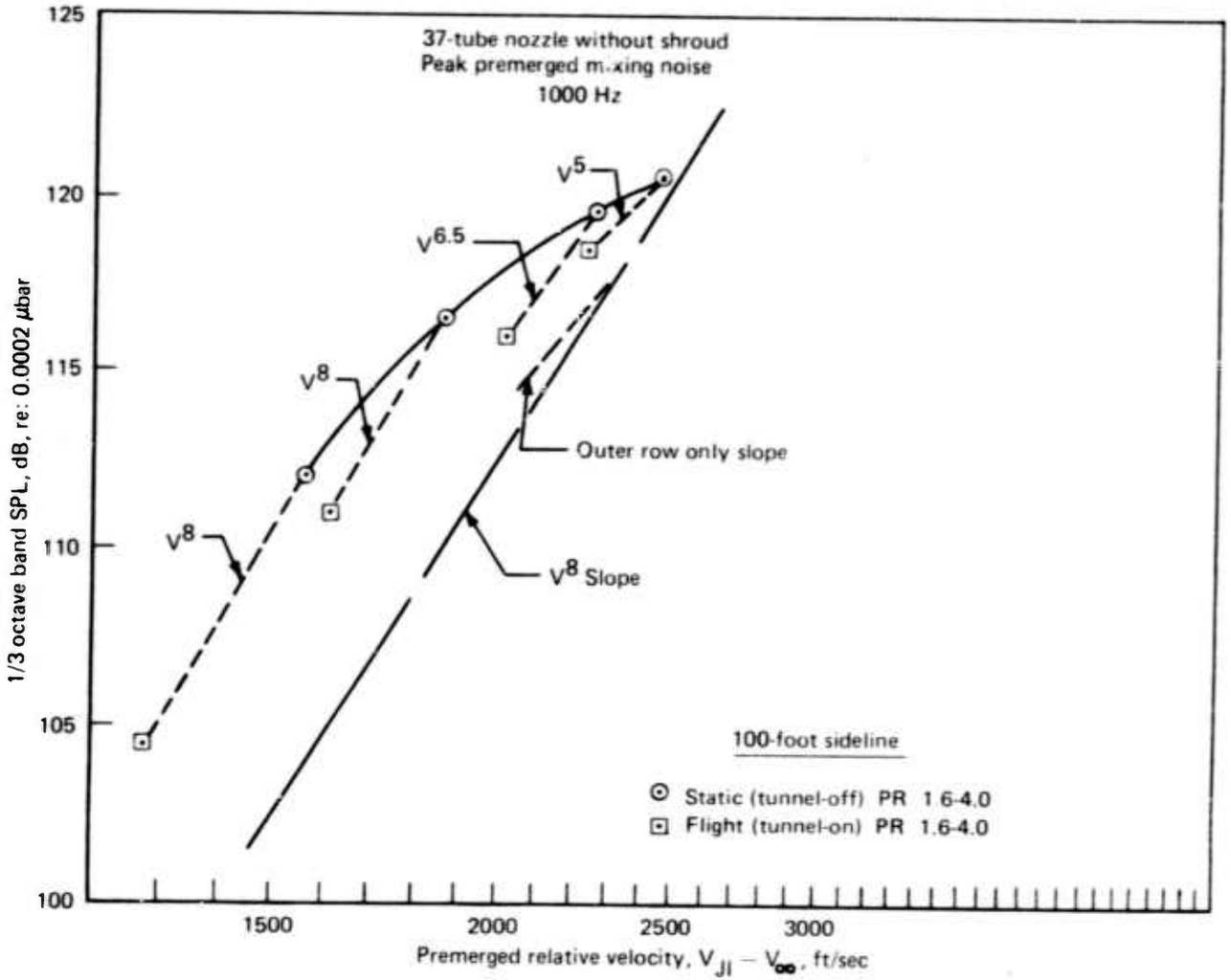

Figure 208.—9 ft by 9 ft Wind Tunnel Test, Premerged Mixing Noise Flight Effect, 37-Tube Nozzle (Ref) Without Shroud

NOTE: The wind tunnel absolute noise values shown for this configuration are not directly comparable with other configurations. (Ref. page 50.)

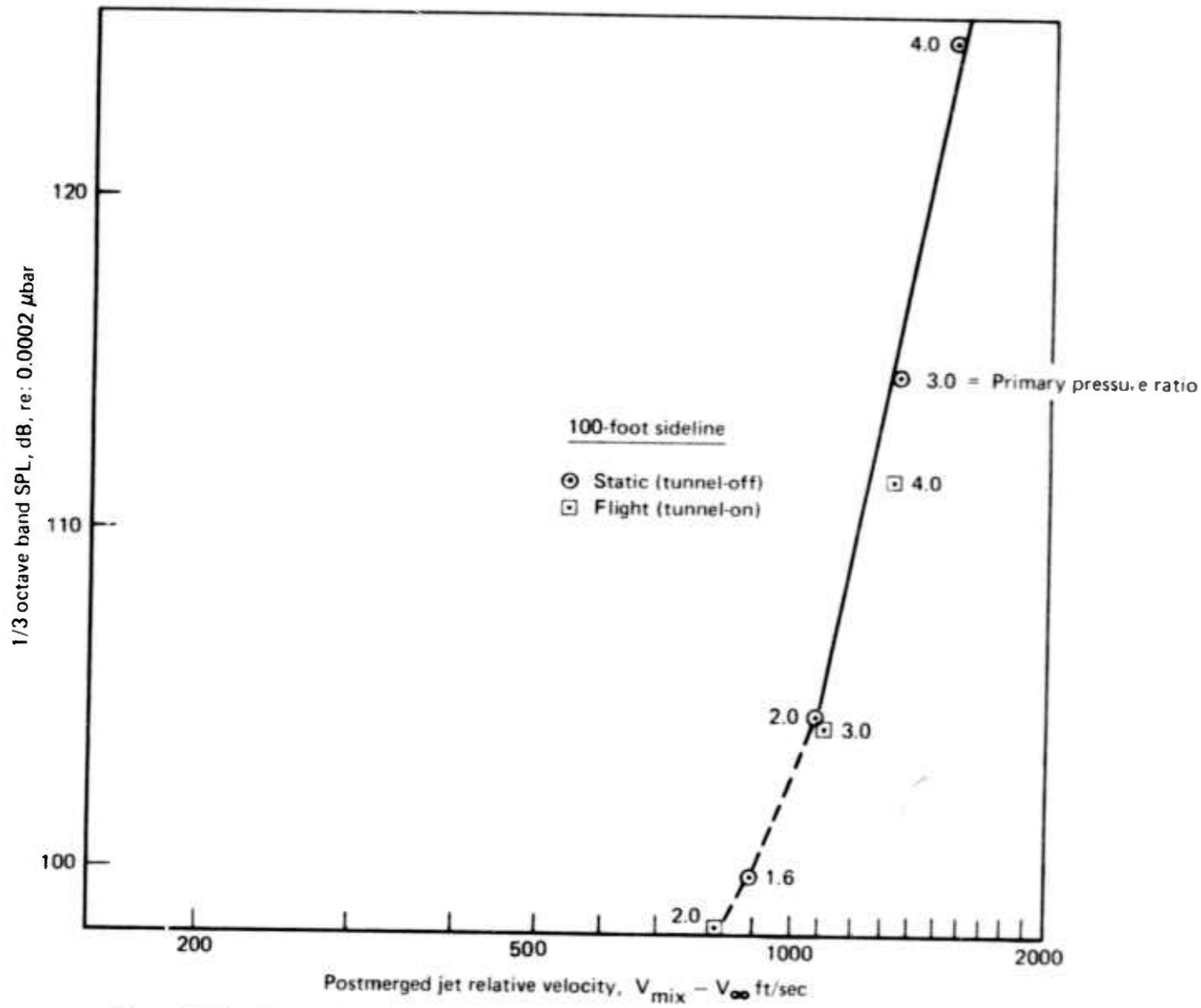

Figure 209.—9 ft by 9 ft Wind Tunnel Test Postmerged Jet-SPL/Relative Velocity Relationship 100 Hz at 160° 37-Tube (Ref) Without Shroud

NOTE: The wind tunnel absolute noise values shown for this configuration are not directly comparable with other configurations. (Ref. page 50.)

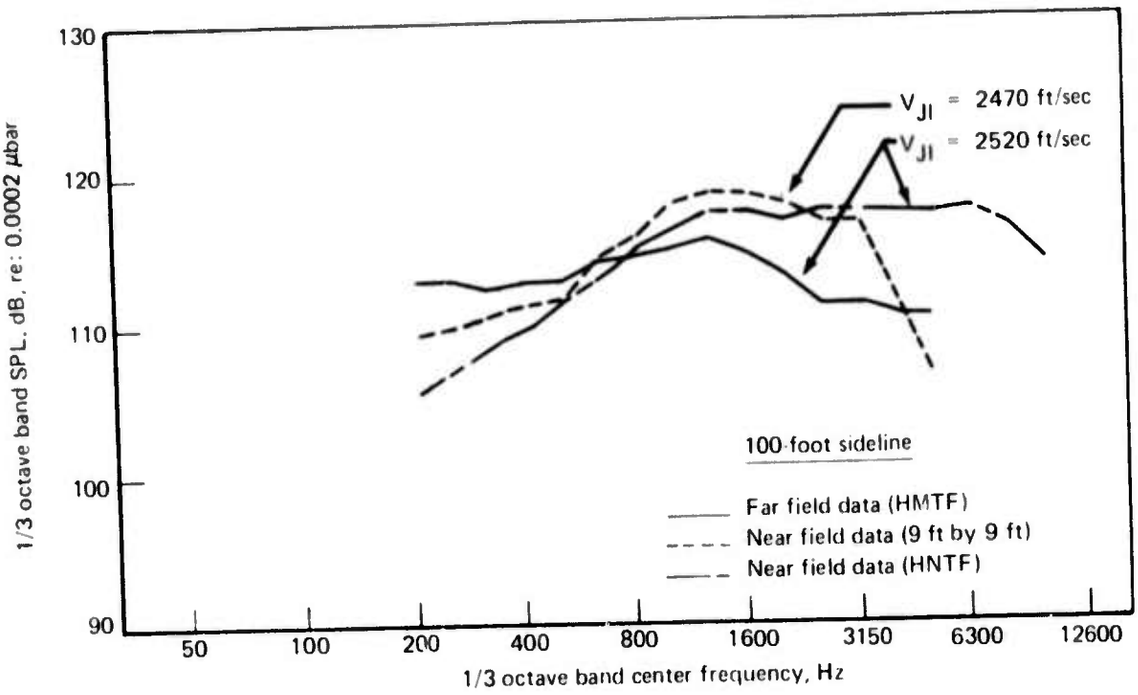

Figure 210.—9 ft by 9 ft Wind Tunnel Noise Test, Comparison of Near- and Far-Field Peak Noise Spectra (120°), 37-Tube Nozzle, With AR 3.7 Shroud, PR 4

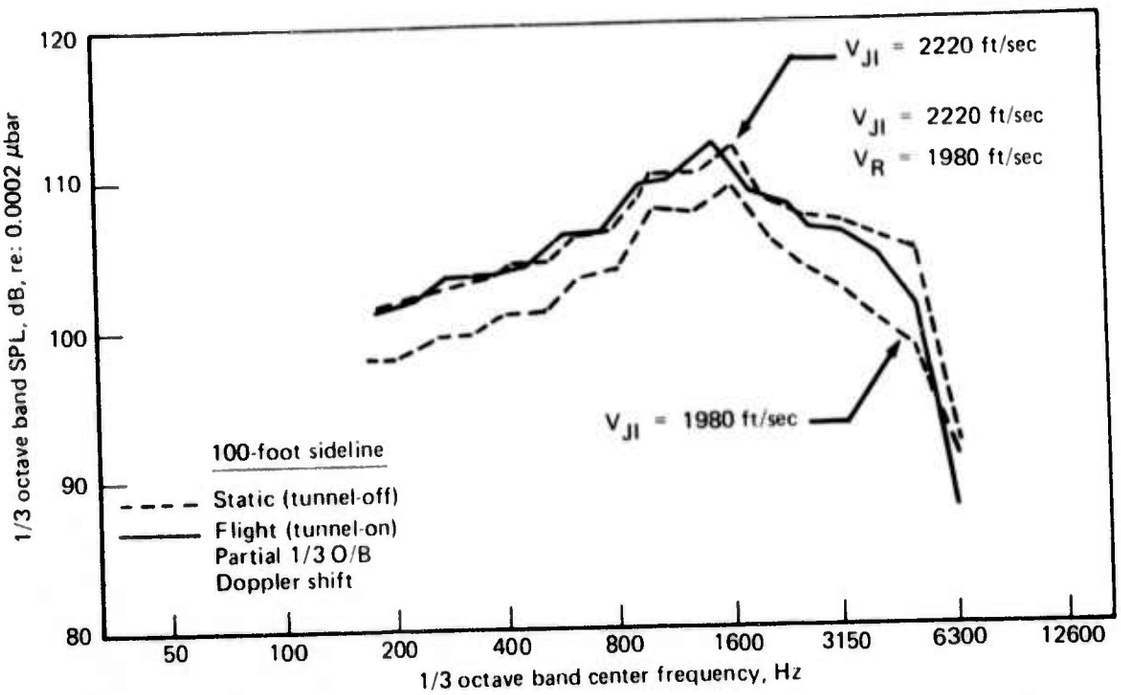

Figure 211.—9 ft by 9 ft Wind Tunnel Noise Test, Comparison of Static and Flight Peak Noise Spectra (115°) 37-Tube Nozzle (Ref) With AR 3.1 Shroud, PR 3

NOTE: The wind tunnel absolute noise values shown for this configuration are not directly comparable with other configurations. (Ref. page 50.)

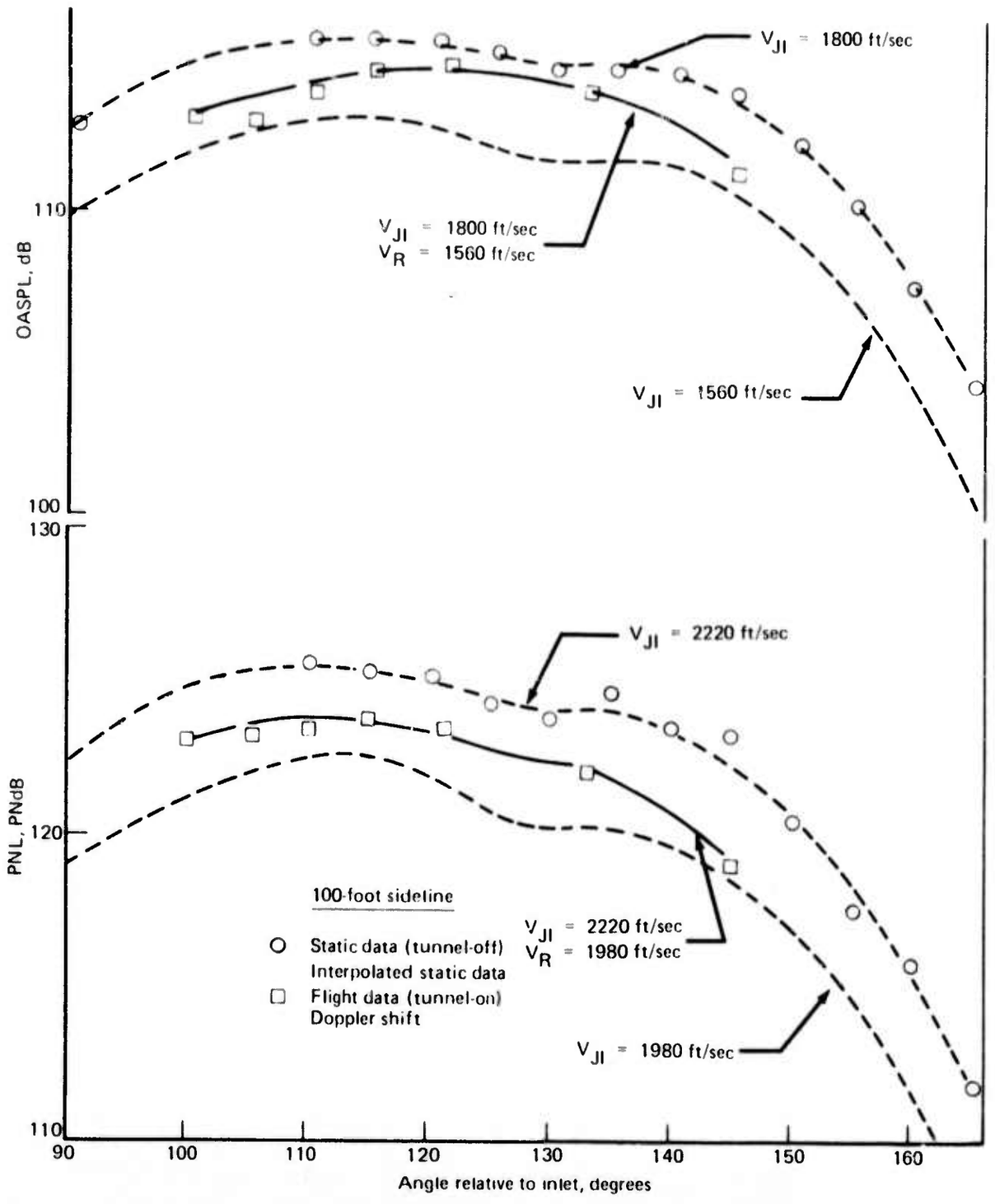

Figure 212.—9 ft by 9 ft Wind Tunnel Noise Test, OASPL and PNL Directivity, Static versus Flight, 37-Tube Nozzle (Ref) With AR 3.1 Shroud, PR 2

NOTE: The wind tunnel absolute noise values shown for this configuration are not directly comparable with other configurations. (Ref. page 50.)

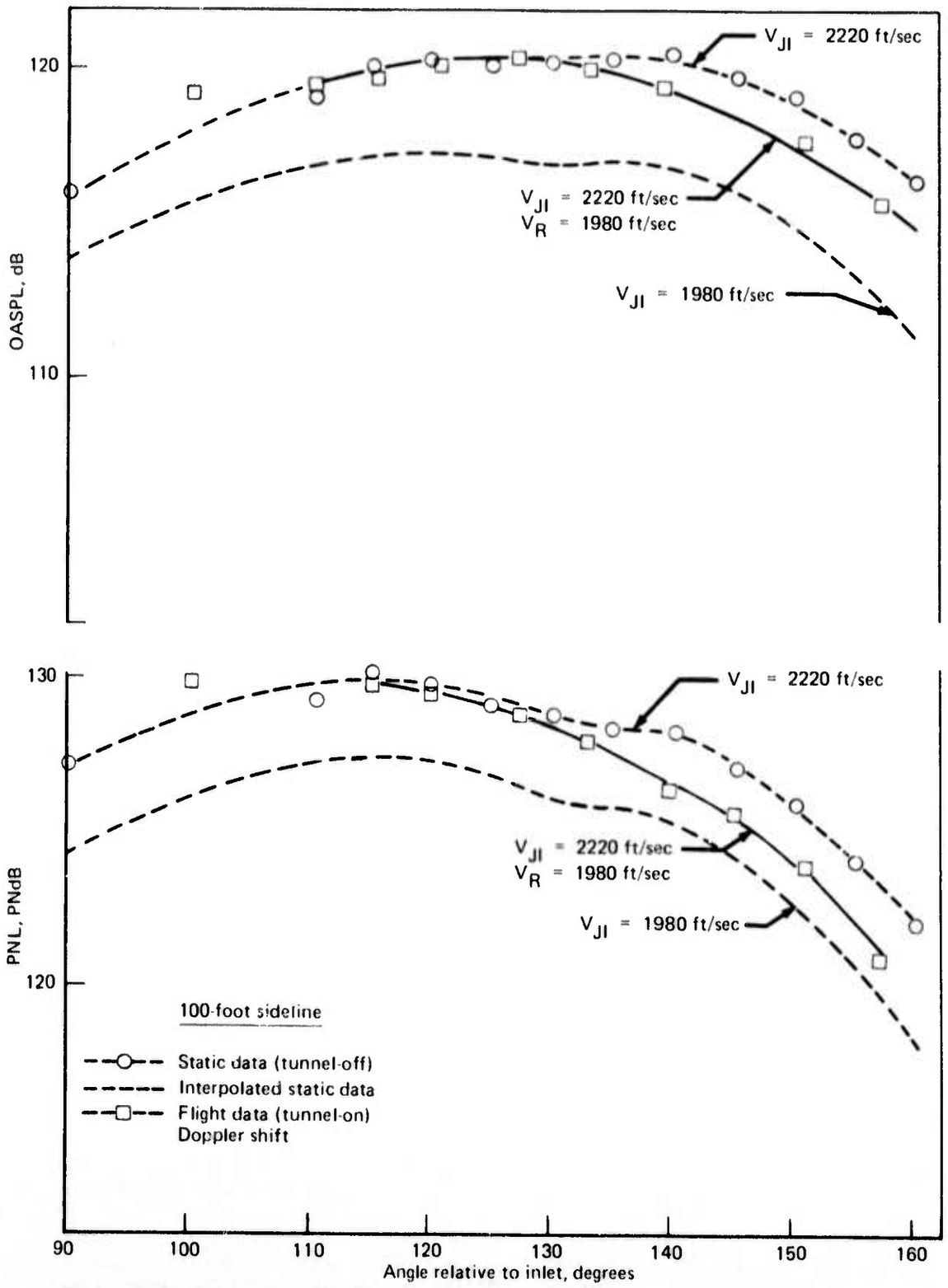

Figure 213.—9 ft by 9 ft Wind Tunnel Noise Test, OASPL and PNL Directivity, Static versus Flight, 37-Tube Nozzle (Ref) With AR 3.1 Shroud, PR 3

NOTE: The wind tunnel absolute noise values shown for this configuration are not directly comparable with other configurations. (Ref. page 50.)

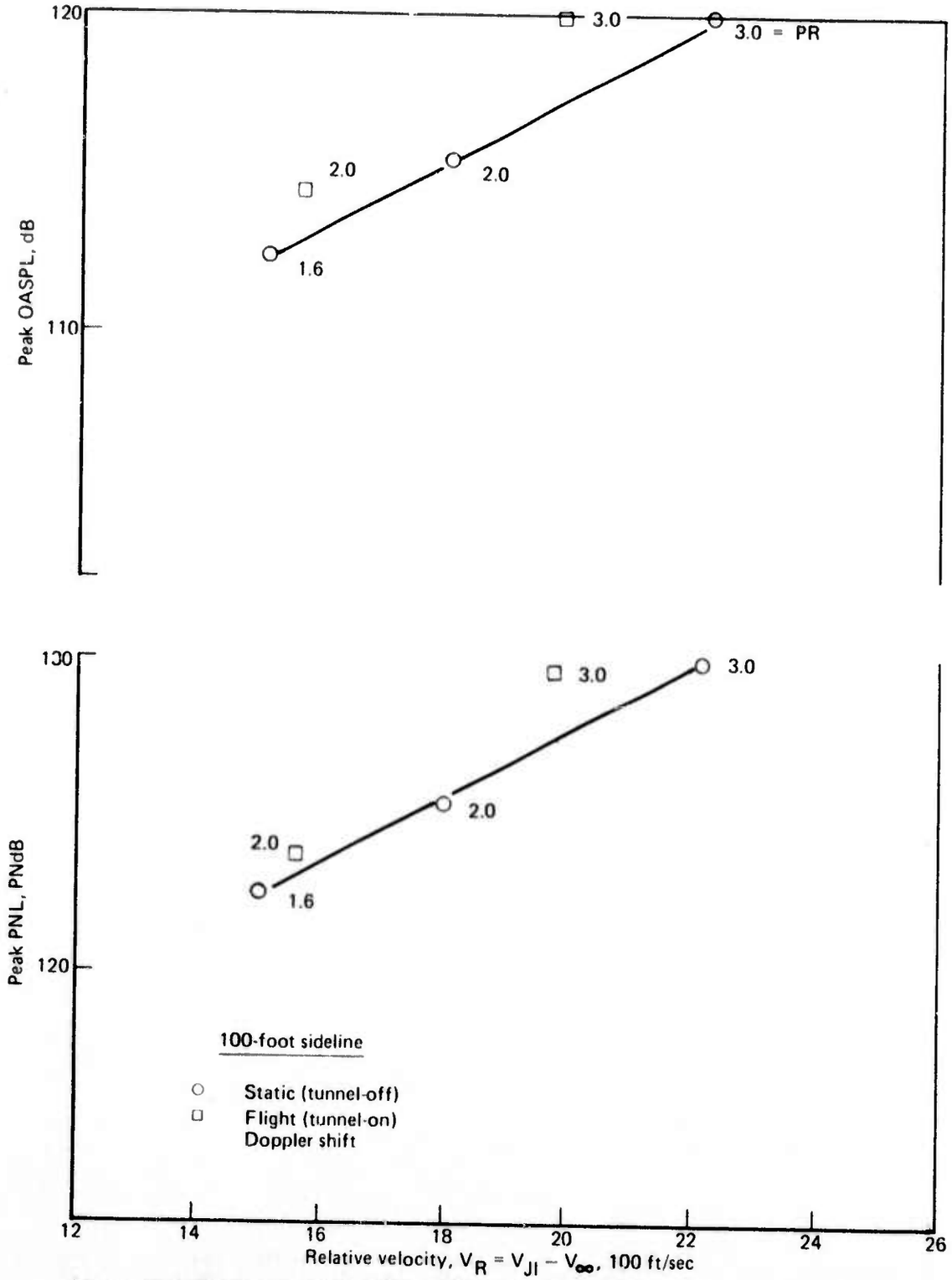

Figure 214.—9 ft by 9 ft Wind Tunnel Noise Test, OASPL and PNL Relative Velocity Relationship, Peak Noise (115°), 37-Tube Nozzle (Ref) With AR 3.1 Shroud

NOTE: The wind tunnel absolute noise values shown for this configuration are not directly comparable with other configurations. (Ref. page 50.)

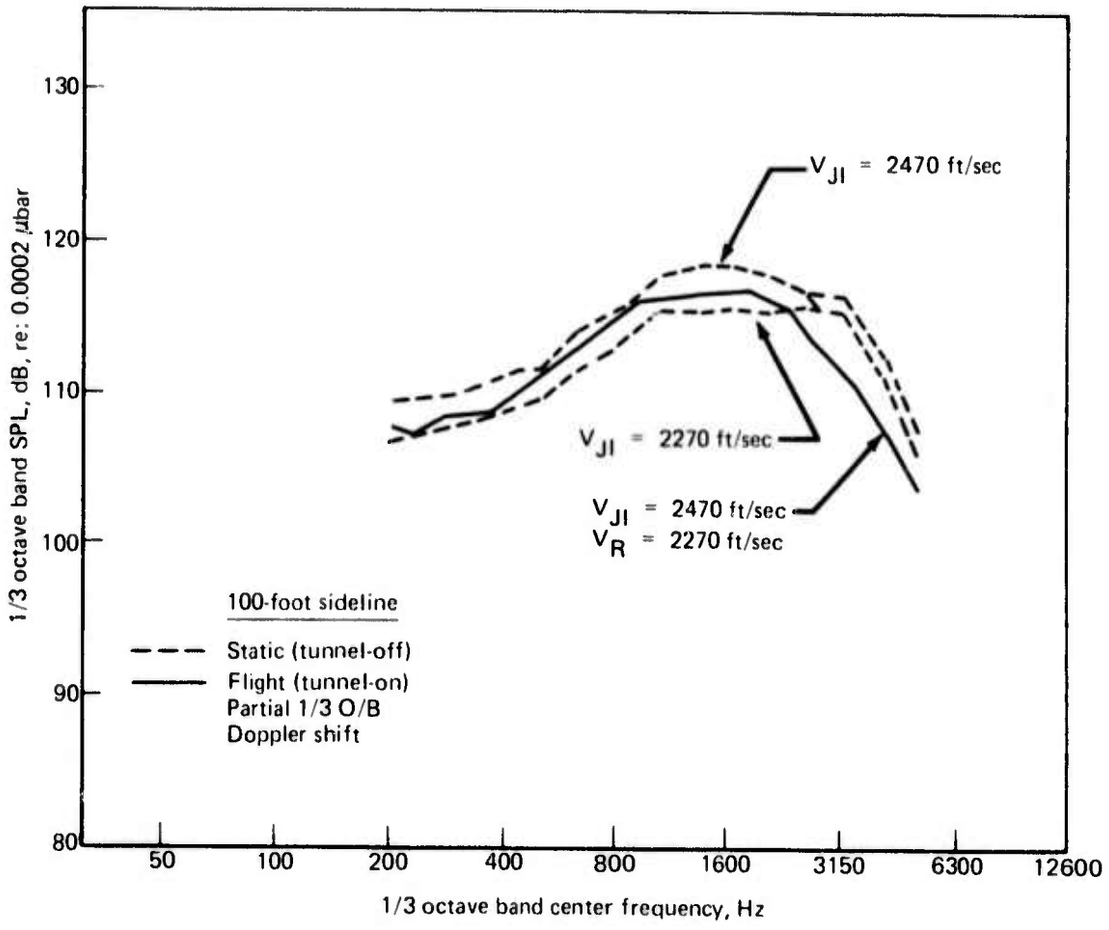

Figure 215.—9 ft by 9 ft Wind Tunnel Noise Test, Comparison of Static and Flight Peak Noise Spectra (120°), 37-Tube Nozzle (Ref) With AR 3.7, Shroud, PR 4

NOTE: The wind tunnel absolute noise values shown for this configuration are not directly comparable with other configurations. (Ref. page 50.)

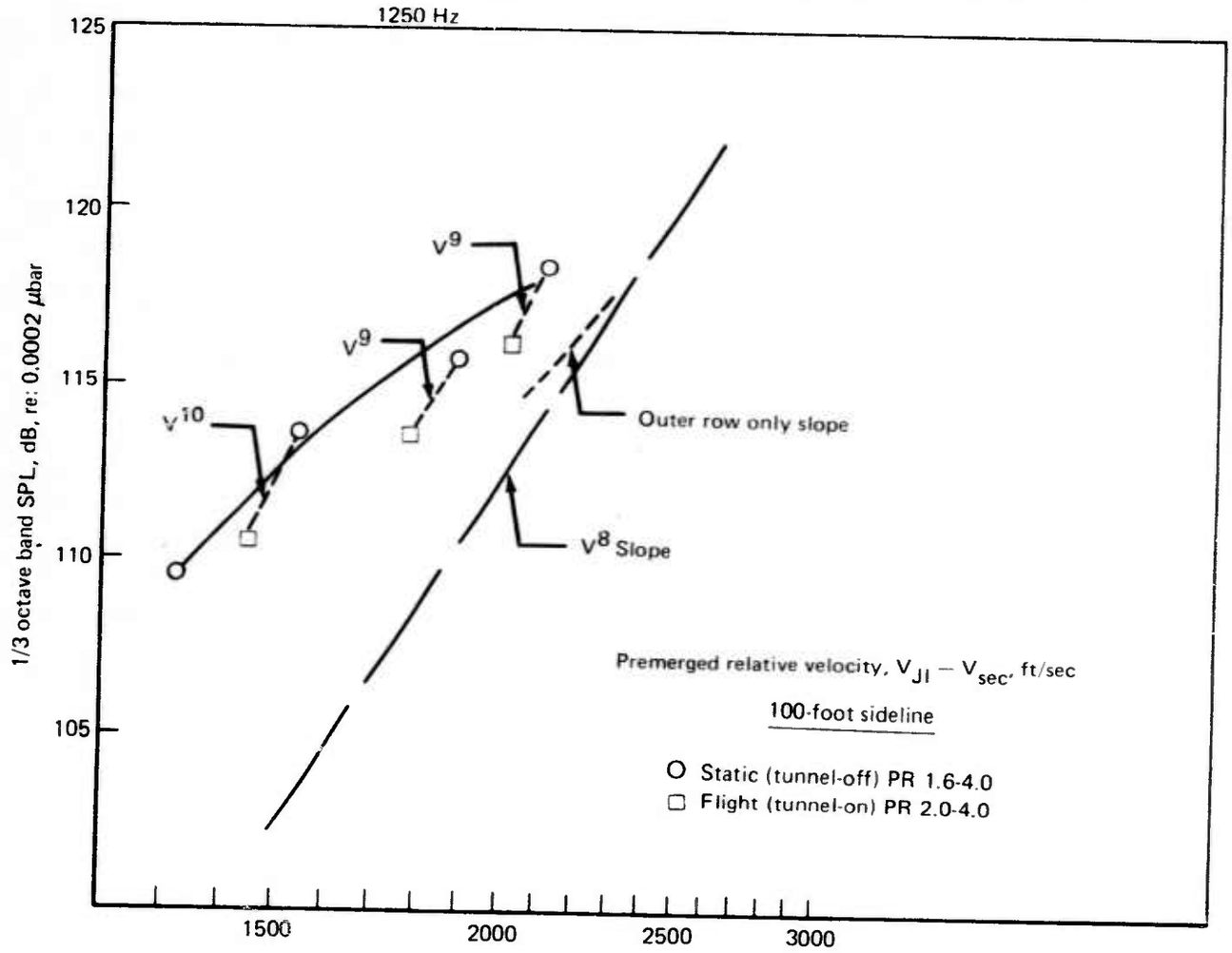

Figure 216. — 9 ft by 9 ft Wind Tunnel Test, Premerged Mixing Noise Flight Effect, 3.7-tube Nozzle (Ref) With AR 3.7 Shroud

NOTE: The wind tunnel absolute noise values shown for this configuration are not directly comparable with other configurations. (Ref. page 50.)

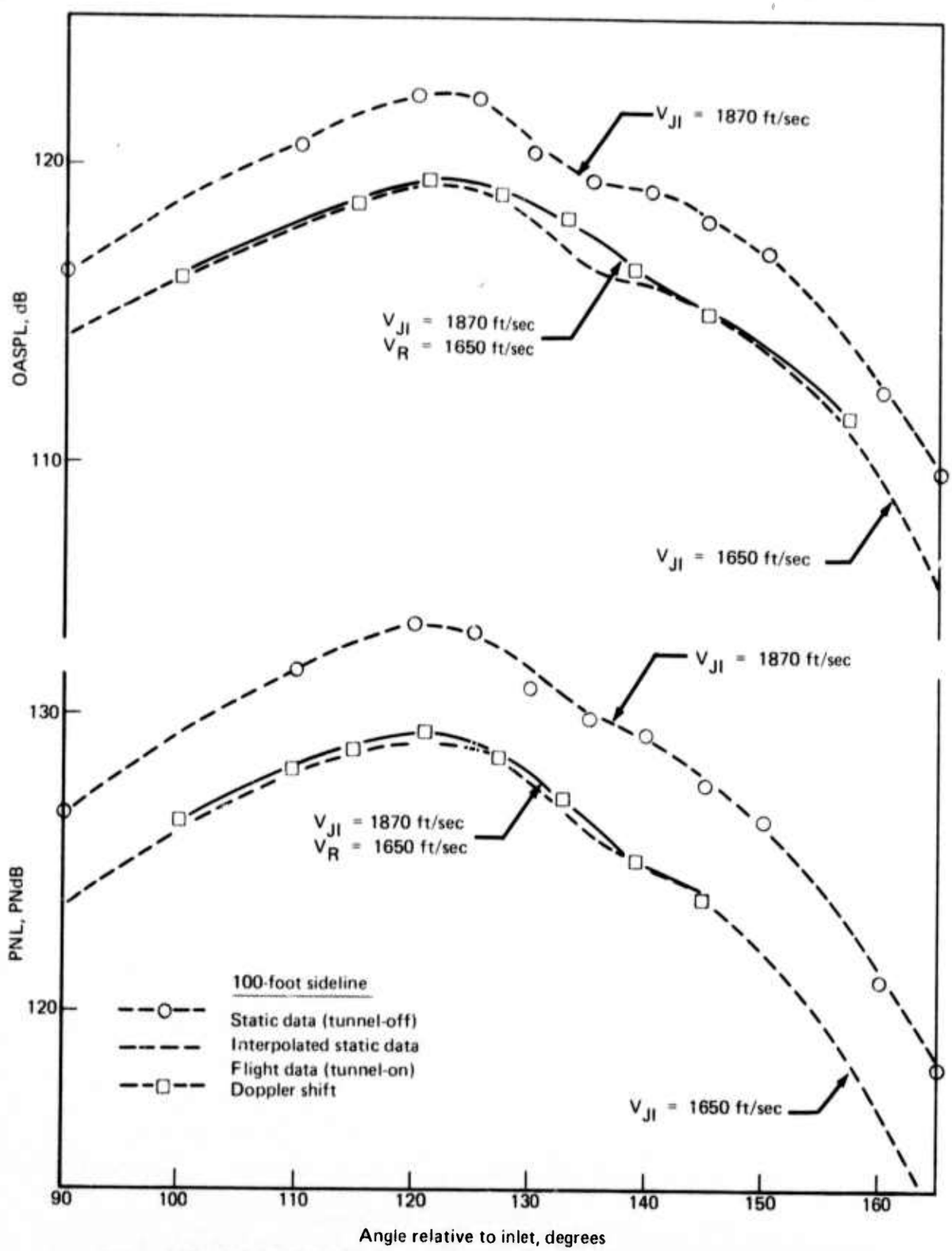

Figure 217.—9 ft by 9 ft Wind Tunnel Noise Test, OASPL and PNL Directivity, Static versus Flight, 37-Tube Nozzle (Ref) With AR 3.7 Shroud, PR 2

NOTE: The wind tunnel absolute noise values shown for this configuration are not directly comparable with other configurations. (Ref. page 50.)

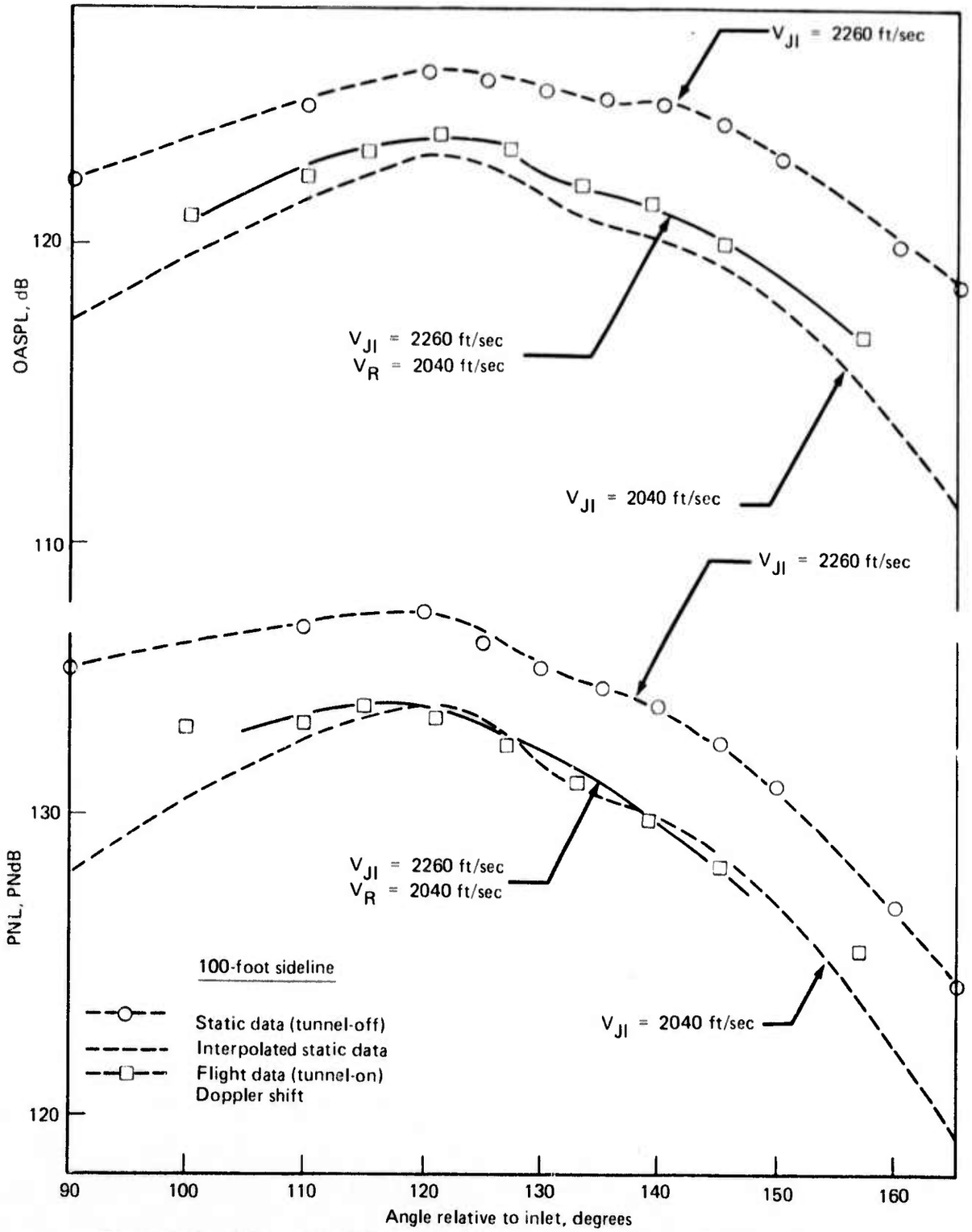

Figure 218.—9 ft by 9 ft Wind Tunnel Noise Test, OASPL and PNL Directivity, Static versus Flight, 37-Tube Nozzle (Ref) With AR 3.7 Shroud, PR 3

NOTE: The wind tunnel absolute noise values shown for this configuration are not directly comparable with other configurations. (Ref. page 50.)

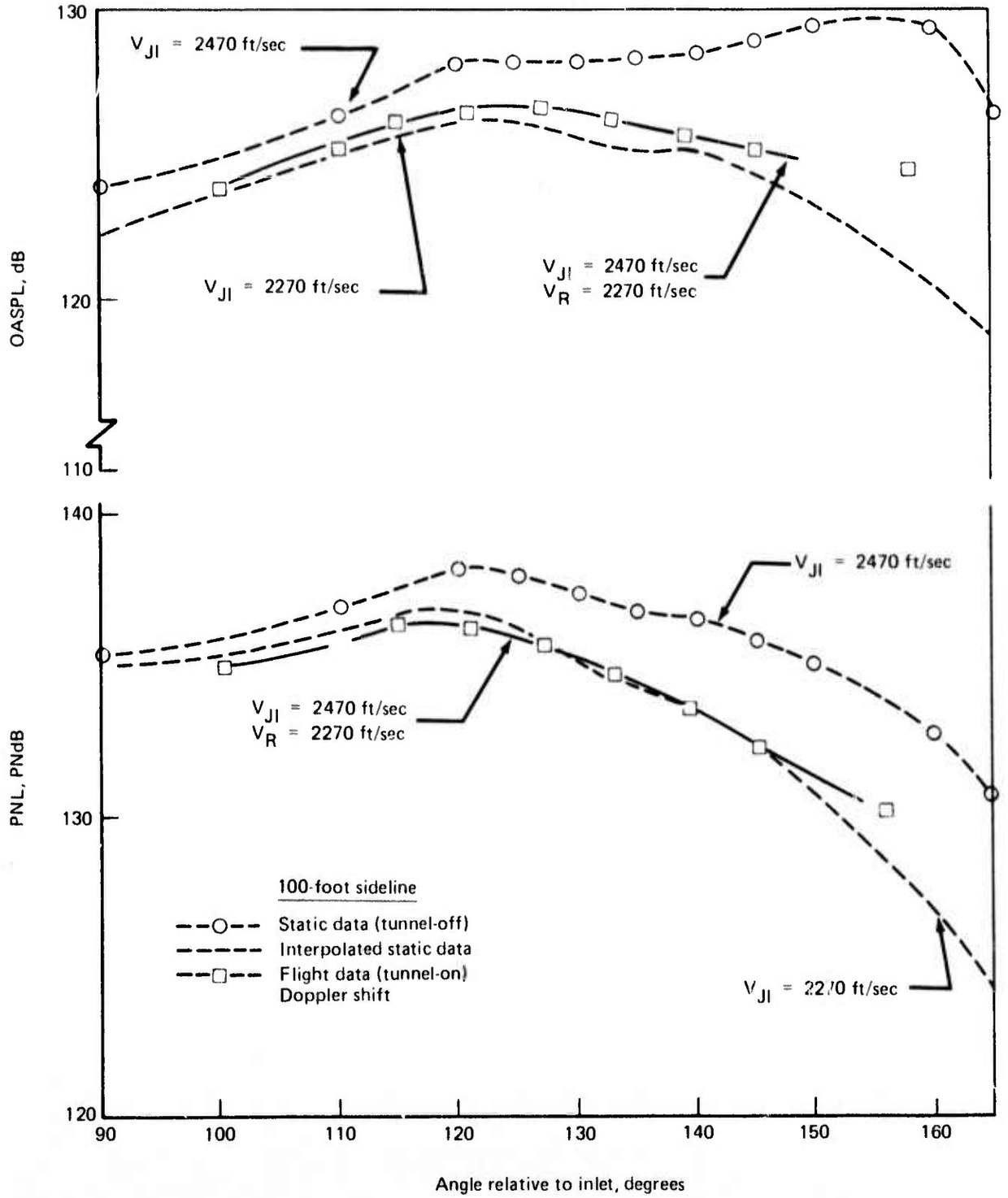

Figure 219.—9 ft by 9 ft Wind Tunnel Noise Test, OASPL and PNL Directivity, Static versus Flight, 37-Tube Nozzle (Ref) With AR 3.7 Shroud, PR 4

NOTE: The wind tunnel absolute noise values shown for this configuration are not directly comparable with other configurations. (Ref. page 50.)

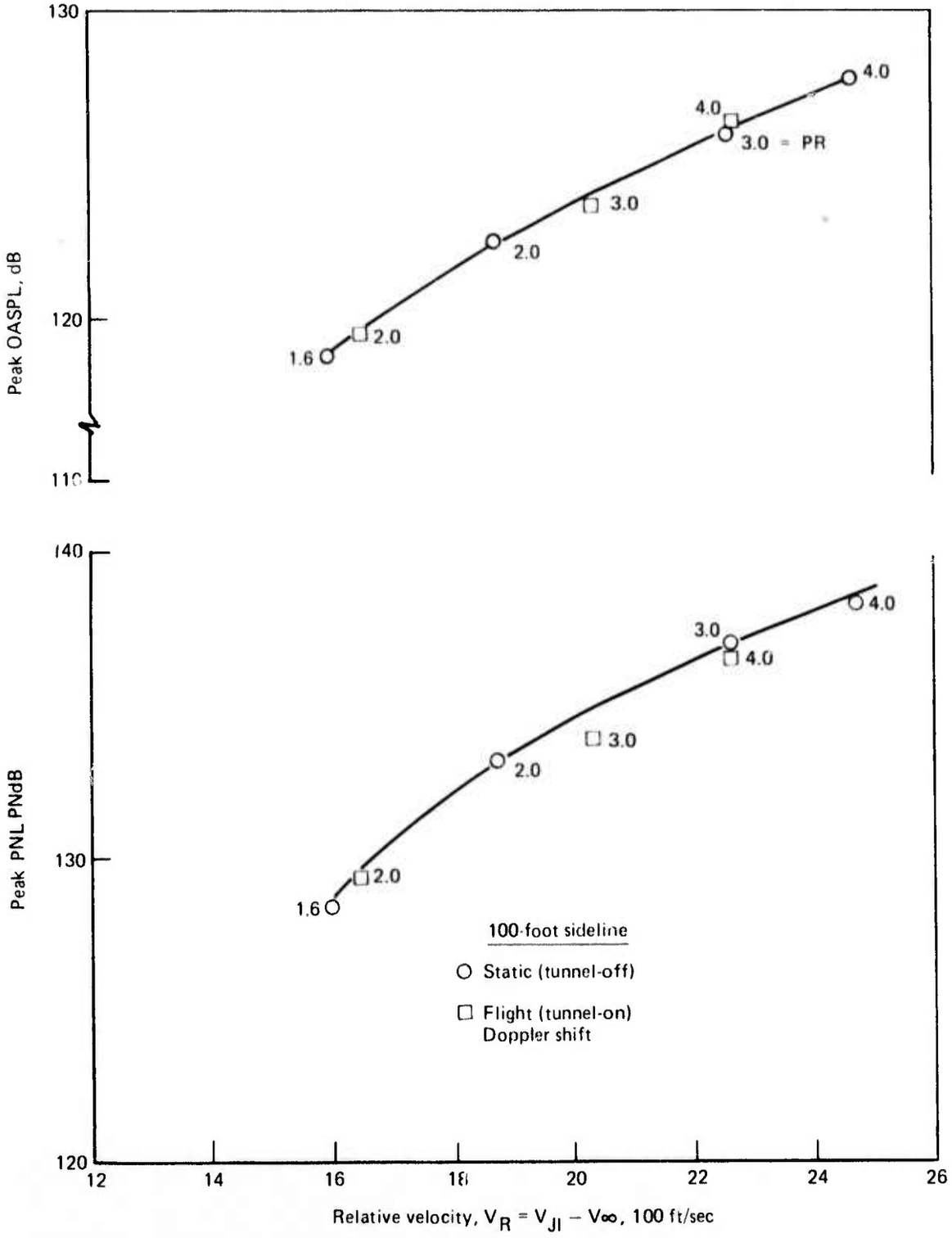

Figure 220.—9 ft by 9 ft Wind Tunnel Noise Test, OASPL and PNL Relative Velocity Relationship, Peak Noise (120°), 37-Tube Nozzle (Ref) With AR 3.7 Shroud

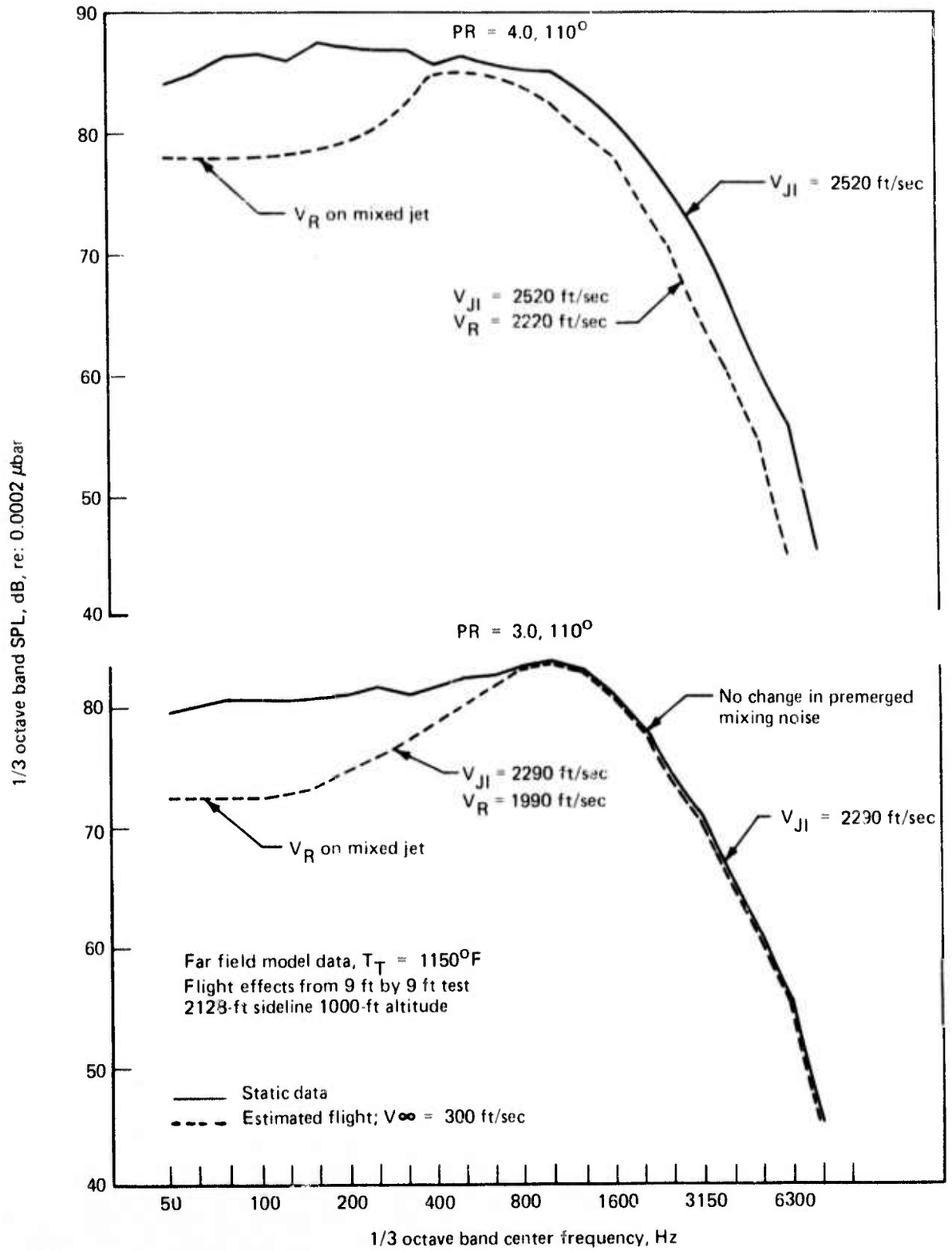

Figure 221.—9 ft by 9 ft Wind Tunnel Noise Test Static and Flight Spectra for 37-Tube Nozzle (Ref) With AR 3.1 Shroud, PR 3 and 4, 2128-ft Sideline

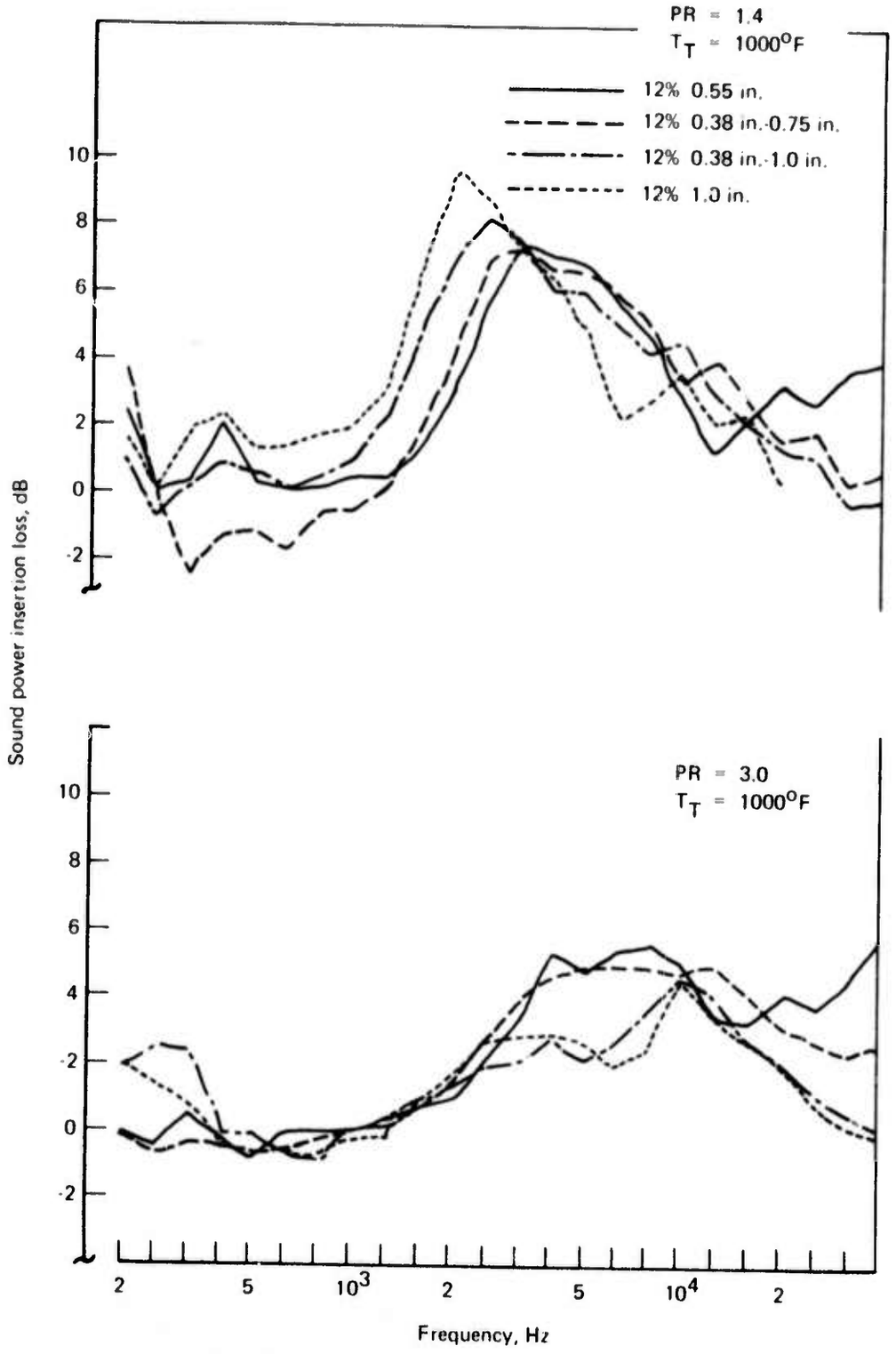

Figure 222.—L/D_E = 4 Ejector With Various Linings

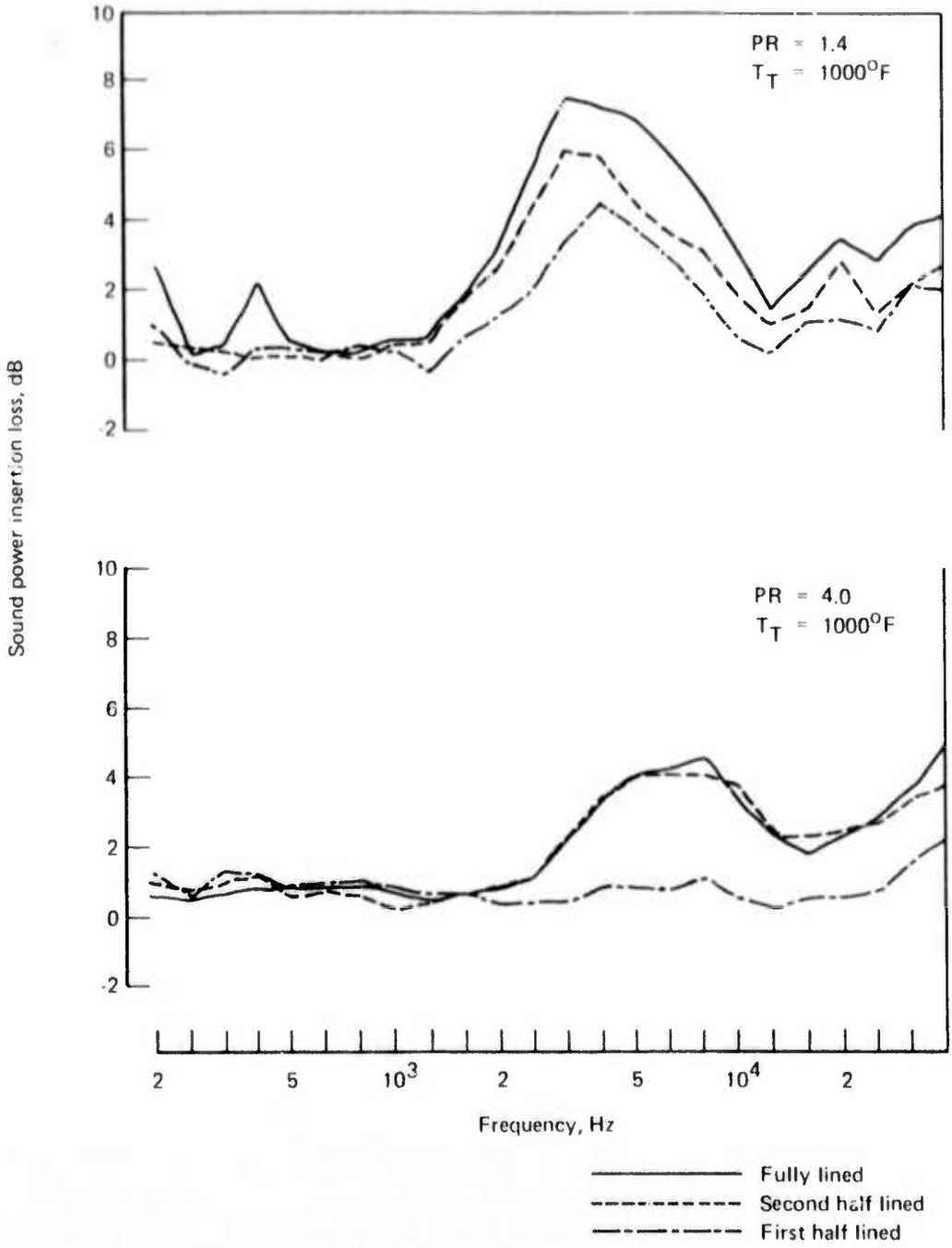

Figure 223.—L/D_E = 4 Ejector With 12% Open Area, 0.55 in. Deep Lining

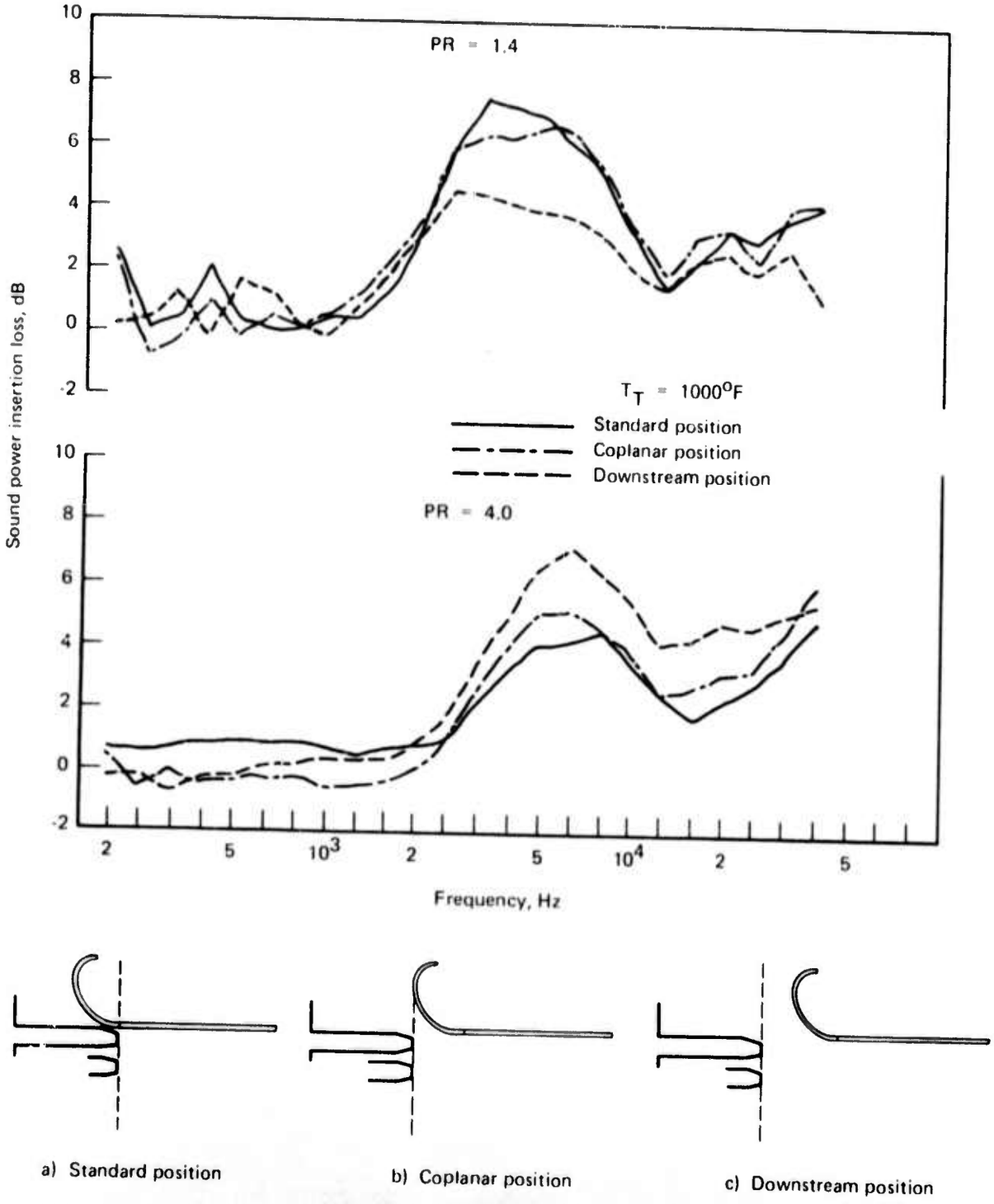

a) Standard position

b) Coplanar position

c) Downstream position

Figure 224.—L/D_E = 4 Ejector With 12% Open Area, 0.55 in. Deep Lining

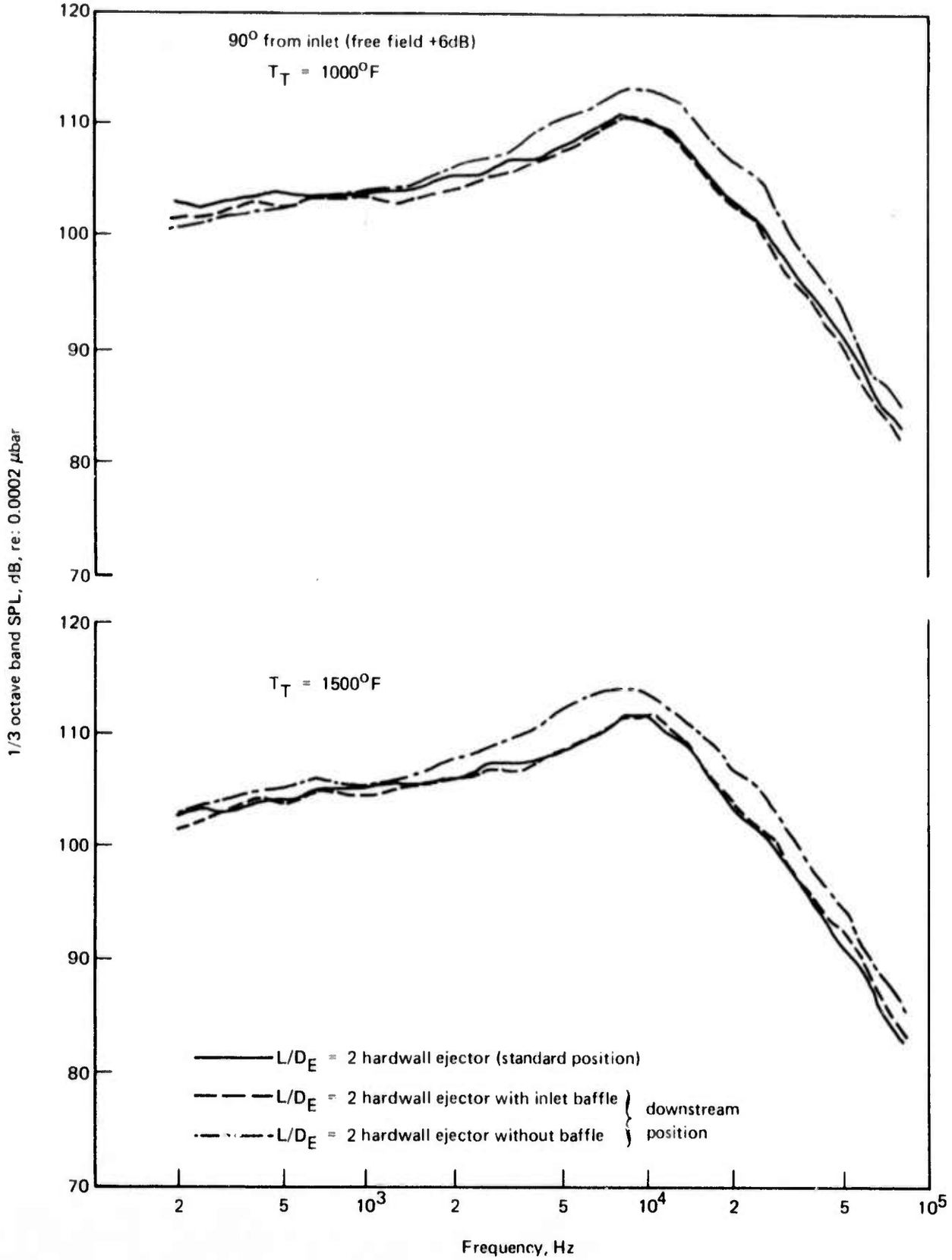

Figure 225.—Ejector Inlet Radiated Noise at Nozzle PR = 4.0

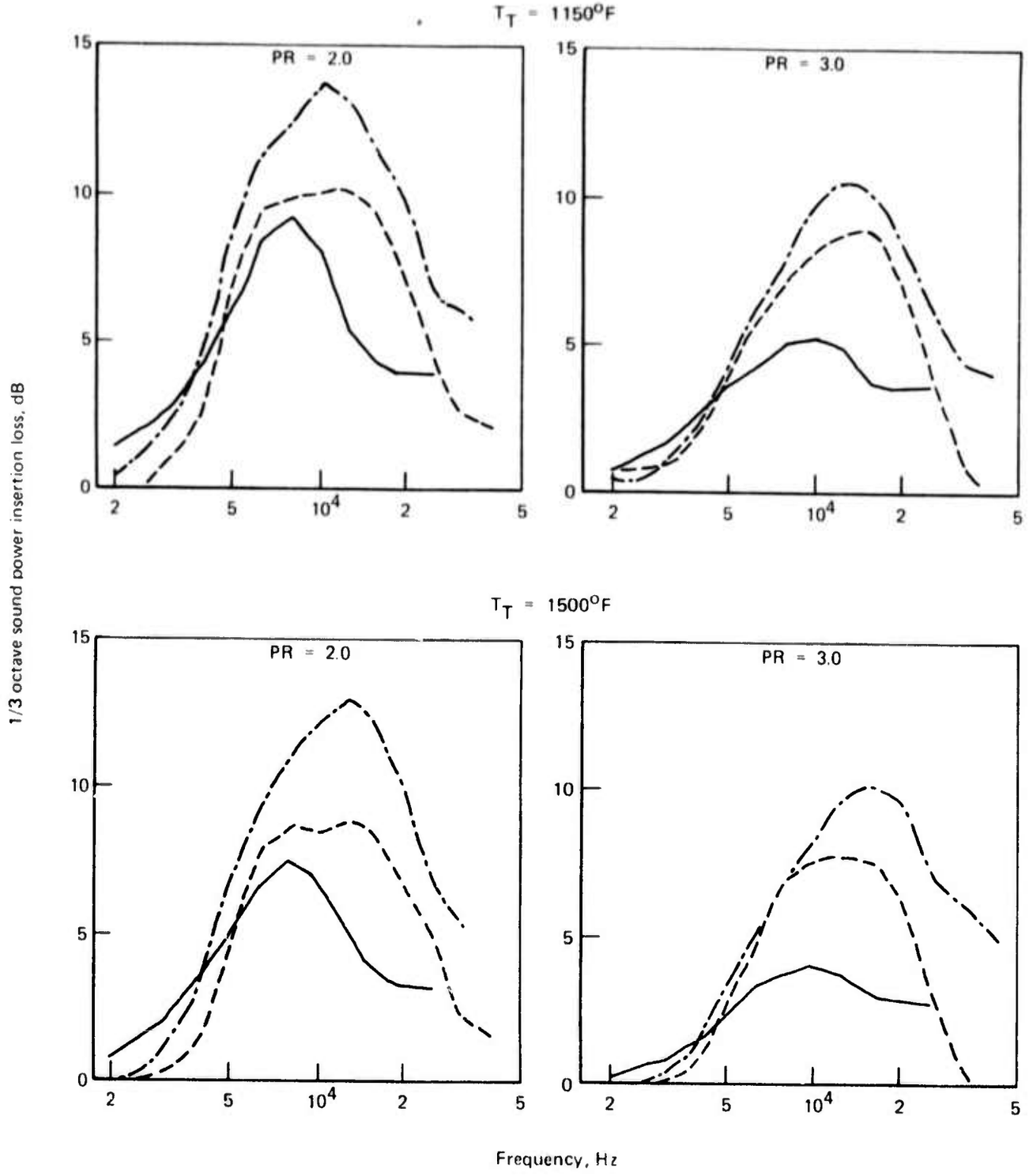

Figure 226.—Lined Ejector Sound-Power Insertion Loss Characteristics

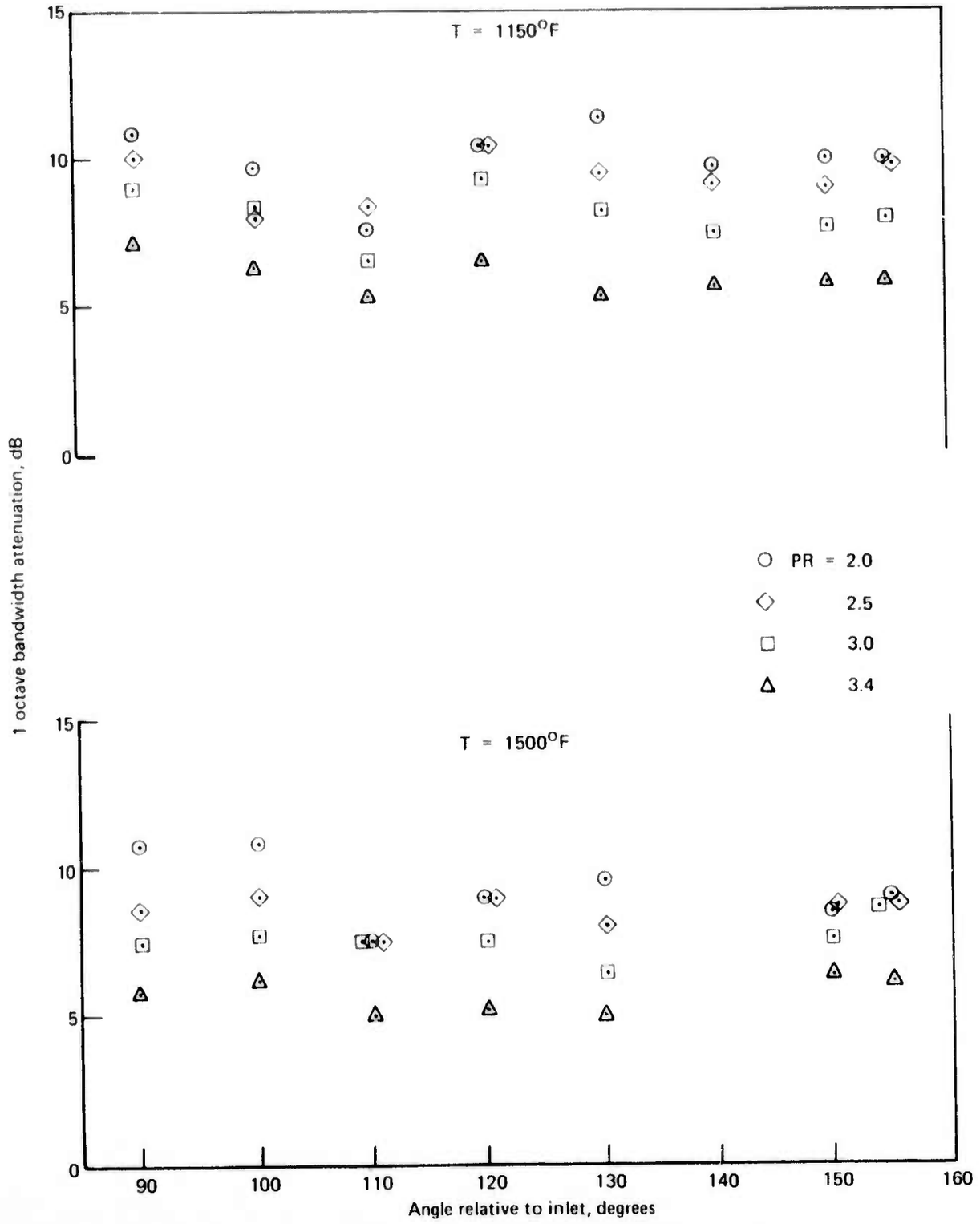

Figure 227.—LNHP-1 Beam Patterns With L/D_E = 2 Ejector and Double-Layer Lining no. 1

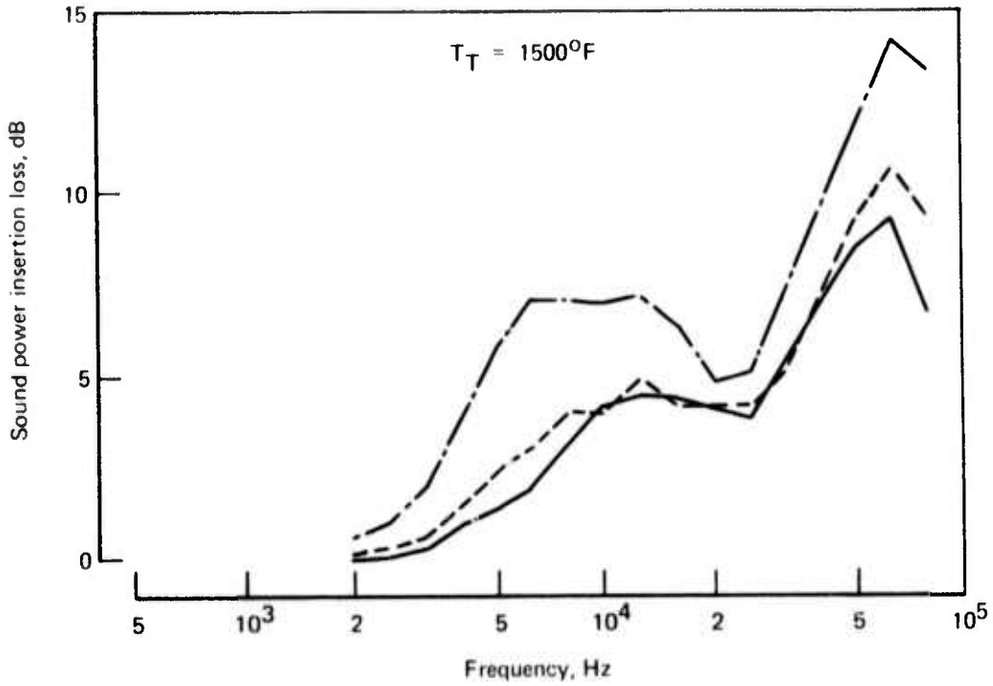

Figure 228.—LNHP-2 Suppressor System With Ejector Setback = 0.8 in. and Lining no. 2

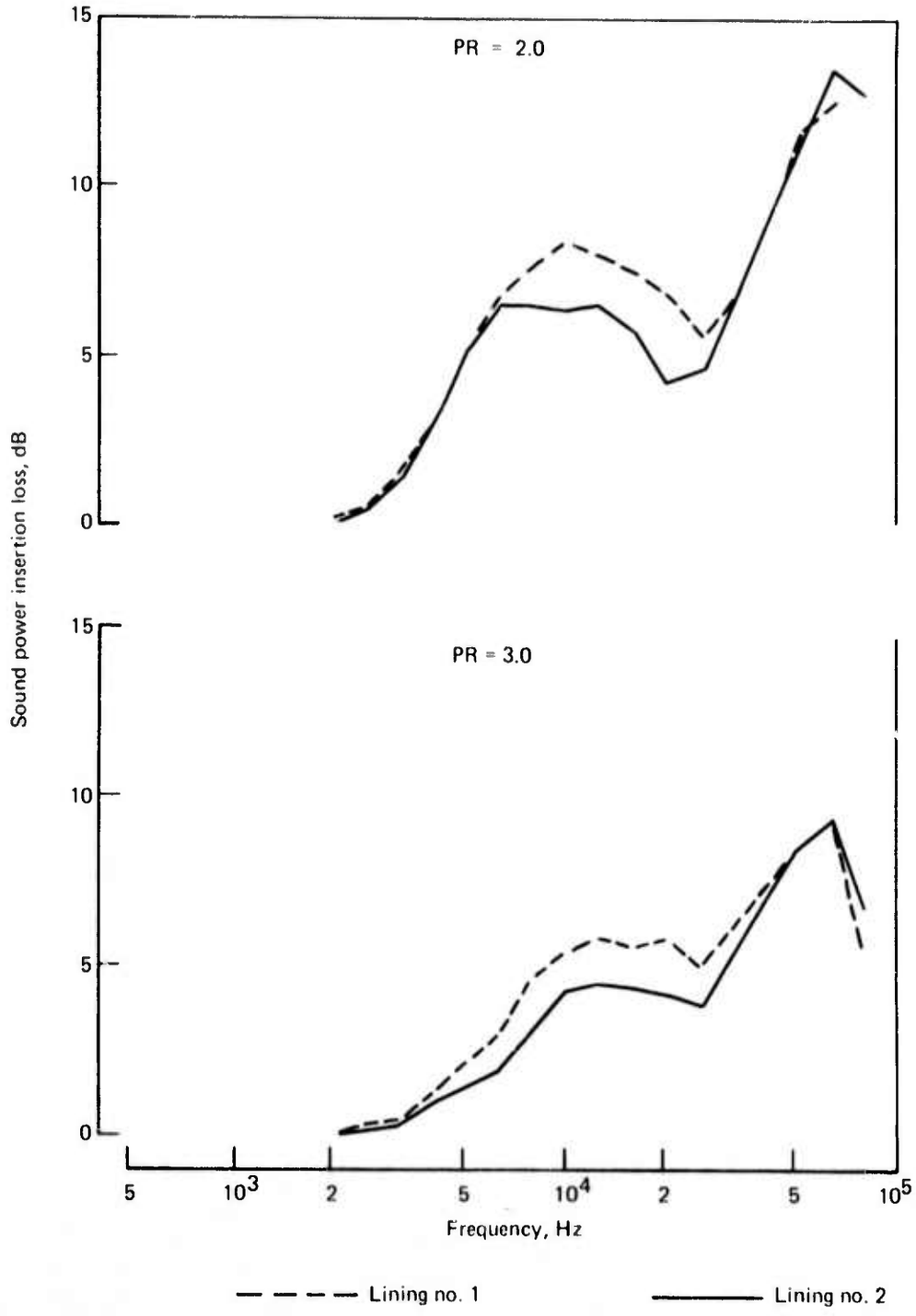

Figure 229.—LNHP-2 Suppressor System at T_T = 1500°F

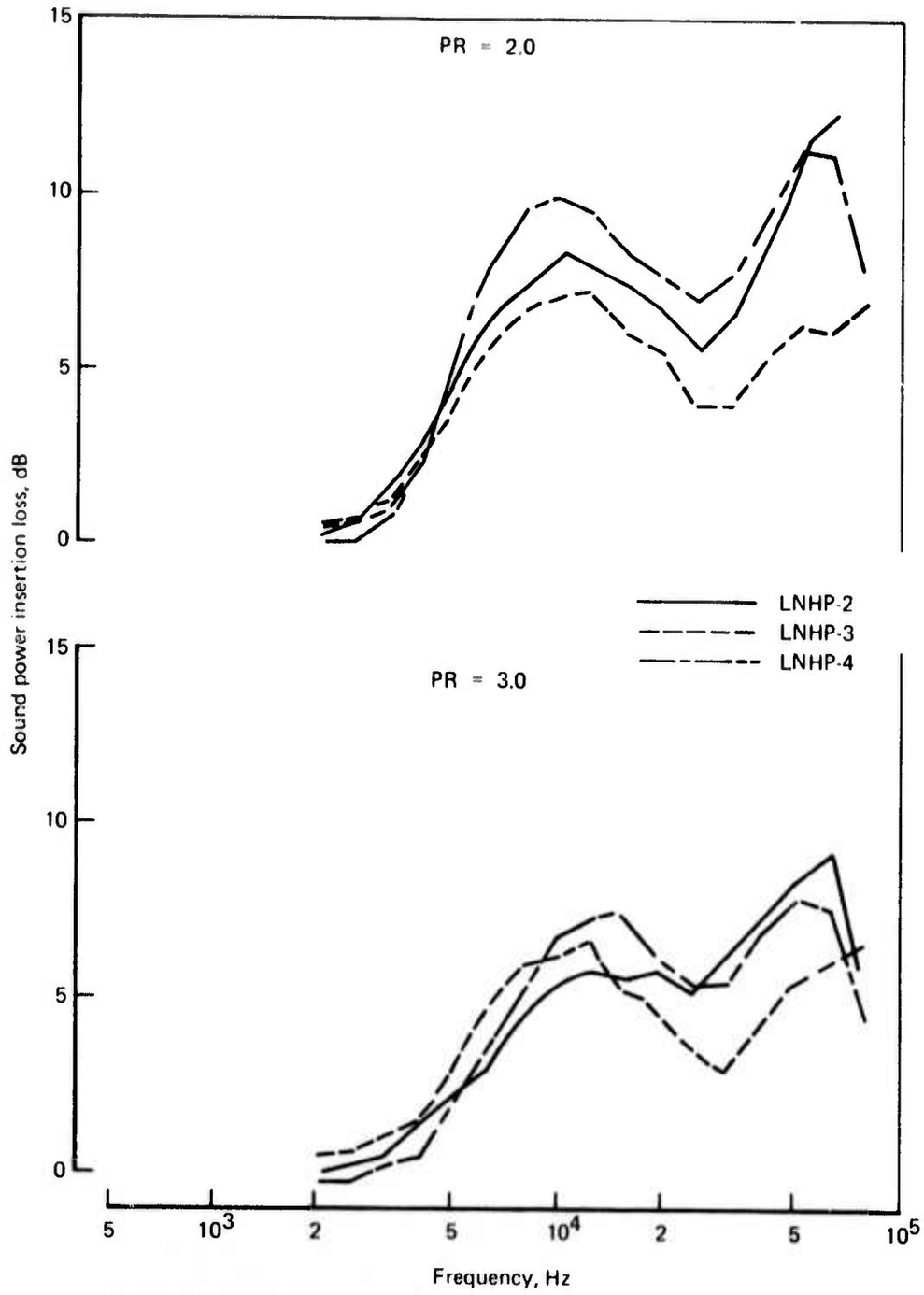

Figure 230.—Lining no. 1 in Combination With Various Noise Sources at T_T = 1500°F

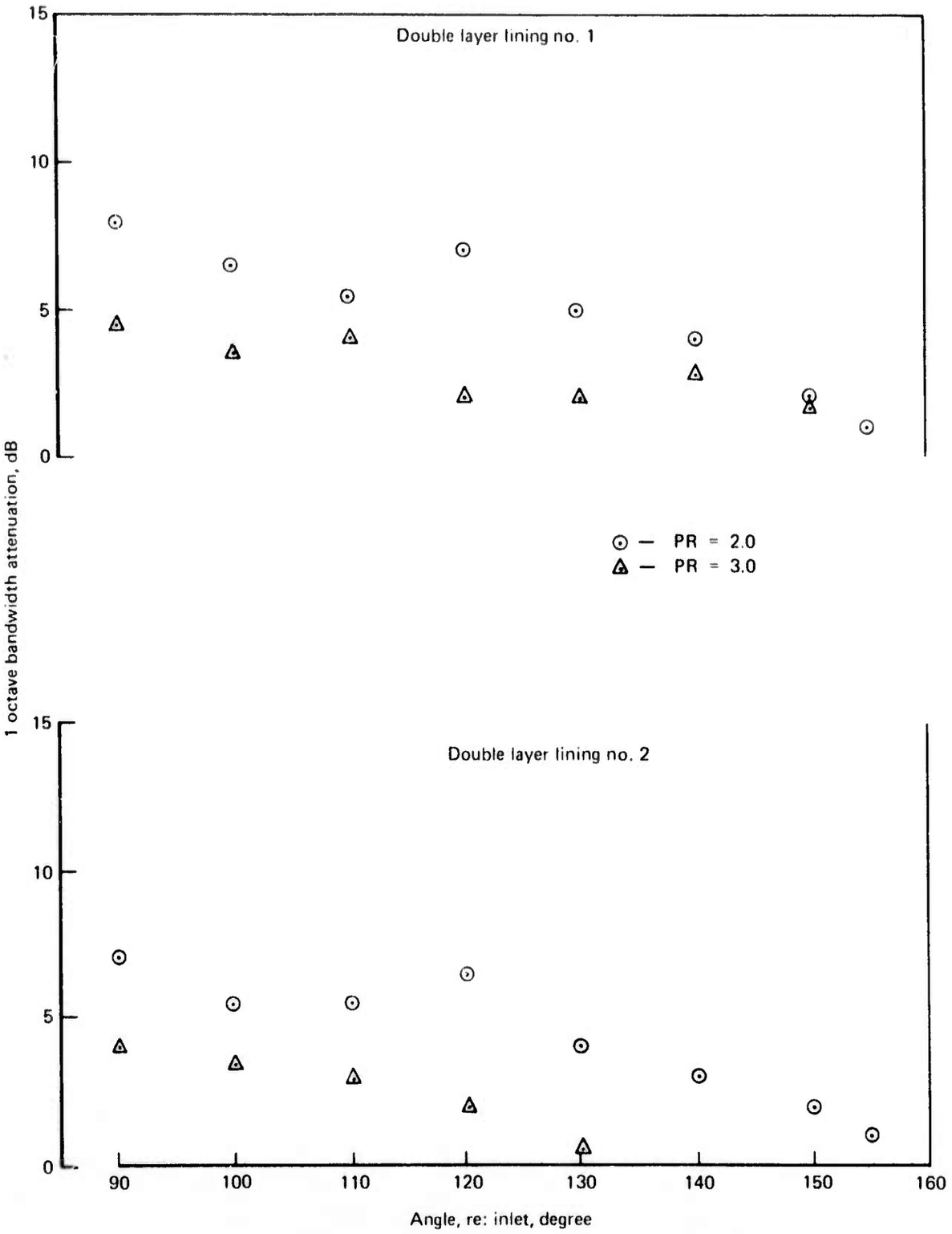

Figure 231. — LNHP-2 Beam Patterns With $L/D_E = 2$ Ejector at $T_T = 1500^oF$

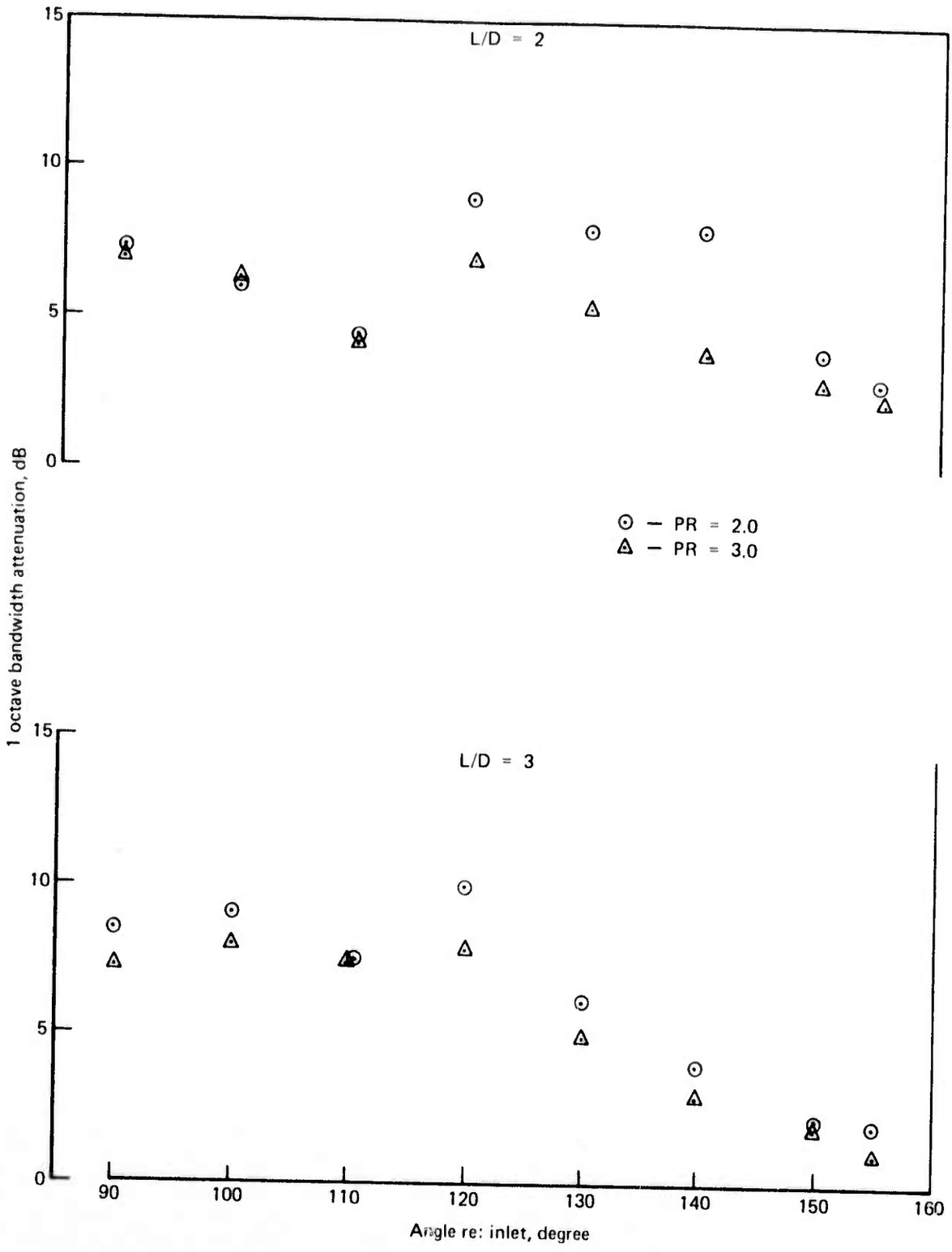

Figure 232.—LNHP-3 Beam Patterns With Double-Layer Lining no. 1 at T_T = 1500°F

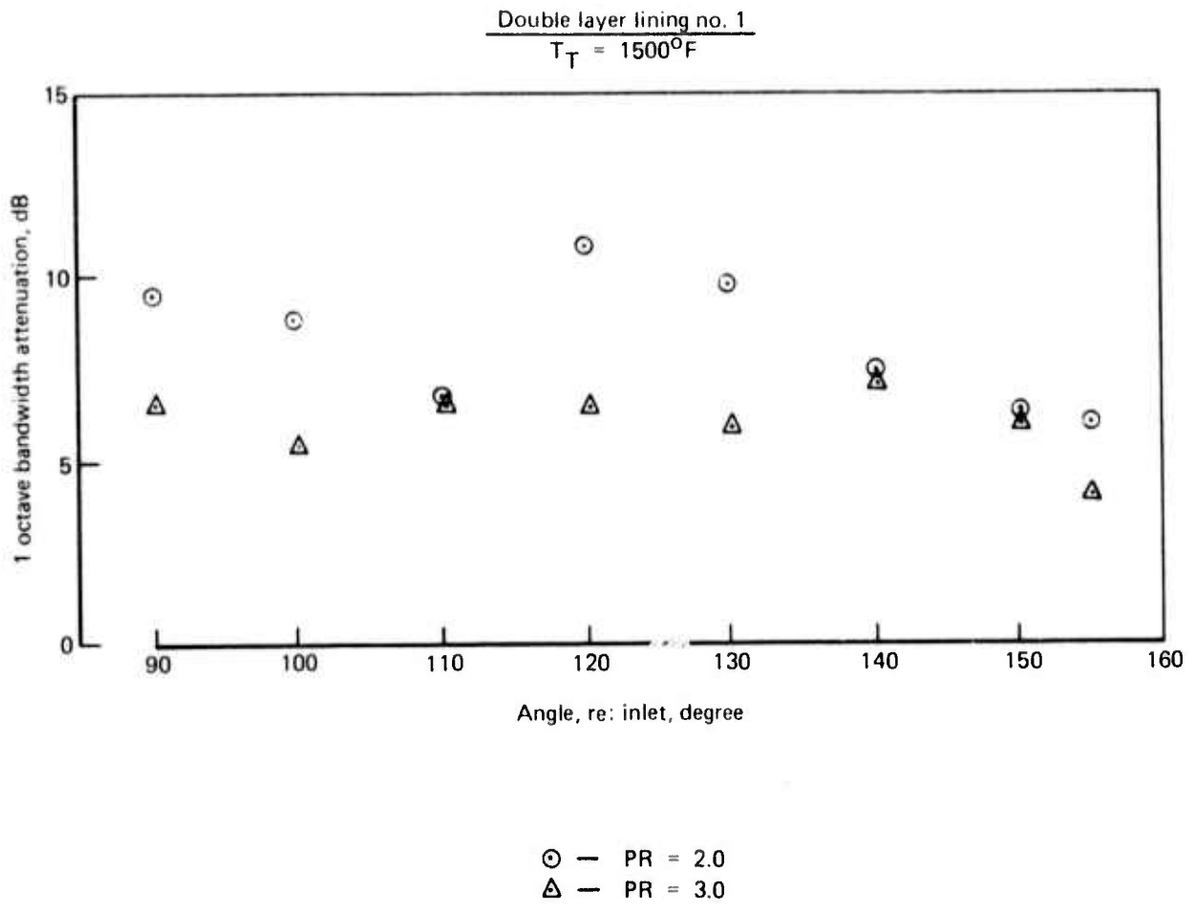

Figure 233.—LNHP-4 Beam Patterns With L/D_E = 2 Ejector

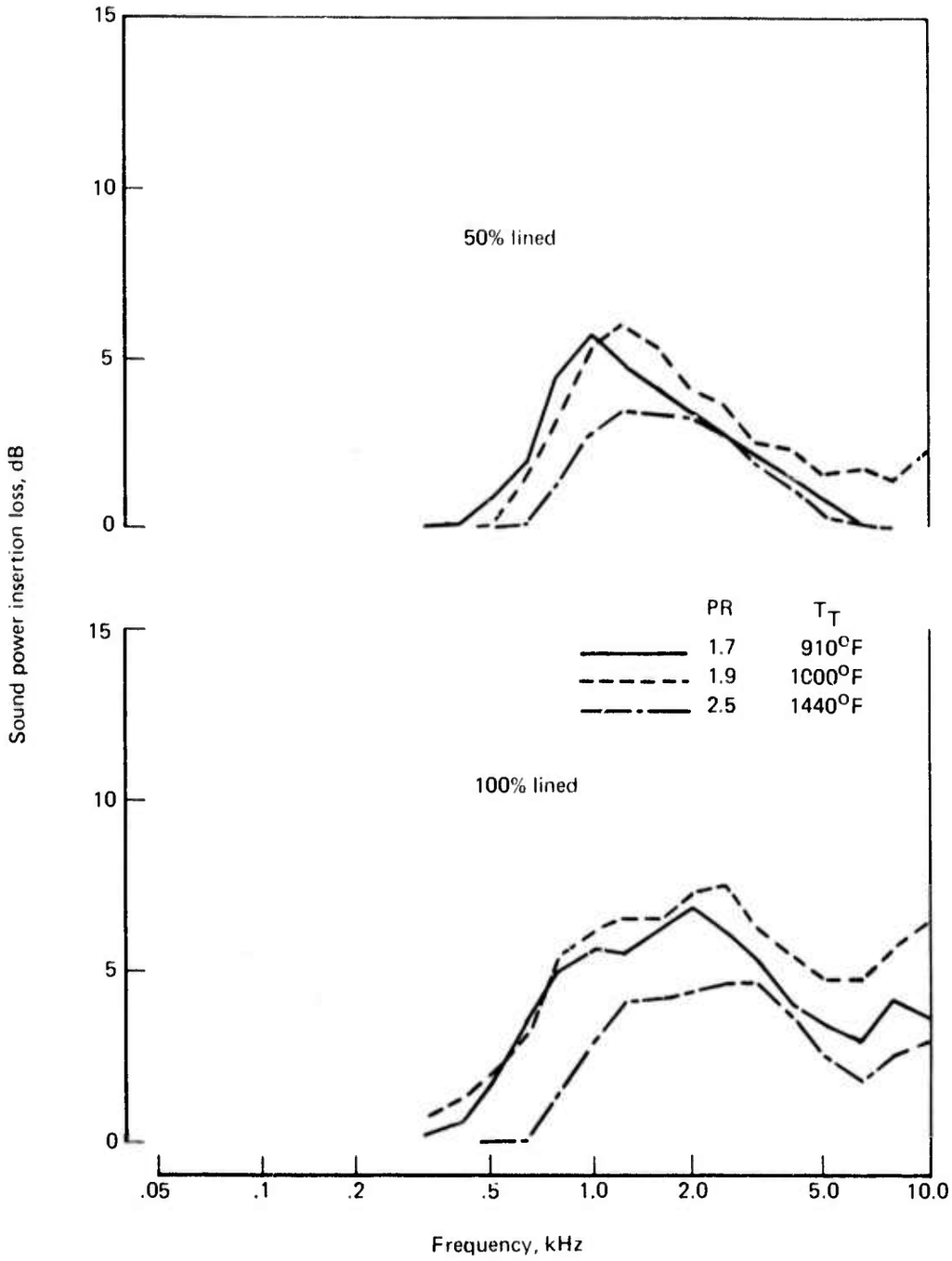

Figure 234.—Full-Scale (J-58) Lined Ejector Results

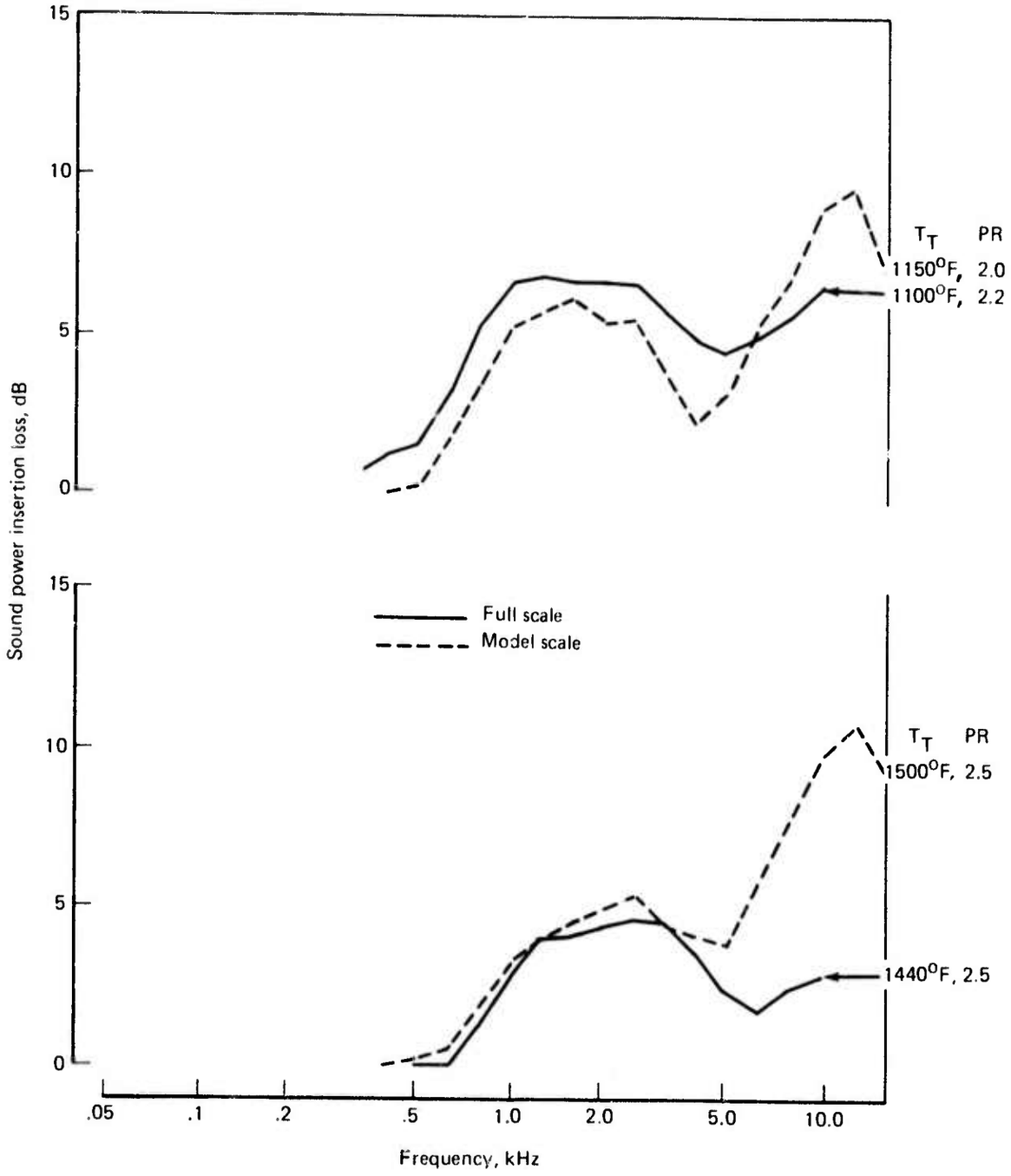

Figure 235.—Lined Ejector Scaling Comparison

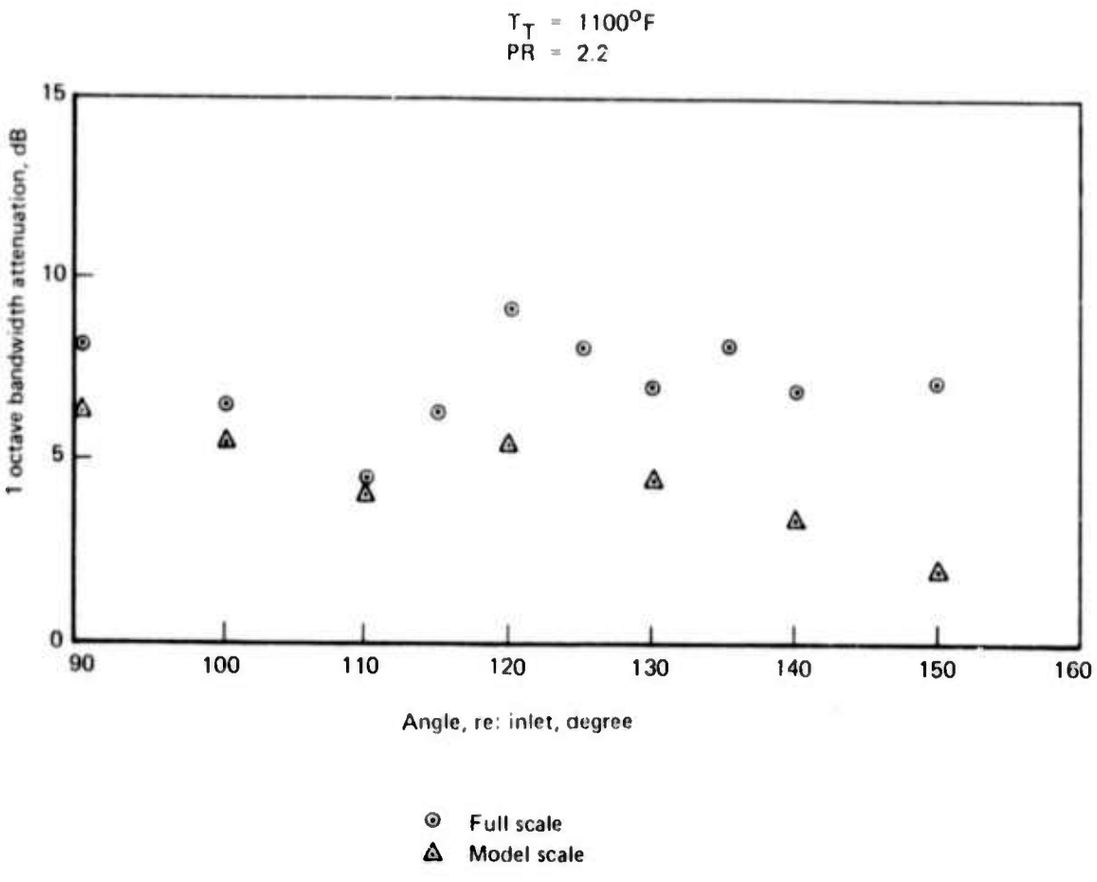

Figure 236.—Lined Ejector Beam Pattern Scaling Comparison

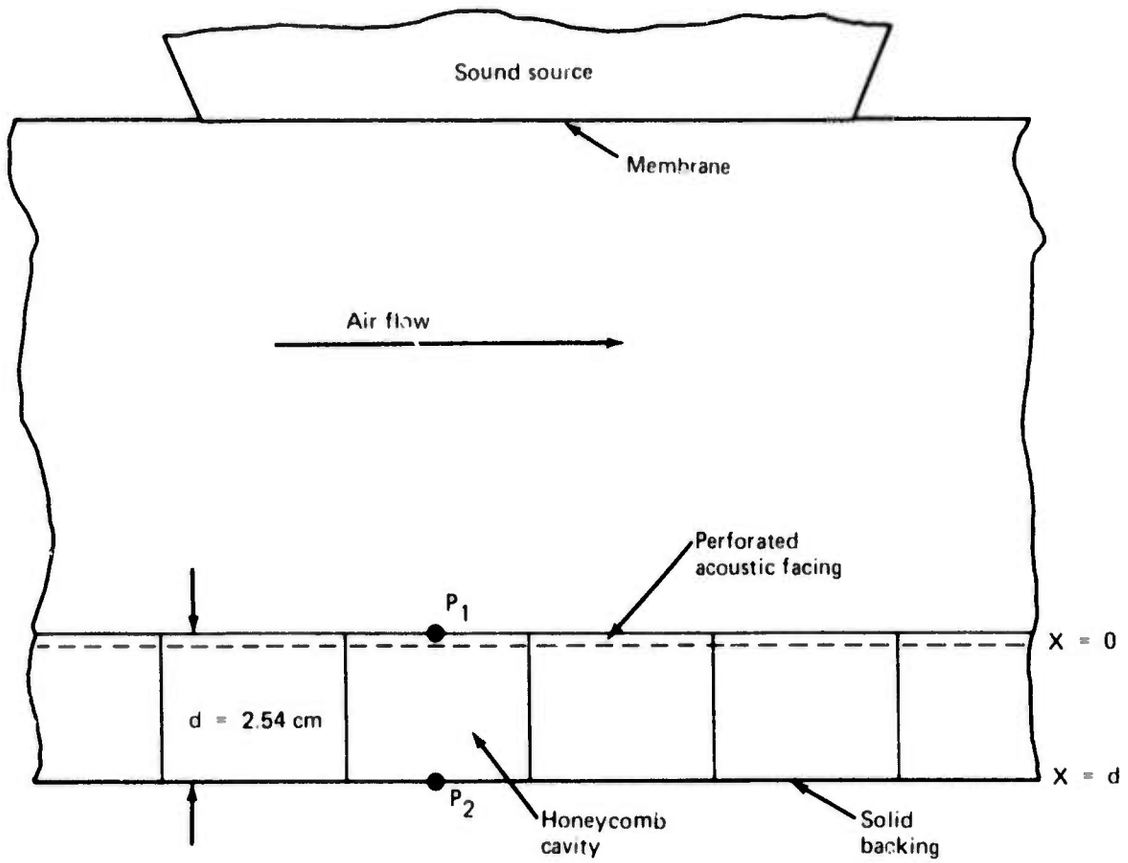

Figure 237.—Impedance Apparatus Test Section Showing Microphone Locations

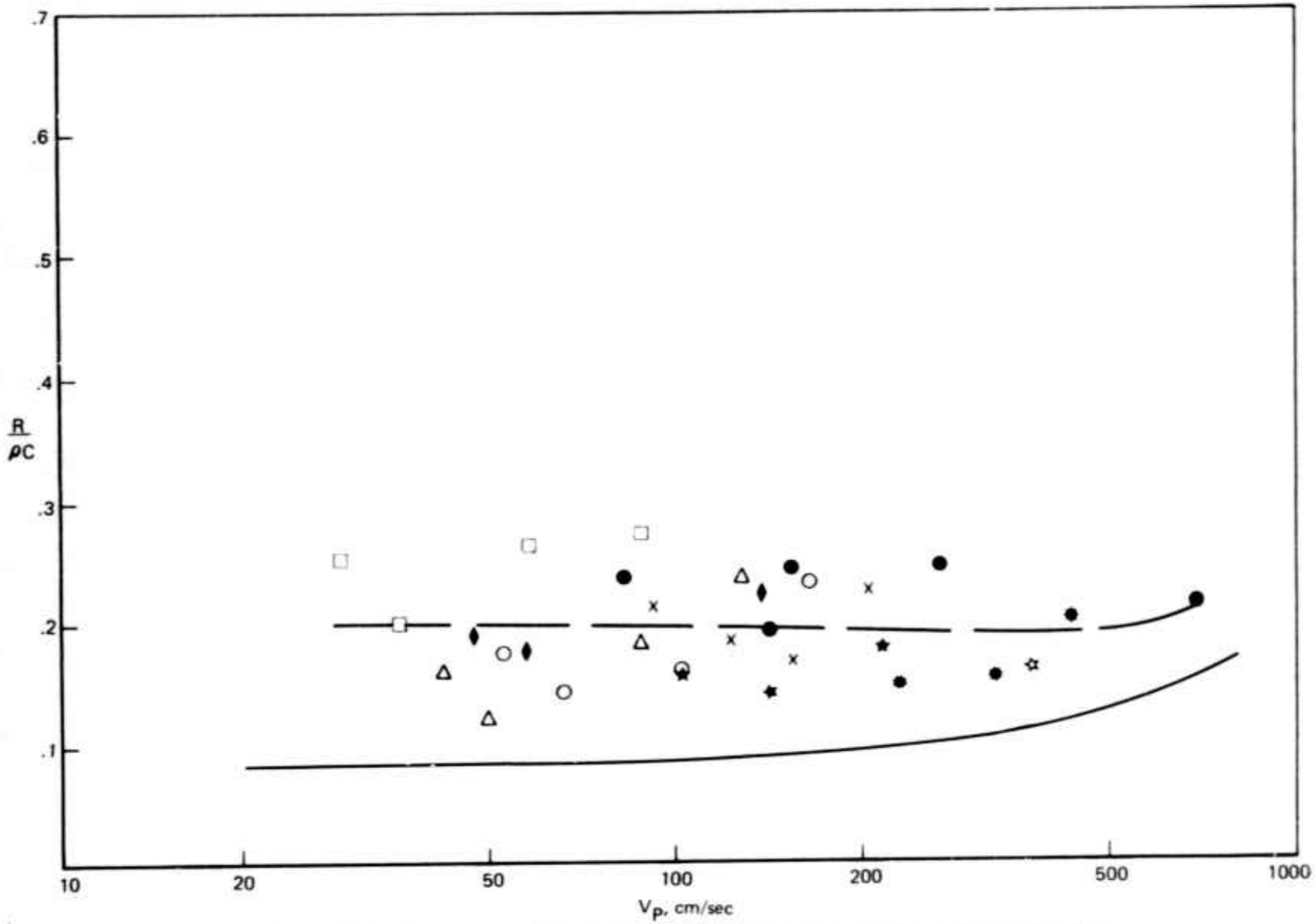

Figure 238.—Experimental Points for the Resistance, Fitted Curve and Curve of the Semi-Empirical Model as a Function of Particle Velocity. M = .20, Perforated Metal Sheet A.

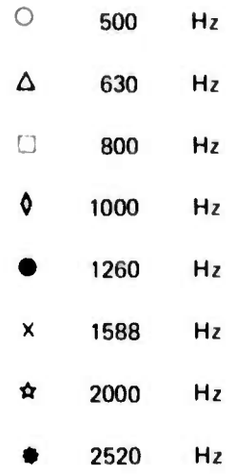

Explanation of Symbols for Figures 239 to 251.

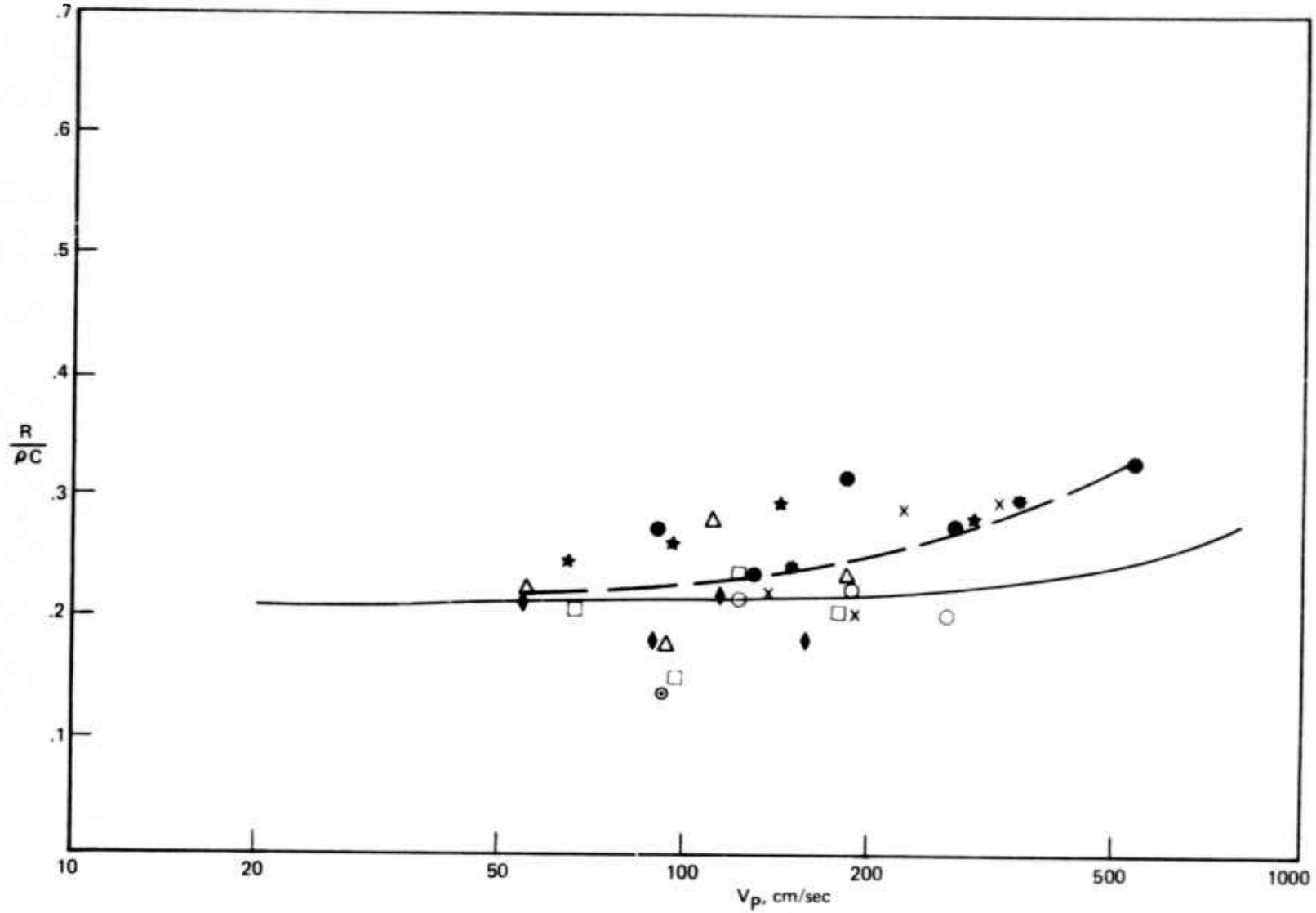

Figure 239.—Experimental Points for the Resistance, Fitted Curve and Curve of the Semi-Empirical Model as a Function of Particle Velocity. M = .40, Thin Boundary Layer. Perforated Metal Sheet A.

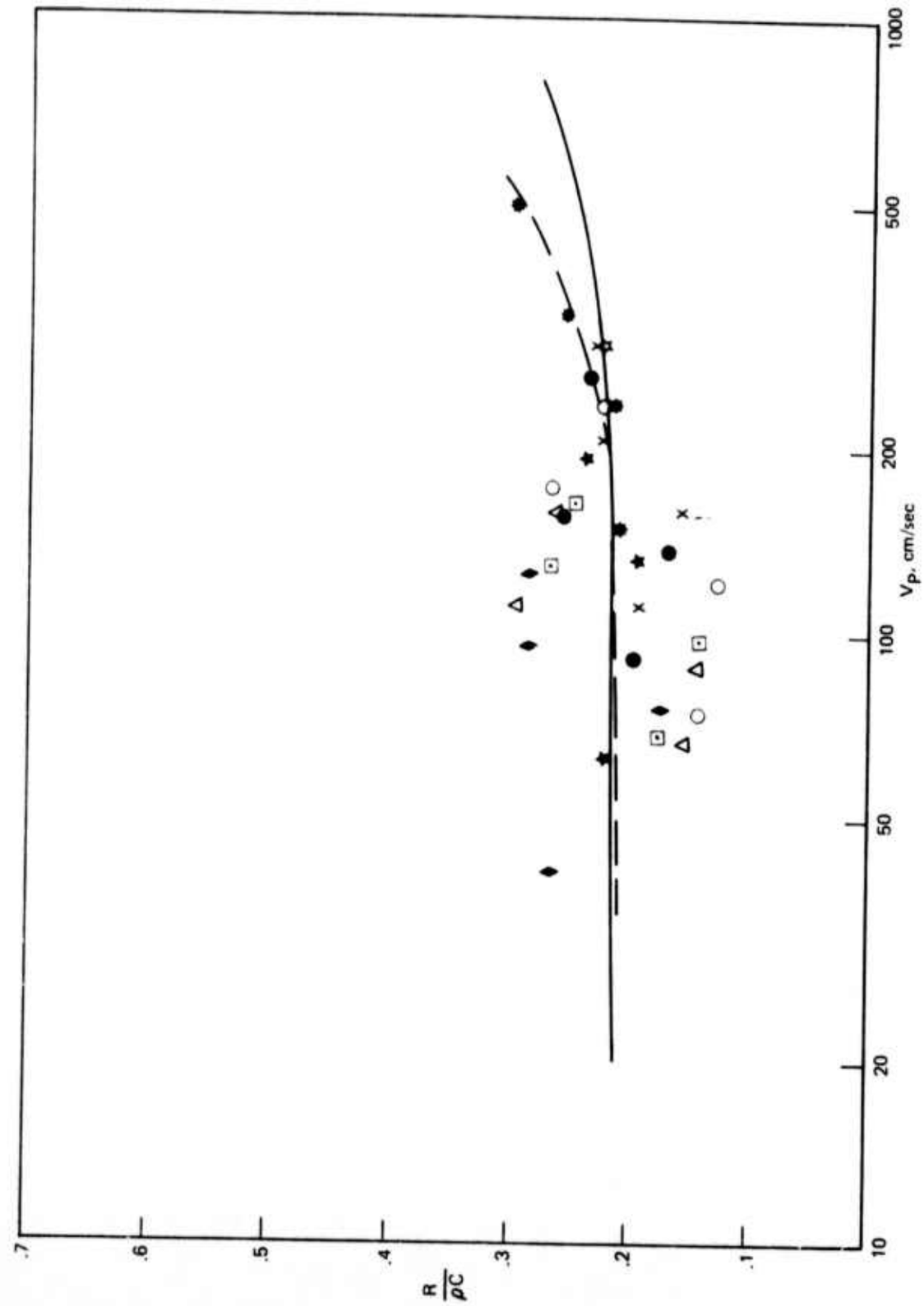

Figure 240.—Experimental Points for the Resistance, Fitted Curve and Curve of the Semi-Empirical Model as a Function of Particle Velocity. M = .40, Thick Boundary Layer. Perforated Metal Sheet A.

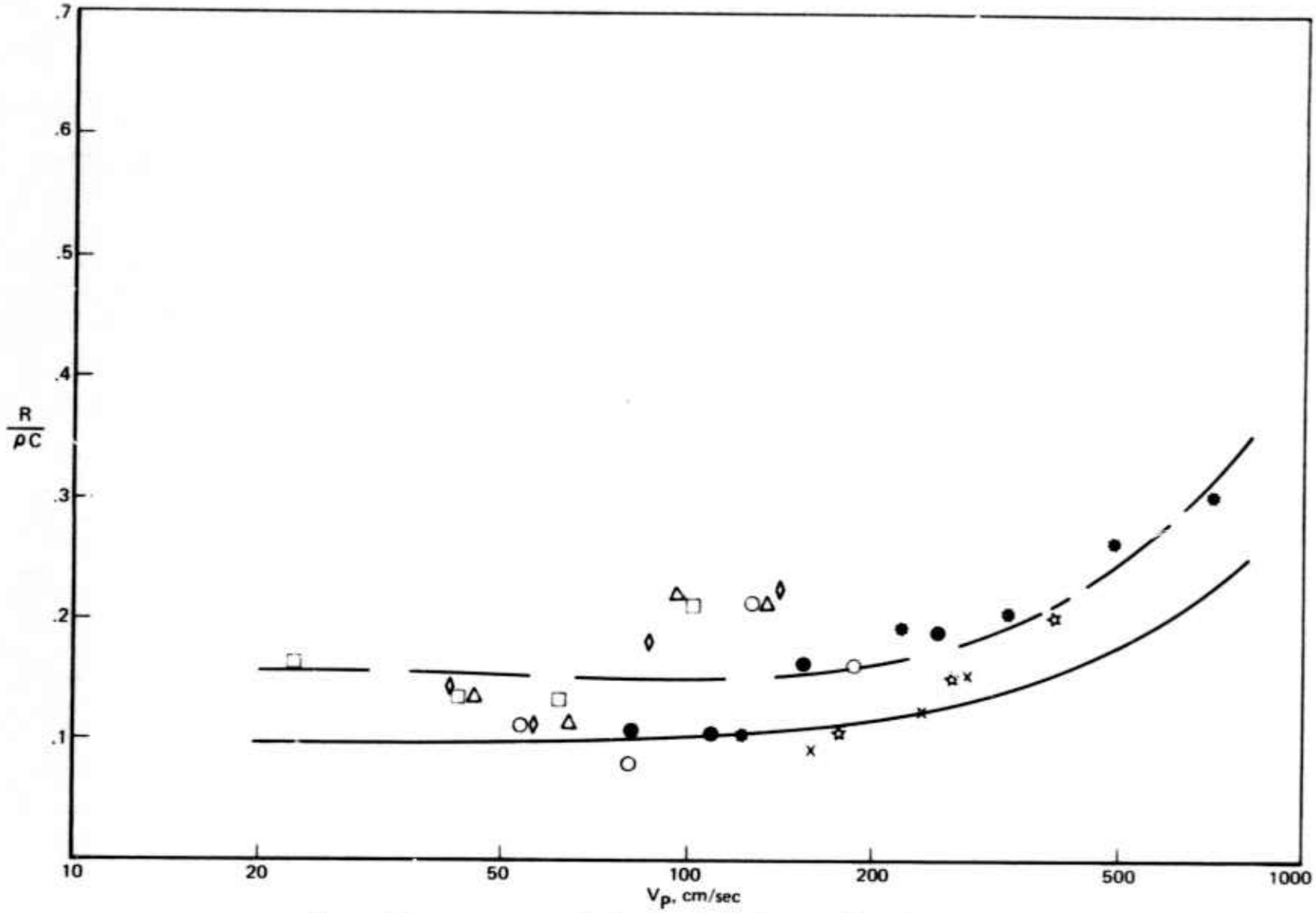

Figure 241.—Experimental Points for the Resistance, Fitted Curve and Curve of the Semi-Empirical Model, as a Function of Particle Velocity. M = .20. Perforated Metal Sheet B.

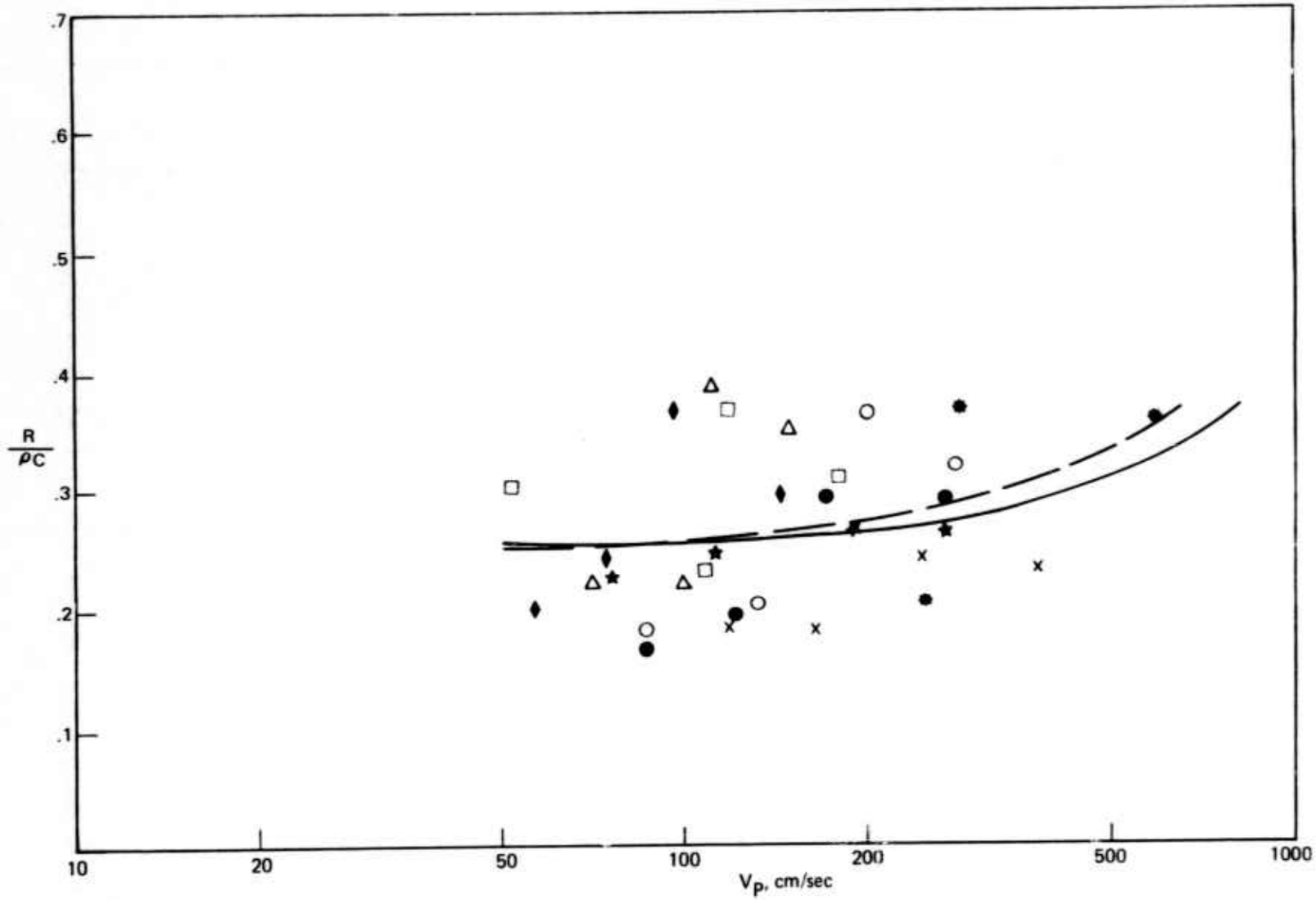

Figure 242.—Experimental Points for the Resistance, Fitted Curve and Curve of the Semi-Empirical Model, as a function of Particle Velocity. M = .40, Thin Boundary Layer. Perforated Metal Sheet B.

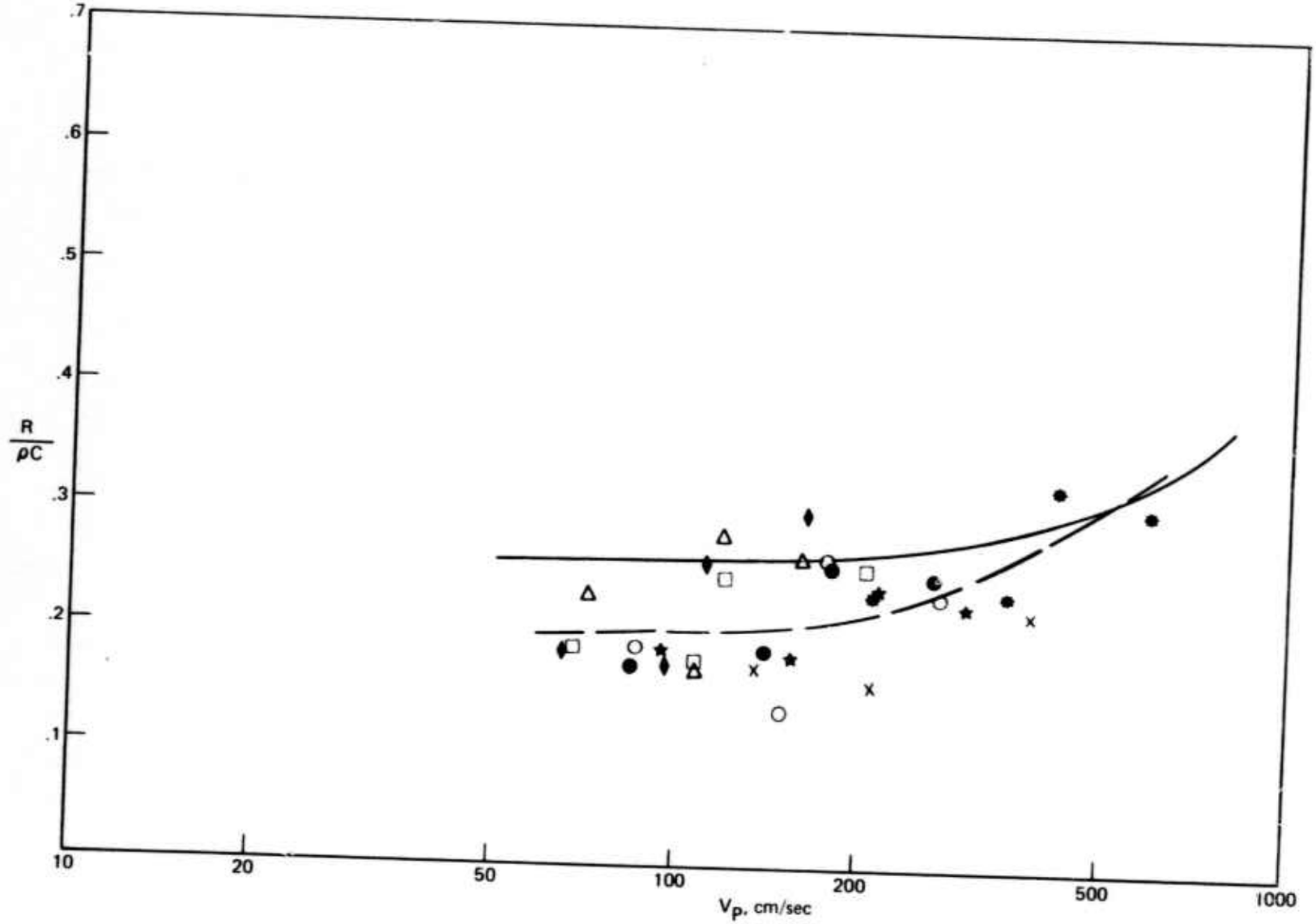

Figure 243.—Experimental Points for the Resistance, Fitted Curve and Curve of the Semi-Empirical Model, as a Function of Particle Velocity. M = .40, Thick Boundary Layer. Perforated Metal Sheet B.

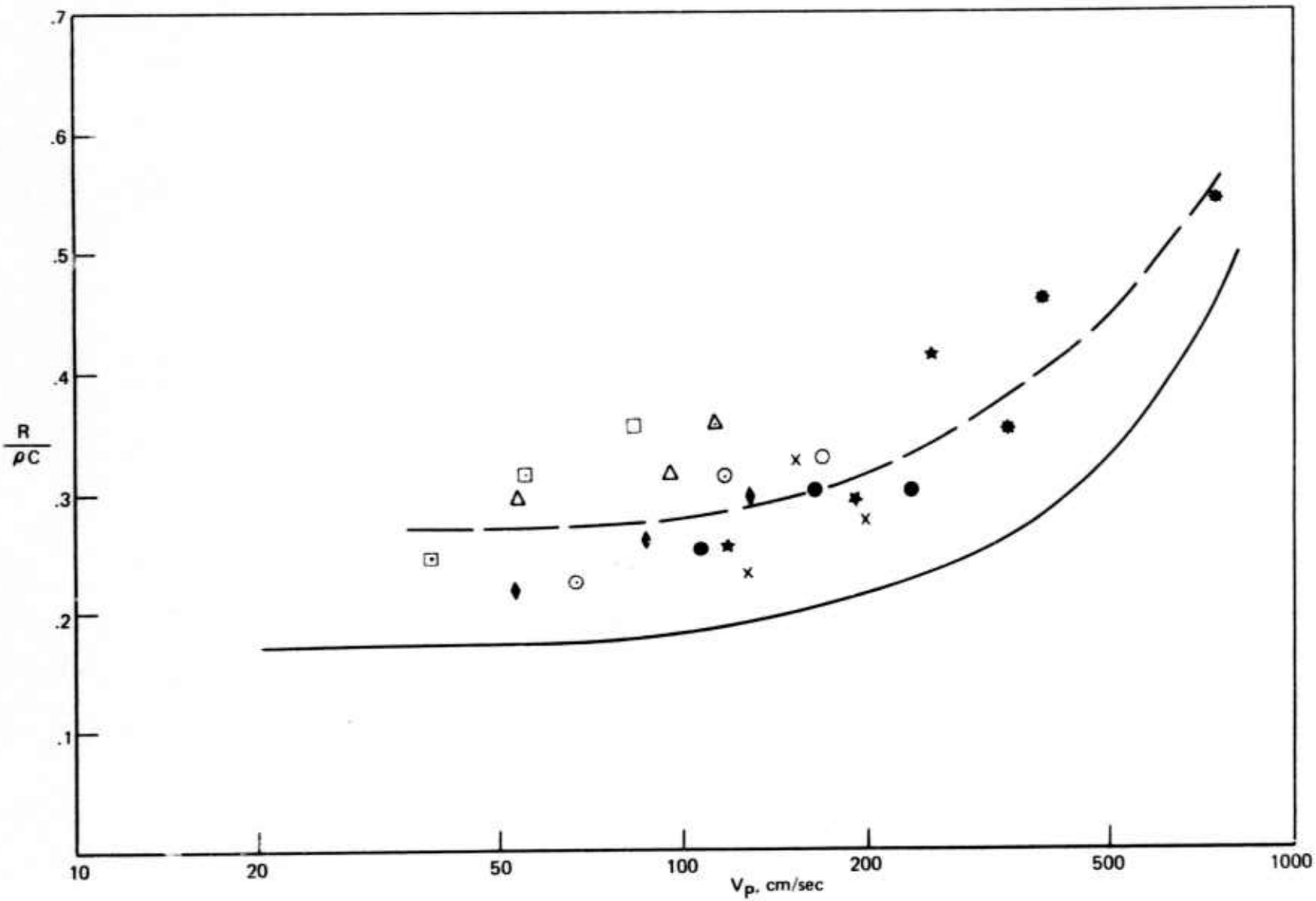

Figure 244.—Experimental Points for the Resistance, Fitted Curve and Curve of the Semi-Empirical Model, as a Function of Particle Velocity. M = .20. Perforated Metal Sheet C.

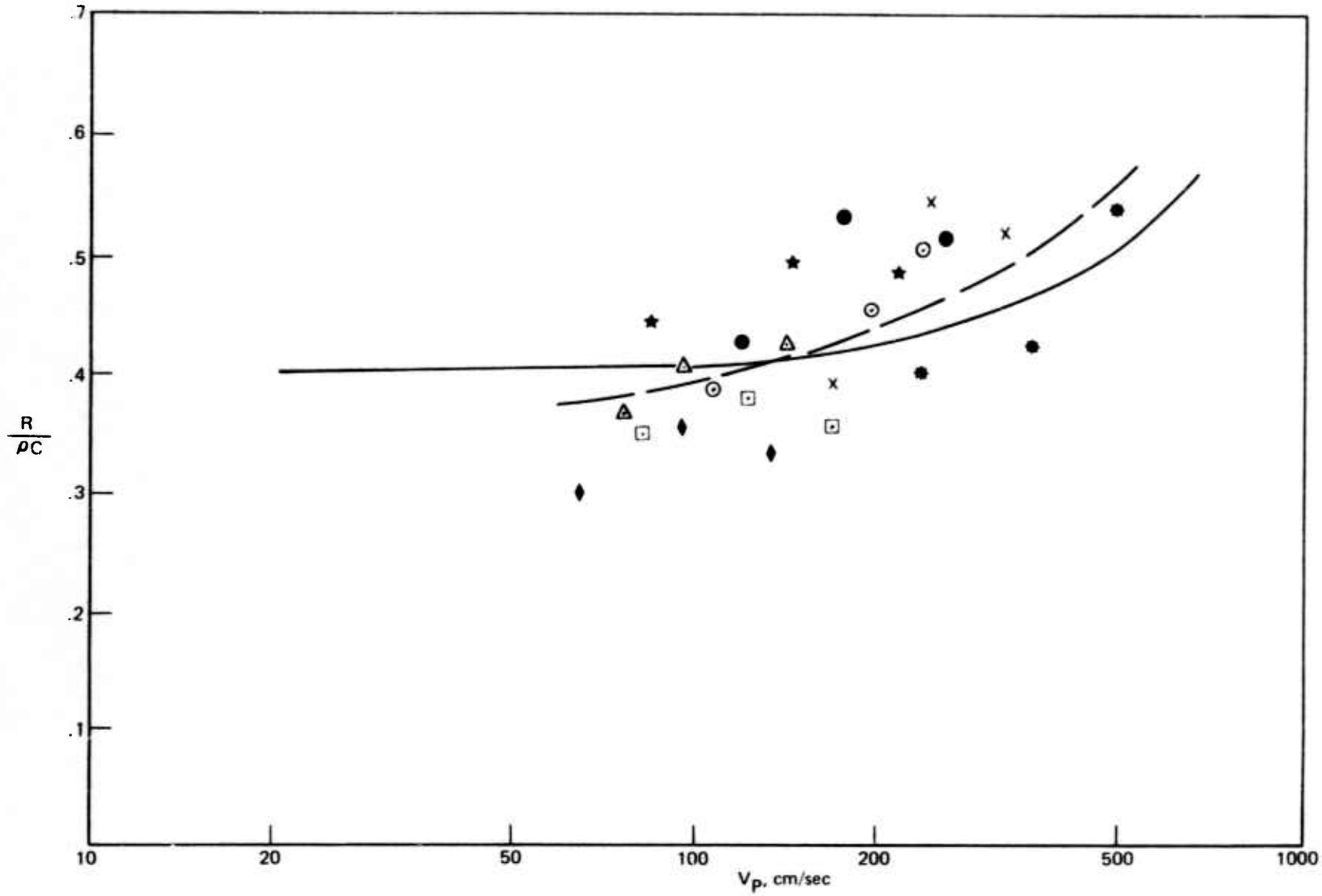

Figure 245.—Experimental Points for the Resistance, Fitted Curve and Curve of the Semi-Empirical Model, as a Function of Particle Velocity. M = .40, Thin Boundary Layer. Perforated Metal Sheet C.

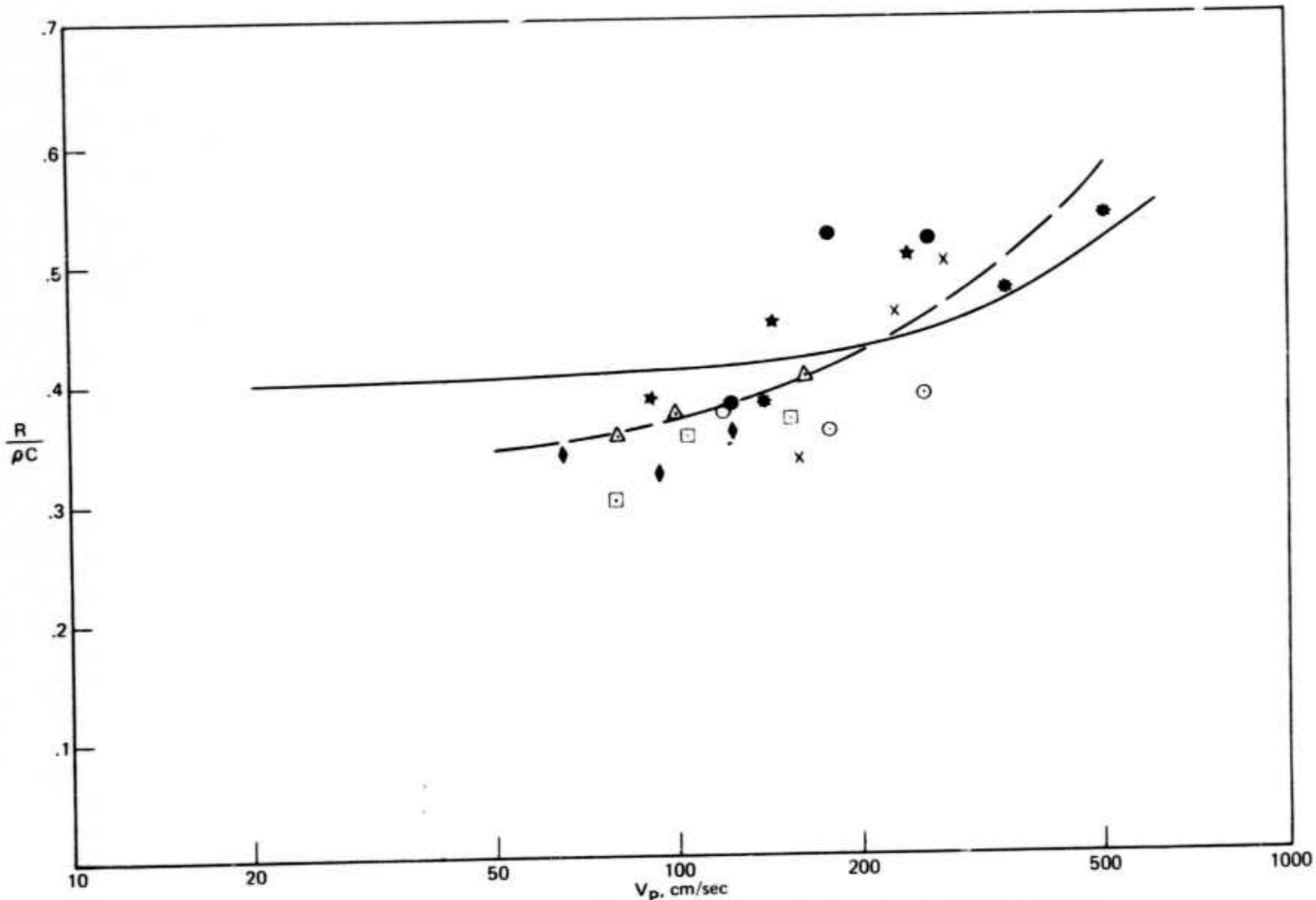

Figure 246.—Experimental Points for the Resistance, Fitted Curve and Curve of the Semi-Empirical Model, as a Function of Particle Velocity. M = .40, Thick Boundary Layer. Perforated Metal Sheet C.

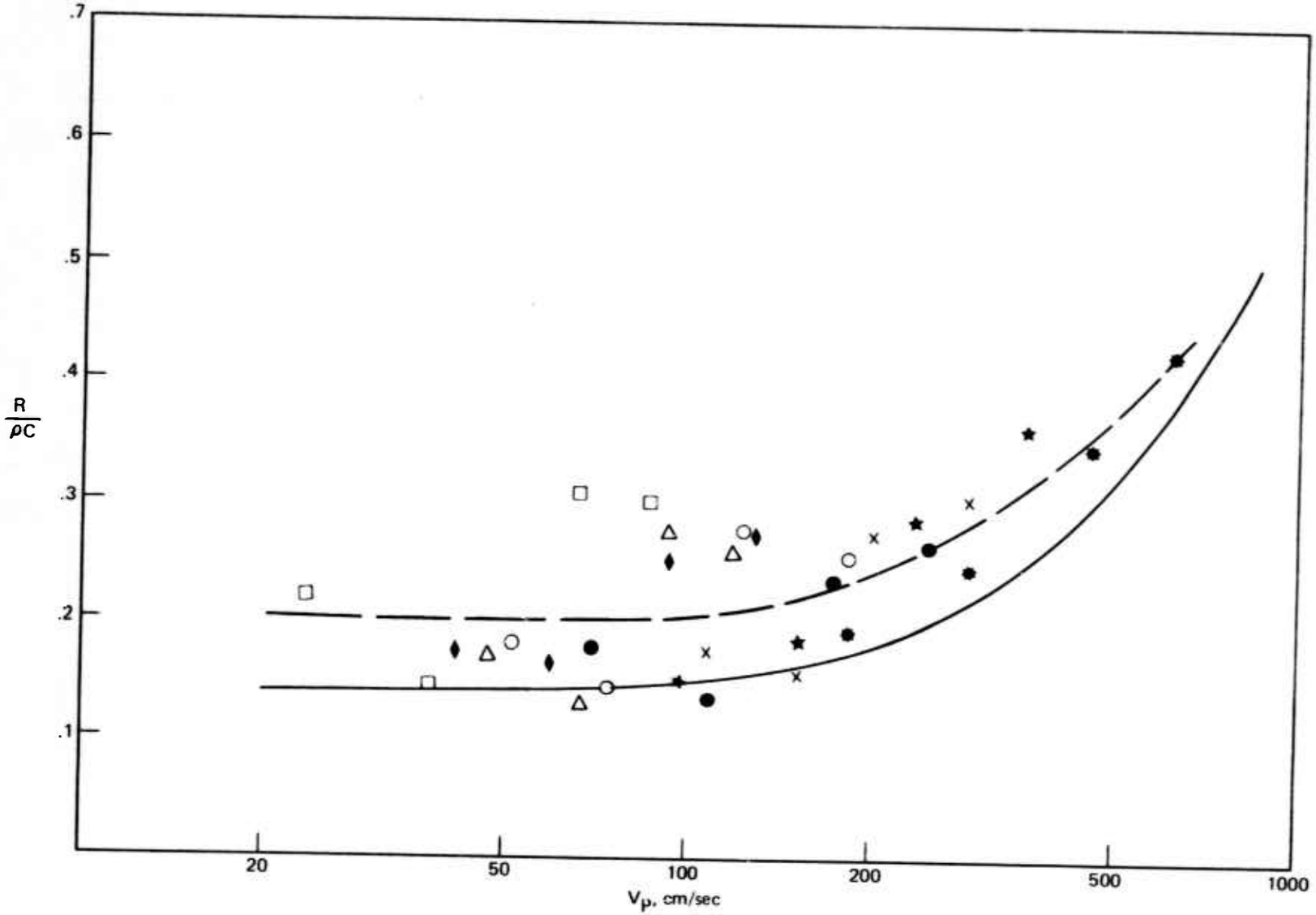

Figure 247. Experimental Points for the Resistance, Fitted Curve and Curve of the Semi-Empirical Model, as a Function of Particle Velocity. M = .20. Perforated Metal Sheet D.

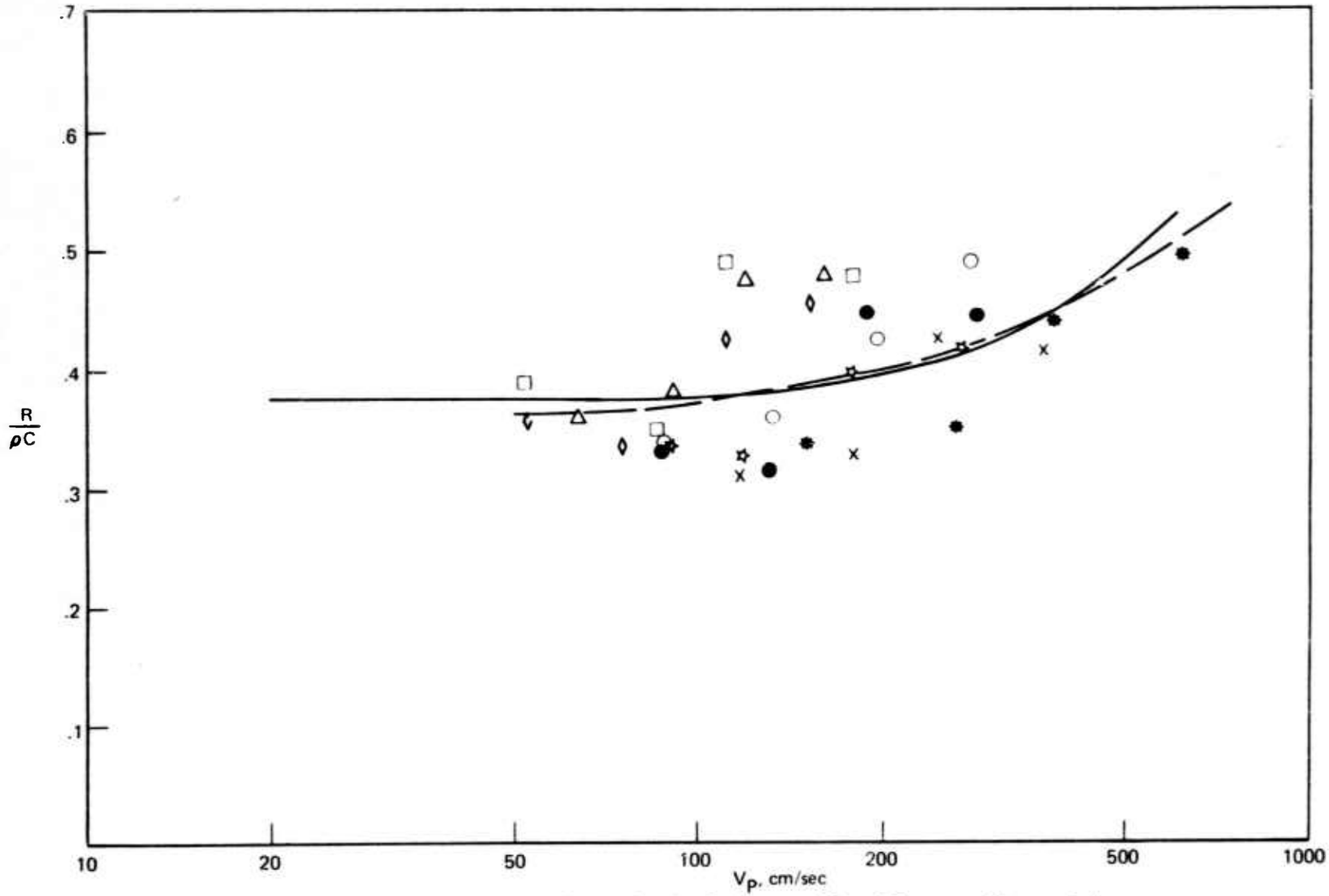

Figure 248.—Experimental Points for the Resistance, Fitted Curve and Curve of the Semi-Empirical Model, as a Function of Particle Velocity. M = .40, Thin Boundary Layer. Perforated Metal Sheet D.

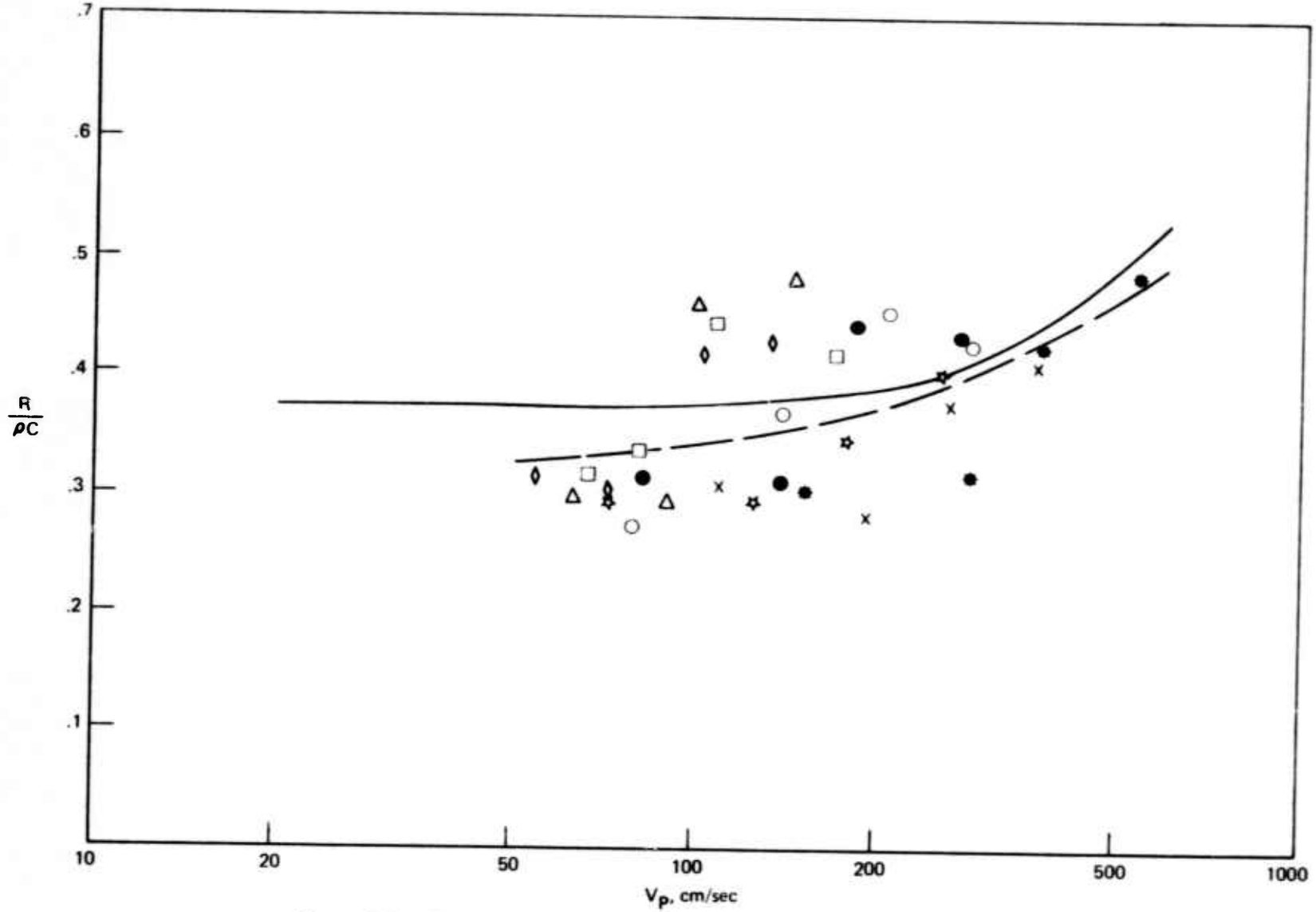

Figure 249.—Experimental Points for the Resistance, Fitted Curve and Curve of the Semi-Empirical Model, as a Function of Particle Velocity. M = .40, Thick Boundary Layer. Perforated Metal Sheet D.

a. Configuration Used in the Analysis of Fan Noise Reduction Prediction.

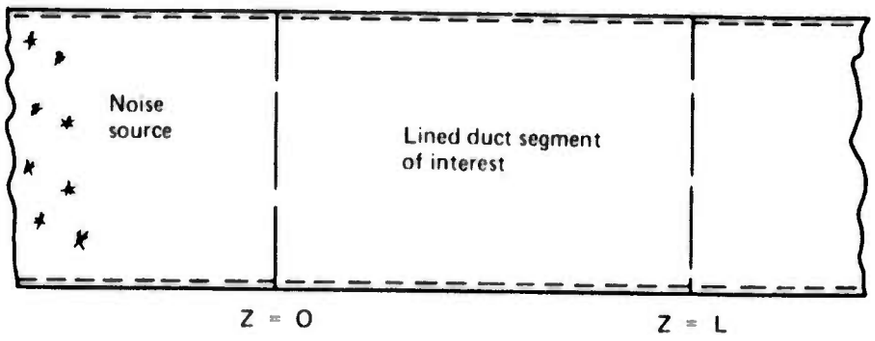

b. Configuration Used for Predicting the Attenuation by Ejector-Suppressors.

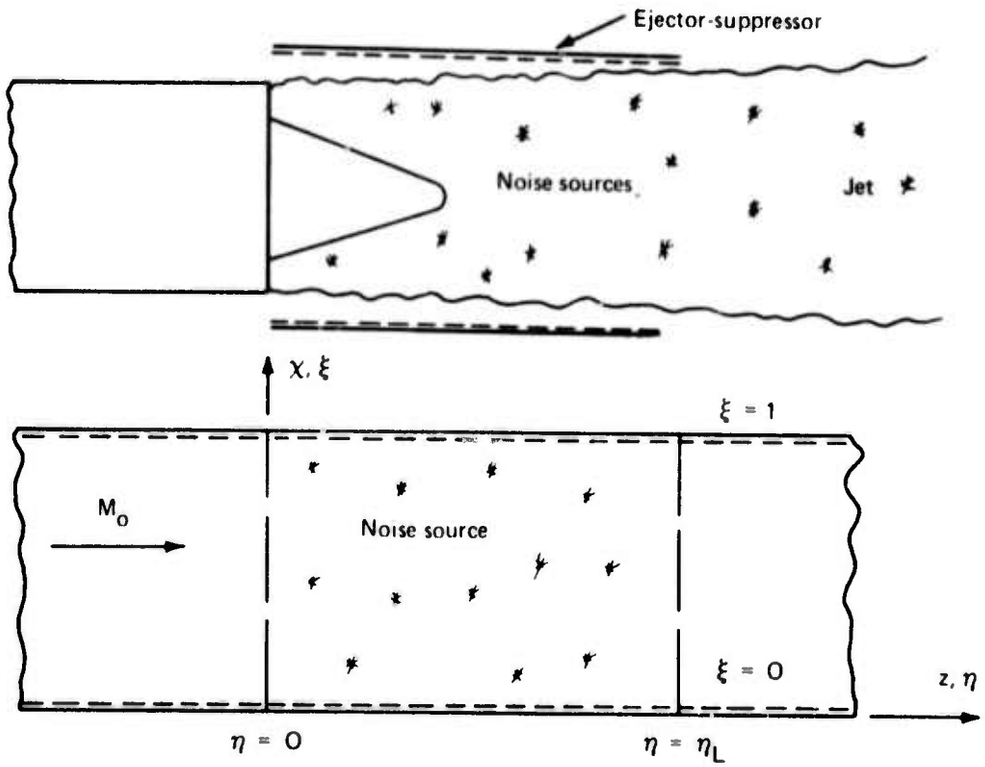

Figure 250.—Sketch of Geometrical Configurations

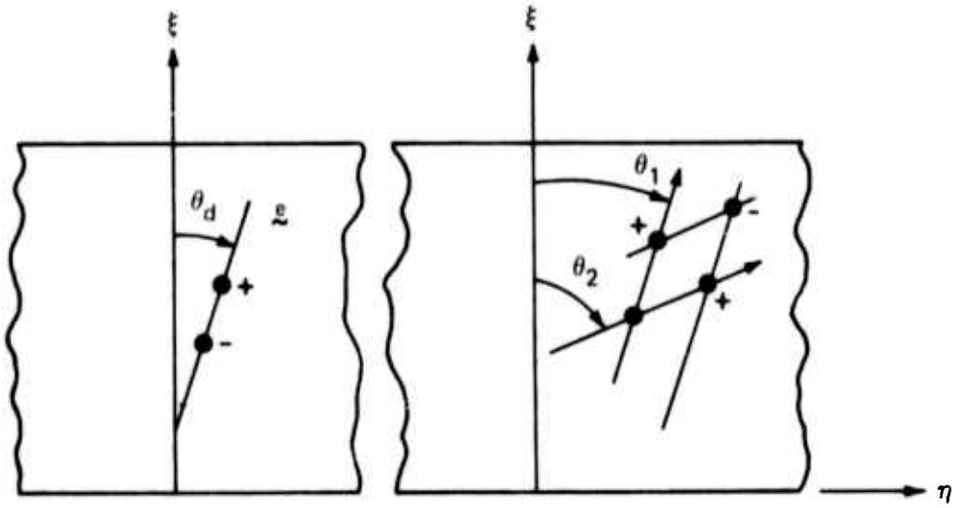

a. Dipole

b. Quadrupole

Figure 251. — Sketch Depicting the Geometry Used to Construct Dipoles and Quadrupoles

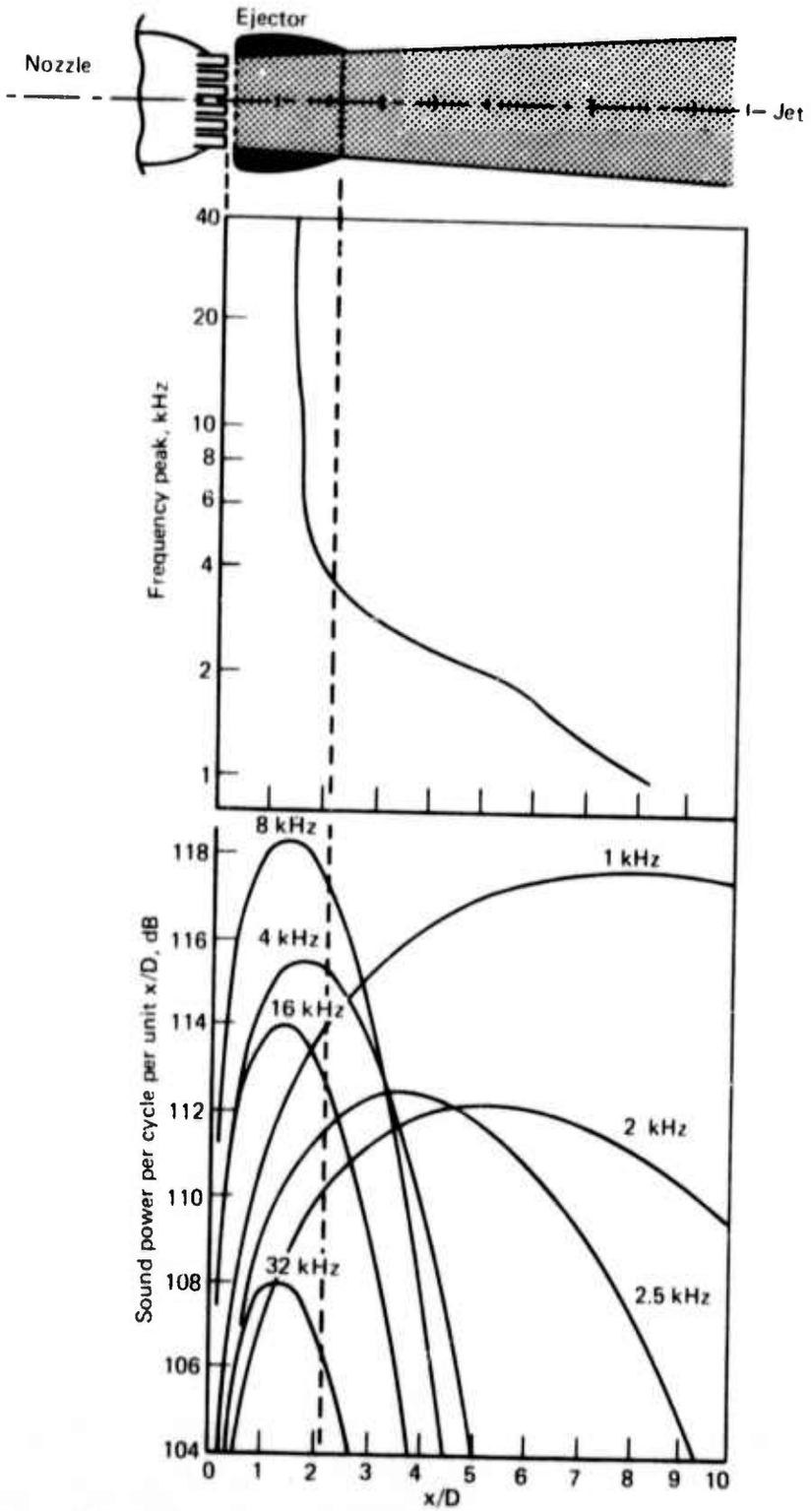

37-tube, AR 3.3 nozzle with L/D_E = 2 ejector at T_T = 1150°F, PR = 3.0

Figure 252.—Sound Power Distribution in a Multitube Jet

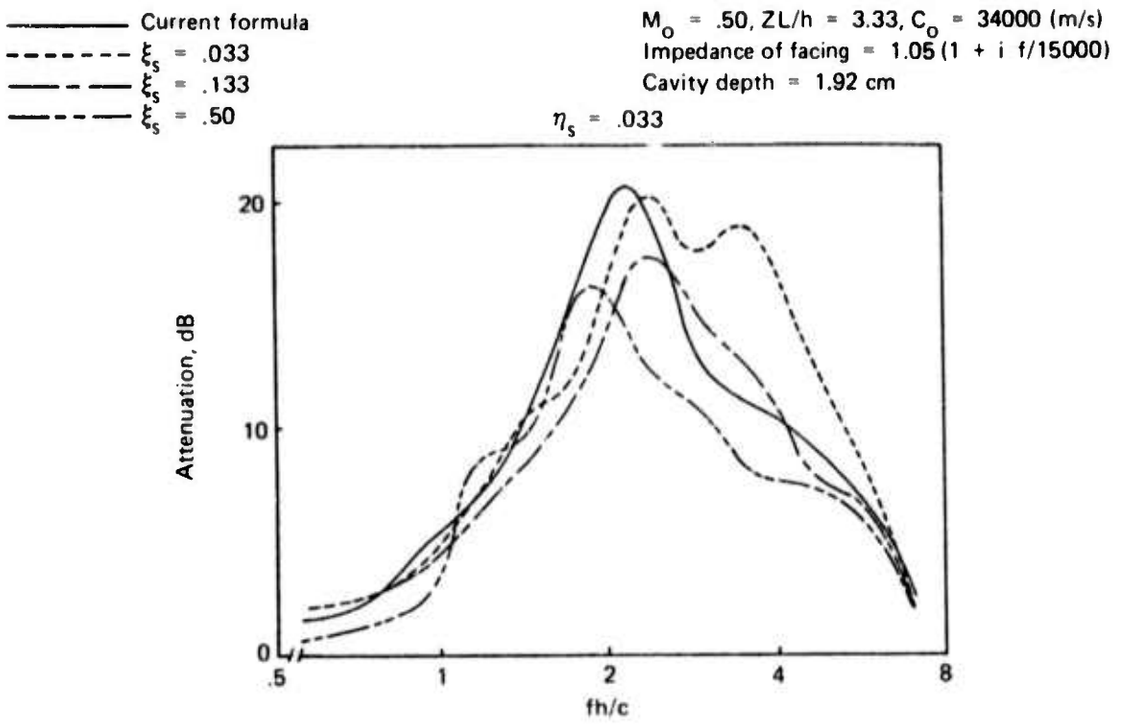

Figure 253.—Attenuation Spectra for Single Monopoles

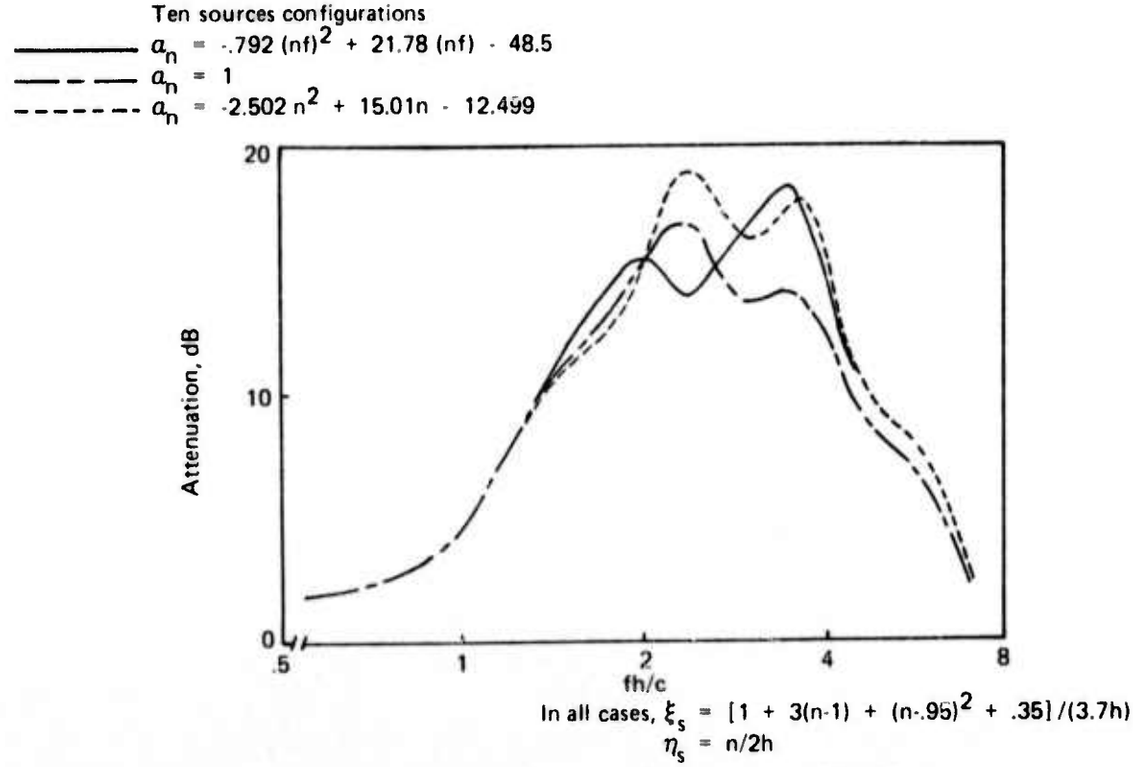

Figure 254.—Attenuation Spectra for a Distribution of Ten Monopoles

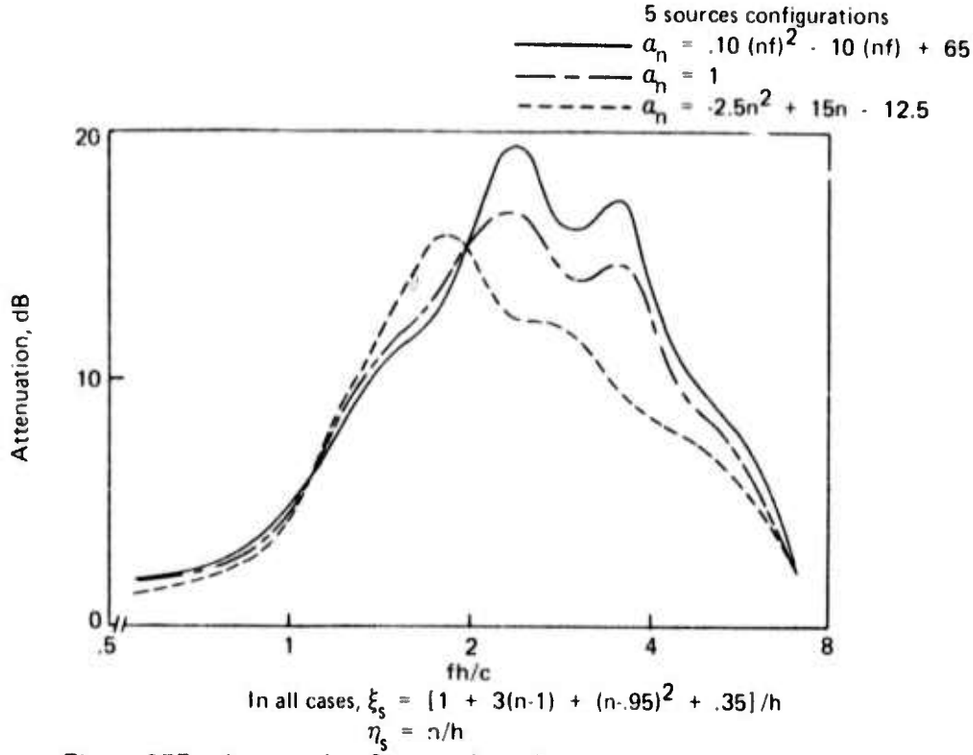

Figure 255.—Attenuation Spectra for a Distribution of Five Monopoles

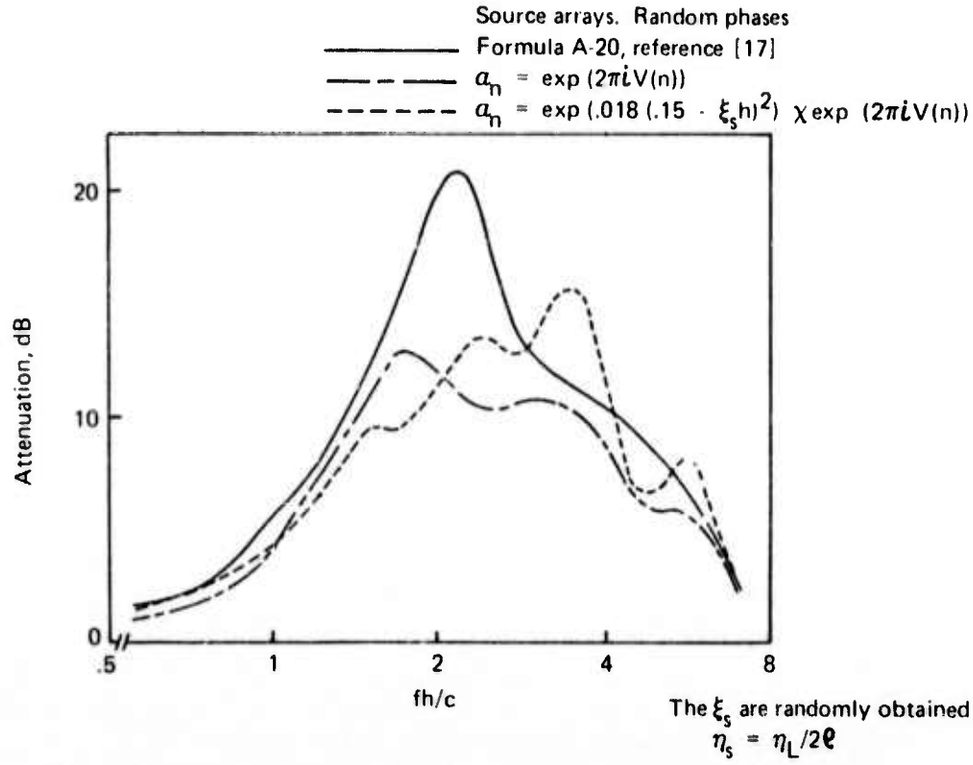

Figure 256.—Attenuation Spectra for a Random Distribution of Twenty Monopoles

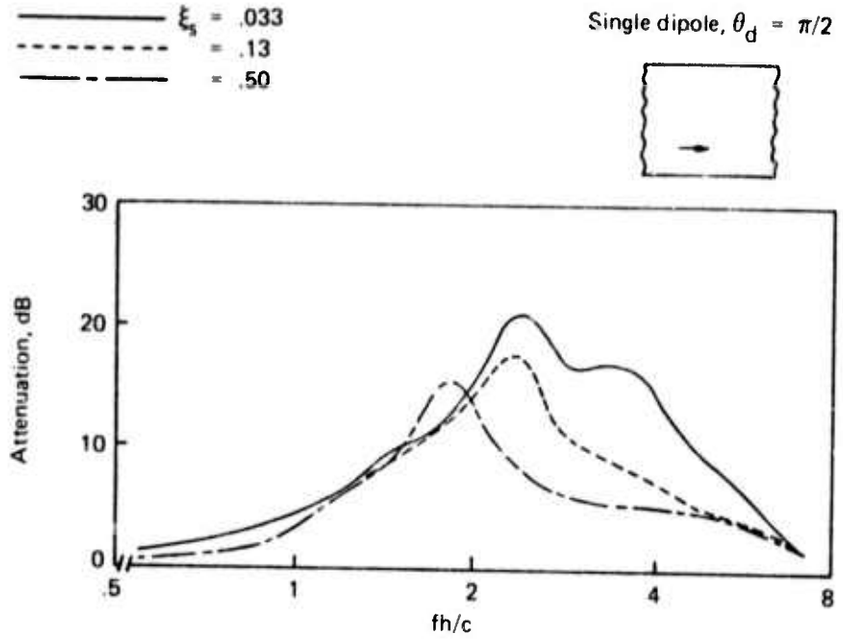

Figure 257.—Attenuation Spectra for Single Dipoles, $\theta_d = \pi/2$

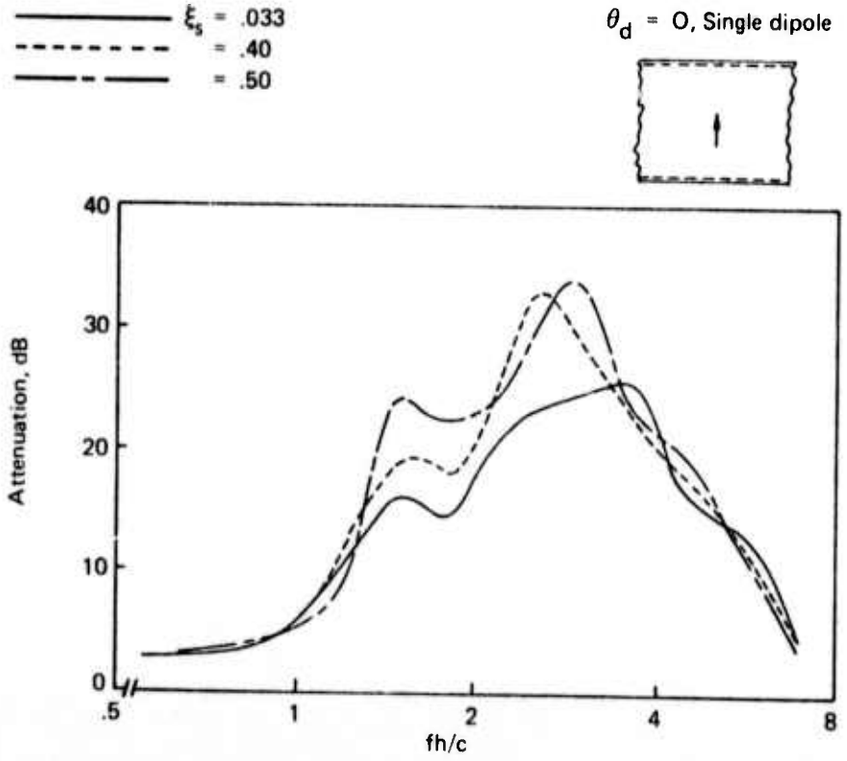

Figure 258.—Attenuation Spectra for Single Dipoles, $\theta_d = O$

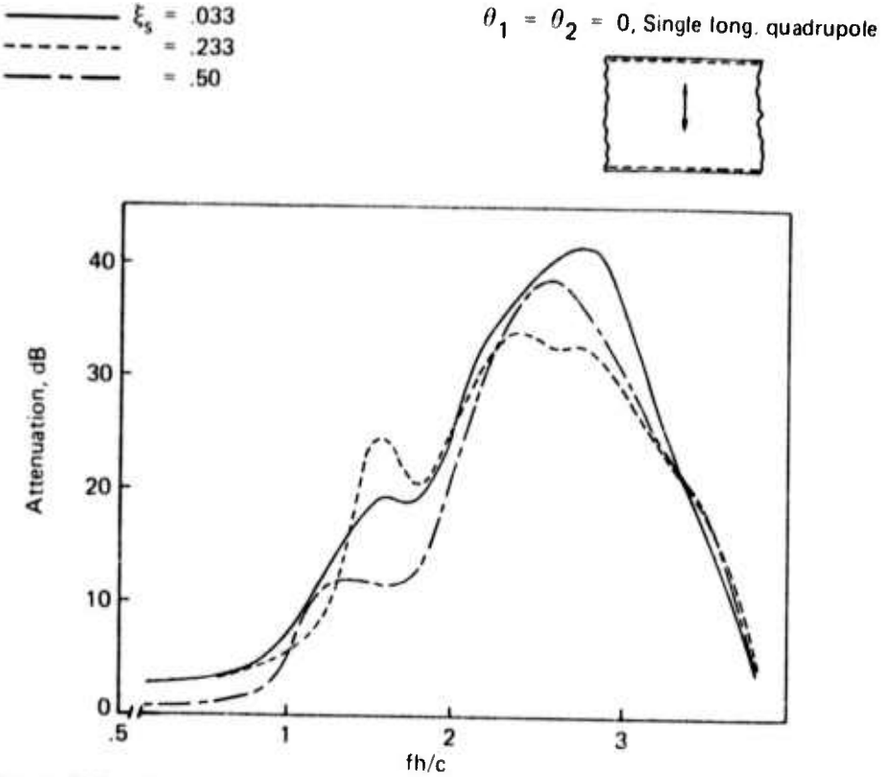

Figure 259.—Attenuation Spectra of Single Quadrupoles Corresponding to the Configuration $\theta_1 = \theta_2 = 0$

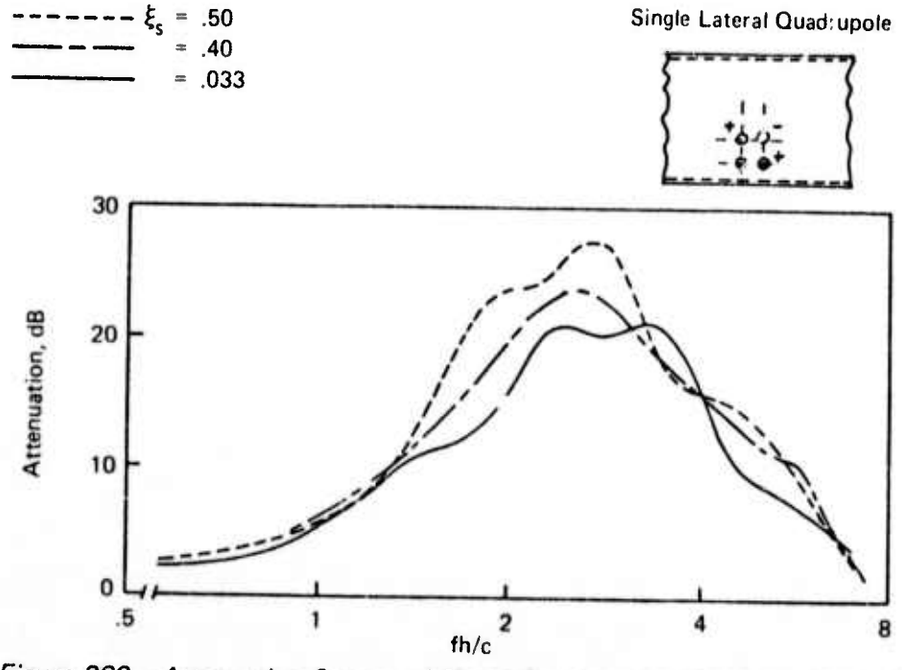

Figure 260.—Attenuation Spectra of Single Quadrupoles Corresponding to the Configuration $\theta_1 = 0, \theta_2 = \pi/2$ (Lateral Quadrupoles)

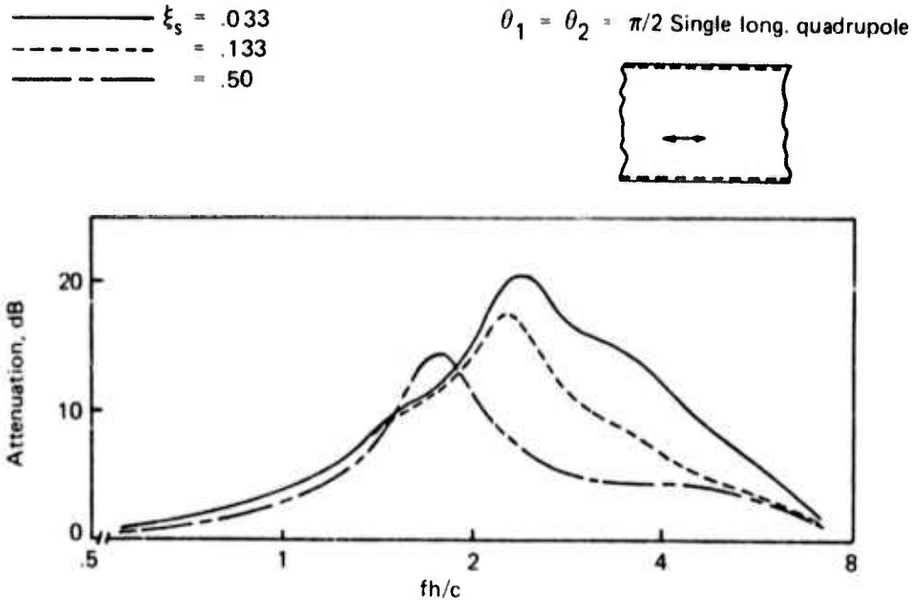

Figure 261.—Attenuation Spectra of Single Quadrupoles Corresponding to the Configuration $\theta_1 = \theta_2 = \pi/2$

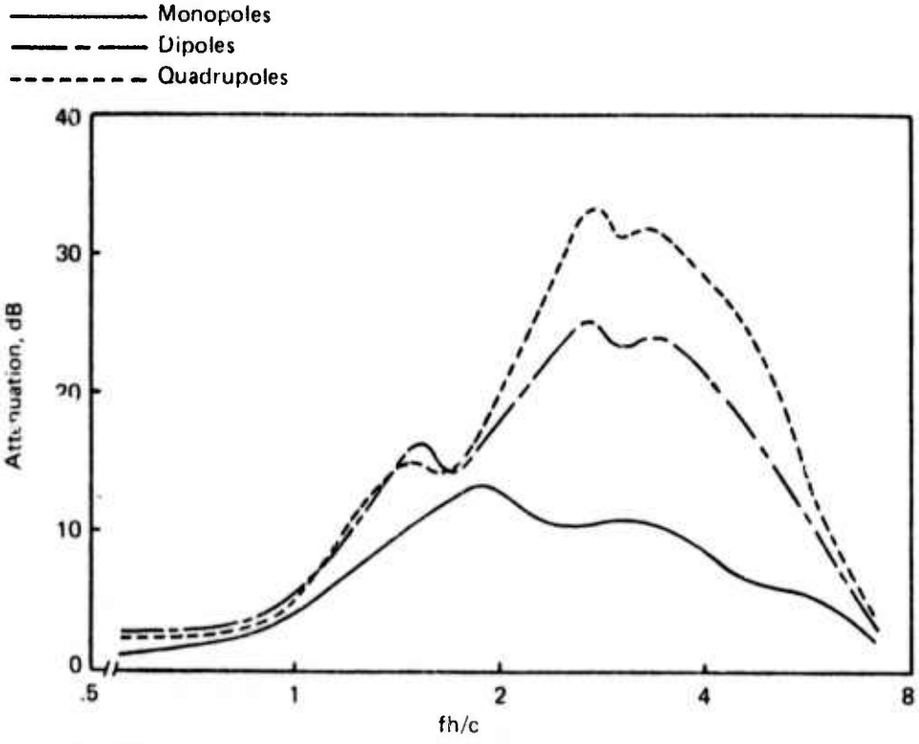

Figure 262.—Attenuation Spectra for Different Noise Sources

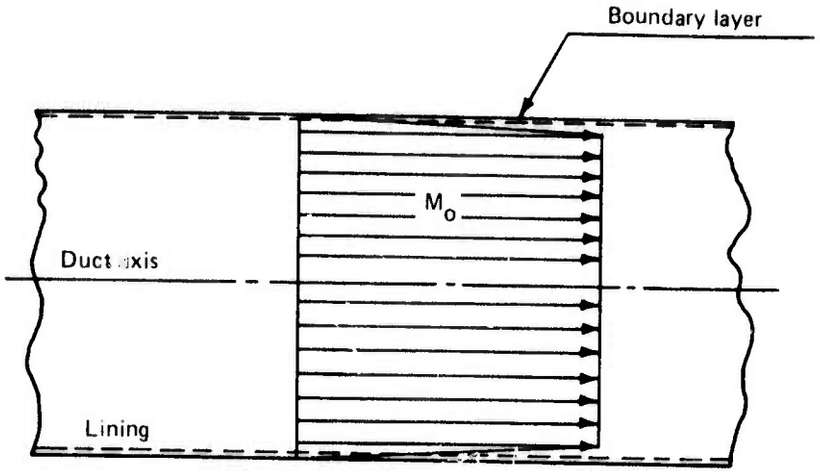

a. Current programs

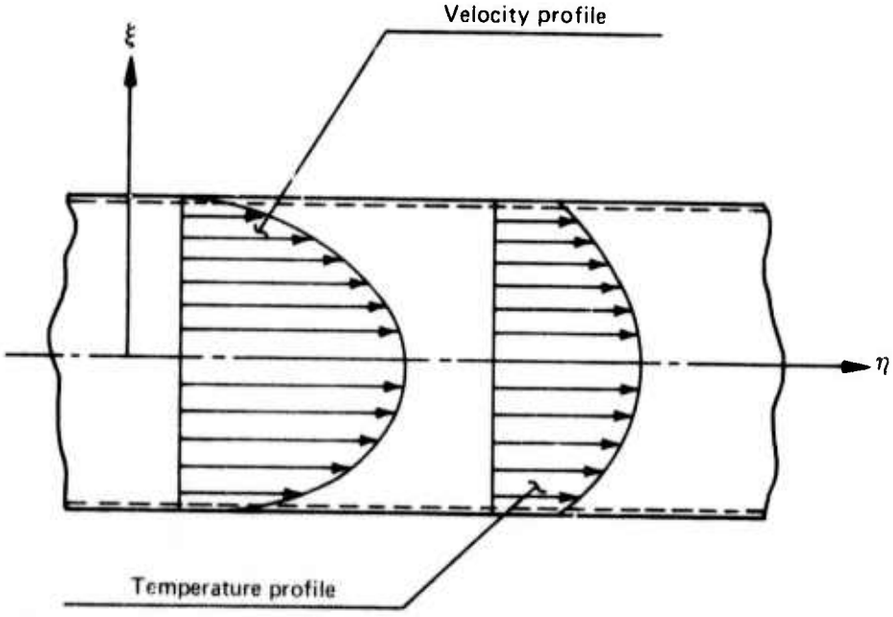

b. Non-uniform velocity and temperature

Figure 263.—Sketch of Geometrical Configuration for Flow Profile Analysis

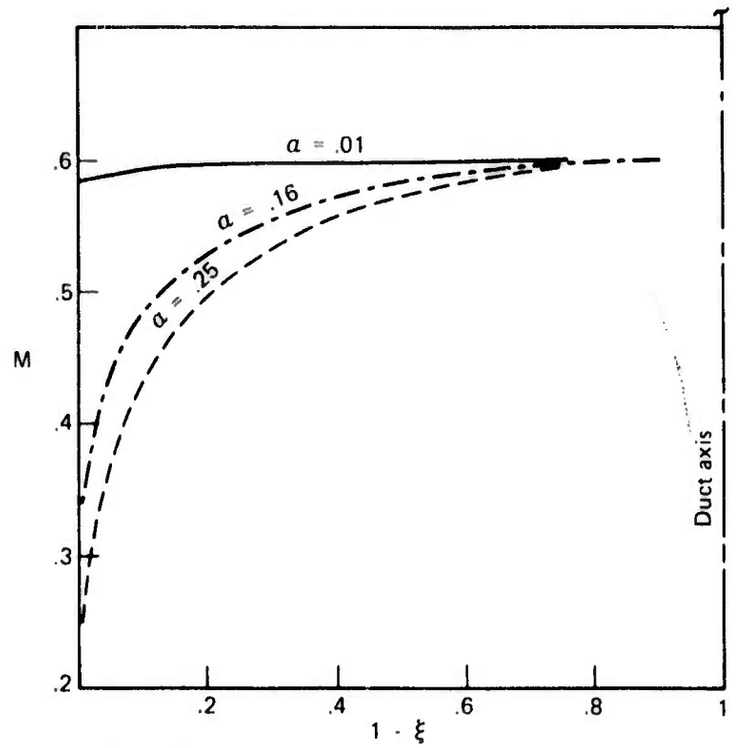

Figure 264.—Parabolic Type Mach Number Profiles

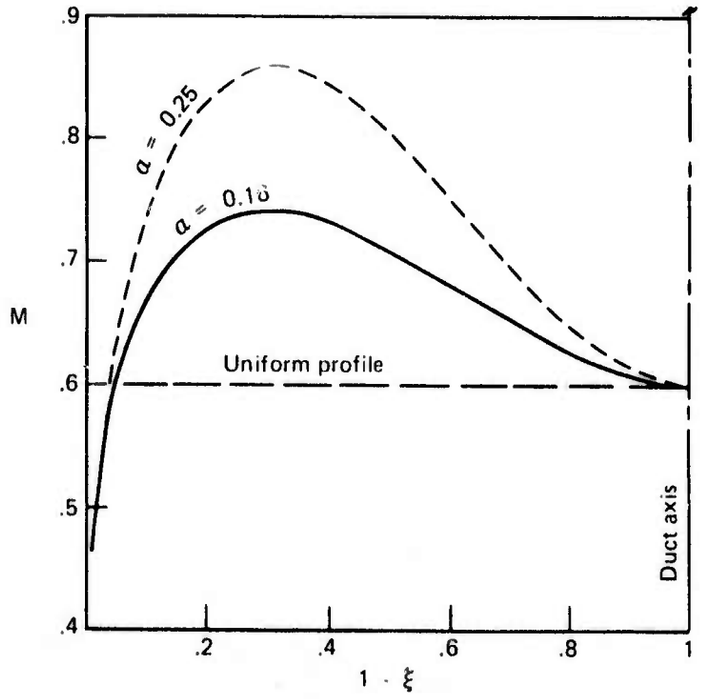

Figure 265.—"Humped" Mach Number Profiles

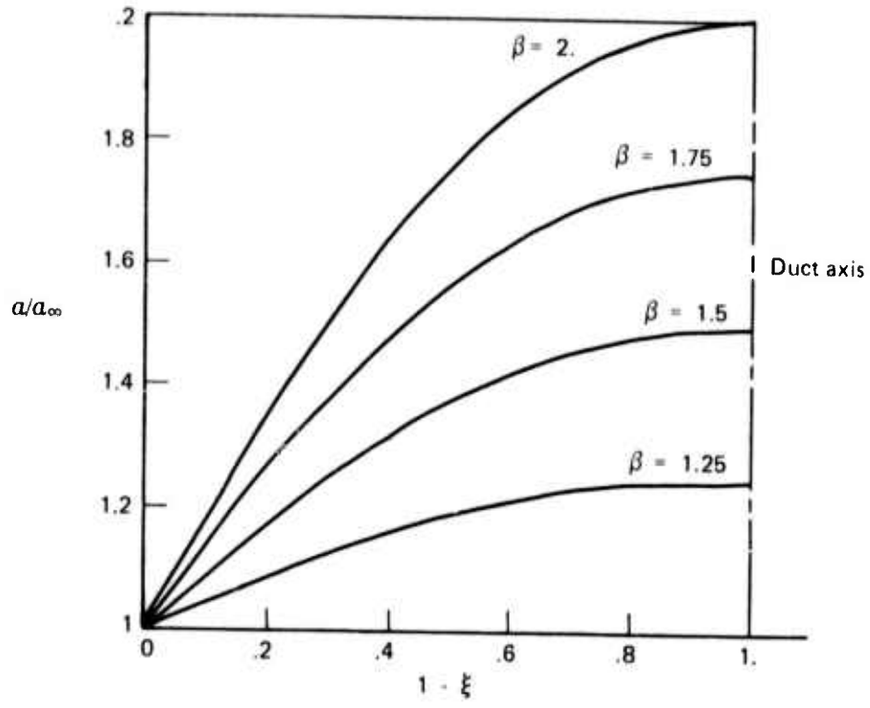

Figure 266.—Speed of Sound Ratio Profiles

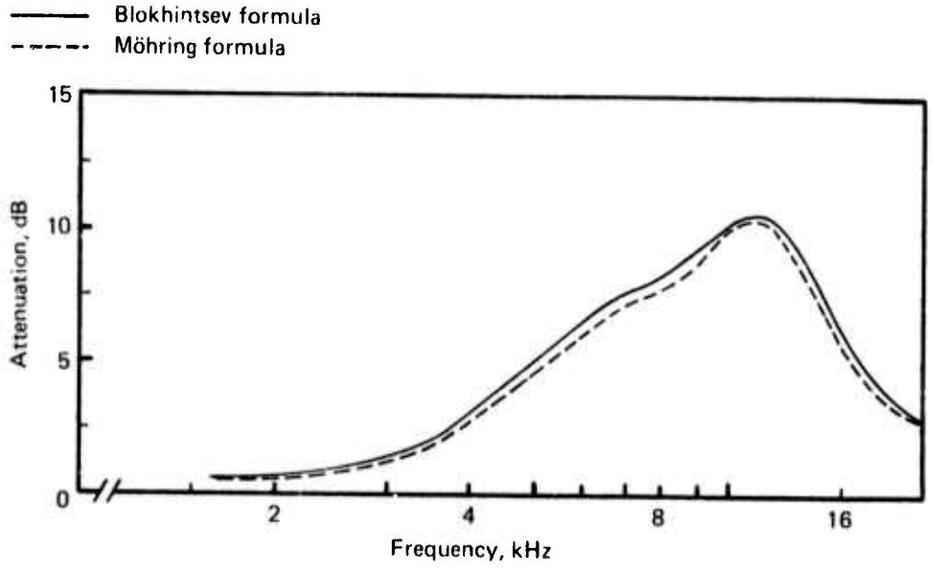

Figure 267.—Attenuation Spectra in Decibels, Obtained Using Blokhintsev and Möhring Formulas for Constant Mach Number Profile

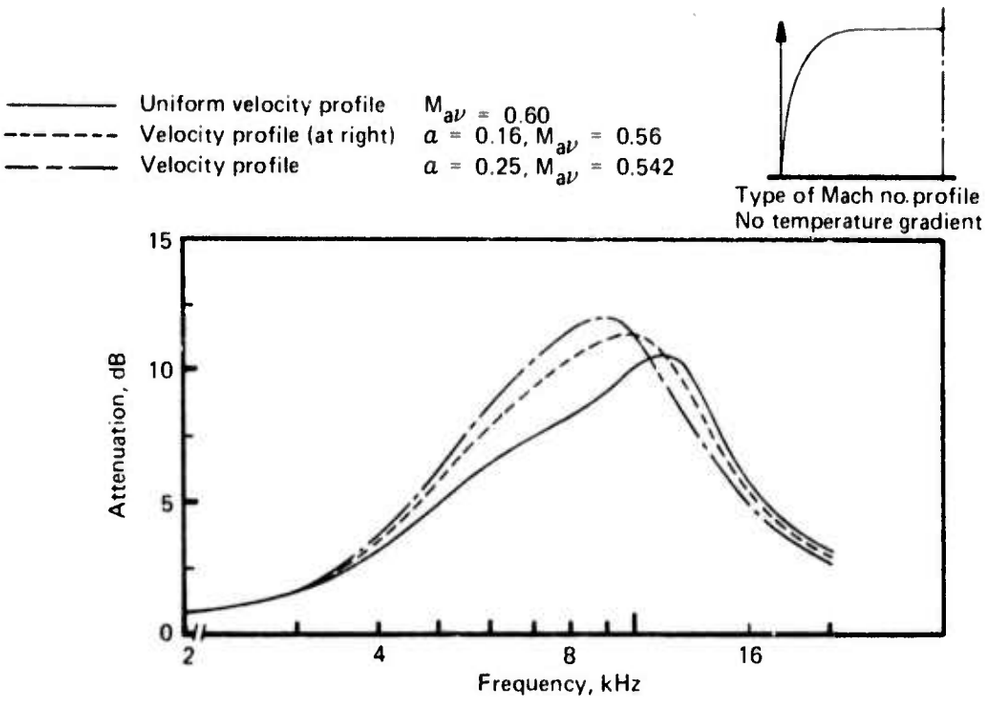

Figure 268.—Attenuation Spectra in Decibels Corresponding to the Parabolic Type of Mach Number Profile. Mach Number on Axis = 0.6

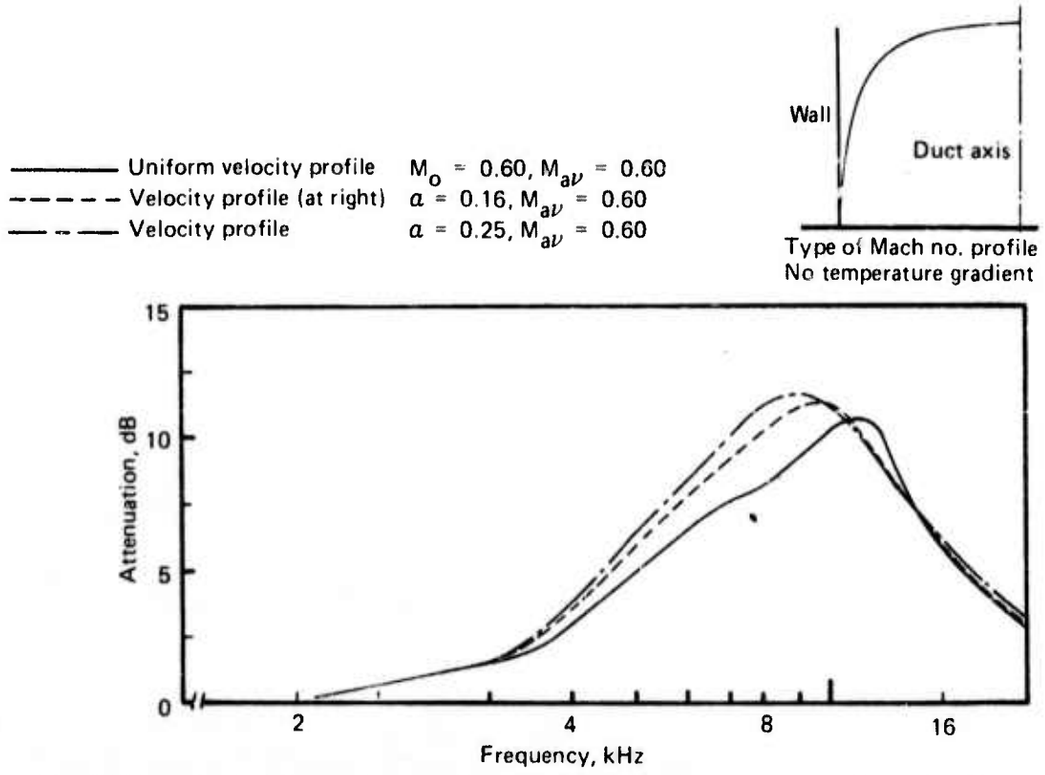

Figure 269.—Attenuation Spectra in Decibels Corresponding to the Parabolic Type of Mach Number Profile. Average Mach Number Constant and Equal to 0.60.

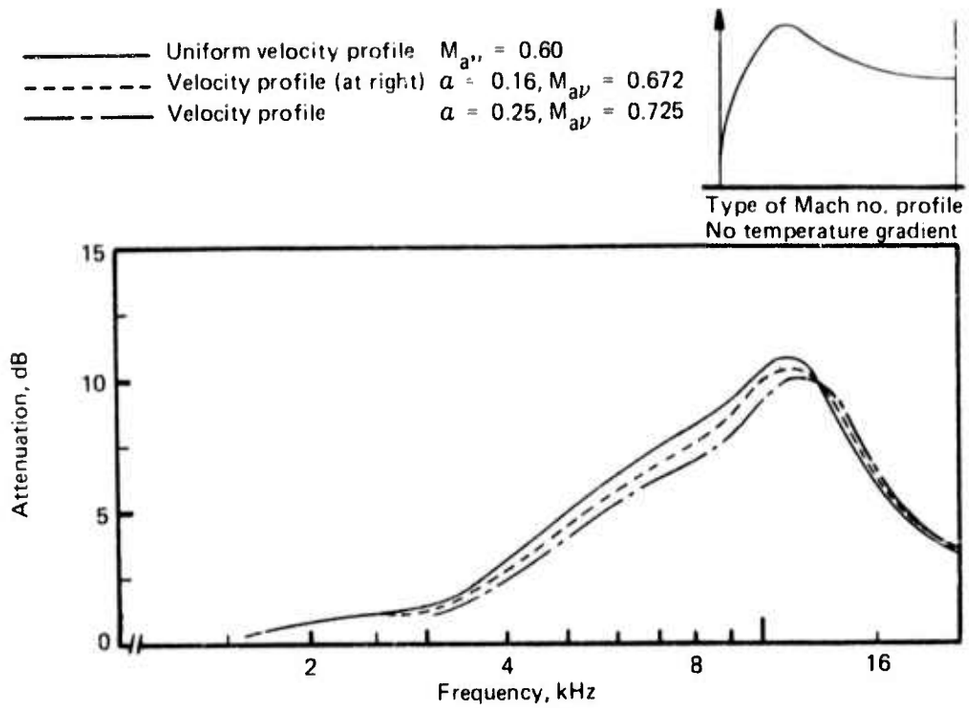

Figure 270.—Attenuation Spectra in Decibels Corresponding to the "Humped" Type of Mach Number Profile. Mach Number on Axis = 0.6

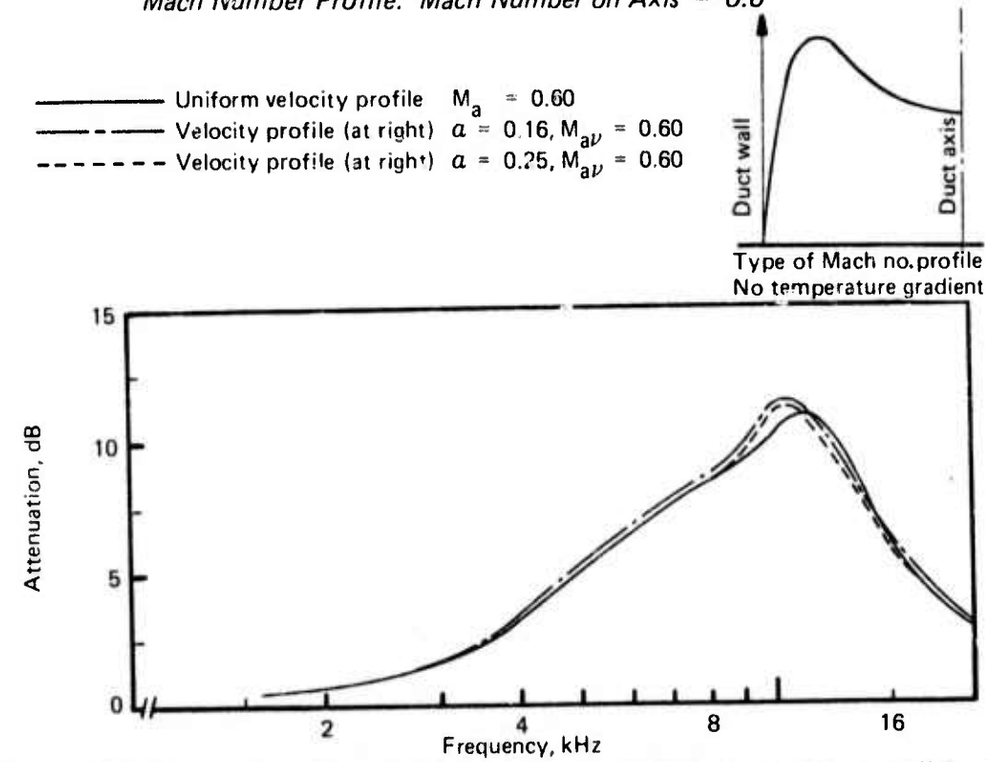

Figure 271.—Attenuation Spectra in Decibels Corresponding to the "Humped" Type of Mach Number Profile When the Average Mach Number is Constant and Equal to 0.60.

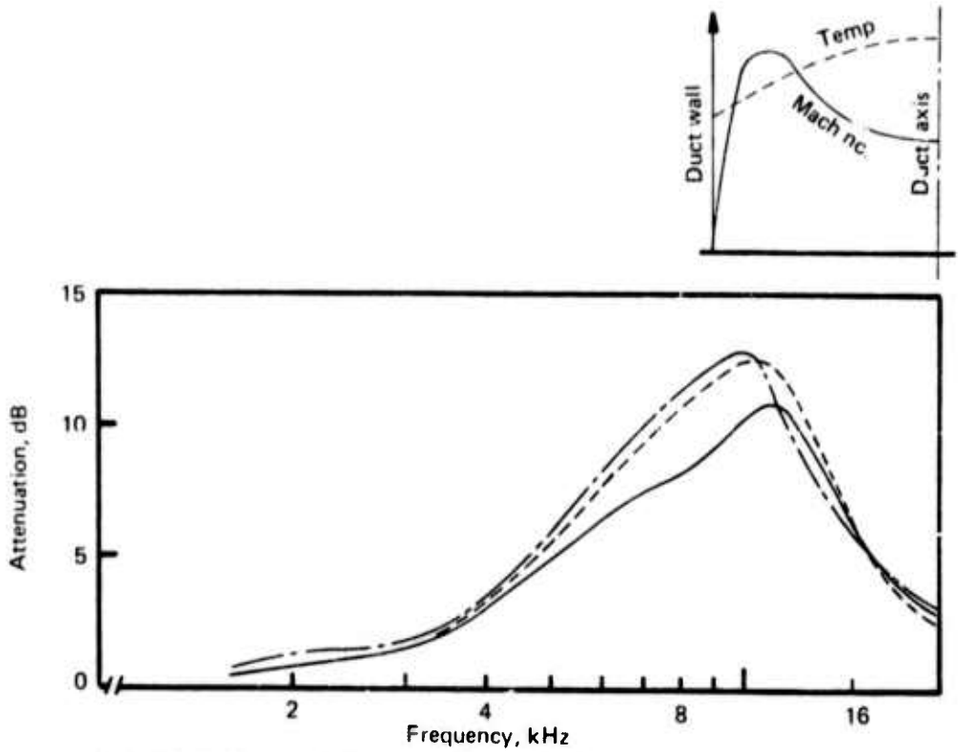

——— Uniform velocity and temperature, $M_{a\nu} = 0.60$
- - - - - - - - Non-uniform velocity and temperature, profiles at right, $M_{a\nu} = 0.60$, $\alpha = 0.25$, $\beta = 1.75$
——— - ——— Uniform velocity, temperature profile at right, $M_{a\nu} = 0.60$, $\alpha = 0$, $\beta = 1.75$

Figure 272.—Attenuation Spectra in Decibels With a Temperature Gradient

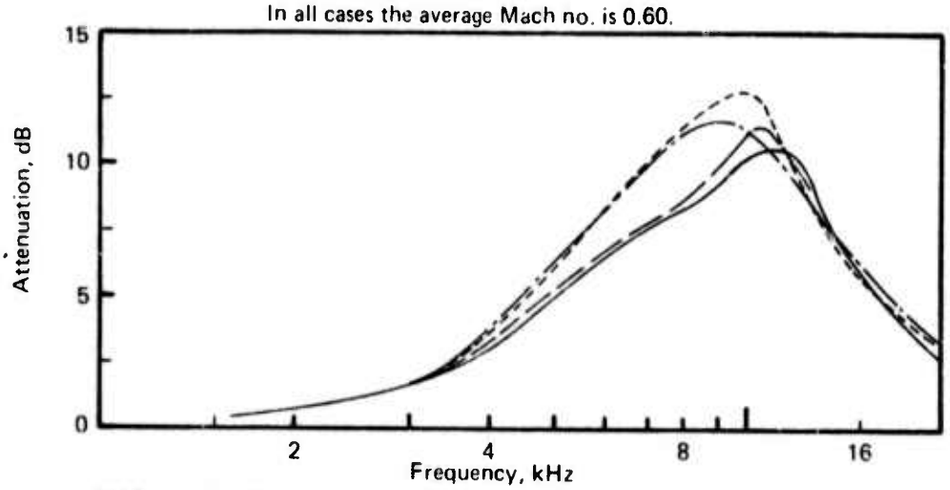

——— Uniform velocity and temperature
——— · ——— Uniform temperature, parabolic Mach no. profile $\alpha = 0.25$
- - - - - - - - Uniform velocity, non-uniform temperature
——— ——— Uniform temperature, humped Mach no. profile $\alpha = 0.16$

Figure 273.—Attenuation Spectra in Decibels Obtained From the Previous Figures to Show the Range of Effects of the Velocity and Temperature Gradients

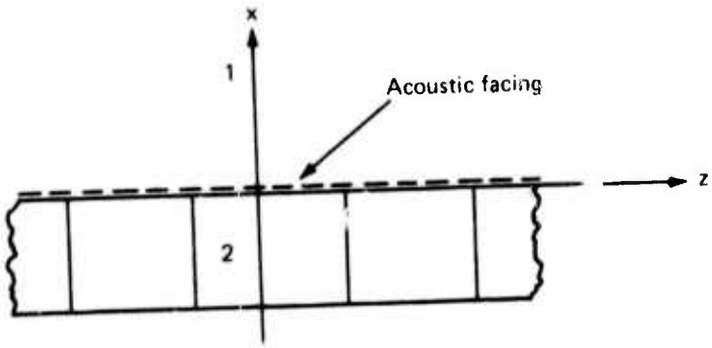

Figure A-1. Sketch of Acoustical Panel Used in the Analysis

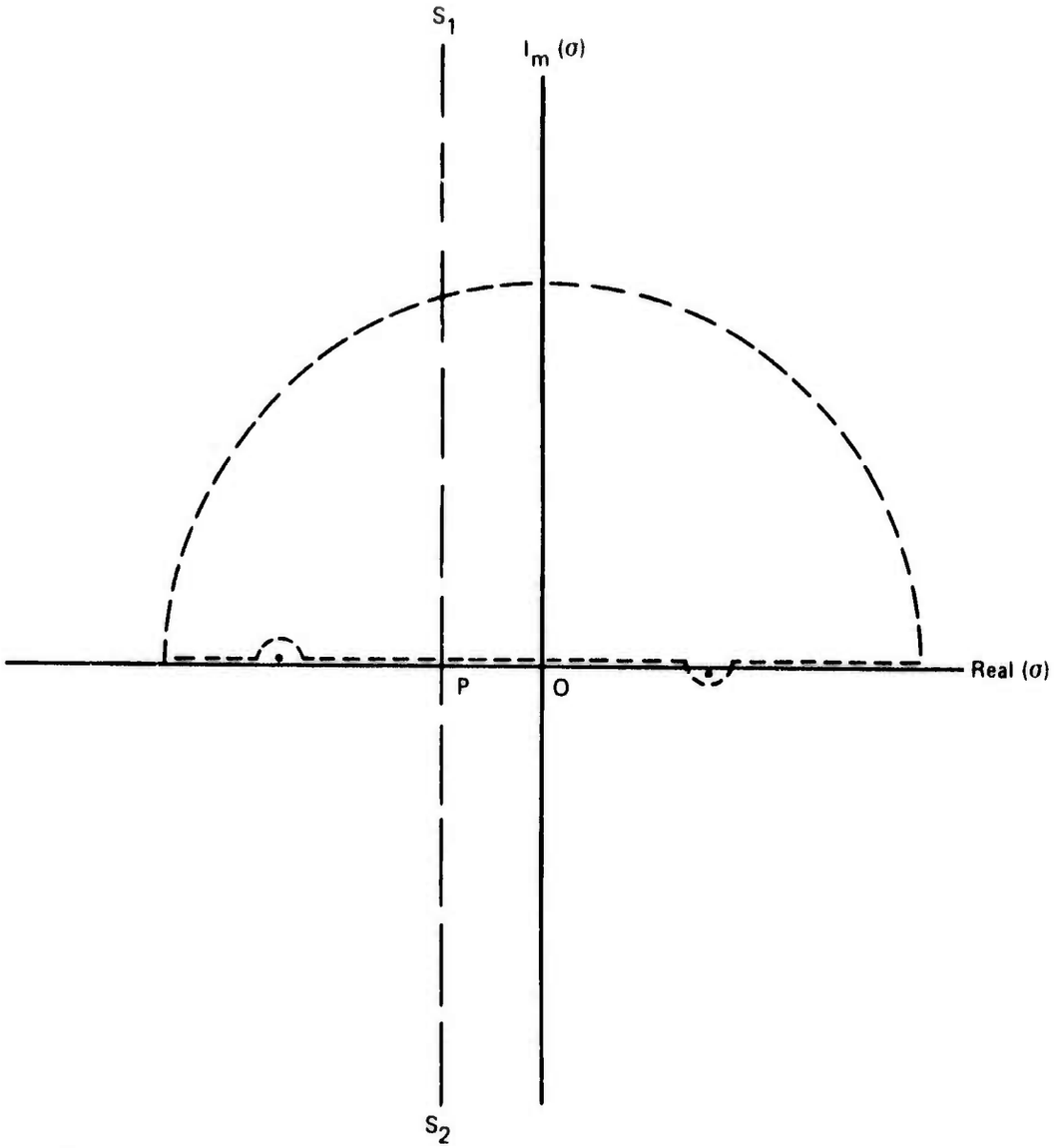

Figure B-1. Location of Poles and Path of Integration for the Hard Wall Case

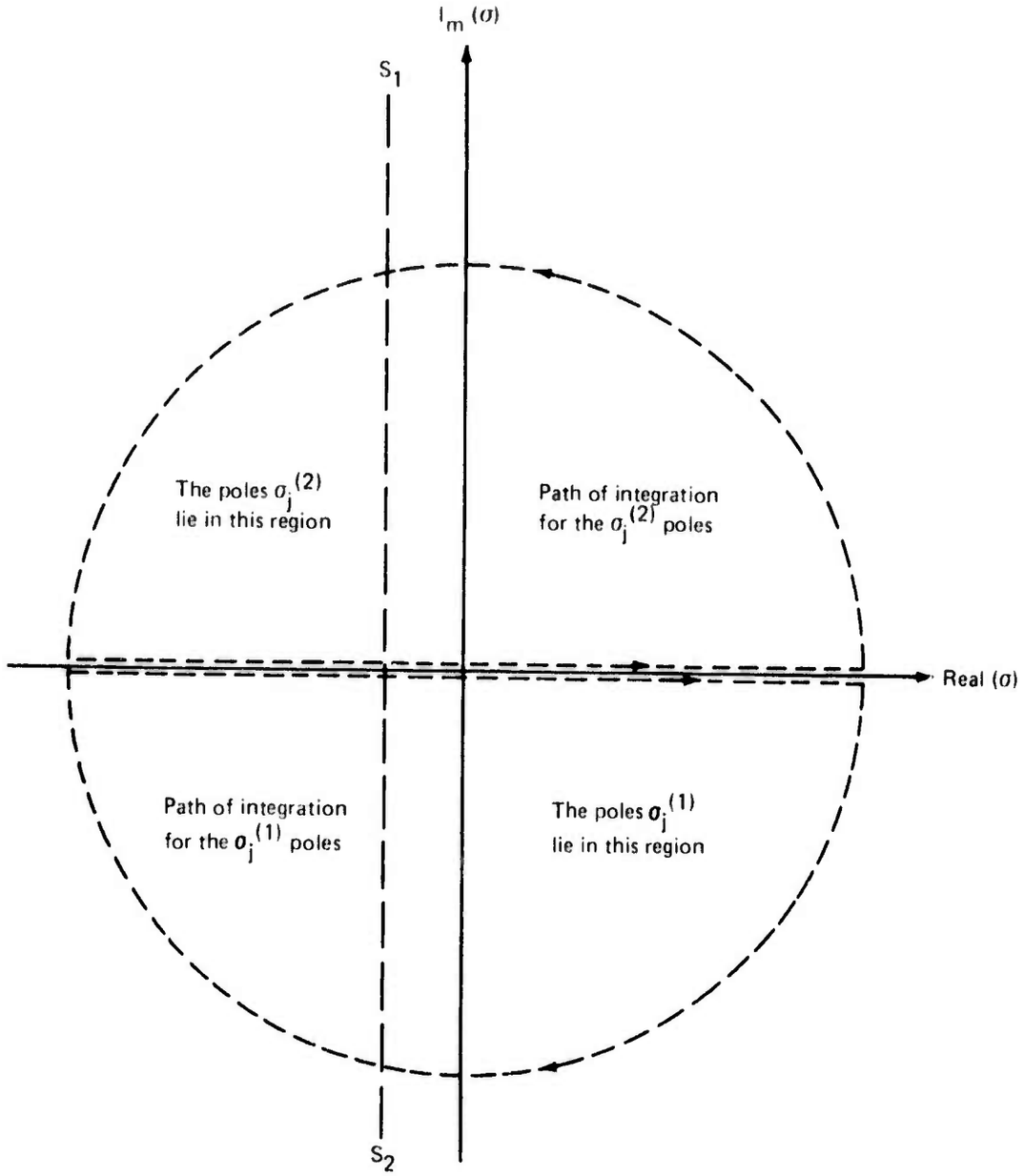

Figure B-2. Location of Poles and Paths of Integration for the Soft Wall Case

REFERENCES

1. C.P. Wright, D.B. Morden and C.D. Simcox, *A Summary of the SST Jet Noise Suppression Test Program*, FAA-SS-72-41, February 1972.

2. H.Y. Lu, D.B. Morden, R.L. Benefiel, and C.D. Simcox, *Performance Evaluation of the NSC-119B Nozzle System — Volume 1, Suppressed Mode*, FAA-SS-72-40-1, February 1972

3. R. C. Potter and J.H. Jones, *An Investigation to Locate the Acoustic Sources in a High Speed Jet Exhaust Stream*, Wyle Laboratories Technical Report WR 68-4, February 1968.

4. G.R. MacGregor and C.D. Simcox, "The Location of Acoustic Sources in Jet Flows by Means of the Wall Isolation Technique," AIAA paper 73-1041, October 1973.

5. J. Atvars, G.C. Paynter, D.Q. Walker, and C.F. Wintermeyer, *Development of Acoustically Lined Ejector Technology for Multitube Jet Noise Suppressor Nozzles by Model and Engine Tests over a Wide Range of Jet Pressure Ratios and Temperatures*, NASA CR-2382, April 1974.

6. "Jet Noise Prediction," AIR 876, SAE, July 1965.

7. "Standard Values of Atmospheric Absorption as a Function of Temperature and Humidity for Use in Evaluating Aircraft Flyover Noise," ARP 866, SAE, August 1964.

8. "Method of Calculating the Attenuation of Aircraft Ground-To-Ground Noise Propagation during Takeoff and Landing," AIR 923, SAE, August, 1965.

9. "Definitions and Procedures for Computing the Perceived Noise Level of Aircraft Noise," ARP 865, SAE, October 1964.

10. Christopher K.W. Tam, "On the Noise of a Nearly Ideally Expanded Supersonic Jet," *Journal of Fluid Mechanics*, vol. 51, no. 1, p. 69, 1972.

11. K. Bushell, "Jet Exhaust Noise Prediction," (2nd Draft Oct. 1973), Presented to the SAE A-21 Committee, October 1973.

12. H.Y. Lu, *Calculation of Axisymmetric Compressible Turbulent Jet Flows*, Boeing Document D6-40611, November 1972.

13. H.T. Nagamatsu, R.E. Sheer, Jr., and M.S. Gill, "Flow and Acoustic Characteristics of Subsonic and Supersonic Jets from Convergent Nozzles," AIAA paper 70-802, July 1970.

14. K. D. Kryter and K.S. Pearsons, "Some Effects of Spectral Content and Duration on Perceived Noise Level," *JASA*, vol. 35, no. 6, June 1963.

PRECEDING PAGE BLANK-NOT FILMED

15. "Noise Standards: Aircraft Type Certification," FAR Part 36, December 1969.

16. Lord Rayleigh, *Theory of Sound*, Dover Publications, vol. 2, 1945, p. 133.

17. J.W. Miles, "On the Reflection of Sound at an Interface of Relative Motion," *JASA*, vol. 29, no. 2, 1951, pp. 226-228.

18. H.S. Ribner, "Reflection, Transmission and Amplification of Sound by a Moving Medium," *JASA*, vol. 29, no. 4, 1957, pp. 435-441.

19. C. Yeh, "Reflection and Transmission of Sound Waves by a Moving Fluid Layer," *JASA*, vol. 41, no. 4, 1967, pp. 817-821.

20. C. Yeh, "A Further Note on the Reflection and Transmission of Sound Waves by a Moving Fluid Layer," *JASA*, vol. 43, no. 6, 1968, pp. 1454-1455.

21. I.S.F. Jones, *Jet Noise Suppression by an Impedance Shroud*, Boeing Scientific Research Lab Document D1-82-0984, 1970.

22. D. Middleton, and P.J.F. Clark, "Assessment and Development of Methods of Acoustic Performance Prediction for Jet Noise Suppressors," *UTIAS*, Tech-Note No. 134, Institute for Aerospace Studies, Univ. of Toronto, April 1969.

23. V.H. Gray, O.A. Gutierrez, and D.Q. Walker, *Assessment of Jets as Acoustic Shields by Comparison of Single and Multiple Suppressor Nozzle Data*, NASA TMX-71450, October 1973.

24. F.B. Greatrex and D.M. Brown, "Progress in Jet Engine Noise Reduction," *Proceedings of First International Congress in the Aeronautical Sciences, Madrid 1958*, Pergaruon, vol. 1, 1960.

25. Vern G. Rollin, *Effect of Multiple Nozzle Geometry on Jet Noise Generation*, NASA TN D-770, September 1961.

26. H.Y. Lu, "Acoustic Far-Field of a Point Source in Cylindrical and Power Parallel Flowing Fluid Layers," AIAA 75-500, 1975.

27. D.L. Armstrong, *Acoustic Grazing Flow Impedance Using Waveguide Principles*, NASA CR 120848, December 1971.

28. E.J. Rice, *Propagation of Waves in an Acoustically-Lined Duct with a Mean Flow*, NASA SP-207, July 1969.

29. S.H. Ko, "Sound Attenuation in Acoustically Lined Circular Ducts in the Presence of Uniform Flow and Shear Flow," *Journal of Sound Vibration*, vol. 22, 1972, p. 193.

30. P. Mungur and G.M.L. Gladwell, "Acoustic Wave Propagation in a Sheared Fluid Contained in a Duct," *Journal of Sound Vibration*, vol. 9, no. 1, 1969.

31. U.J. Kurze and C.H. Allen, "Influence of Flow and High Sound Level on the Attenuation in a Lined Duct," *Journal of the Acoustic Society of America*, vol. 49, 1971, p. 1643.

32. A. Kapur, A. Cummings, and P. Mungur, "Sound Propagation in a Combustion Can with Axial Temperature and Density Gradients," *Journal of Sound Vibration*, vol. 25, no. 1, 1972, pp. 129-138.

33. D.L. Lansing and W.E. Zorumski, "Effect of Wall Admittance Changes on Duct Transmission and Radiation of Sound," *Journal of Sound Vibration*, vol. 27, no. 1, 1973, pp. 85-100.

34. B.J. Tester, "The Propagation and Attenuation of Sound in Lined Ducts Containing Uniform or 'Plug' Flow," *Journal of Sound Vibration*, vol. 28, no. 2, 1973, pp. 151-203.

35. B. J. Tester, "The Optimization of Modal Sound Attenuation in Ducts, in the Absence of Mean Flows," *Journal of Sound Vibration*, vol. 27, 1973, pp. 477-513.

36. M.A. Isakovich, "Scattering of Sound Waves by Small Nonuniformities in a Waveguide," *Soviet Physics-Acoustics*, vol. 3, 1957, pp. 35-45.

37. A.D. Lapin, "Sound Propagation in a Waveguide Having Rectangular Grooves in the Walls," *Soviet Physics-Acoustics*, vol. 3, no. 6, 1960, pp. 233-238.

38. A.D. Lapin, "Sound Propagation in a Waveguide with Side Branches and Volume Resonators in the Walls," *Soviet Physics-Acoustics*, vol. 7, no. 2, 1961, pp. 171-175.

39. I.N. Sneddon, *Fourier Transforms*, McGraw-Hill Book Co., (New York), 1951.

40. H.S. Ribner, "The Noise of Aircraft," *International Council of the Aeronautic Sciences Fourth Congress*, Paris, August 24-28, 1968.

41. H.S. Ribner, "Aerodynamic Sound from Fluid Dilatations," *UTIA* report no. 86, July 1962.

42. P.M. Morse and K.U. Ingard, *Theoretical Acoustics*, McGraw-Hill Co., (New York), 1968.

43. D.I. Blokhintsev, *Acoustics of a Non-Homogeneous Moving Medium*, (Translated from the Russian), NASA TM-1399, 1956.

44. S. Mariano, "Effect of Wall Shear Layers on the Sound Attenuation by Broad Band-Width Linings," *Acoustica*, vol. 29, no. 3, 1973.

45. B. J. Tester, "Acoustic Energy Flow in Lined Ducts Containing Uniform or 'Plug' Flow," *Journal of Sound Vibration*, vol. 28, no. 2, 1973, pp. 205-215.

46. C.L. Morfey, "Acoustic Energy in Non-Uniform Flows," *Journal of Sound Vibration*, vol. 14, 1971, pp. 159-170.

47. W. Möhring, "Energy Flux in Duct Flow," *Journal of Sound Vibration*, vol. 18, 1971, pp. 101-109.

48. P. Mungur, and G.M.L. Gladwell, "Acoustic Wave Propagation in a Sheared Fluid Contained in a Duct," *Journal of Sound Vibration*, vol. 9, no. 1, 1969, pp. 28-48.

49. S. Mariano, "Effect of Wall Shear Layers on the Sound Attenuation in Acoustically Lined Rectangular Ducts," *Journal of Sound Vibration*, vol. 19, no. 3, 1971, pp. 261-275.

50. S.H. Ko, "Sound Attenuation in Acoustically Lined Circular Duct in the Presence of Uniform Flow and Shear Flow," *Journal of Sound Vibration*, vol. 22, 1972.

51. V.J. Kurze, and C.H. Allen, "Influence of Flow and High Sound Level on the Attenuation in a Lined Duct," *Journal of Acoustic Society of America*, vol. 49, 1971.

52. A. Kapur and P. Mungur, "On the Propagation of Sound in a Rectangular Duct with Gradients of Mean Flow and Temperature in Both Transverse Directions," *Journal of Sound Vibration*, vol. 23, no. 3, August 1972, pp. 401-404.

53. R.J. Beckemeyer, "On the Effect of Thin Shear Layers with Flow and Density Gradients on Small Disturbances in Inviscid, Compressible Fluid," *Journal of Sound Vibration*, vol. 31, no. 2, 1973, pp. 251-256.

54. B. Noble, *Numerical Methods (II)*, Interscience Publishers, Inc. (New York); Oliver and Boyd (London).

55. S. Mariano, "Effect of Wall Shear Layers on the Sound Attenuation by Broad Band-Width Linings," *Acoustica*, vol. 29, 1973, pp. 148-156.

56. W. Möhring, "Energy Flux in Duct Flow," *Journal of Sound Vibration*, vol 18, 1971, pp. 101-109.

57. C.L. Morfey, "Acoustic Energy in Non-Uniform Flows," *Journal of Sound Vibration*, vol. 14, 1971, pp. 139-170.

APPENDIX A
DERIVATION OF BOUNDARY CONDITIONS FOR PRESSURE FIELD OF MONOPOLES

At the face of the acoustic treatment the particle displacement must be the same in regions 1 and 2 of figure A-1.

$$\frac{ds_1}{dt} = u_1 = \frac{\partial s_1}{\partial t} + V_o \frac{\partial s_1}{\partial z} \tag{A-1}$$

$$\frac{ds_2}{dt} = u_2 = \frac{\partial s_2}{\partial t} \tag{A-2}$$

Assume a time dependence of the type $e^{i\omega t}$, then:

$$u_1 = i\omega s_1 + V_o \frac{\partial s_1}{\partial t} \tag{A-3}$$

$$u_2 = i\omega s_2 \tag{A-4}$$

By definition, $u_2 = Yp_1$; hence,

$$s_2 = \frac{Yp_1}{i\omega} \tag{A-5}$$

(A-6)

Since, $s_1 = s_2$

the, from A-3,

$$u_1 = Yp_1 + \frac{V_o Y}{i\omega} \frac{\partial p_1}{\partial z} \tag{A-7}$$

From the x-momentum equation the following is obtained:

$$i\omega u_1 + V_o \frac{\partial u_1}{\partial z} = -\frac{1}{\rho_o} \frac{\partial p_1}{\partial x} \tag{A-8}$$

From equations A-7 and A-8 u_1 can be eliminated. Then:

$$\frac{\partial p_1}{\partial x} = -i\omega\rho_o Y \left[p_1 + \frac{2 V_o}{i\omega} \frac{\partial p_1}{\partial z} - \frac{V_o^2}{\omega^2} \frac{\partial^2 p_1}{\partial z^2} \right] \tag{A-9}$$

which can be written in the nondimensional form, as follows:

$$\frac{\partial p_1}{\partial \xi} = -isY' \left[p_1 - 2i \frac{M_o}{s} \frac{\partial p_1}{\partial \eta} - \frac{M_o^2}{s^2} \frac{\partial^2 p_1}{\partial \eta^2} \right] \tag{A-10}$$

If the η-dependence is of the form $e^{-ik_z' \eta}$, then:

$$\frac{\partial p_1}{\partial \xi} = -isY' \left(1 - \frac{M_o}{s} k_z' \right)^2 p_1 \tag{A-11}$$

where $k_z' = k_z h$.

APPENDIX B
ANALYSIS OF THE INTEGRATION REQUIRED TO OBTAIN $p(\xi, \eta)$

1. MONOPOLES

The poles of $\overline{P}_m(\sigma)$ are given by:

$$R_m = 0 \text{ and } D = 0 \tag{B-1}$$

a. If the hardwall case is studied, the only possible solution is

$$R_m(\sigma) = o, \text{ i.e.}$$

$$R_m = -(1 - M_o^2)(\sigma - \sigma_1)(\sigma - \sigma_2) \tag{B-2}$$

where σ_1 and σ_2 are the roots corresponding to each branch

$$\left.\begin{matrix}\sigma_1 \\ \sigma_2\end{matrix}\right\} = s\,\frac{-M_o \pm \sqrt{i\text{-}(1 - M_o^2)(m\pi/s)^2}}{1 - M_o^2} \tag{B-3}$$

$$\sigma_1 > -\frac{M_o}{1 - M_o^2} \qquad \sigma_2 < -\frac{M_o}{1 - M_o^2}$$

In figure B-1 the location of the poles has been depicted. The distance OP defining the position of the line $s_1 s_2$ is equal to $-M_o/(1-M_o^2)$. When $m > s/(\pi \sqrt{1 - M_o^2})$, σ_1 and σ_2 become complex quantities; in this instance, the poles given by σ_1 are located on the line Ps_2 while those given by σ_2 can be found on Ps_1. Since these complex poles correspond to cut-off modes for the hardwall duct they will not be considered here.

Where $R_m = 0$ $D \to \infty$ (assuming that Y_1' and Y_2' have a very small value, non-zero)

$$D = \left(1 + \frac{s^2 Y_1' Y_2'}{\lambda^2}\right) - i\frac{s}{\lambda}\left(Y_1' + Y_2'\right)\cot\lambda \tag{B-4}$$

$$\lambda = \sqrt{s^2 - \left(1 - M_o^2\right)\sigma^2 - 2\sigma x M_o}$$

Expression B-4 will be verified below. When hardwalls exist $\lambda = m\pi$. The interesting fact is that D (equation 54) is denominator of an expression whose numerator also becomes infinite.

By performing the algebra, the main parts of D and the numerator (assuming that Y_1' and Y_2' have, for the time being, a small value) are:

$$\text{Numerator} = (-1)^{m+1}\left(Y_1' + Y_2'\right)\frac{i\cos\lambda\xi_s}{\lambda\sin\lambda}$$

$$D = i(-1)^{m+1}\frac{s}{\lambda}\frac{Y_1' + Y_2'}{\sin\lambda}$$

Hence,

$$\frac{\text{Numerator}}{D} = \cos(m\pi\xi_s) \tag{B-5}$$

In the case of hardwalls, then:

$$\overline{P}_{m1}(\sigma) = \frac{2\,Ah^2\exp(i\sigma\eta_s)\cos(m\pi\xi_s)}{2\pi\left(1 - M_o^2\right)(\sigma_1 - \sigma_2)} \tag{B-6}$$

Figure B-1 depicts the location of the pole σ_1 and σ_2 in the complex σ-plane and the path of integration. A small imaginary part, that in calculations $\to 0$, is assumed for σ_1 and σ_2 such that the radiation condition at ∞ is satisfied. Since the poles are basically lying on the real axis, it is necessary to multiply by πi instead of $2\pi i$ · $p(\xi, \eta)$ is then given by:

$$p(\xi,\eta) = \frac{Ah^2 i}{1 - M_o^2}\sum_{m=0}^{\infty}\in_m \frac{\cos(m\pi\xi_s)\cos(m\pi\xi)}{\sigma_1 - \sigma_2}\begin{cases} e^{i\sigma_1(\eta_s - \eta)}, & \eta > \eta_s \\ e^{i\sigma_2(\eta_s - \eta)}, & \eta < \eta_s \end{cases} \tag{B-7}$$

Expression B-7 looks like a Green's function, but it does not satisfy the reciprocity relations. It would satisfy these relations if the Mach number change sign. In order to avoid confusion it is referred to as the "acoustic propagator". This function can be used as a Green's function provided it is not necessary to apply the reciprocity theorem.

b. **For the softwall case**

$$D = 0$$

The roots must be complex. R_m cannot be zero in this case since the roots for R_m are real numbers.

It is possible to obtain the following expressions:

$$\begin{aligned} S_1 &= 1/\lambda\sin\lambda \\ S_2 &= \cos\lambda\xi_s/\lambda\sin\lambda \\ S_3 &= (\sin\lambda\xi_s + \cot\lambda\cdot\cos\lambda\xi_s)/\lambda \end{aligned} \tag{B-8}$$

$$S_4 = \cot\lambda/\lambda$$

where,

$$\lambda = \left[s^2 - \left(1 - M_o^2\right) \sigma^2 - 2s\sigma M_o \right]^{1/2}$$

Replacing the first and last of these expressions into equation 52, the latter becomes:

$$D = \left(1 + \frac{s^2}{\lambda^2} Y_1' Y_2'\right) - i\frac{s}{\lambda}\left(Y_1' + Y_2'\right) \cot\lambda \qquad \text{(B-4)}$$

Therefore, the poles are given by the expression:

$$\left(\lambda^2 + s^2 Y_1' Y_2'\right) \tan\lambda = i\lambda\left(Y_1' + Y_2'\right) \qquad \text{(B-9)}$$

which is the usual expression, (ref. 17 and 22) required in order to determine the eigenvalues for a rectangular duct when opposite duct walls have linings of dissimilar admittances.

The location of the poles $\sigma_j^{(1)}$ and $\sigma_j^{(2)}$ in the complex σ-plane and the paths of integration are shown in figure B-2. As customary, the path of integration is positive when counter-clockwise. The poles are differentiated according to:

$$\text{Im}\left(\sigma_j^{(1)}\right) < o, \quad \text{Real}\left(\sigma_j^{(1)}\right) > -\frac{M_o}{1 - M_o^2}$$

$$\text{Im}\left(\sigma_j^{(2)}\right) > o, \quad \text{Real}\left(\sigma_j^{(2)}\right) < -\frac{M_o}{1 - M_o^2}$$

The double poles mentioned by Tester (ref. 45) are unlikely to exist when opposite walls have linings of dissimilar admittance. These double poles arise when the two opposite walls have linings of the same admittance and when the lining is optimized for one frequency; most likely, these double poles do not exist when the lining is optimized for a frequency band.

The investigation of the poles for a similar equation to that of B-9 has already been done by Tester (ref. 34 and 35) and it will not be repeated here. The poles are of first order and the residues are given by:

$$\text{Res} = \frac{\left(\sigma - \sigma_j^{(\nu)}\right)}{D} \frac{s\, e^{i\sigma\eta_s}}{R_m} \left[Y_1' C_1(\sigma) - (-1)^m Y_2' C_2(\sigma) \right] \qquad \text{(B-10)}$$

$$\nu = 1, 2$$

Using l' Hospital rule, get

$$\text{Residue} = Z_{m,j}^{(\nu)} \exp\left(i\sigma_j^{(\nu)}\eta_s\right)$$

$$Z_{m,j}^{(\nu)} = \frac{-\lambda s\left[Y_1' C_1\left(\sigma_j^{(\nu)}\right) - (-1)^m Y_2' C_2\left(\sigma_j^{(\nu)}\right)\right]}{\left[\frac{-2s^2 Y_1' Y_2'}{\lambda^3} + \left(\frac{\cot\lambda}{\lambda^2} - \frac{1}{\lambda\sin^2\lambda}\right) is\left(Y_1' + Y_2'\right)\right]\left[1 - M_o^2\,\sigma_j^{(\nu)} + sM_o\right] R_m\,\sigma_j^{(\nu)}} \tag{B-11}$$

$$C_1\left(\sigma_j^{(\nu)}\right) = s\,Y_2'\,S_1\,S_2 - i\,S_3\left(1 - is\,Y_2'\,S_4\right)$$

$$C_2\left(\sigma_j^{(\nu)}\right) = i\,S_2\left(1 - is\,Y_1'\,S_4\right) - s\,Y_1'\,S_3\,S_1$$

when $Y_1' \to 0$ and $Y_2' \to 0$ expression B-11 gives the result corresponding to the hardwall case. The pressure (acoustic propagator) for this case can be written in the form:

$$p(\xi,\eta) = Ah^2 i \sum_{m=0}^{\infty} \epsilon_m \cos(m\pi\xi) \sum_{j=1}^{\infty} \begin{cases} Z_{m,j}^{(1)}\, e^{i\sigma_j^{(1)}(\eta_s - \eta)}, & \eta > \eta_s \\ Z_{m,j}^{(2)}\, e^{i\sigma_j^{(2)}(\eta_s - \eta)}, & \eta < \eta_s \end{cases} \tag{B-12}$$

The solution B-12 gives the pressure for all points inside the duct including the walls, however, it cannot give the ξ-component of the particle velocity at the wall. This velocity component at the facing of the lining is obtained from expressions 38 and 42.

The number of poles required for the expression B-12 to converge increases when the frequency increases, but for practical purposes this number is seldom larger than 20. In this context, the series is meant to converge when the remaining terms contribute less than 1% of the total result in absolute value.

The ξ-component of the particle velocity at the wall is given by:

$$u^{(\nu)} = \frac{(-1)^\nu}{i\rho_o c_o\left(1 - \sigma_j^{(\nu)}\frac{M_o}{s}\right)} f_\nu(\eta) \tag{B-13}$$

where

$$f_\nu(\eta) = s\,\frac{Y_\nu' Ah^2}{2\pi} \int_{-\infty}^{+\infty} C_\nu \frac{e}{D}^{i\sigma(\eta_s - \eta)}\, d\sigma \tag{B-14}$$

$$\nu = 1, 2$$

Hence

$$u^{(1)} = \frac{Y_1\, Ah^2}{\rho_o c_o} \sum_{j=1}^{\infty} \begin{cases} U_j^{(1)}\, e^{i\sigma_j^{(1)}(\eta_s - \eta)}, & \eta > \eta_s \\ U_j^{(2)}\, e^{i\sigma_j^{(2)}(\eta_s - \eta)}, & \eta < \eta_s \end{cases} \tag{B-15}$$

where

$$U_j^{(\nu)} = \frac{-\lambda C_1}{\left(1 - \sigma_j^{(\nu)} \frac{M_o}{s}\right)\left[\frac{-2\, s^2\, Y_1'\, Y_2'}{\lambda^2} + \left(\frac{\cot\lambda}{\lambda^3} - \frac{1}{\lambda \sin^2\lambda}\right) is\left(Y_1' + Y_2'\right)\right]\left[\left(1 - M_o^2\right)\sigma_j^{(\nu)} + sM_o\right]} \tag{B-16}$$

In the expression above, the numerator and the denominator are functions of $\sigma_j^{(\nu)}$

u_2 can be expressed in a similar manner.

2. DIPOLES AND QUADRUPOLES

In order to obtain the pressure fields for dipoles and quadrupoles it is not necessary to go through the entire process done for monopoles. They can be obtained directly by performing certain operations on equation B-12. These operations, done with respect to the variables ξ_s and η_s, are possible because linearity considerations and they are defined by the right hand side of equations 57 and 58.

Then the pressure field corresponding to one dipole positioned at ξ_s, η_s is given by

$$pd(\xi, \eta) = Ah^2 i \sum_{m=0}^{\infty} \in_m \cos(m\pi\xi) \sum_{j=1}^{\infty} \begin{cases} D_{m,j}^{(1)}\, e^{i\sigma_j^{(1)}(\eta_s - \eta)}, & \eta > \eta_s \\ D_{m,j}^{(2)}\, e^{i\sigma_j^{(2)}(\eta_s - \eta)}, & \eta < \eta_s \end{cases} \tag{B-17}$$

where

$$D_{m,j}^{(\nu)} = \cos\theta_d \frac{d\, Z_{m,j}^{(\nu)}}{d\, \xi_s} + i\sigma_j^{(\nu)} \sin\theta_d\, Z_{m,j}^{(\nu)} \qquad \nu = 1, 2 \tag{B-18}$$

The pressure field of a quadrupole is given by

$$p_q(\xi,\eta) = Ah^2 i \sum_{m=0}^{\infty} \epsilon_m \cos(m\pi\xi) \sum_{j=1}^{\infty} \begin{cases} Q_{m,j}^{(1)}\, e^{i\sigma_j^{(1)}(\eta_s - \eta)}, & \eta > \eta_s \\ Q_{m,j}^{(2)}\, e^{i\sigma_j^{(2)}(\eta_s - \eta)}, & \eta < \eta_s \end{cases} \tag{B-19}$$

where

$$Q_{m,j}^{(\nu)} = \cos\theta_1 \cdot \cos\theta_2 \frac{d^2 Z_{m,j}^{(\nu)}}{d\ \xi_s^2} + i\sigma_j^{(\nu)} \sin(\theta_1 + \theta_2) \frac{d\ Z_{m,j}^{(\nu)}}{d\ \xi_s} - \sigma_j^{(2)(\nu)} \sin\theta_1 \cdot \sin\theta_2\, Z_{m,j}^{(\nu)}$$

$$\nu = 1, 2 \tag{B-20}$$

The ξ-component of the particle velocity at the wall for dipoles and quadrupoles is obtained by operating on the result given by expression B-16 corresponding to monopoles.

Hence, for dipoles it is

$$u_d^{(1)} = \frac{Ah^2\, Y_1'}{\rho_o c_o} \sum_{j=1}^{\infty} \begin{cases} \left[\cos\theta_d \frac{d\ U_j^{(1)}}{d\ \xi_s} + i\sigma_j^{(1)} \sin\theta_d\, U_j^{(1)}\right] e^{i\sigma_j^{(1)}(\eta_s - \eta)}, & \eta > \eta_s \\ \left[\cos\theta_d \cdot \frac{d\ U_j^{(2)}}{d\ \xi_s} + i\sigma_j^{(2)} \sin\theta_d\, U_j^{(2)}\right] e^{i\sigma_j^{(2)}(\eta_s - \eta)}, & \eta < \eta_s \end{cases} \tag{B-21}$$

and, for quadrupoles

$$u_q^{(1)} = \frac{Ah^2\, Y_1'}{\rho_o\, c_o} \sum_{j=1}^{\infty} \begin{cases} U_{q,j}^{(1)}\, e^{i\sigma_j^{(1)}(\eta_s - \eta)}, & \eta > \eta_s \\ U_{q,j}^{(2)}\, e^{i\sigma_j^{(2)}(\eta_s - \eta)}, & \eta < \eta_s \end{cases} \tag{B-22}$$

where

$$U_{q,j}^{(\nu)} = \cos\theta_1 \cdot \cos\theta_2 \frac{d^2\, U_j^{(\nu)}}{d\ \xi_s^2} + i\sigma_j^{(\nu)} \sin(\theta_1 + \theta_2) \frac{d\ U_j^{(\nu)}}{d\ \xi_s} - \sigma_j 2(\nu) \sin\theta_1 \cdot \sin\theta_2\, U_j^{(\nu)}$$

$$\nu = 1, 2 \tag{B-23}$$

APPENDIX C
EVALUATION OF THE ACOUSTIC ENERGY FLUX IN A DUCT

1. SINGLE SOURCE: MONOPOLES

The case where $\eta > \eta_s$ is of concern. Then:

$$p(\xi, \eta) = Ah^2 i \sum_{m=0}^{\infty} \in_m \cos(m\pi\xi) \sum_{j=1}^{\infty} Z^{(1)}_{m,j} \; e^{i\sigma_j^{(1)}(\eta_s - \eta)} \tag{C-1}$$

where $Z^{(1)}_{m,j}$ was defined in appendix B.

Also,

$$u = \frac{-1}{i\rho_o c_o (1 - \sigma_j^{(1)} M_o/s)\, s} \cdot \frac{\partial p}{\partial \xi} \tag{C-2}$$

$$w = \frac{-1}{i\rho_o c_o (1 - \sigma_j^{(1)} M_o/s)\, s} \cdot \frac{\partial p}{\partial \eta} \tag{C-3}$$

Hence:

$$u = \frac{Ah^2}{\rho_o c_o s} \sum_{m=0}^{\infty} (m\pi) \in_m \sin(m\pi\xi) \sum_{j=1}^{\infty} \frac{Z^{(1)}_{m,j}}{1 - \sigma_j^{(1)} M_o/s} \; e^{i\sigma_j^{(1)}(\eta_s - \eta)} \tag{C-4}$$

$$w = \frac{Ah^2 i}{\rho_o c_o s} \sum_{m=0}^{\infty} \in_m \cos(m\pi\xi) \sum_{j=1}^{\infty} \frac{\sigma_j^{(1)} Z^{(1)}_{m,j}}{1 - \sigma_j^{(1)} M_o/s} \; e^{i\sigma_j^{(1)}(\eta_s - \eta)} \tag{C-5}$$

By using equations 61 and 62 of the main body of this report, the following is obtained:

$$Q = \frac{(Ah^2)^2 h}{8\rho_o c_o} \sum_{m=0}^{\infty} \in_m^2 \sum_{j=1}^{\infty} \left[\frac{M_o \left(\frac{m\pi}{s}\right)^2 + 2\tau_m \mathrm{Real}\left(\frac{\sigma_j^{(1)}}{s}\right) - \tau_m \left|\frac{\sigma_j^{(1)}}{s}\right|^2 M_o}{\left|1 - \sigma_j^{(1)} \frac{M_o}{s}\right|^2} + \tau_m M_o \right] Z^{(1)}_{m,j} \, Z^{*(1)}_{m,j} \, e^{-2\mathrm{Im}(\sigma_j^{(1)})(\eta_s - \eta)} \tag{C-6}$$

where

$$\tau_m = \begin{cases} 2, & m=0 \\ 1, & m \neq 0 \end{cases}$$

2. SOURCE DISTRIBUTION. (MORE THAN ONE SOURCE)

Let us define

$$T_{m,j} = Z_{m,j}\, e^{i\sigma_j^{(1)}(\eta_s - \eta)} \tag{C-7}$$

$$V_{m,j} = \frac{T_{m,j}}{1 - \sigma_j^{(1)} M_o/s} \tag{C-8}$$

So. if there is more than one source, p, u and w can be expressed by:

$$p = \sum_{m=0}^{\infty} Ah^2 i \in_m \cos(m\pi\xi) \sum_{j=1}^{J} \sum_{n=1}^{N} \alpha_n\, T_{m,j}^{(n)} \tag{C-9}$$

$$u = \frac{Ah^2}{\rho_o c_o s} \sum_{m=0}^{\infty} \in_m \sin(m\pi\xi) \sum_{j=1}^{J} \sum_{n=1}^{N} \alpha_n\, V_{m,j}^{(n)} \tag{C-10}$$

$$w = \frac{Ah^2_i}{\rho_o c_o s} \sum_{m=0}^{\infty} \in_m \cos(m\pi\xi) \sum_{j=1}^{J} \sum_{n=1}^{N} \sigma_j^{(1)} \alpha_n\, V_{m,j}^{(n)} \tag{C-11}$$

In the expressions above J is the number of poles used and N the number of sources. The weighting parameter α_n can be a function of frequency and source locations; in general, it is a complex quantity.

The composite total acoustic energy flux is given by:

$$Q = \frac{(Ah^2)^2 h}{\rho_o c_o} \sum_{\ell=1}^{L} \sum_{m=0}^{\infty} \in_m^2 \left\{ M_o \left(\frac{m\pi}{s}\right)^2 \left| \sum_{j=1}^{J} \sum_{n=1}^{N} \alpha_n\, V_{m,j}^{(n)} \right|^2 \right.$$

$$+ M_o \tau_m \left| \sum_{j=1}^{J} \sum_{n=1}^{N} \sigma_j^{(1)} \alpha_n\, V_{m,j}^{(n)} \right|^2 + M_o \tau_m \left| \sum_{j=1}^{J} \sum_{n=1}^{N} \alpha_n\, T_{m,j}^{(n)} \right|^2$$

$$\left. + 2\tau_m \mathrm{Real} \left[\sum_{j=1}^{J} \sum_{n-1}^{N} \alpha_n\, T_{m,j}^{(n)} \times \sum_{j=1}^{J} \sum_{n=1}^{N} \sigma_j^{*(1)} \alpha_n^*\, V_{m,j}^{*(n)} \right] \right\} \tag{C-12}$$

where L is the number of cross-sections containing sources while N is the number of sources in each of these cross-sections. In the expression above the sources lying on a specific cross-section are assumed to be correlated and they give a composite energy flux. On the other hand, no correlation exists for the sources lying on dissimilar η_s; the, the total energy flux is the sum of the individual fluxes of each source.

All the expressions obtained in this appendix can easily be extended to dipoles and quadrupoles.

APPENDIX D
PRESSURE FIELD PRODUCED BY GENERALIZED SOURCE DISTRIBUTIONS

Assume that there is a source distribution function $H(\xi_s, \eta_s, \omega)$. It is of interest to obtain the pressure generated by this source distribution. Only the case $\eta > \eta_s$ will be analyzed here since the other case, when $\eta < \eta_s$ follows the same procedure.

From B-12, appendix B:

$$\Gamma^{(1)}(\xi, \eta; \xi_s, \eta_s) = Ah^2 i \sum_{m=0}^{\infty} \epsilon_m \cos(m\pi\xi) \sum_{j=1}^{J} Z_{m,j}\, e^{i\sigma_j^{(1)}(\eta_s - \eta)} \tag{D-1}$$

Performing the algebra, $Z_{m,j}$ can be written in the form:

$$Z_{m,j} = \Psi \left\{ \left[\frac{s\, Y_1' Y_2'}{\lambda^2} - \frac{(-1)^m i\, Y_2'}{\lambda \sin\lambda} - i \frac{Y_1' \cot\lambda}{\lambda} \right] \cos\lambda\xi_s \right.$$
$$\left. - \left[\frac{i\, Y_1'}{\lambda} + \frac{s\, Y_1 Y_2' \cot\lambda}{\lambda^2} + \frac{(-1)^{m+1} s\, Y_2' Y_1'}{\lambda^2 \sin\lambda} \right] \sin\lambda\xi_s \right\} \tag{D-2}$$

where

$$\Psi = \frac{-\lambda_s}{\left[\frac{-2s^2 Y_1' Y_2'}{\lambda^3} + \left(\frac{\cot\lambda}{\lambda^2} - \frac{1}{\lambda \sin^2\lambda} \right) is \left(Y_1' + Y_2' \right) \right] \left[\left(1 - M_o^2 \right) \sigma_j^{(1)} + sM_o \right] R_m\left(\sigma_j^{(1)}\right)}$$

The $\cos\lambda\xi_s$ and $\sin\lambda\xi_s$ must be expanded in function of $\cos(m\pi\xi)$. In this way, $Z_{m,j}$ can be transformed into:

$$Z_{m,j} = \Psi \sum_{n=0}^{\infty} \epsilon_n \left(c_{m,j} L_n^{(j)} - d_{m,j} M_n^{(j)} \right) \cos n\pi\xi \tag{D-3}$$

where

$$c_{m,j} = \frac{s\, Y_1' Y_2'}{\lambda^2} + \frac{(-1)^{m+1} i\, Y_2'}{\lambda \sin\lambda} - i \frac{Y_1' \cot\lambda}{\lambda}$$

$$d_{m,j} = \frac{i\, Y_1'}{\lambda} + \frac{s\, Y_1' Y_2' \cot\lambda}{\lambda^2} + \frac{(-1)^{m+1} s\, Y_1' Y_2'}{\lambda^2 \sin\lambda} \tag{D-4}$$

PRECEDING PAGE BLANK-NOT FILMED

$$L_n^{(j)} = \frac{(-1)^n \lambda \sin\lambda}{\lambda^2 - (n\pi)^2}$$

$$M_n^{(j)} = \frac{\lambda \left[1 - (-1)^n \cos\lambda\right]}{\lambda^2 - (n\pi)^2} \qquad \text{(D-4)}$$

So, the acoustic propagator becomes:

$$\Gamma^{(1)}(\xi, \eta; \xi_s, \eta_s) = Ah^2 i \sum_{m=0}^{\infty} \in_m \cos(m\pi\xi) \sum_{j=1}^{J} e^{i\sigma_j^{(1)}(\eta_s - \eta)} \sum_{n=0}^{\infty} \Psi \in_n q_{n,m}^{(j)} \cos(n\pi\xi_s) \qquad \text{(D-5)}$$

where

$$q_{n,m}^{(j)} = c_{m,j} L_n^{(j)} - d_{m,j} M_n^{(j)}$$

The composite pressure given by the distribution function $H(\xi_s, \eta_s, \omega)$ can be written in the form:

$$p_\omega = \int_{\eta_s=\eta_s^{(1)}}^{\eta_s=\eta_s^{(2)}} \int_0^1 H(\xi_s, \eta_s, \omega)\ \Gamma(\xi, \eta; \xi_s, \eta_s)\, d\xi_s\, d\eta_s \qquad \text{(D-6)}$$

It was assumed that the sources lie in the region $\eta_s^{(1)} < \eta_s^{(2)} < \eta$ and $0 < \xi_s < 1$

Replacing the expression D-5 of the acoustic propagator into D-6, the latter becomes:

$$p_\omega = Ah^2 i \sum_{m=0}^{\infty} \in_m \cos(m\pi\xi) \int_{\eta_s=\eta_s^{(1)}}^{\eta_s=\eta_s^{(2)}} \sum_{j=1}^{J} e^{i\sigma_j^{(1)}(\eta_s - \eta)} \sum_{n=0}^{\infty} \in_n \Psi\, q_{n,m}^{(j)}\, h_n\, d\eta_s \qquad \text{(D-7)}$$

where

$$h_n(\omega, \eta_s) = \int_0^1 H(\xi_s, \eta_s, \omega) \cos(n\pi\xi_s)\, d\xi_s \qquad \text{(D-8)}$$

If the distribution function $H(\xi_s, \eta_s, \omega)$ is a constant, the pressure p_ω is:

$$p_\omega = Ah^2 i \sum_{m=0}^{\infty} \epsilon_m \cos(m\pi\xi) \sum_{j=1}^{J} \left[\frac{e^{i\sigma_j^{(1)}\eta_s^{(2)}} - e^{i\sigma_j^{(1)}\eta_s^{(1)}}}{\sigma_j^{(1)}} \right] \Psi\, q_{n,m}^{(j)}\, e^{-i\sigma_j^{(1)}\eta} \qquad \text{(D-9)}$$

$$\eta > \eta_2$$

Formula D-9 gives the composite pressure for a uniform distribution of sources.